

Annual Research Briefs – 2006

Center for Turbulence Research

December 2006

DISTRIBUTION STATEMENT A
Approved for Public Release
Distribution Unlimited



Annual Research Briefs – 2006

Center for Turbulence Research

December 2006



CONTENTS

Preface	1
Uncertainty quantification in simple linear and non-linear problems T. CHANTRASMI, P. CONSTANTINE, N. ETEMADI, G. IACCARINO AND Q. WANG	3
Strain and stress analysis of uncertain engineering systems. D. GHOSH, C. FARHAT AND P. AVERY	17
Separated flow in a three-dimensional diffuser: preliminary validation. E. M. CHERRY, G. IACCARINO, C. J. ELKINS AND J. K. EATON	31
A dynamic global-coefficient subgrid-scale eddy-viscosity model for large-eddy simulation in complex geometries. D. YOU AND P. MOIN	41
Three-dimensional wall filtering formulation for large-eddy simula- tion. M. SHOEYBI AND J. A. TEMPLETON	55
Application of a local subgrid model based on coherent structures to complex geometries. H. KOBAYASHI AND X. WU	69
Computational study of aero-optical distortions by a turbulent wake. A. MANI, M. WANG AND P. MOIN	79
Simulation of the incompressible flow through a jet engine fuel nozzle rig. X. WU, G. IACCARINO, F. HAM AND P. MOIN	93
On the optimization of artificial neural networks for application to the approximation of chemical systems. M. IHME, A.L. MARSDEN AND H. PITSCHE	105
A dynamic front propagation model for large eddy-simulation of tur- bulent premixed combustion. E. KNUDSEN, M. HERRMANN AND H. PITSCHE	119
Consistent and accurate state evaluations in variable-density flow sim- ulations. L. SHUNN AND F. HAM	135
Scalar gradient and small-scale structure in turbulent premixed com- bustion. S. H. KIM AND H. PITSCHE	149
A balanced force refined level set grid method for two-phase flows on unstructured flow solver grids. M. HERRMANN	167
Toward two-phase simulation of the primary breakup of a round liq- uid jet by a coaxial flow of gas. D. KIM, O. DESJARDINS, M. HERRMANN AND P. MOIN	185
Stable and high-order accurate finite difference schemes on singular grids. M. SVÄRD AND E. VAN DER WEIDE	197

Stable and compact finite difference schemes. K. MATTSSON, M. SVÄRD AND M. SHOEYBI	211
Efficient wave propagation on complex domains. K. MATTSSON, F. HAM AND G. IACCARINO	223
A stable, efficient, and adaptive hybrid method for unsteady aerodynamics. J. NORDSTRÖM, M. SVÄRD, M. SHOEYBI, F. HAM, K. MATTSSON, G. IACCARINO, E. VAN DER WEIDE AND J. GONG	235
Accurate and stable finite volume operators for unstructured flow solvers. F. HAM, K. MATTSSON AND G. IACCARINO	243
Coupled high-fidelity URANS simulation for helicopter applications. S. HAHN, K. DURAISAMY, G. IACCARINO, S. NAGARAJAN, J. SITARAMAN, X. WU, J. J. ALONSO, J. D. BAEDER, S. K. LELE, P. MOIN AND F. SCHMITS	263
Integrated RANS/LES computations of turbulent flow through a turbobfan jet engine. G. MEDIC, G. KALITZIN, D. YOU, M. HERRMANN, F. HAM, E. VANDER WEIDE, H. PITSCHE AND J. ALONSO	275
An approach for coupling RANS and LES in integrated computations of jet engines. G. MEDIC, D. YOU AND G. KALITZIN	287
Low frequency sound sources in high-speed turbulent jets. D. J. BODONY AND S. K. LELE	299
Improved near-wall accuracy for solutions of the Helmholtz equation using the boundary element method. Y. KHALIGHI AND D. J. BODONY	313
Evaluation of active control of a laminar separation bubble based on linear stability theory. O. MARXEN, R. B. KOTAPATI AND D. YOU	323
Large-eddy simulation of flow separation over an airfoil with synthetic jet control. D. YOU AND P. MOIN	337
Asymptotic analysis of the constant pressure turbulent boundary layer. T. S. LUNDGREN	347
Convection in an internally cooled fluid layer heated from below. T. HARTLEP AND F. H. BUSSE	355
Magnetic waves in a two-component model of galactic dynamo: metastability and stochastic generation. S. FEDOTOV AND S. ABARZHI	363
Appendix: Center for Turbulence Research 2006 Roster	371

Preface

This volume contains the 2006 annual progress reports of the CTR postdoctoral fellows and visiting scholars. A separate report of the proceedings of the eleventh biennial CTR Summer Program was published earlier this year. CTR will be twenty years old by the time this volume reaches its worldwide readership. In the past twenty years CTR research has evolved significantly. Many of the fundamental research areas of the early days of CTR, such as direct numerical simulation of canonical shear flows and combustion phenomenon have now been adopted as mainstream research tools in the engineering science community. As is evident from the technical reports in this and recent volumes of the Annual Research Briefs, current CTR scholars are tackling much more complex and interdisciplinary problems. However, the most important feature that remains the same is the continued emphasis on the development of computational tools for conducting experiments of discovery and for flow prediction in engineering analysis. To conduct effective research in predictive science in complex systems, CTR has strived to maintain a critical mass in numerical analysis, computer science and physics based modeling, all under one roof. CTR has also always maintained close ties to laboratory experiments and experimentalists in several institutions. Over the last ten years, this infrastructure has benefited greatly from the sustained financial and intellectual support of the Department of Energy's Advanced Simulation and Computing Program.

The first group of papers in this volume are concerned with uncertainty quantification and validation of numerical simulations. This is an emerging area of importance in computational science, and we have assembled a strong group of students, postdoctoral fellows and faculty to meet the challenges in this area. The next group of papers are concerned with fundamental developments in LES, including new subgrid scale models, and its applications in multi-physics areas such as aero-optics and combustion. There was a substantial effort in numerical analysis of partial differential equations, which are reported in the next group of papers. Provable stable schemes were developed and implemented in complex flow applications. An important pacing item in computational science for complex systems is the problem of integration of multiple codes simulating multiple physical effects. The utility of the coupler code and environment for integrated simulations was demonstrated in two massive calculations: end to end hybrid simulation of a gas turbine engine and a hybrid simulation of flow around helicopter rotors and the associated acoustics. Computational acoustics, and flow control are receiving renewed attention at CTR in part because of the development of high fidelity large eddy simulation technology for computation of realistic flows of aeronautical interest. Several papers on these and more fundamental studies of turbulence constitute the final group of papers in this volume.

We are grateful to Dr. Donghyun You for his skillful editing of this report. Thanks are due to Ms. Lan Tang and Tricia Armstrong for their help in the production of the report. The CTR roster for 2006 is provided in the Appendix. This report is available on the CTRs site on the world wide web (<http://www.stanford.edu/group/ctr/>).

Parviz Moin
Nagi N. Mansour

Uncertainty quantification in simple linear and non-linear problems

By T. Chantrasmi[†], P. Constantine, N. Etemadi[‡],
G. Iaccarino AND Q. Wang

1. Motivation and objectives

Despite the considerable success of computer simulation technology in science and engineering, it remains difficult to provide objective confidence measures of the numerical predictions. This difficulty arises from the uncertainties associated with the inputs of any computation attempting to model a physical system. Uncertainties are typically classified as *aleatory* and *epistemic*. Aleatory uncertainty (also called variability) arises naturally from randomness in the system, and is studied using probabilistic approaches. The determination of material properties or operating conditions of a physical system typically leads to aleatory uncertainties; additional experimental characterization of such quantities might provide more conclusive evidence and characterization of their variability, but in practical situations it is not possible reduce this type of uncertainty completely. On the other hand, epistemic uncertainty is typically due to incomplete knowledge (or ignorance). This can arise from assumptions introduced in the derivation of the mathematical model or simplifications related to the correlation or dependence between physical processes. It is possible to *reduce* the epistemic uncertainty by using, for example, a combination of calibration, inference from experimental observations, and improvement of the physical models.

In this report, we consider two test problems to explore various numerical techniques to identify, propagate, and quantify uncertainties. The first problem involves transient heat conduction (a problem governed by a linear PDE) and corresponds to a test problem proposed by Sandia National Laboratory (Dowding *et al.* 2006). In this case, both aleatory and epistemic uncertainties are considered. The second problem is related to transient non-linear advection (Burgers' equation), and only variability in the initial conditions is considered.

2. Uncertainty analysis for a linear problem: heat conduction

The design and analysis of complex engineering systems is challenging not only because of the physical processes involved but also as a result of the limited amount of precise characterization of the overall conditions. This is in stark contrast to the assumptions in a computational model that typically requires well-defined (deterministic) inputs. For example, the material property of a certain component might be a function of the manufacturing process and exhibit a strong random variability. In a validation workshop organized by Sandia National Laboratory, three nominally simple problems were proposed to identify procedures and techniques to determine confidence bounds on the predictions. We describe the first of these problems in the following.

[†] Authors are listed in alphabetical order.

[‡] University of Illinois at Chicago

Data set	Samples	k [W/mC]	$\rho C_p \times 10^{-5}$ [J/m ³ C]
Low data	6	[0.0496:0.0796]	[3.38:4.52]
Medium data	20	[0.0455:0.0796]	[3.38:4.69]
High data	30	[0.0455:0.0811]	[3.37:4.69]

TABLE 1. Measured material properties.

2.1. Description of the problem: the Sandia thermal challenge

Consider a 1-D slab with a known heat flux applied at one end and an adiabatic boundary condition at the other. The thermal conductivity (k) and specific heat coefficient (ρC_p) of the slab material are known with a degree of variability; these are the only two sources of aleatory uncertainty. The objective is to determine the probability that after a certain amount of time (1000 seconds) the temperature in the slab is above a critical value ($T_c = 900^\circ C$); this is referred to as the regulatory assessment. The source of epistemic uncertainty is the choice of the numerical model to represent the physical system. Instead of considering the PDE describing the 1-D heat conduction in the slab, the challenge is built around an *exact* solution to the PDE, expressed as a series:

$$T(x, t) = T_{init} + \frac{qL}{k} \left[\frac{(k/\rho C_p)t}{L^2} + \frac{1}{3} - \frac{x}{L} + \frac{1}{2} \left(\frac{x}{L} \right)^2 \right] - \frac{2qL}{\pi^2 k} \sum_{n=1}^6 \frac{1}{n^2} e^{-n^2 \pi^2 \frac{(k/\rho C_p)t}{L^2}} \cos \left(n\pi \frac{x}{L} \right), \quad (2.1)$$

where $T(x, t)$ is the temperature within the slab, T_{init} the initial condition, L the slab length and q the heat flux applied at one end of the slab ($x = 0$). Note that both q and L are assumed known without uncertainty. Experimental data are provided for the material properties as a collection of samples. In addition, measured temperature distributions for five choices of q and L are given. These measurements are repeated few times and, therefore, several temperature dataset are available for the same nominal conditions (q and L), but without a reference to the material characterization experiments. In other words, the material properties of the slab used for the temperature measurements are unknown. Moreover, the conditions used in these experiments are different from the conditions specified for the regulatory assessment, and therefore, a direct validation of the predictions is not possible.

2.2. Characterization of the aleatory uncertainty

The first step of any uncertainty quantification (UQ) study is to characterize the sources of variability. Thirty measured values are provided for k and ρC_p . The samples are organized in three groups corresponding to *low*, *medium*, or *high* volume of data with the first set including only 6 samples, the other two including 20 and 30 samples, respectively. The objective is to identify the effect of a better characterization of the input parameters on the confidence bounds for the predictions. Note that the last set includes the first two sets plus 10 new samples.

Initially we analyzed the three data sets to verify their *consistency*. Using the three datasets sample, and assuming that k and ρC_p are random variables independent of

Data set	Samples	k [W/mC]	$\rho C_p \times 10^{-5}$ [J/m^3C]
<i>Low data</i>	6	[0.0127:0.1073]	[2.047:6.063]
<i>Medium data</i>	20	[0.0416:0.0833]	[3.153:4.892]
<i>High data</i>	30	[0.0423:0.0822]	[3.189:4.689]

TABLE 2. Material characterization for the thermal problem, assuming a Gaussian distribution of the variables within the intervals reported in Table 1

everything else, we can compute the 99.5% confidence interval from a student-t distribution. The obtained intervals are reported in Table 2. The addition of more samples allows to reduce the variation interval for both quantities: the three sets of samples are consistent.

2.3. Predicting confidence intervals using direct sampling

The next step is to determine the confidence intervals of the predicted temperature at $x = 0$ and $t = 1000\text{sec}$ from the formula (2.1). Noting that T decreases monotonically with respect to ρC_p , we can calculate the confidence interval by evaluating Eq. (2.1) using the two ends of the 99.5% confidence interval of ρC_p , and sampling inside the 99.5% confidence interval of k . This produces a 99% confidence interval of temperature T . The predictions obtained in this way are compared to the experimental measurements for all the cases available. In Fig. 1 the results obtained for one of the configurations (corresponding to $L = 0.019m$ and $q = 3000W/m^2$) are reported. The experimental data fall within the predicted bounds, and moreover, as we include more information, the confidence interval tightens.

Applying the same procedure to the regulatory assessment conditions, we obtain the predictions reported in Fig. 1. Repeating the predictions for the three sets of material properties previously identified yields the following predicted values and confidence bounds: 1306 ± 682 , 906.0 ± 220 , and 900.5 ± 217.5 respectively. Note that although the confidence interval gets tighter as the material characterization data increase, the 99% confidence interval is not entirely below $900C$.

To identify the effect of the assumed stochastic distribution of the material properties, we also considered the case of k and ρC_p uniformly distributed within the minimum and maximum in the experimental samples (see Table 1. We evaluated Eq. (2.1) using the same statistical sampling discussed earlier and obtained the results reported in Fig. 2. The bounds are somewhat reduced in this case (due to the elimination of the tails in the assumed distribution of the material properties), but still the system has a large probability of achieving temperatures above the critical temperature indicated in the Sandia challenge.

Therefore, we cannot safely conclude that the system satisfies the regulatory requirement. More material properties' measurements might be required to improve the characterization of the distributions of k or ρC_p , or a different model must be developed to identify the epistemic uncertainty. In the following section, we consider the heat conduction PDE and apply a probabilistic approach to propagate the distributions of the material properties.

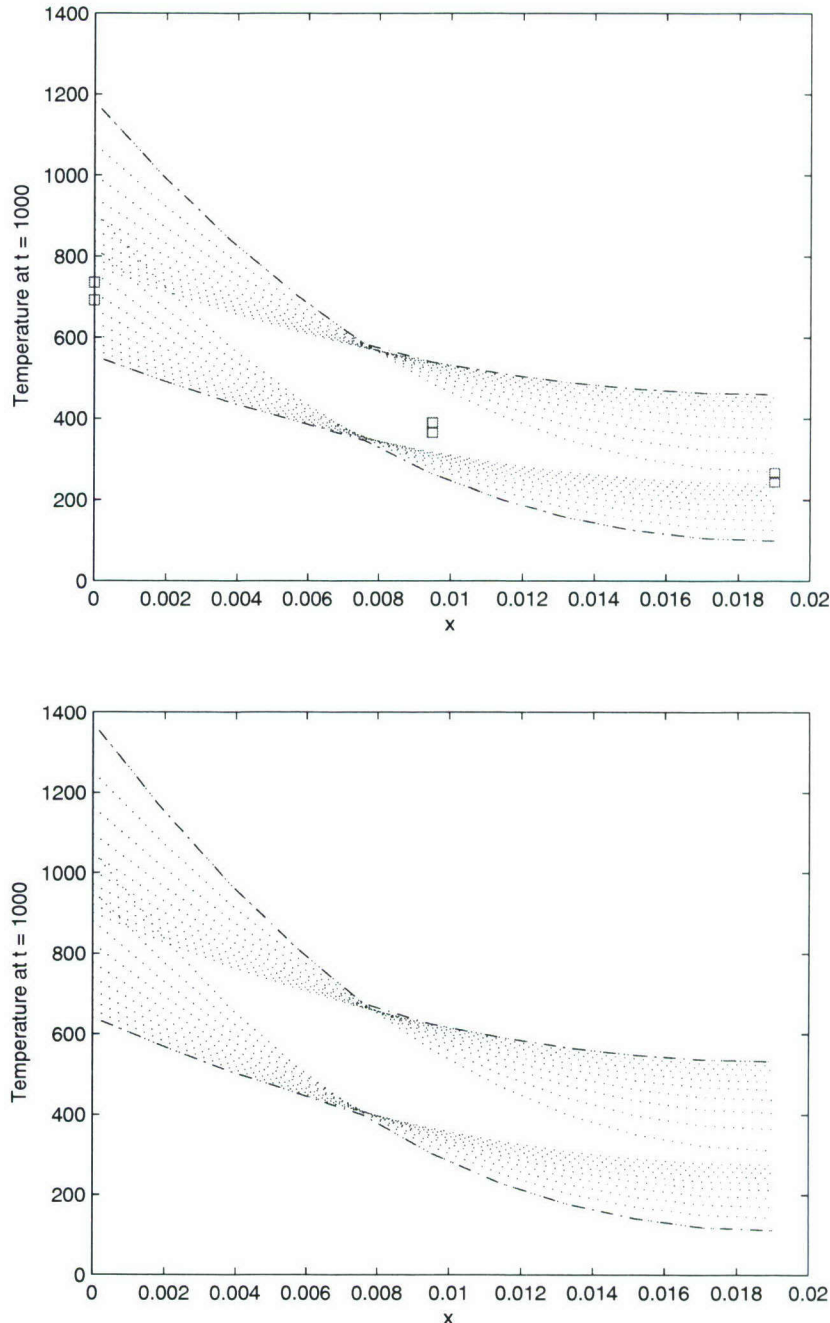


FIGURE 1. 99% confidence interval of T assuming Gaussian distribution for k and ρC_p . The conditions correspond to $L = 0.019m$ and $q = 3000W/m^2$ (top) and to the regulatory assessment $L = 0.019m$ and $q = 3500W/m^2$ (bottom). \square : experimental data -: Eq. 2.1 - - - - : computed confidence bounds.

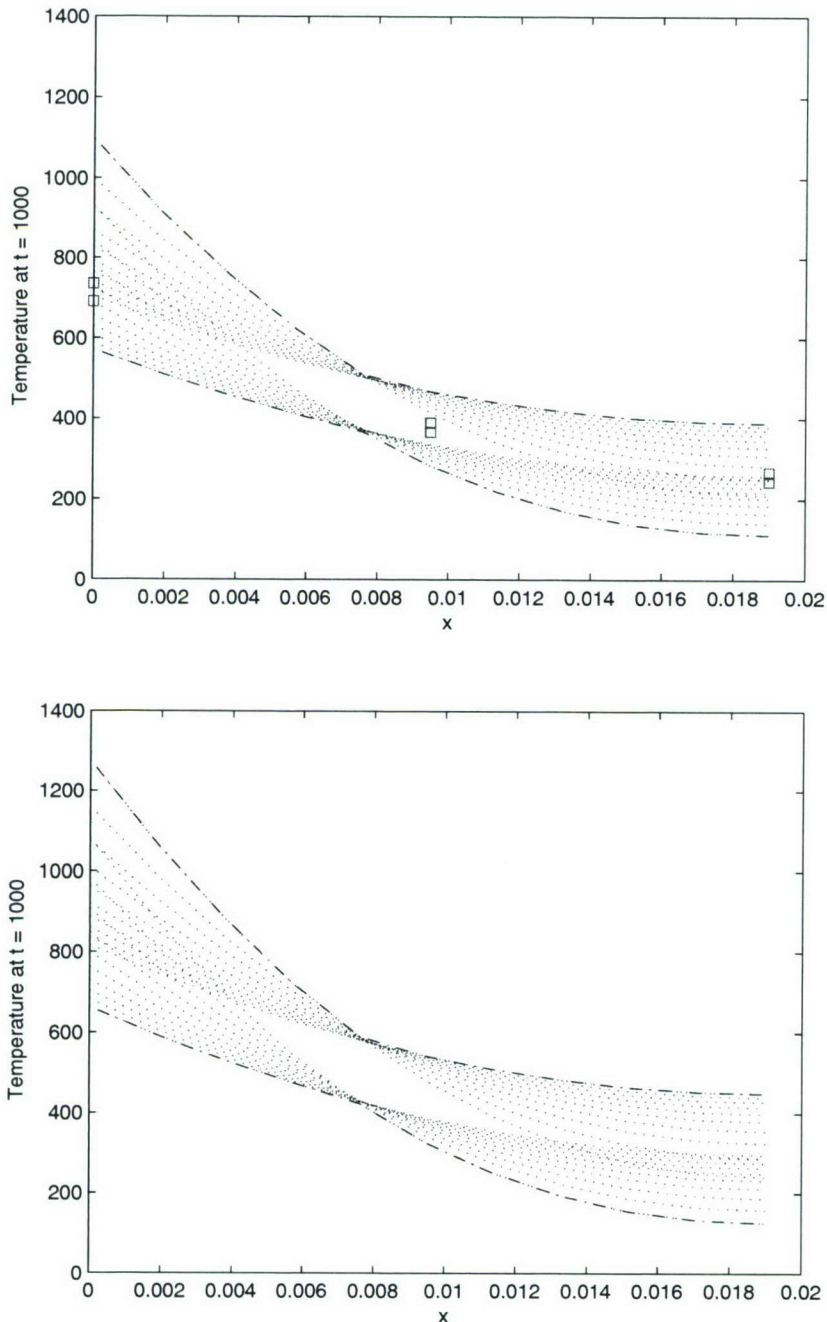


FIGURE 2. 99% confidence interval of T assuming uniform distribution for k and ρp_c . The conditions correspond to $L = 0.019m$ and $q = 3000W/m^2$ (top) and to the regulatory assessment $L = 0.019m$ and $q = 3500W/m^2$ (bottom). \square : experimental data -: Eq. 2.1 - - - - -: computed confidence bounds.

2.4. Predicting probability bounds using a polynomial chaos approach

In this section, we illustrate the application of the polynomial chaos expansion (PCE) to solve the present 1-D heat conduction problem. The PCE approach has its foundation in the work of Wiener (1938), who represented a Gaussian process as an infinite series of Hermite polynomials that take a vector of random variables as arguments. Ghanem and Spanos (1991) used this representation to develop the stochastic finite element method. Xiu and Karniadakis (2002) extended the theoretical framework to non-Gaussian process by employing different polynomial basis functions. This generalized polynomial chaos approach was used to address the problem of heat transfer with random material properties by Wan *et al.* 2004.

The PCE is a representation of a random variable, more generally a stochastic process, with an infinite series of orthogonal polynomials that take a vector of independent and identically distributed random variables as arguments. Denote the set of orthogonal polynomials by $\{\Phi_i(\xi(\omega))\}$, $i \geq 0$, where $\xi(\omega)$ is a vector of i.i.d. random variables. Then $\{\Phi_i(\xi(\omega))\}$ have the following properties:

$$\langle \Phi_0 \rangle = 1, \quad \langle \Phi_i \rangle = 0 \text{ for } i > 0, \quad \langle \Phi_j \Phi_k \rangle = \delta_{jk} \text{ for } j, k \geq 0,$$

where $\langle \cdot \rangle$ is the expectation and δ_{jk} is the Kronecker delta. By the Cameron-Martin theorem (1947), the PCE converges in the L_2 sense. So, for example, if we represent $T = \sum_{i=0}^{\infty} T_i(x, t) \Phi_i(\xi(\omega))$, where $\{T_i(x, t)\}$ are the PCE coefficients, then

$$\left\langle \left(T - \sum_{i=0}^N T_i \Phi_i(\xi(\omega)) \right)^2 \right\rangle \rightarrow 0$$

as $N \rightarrow \infty$. The L_2 convergence of this expansion justifies an approximation of the random quantities by a truncated finite series. For the example above, we approximate

$$T \approx \sum_{i=0}^P T_i(x, t) \Phi_i(\xi(\omega)),$$

where P is the order of the truncated PCE. The value of P is determined by the number d of random dimensions - the length of $\xi(\omega)$ - and the highest degree n of polynomial employed. In particular, we have the formula

$$(P + 1) = \frac{(n + d)!}{n! d!}.$$

In the heat conduction problem considered above, we assume that $\rho C_p(\omega_1)$ is a uniformly distributed random variable over the interval $[(\rho C_p)_a, (\rho C_p)_b]$ and let $k(\omega_2)$ be a uniformly distributed random variable over $[k_a, k_b]$ such that ρC_p and k are independent; we use the arguments ω_1 and ω_2 to emphasize that ρC_p and k are random quantities. Then we consider the following differential equation:

$$\rho C_p \frac{\partial T}{\partial t} = k \frac{\partial^2 T}{\partial x^2}, \quad (2.2)$$

where

$$k \frac{\partial T}{\partial x} \bigg|_{x=0} = q, \quad k \frac{\partial T}{\partial x} \bigg|_{x=L} = 0, \quad T(x, 0) = T_{init}.$$

over the domain $x \in [0, L]$, $t \in [0, t_f]$, where T is in general a function of time, space, and the two random variables ω_1 and ω_2 .

By choosing a uniform distribution to model k and ρC_p , we ensure that their support is bounded. If we had chosen some other distribution, say Gaussian, that has support in the negative real line, then we risk attempting to solve the backward heat equation, which is unstable.

Given (2.2), the objective is to compute the mean and variance of T , both of which are functions of x and t using the PCE approach. Since ρC_p and k are both uniform random variables, we can achieve exponential convergence of the PCE coefficients of T by choosing $\{\Phi_i(\xi_1(\omega_1), \xi_2(\omega_2))\}$ to be the 2-D Legendre polynomials with each $\xi_i, i = 1, 2$ distributed uniformly over the interval $[-1, 1]$, as described in Xiu and Karniadakis (2002). For reference, the first few 2-D Legendre polynomials are given by

$$\begin{aligned}\Phi_0 &= 1 \\ \Phi_1 &= \xi_1(\omega_1) \\ \Phi_2 &= \xi_2(\omega_2) \\ \Phi_3 &= \frac{1}{2}(3\xi_1(\omega_1)^2 - 1) \\ \Phi_4 &= \xi_1(\omega_1)\xi_2(\omega_2) \\ \Phi_5 &= \frac{1}{2}(3\xi_2(\omega_2)^2 - 1).\end{aligned}\tag{2.3}$$

Equipped with these basis polynomials, we now represent

$$\begin{aligned}\rho C_p &\approx \sum_{i=0}^P (\rho C_p)_i \Phi_i(\xi_1(\omega_1), \xi_2(\omega_2)), \\ k &\approx \sum_{i=0}^P k_i \Phi_i(\xi_1(\omega_1), \xi_2(\omega_2)), \\ T &\approx \sum_{i=0}^P T_i \Phi_i(\xi_1(\omega_1), \xi_2(\omega_2)).\end{aligned}$$

In general, since the distributions of ρC_p and k are known, we can compute their PCE coefficients by taking advantage of the orthogonality of $\{\Phi_i\}$. In particular, we have the following formulas:

$$(\rho C_p)_i = \frac{\langle \rho \Phi_i \rangle}{\langle \Phi_i^2 \rangle}, \quad k_i = \frac{\langle k \Phi_i \rangle}{\langle \Phi_i^2 \rangle}.$$

In this simple case, however, we note that the PCEs of ρC_p and k are simply scalings of their respective ranges, i.e.,

$$\rho = \frac{\rho_b + \rho_a}{2} + \frac{\rho_b - \rho_a}{2} \xi_1(\omega_1), \quad k = \frac{k_b + k_a}{2} + \frac{k_b - k_a}{2} \xi_2(\omega_2).$$

Then the PCE coefficients are

$$\rho_0 = \frac{\rho_b + \rho_a}{2}, \quad \rho_1 = \frac{\rho_b - \rho_a}{2}, \quad \rho_2 = 0, \quad \rho_i = 0, \quad i > 2$$

and

$$k_0 = \frac{k_b + k_a}{2}, \quad k_1 = 0, \quad k_2 = \frac{k_b - k_a}{2}, \quad k_i = 0, \quad i > 2.$$

When we substitute the PCE representations into the differential equation, the problem

becomes

$$[(\rho C_p)_0 + (\rho C_p)_1 \xi_1(\omega_1)] \sum_{i=0}^P \frac{\partial T_i(x, t)}{\partial t} \Phi_i(\xi_1(\omega_1), \xi_2(\omega_2)) = \\ (k_0 + k_2 \xi_2(\omega_2)) \sum_{i=0}^P \frac{\partial^2 T_i(x, t)}{\partial x^2} \Phi_i(\xi_1(\omega_1), \xi_2(\omega_2)) \quad (2.4)$$

with boundary and initial conditions prescribed as:

$$(k_0 + k_2 \xi_2(\omega_2)) \sum_{i=0}^P \frac{\partial T_i}{\partial x} \Big|_{x=0} \Phi_i(\xi_1(\omega_1), \xi_2(\omega_2)) = q \quad (2.5)$$

$$(k_0 + k_2 \xi_2(\omega_2)) \sum_{i=0}^P \frac{\partial T_i}{\partial x} \Big|_{x=L} \Phi_i(\xi_1(\omega_1), \xi_2(\omega_2)) = 0 \quad (2.6)$$

$$\sum_{i=0}^P T_i(x, 0) \Phi_i(\xi_1(\omega_1), \xi_2(\omega_2)) = T_{init}. \quad (2.7)$$

To solve this set of equations for the coefficients $T_i(x, t)$, we multiply each equation by Φ_k for $k = 0, \dots, P$ and take the expectation of both sides. Then, by the orthogonality of $\{\Phi_i\}$, we're left with a system of linear differential equations for the PCE coefficients. By using second-order central differencing in space and the Crank-Nicholson scheme in time, we obtain a linear system to be solved at each time step. Once we have computed these coefficients, we can compute the expectation and variance of T at each grid point j and time instant n with the following formulas:

$$\bar{T}_j^n \equiv \langle T \rangle = (T_0)_j^n, \quad \hat{T}(j) \equiv \langle (T - \langle T \rangle)^2 \rangle = \sum_{i=1}^P (T_i)_j^n \langle \Phi_i^2 \rangle.$$

To address the Sandia thermal challenge, we choose the material property intervals obtained from the *high* volume dataset, reported in Table 1. We then represent T with a truncated PCE in two random dimensions with second-degree orthogonal polynomials, so $P = (2+2)!/2!2! = 6$. We discretize the spatial domain with $N = 33$ grid points; the size of the linear system to be solved at each time step is then $(N \times P)^2 = 198^2$. There is no time-step restriction using the Crank-Nicolson scheme, so we choose $\Delta t = 10\Delta x$.

Although the present approach has been compared to all the experimental data provided, we only illustrate the results obtained for the configuration reported earlier, corresponding to $L = 0.019m$ and $q = 3000W/m^2$. As previously mentioned, there are two measured values of T at $x = 0$, $L/2$, and L , and t a multiple of 50 from 0 up to 1,000 seconds. We compare the results of the simulation at time 1000 seconds with the experimental data in Fig. 3.

The results show that the predicted results envelop the measured data, providing confidence that the material property variability is well characterized in these simulations. The application of the same numerical approach to the regulatory assessment is also illustrated in Fig. 3.

Once we have the PCE coefficients at $x = 0$ and $t = 1000$, we can generate samples from a uniform distribution over $[-1, 1]$ and evaluate the PCE representation of $T(0, 1000)$. The percentage of those realizations that are above T_c is approximately:

$$P(T(0, 1000) > T_c) \approx 0.2145$$

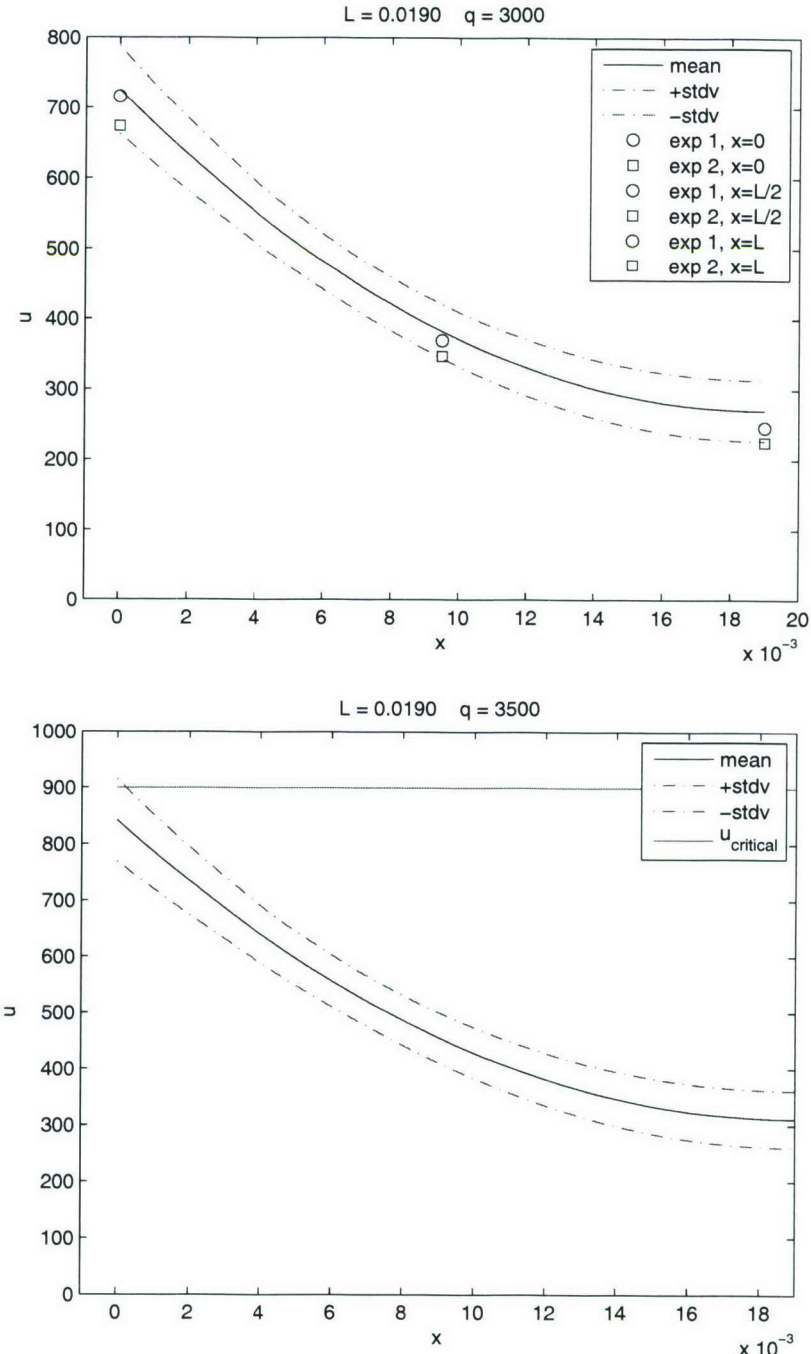


FIGURE 3. Polynomial chaos solution to the 1-D heat conduction problem assuming uniform distribution for k and ρC_p . The conditions correspond to the $L = 0.019m$ and $q = 3000W/m^2$ (top) and to the regulatory assessment $L = 0.019m$ and $q = 3500W/m^2$ (bottom). \square : experimental data - - - - : Eq. 2.1 - - - - : computed confidence bounds.

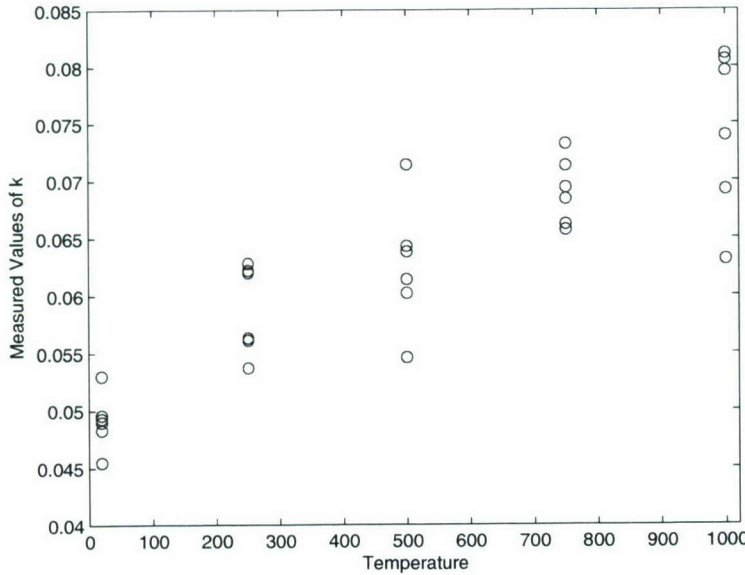


FIGURE 4. Measured thermal conductivity as a function of the experimental temperature

If we follow this approach, we conclude that the device does not meet the regulatory requirement described by the Sandia challenge problem. How confident are we in this assessment? There are, of course, the numerical errors resulting from the spatial and temporal discretization. The PCE representations of ρC_p and k are exact, but error associated with the truncation of the PCE of T is still an area of open research. We compared the PCE solution with a simple Monte Carlo simulation that generated realizations of ρC_p and k , and solved the resulting deterministic problem. We found that the PCE solution was sufficiently close to the Monte Carlo simulation to conclude that the two had converged. Currently this is the only available method for evaluating the accuracy of the truncated PCE.

None of these relatively small errors undermines our confidence in the assessment. The more troubling assumptions are the ones we used to model the uncertain parameters. Supposing that ρC_p and k are uniformly distributed, how do we know that they are actually distributed over the minimum and maximum of their measured values? Their respective ranges could be much larger, and this could affect the final computed probability. For example, running the simulation with a 20% increase in upper bound for k results in $P(T(0, 1000) > T_c) \approx 0.1480$, a significant decrease from the result above.

In addition, the assumption that k is constant and independent of everything else might be incorrect. A more careful analysis of the conductivity data provided in the Sandia challenge problem is presented in Fig. 4, where the samples are organized as a function of the experimental temperature. With linear regression, we find that there is *likely* a linear relationship between temperature and conductivity, i.e., $k(u) = \alpha + \beta T$. This is not a surprising physical behavior for many materials. Future work on this problem might involve modeling k as a linear function of T with random slope and/or intercept. This improved assumption should decrease $P(T(0, 1000) > T_{\text{critical}})$, but the resulting non-linear equation is much more complicated.

3. Uncertainty propagation for a non linear problem: Burgers' equation

Uncertainty analysis in non-linear problems introduces additional complications. In this section, we apply the polynomial chaos approach introduced earlier to a simple non-linear Burgers' equation. We also introduce a hybrid approach based on the combination of deterministic modeling and stochastic sampling.

3.1. Description of the problem

We study the classical problem of non-linear advection in one dimension. The problem is governed by the Burgers equation:

$$u_t + \left(\frac{u^2}{2} \right)_x = 0 \quad 0 \leq x \leq 1. \quad (3.1)$$

We will assume that the uncertainty is only related to the initial conditions, and in particular, consists of random perturbation of a sinusoidal wave, i.e.,

$$u(x, 0) = \sin(2\pi x) + \sigma\xi, \quad (3.2)$$

where ξ is a standard Gaussian random variable and σ is the magnitude of perturbation. The simplicity of this problem allows us to find an exact solution for the evolution of the mean and the variance of the solution. In the next section, the polynomial chaos framework is discussed, followed by a hybrid method.

3.2. Polynomial chaos approach

As previously illustrated, within the polynomial chaos framework we represent the solution of the Burgers' equation as

$$\mathbf{u}(x, t) = \sum_{i=0}^{\infty} u_i(x, t) \Phi_i(\xi), \quad (3.3)$$

where Φ_i is the i th-order Hermite polynomial (as mentioned earlier, this choice is motivated by the distribution of the random variable)

$$\Phi_0(\xi) = 1 \quad (3.4)$$

$$\Phi_1(\xi) = 2\xi \quad (3.5)$$

$$\Phi_{n+1}(\xi) = 2\xi\Phi_n(\xi) - 2n\Phi_{n-1}(\xi). \quad (3.6)$$

As before, we truncate the infinite series (3.3) to order P . Inserting the truncated polynomial chaos expansion into the Burgers equation results in

$$\sum_{i=0}^P \frac{\partial u_i}{\partial t} \Phi_i(\xi) + \sum_{i=0}^P \sum_{j=0}^P \frac{\partial(u_i u_j)}{\partial x} \Phi_i(\xi) \Phi_j(\xi) = 0. \quad (3.7)$$

Applying Galerkin projection in the probability space yields:

$$\frac{\partial u_k}{\partial t} + \sum_{i=0}^P \sum_{j=0}^P C_{ijk} \frac{\partial(u_i u_j)}{\partial x} = 0 \quad 0 \leq k \leq P, \quad (3.8)$$

where $C_{ijk} = \langle \Phi_i \Phi_j \Phi_k \rangle$.

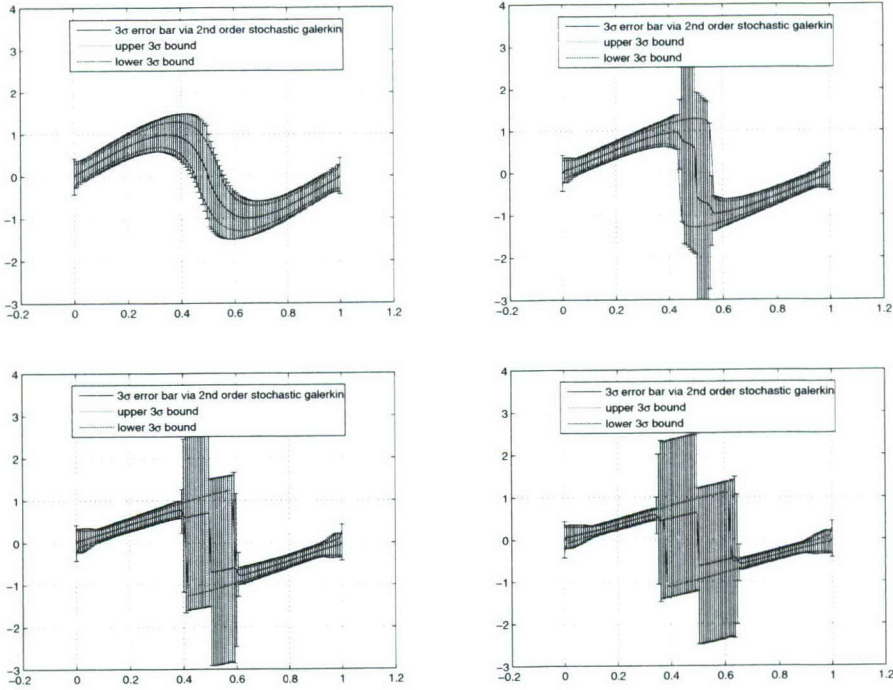


FIGURE 5. Evolution of the computed error bars at various times: $t=0.1, 0.2, 0.3, 0.4$. Note that the exact solution is also reported in the plots.

Equation (3.8) is again a system of partial differential equations that we can solve numerically. In order to ensure stability of the numerical scheme, the time step must be much smaller than the restriction imposed by the CFL number in the deterministic analogue. The details are not discussed in this report. After we obtain a numerical solution for $u_i(x, t)$, $i = 0, \dots, P$, we can reconstruct the stochastic solution of (3.1) and its mean and variance. The standard deviation of the solution is given by the formula

$$u_\sigma(x, t) = \left(\sum_{i=1}^P u_i^2(x, t) \langle \Phi_i^2 \rangle \right)^{1/2}. \quad (3.9)$$

A 99.7% confidence interval can therefore be constructed as

$$u(x, t) = u_0(x, t) \pm 3u_\sigma(x, t). \quad (3.10)$$

Figure 5 illustrates the confidence interval we constructed using second-order polynomial chaos ($P = 2$) and compared to the exact bounds. It is also interesting to note the PCE coefficients corresponding to the computed solution during the time evolution (Fig. 6).

The comparison with the available exact solution (Fig. 5) shows that the second order polynomial chaos method captures the uncertainty in the location of the shock wave very well.

3.3. A deterministic/stochastic hybrid approach

In this section, we report our initial efforts in developing a different approach for uncertainty propagation. As previously mentioned, the uncertainty is introduced into the

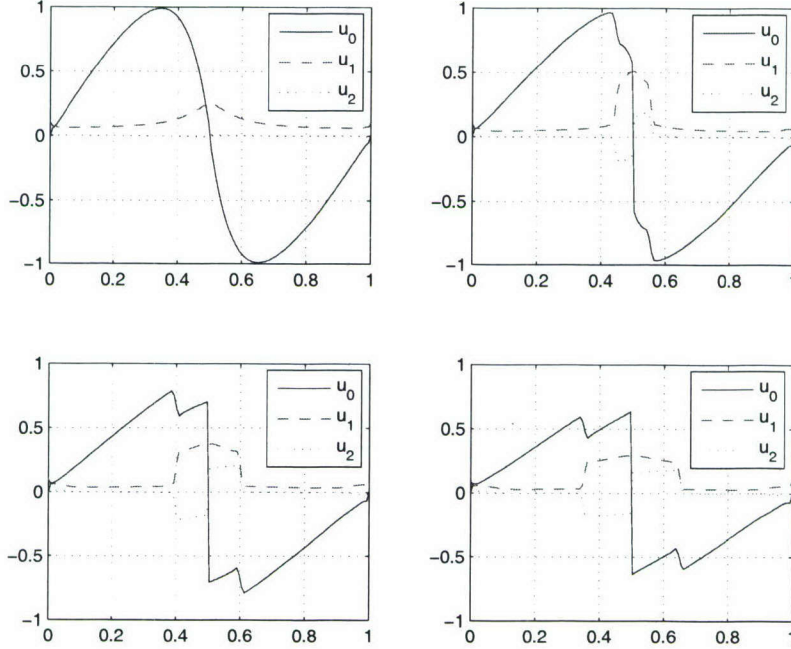


FIGURE 6. Coefficients of polynomial expansion at various instants during the time evolution.
 $t = 0.1, 0.2, 0.3, 0.4$

initial condition $u_0 = u_0(x, t = 0, \omega)$, where $\omega \in \Omega$ is the sample space. Thus u is a function of x , t , and ω , and the objective is to compute the statistics of u . In particular, we desire the mean \bar{u} and the variance \hat{u} , defined as

$$\bar{u} \equiv \langle u \rangle = \int_{\omega \in \Omega} u dP(\omega), \quad \hat{u} \equiv \text{var}(u) = \frac{1}{2} \int_{\omega \in \Omega} (u - \bar{u})^2 dP(\omega). \quad (3.11)$$

Note that other definitions of the mean are possible. If we decompose the unknown u into the mean part and fluctuation part: $u = \bar{u} + u'$, plug in into (3.1), and integrate over the sample space, we obtain an evolution equation for the mean. Higher-order equations can also be generated by multiplying (3.1) with $(u')^n$ and integrating. Below are the equations for the mean and the variance.

$$\frac{\partial \bar{u}}{\partial t} + \bar{u} \frac{\partial \bar{u}}{\partial x} = - \int_{\omega \in \Omega} u' \frac{\partial u'}{\partial x} dP(\omega), \quad (3.12)$$

$$\frac{\partial \hat{u}}{\partial t} + \bar{u} \frac{\partial \hat{u}}{\partial x} + 2\hat{u} \frac{\partial \bar{u}}{\partial x} = - \int_{\omega \in \Omega} u' u' \frac{\partial u'}{\partial x} dP(\omega). \quad (3.13)$$

Note that these equations describe the evolution of the statistics of the solutions. The terms on the right-hand side are not known (*unclosed*) and must be modeled or approximated. This is similar in many ways to the process of deriving the Reynolds-Averaged Navier-Stokes equations.

In a Monte Carlo approach, one would solve the PDE (3.1) many times with different initial conditions and average over the realizations. In the present hybrid approach, we use Monte Carlo (or other approaches) to approximate the unclosed terms in (3.12) and (3.13), then solve these equations in a deterministic sense.

We proved that, if we simply use Monte Carlo sampling to approximate the unclosed terms, then solve (3.12) and (3.13), the result is identical to using the samples directly to obtain the mean. This conclusion applies even when the process is not converged, namely if we use only a limited number of sample, provided we use the same samples in both methods. However, the former method allows us to incorporate a *model* for the unclosed terms. For instance, we could attempt to model the unclosed term in (3.12) as a diffusion process. One possible model could be written as $\beta t \sigma^2 \partial^2 \bar{u} / \partial x^2$, where σ is the standard deviation in the initial condition and β is a constant that can be approximated by sampling. Current research is focused on an efficient way to obtain β . We have also investigated the use of bootstrap or a reduced order model (ROM). Only the latter is briefly described here. The idea is to perform Monte Carlo sampling on coarser grids (the simplest ROM in the present problem) and to construct the approximate unclosed terms. To improve the sampling quality we also considered a few realizations obtained directly on the fine grid. For example, for the Burgers equation problem described earlier, about 1000 realizations are needed to obtain converged statistics using the Monte Carlo approach. In the two-grid method, we can achieve the same accuracy with 1000 realizations on the coarse grid (half the grid points) and 100 realizations on fine grid; the overall reduction of the computational cost is approximately 40%. The benefit will be obviously more significant in higher dimensions.

Acknowledgments

This work is supported by the Department of Energy within the Advanced Simulation and Computing Program.

REFERENCES

CAMERON R. AND MARTIN W. 1947. The orthogonal development of nonlinear functionals in series of Fourier-Hermite functionals *Ann. of Math.* **28**, 285-392.

DOWDING, K., PILCH, M., AND HILLS, R. G. 2006. Model Validation Challenge Problem: Thermal Problem, Sandia Validation Workshop, *Sandia National Laboratory*, May 2005.

GHANEM R. AND SPANOS P. 1991. *Stochastic Finite Elements: A Spectral Approach* Springer-Verlag, New York.

WAN X., XIU, D. AND KARNIADAKIS, G. E. 2004. Modeling uncertainty in three-dimensional heat transfer problems in Advanced Computational Methods in Heat Transfer VIII, Proceedings of the Eighth International Conference on Advanced Computational Methods in Heat Transfer, Lisbon, Portugal, 2004, B. Sundén, C. Brebbia, and A. Mendes, eds., WIT Press, Southampton, UK.

WIENER, N. 1938. The homogeneous chaos *Amer. J. Math.* **60** 897-936.

XIU D. AND KARNIADAKIS, G. E. 2002. The WienerAskey polynomial chaos for stochastic differential equations *SIAM J. Sci. Comput.* **24**, 619-644.

Strain and stress analysis of uncertain engineering systems

By D. Ghosh, C. Farhat AND P. Avery

1. Motivation and objectives

Structural properties of any material show variability among different samples of the material resulting from natural variability in microstructure and from the manufacturing process. The manufacturing process also causes variability in the geometric properties of the components made from these materials. These variabilities induce uncertainty in the predicted response of a physical system. Additional factors such as uncertainty in external loading, and in some cases insufficient details about the underlying physics such as behavior of the joints contribute to magnify the uncertainty in this predicted response. These uncertainties can be modeled and their effects can be analyzed using a probability theory based framework.

Among the response quantities, the strains and stresses are often of the greatest interest in an engineering problem. However, the current literature on probabilistic engineering mechanics focuses on the issue of finding the displacement field; the issue of finding the strains and stresses is not sufficiently addressed. This paper addresses the computational issues related to strain and stress computation. Here the problem of uncertainty analysis is posed in a stochastic finite elements framework.

Among the probabilistic methods of uncertainty analysis, Stochastic Finite Element Methods (SFEM) (Ghanem & Spanos 2003) have gained considerable attention recently. The major advantages of these methods are their ability to handle stochastic processes, encapsulated representation of random quantities, and lower computational cost.

Let (Ω, \mathcal{F}, P) denote a probability space, where Ω is the set of the outcomes θ of physical experiments, \mathcal{F} is a σ -algebra in Ω , and P is a probability measure on \mathcal{F} . Let \mathcal{X} denote the physical domain of the system. Consider

$$\mathcal{L}(u) = f, \quad (1.1)$$

where $\mathcal{L} = \mathcal{L}(\theta)$ and $f = f(\theta)$. Randomness in the parameters of the underlying physical system induces randomness in \mathcal{L} and f . Some of these random parameters can be modeled as random variables $\{\eta_i(\theta)\}_{i=1}^{i=r}$ and some as random processes $\kappa(\mathbf{x}, \theta)$, where $\mathbf{x} \in \mathcal{X}$. For example, a spring stiffness can be modeled as a random variable, whereas the thickness of a plate can be modeled as a random field. The processes $\kappa(\mathbf{x}, \theta)$ can be discretized using a random basis set $\{\eta_i(\theta)\}_{i=r+1}^{i=s}$ in $L_2(\Omega, \mathcal{F}, P)$, where the coefficients of the random variables $\{\eta_i(\theta)\}_{i=r+1}^{i=s}$ turn out to be functions of the parameter \mathbf{x} . For example, if the covariance function $C(\mathbf{x}_1, \mathbf{x}_2)$ of the process $\kappa(\mathbf{x}, \theta)$ is known then the process can be discretized using the Karhunen-Loëve expansion (Ghanem & Spanos 2003) as

$$\kappa(\mathbf{x}, \theta) = \sum_{i=0}^{\infty} \sqrt{\lambda_i} \phi^{(i)}(\mathbf{x}) \eta_i(\theta) , \quad (1.2)$$

where λ_i are the eigenvalues of the covariance kernel $C(\mathbf{x}_1, \mathbf{x}_2)$, arranged in descending

order, $\phi^{(i)}$ are the corresponding eigenvectors, and $\eta_i(\theta)$ are zero-mean and orthonormal random variables. For computational convenience this series is truncated after the first few terms. The set of all random variables $\{\eta_i(\theta)\}_{i=1}^{i=s}$ completely characterizes the uncertainty in the underlying system. These random variables are characterized by their joint probability measure, if this measure is not Gaussian, these variables can be transformed into a nonlinear functional of an independent Gaussian vector $\{\xi_i(\theta)\}_{i=1}^{i=m}$ (Ghanem & Doostan 2006, Das *et al.* 2006); the integer m is often referred as stochastic dimension of the problem (Ghanem & Spanos 2003, Debusschere *et al.* 05). This new set of independent standard random variables will be denoted by an m -dimensional vector ξ . Thus, $\mathcal{L}(\theta)$ and $f(\theta)$ can now also be denoted by $\mathcal{L}(\xi)$ and $f(\xi)$. The solution u is also a function of ξ , yielding the notation $u(\xi)$, or more specifically $u(\mathbf{x}, \xi)$. The formulation presented in this paper is valid for ξ being non-Gaussian as well, and thus it is equally applicable to a variety of expansions (Xiu & Karniadakis 2003, LeMaitre *et al.* 2004).

Once $\mathcal{L}(\xi)$ and $f(\xi)$ are constructed, the solution $u(\mathbf{x}, \xi)$ is next represented in polynomial chaos expansion (PCE) (Ghanem & Spanos 2003), where a square-integrable random process is expressed as

$$u(\mathbf{x}, \xi) = \sum_{i=0}^{\infty} u^{(i)}(\mathbf{x}) \psi_i(\xi) , \quad (1.3)$$

where $\psi_i(\xi)$ are the Hermite polynomials, and $u^{(i)}(\mathbf{x})$ are deterministic coefficients called as *chaos coefficients*. For computational purposes, the series is truncated after a finite number of terms, yielding

$$u(\mathbf{x}, \xi) = \sum_{i=0}^{P-1} u^{(i)}(\mathbf{x}) \psi_i(\xi) . \quad (1.4)$$

The index P is determined by the stochastic dimension and the highest order of polynomial chaos to be retained in the expansion. For example, in a second-order expansion in two stochastic dimension $P = 6$ and the polynomials $\psi_i(\xi_1, \xi_2)$ are (Ghanem & Spanos 2003)

$$\begin{aligned} \psi_0(\xi_1, \xi_2) &= 1 , & \psi_1(\xi_1, \xi_2) &= \xi_1 , & \psi_2(\xi_1, \xi_2) &= \xi_2 , \\ \psi_3(\xi_1, \xi_2) &= \xi_1^2 - 1 , & \psi_4(\xi_1, \xi_2) &= \xi_1 \xi_2 , & \psi_5(\xi_1, \xi_2) &= \xi_2^2 - 1 . \end{aligned}$$

The chaos coefficients $u^{(i)}(\mathbf{x})$ can be computed by minimizing either the error in the solution or the residual in the equation (Ghanem & Spanos 2003). In both cases, a Galerkin approach is used to find the optimal solution. The second method, when applied to a linear statics problem of the form

$$K(\xi)u(\xi) = f(\xi) , \quad K(\xi) \in \mathbb{R}^{n \times n} , \quad u(\xi), f(\xi) \in \mathbb{R}^n , \quad (1.5)$$

where

$$\begin{aligned} K(\xi) &= \sum_{i=0}^{L-1} K^{(i)} \psi_i(\xi) , & f(\xi) &= \sum_{i=0}^{M-1} f^{(i)} \psi_i(\xi) , & u(\xi) &= \sum_{i=0}^{P-1} u^{(i)} \psi_i(\xi) , \\ P > L, M, \quad K^{(i)} &\in \mathbb{R}^{n \times n} , & f^{(i)}, u^{(i)} &\in \mathbb{R}^n , \end{aligned} \quad (1.6)$$

yields a system of linear deterministic equations of the form

$$\mathbf{K}\mathbf{u} = \mathbf{f}, \quad \mathbf{K} \in \mathbb{R}^{n^P \times n^P}, \quad \mathbf{u}, \mathbf{f} \in \mathbb{R}^{n^P}, \quad (1.7)$$

where

$$\mathbf{K} = \begin{bmatrix} \sum_{i=0}^{L-1} K^{(i)} \langle \psi_i \psi_0 \psi_0 \rangle & \sum_{i=0}^{L-1} K^{(i)} \langle \psi_i \psi_1 \psi_0 \rangle & \dots & \sum_{i=0}^{L-1} K^{(i)} \langle \psi_i \psi_{P-1} \psi_0 \rangle \\ \sum_{i=0}^{L-1} K^{(i)} \langle \psi_i \psi_0 \psi_1 \rangle & \sum_{i=0}^{L-1} K^{(i)} \langle \psi_i \psi_1 \psi_1 \rangle & \dots & \sum_{i=0}^{L-1} K^{(i)} \langle \psi_i \psi_{P-1} \psi_1 \rangle \\ \dots & \dots & \dots & \dots \\ \sum_{i=0}^{L-1} K^{(i)} \langle \psi_i \psi_0 \psi_{P-1} \rangle & \sum_{i=0}^{L-1} K^{(i)} \langle \psi_i \psi_1 \psi_{P-1} \rangle & \dots & \sum_{i=0}^{L-1} K^{(i)} \langle \psi_i \psi_{P-1} \psi_{P-1} \rangle \end{bmatrix}, \quad (1.8)$$

$$\mathbf{u} = \begin{Bmatrix} u^{(0)} \\ u^{(1)} \\ \vdots \\ u^{(P-1)} \end{Bmatrix}, \quad \mathbf{f} = \begin{Bmatrix} \langle \psi_0^2 \rangle f^{(0)} \\ \langle \psi_1^2 \rangle f^{(1)} \\ \vdots \\ \langle \psi_{M-1}^2 \rangle f^{(M-1)} \\ 0 \end{Bmatrix}, \quad (1.9)$$

and $\langle \cdot \rangle$ denotes the mathematical expectation operator:

$$\langle g(\boldsymbol{\xi}) \rangle = \int_{\mathbb{R}^m} g(\boldsymbol{\xi}) p(\boldsymbol{\xi}) d\boldsymbol{\xi}, \quad (1.10)$$

where $g(\boldsymbol{\xi})$ is any function of the m -dimensional random vector $\boldsymbol{\xi}$ and $p(\boldsymbol{\xi})$ is the joint probability density function (PDF) of $\boldsymbol{\xi}$. To solve (1.7) efficiently, the sparsity of matrix \mathbf{K} can be exploited and iterative solvers can be employed, as described in Section 4. Once the coefficients $u^{(i)}$ are estimated, any statistical moment and the PDF of $u(\mathbf{x}, \boldsymbol{\xi})$ can be computed using (1.4). For example, the mean (the first moment) and standard deviation (square root of the second moment about the mean) are

$$\langle u(\mathbf{x}, \boldsymbol{\xi}) \rangle = u^{(0)}(\mathbf{x}), \quad (1.11)$$

and

$$stddev(u(\mathbf{x}, \boldsymbol{\xi})) = \sqrt{\sum_{i=1}^{P-1} u^{(i)}^2(\mathbf{x}) \langle \psi_i^2(\boldsymbol{\xi}) \rangle}, \quad (1.12)$$

respectively.

However, in a real engineering problem the displacement field is of very little interest; the strains and stresses are considered to be more important. It will be shown here that often computation of the statistical moments of strains and stresses is not as simple as that of the displacement field. This is because an orthogonal expansion such as PCE is not easily obtainable for such strains and stresses (explained in details in the following section). Von Mises stress by any numerical method using 50,000 grid points takes about

45 minutes, which is significant. There may be additional quantities of interest such as strains, which will require additional computational time. Moreover, as previously mentioned, these numerical techniques will bring additional overhead of computational and programming complexity.

These issues are not addressed at length in the current literature, the goal of this paper is to discuss these issues and to find a set of feasible solutions. Cases where numerical integration must be used are identified, and a few integration techniques are considered. These techniques are further studied for their computational cost and complexity in implementation.

The stress tensor components σ_{ij} can be derived from the strain tensor components ε_{ij} using the constitutive relationship. For the isotropic materials these stress components are

$$\sigma_{ii} = \frac{E}{(1-2\nu)(1+\nu)} \{ (1-\nu)\varepsilon_{ii} + \nu\varepsilon_{jj} + \nu\varepsilon_{kk} \} \quad i \neq j \neq k , \quad (1.13)$$

and

$$\sigma_{ij} = \frac{E}{2(1+\nu)} \varepsilon_{ij} \quad i \neq j , \quad (1.14)$$

where E denotes the Young's modulus and ν denotes the Poisson's ratio. The Von Mises stress can be computed as

$$\sigma_{VM} = \sqrt{I_1^2 - 3I_2} , \quad (1.15)$$

where

$$I_1 = \sigma_{ii} + \sigma_{jj} + \sigma_{kk} \quad \text{and} \quad I_2 = \sigma_{ii}\sigma_{jj} + \sigma_{jj}\sigma_{kk} + \sigma_{kk}\sigma_{ii} - \tau_{ij}^2 - \tau_{jk}^2 - \tau_{ki}^2 . \quad (1.16)$$

Evaluation of the mean and standard deviation of these stress and strain quantities will be considered next. In a nondeterministic case the displacement field in three spatial directions can be represented in a form similar to (1.4) as

$$u_i(\mathbf{x}, \boldsymbol{\xi}) = \sum_{p=0}^{P-1} u_i^{(p)}(\mathbf{x}) \psi_p(\boldsymbol{\xi}) \quad i, j = 1, 2, 3 . \quad (1.17)$$

The strain tensor components are derived from the displacement field as

$$\varepsilon_{ii} = \frac{\partial u_i}{\partial x_i} \quad \text{and} \quad \varepsilon_{ij} = \frac{\partial u_i}{\partial x_j} + \frac{\partial u_j}{\partial x_i} \quad \text{for} \quad i \neq j ; \quad i, j = 1, 2, 3 . \quad (1.18)$$

For an uncertain system, using (1.17) and (1.18), the representation of the strain components become

$$\varepsilon_{ij}(\mathbf{x}, \boldsymbol{\xi}) = \sum_{p=0}^{P-1} \varepsilon_{ij}^{(p)}(\mathbf{x}) \psi_p(\boldsymbol{\xi}) . \quad (1.19)$$

For brevity, the arguments \mathbf{x} and $\boldsymbol{\xi}$ are dropped hereafter. The principal strains ε_{pr_i} ($i = 1, 2, 3$) are eigenvalues of the matrix \mathbf{E} , thus they are highly nonlinear functions of the strain components ε_{ij} . Thus mean and standard deviations of the principal strains cannot be easily computed using orthogonality among the polynomials; a numerical technique is needed for this. The same is true for the Von Mises strains.

A numerical integration technique is therefore needed for computing the statistical moments of the terms that cannot be evaluated using the orthogonality property of chaos polynomials. A few techniques are considered and compared here for their computational efficiency and algorithmic complexity. These are (i) Monte Carlo simulation, (ii) Latin hypercube sampling, (iii) Gaussian quadrature on the standard tensor product grid, and (iv) Smolyak cubature. These methods are presented below.

2. Numerical integration

The integral of the following form will be considered here:

$$I = \int_{\mathcal{D}} g(s)p(s)ds , \quad (2.1)$$

where $\mathcal{D} \in \mathbb{R}^k$ is the domain of integration, $g(s)$ is the integrand, and $p(s)$ is the weighing function. For example, in a probabilistic context, if $p(s)$ is a joint probability density function of a random vector s then the above integral yields the statistical moment of the function $g(s)$. In our case $k = m$ and $s = \xi$. A numerical integration rule to evaluate this integral typically looks like

$$\hat{I} = \sum_{i=1}^N w_i g(s_i) , \quad (2.2)$$

where s_i are the points where the function $g(s)$ is evaluated according to the integration scheme and w_i are the corresponding weights. In this paper the terms *quadrature points* and *nodal points* will be used synonymously. In the probabilistic methods of integration these points are often referred as realizations of the random variable s and N is called sample size. Evaluation of multi-dimensional integrals deserves special attention to manage the increasing computational cost with dimension. Numerical integration can be categorized into two different classes, probabilistic methods (Evans & Swartz 2000, Liu 2001) and deterministic methods (Abramowitz & Stegun 1984, Stroud & Secresr 1966). Here two probabilistic methods, Monte Carlo simulation and Latin hypercube sampling, and two deterministic methods, Gaussian quadrature with standard tensor product and Smolyak cubature are considered.

2.1. Monte Carlo (MC) simulation

In this method the quadrature points s_i are generated using a random number generator such that their probability density function becomes $p(s)$. The weights w_i are $1/N$ (Evans & Swartz 2000, Liu 2001). The procedure is explained with a specific example: computing the statistical moments of the Von Mises stress. To do this, at first realizations of random numbers ξ are generated. Each of these realizations corresponds to a realization of the random system model. Then for each realization, the following steps are followed. First, using (1.19), realization of the strain tensor components is computed, simultaneously realization of the material properties such as E, ν is computed, which yields the corresponding realization of the constitutive matrix. From the strain tensor components and constitutive matrix, realization of the stress tensor components is computed. Then the corresponding realization of Von Mises stress is computed using (1.15) and (1.16). Finally, over numerous realizations the statistical moments of the Von Mises stress are computed. The main advantage of this method is its straightforward implementation.

However, this method needs a large number of realizations to obtain a good estimate of the statistical moments; thus it is computation intensive.

2.2. Latin hypercube sampling

Latin hypercube sampling (LHS) (Mckay *et al.* 1979) is a method of selecting the integration points to achieve faster convergence than the standard Monte Carlo method. This is a variance reduction technique (pp 391 of Davis & Rabinowitz 1984, pp 183 of Evans & Swartz 2000). As a result, for any fixed error level LHS requires a smaller sample size than MC to estimate the integral. The computational procedure of the integral evaluation is exactly the same as the Monte Carlo simulation, only the sampling points (that is, the realizations of random numbers ξ) are different. Usage of LHS in SFEM applications has also been addressed in (Choi *et al.* 2004, Olsson & Sandberg 2002, Ghiocel & Ghanem 2002),

2.3. Gaussian quadrature on standard tensor product grid

This is a deterministic quadrature rule (Abramowitz & Stegun 1984, Stroud & Secresr 1966) that has also been used in SFEM (Field 2002). For an integration of form (2.1) this method can evaluate the integral exactly if $g(s)$ is a polynomial. In our case, the $p(s)$ is the distribution of a Gaussian random vector. Gaussian quadrature with Gaussian distribution as weighing function is also known as Gauss-Hermite quadrature. In one dimension, an N -point quadrature rule can exactly evaluate the integral of a polynomial of order up to $(2N - 1)$. For a given quadrature rule in one dimension, its extension to a multidimensional case is as follows.

Let an m_i point numerical integration rule for a function g of one variable s^i be

$$U^i(g) = \sum_{j=1}^{m_i} a_j^i g(s_j^i), \quad (2.3)$$

where s_j^i are quadrature points, and a_j^i are weights. This integration rule can then be extended to a d -dimensional integration using the Kronecker product as

$$\hat{I} = (U^{i_1} \otimes \cdots \otimes U^{i_d})(g) = \sum_{j_1=1}^{m_{i_1}} \cdots \sum_{j_d=1}^{m_{i_d}} (a_{j_1}^{i_1} \otimes \cdots \otimes a_{j_d}^{i_d}) g(s_{j_1}^{i_1} \cdots s_{j_d}^{i_d}), \quad (2.4)$$

where m_{i_1}, \dots, m_{i_d} are the number of quadrature points used for defining integration rule in variables s^{i_1}, \dots, s^{i_d} , respectively. Thus, computation of the above integral needs $(m_{i_1} \cdots m_{i_d})$ function evaluations. For example, if an m -point integration rule is used in each dimension in a d -dimensional space, then evaluation of a d -dimensional integral in this space needs m^d function evaluations. The computational burden therefore increases significantly with dimension d . This is often referred as the *curse of dimensionality*.

2.4. Smolyak cubature

In order to avoid the so-called *curse of dimensionality*, another approach of numerical integration, Smolyak cubature (Smolyak 1963), is widely used. Here, instead of using the full tensor product grid a recursive contribution of lower-order tensor products is used to estimate the integral, stated as

$$\hat{I}_{q,d} = \sum_{q-d+1 \leq |\mathbf{i}| \leq q} (-1)^{q-|\mathbf{i}|} \binom{d-1}{q-|\mathbf{i}|} (U^{i_1} \otimes \cdots \otimes U^{i_d})(g), \quad (2.5)$$

$$\mathbf{i} = \{i_1, \dots, i_d\}, \quad |\mathbf{i}| = i_1 + \dots + i_d.$$

Here $\hat{I}_{q,d}$ is the cubature rule, $q \geq d$ is a parameter to be selected, \mathbf{i} is a d -dimensional index set, U^{i_k} are 1-dimensional quadrature rules as in (2.3), and $m_{i_j} \neq m_{i_k}$ for $i_j \neq i_k$. Instead of considering $U^{i_k}(g)$ as the integration rule in any particular variable s^{i_k} , it can be viewed as a quadrature rule for any dimension. In fact, a closer examination of (2.5) reveals that the one-dimensional quadrature rules are permuted in all dimensions. These 1-dimensional quadrature rules can be selected as Gaussian quadrature rules, with $m_{i_1} = 1, m_{i_2} = 2, \dots$. Computational cost saving in Smolyak cubature compared to the standard tensor product integration rule increases as d , the dimension of the problem grows. It is proved in (Heiss & Winschel 2006) that if every univariate quadrature rule U^i as in (2.3) in the sequence $\{U^i, i = i_1, i_2, \dots\}$ can integrate any univariate polynomial of order up to $(2m_i - 1)$ exactly, then the Smolyak quadrature (2.5) yields the exact integral of a d -variate polynomial of total order up to $(2M - 1)$, where

$$M = \max_{i_1 \leq i_k \leq i_d} m_{i_k}. \quad (2.6)$$

3. Numerical integration of a polynomial integration: dimension reduction

When the integrand admits a polynomial form and the order of the polynomial is less than the dimension or the number of independent variables involved, then the integration cost can be reduced significantly by using a reduced dimensional integration, described here. Let us define the term *effective dimension* of a function to refer to the maximum number of independent random variables ξ_i present in the function; for example, the *effective dimension* of $\xi_5^4 \xi_8$ is 2, since it involves two independent random variables: ξ_5 and ξ_8 . Let a random quantity be expressed as an expansion of polynomials of d -dimensional orthonormal random variables, and the highest order of the polynomial in the expansion be p . If $p < d$ then the highest *effective dimension* of any term in the expansion is p , and not d . Obviously a p -dimensional integration rule is computationally more efficient than a d -dimensional rule. If a d -dimensional integration rule is used to evaluate such function, it only contributes to increase the computational cost, without affecting the result. Thus in this situation a p -dimensional integration rule is sufficient and computationally more efficient. In this paper such reduced dimensional integration will be referred as Integration in Reduced Dimension (IRD). For general cases where IRD is not used, and instead a full dimensional integration is carried out which will be referred to as Integration in Full Dimension (IFD).

4. Numerical study

Two numerical studies are conducted and presented here. In the first study numerical integration of a polynomial expansion is considered. Three deterministic integration techniques are compared regarding the computational cost to integrate a fourth order polynomial expansion. These techniques are: (i) Gaussian quadrature with standard tensor product grid in full dimension (IFD), (ii) Gaussian quadrature with standard tensor product grid in reduced dimension (IRD), and (iii) Smolyak cubature. In the second numerical study a plate model with random material properties is considered and the first two statistical moments of a few strain and stress quantities of this model are computed using some of the methods described previously. Computational issues such as speed and complexity in implementation are discussed.

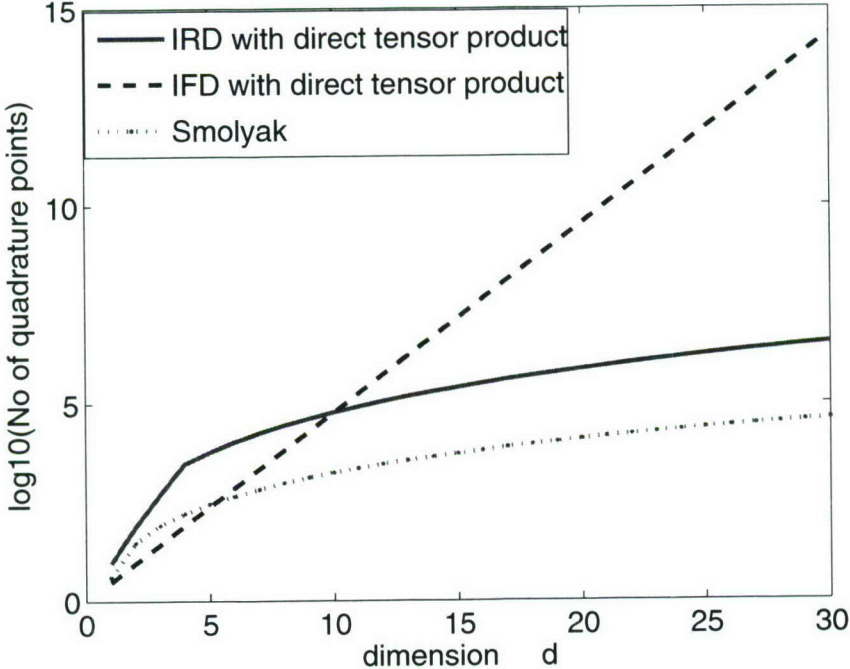


FIGURE 1. Number of quadrature points needed in different deterministic integration schemes: fourth degree polynomial expansion

4.1. Example 1

Throughout this paper the Gauss-Hermite quadrature is used as the basic univariate integration rule for the deterministic integration techniques, that is, as $U^i(g)$ in (2.3) and as $U^{i_1}(g)$ in (2.5). For a fourth order polynomial expansion, the number of quadrature points needed by three exact (and deterministic) methods, IFD with Kronecker product, IRD with Kronecker product, and Smolyak cubature are plotted in Fig. 1. From this plot it is noted that IRD with Kronecker product yields a significant improvement over IFD with Kronecker product, especially as the dimension increases. The Smolyak cubature is found to be the most computational efficient among the three methods. It is further noted that for lower dimensional integration, the number of quadrature points needed by Smolyak cubature exceeds the number of points needed by IFD with direct tensor product. It is experienced that in terms of complexity in implementation, the sequence is reverse. That is Smolyak is the most complex and IFD with Kronecker product is the simplest. The complexity of Smolyak algorithm arises primarily from the need of some recursive functions to generate the grid points.

4.2. Example 2

In the second study a square plate model is used to compare numerical integration schemes to compute the statistical moments of stresses and strains. The dimensions of the plate are $2.3m \times 2.3m \times 5mm$. The plate is built using 20 metal strips joined side by side along the edges, and the dimensions of each strip are $2.3m \times 0.115m \times 5mm$, as shown in Fig. 2. Young's modulus of the strips are assumed to be random, modeled as

$$E_i = \bar{E}_i + stdev_{E_i} \xi_i \quad i = 1, \dots, 20, \quad (4.1)$$

thus $L = 20$ in (1.6). Here \bar{E}_i and $stdev_{E_i}$ are the mean and standard deviation of the Young's modulus of the material in strip i , and ξ_i are independent standard normal random variables. The plate is fixed along its four edges. A finite element model with 400 square elements is used. Out of the twenty different materials, ten are chosen to be of mean Young's modulus 2.0 MPa and ten of mean 2.1 MPa ; standard deviations for all the materials are 20% of the respective mean values. Density of the plate material is assumed to be 7860 Kg/m^3 , the same as steel. In addition to the self-weight, the plate is loaded by three concentrated forces in its center, 400 KN , 300 KN , and -2 KN in directions x , y , and z , respectively. Displacement is represented using second-order chaos expansion as in (1.4) with $P = 231$. The chaos coefficients are computed by solving (1.7). To solve the system of deterministic equations a preconditioned conjugate gradient method is used with Block-Jacobi preconditioner. The matrix-vector (mat-vec) product computation is optimized by performing them in the block level (Pellissetti & Ghanem 2000). After estimating the chaos coefficients $u^{(i)}$ of the displacement field, standard deviation of the Von Mises stress are computed by Smolyak cubature and plotted in Fig. 3. Techniques for computing the chaos polynomials at a given grid point can be found in (Ghanem & Spanos 2003, Debusschere *et al.* 05). Next using MC simulation, LHS, and Smolyak cubature $\bar{\sigma}_{vm}$ and $stdev(\sigma_{vm})$ are computed. Values of these quantities at an arbitrary chosen node (node 45) are plotted in Figs. 4 - 5 against the number of quadrature points used. In this paper the random numbers are generated using Matlab. Usually the computer-generated random numbers do not satisfy the orthonormal properties for a finite sample size. Thus the generated random numbers are orthonormalized using a transformation (Ang & Tang 1984), and the new numbers are used for MC- and LHS-related computation. From (1.15), it is clear that the σ_{VM}^2 is a sixth order polynomial expansion. Following the discussion in Section 2.4, the cubature rule needs $M = 4$ for the exact evaluation of $\langle \sigma_{VM}^2 \rangle$, where M is defined in (2.6). For $d = 20$, it is found that the numbers of quadrature points in Smolyak cubature are 861, 12341, and 135751 for $M = 2$, 3, and 4, respectively.

The results of our study led to the following observations. Although it is previously shown that for Smolyak cubature $M = 4$ or 135751 quadrature points are needed to exactly evaluate $\langle \sigma_{VM}^2 \rangle$, it is observed from the plots that $M = 3$ or 12341 quadrature points suffice. Although not plotted here, this trend was observed for most other FE nodes as well. There were only a few nodes for which changing M from 3 to 4 changed the estimate of the integral to some extent. Thus, for most of the nodes, contribution from the higher-order terms in the expansion of $\langle \sigma_{VM}^2 \rangle$ is very small. It is also observed that in general all the three methods MC, LHS and Smolyak cubature provided a fair level of approximation of the statistical moments.

Transformation of the machine-generated random numbers helped improving the convergence of MC and LHS. No significant difference is noticed between the performance of MC and LHS. One possible reason is that the integrands are not monotonic functions of the arguments, thus variance reduction in LHS is not guaranteed (Mckay *et al.* 1979).

5. Conclusions

Stochastic dimension of the system, that is, the number of basic random variables involved in uncertainty modeling, is an important factor in selecting an integration al-

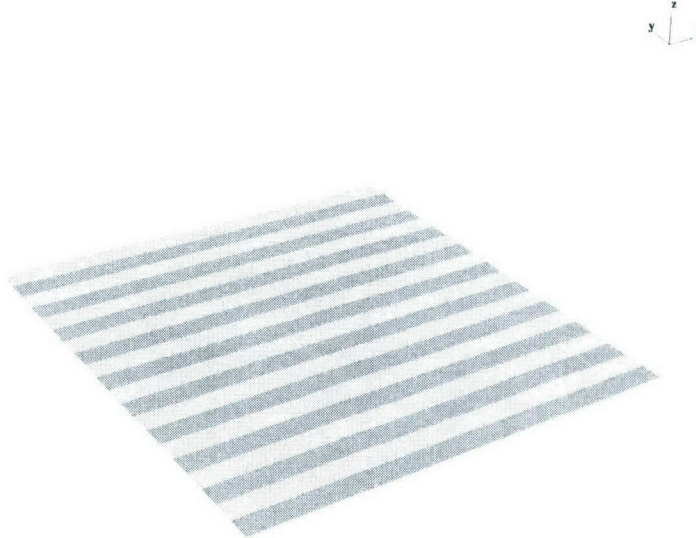


FIGURE 2. The plate model

gorithm. If the dimension is very low (say less than four or five) then computational cost is not very high for any of the methods. In that case even Gaussian quadrature with full tensor product rule can be used to achieve good accuracy as well as to enjoy lower algorithmic complexity. As the dimension increases, the computational cost of this method becomes prohibitive, and more advanced techniques such as Monte Carlo sampling, Latin hypercube sampling, or Smolyak cubature should be used. It is observed from the numerical experiments that all of these three methods work satisfactorily. In the simulation-based methods, the error is random, thus there is a probability of the error being higher than tolerance. This probability decreases as more number of realizations or quadrature points are included.

Thus according to the increasing computational cost, the deterministic methods can be arranged as Smolyak cubature, Integration in Reduced Dimension, Integration in Full Dimension (IFD) in Kronecker tensor product grid. According to the increasing complexity in implementation, the sequence becomes Integration in Full Dimension with Kronecker tensor product, Integration in Reduced Dimension, Smolyak cubature. Implementation of Monte Carlo and Latin hypercube sampling are as easy as Integration in Full Dimension with Kronecker tensor product grid, excluding the additional complexity to generate the random numbers needed for these methods. The choice of a particular integration scheme depends upon complexity level that can be afforded, availability of subroutine, and level of accuracy needed.

6. Future plans

According to the current literature SFEM has been applied to a variety of problems. However, most of these applications are on fairly small-scale problems. Thus, with the vision of analyzing and quantifying uncertainty of real-life problems currently we are working on applying domain decomposition techniques to solve SFEM-related problems in large-scale systems.

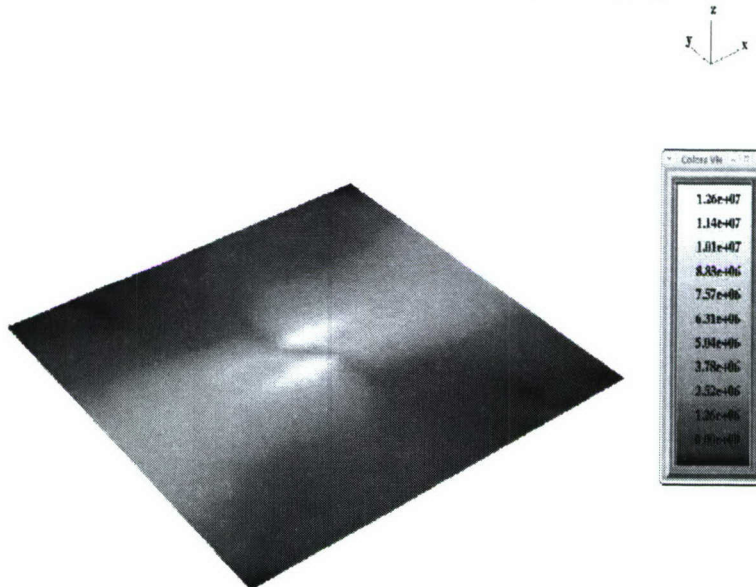


FIGURE 3. Standard deviation of Von Mises stress ($stdev(\sigma_{vm})$) computed by IFD, used Smolyak cubature with $M = 4$

Acknowledgment

Financial support from the Advanced Simulation and Computing Program of the Department of Energy is gratefully acknowledged.

REFERENCES

CHOI, S. K. & GRANDHI, R. V. & CANFIELD, R. A. & PETTIT, C. L. 2004 Polynomial chaos expansion with Latin hypercube sampling for estimating response variability. *AIAA Journal* **42**(6), 1191-1198.

DAS S. & GHANEM R. & SPALL J. 2006, Asymptotic sampling distribution for polynomial chaos representation of data: A maximum entropy and Fisher information approach. *45th IEEE Conference on Decision and Control, San Diego, CA* December 13-15.

DEBUSSCHERE JB & NAJM HN & PBAY PP & KNIO OM & GHANEM RG & LE MAÎTRE OP 2005 Numerical challenges in the use of polynomial chaos representations for stochastic processes *SIAM Journal on Scientific Computing archive* **26**(2), 698-719.

FIELD R. V. JR. 2002 Numerical methods to estimate the coefficients of the polynomial chaos expansion *15th ASCE Engineering Mechanics Conference, Columbia University, New York, NY* June 2-5

GHANEM R. & DOOSTAN A. 2006 On the construction and analysis of stochastic predictive models: Characterization and propagation of the errors associated with limited data. *Journal of Computational Physics* **217**(1), 63-81.

GHIOCEL D. M. & GHANEM R. 2002 Stochastic finite-element snalysis of seismic soil-structure interaction *Journal of Engineering Mechanics* **128**(1), 66-77.

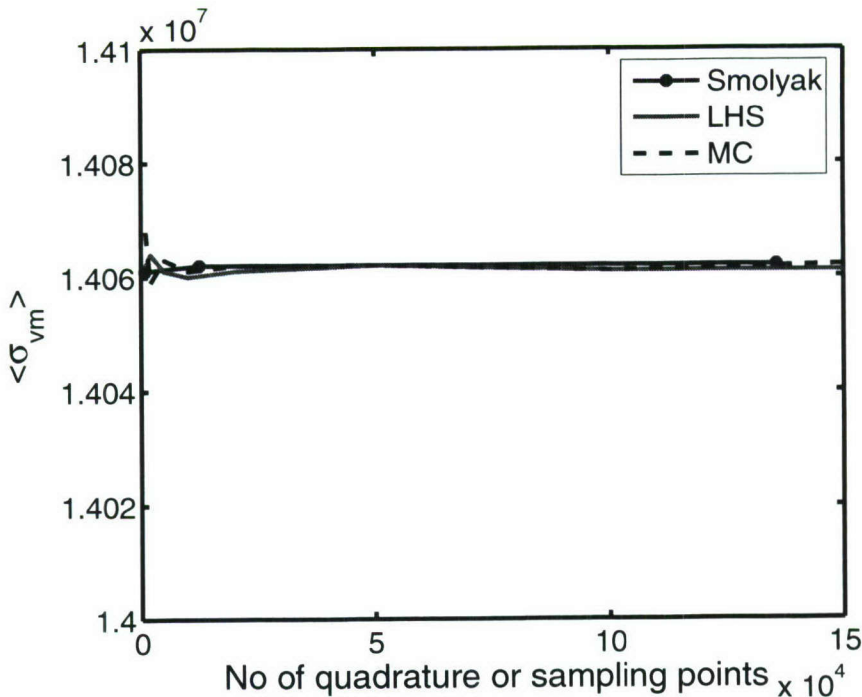


FIGURE 4. Mean Von Mises stress $\bar{\sigma}_{vm}$ (or $\langle \sigma_{vm} \rangle$) at node 45: convergence of different methods

HEISS F. & WINSCHEL V. 2006 Estimation with numerical integration on sparse grids
Discussion Papers in Economics **15**

LE MAITRE O. P. & NAJM H. & GHANEM R. & KNIO O. 2004 Multi-resolution analysis of wiener-type uncertainty propagation schemes. *J. Comp. Ph.* **197(2)**, 502-531.

MATLAB User's Guide, Version 7 *The MathWorks, Inc. MA*

MCKAY M. D. & BECKMAN R. J. & CONOVER W. J. 1979 A comparison of three methods for selecting input variables in the analysis of output from a computer code. *Technometrics* **21(2)**, 239-245.

OLSSON A. M. J. & SANDBERG G. E. 2002 Latin hypercube sampling for stochastic finite element analysis *Jl. Engng. Mech.* **128(1)**, 121-125.

PELLISSETTI M. & GHANEM R. 2000 Iterative solution of systems of linear equations arising in the context of stochastic finite elements *Advances in Engng. Software* **31**, 607-616.

SMOLJAK S. A. 1963 Quadrature and interpolation formulas for tensor products of certain classes of functions *Soviet Math. Dokl.* **4**, 240-243.

ABRAMOWITZ M. & STEGUN I. 1984 Handbook of mathematical functions with formulas, graphs, and mathematical tables *John Wiley & Sons Inc.*

ANG A. H.-S. & TANG W. H. 1984 Probability Concepts in Engineering Planning and Design, Vol II Decision, Risk and Reliability *John Wiley & Sons*

GHANEM R. & SPANOS P. D. 2003 Stochastic Finite Elements: A Spectral Approach *Revised Edition, Dover Publications*

DAVIS P.J. & RABINOWITZ P. 1984 Methods of numerical integration *Academic Press*

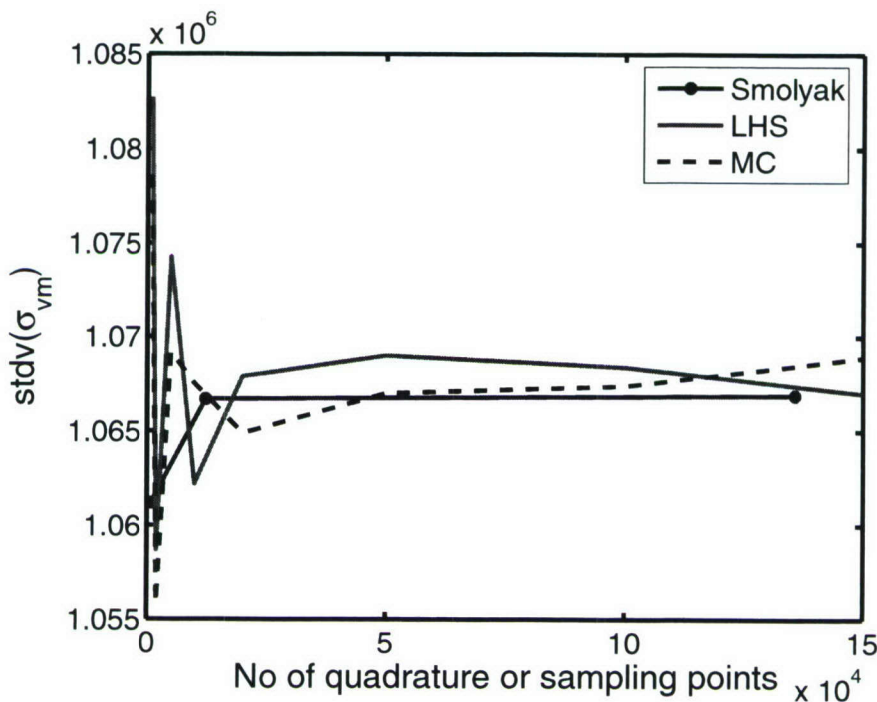


FIGURE 5. Standard deviation of Von Mises stress $stdev(\sigma_{vm})$ at node 45: convergence of different methods

EVANS M. & SWARTZ T. Approximating integrals via Monte Carlo & deterministic methods *Oxford University Press*

LIU J. S. 2001 Monte Carlo strategies in scientific computing *Springer-Verlag*

STROUD A. H. & SECRESR D. 1966 Gaussian quadrature formulas *Prentice-Hall Inc*

XIU D. & KARNIADAKIS G. 2003 Modeling uncertainty in flow simulations via generalized polynomial chaos. *J. Comp. Phys.* **187**(1), 137-167.

Separated flow in a three-dimensional diffuser: preliminary validation

By E. M. Cherry, G. Iaccarino, C. J. Elkins AND J. K. Eaton

1. Motivation and objectives

In gas turbine engines, the final stage of air compression occurs within the annular diffuser just upstream of the combustor. This component must satisfy conflicting goals of recovering kinetic energy exiting the compressor while supplying reasonably uniform flow and consistent mass splits into the various sections of the combustor. The key challenge in designing the diffuser is to make it as short as possible while avoiding any possibility of massive flow separation. Pressure losses due to the separated flow reduce engine performance while unsteadiness and recirculating flow associated with separation can cause catastrophic engine failure. An optimal design probably operates very near separation for some part of the engine's operating envelope. Accurate design analysis tools are needed to find the optimum and to avoid unexpected failures during prototype testing.

Previous experimental investigations (Obi *et al.* 1993; Buice & Eaton 2000) considered a planar geometry and provided a large amount of measurements both in terms of mean velocity and turbulent quantities. In order to guarantee the two-dimensionality of the flow, a very high aspect ratio duct was considered. Durbin (1995) and Iaccarino (2001) performed Reynolds-Averaged Navier-Stokes (RANS) simulations of the diffuser and concluded that good overall agreement with the experiments was obtained using the V2F turbulence model; discrepancies were observed in the recovery region (after the flow reattachment). Additional numerical studies carried out using Large-Eddy Simulations (LES) were conducted by Kalthenbach *et al.* (1999) and later by Wu *et al.* (2006); the agreement was again satisfactory although in the region downstream of the separation proved to be the most difficult to reproduce numerically. It was hypothesized that the flow in this region is characterized by long-time unsteadiness and potential flow three-dimensionality. The difficulty in exactly defining the flow conditions in the direction perpendicular to the diffuser plane might prevent reproduction of the experimental configuration in the simulations.

The objective of the present work is to complement the above mentioned study by performing experiments and simulations of a *truly* 3-D diffuser with simple and well-specified boundary conditions. The experimental setup is designed to provide a challenging test case for numerical models: it involves a well-defined 3-D recirculation region, and a considerable amount of data are collected at realistic Reynolds numbers. In addition, the effect of a small change in the expansion ratio is used to evaluate the ability of the numerical methods to predict trends and sensitivity to the geometry. Current measurements are obtained using Magnetic Resonance Velocimetry (MRV) (Elkins *et al.* 2003). Simulations are based on a novel unstructured-grid method developed for high-fidelity LES (Mahesh *et al.* 2004; Ham & Iaccarino 2004). Predictions using RANS turbulence models are also considered to identify the limitations of conventional turbulence models.

An additional objective of this work is to develop a procedure to objectively validate the numerical predictions in a case where detailed volumetric measurements exist. In

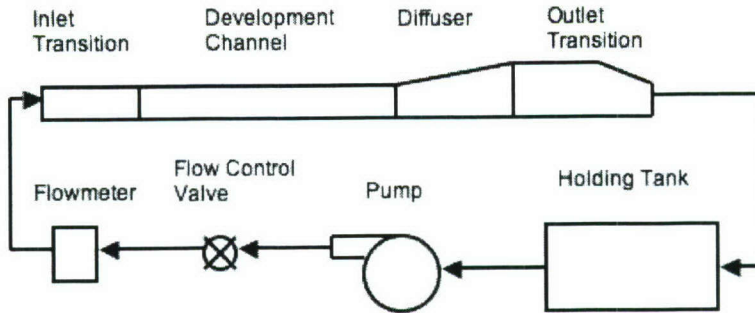


FIGURE 1. Sketch of the experimental setup.

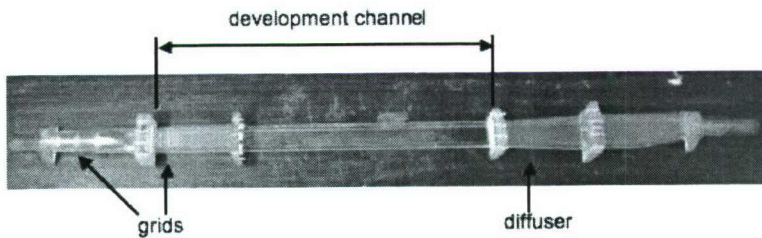


FIGURE 2. The development channel, the diffuser, and the outlet transition duct as fabricated using stereolithography manufacturing (see Fig. 1)

the present situation, the experiments consist of three-component mean velocity vectors within the entire diffuser volume. This makes *classical* comparisons based on the extraction of few selected velocity profiles possibly insufficient (although still useful).

2. Experimental setup

The working fluid for all of the experiments was water. A gadolinium-based contrast agent (Omniscan, Nycomed, Inc.) was added to the water in a concentration of 0.5 %. The schematic of the recirculating flow loop is shown in Fig. 1. A centrifugal pump (Little Giant model no. TE-6MD-HC) circulated water at a flow rate of 20.3 L/min. The average volume flow rate was measured using a Signet Scientific MK315.P90 paddle wheel flow meter, which was calibrated using the bucket and stopwatch method described by Elkins *et al.* (2003) with an estimated uncertainty of 5%. The pump was placed approximately 3 meters from the magnet, and no other metallic parts were used in the loop to avoid influencing the signal detected by the magnetic resonance imaging (MRI) system. Flexible plastic tubing with an inner diameter of 25.4 cm was used to complete the flow loop.

Figure 2 is a photograph of the transition piece, development channel, and test diffuser. The diffuser itself was preceded by three inlet parts made of Plexiglas and stereolithography (SLA) resin. The SLA pieces were fabricated with a normal resolution of 100 μ m by Mr. Frank Medina of Keck Laboratory at the University of Texas El Paso.

The upstream transition piece was designed to smoothly morph the cross-section of the flow from a 25.4 cm diameter circle to a rectangle with the same dimensions as the development channel. This section included three sets of grids with 2 mm square holes and a 60% open area to keep the flow from separating and provide uniform mean flow

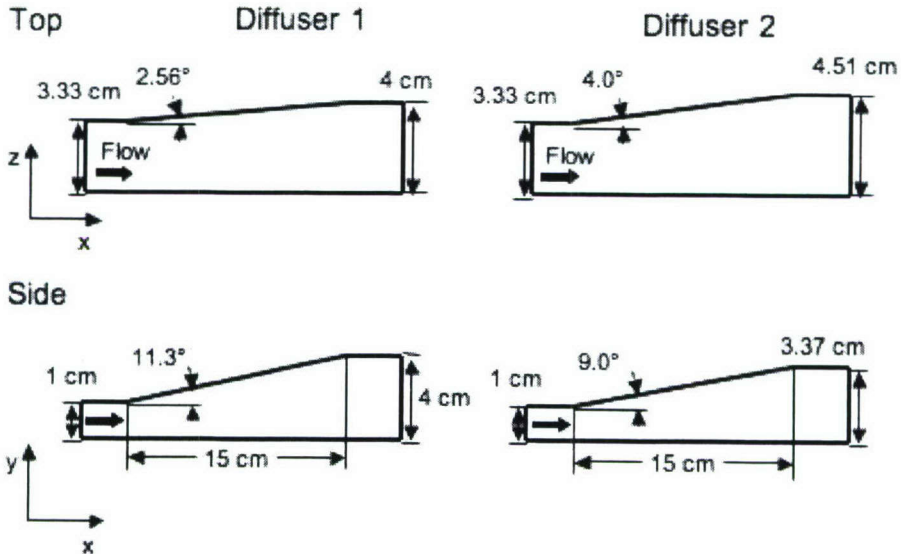


FIGURE 3. Geometrical details of the two diffuser configurations used in the present study.

and turbulence at the development section inlet. The 60-cm-long development channel had a constant rectangular cross section of height 1 cm and aspect ratio 1:3.33. Three grids were included at the upstream end of the development section to achieve a greater flow uniformity. Velocity data a few centimeters upstream of the diffuser inlet showed that the flow was fully developed by the end of this channel.

The test diffuser is attached directly to the development channel exit. Diffuser 1 has a rectangular inlet of height 1 cm and aspect ratio 1:3.33 and a 4 cm square outlet, giving an area expansion ratio of 4.8. The diffuser is 15 cm long. One side wall expands at an angle of 2.56° degrees, and the top wall expands at an angle of 11.3° degrees. The other two walls are straight. Diffuser 2 is also 15 cm long and has the same inlet as Diffuser 1, but its outlet is 4.51 cm x 3.37 cm, giving an area expansion ratio of 4.56. The top wall of Diffuser 2 expands at an angle of 9° degrees and its side wall expands at an angle of 4° degrees. The Reynolds number in both diffusers based on the height of the inlet channel is set to approximately 10,000. Different outlet transition sections are used for the two diffusers because it is necessary to match the dimensions of the diffuser outlet. Both outlet transitions have 10 cm of constant-cross-section channel and then a 10-cm contraction into a circular outlet 25.4 cm diameter.

Velocity data are collected using the method of magnetic resonance velocimetry (MRV) described by MRV uses magnetic resonance imaging to measure the three-component mean velocity vectors in a three-dimensional volume.

All experiments were performed at the Richard M. Lucas Center for Magnetic Resonance Spectroscopy and Imaging at Stanford University. A 1.5-T MR system (GE Signa CV/I, Gmax = 40 mT/m, rise time = 268 s), with a single channel, head receive coil was used. Data were collected with a sagittal slab 74 mm thick in the spanwise direction and a field-of-view (FOV) of 24 cm in the streamwise and cross stream directions. The imaging matrix was 74 × 256 × 256 yielding 1 mm resolution in the spanwise direction and 0.9 mm

in the streamwise and cross stream directions. A total of 16 complete scans of the flow were averaged to produce the final velocity field.

The mean velocity uncertainty was estimated to be less than 10% following the analysis of Elkins *et al.* (2003) and Elkins *et al.* (2004).

Velocity field data were processed using Matlab. The coordinate system was rotated and translated to match the coordinate system of the Solidworks model of each diffuser. The data were then averaged in the streamwise direction using a five-point Gaussian filter.

3. Numerical setup

As discussed in the previous section, the diffuser geometry was designed to be easily defined; the presence of planar surfaces and simple rectangular inlet and outlet ducts facilitates the construction of a very high-quality hexahedral-only mesh. The grid is clustered at the walls to provide good resolution of the near-wall region. In Fig. 4 several cross-sections are reported in the region of the diffuser. The computational domain also includes the development duct and the outlet region (as defined earlier). Most of the calculations reported herein are obtained on a mesh consisting of 1.8 million grid cells (referred to as the coarse grid); an additional mesh (fine grid) consisting of 14 millions cells is also considered for the LES simulations. This is obtained by splitting each hexahedral in the coarse grid into eight elements.

Boundary conditions are simple no-slip walls, velocity inlet and outflow. At the inlet plane, a constant velocity matching the experimental mass flow rate is specified. No fluctuations are added, as the inflow plane is far from the diffuser region. The outlet is treated as a *classical* convective outlet.

The numerical simulations using LES are performed using CDP, a parallel, unstructured code for accurate flow simulations (Mahesh *et al.* 2004; Ham & Iaccarino 2004). The incompressible Navier-Stokes equations are solved on general polyhedral meshes using a fractional-step procedure. Second-order symmetric discretization in time and space is used. This results in an algorithm that conserves kinetic energy, and introduces no numerical dissipation. The subgrid scale Reynolds stresses are modeled using the dynamic Smagorinsky closure.

In addition to the LES, computations using a commercial software (Fluent) are considered to evaluate the predictive abilities of conventional RANS turbulence models. Several models have been tested, but only the results using the $k-\omega$ SST model (Menter 1994) are presented herein. Results obtained with other eddy-viscosity models are comparable.

The LES computations are performed using unity CFL; this results in a timestep approximately equal to 0.00015 seconds on the coarse mesh. The simulation has been run for approximately 25,000 timesteps to achieve statistical convergence. Afterward the flowfield has been averaged for about 2.5 seconds (or equivalently 15,000 timesteps). On the other hand, the computations on the fine grid have been averaged only for about 8,000 timesteps and have not achieved sufficient convergence of the velocity statistics. The preliminary results are presented in the following section although the computations are ongoing. Calculations on the two grids have been carried out using 128 processors of the ALC Linux cluster at Lawrence Livermore National Laboratory.

Fluent computations are carried out solving the steady RANS equations using 16 processors and have been completed only on the mesh consisting on 1.8 million grid elements.

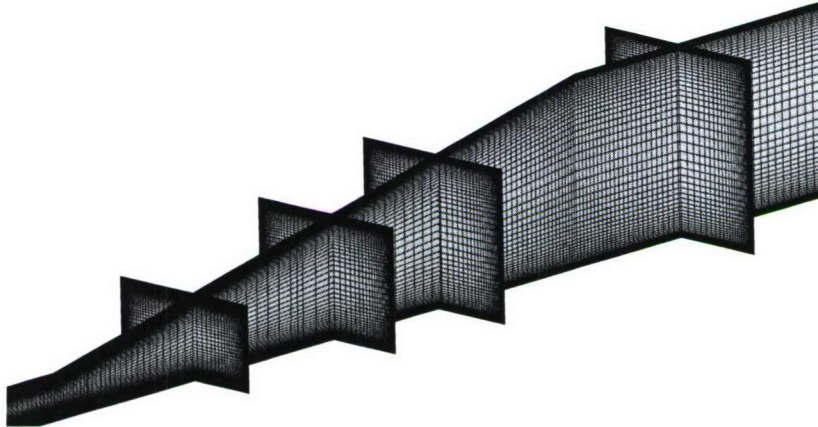


FIGURE 4. Cross-section of the computational grid consisting of 1.8 million hexahedrals. The mesh is clustered toward the no-slip walls. The computational domain includes the development channel, the diffuser, and the outlet region.

4. Quantitative comparisons

Comparisons between numerical predictions and measurements are reported in Figs. 5 and 6. The development of the flow in the diffuser 1 is illustrated in Fig. 5 in terms of streamwise velocity isocontours in axial cross-sections. The experiments show the presence of a 3D separation that originates in the top-right corner and then propagates to become almost 2D in the upper part of the diffuser. The RANS simulations strongly overpredict the strength of the separation and result in a flow that is recirculating well in the outlet region. In addition, the flow is separated on the right side of the diffuser as opposed to the measurements that show a recirculation area on the top wall. Mass conservation implies strong acceleration in the left part of the diffuser, resulting in very different velocity distributions in the cross-sections. On the other hand, the LES computations show a much better agreement with the data, especially for the fine grid, although the temporal averages are not converged. In Fig. 6, the streamwise velocity in a longitudinal plane at the mid-span of the development channel cross-section is reported. This plot can be compared directly to the results presented in the 2D diffuser simulated in Iaccarino (2001). The results confirm that the RANS predictions severely over-estimate the strength of the recirculation, while the LES (especially on the fine grid) appear to be in reasonable agreement with the experiments.

In order to provide a more quantitative analysis of the predictions and measurements, six velocity profiles are extracted from the longitudinal plane reported in Fig. 5. The comparisons are reported in Fig. 7. The experiments clearly show a large separated region on the top wall of the diffuser, but the detachment point is approximately located at $x = 8\text{mm}$ downstream of the diffuser inlet. This is in strong contrast with the predictions of both RANS and LES, which result in a separation occurring almost immediately at the diffuser inlet. The LES predictions on the fine grid, however, appear to be in much better agreement with the measurements. All of the numerical simulations predict a thinner boundary layer on the bottom wall compared to the measurements.

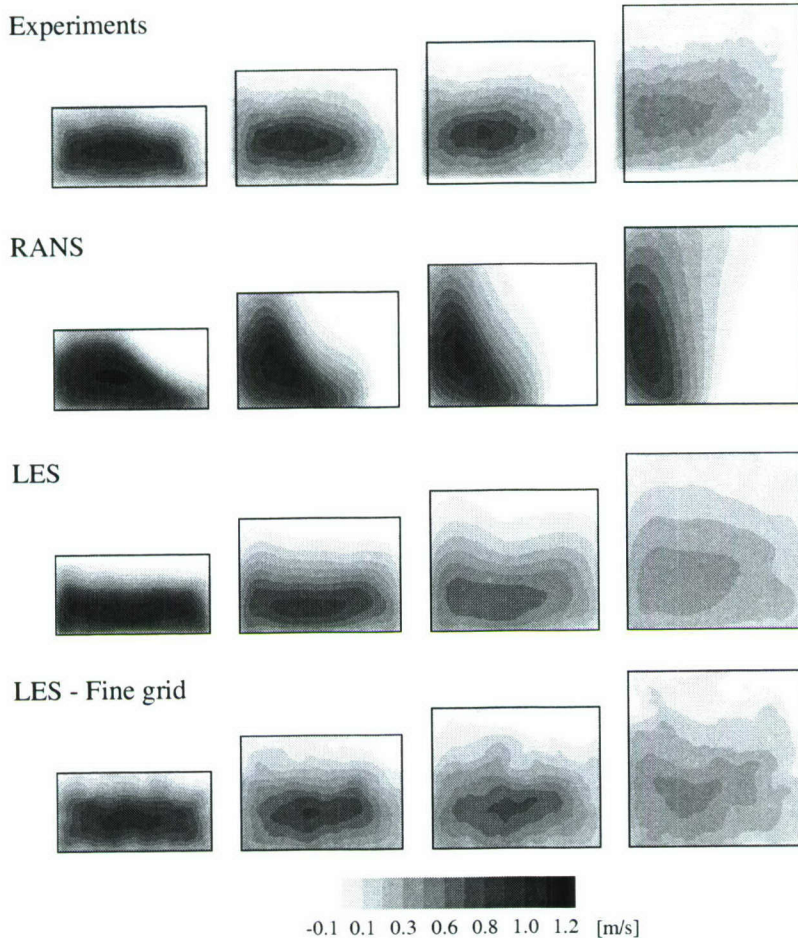


FIGURE 5. Streamwise velocity isolevels in four cross-sections along the diffuser 1. The columns represent sections at $x = 4\text{mm}$, 8mm , 12mm , and 16mm from left to right (the origin of the x -coordinate is fixed at the diffuser inlet).

5. Ongoing and future work

The experimental and numerical results presented in this report have been collected during the first part of this research activity. Current experimental work is focused on the characterization of the second diffuser geometry. On the numerical side, the predictions obtained on the fine grid are considered to be preliminary because the flow statistics have not been averaged for sufficient time. The simulation is ongoing. The computational grid for the second diffuser has been generated but the flow computations have not yet started. In addition to completing these simulations, we intend to perform simulations using a Reynolds stress model to evaluate the limitations introduced by the eddy viscosity approximation.

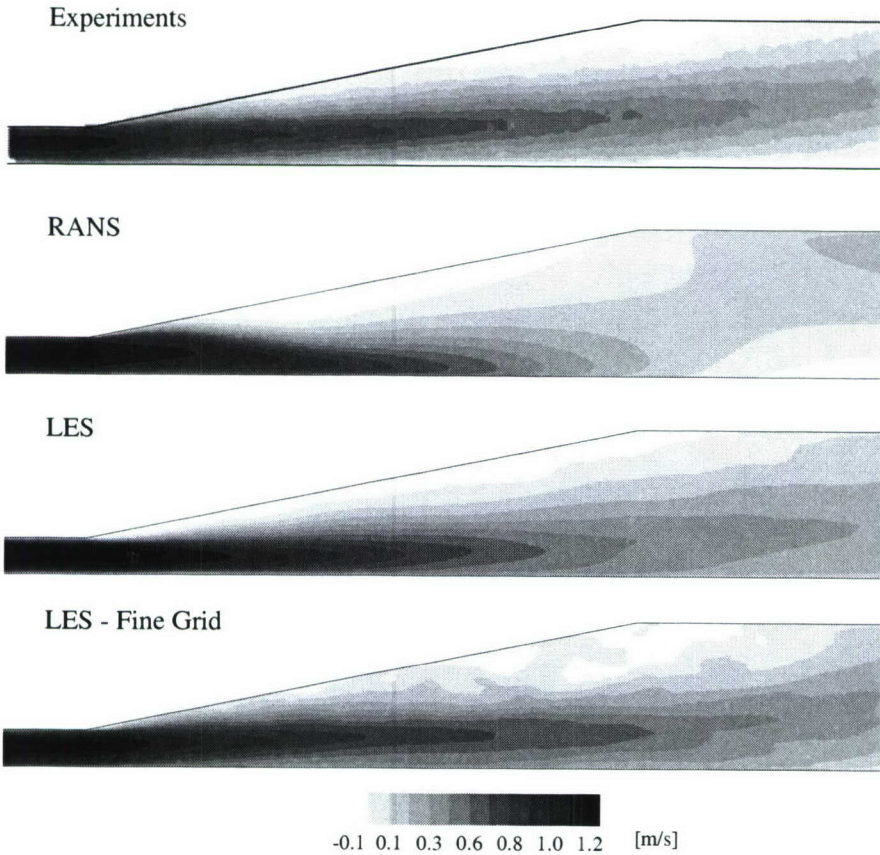


FIGURE 6. Streamwise velocity isolevels in a longitudinal section midspan in the diffuser 1.

Another important aspect of the present joint experimental and numerical study is the development of objective measures of the agreement between the datasets. The availability of massive amounts of measurements (in the present case about 400,000 velocity vectors in the diffuser region) makes *conventional* comparisons such as the one presented in Fig. 7 limited and potentially misleading, as they only focus on a limited region of the domain. In particular, the last profile in Fig. 7 seems to suggest a potential difference in the overall mass flux through the diffuser. In practice, the overall mass flow has been verified to be conserved and in close agreement between experiments and simulations. Each velocity profile in Fig. 7 is a 1D sample of a strongly 2D flow in the corresponding cross-section; mass conservation, on the other hand, is a scalar measure of the flow characteristic in the cross-section. In an attempt to capture the entire flow as a 3D entity, the probability density functions of the velocity vectors are reported in Fig. 8; this represents a global measure of *proximity* between measurements and numerical predictions although it is only qualitative because by construction it includes a scaling (the integral of the PDF is unity). Figure 8 shows the mean velocity statistics in the recirculating region and the much better agreement of the LES predictions as compared to the RANS

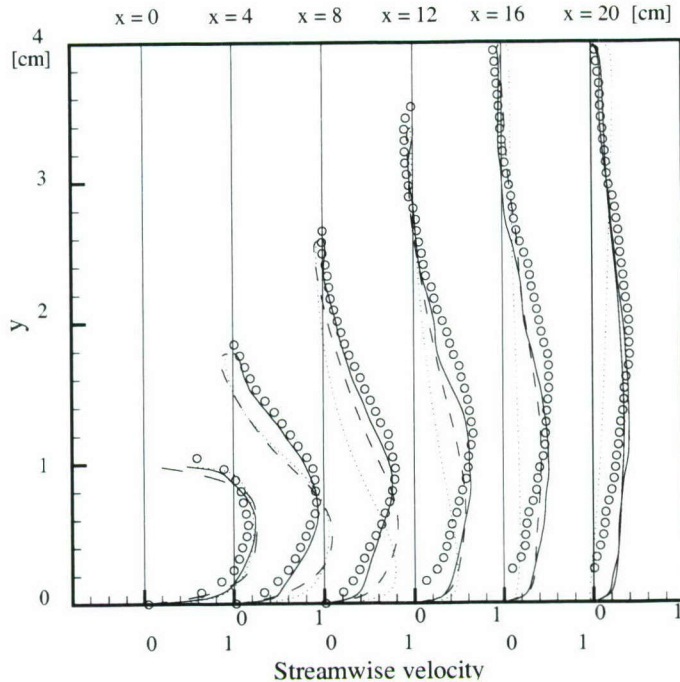


FIGURE 7. Streamwise velocity profiles in a longitudinal section midspan in the diffuser 1. Symbols are experiments; dotted lines are the RANS predictions; dashed and solid lines are the LES predictions on the coarse and fine grid, respectively.

one (although only the coarse grid results are reported here for the LES). In addition, the PDF of the vertical velocity illustrates a strong asymmetry, while the cross-flow velocity is nearly Gaussian. Future work will focus on ways to compare quantitatively the predictions based on distribution functions and as well as determine local comparison metrics.

Another important component of the validation process is the determination of the uncertainties. Although the experimental characterization has been performed (following what was done earlier in Elkins *et al.*, 2003), we have not included uncertainty bars in the present data as they are not yet available for the computational results. Future work will address this aspect of the numerical simulations.

Acknowledgments

This work is supported by the ONR and the Department of Energy within the Advanced Simulation and Computing Program.

REFERENCES

ASHJAAE, J. & JOHNSON, J.P. 1980. Subsonic Turbulent Flow in Plane Wall Diffusers: Peak Pressure Recovery and Transitory Stall. *Journal of Fluids Engineering* **102**(3), 275–282.

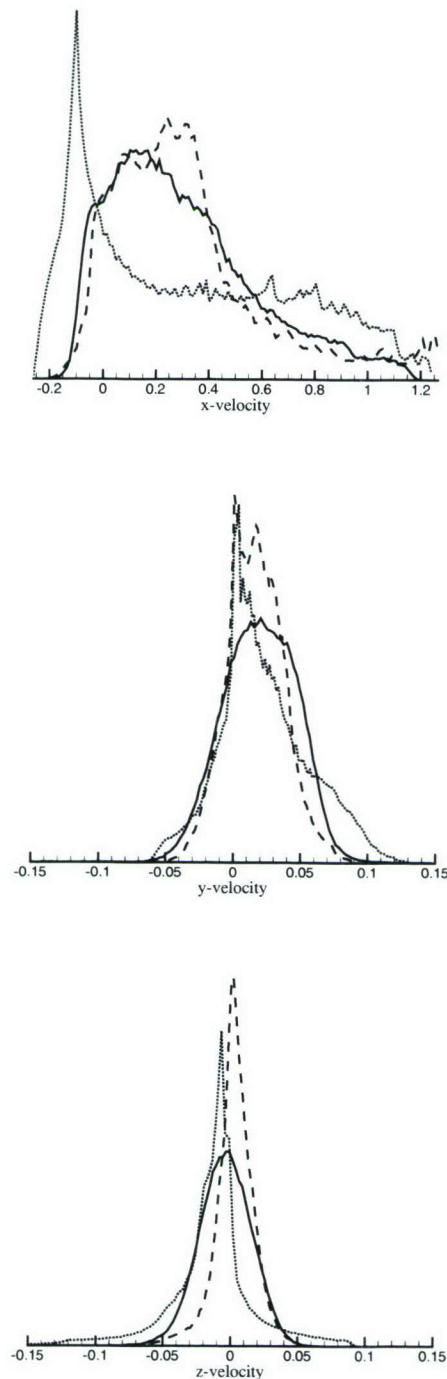


FIGURE 8. Probability density function of the three velocity components within the diffuser region. Solid lines are the experimental data, dotted and dashed lines are the RANS and the LES predictions respectively (on the coarse mesh).

BUICE, C.U. & EATON, J.K. 2000. Experimental Investigation of Flow through an Asymmetric Plane Diffuser. *Journal of Fluids Engineering* **122**(2), 433–435

DURBIN, P. 1995. Separated Flow Computations with the $k-\epsilon-v^2$ Model. *AIAA J.* **33**, 659–664.

ELKINS, C.J., MARKL, M., PELC, N. & EATON, J.K., 2004. Full-Field Velocity and Temperature Measurements Using Magnetic Resonance Imaging in Turbulent Complex Internal Flows. *International Journal of Heat and Fluid Flow* **25** 702–710.

ELKINS, C.J., MARKL, M., PELC, N. & EATON, J.K., 2003. 4D magnetic resonance velocimetry for mean flow measurements in complex turbulent flows. *Exp. Fluids* **34**, 494–503.

HAM, F. & IACCARINO, G. 2004. Energy Conservation in Colocated Discretization Schemes on Unstructured Meshes. *Annual Research Briefs, Center for Turbulence Research* 3–14.

IACCARINO, G. 2001. Prediction of a turbulent separated flow using commercial CFD codes. *J. Fluids Engng.* **123**, 819–828.

JOHNSON, J.P. 1998. Review: Diffuser Design and Performance Analysis by a Unified Integral Method. *Journal of Fluids Engineering* **120**(1), 6–18.

KALTENBACH, H. J., FATICA, M., MITTAL, R., LUND, T. S. & MOIN, P. 1999. Study of flow in a planar asymmetric diffuser using large eddy simulation. *J. Fluid Mech.* **390**, 151–185.

MAHESH, K., CONSTANTINESCU, G. & MOIN, P. 2004. A numerical method for large eddy simulation in complex geometries. *J. Comput. Phys.* **197**, 215–240.

MENTER, F. R. 1994. Two equation eddy viscosity turbulence models for engineering applications. *AIAA J.* **32**, 1598–1605.

OBI, S., AOKI, K., & MASUDA, S. 1993. Experimental and Computational Study of Separating Flow in an Asymmetric Plane Diffuser. *9th Symposium on Turbulent Shear Flows*, Kyoto, Japan, August 16–18, 305–1–305–4

SIMPSON, R.L. 1981. Review of Some Phenomena in Turbulent Flow Separation. *Journal of Fluids Engineering* **103**(4), 520–532.

SONG, S. & EATON, J.K. 2004. Reynolds Number Effects on a Turbulent Boundary Layer with Separation, Reattachment, and Recovery, *Experiments in Fluids* **36**, 246–258.

STOCK, H.W., LEICHER, S., & SEIBERT, W. 1988. Investigation of Flow Separation in a 3D Diffuser Using a Coupled Euler and Boundary Layer Method. *Zeitschrift Fur Flugwissen Schaffen und Weltraumforschung* **12**(5–6), 347–357.

TSUI, Y.Y. & WANG, C.K. 1995. Calculation of Laminar Separated Flow in Symmetric 2D Diffusers. *Journal of Fluids Engineering*, **117**(4), 612–616.

XU, D., LESCHZINER, M.A., KHOO, B.C., & SHU, C. 1997. Numerical Prediction of Separation and Reattachment of Turbulent Flow in an Axisymmetric Diffuser. *Computers and Fluids*. **26**, no. 4, pp(4), 417–423.

WU, X., SCHLUTER, J., MOIN, P., PITSCH, H., IACCARINO, G., & HAM, F. 2006. Computational study on the internal layer in a diffuser. *J. Fluid Mech.* **(550)** 391–412.

A dynamic global-coefficient subgrid-scale eddy-viscosity model for large-eddy simulation in complex geometries

By D. You AND P. Moin

1. Motivation and objectives

A major drawback of the Smagorinsky subgrid-scale eddy-viscosity model used in large-eddy simulations is that the model needs to be closed with an empirical constant, which has been found far from being universal and difficult to adjust to the characteristics of the turbulent flow field and computational resolution (Germano *et al.* 1991). Furthermore, the Smagorinsky model predicts non-vanishing subgrid-scale eddy viscosity in the regions where the flow is laminar, or the eddy viscosity should be zero. These shortcomings of the Smagorinsky model were overcome by Germano *et al.* (1991) through a dynamic procedure for determining the model coefficient. In the dynamic Smagorinsky model, the model coefficient is dynamically determined as a function of space and time using the scale-invariance concept and the “local-equilibrium” hypothesis (i.e., an equilibrium between the subgrid-scale dissipation and the viscous dissipation at the same physical location).

Although the dynamic model coefficient vanishes where the flow is laminar or fully resolved, it can cause numerical instability since its value often becomes negative and/or highly fluctuates in space and time. The numerical instability is remedied by additional numerical procedures such as an averaging of the model coefficient over statistically homogeneous directions or an ad hoc clipping procedure. The numerical stabilization procedure becomes complicated when the dynamic model is applied to a complex flow configuration in which there are no homogeneous directions. A number of novel approaches have been proposed (e.g., the dynamic localization model by Ghosal *et al.* (1994) and the Lagrangian dynamic model by Meneveau *et al.* (1996)) to address this issue. For example, the Lagrangian dynamic subgrid-scale model has been successfully employed for large-eddy simulations of flow through a real jet engine combustor (Moin 2002) and the tip-leakage flow in a turbomachinery cascade (You *et al.* 2004). However, the iterative solution procedure to solve an integral equation in the dynamic localization procedure (Ghosal *et al.* 1994) or the interpolation required for the pathline averaging in the Lagrangian dynamic model (Meneveau *et al.* 1996) demands a non-trivial effort in implementation, results in computational overhead, and may still require non-physical clipping operations.

Recently, Vreman (2004) developed a new subgrid-scale eddy-viscosity model that appears to offer several advantages over the Smagorinsky model with a constant coefficient. In this model, vanishing subgrid-scale dissipation for various laminar shear flows is theoretically guaranteed even with a non-zero constant empirical model coefficient. Since the model provides desirable features for successful large-eddy simulation even with a spatially uniform model coefficient and does not require any averaging or clipping procedures for numerical stabilization, it is especially suitable for complex flow configurations. Vre-

man (2004) showed that the model with a fixed coefficient predicts turbulence statistics for channel flow without introducing any wall-damping functions.

However, more recently, Park *et al.* (2006) showed that the model coefficient is not universal for all turbulent flows and needs to be adjusted according to the turbulent flow field simulated. They proposed a dynamic procedure for determining the model coefficient utilizing the “global equilibrium” between the subgrid-scale dissipation and the viscous dissipation (da Silva & Metais 2002). In this approach, the model coefficient is globally constant in space but varies in time, and it still guarantees zero eddy viscosity in the laminar-flow regions. Furthermore, the model does not require any ad hoc numerical stabilization or clipping operations. The dynamic procedure was found quite effective in determining the model coefficient and predicted superior results to those obtained by using the fixed-coefficient Smagorinsky model in a number of applications including turbulent channel flow and flows over a circular cylinder and a sphere (Park *et al.* 2006).

In this study, we propose an improvement of the dynamic global-coefficient subgrid-scale eddy-viscosity model of Park *et al.* (2006). The present dynamic procedure is also based on the “global equilibrium” between the subgrid-scale and viscous dissipation. In contrast to the dynamic procedure of Park *et al.* (2006) which requires two-level test filters, the present model requires only a single-level test filter, and therefore is more suitable for large-eddy simulation in complex geometries. The present dynamic procedure guarantees a model coefficient which is free from the influence of the computational domain size over which the volume averaging is taken while it is controlled by a scale-invariance concept in the model of Park *et al.* (2006).

The original Vreman model and the dynamic model of Park *et al.* (2006) are briefly introduced in section 2. Then, in section 3, the present dynamic model is derived and its characteristics are discussed. In section 4, the predictive capability of the present model is evaluated by considering turbulent channel flow and flow over a circular cylinder. A brief summary is presented in section 5.

2. Vreman-type subgrid-scale eddy-viscosity models

The incompressible Navier-Stokes and continuity equations are:

$$\frac{\partial u_i}{\partial t} = -\frac{\partial u_i u_j}{\partial x_j} - \frac{\partial p}{\partial x_i} + \nu \frac{\partial^2 u_i}{\partial x_j \partial x_j}, \quad (2.1)$$

$$\frac{\partial u_i}{\partial x_i} = 0. \quad (2.2)$$

By applying a “grid” filter $\overline{(\cdot)}$ to (2.1) and (2.2), one obtains the filtered equations of motions

$$\frac{\partial \overline{u}_i}{\partial t} = -\frac{\partial \overline{u}_i \overline{u}_j}{\partial x_j} - \frac{\partial \overline{p}}{\partial x_i} + \nu \frac{\partial^2 \overline{u}_i}{\partial x_j \partial x_j} - \frac{\partial \tau_{ij}}{\partial x_j}, \quad (2.3)$$

$$\frac{\partial \overline{u}_i}{\partial x_i} = 0, \quad (2.4)$$

where τ_{ij} is the subgrid-scale stress tensor. The subgrid-scale stress tensor τ_{ij} is modeled by an eddy-viscosity model:

$$\tau_{ij} - \frac{1}{3}\delta_{ij}\tau_{ij} = -2\nu_T \bar{S}_{ij}, \quad (2.5)$$

where ν_T is the eddy viscosity. In the present study, the Vreman-type eddy-viscosity models are considered for determining ν_T .

2.1. Subgrid-scale model with a fixed model coefficient

Vreman (2004) proposed a subgrid-scale eddy-viscosity model for ν_T in the following form:

$$\nu_T = C_v \bar{\Pi}, \quad (2.6)$$

where

$$\bar{\Pi} = \sqrt{\frac{\bar{B}_\beta}{\bar{\alpha}_{kl}\bar{\alpha}_{kl}}},$$

$$\bar{B}_\beta = \bar{\beta}_{11}\bar{\beta}_{22} - \bar{\beta}_{12}\bar{\beta}_{12} + \bar{\beta}_{11}\bar{\beta}_{33} - \bar{\beta}_{13}\bar{\beta}_{13} + \bar{\beta}_{22}\bar{\beta}_{33} - \bar{\beta}_{23}\bar{\beta}_{23},$$

$$\bar{\beta}_{ij} = \sum_{m=1}^3 \bar{\Delta}_m^2 \bar{\alpha}_{mi} \bar{\alpha}_{mj},$$

$$\bar{\alpha}_{ij} = \frac{\partial \bar{u}_j}{\partial x_i}, \quad (2.7)$$

$\bar{\Delta}_m$ is the grid-filter width in the m -direction, and C_v is the model coefficient. A novel feature of the model that makes it superior to the Smagorinsky model with a constant coefficient, is that the kernel $\bar{\Pi}$ becomes zero for canonical cases where the eddy viscosity should be zero. More details of the derivation of the model and its characteristics can be found in Vreman (2004).

For homogeneous turbulent flow, Vreman (2004) proposed C_v of 0.07 and showed favorable results. However, the value is found not universal and needs to be adjusted according to the flow and computational resolution as noted by Park *et al.* (2006).

2.2. Dynamic model with two-level test filters

Park *et al.* (2006) proposed a dynamic procedure for the determination of the model coefficient. They considered a transport equation for τ_{ii} ($= \bar{u}_i \bar{u}_i - \bar{u}_i \bar{u}_i$):

$$\begin{aligned} \frac{\partial \tau_{ii}}{\partial t} = & \underbrace{\frac{\partial}{\partial x_j} \left\{ -(\bar{u}_i \bar{u}_i \bar{u}_j - \bar{u}_i \bar{u}_i \bar{u}_j) - 2(\bar{u}_j \bar{p} - \bar{u}_j \bar{p}) + \nu \left(\frac{\partial \bar{u}_i \bar{u}_i}{\partial x_j} - \frac{\partial \bar{u}_i \bar{u}_i}{\partial x_j} \right) + 2\tau_{ij} \bar{u}_i \right\}}_{\Gamma} \\ & - \underbrace{2\nu \left(\frac{\partial \bar{u}_i}{\partial x_j} \frac{\partial \bar{u}_i}{\partial x_j} - \frac{\partial \bar{u}_i}{\partial x_j} \frac{\partial \bar{u}_i}{\partial x_j} \right)}_{\varepsilon_\nu} - \underbrace{2\tau_{ij} \bar{S}_{ij}}_{\varepsilon_{SGS}}, \end{aligned} \quad (2.8)$$

where Γ is the redistribution term, and ε_ν and ε_{SGS} are the viscous and the subgrid-scale dissipation terms, respectively. Taking the volume average $\langle \rangle$ of the terms in (2.8) over the entire computational domain yields

$$\langle \tau_{ij} \bar{S}_{ij} \rangle = -\nu \langle \bar{\alpha}_{ij} \bar{\alpha}_{ij} - \bar{\alpha}_{ij} \bar{\alpha}_{ij} \rangle, \quad (2.9)$$

assuming the volume averages of the redistribution term and the time variation of τ_{ii} are negligible (Piomelli *et al.* 1996; da Silva & Metais 2002; Park *et al.* 2006). The relationship in (2.9) was referred to as the “global equilibrium” between the viscous dissipation and the subgrid-scale dissipation (Park *et al.* 2006; da Silva & Metais 2002). da Silva & Metais (2002) and Park *et al.* (2006) found that the equilibrium between the viscous and subgrid-scale dissipation is only observed “globally” (not locally).

Replacing τ_{ij} in (2.9) with (2.6) results in

$$C_v = \frac{\nu}{2} \cdot \frac{(\gamma - 1) \langle \bar{\alpha}_{ij} \bar{\alpha}_{ij} \rangle}{\langle \bar{\Pi} \bar{S}_{ij} \bar{S}_{ij} \rangle}, \quad (2.10)$$

where the following closure assumption has been made

$$\langle \bar{\alpha}_{ij} \bar{\alpha}_{ij} \rangle = \gamma \langle \bar{\alpha}_{ij} \bar{\alpha}_{ij} \rangle. \quad (2.11)$$

The model uses the following scale-invariance assumption:

$$\gamma = \frac{\langle \bar{\alpha}_{ij} \bar{\alpha}_{ij} \rangle}{\langle \bar{\alpha}_{ij} \bar{\alpha}_{ij} \rangle} = \kappa \frac{\langle \bar{\alpha}_{ij} \bar{\alpha}_{ij} \rangle}{\langle \tilde{\alpha}_{ij} \tilde{\alpha}_{ij} \rangle} \approx \kappa^2 \frac{\langle \tilde{\alpha}_{ij} \tilde{\alpha}_{ij} \rangle}{\langle \hat{\alpha}_{ij} \hat{\alpha}_{ij} \rangle}, \quad (2.12)$$

where κ is another unknown parameter to be determined together with γ . $\tilde{\alpha}_{ij}$ and $\hat{\alpha}_{ij}$ are the first- and second-level test-filtered tensors, respectively, and $\tilde{\Delta} = 2\bar{\Delta}$ and $\hat{\Delta} = 2\tilde{\Delta}$ are assumed. From (2.12), κ and γ are readily obtained as follows:

$$\kappa = \frac{\langle \hat{\alpha}_{ij} \hat{\alpha}_{ij} \rangle \langle \bar{\alpha}_{ij} \bar{\alpha}_{ij} \rangle}{\langle \tilde{\alpha}_{ij} \tilde{\alpha}_{ij} \rangle^2}, \quad \gamma = \frac{\langle \hat{\alpha}_{ij} \hat{\alpha}_{ij} \rangle \langle \bar{\alpha}_{ij} \bar{\alpha}_{ij} \rangle^2}{\langle \tilde{\alpha}_{ij} \tilde{\alpha}_{ij} \rangle^3}. \quad (2.13)$$

Equations (2.10) and (2.13) complete the model with two-level test filters. In this approach, the model coefficient is globally constant in space but varies in time.

3. New dynamic model with a single test filter

In the proposed model, we start with the test-filtered incompressible Navier-Stokes and continuity equations:

$$\frac{\partial \tilde{u}_i}{\partial t} = -\frac{\partial \tilde{u}_i \tilde{u}_j}{\partial x_j} - \frac{\partial \tilde{p}}{\partial x_i} + \nu \frac{\partial^2 \tilde{u}_i}{\partial x_j \partial x_j} - \frac{\partial T_{ij}}{\partial x_j}, \quad (3.1)$$

$$\frac{\partial \tilde{u}_i}{\partial x_i} = 0, \quad (3.2)$$

where $\tilde{(\cdot)}$ denotes $\hat{(\cdot)}$ and $T_{ij} = \tilde{u}_i \tilde{u}_j - \tilde{u}_i \tilde{u}_j$.

The test-filter-level large-scale turbulent kinetic energy equation is

$$\frac{\partial \tilde{u}_i \tilde{u}_i}{\partial t} = \frac{\partial}{\partial x_j} \left\{ -\tilde{u}_i \tilde{u}_i \tilde{u}_j - 2\tilde{u}_j \tilde{p} + \nu \frac{\partial \tilde{u}_i \tilde{u}_i}{\partial x_j} - 2T_{ij} \tilde{u}_i \right\} - 2\nu \frac{\partial \tilde{u}_i}{\partial x_j} \frac{\partial \tilde{u}_i}{\partial x_j} + 2T_{ij} \tilde{S}_{ij}. \quad (3.3)$$

Subtracting (3.3) from the test-filtered total kinetic energy equation results in a transport equation for T_{ii} :

$$\begin{aligned} \frac{\partial T_{ii}}{\partial t} = & \frac{\partial}{\partial x_j} \left\{ -(\tilde{u}_i \tilde{u}_i \tilde{u}_j - \tilde{u}_i \tilde{u}_i \tilde{u}_j) - 2(\tilde{u}_j \tilde{p} - \tilde{u}_j \tilde{p}) + \nu \left(\frac{\partial \tilde{u}_i \tilde{u}_i}{\partial x_j} - \frac{\partial \tilde{u}_i \tilde{u}_i}{\partial x_j} \right) + 2T_{ij} \tilde{u}_i \right\} \\ & - 2\nu \left(\frac{\partial \tilde{u}_i}{\partial x_j} \frac{\partial \tilde{u}_i}{\partial x_j} - \frac{\partial \tilde{u}_i}{\partial x_j} \frac{\partial \tilde{u}_i}{\partial x_j} \right) - 2T_{ij} \tilde{S}_{ij}. \end{aligned} \quad (3.4)$$

By subtracting test-filtered (2.8) from (3.4), one finally obtains a transport equation for L_{ii} ($= T_{ii} - \hat{\tau}_{ii}$)

$$\begin{aligned} \frac{\partial L_{ii}}{\partial t} = & \frac{\partial}{\partial x_j} \left\{ -(\widehat{\bar{u}_i \bar{u}_i \bar{u}_j} - \bar{u}_i \bar{u}_i \bar{u}_j) - 2(\widehat{\bar{u}_j \bar{p}} - \bar{u}_j \bar{p}) + \nu \left(\frac{\partial \widehat{\bar{u}_i \bar{u}_i}}{\partial x_j} - \frac{\partial \bar{u}_i \bar{u}_i}{\partial x_j} \right) - 2(\widehat{\bar{\tau}_{ij} \bar{u}_i} - T_{ij} \bar{u}_i) \right\} \\ & - 2\nu \left(\frac{\partial \widehat{\bar{u}_i}}{\partial x_j} \frac{\partial \widehat{\bar{u}_i}}{\partial x_j} - \frac{\partial \bar{u}_i}{\partial x_j} \frac{\partial \bar{u}_i}{\partial x_j} \right) + 2(\widehat{\bar{\tau}_{ij} \bar{S}_{ij}} - T_{ij} \bar{S}_{ij}). \end{aligned} \quad (3.5)$$

Taking the volume average of (3.5) assuming “global equilibrium” finally results in

$$C_v = -\frac{\nu}{2} \cdot \frac{\langle \widehat{\bar{\alpha}_{ij} \bar{\alpha}_{ij}} - \tilde{\alpha}_{ij} \tilde{\alpha}_{ij} \rangle}{\langle \widehat{\bar{\Pi} \bar{S}_{ij} \bar{S}_{ij}} - \tilde{\Pi} \tilde{S}_{ij} \tilde{S}_{ij} \rangle}, \quad (3.6)$$

where the subgrid-scale quantities $\overline{(\cdot)}$ are defined in (2.7) and

$$\begin{aligned} T_{ij} - \frac{1}{3} T_{kk} \delta_{ij} &= -2C_v \tilde{\Pi} \tilde{S}_{ij}, \\ \tilde{\Pi} &= \sqrt{\frac{\tilde{B}_\beta}{\tilde{\alpha}_{kl} \tilde{\alpha}_{kl}}}, \\ \tilde{\beta}_\beta &= \tilde{\beta}_{11} \tilde{\beta}_{22} - \tilde{\beta}_{12} \tilde{\beta}_{12} + \tilde{\beta}_{11} \tilde{\beta}_{33} - \tilde{\beta}_{13} \tilde{\beta}_{13} + \tilde{\beta}_{22} \tilde{\beta}_{33} - \tilde{\beta}_{23} \tilde{\beta}_{23}, \\ \tilde{\beta}_{ij} &= \sum_{m=1}^3 \tilde{\Delta}_m^2 \tilde{\alpha}_{mi} \tilde{\alpha}_{mj}, \\ \tilde{\alpha}_{ij} &= \frac{\partial \tilde{u}_j}{\partial x_i}. \end{aligned} \quad (3.7)$$

The present model coefficient is dynamically determined from the instantaneous flow field and computational resolution by utilizing only a single-level test filter.

Figure 1 shows the temporal evolution of the model coefficient predicted by (3.6) for turbulent channel flow at $Re_\tau = 395$ after the flow has reached a statistically steady state. The temporal variation of the model coefficient is mild and the mean value of the coefficient is approximately 0.05, which differs from the value of 0.07 proposed by Vreman (2004) for channel flow and mixing layer simulations. The present dynamic model shows favorable agreement with the direct numerical simulation results of Moser *et al.* (1999) (see section 4.1 for details).

The present model shares the important features of the original Vreman model (Vreman 2004) and the dynamic model of Park *et al.* (2006). Even with the spatially constant model coefficient, the model predicts zero eddy viscosity in regions where the vanishing eddy viscosity is theoretically expected. For example, figure 2a shows the instantaneous spanwise vorticity contours of the flow over a circular cylinder. The flow configuration consists of a variety of different flow regimes such as laminar uniform flow (Ω_l), laminar boundary layer ($\partial\Omega_w$), and turbulent wake (Ω_t). The present model predicts vanishing

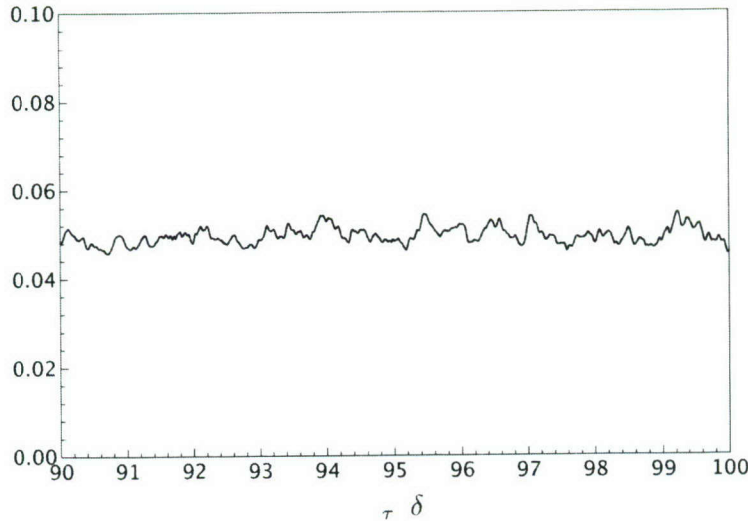


FIGURE 1. Temporal evolution of C_v predicted by the present dynamic procedure for turbulent channel flow at $Re_\tau = 395$.

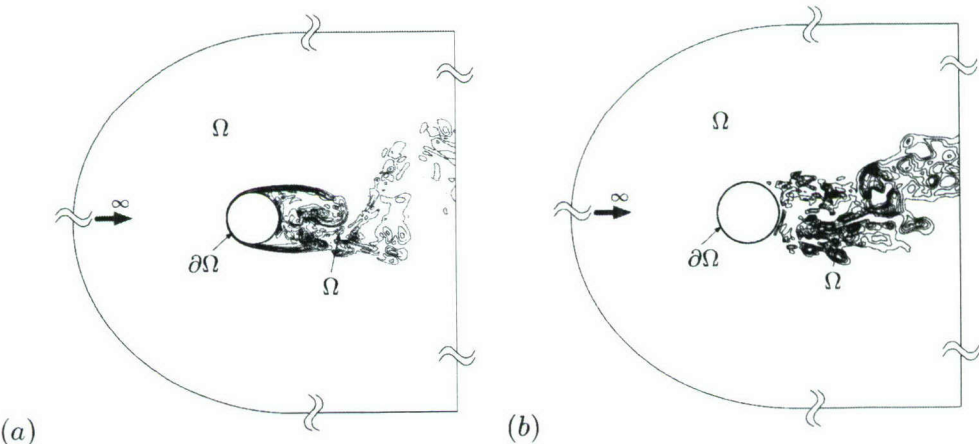


FIGURE 2. Contour plots of (a) the instantaneous spanwise vorticity and (b) the ratio of eddy viscosity to molecular viscosity ν_T/ν predicted by large-eddy simulation with the present dynamic model in the circular cylinder flow at $Re_D = 3900$. 20 contour levels in the range of $-20 \sim 20$, and $0.5 \sim 5$ are shown in (a) and (b), respectively. Ω_l , Ω_t , and $\partial\Omega_w$ represent laminar uniform, turbulent wake, and boundary layer flow regimes, respectively.

eddy viscosity in the regions of laminar flow (Ω_l and $\partial\Omega_w$) as shown in figure 2b. The large-eddy simulation of circular cylinder flow is discussed in detail in section 4.2.

Besides the advantage of utilizing only a single-level test filter, which improves the applicability of the model for complex flow configurations (especially with unstructured grid topology where defining the second-level test filter is not straightforward), the present volume-averaging process in (3.6) obviates a possibility of obtaining different model coefficients when two different computational domains that contain the same turbulence flow field but different laminar shear flow regions are employed. This is because both the viscous dissipation ($\nu(\widehat{\alpha_{ij}\alpha_{ij}} - \widetilde{\alpha_{ij}\alpha_{ij}})$) and the subgrid-scale dissipation ($\widehat{\Pi\tilde{S}_{ij}\tilde{S}_{ij}} - \widetilde{\Pi\tilde{S}_{ij}\tilde{S}_{ij}}$)

Re_τ	L_x	L_y	L_z	N_x	N_y	N_z	Δx^+	Δy_{min}^+	Δz^+
590	$2\pi\delta$	2δ	$\pi\delta$	64	97	64	57	0.59	29
395	$2\pi\delta$	2δ	$\frac{2}{3}\pi\delta$	48	65	48	48	0.95	18

TABLE 1. Grid parameters for large-eddy simulation of turbulent channel flows. L_x , L_y , and L_z are the streamwise, vertical, and spanwise domain sizes, respectively. $N_{x(y,z)}$ and $\Delta x(y,z)^+$ are the number of mesh points and the resolution in wall units, respectively.

in (3.6) vanish in the laminar flow region. Therefore, in the present method, the regions where both the subgrid-scale dissipation and the viscous dissipation vanish are naturally excluded from the averaging process in (3.6). In the dynamic model of Park *et al.* (2006), the influence of the computational domain size in the volume-averaging procedure is controlled by γ in (2.10).

4. Results and discussion

4.1. Large-eddy simulation of turbulent channel flow

Turbulent flow through a plane channel has been widely considered as a benchmark for validating turbulence models. Reynolds numbers of 590 and 395 based on the channel half height δ and friction velocity u_τ are considered. Large-eddy simulation results with three different Vreman-type closures including the present dynamic model and the dynamic Smagorinsky model (Germano *et al.* 1991) with Lilly (1992)'s modification are compared with the direct numerical simulation results of Moser *et al.* (1999). The computational parameters for large-eddy simulations at the two different Reynolds numbers are summarized in table 1. For the simulation at $Re_\tau = 590$, a second-order finite-volume solver (Mahesh *et al.* 2006) on a collocated grid arrangement of the primary variables is employed, while a second-order finite-difference solver (Templeton *et al.* 2006) on a staggered grid is used in the case of $Re_\tau = 395$.

In figure 3, the profiles of the mean streamwise velocity and rms velocity fluctuations at $Re_\tau = 590$ obtained using the present dynamic model, the dynamic model of Park *et al.*, the Vreman model with a fixed coefficient of 0.07, and the dynamic Smagorinsky model are compared with the direct numerical simulation data of Moser *et al.* (1999). The time-averaged model coefficients for the present channel flow are much smaller than the coefficient suggested by Vreman (2004) (0.07), and are 0.010 and 0.008 in the present dynamic model and Park *et al.*'s dynamic model, respectively. The present dynamic model (solid line) and the dynamic model of Park *et al.* (dashed line) predict similar results. The collocated grid method used in the present simulation requires finer resolution in the spanwise direction to predict similar results predicted by the staggered grid approach (Ham & Iaccarino 2004). The present and Park *et al.*'s dynamic models predict superior results to those obtained with the Vreman model (chain-dotted line) with the coefficient of 0.07, which is not optimal in the present simulation. The present results are comparable or superior to those obtained with the dynamic Smagorinsky model (dotted line). In the mean velocity profile, the upward shift in the log-layer is a little bit smaller than that of the dynamic Smagorinsky model, while the Vreman model with a non-optimal model

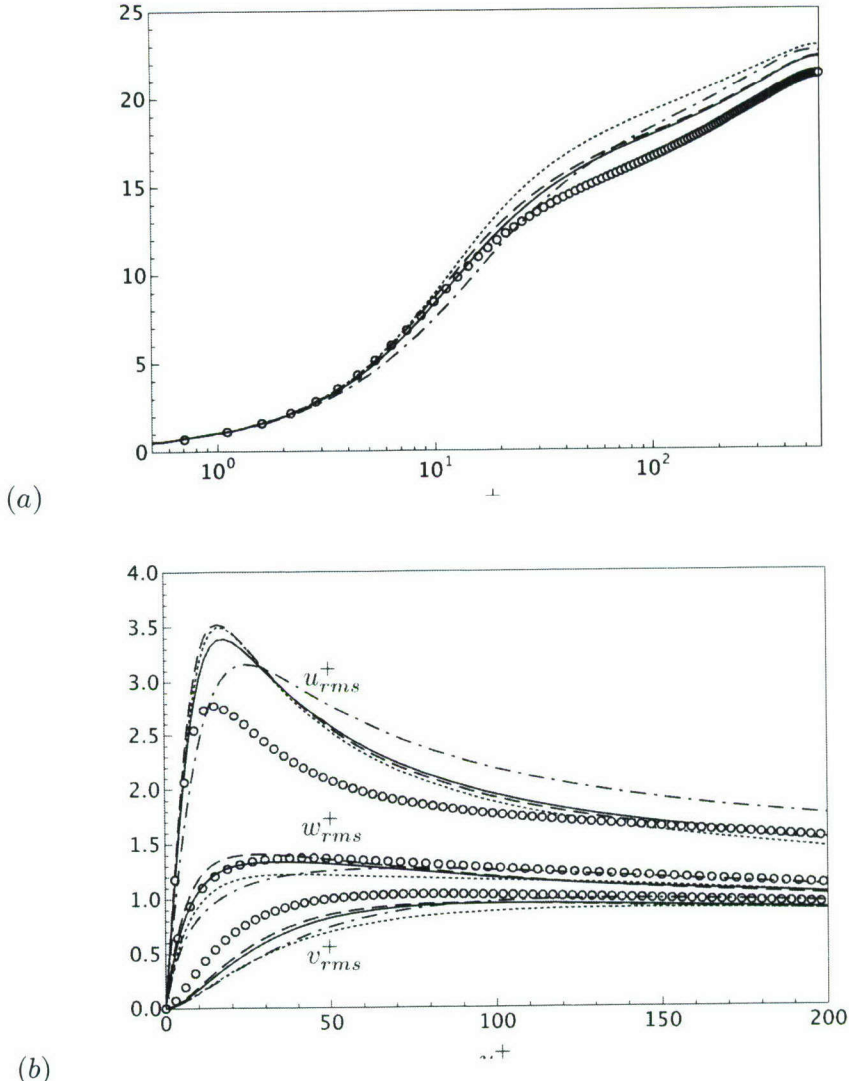


FIGURE 3. Profiles of (a) the mean streamwise velocity and (b) rms velocity fluctuations in turbulent channel flow at $Re_\tau = 590$. Solid line, the present dynamic model; dashed line, dynamic model of Park *et al.*; dotted line, dynamic Smagorinsky model; chain-dotted line, Vreman model with $C_v = 0.07$; symbol, direct numerical simulation (Moser *et al.* 1999).

coefficient ($C_v = 0.07$) predicts deficiency both in the mean streamwise velocity and rms velocity fluctuations, which are under-predicted in the overlap layer.

The time-averaged model coefficients for the channel flow at $Re_\tau = 395$ are approximately 0.05 in both the present dynamic model and the dynamic model of Park *et al.* Also at this Reynolds number, the present dynamic and Park *et al.*'s dynamic models are slightly superior to the dynamic Smagorinsky model in predicting the mean and turbulence statistics provided by the direct numerical simulation of Moser *et al.* (1999).

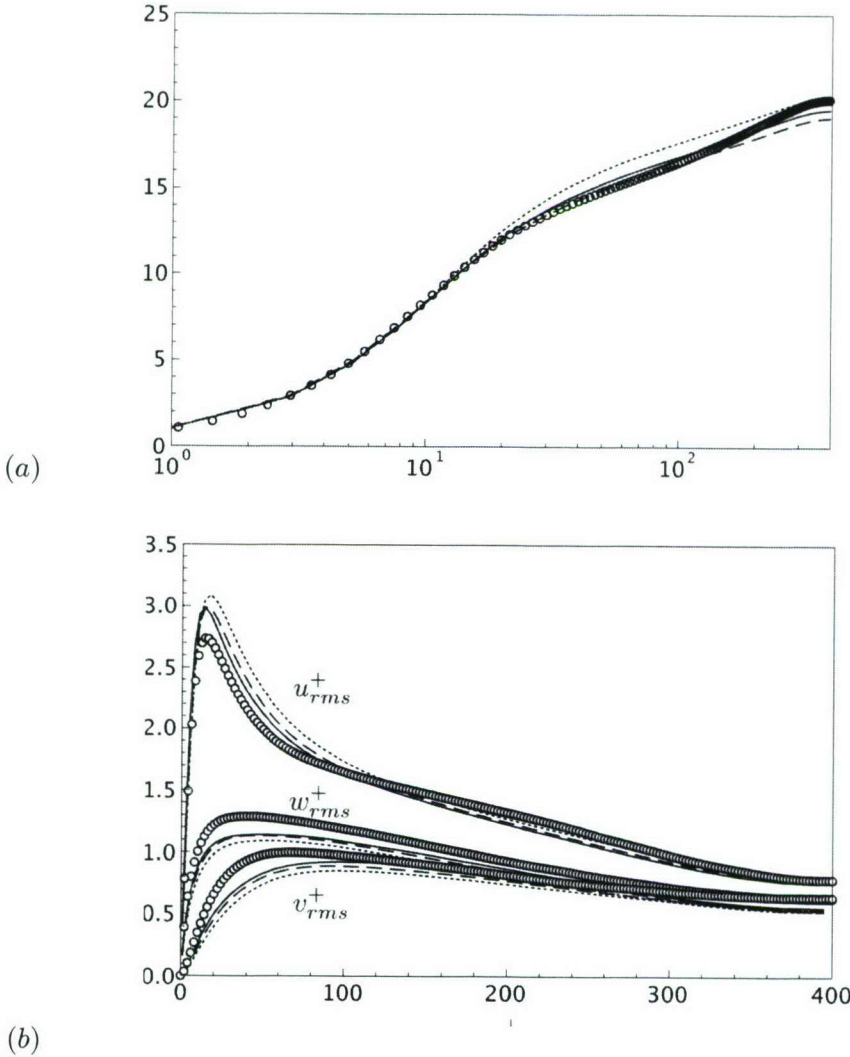


FIGURE 4. Profiles of (a) the mean streamwise velocity and (b) rms velocity fluctuations in turbulent channel flow at $Re_\tau = 395$. Solid line, the present dynamic model; dashed line, dynamic model of Park *et al.*; dotted line, dynamic Smagorinsky model; symbol, direct numerical simulation (Moser *et al.* 1999).

4.2. Large-eddy simulation of flow over a circular cylinder

The effectiveness of the present dynamic model is further assessed in the large-eddy simulation of flow over a circular cylinder at $Re_D = 3900$. The circular cylinder flow consists of a variety of flow regimes including laminar uniform flow, laminar boundary layer, laminar shear layer, transition, and turbulent wake. Therefore, it is an excellent benchmark for assessing the predictive capability of the proposed subgrid-scale model. Results predicted by the present dynamic model are compared with those predicted by the large-eddy simulation performed with the dynamic Smagorinsky model and a high-order

L_x	L_y	L_z	N_θ	N_z	$N_{BL}(\theta = 90^\circ)$	$N_{BL}(\theta = 170^\circ)$	N_{total}
$-30D \sim 20D$	$-30D \sim 30D$	πD	300	65	24	13	7,543,680

TABLE 2. Grid parameters for cylinder flow simulation at $Re_D = 3900$. L_x , L_y , and L_z are the streamwise, vertical, and spanwise domain sizes, respectively. N_θ , N_z , and N_{BL} are the numbers of mesh points in the circumferential and spanwise directions and in the boundary layer, respectively. N_{total} denotes the total number of mesh points.

	\bar{C}_D	$C_{L_{rms}}$	$-C_{pb}$	St
LES with DM1	1.01	0.12	0.92	0.211
LES with DSM*	1.04	.	0.94	0.210
Experiments	$0.99 \pm 0.05^\dagger$	$0.1 \pm 0.05^\dagger$	$0.88 \pm 0.05^\dagger$	$0.215 \pm 0.05^\ddagger$

TABLE 3. Summary of cylinder flow computations at $Re_D = 3900$. \bar{C}_D , $C_{L_{rms}}$, $-C_{pb}$, and St are the mean-drag, rms-lift, base-pressure coefficients and the Strouhal number, respectively. DM1 and DSM denote the present dynamic model and the dynamic Smagorinsky model, respectively. *Kravchenko & Moin (2000), [†]Norberg (1987), and [‡]Ong & Wallace (1996).

numerical scheme (B-spline method; Kravchenko & Moin 2000) and experimental data (Norberg 1987; Ong & Wallace 1996). Grid parameters used in the present simulation are summarized in table 2. The numerical method is a second-order finite-volume method and an unstructured grid is employed (Ham & Iaccarino 2004). The total number of grid points is similar to those employed in other previous large-eddy simulations performed with a second-order finite-difference method (Kim & Choi 2005; Park *et al.* 2006).

As shown in figure 2, the present model predicts eddy-viscosity distribution that is qualitatively expected from the physical characteristics of the flow (figure 2). High levels of eddy viscosity occur in the turbulent near wake. On the other hand, Beaudan & Moin (1994) found, with a constant-coefficient Smagorinsky model, that the largest mean eddy viscosity is generated in the separated shear layers that are laminar at $Re_D = 3900$. In the simulation with the present dynamic model, the peak ratio of the eddy viscosity to the molecular viscosity is not greater than 5 (figure 2).

The global flow quantities such as the drag, rms-lift, base pressure coefficients, and the Strouhal number are compared with numerical (Kravchenko & Moin 2000) and experimental data (Norberg 1987; Ong & Wallace 1996) and are summarized in table 3. In general, the present simulation results are in favorable agreement with the other numerical and experimental data.

The profiles of the mean streamwise velocity and streamwise velocity fluctuations obtained in three different near-wake locations are compared with the numerical data of Kravchenko & Moin (2000) in figure 5. The present large-eddy simulation with the dynamic model performs well and predicted comparable results to those predicted by Kravchenko & Moin (2000) with the dynamic Smagorinsky model. However, it is worth

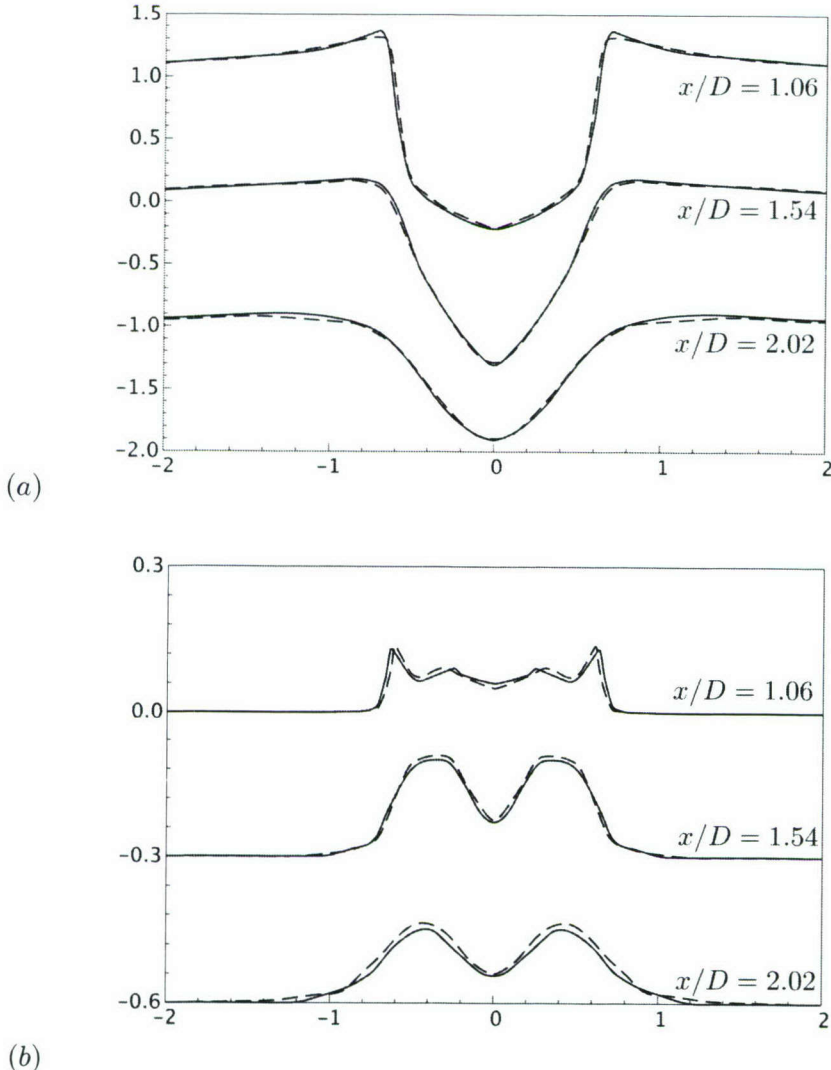


FIGURE 5. Profiles of (a) the mean streamwise velocity and (b) streamwise-velocity fluctuations at three locations in the wake of a circular cylinder at $Re_D = 3900$. Solid line, large-eddy simulation with the present dynamic model; dashed line, large-eddy simulation with the dynamic Smagorinsky model (Kravchenko & Moin 2000).

noting that, in the large-eddy simulation of Kravchenko & Moin (2000), it was necessary to discard negative model coefficients by ad hoc clipping operations for numerical stability (Kravchenko & Moin 1998).

5. Summary

A dynamic procedure for closure of the subgrid-scale model developed by Vreman (2004) using a single-level test filter has been proposed. The dynamic procedure of determining model coefficient is based on the “global equilibrium” between the subgrid-scale

dissipation and the viscous dissipation as utilized by Park *et al.* (2006). Like the fixed-coefficient (Vreman 2004) and dynamic-coefficient (Park *et al.* 2006) Vreman models, the present model predicts zero eddy-viscosity in regions where the vanishing eddy viscosity is theoretically expected. In contrast to the dynamic procedure by Park *et al.* (2006), which employs two-level test filters, the present model necessitates only a single-level test filter, and therefore is more suitable for large-eddy simulation in complex geometries. The present model is not more complicated than the dynamic Smagorinsky model in implementation and does not require any ad hoc spatial and temporal averaging or clipping of the model coefficient for numerical stabilization. In addition, the computational cost is not more expensive than that of the dynamic Smagorinsky model. The present dynamic procedure has been found quite effective in determining the model coefficient and predicted excellent results in large-eddy simulations of turbulent channel flow and flow over a circular cylinder.

Acknowledgments

The authors would like to thank Professor Haecheon Choi for allowing us to access the preprint of Park *et al.* [Phys. Fluids **18**, 125109 (2006)].

REFERENCES

BEAUDAN, P. & MOIN, P. 1994 Numerical experiments on the flow past a circular cylinder at sub-critical Reynolds number. Report TF-62. Department of Mechanical Engineering, Stanford University, Stanford, California.

DA SILVA, C. B. & METAIS, O. 2002 On the influence of coherent structures upon interscale interaction in turbulent plane jets. *Journal of Fluid Mechanics* **473**, 103–145.

GERMANO, M., PIOMELLI, U., MOIN, P. & CABOT, W. H. 1991 A dynamic subgrid-scale eddy-viscosity model. *Physics of Fluids A* **3** (7), 1760–1765.

GHOSAL, S., LUND, T. S., MOIN, P. & AKSELVOLL, K. 1994 A dynamic localization model for large-eddy simulation of turbulent flows. *Journal of Fluid Mechanics* **282**, 1–27.

HAM, F. & IACCARINO, G. 2004 Energy conservation in collocated discretization schemes on unstructured meshes. Annual Research Briefs, 3–14, Center for Turbulence Research, Stanford, California.

KIM, J. & CHOI, H. 2005 Distributed forcing of flow over a circular cylinder. *Physics of Fluids* **17**, 033103.

KRAVCHENKO, A. G. & MOIN, P. 1998 B-spline methods and zonal grids for numerical simulations of turbulent flows. Report TF-73. Department of Mechanical Engineering, Stanford University, Stanford, California.

KRAVCHENKO, A. G. & MOIN, P. 2000 Numerical studies of flow over a circular cylinder at $Re_D = 3900$. *Physics of Fluids* **12** (2), 403–417.

LILLY, D. K. 1992 A proposed modification of the Germano subgrid-scale closure model. *Physics of Fluids A*, **4** (3), 633–635.

MAHESH, K., CONSTANTINESCU, G., APTE, S., IACCARINO, G., HAM, F. & MOIN, P. 2006 Large-eddy simulation of reacting turbulent flows in complex geometries. *Journal of Applied Mechanics* **73**, 374–381.

MENEVEAU, C., LUND, T. S. & CABOT, W. H. 1996 A Lagrangian dynamic subgrid-scale model of turbulence. *Journal of Fluid Mechanics* **319**, 233–242.

MOIN, P. 2002 Advances in large eddy simulation methodology for complex flows. *International Journal of Heat and Fluid Flow* **23**, 710–720.

MOSER, R. D., KIM, J. & MANSOUR, N. N. 1999 Direct numerical simulation of turbulent channel flow up to $Re_\tau=590$. *Physics of Fluids* **11** (4), 943–945.

NORBERG, C. 1987 Effects of Reynolds number and a low-intensity freestream turbulence on the flow around a circular cylinder. Publication 87/2. Department of Applied Thermodynamics and Fluid Mechanics, Chalmers University of Technology, Sweden.

ONG, L. & WALLACE, J. 1996 The velocity field of the turbulent very near wake of a circular cylinder. *Experiments in Fluids* **20**, 441–453.

PARK, N., LEE, S., LEE, J. & CHOI, H. 2006 A dynamic subgrid-scale eddy-viscosity model with a global model coefficient. *Physics of Fluids* **18**, 125109.

PIOMELLI, U., YU, Y. & ADRIAN, R. J. 1996 Subgrid-scale energy transfer and near-wall turbulence structure. *Physics of Fluids* **8**(1), 215–224.

TEMPLETON, J. A., WANG, M. & MOIN, P. 2006 An efficient wall model for large-eddy simulation based on optimal control theory. *Physics of Fluids* **18**, 025101.

VREMAN, A. W. 2004 An eddy-viscosity subgrid-scale model for turbulent shear flow: algebraic theory and applications. *Physics of Fluids* **16** (10), 3670–3681.

YOU, D., MITTAL, R., WANG, M. & MOIN, P. 2004 Computational methodology for large-eddy simulation of tip-clearance flows. *AIAA Journal* **42** (2), 271–279.

Three-dimensional wall filtering formulation for large-eddy simulation

By M. Shoeybi AND J. A. Templeton†

1. Motivation and objectives

Large-eddy simulation (LES) is a method for computing the solution of the spatially low-pass filtered Navier-Stokes equations. In most formulations, the filtering operation is not taken to pass through boundaries. Instead, the wall-normal filter width approaches zero at walls to allow the application of the no-slip condition (e.g., Carati 2001; Sagaut 2002). However, this introduces commutation error and adds modeling complexity due to filter anisotropy.

One approach to reduce this error is to use one-sided commuting filters near the wall which have less commutation error than the numerical differentiation error in the simulation (Vasilyev *et al.* 1998). The drawback of one-sided filters is that they require slip velocities at the wall. Prescribing slip conditions both on (Iovieno *et al.* 2004; Borggaard & Illiescu 2006) and off (Baggett 1997) the wall has proven quite challenging.

A recently proposed alternative involves filtering the wall in conjunction with the optimal LES technique (Moser *et al.* 2005). This method has thus far been applied only to channel flow, allowing periodic conditions to be used in the wall-normal directions. Recently, Templeton & Shoeybi (2006) proposed an approach based on filtering the solution over an infinite domain for 1-D problems. This allows the LES equations, including boundary conditions, to be precisely defined without any commutation error.

This work considers formulating the LES problem in such a way that the filtering operation can take place through the wall. This forms a fully consistent LES system that has compact support, precise boundary conditions, and known forcing terms. Thus, the LES equations can be solved without any ambiguity concerning the boundary conditions and filter definition. To clarify the presentation in three dimensions, we will first briefly review the work of Templeton & Shoeybi (2006) for the 1-D Burgers' equation. This method will then be extended to the incompressible Navier-Stokes equations.

2. 1-D formulation for the Burgers' equation

The key idea of this work is to alter the formulation of the dynamical equations such that they are consistent with wall-normal filtering. Such a formulation is accomplished by considering a limiting process of solutions on an infinite domain with an appropriate forcing term that ensures the solutions have compact support. This will enable LES to be constructed using constant width filters. In addition, the proper boundary conditions will be determined and can be applied precisely.

Consider the Burgers' equation with Dirichlet boundary conditions for the dependent variable, u ,

$$\frac{\partial u}{\partial t} + \frac{1}{2} \frac{\partial u^2}{\partial x} - \nu \frac{\partial^2 u}{\partial x^2} = f \quad \forall x \in (0, L), \quad (2.1)$$

† Presently at Sandia National Laboratories, Livermore, CA

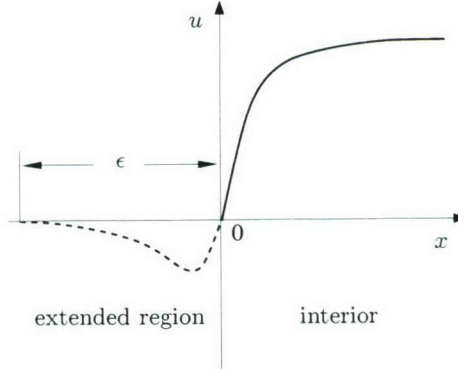


FIGURE 1. Constructed solution schematic.

where ν is the viscosity and f is an arbitrary source term. The method consists of constructing a family of solutions for $\epsilon > 0$ such that each solution has its domain of support on $[-\epsilon, L + \epsilon]$ (see figure 1). We begin by fixing $\epsilon > 0$, and indexing the solutions for each ϵ by u_ϵ . On the domain $(0, L)$, the solution has initial conditions $u_\epsilon(x, t) = u(x, 0) \in C^2(x)$ and is subject to a source term, f , both of which are independent of ϵ . At $x = 0$ and L , the solution is constrained to be zero. For $x \leq -\epsilon$ and $x \geq L + \epsilon$, the initial conditions and source term are set to zero. In order to make all of these constraints consistent, the solution in the regions $[-\epsilon, 0]$ and $[L, L + \epsilon]$ will have a specified form enforced by the, as yet undefined, source term f_ϵ . In the remainder of this section, the method will be formulated only at the lower boundary to simplify the presentation.

The solution imposed between $-\epsilon$ and zero must be C^2 in space and satisfy the constraints that it matches the value, first derivative, and second derivative of u_ϵ at $x = 0$ and $x = -\epsilon$. This results in six constraints, indicating that u_ϵ can be represented by a fifth-order polynomial. At $x = -\epsilon$ the constraints are such that u , $\frac{\partial u}{\partial x}$ and $\frac{\partial^2 u}{\partial x^2}$ are all zero, so it is useful to write the polynomial as a function of $x^* = x + \epsilon$. This makes the first three coefficients zero, with the resulting polynomial being

$$u_\epsilon(x, t) = ax^{*3} + bx^{*4} + cx^{*5} \quad \forall x^* \in [0, \epsilon]. \quad (2.2)$$

The other three coefficients can be uniquely determined such that the first two derivatives exist and are continuous at $x = 0$. This gives three expressions for a , b , and c in terms of ϵ , $\frac{\partial u}{\partial x}|_{x=0}^+$ and $\frac{\partial^2 u}{\partial x^2}|_{x=0}^+$. The source term f_ϵ is chosen such that u_ϵ obeys the prescribed solution (2.2). This results in f_ϵ being a ninth-order polynomial in x . Using $\tilde{x} = x^*/\epsilon$, where $\tilde{x} \in [0, 1]$, the leading order terms in ϵ can be written as

$$f_\epsilon(x) = \frac{\nu}{\epsilon} (24\tilde{x} - 84\tilde{x}^2 + 60\tilde{x}^3) \frac{\partial u}{\partial x} \Big|_{x=0}^+ + \nu (-3\tilde{x} + 12\tilde{x}^2 - 10\tilde{x}^3) \frac{\partial^2 u}{\partial x^2} \Big|_{x=0}^+ + O(\epsilon). \quad (2.3)$$

2.1. Governing equations of the filtered solution

The exact solution u is spatially filtered to produce the LES solution, \hat{u} , which contains the large scales of the problem. In this work, the LES solution, like the exact solution, is defined on an infinite domain. This means that the interior domain, wall, and exterior domain can all be filtered directly. This eliminates commutation error between the filtering and differentiation operations because a homogenous filter is used. In addition, the LES boundary conditions are known by construction while the forcing term coming from the DNS boundary conditions can be determined analytically.

Proceeding directly, the LES velocity field is defined as

$$\hat{u}(x, t) = \int_{-\infty}^{\infty} u(x - y, t) G(y) dy, \forall x \in (-\infty, \infty). \quad (2.4)$$

Here, G is the filter kernel, which is spatially convolved with the exact solution. We require that G have compact support so that \hat{u} will as well. In this work, we will consider the filter to be a top-hat filter such that $G(y) = 1/2\Delta$ for $y \in [-\Delta, \Delta]$. However, it is important to note that any low-pass filter with compact support such that $\int_{-\infty}^{\infty} G(x) dx = 1$ and $\int_{-\infty}^{\infty} |G(x)| dx < \infty$ would be an appropriate filter in this formulation.

Unlike standard LES constructions, the domain of support of \hat{u} in this formulation is $[-\Delta, L + \Delta]$ instead of $[0, L]$. This property implies that when computationally solving for \hat{u} , the geometry must be extended. When performing such simulations, it will be necessary to prescribe boundary conditions. Given the above domain of support, it is clear that $\hat{u} = 0$ at $x = -\Delta$ and $L + \Delta$ (subsequently referred to as the LES boundaries), implying that Dirichlet conditions are appropriate. However, the continuity of $\frac{\partial \hat{u}}{\partial x}$ also implies that it too is zero at the LES boundaries. Thus, two boundary conditions, a Dirichlet and a Neumann, are valid at each boundary.

To derive the governing equations for the LES field, we will apply the filtering procedure to the equations governing u_{ϵ} and take the limit as $\epsilon \rightarrow 0$ to obtain

$$\frac{\partial \hat{u}}{\partial t} + \frac{1}{2} \frac{\partial \hat{u}^2}{\partial x} - \nu \frac{\partial^2 \hat{u}}{\partial x^2} = \hat{f} + \hat{f}_w. \quad (2.5)$$

The key step in formulating the LES equations is determining the filtered value of f_{ϵ} . This is done by simply filtering (2.3). Then the wall force, f_w , is defined to be $\lim_{\epsilon \rightarrow 0} \hat{f}_{\epsilon}$ and is given by

$$f_w(x) = -\frac{\nu}{2\Delta} \frac{\partial u}{\partial x} \Big|_{x=0}^+ \quad \forall x \in [-\Delta, \Delta]. \quad (2.6)$$

Using the top-hat filter kernel and applying the fundamental theorem of calculus, it can be rigorously shown that

$$\lim_{\epsilon \rightarrow 0} \frac{\partial^2 \hat{u}_{\epsilon}}{\partial x^2} \Big|_{x=-\Delta}^+ = \frac{1}{2\Delta} \frac{\partial u}{\partial x} \Big|_{x=0}^+. \quad (2.7)$$

When (2.7) is combined with (2.6), an expression for f_w is obtained:

$$f_w = -\nu(2\Delta G(x)) \frac{\partial^2 \hat{u}}{\partial x^2} \Big|_{x=-\Delta}^+. \quad (2.8)$$

This forcing makes the system with over-determined boundary conditions well posed by ensuring that $\hat{u}(x = -\Delta)$ always remains zero.

2.2. Results

Here we consider the stochastically forced Burgers' equation by using independent Gaussian random variables to provide the forcing at each DNS grid point. This forcing is changed at a rate of Δt_r , at which time a new set of independent random variables represent the force. In order to make the equations non-dimensional, $\sqrt{\sigma L}$ is used as the velocity scale where σ is the square root of the variance of the random variables. When performing LES computations, this noise is filtered to determine the source term \hat{f} . To

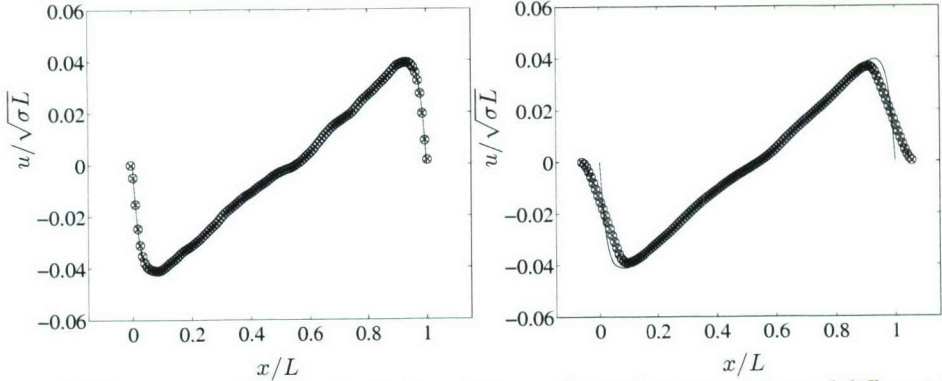


FIGURE 2. Time-averaged stochastically forced Burgers' equation, comparison of different filter widths with $\Delta/L = 0.0078125$ (left) and $\Delta/L = 0.0625$ (right): —, DNS; \circ , filtered DNS; \times , LES.

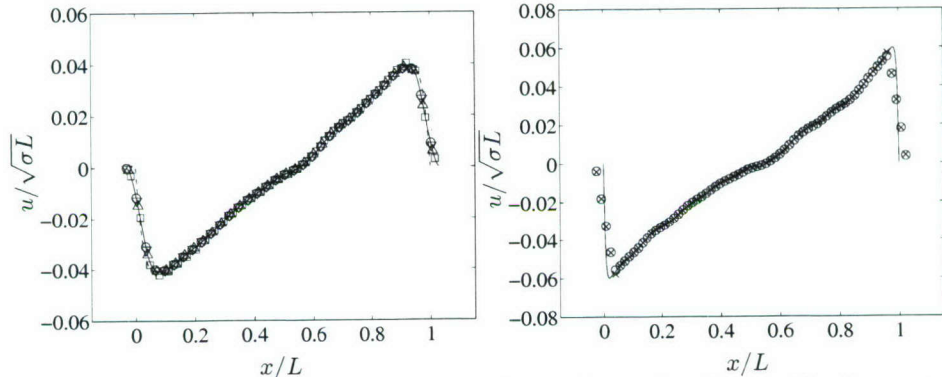


FIGURE 3. Time-averaged stochastically forced Burgers' equation. Left: grid refinement with $\Delta/L = 0.03125$: —, DNS; —, filtered DNS; \circ , LES with $\Delta x_{LES} = \Delta x_{DNS}$; ∇ , $\Delta x_{LES} = 2\Delta x_{DNS}$; \triangle , $\Delta x_{LES} = 4\Delta x_{DNS}$; \square , $\Delta x_{LES} = 8\Delta x_{DNS}$. Right: Reynolds number dependence for the case at $Re = 2000$ with $\Delta/L = 0.03125$: —, DNS; \circ , filtered DNS; \times , LES.

examine the effect of the proposed filtering treatment only, the DNS solution is used to provide the SGS stress directly. See Templeton & Shoeybi (2006) for further details.

Time-averaged velocity profiles are shown in figure 2 with $Re = 500$. In these simulations, 255 interior grid points were used in the DNS computation and the same resolution was retained for the LES. Filter widths of $\Delta = 0.00781L$ ($2\Delta x_{DNS}$) and $\Delta = 0.0625L$ ($16\Delta x_{DNS}$) are considered. These results indicate that the LES solution is able to accurately capture the filtered time-averaged velocity profile from the DNS solution. The effect of resolution and Reynolds number are shown in figure 3. To test the effect of resolution, the LES is computed on a wide range of grids, and the time-averaged velocity profiles are presented using $\Delta = 0.03125L$ ($8\Delta x_{DNS}$). All show good agreement with the filtered DNS solution, up to the ratio of Δx_{LES} to Δ being unity. To examine the Reynolds number dependence of the method, we consider a test case at $Re = 2000$ with a filter width of $\Delta = 0.03125L$ ($8\Delta x_{DNS}$) on a grid with $\Delta x_{LES} = 4\Delta x_{DNS}$. Thus, the method can be applied over a range of flow and numerical parameters.

3. 3-D formulation for incompressible Navier-Stokes equations

We next extend the previous formulation to the incompressible Navier-Stokes equations in three dimensions. Only pressure-driven 3-D plane periodic channel flow will be considered. The equations are non-dimensionalized using the channel half-height and friction velocity. The DNS domain is defined as $0 \leq x_1 < L_1$, $0 < x_2 < 2$ and $0 \leq x_3 < L_3$, and the flow is taken to be periodic in the x_1 and x_3 directions while no-slip walls bound the domain in the x_2 direction. The non-dimensionalized governing equations are

$$\frac{\partial u_i}{\partial t} + \frac{\partial u_i u_j}{\partial x_j} + \frac{\partial p}{\partial x_j} - \frac{1}{Re_\tau} \frac{\partial^2 u_i}{\partial x_j \partial x_j} = f_i, \quad (3.1)$$

$$\frac{\partial u_j}{\partial x_j} = 0, \quad (3.2)$$

where $f_1 = 1$ and $f_2 = f_3 = 0$.

To define the LES field, 3-D filters will be applied to the DNS solution. Filtering operations can pass through the periodic boundaries since the data outside those boundaries are available. This is not the case in the wall-normal direction, where no information is provided outside the DNS domain. Therefore, we extend the solution outside the DNS domain in the wall-normal directions such that (3.1) and (3.2) hold over all of \mathbf{R}^3 . Unlike the 1-D case, the pressure must be included in this extension in addition to the velocity field. The following sections describe this extension for the lower wall of the channel ($x_2 = 0$), with similar results holding for the upper wall.

3.1. Extension of the velocity and pressure fields

Analogously to the 1-D case, we begin by defining the solution for any fixed $\epsilon > 0$ as u_i^ϵ and p^ϵ . On the domain $x_2 \in (0, 2)$, the solution is identical to the DNS, denoted by u_i and p . For $-\infty < x_2 < -\epsilon$ and $2 + \epsilon < x_2 < \infty$, the pressure and velocities in the streamwise and spanwise directions are set to zero. In the rest of the domain, the dependent variables will be constructed such that they are C^2 for any $\epsilon > 0$. Using the coordinate transformation $x_2^* = x_2 + \epsilon$ for $x_2 \in [-\epsilon, 0]$, u_i^ϵ can be written as

$$u_i^\epsilon = a_i(x_1, x_3) x_2^{*3} + b_i(x_1, x_3) x_2^{*4} + c_i(x_1, x_3) x_2^{*5} \quad i = 1, 3, \quad x^* \in [0, \epsilon]. \quad (3.3)$$

Satisfying the three constraints at $x_2 = 0$ requires

$$\begin{aligned} a_i &= \frac{1}{2\epsilon} \frac{\partial^2 u_i}{\partial x_2^2} \bigg|_{x_2=0}^+ - \frac{4}{\epsilon^2} \frac{\partial u_i}{\partial x_2} \bigg|_{x_2=0}^+, \\ b_i &= -\frac{1}{\epsilon^2} \frac{\partial^2 u_i}{\partial x_2^2} \bigg|_{x_2=0}^+ + \frac{7}{\epsilon^3} \frac{\partial u_i}{\partial x_2} \bigg|_{x_2=0}^+, \\ c_i &= \frac{1}{2\epsilon^3} \frac{\partial^2 u_i}{\partial x_2^2} \bigg|_{x_2=0}^+ - \frac{3}{\epsilon^4} \frac{\partial u_i}{\partial x_2} \bigg|_{x_2=0}^+. \end{aligned}$$

In contrast, the wall-normal velocity field is extended to enforce continuity:

$$u_2^\epsilon = a_2(x_2^{*4} - \epsilon^4) + b_2(x_2^{*5} - \epsilon^5) + c_2(x_2^{*6} - \epsilon^6), \quad (3.4)$$

where

$$a_2 = -\frac{\frac{\partial a_1}{\partial x_1} + \frac{\partial a_3}{\partial x_3}}{4}, \quad b_2 = -\frac{\frac{\partial b_1}{\partial x_1} + \frac{\partial b_3}{\partial x_3}}{5}, \quad c_2 = -\frac{\frac{\partial c_1}{\partial x_1} + \frac{\partial c_3}{\partial x_3}}{6}.$$

Since u_1^ϵ and u_3^ϵ are C^2 at $x_2 = 0$, (3.3) and (3.4) can be used to take the derivatives of the wall-normal velocity at $x_2 = 0$ as

$$\begin{aligned}\frac{\partial u_2^\epsilon}{\partial x_2}\Big|_{x_2=0} &= -\frac{\partial u_1}{\partial x_1}\Big|_{x_2=0}^+ - \frac{\partial u_3}{\partial x_3}\Big|_{x_2=0}^+ = \frac{\partial u_2}{\partial x_2}\Big|_{x_2=0}^+, \\ \frac{\partial^2 u_2^\epsilon}{\partial x_2^2}\Big|_{x_2=0} &= -\frac{\partial^2 u_1}{\partial x_2 \partial x_1}\Big|_{x_2=0}^+ - \frac{\partial^2 u_3}{\partial x_2 \partial x_3}\Big|_{x_2=0}^+ = \frac{\partial^2 u_2}{\partial x_2^2}\Big|_{x_2=0}^+, \end{aligned}$$

showing the constructed wall-normal velocity field is C^2 at $x_2 = 0$.

As opposed to the streamwise and spanwise directions for which the solution and all the derivatives are zero at $x_2 = -\epsilon$, the wall-normal velocity u_2^ϵ is of the order of ϵ^2 . Since $\frac{\partial u_2^\epsilon}{\partial x_2}$, $\frac{\partial^2 u_2^\epsilon}{\partial x_2^2}$ vanish at $x_2 = -\epsilon$, we can define the u_2 velocity in the region $x_2 \in (-\infty, -\epsilon)$ to be independent of x_2 and to remain of the order of ϵ^2 everywhere on that region. As with the 1-D case, terms of the order ϵ^2 and higher will have no contribution to the LES equations in the limit $\epsilon \rightarrow 0$. This implies the LES solution has compact support even though the DNS for fixed $\epsilon > 0$ does not.

A similar expansion can be used to construct the pressure on the region $x_2 \in [-\epsilon, 0]$. Since the pressure in the Navier-Stokes equation is undetermined up to a constant, the polynomial expansion is written as

$$p^\epsilon = p^* - p_{ave}(t) = a_p x_2^{*3} + b_p x_2^{*4} + c_p x_2^{*5}, \quad (3.5)$$

where $p_{ave}(t)$ is an arbitrary constant and p^* is the singular pressure. Ensuring that p^ϵ is C^2 requires

$$\begin{aligned}a_p &= \frac{10}{\epsilon^3} p|_{x_2=0} - \frac{4}{\epsilon^2} \frac{\partial p}{\partial x_2}\Big|_{x_2=0}^+ + \frac{1}{2\epsilon} \frac{\partial^2 p}{\partial x_2^2}\Big|_{x_2=0}^+, \\ b_p &= -\frac{15}{\epsilon^4} p|_{x_2=0} + \frac{7}{\epsilon^3} \frac{\partial p}{\partial x_2}\Big|_{x_2=0}^+ - \frac{1}{\epsilon^2} \frac{\partial^2 p}{\partial x_2^2}\Big|_{x_2=0}^+, \\ c_p &= \frac{6}{\epsilon^5} p|_{x_2=0} - \frac{3}{\epsilon^4} \frac{\partial p}{\partial x_2}\Big|_{x_2=0}^+ + \frac{1}{2\epsilon^3} \frac{\partial^2 p}{\partial x_2^2}\Big|_{x_2=0}^+. \end{aligned}$$

3.2. Modified governing equations

To enforce the prescribed fields, an extra source term, \vec{f}^ϵ , is required on the right-hand side of the momentum equations. The forcing terms are determined by inserting the constructed velocity field into the governing equations and are active only in the region $x_2 \in [-\epsilon, 0]$. We decompose the resulting forcing term into two parts. The first part is a function of the DNS velocity field, $\vec{f}^{\epsilon,u}$, while the second part contains contributions from the DNS pressure, $\vec{f}^{\epsilon,p}$. For the streamwise and spanwise velocities, it is an eleventh-order polynomial in x_2 , which has leading-order terms in ϵ of

$$\begin{aligned}f_i^{\epsilon,u}(x_1, x_2, x_3) &= \epsilon^{-1} \frac{1}{Re_\tau} (24\tilde{x}_2 - 84\tilde{x}_2^2 + 60\tilde{x}_2^3) \frac{\partial u_i}{\partial x_2}\Big|_{x_2=0}^+ \\ &+ \frac{1}{Re_\tau} (-3\tilde{x}_2 + 12\tilde{x}_2^2 - 10\tilde{x}_2^3) \frac{\partial^2 u_i}{\partial x_2^2}\Big|_{x_2=0}^+ + O(\epsilon), \quad i = 1, 3 \end{aligned} \quad (3.6)$$

for the wall-parallel velocities and

$$f_2^{\epsilon,u}(x_1, x_2, x_3) = \frac{1}{Re_\tau} (12\tilde{x}_2^2 - 28\tilde{x}_2^3 + 15\tilde{x}_2^4) \frac{\partial^2 u_2}{\partial x_2^2} \Big|_{x_2=0}^+ + O(\epsilon) \quad (3.7)$$

for the wall-normal velocity, where $\tilde{x}_2 = \frac{x_2^*}{\epsilon} \in [0, 1]$. Similarly, $\vec{f}^{\epsilon,p}$ can be written as

$$f_i^{\epsilon,p}(x_1, x_2, x_3) = (10\tilde{x}_2^3 - 15\tilde{x}_2^4 + 6\tilde{x}_2^5) \frac{\partial p}{\partial x_i} \Big|_{x_2=0}^+ + O(\epsilon). \quad i = 1, 3 \quad (3.8)$$

and

$$\begin{aligned} f_2^{\epsilon,p}(x_1, x_2, x_3) &= \epsilon^{-1} (30\tilde{x}_2^2 - 60\tilde{x}_2^3 + 30\tilde{x}_2^4) p|_{x_2=0} \\ &+ (-12\tilde{x}_2^2 + 28\tilde{x}_2^3 - 15\tilde{x}_2^4) \frac{\partial p}{\partial x_2} \Big|_{x_2=0}^+ + O(\epsilon). \end{aligned} \quad (3.9)$$

From the modified momentum equation, we can derive a new pressure-Poisson equation consistent with the new formulation by taking the divergence of the momentum equations. The governing equations on the bounded spatial domain $x_2 \in [0, 2]$ are not subject to any changes, resulting in the same Poisson equation for pressure as the original equations. For $x_2 \in [-\epsilon, 0]$, the divergence of the added source term is present on the right-hand side of the pressure-Poisson equation:

$$\nabla^2 p = -\frac{\partial}{\partial x_i} \frac{\partial u_i^\epsilon u_j^\epsilon}{\partial x_j} + \vec{\nabla} \cdot \vec{f}^\epsilon. \quad (3.10)$$

Here we use the decomposition $\vec{f}^\epsilon = \vec{f}^{\epsilon,u} + \vec{f}^{\epsilon,p}$ to analyze the second term on the right-hand side of (3.10). By taking the wall-parallel derivatives of (3.6) and wall-normal derivative of (3.7), we see that

$$\vec{\nabla} \cdot \vec{f}^{\epsilon,u} = O(1), \quad \forall \epsilon > 0. \quad (3.11)$$

As we will see later, terms order one and higher in ϵ will have no contribution to the governing equations when the equations are filtered and $\epsilon \rightarrow 0$. However, the divergence of the pressure force, $\frac{\partial f_2^{\epsilon,p}}{\partial x_2}$, will be present and have contributions of orders ϵ^{-2} and ϵ^{-1} as

$$\vec{\nabla} \cdot \vec{f}^{\epsilon,p} = \delta_d(x_2, \epsilon) p \Big|_{x_2=0} + \epsilon^{-1} (-24\tilde{x}_2 + 84\tilde{x}_2^2 - 60\tilde{x}_2^3) \frac{\partial p}{\partial x_2} \Big|_{x_2=0}^+ + O(1). \quad (3.12)$$

where

$$\delta_d(x_2, \epsilon) = \epsilon^{-2} (60\tilde{x}_2 - 180\tilde{x}_2^2 + 120\tilde{x}_2^3). \quad (3.13)$$

3.3. Construction of the filtered equations

As in the 1-D case, we define the filtering procedure as the convolution of a state variable ϕ with a spatial filter kernel $G(x_1, x_2, x_3)$:

$$\hat{\phi}(\vec{x}, t) = \int_{-\infty}^{\infty} \int_{-\infty}^{\infty} \int_{-\infty}^{\infty} \phi(\vec{x} - \vec{y}, t) G(\vec{y}) d\vec{y}. \quad (3.14)$$

We require the filter to have compact support in physical space, and hence it can efficiently solve a discrete approximation to the problem. We limit the discussion here to

the top-hat filter $G(x_1, x_2, x_3) = G_1(x_1)G_2(x_2)G_3(x_3)$, where

$$G_i(x) = \begin{cases} \frac{1}{2\Delta_i} & -\Delta_i \leq x_i \leq \Delta_i \text{ for } i=1,2,3, \\ 0 & \text{otherwise} \end{cases} \quad (3.15)$$

although many of the results hold for 3-D extensions of higher-order B-spline filters (Templeton & Shoeybi 2006). For such a filter, the filtering operation reduces to

$$\hat{\phi}(\vec{x}, t) = \frac{1}{2\Delta_2} \int_{x_2 - \Delta_2}^{x_2 + \Delta_2} \tilde{\phi}(x_1, y_2, x_3, t) dy_2, \quad (3.16)$$

where

$$\tilde{\phi}(x_1, x_2, x_3, t) = \frac{1}{4\Delta_1\Delta_3} \int_{x_1 - \Delta_1}^{x_1 + \Delta_1} \int_{x_3 - \Delta_3}^{x_3 + \Delta_3} \phi(y_1, x_2, y_3, t) dy_1 dy_3. \quad (3.17)$$

To derive the LES equations, we first filter the Navier-Stokes equations for any $\epsilon > 0$:

$$\frac{\partial \hat{u}_i^\epsilon}{\partial t} + \frac{\partial \hat{u}_i^\epsilon u_j^\epsilon}{\partial x_j} + \frac{\partial \hat{p}^\epsilon}{\partial x_j} - \frac{1}{Re_\tau} \frac{\partial^2 \hat{u}_i^\epsilon}{\partial x_j \partial x_j} = \hat{f}_i + \hat{f}_i^{\epsilon,u} + \hat{f}_i^{\epsilon,p}, \quad (3.18)$$

$$\nabla^2 \hat{p}^\epsilon = -\frac{\partial}{\partial x_i} \frac{\partial \hat{u}_i^\epsilon u_j^\epsilon}{\partial x_j} + \vec{\nabla} \cdot \widehat{\vec{f}^{\epsilon,p}}. \quad (3.19)$$

Given the exact expression for the added source terms on the right-hand side of the momentum and Poisson equations, their filtered value when the filter kernel encompasses the region $x_2 \in [-\epsilon, 0]$ can be written as

$$\hat{f}_i^{\epsilon,u} = -\frac{1}{Re_\tau} G_2(x_2) \frac{\partial \tilde{u}_i}{\partial x_2} \Big|_{x_2=0}^+ + O(\epsilon) \quad i = 1, 3, \quad \hat{f}_2^{\epsilon,u} = O(\epsilon) \quad (3.20)$$

$$\hat{f}_2^{\epsilon,p} = G_2(x_2) \tilde{p} \Big|_{x_2=0} + O(\epsilon), \quad \hat{f}_i^{\epsilon,p} = O(\epsilon) \quad i = 1, 3 \quad (3.21)$$

and

$$\vec{\nabla} \cdot \widehat{\vec{f}^{\epsilon,p}} = G_2(x_2) \frac{\partial \tilde{p}}{\partial x_2} \Big|_{x_2=0}^+ + O(\epsilon). \quad (3.22)$$

Note that when the filter integrand contains the ϵ region in the x_2 direction, all the terms on the right-hand side of the governing equations will be bounded as $\epsilon \rightarrow 0$ except the first term on the right-hand side of (3.12), $\delta_d(x_2, \epsilon) p \Big|_{x_2=0}$, which varies with ϵ^{-2} . Although its filtered value vanishes when the filter encompasses the whole ϵ region, its contribution to the filtered solution on the regions $x_2 \in [-\Delta_2 - \epsilon, -\Delta_2]$ or $x_2 \in [\Delta_2 - \epsilon, \Delta_2]$ will be of order ϵ^{-1} and not negligible in the limit as $\epsilon \rightarrow 0$. On $x_2 \in [\Delta_2 - \epsilon, \Delta_2]$

$$\delta_d(x_2, \epsilon) \widehat{p} \Big|_{x_2=0} = \hat{\delta}_d(x_2, \epsilon) \tilde{p} \Big|_{x_2=0}, \quad (3.23)$$

where

$$\hat{\delta}_d(x_2, \epsilon) = G_2(x_2) \frac{-30(1 + \frac{x_2 - \Delta_2}{\epsilon})^2 (\frac{x_2 - \Delta_2}{\epsilon})^2}{\epsilon}. \quad (3.24)$$

Now we define the LES equations as the limit $\epsilon \rightarrow 0$ of filtered governing equations (3.18) and (3.19). As previously shown for the 1-D case, the constructed velocity and pressure fields will have no contribution to the LES solution, i.e., $\hat{u}_i = \lim_{\epsilon \rightarrow 0} \hat{u}_i^\epsilon$ and $\hat{p} = \lim_{\epsilon \rightarrow 0} \hat{p}^\epsilon$, while the source terms will be non-zero in the limit. The LES governing equations

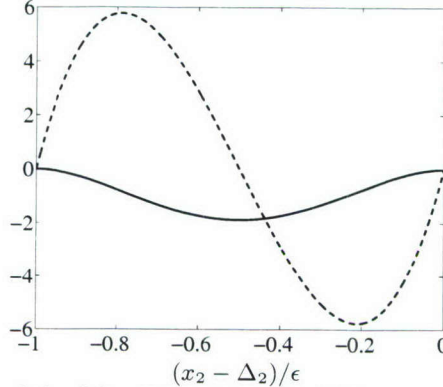


FIGURE 4. Schematic of the delta differentiator for finite ϵ ; \cdots , $\epsilon^2 \delta_d$; --- , $\epsilon \frac{\delta_d}{G_2}$

can be written as

$$\frac{\partial \hat{u}_i}{\partial t} + \frac{\partial \hat{u}_i \hat{u}_j}{\partial x_j} + \frac{\partial \hat{p}}{\partial x_j} - \frac{1}{Re_\tau} \frac{\partial^2 \hat{u}_i}{\partial x_j \partial x_j} = \hat{f}_i + \hat{f}_i^{w,u} + \hat{f}_i^{w,p}, \quad (3.25)$$

$$\nabla^2 \hat{p} = - \frac{\partial}{\partial x_i} \frac{\partial \hat{u}_i \hat{u}_j}{\partial x_j} + S^{w,p}, \quad (3.26)$$

where

$$\hat{f}_i^{w,u} = \lim_{\epsilon \rightarrow 0} \hat{f}_i^{\epsilon,u} = - \frac{1}{Re_\tau} G_2(x_2) \frac{\partial \hat{u}_i}{\partial x_2} \Big|_{x_2=0}^+ \quad i = 1, 3 \quad , \quad \hat{f}_2^{w,u} = \lim_{\epsilon \rightarrow 0} \hat{f}_2^{\epsilon,u} = 0 \quad (3.27)$$

$$\hat{f}_2^{w,p} = \lim_{\epsilon \rightarrow 0} \hat{f}_2^{\epsilon,p} = G_2(x_2) \tilde{p}|_{x_2=0}, \quad \hat{f}_i^{w,p} = \lim_{\epsilon \rightarrow 0} \hat{f}_i^{\epsilon,p} = 0 \quad i = 1, 3 \quad (3.28)$$

and

$$S^{w,p} = \lim_{\epsilon \rightarrow 0} \vec{\nabla} \cdot \widehat{\vec{f}}^{\epsilon,p} = \frac{\partial G_2}{\partial x_2} (x_2) \tilde{p}|_{x_2=0} + G_2(x_2) \frac{\partial \tilde{p}}{\partial x_2} \Big|_{x_2=0}^+. \quad (3.29)$$

The first term on the right-hand side of (3.29) is a result of taking the limit as $\epsilon \rightarrow 0$ of (3.23), which holds on the interval $x_2 \in [\Delta_2 - \epsilon, \Delta_2]$. This term is zero at both boundaries of this interval and will go to infinity as ϵ goes to zero while its integral over the region $x_2 \in [\Delta_2 - \epsilon, \Delta_2]$ is bounded and equal to -1 . In the limit, the interval will shrink to a single point, suggesting the source term is a one-sided delta function. This is equivalent to the derivative of the filter kernel. The property implies that δ_d in (3.13) is a delta differentiator for which

$$\lim_{\epsilon \rightarrow 0} \int G(x) \delta_d(x - x_0, \epsilon) dx = \frac{\partial G}{\partial x} \Big|_{x=x_0}. \quad (3.30)$$

Figure 4 shows a schematic of the delta differentiator for a finite ϵ . The dashed line represents the delta differentiator itself while the solid line is simply its integral. As shown in the figure, the net integral of δ_d over the region $x_2 \in [-\epsilon, 0]$ is zero while as the integrand contains the ϵ region, it produces a net force that varies as ϵ^{-1} and acts as a δ function.

Using the filter kernel with compact support of length $2\Delta_2$ extends the domain of support from $x_2 \in [0, 2]$ to $x_2 \in [-\Delta_2, 2 + \Delta_2]$. Although the new LES equations in (3.25) and (3.26) are defined everywhere on \mathbf{R}^3 , the velocity and pressure fields are zero outside the domain $x_2 \in [-\Delta_2, 2 + \Delta_2]$. The LES field can then be found by simulating

only the extended domain. However, this requires a new set of boundary conditions at the LES boundaries $x_2 = -\Delta_2$ and $x_2 = 2 + \Delta_2$. Just as in the 1-D case, both Dirichlet and Neumann boundary conditions are valid at each boundary for the velocity field. For the wall-normal velocity, mass conservation provides extra smoothness, making $\partial^2 u_2 / \partial x_2^2$ zero at boundaries. Since the unfiltered pressure is non-zero at DNS boundaries, a Neumann boundary condition does not hold and only a Dirichlet condition is appropriate. As will be shown, the Dirichlet condition can also be removed via a pressure decomposition.

We derive the LES pressure-Poisson equation by taking the divergence of the unfiltered momentum equations, filtering them, and taking the limit as $\epsilon \rightarrow 0$. To illustrate the consistency of the equations, we use a different approach and derive the pressure-Poisson equation by taking the divergence of the LES equations for velocity. This is done by taking the divergence of (3.25) as

$$\nabla^2 \hat{p} + \frac{\partial}{\partial x_i} \frac{\partial \widehat{u_i u_j}}{\partial x_j} = \vec{\nabla} \cdot \vec{f} + \vec{\nabla} \cdot \vec{f}^{w,u} + \vec{\nabla} \cdot \vec{f}^{w,p}, \quad (3.31)$$

where

$$\begin{aligned} \vec{\nabla} \cdot \vec{f} &= 0, \\ \vec{\nabla} \cdot \vec{f}^{w,u} &= -\frac{1}{Re_\tau} G_2(x_2) \left(\frac{\partial^2 \tilde{u}_1}{\partial x_1 \partial x_2} + \frac{\partial^2 \tilde{u}_3}{\partial x_3 \partial x_2} \right) \Big|_{x_2=0}^+ = \frac{1}{Re_\tau} G_2(x_2) \frac{\partial^2 \tilde{u}_2}{\partial x_2^2} \Big|_{x_2=0}^+, \\ \vec{\nabla} \cdot \vec{f}^{w,p} &= \frac{\partial G_2}{\partial x_2}(x_2) \tilde{p} \Big|_{x_2=0}. \end{aligned}$$

The LES Poisson equation can be written as

$$\nabla^2 \hat{p} + \frac{\partial}{\partial x_i} \frac{\partial \widehat{u_i u_j}}{\partial x_j} = \frac{1}{Re_\tau} G_2(x_2) \frac{\partial^2 \tilde{u}_2}{\partial x_2^2} \Big|_{x_2=0}^+ + \frac{\partial G_2}{\partial x_2}(x_2) \tilde{p} \Big|_{x_2=0}. \quad (3.32)$$

We know from the Navier-Stokes equations that

$$\frac{1}{Re_\tau} \frac{\partial^2 \tilde{u}_2}{\partial x_2^2} \Big|_{x_2=0}^+ = \frac{\partial \tilde{p}}{\partial x_2} \Big|_{x_2=0}. \quad (3.33)$$

This again implies, consistently, the LES pressure equation derived in this formulation is identical to that derived in (3.26) and (3.29).

3.4. Approximate solution

Given the LES governing equations and their source terms, we need to determine a method to solve them. Therefore, we will do an LES pressure solve as a Lagrange multiplier to enforce continuity exactly as it is done in DNS. The LES forcing terms will therefore not be responsible for satisfying the LES continuity equation. Instead, the pressure is decomposed into two parts: $\hat{p} = \hat{p}_c + \hat{p}_f$ as

$$\nabla^2 \hat{p}_f = \frac{\partial G_2}{\partial x_2}(x_2) \tilde{p} \Big|_{x_2=0} + \frac{1}{Re_\tau} G_2(x_2) \frac{\partial^2 \tilde{u}_2}{\partial x_2^2} \Big|_{x_2=0}^+, \quad (3.34)$$

$$\nabla^2 \hat{p}_c = -\frac{\partial}{\partial x_i} \frac{\partial \widehat{u_i u_j}}{\partial x_j}. \quad (3.35)$$

Since these terms are active only near the wall and exhibit stronger variations in the wall-normal direction, we use the approximation $\nabla^2 \hat{p}_f \approx \frac{\partial^2 \hat{p}_f}{\partial x_2^2}$. Taylor series expansion

shows that this is reasonable near the LES wall, although its accuracy begins to decrease near the edge of the LES wall region. However, the assumption implies the following formula

$$\frac{\partial \hat{p}_f}{\partial x_2} = G_2(x_2) \tilde{p}|_{x_2=0} + \frac{1}{Re_\tau} \frac{\partial^2 \tilde{u}_2}{\partial x_2^2} \Big|_{x_2=0}^+ \int_{-\Delta}^{x_2} G_2(y) dy, \quad (3.36)$$

in the near wall region. The first term is an artifact of setting the outside pressure to the arbitrary value of zero and cancels with this arbitrary pressure acting in the u_2 equation. This can be easily seen for the top-hat filter. The second term we apply directly through inversion. In this way, the LES pressure is decomposed, and the forces are applied in an appropriate manner.

It should be noted that second term on the right-hand side of (3.36) makes the velocity force $\tilde{f}^{w,u}$ in (3.27) divergence-free. From (3.10) we conclude that $\lim_{\epsilon \rightarrow 0} \tilde{\nabla} \cdot \widehat{\tilde{f}^{\epsilon,u}} = 0$ while from (3.27), $\tilde{\nabla} \cdot (\lim_{\epsilon \rightarrow 0} \widehat{\tilde{f}^{\epsilon,u}}) = \frac{1}{Re_\tau} G_2(x_2) \frac{\partial^2 \tilde{u}_2}{\partial x_2^2} \Big|_{x_2=0}^+$. This suggests that making the velocity force in the LES formulation divergence-free is equivalent to adding the second term on the right-hand side of (3.36) to the wall-normal momentum equation. Numerical experiments demonstrate similar results for both approximations.

Combining all the expressions, our LES equations are given by

$$\frac{\partial \hat{u}_i}{\partial t} + \frac{\partial \hat{u}_i \hat{u}_j}{\partial x_j} + \frac{\partial \hat{p}_c}{\partial x_j} - \frac{1}{Re_\tau} \frac{\partial^2 \hat{u}_i}{\partial x_j \partial x_j} = \hat{f}_i + \hat{f}_i^w, \quad (3.37)$$

$$\nabla^2 \hat{p}_c = - \frac{\partial}{\partial x_i} \frac{\partial \hat{u}_i \hat{u}_j}{\partial x_j}, \quad (3.38)$$

where

$$\begin{aligned} \hat{f}_i^w &= - \frac{1}{Re_\tau} (2\Delta_2 G_2(x_2)) \frac{\partial^2 \hat{u}_i}{\partial x_2^2} \Big|_{x_2=-\Delta_2}^+ \quad i = 1, 3 \quad , \\ \hat{f}_2^w &= - \frac{1}{Re_\tau} \frac{\partial^3 \hat{u}_2}{\partial x_2^3} \Big|_{x_2=-\Delta_2}^+ \int_{-\Delta_2}^{x_2} 2\Delta_2 G_2(y) dy. \end{aligned} \quad (3.39)$$

These equations, supplemented with the boundary conditions, need to be discretized and solved numerically. Filter inversion is used to compute the DNS quantities.

4. Results and discussion

Preliminary results have been obtained using the formulation described in the preceding section for periodic plane channel flow. Simulations were performed using the second-order centered finite difference code described in Templeton *et al.* (2005).

The test case we consider here is pressure-driven channel flow at $Re_\tau = 180$ of dimensionless size $4\pi \times 2 \times 4\pi/3$. The flow is resolved on a uniform grid using $48 \times 57 \times 48$ points. The equivalent wall-normal resolution without extension is 49 points, which is relatively coarse. A homogeneous top-hat filter is used with a large filter width $2\Delta_i = 8\Delta x_i$. However, the filter width is not tied to the grid resolution; this choice is simply for convenience. Since the LES equations are still unclosed due to the presence of the sub-grid scale (SGS) stresses, the dynamic Smagorinsky model (Germano *et al.* 1991) is also included in the LES equations with a test filter size of twice the filter width. Since we wish to separate the effects of the wall-forcing terms from the SGS modeling, the dynamic model is applied away from the LES walls over the domain $x_2 \in [\Delta_2, 2 - \Delta_2]$.

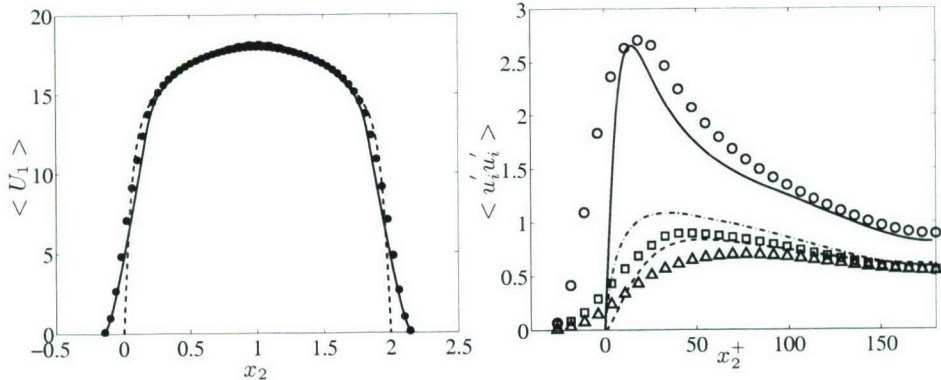


FIGURE 5. Left: Mean velocity profile; ----, DNS; —, filtered DNS ; •, LES. Right: RMS velocity fluctuations; —, $\langle u_1'^2 \rangle$ DNS; ---, $\langle u_2'^2 \rangle$ DNS; -·-, $\langle u_3'^2 \rangle$ DNS; ○, $\langle u_1'^2 \rangle$ LES; △, $\langle u_2'^2 \rangle$ LES; □, $\langle u_3'^2 \rangle$ LES .

Results for the mean velocity profile and rms velocity fluctuations are shown in figure 5. Good agreement is obtained between the results of the present LES and the filtered mean velocity from the DNS of Moser *et al.* (1999), with the greatest discrepancy occurring in the outer part of the LES wall layer (approximately $x_2 \in [0, \Delta_2]$). There are two likely causes of this discrepancy. The first is that the assumptions used in the pressure-forcing term are less accurate in this region than they are nearer the wall. The second is uncertainty related to the lack of an SGS model in this region when it is known that the SGS stresses are significant. However, the dynamic model, being purely dissipative, often has difficulty in this region where turbulence production is significant (Gullbrand & Chow 1999).

This point is emphasized by the well-known over-prediction of the peak streamwise velocity fluctuations. Note that the LES values are directly compared with the DNS curves, although the appropriate comparison would be to the filtered DNS fluctuations (a subject of future work). Certain points can be made using the present comparison, however. In the spanwise and wall-normal directions, the LES fluctuations are less than the DNS fluctuations, a qualitatively correct result, and smoothly approach zero at the LES wall after having the boundary layer ‘‘smeared’’ by the filtering. In the streamwise direction, the peak is slightly over-predicted, although this over-prediction is less than in corresponding wall-resolved simulations. This may be partly due to the ability of the wall-forcing terms to add energy to the flow, although further study of the energetics of the boundary terms and SGS model is required. Finally, it should be noted that since the streamwise fluctuations exhibit a steeper boundary layer, the Neumann condition at the wall is more difficult to capture. Thus, there may be limits on the wall resolution that can be used with this approach.

These results suggest that filtering the wall may be a viable formulation for LES of bounded flows. Reasonable predictions of the mean and fluctuating velocity components have been obtained, although much work is still needed to fully assess the accuracy of the method. Comparisons between the LES and filtered DNS turbulence are required, along with an improved understanding of the energy balance involving the LES wall forces and SGS model.

Acknowledgements

Funding for this work was provided by Franklin P. Johnson Graduate Fellowship and the AFOSR Grant # F49620-03-1-0132. Computer time was provided by the DOD High Performance Computing Modernization Program through NRL-DC. The authors would like to thank Professor Parviz Moin for his helpful suggestions during the preparation of this manuscript.

REFERENCES

BAGGETT, J.S. 1997 Some modelling requirements for wall models in large-eddy simulation. *Annual Research Briefs 1997* Center for Turbulence Research, Stanford University, CA, 123–134.

BORGGAARD, J. & ILLIESCU, T. 2006 Approximate deconvolution boundary conditions for large eddy simulation. *Appl. Math Letters* **19**, 735–740.

CARATI, D. 2001 *Large-eddy simulation for turbulent flows: from mathematical foundations to practical applications*. Technical report, Université Libre de Bruxelles.

GERMANO, M., PIOMELLI, U., MOIN, P. & CABOT, W. 1991 A dynamic subgrid-scale eddy-viscosity model. *Phys. Fluids A* **3**(7), 1760–1765.

GULLBRAND, J. & CHOW, F.K. 2003 The effect of numerical errors and turbulence models in large-eddy simulations of channel flow, with and without explicit filtering. *J. Fluid Mech.* **495**, 323–341.

IOVINO, M., PASSONI, G. & TORDELLA, D. 2004 A new large-eddy simulation near-wall treatment. *Phys. Fluids* **16**(11), 3935–3944.

MOSER, R.D., DAS, A. & BHATTACHARYA, A. 2005 *Filtering the wall as a solution to the wall-modeling problem*. Limmasol, Cypress, Conference on Complex Effects in Large-Eddy Simulation.

MOSER, R., KIM, J. & MANSOUR, N. 1999 Direct numerical simulation of turbulent channel flow up to $Re_\tau = 590$. *Phys. Fluids* **11** (4), 943–945.

SAGAUT, P. 2002 *Large Eddy Simulation for Incompressible Flows*. Springer, Berlin.

TEMPLETON, J.A. & SHOEYBI, M. 2006 Towards wall-normal filtering for large eddy simulation. *Multiscale Model. Simul.* **5**(2), 420–444.

TEMPLETON, J.A., WANG, M. & MOIN, P. 2005 An efficient wall model for large-eddy simulation based on optimal control theory. *Phys. Fluids* **18** (2), 025101–025113.

VASILEYEV, O.V., LUND, T.S. & MOIN, P. 1998 A general class of commutative filters for LES in complex geometries. *J. Comp. Phys.* **146**, 82–104.

Application of a local subgrid model based on coherent structures to complex geometries

By H. Kobayashi[†] AND X. Wu

1. Motivation and objectives

Fine-scale coherent eddies are an important feature of turbulence. These eddies scale with the Kolmogorov microscale, and have been found universally in homogeneous isotropic turbulence, planar channel flow, and mixing layers using direct numerical simulation (Miyauchi & Tanahashi 2001). Recently, Kobayashi (2005) proposed a coherent structure model (CSM) as a subgrid scale (SGS) model. This model has been tested in a series of canonical turbulent flows including rotating and non-rotating channel flows and was found to yield a level of accuracy similar to that obtained by using the dynamic Smagorinsky model (DSM) (Germano *et al.* 1991). Compared to the DSM, the newly proposed CSM has advantages of local determination of the SGS model parameter and of faster computation. Simple and stable SGS models are suitable for engineering applications without any homogeneous directions for averaging. Since the model parameter of the CSM has a positive, finite small variance, it is stable in spite of local determination of the model parameter. This local model is suitable for complex geometries.

In this study, the applicability of the CSM is further assessed in the simulations of flow over a backward-facing step and flow in an asymmetric plane diffuser.

2. Coherent structure model

In LES, coherent structures are extracted by the second invariant Q in a resolved-scale field, which is given by

$$Q = \frac{1}{2} (\bar{W}_{ij} \bar{W}_{ij} - \bar{S}_{ij} \bar{S}_{ij}), \quad \bar{S}_{ij} = \frac{1}{2} \left(\frac{\partial \bar{u}_j}{\partial x_i} + \frac{\partial \bar{u}_i}{\partial x_j} \right), \quad \bar{W}_{ij} = \frac{1}{2} \left(\frac{\partial \bar{u}_j}{\partial x_i} - \frac{\partial \bar{u}_i}{\partial x_j} \right), \quad (2.1)$$

where \bar{S}_{ij} is the strain-rate tensor, and \bar{W}_{ij} is the vorticity tensor.

In the present study, the second invariant is applied to the model parameter C of the Smagorinsky model (Smagorinsky 1963):

$$\tau_{ij} = -2C\bar{\Delta}^2 |\bar{S}| \bar{S}_{ij}, \quad |\bar{S}| = \sqrt{2\bar{S}_{ij} \bar{S}_{ij}}, \quad (2.2)$$

where τ_{ij} is the traceless SGS stress tensor, $\bar{\Delta}$ is the filter width, and $|\bar{S}|$ is the magnitude of the strain-rate tensor \bar{S}_{ij} . The model parameter C is determined as follows:

$$\begin{aligned} C &= C' |F_{CS}|^{3/2} F_\Omega, \quad F_{CS} = \frac{Q}{E}, \quad F_\Omega = 1 - F_{CS}, \\ E &= \frac{1}{2} (\bar{W}_{ij} \bar{W}_{ij} + \bar{S}_{ij} \bar{S}_{ij}), \quad C' = \frac{1}{22}, \end{aligned} \quad (2.3)$$

where F_{CS} is the coherent structure function, which is normalized by a magnitude of the

[†] Permanent address: Keio University, Japan

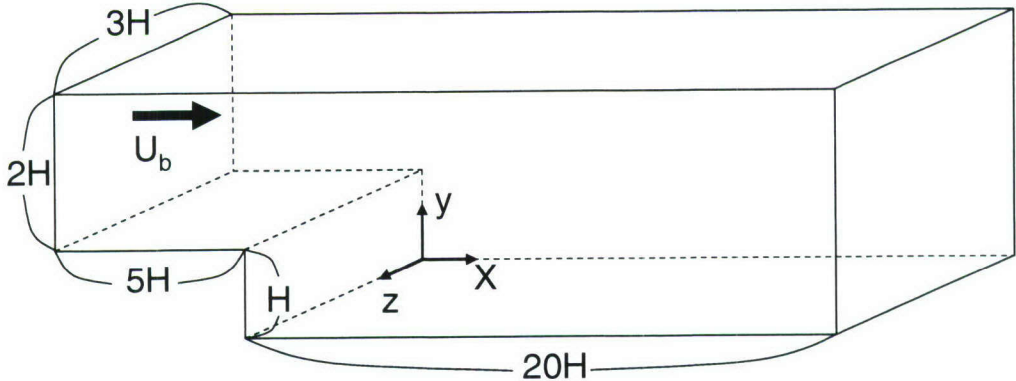


FIGURE 1. Computational domain for a backward-facing step.

shear E ; F_Ω is the energy-decay suppression function. The parameter C' is determined by *a priori* tests in isotropic homogeneous and channel turbulent flows, and its value is fixed as 1/22. This model is called a coherent structure model (CSM) (Kobayashi 2005).

This model is very simple because one has only to calculate vorticities in a resolved-scale field. This model also realizes a suppression of the energy decay in a flow field with a high rotation because F_Ω gives a suppression of the dissipation with the increase in an angular velocity (Kobayashi 2005). The functions of F_{CS} and F_Ω have distinct upper and lower limits:

$$-1 \leq F_{CS} \leq 1, \quad 0 \leq |F_{CS}| \leq 1, \quad 0 \leq F_\Omega \leq 2. \quad (2.4)$$

As a result, the model parameter C of the CSM has a finite small variance, and the numerical simulation with the CSM is stably carried out even though the model parameter is locally determined.

The model parameter of the DSM (Germano *et al.* 1991) is determined using a least square procedure proposed by Lilly (1992) with an average in homogeneous directions.

3. Backward-facing step flow

Figure 1 shows the computational domain for a turbulent flow over a backward-facing step. The grid resolution is $256 \times 96 \times 64$ in the x , y , and z directions, respectively; x is the streamwise direction, y is the one normal to the walls, and z is the spanwise one. The Reynolds number based on the step height H and bulk velocity U_b was 4800. This value is close to 4775 in the experiment by Kasagi and Matsunaga (1995); the Reynolds number based on the step height and a centerline velocity at the inlet is 5500. The domain depth in z direction is $3H$. The grid was stretched out with the factors; $4(x = -5) : 4(x = -1) : 1(x = 0) : 2(x = 2) : 2(x = 10) : 4(x = 20)$ in the x direction; $1(y = 0) : 10(y = 0.5) : 1(y = 1) : 20(y = 2) : 1(y = 3)$ in the y direction. An inflow condition is imposed at $x = -5$, and the inflow profile is given a fully developed channel flow at $Re_\tau = 290$. The time step is $0.01H/U_b$. A convective condition is applied at the outflow boundary. Statistics for the CSM, the DSM, and no model are accumulated over 20,000 time steps (200 time units), respectively.

This simulation was performed using JETCODE (CHUCK'S CODE), a structured incompressible flow solver developed at the Center for Turbulence Research and based on

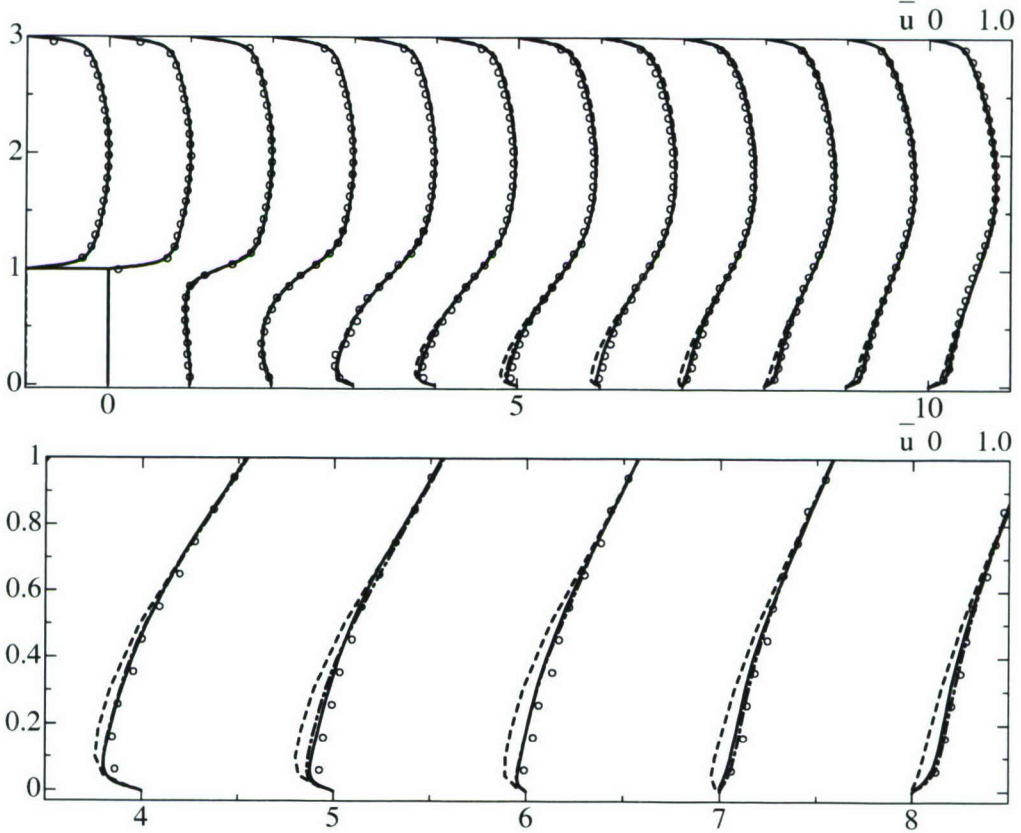


FIGURE 2. Streamwise mean velocity profiles; (upper figure): inlet $\leq x \leq 10$, $0 \leq y \leq 3$; (lower figure): $4 \leq x \leq 8$, $0 \leq y \leq 1$. —, CSM; -·-, DSM; -·-, no model; \circ , experimental data by Kasagi and Matsunaga (1995).

a second-order central-discretization on a staggered-grid, a second-order time advancement, and a Poisson equation for pressure (see Akselvoll & Moin 1995; Pierce 2001).

Figure 2 shows the profiles of streamwise mean velocities for the CSM, the DSM, and no model in comparison with the particle-tracking velocimetry (PTV) data by Kasagi and Matsunaga (1995). The lower figure in Fig. 2 shows the close-up of the upper figure in a reattachment region near a lower wall. Whereas the overall profiles of the CSM, the DSM, and no model in the upper figure are almost the same, the lower figure shows that no model simulation gives under-predictions from $x = 4$ to $x = 8$ in a reattachment region near a lower wall. The CSM and DSM, however, agree well with the PTV data. The CSM gives a level of accuracy similar to the DSM in spite of a local model.

Figures 3 and 4 show the profiles of streamwise rms velocities and Reynolds shear stress for the CSM, the DSM, and no model in comparison with the PTV data by Kasagi and Matsunaga (1995). Whereas the profiles of the CSM, the DSM, and no model in Fig. 3 are almost the same, in Fig. 4 no model simulation gives under-predictions from $x = 3$ to $x = 7$ at $y = 1$ in comparison with the CSM and DSM. The profile of the CSM agrees well with that of the DSM, although the CSM is a local SGS model.

Figure 5 shows the ratios of the SGS eddy viscosity ν_t and the molecular viscosity ν for the CSM and the DSM. The ratio for the CSM becomes small at $y = 1$ because the

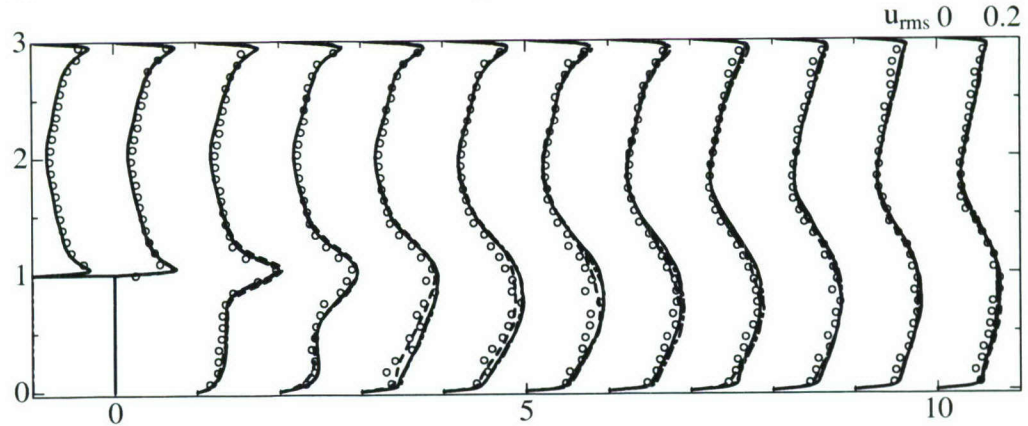


FIGURE 3. Streamwise rms velocity profiles. —, CSM; - - -, DSM; - · - , no model; \circ , experimental data by Kasagi and Matsunaga (1995).

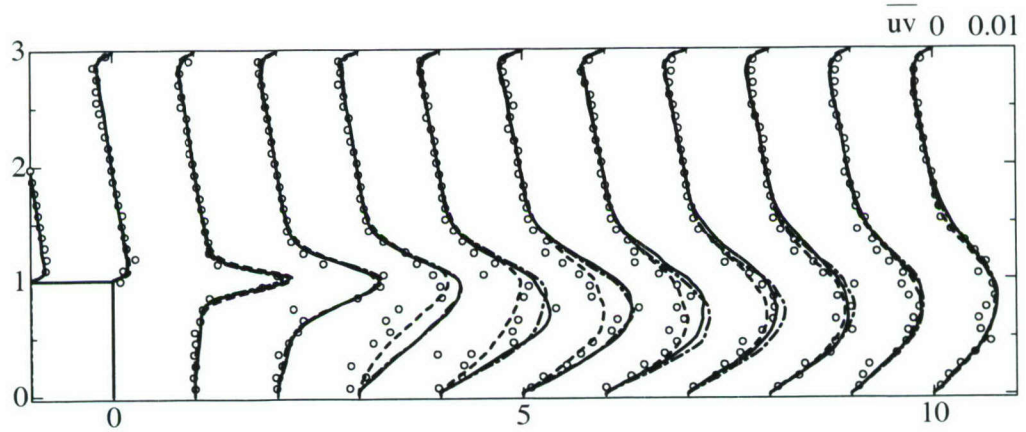


FIGURE 4. Reynolds shear stress profiles. —, CSM; - - -, DSM; - · - , no model; \circ , experimental data by Kasagi and Matsunaga (1995).

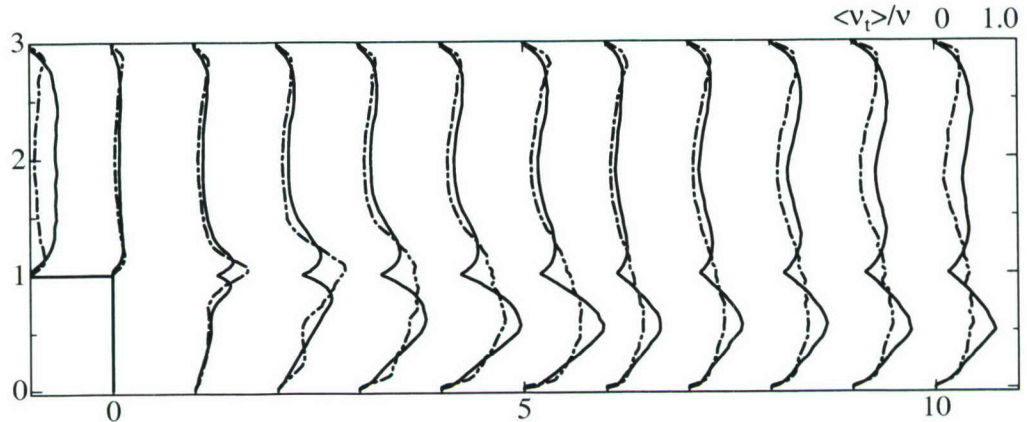


FIGURE 5. Ratios of the SGS eddy viscosity and the molecular viscosity. —, CSM; - - -, DSM.

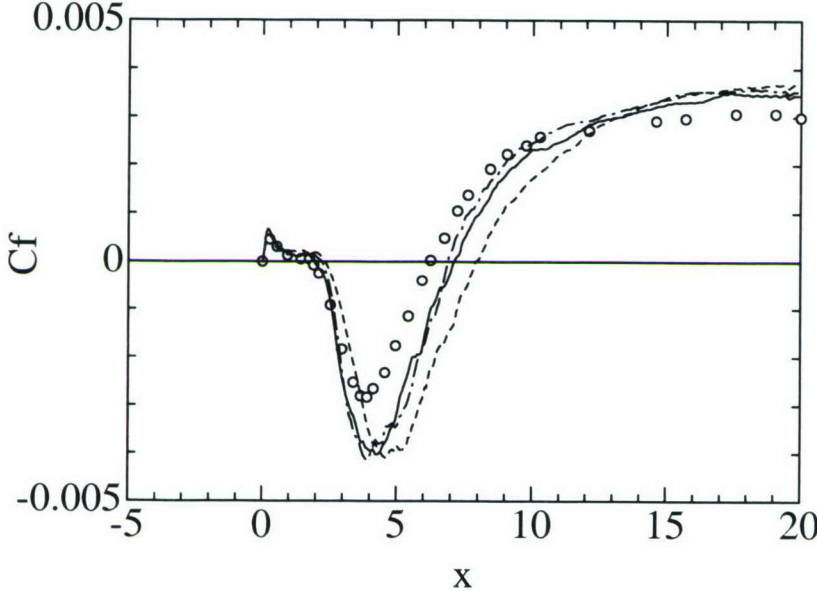


FIGURE 6. Skin friction profiles. —, CSM; - - -, DSM; - - - -, no model; \circ , DNS result by Le, Moin & Kim (1997).

SGS eddy viscosity depends on $\bar{\Delta}_y$ in $\bar{\Delta} = (\bar{\Delta}_x \bar{\Delta}_y \bar{\Delta}_z)^{2/3}$, and the $\bar{\Delta}_y$ is stretched out to create the finest mesh. On the other hand, in the present study the ratio for the DSM does not depend on $\bar{\Delta}_y$ because the SGS eddy viscosity is determined using an average in homogeneous directions and not using a filtering for the y direction (Germano *et al.* 1991; Lilly 1992). In the DSM the filtering in the y direction is "optional", and in some studies the filtering is carried out. In that situation the DSM would give a similar profile at $y = 1$ to the CSM.

However, the sharp profile of the CSM seems to be valid because in the small mesh the effect of ν_t to ν should be small. Although the SGS eddy viscosity of the CSM sharply changes at $y = 1$, the statistics of the first and second moments of the CSM were almost the same as those of the DSM. In addition, the CSM was numerically stable.

The CSM ran 15% faster in total CPU time than the DSM, which gives it a significant advantage over the DSM.

Figure 6 shows the skin friction profiles for the CSM, the DSM, no model, and the DNS result by Le, Moin & Kim (1997). The Reynolds number for the DNS is 5100 based on a centerline velocity and a step height. This Reynolds number is similar to 5500 in our simulation. The slight difference of the amplitude in the skin friction between the DNS and the other results comes from the difference of the expansion ratio of the backstep configuration. In our case the expansion ratio of 1.5 is used, while in the DNS that of 1.2 was used. The skin friction profiles of the CSM and DSM agree well, whereas that of no model gives a far reattachment point. The reattachment lengths for the CSM, DSM, and no model are 7.09, 6.87, and 7.88, respectively. However, an experimental result by Kasagi and Matsunaga (1995) was 6.51. A higher grid resolution of $384 \times 192 \times 64$ with the same stretch factors as the lower one was examined to confirm the reattachment length. In that study, the reattachment lengths for the CSM, DSM, and no model are 6.81, 6.75, and 7.13, respectively. For each resolution, it is confirmed that the CSM gives a similar prediction to the DSM.

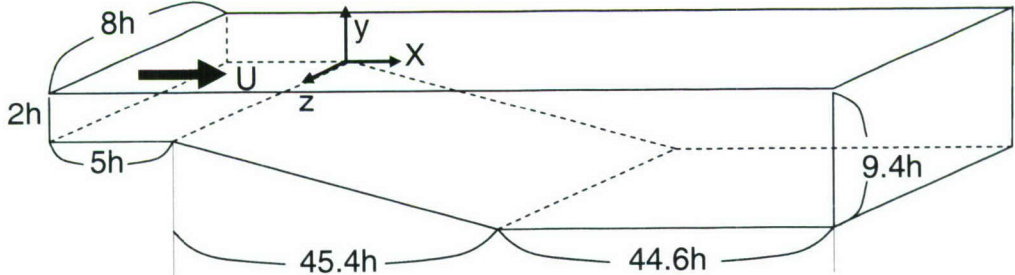


FIGURE 7. Computational domain for an asymmetric plane diffuser.

4. Diffuser flow

Figure 7 shows the computational domain for a turbulent flow through an asymmetric plane diffuser. The diffuser has a total expansion ratio of $4.7h$ and a single-sided deflection wall of 10° . An experiment for this configuration was carried out by Obi *et al.* (1993); more detailed experiments were conducted by Buice and Eaton (1997). The grid resolution is $400 \times 80 \times 80$ in the x , y , and z directions, respectively (x is the streamwise direction, y the one normal to the walls, z the spanwise one). An inflow condition is imposed at $x = -5$, and the unsteady inflow profile is given a fully developed channel flow at $Re_\tau = 500$. A convective condition is applied at the outflow boundary.

This simulation was carried out using an unstructured LES solver CDP, developed at the Center for Turbulence Research. The filtered momentum equations are solved on a cell-centered unstructured mesh with a second-order accurate central difference spatial discretization. An implicit time-advancement procedure is applied. The Poisson equation is solved to determine the pressure field. For further details about the numerical algorithm, see Ham & Iaccarino (2004); for more information about the diffuser simulation, see Wu *et al.* (2006) and Schlüter *et al.* (2005). In this study, two times larger filter width was used for the CSM.

Figure 8 shows the streamwise profiles of mean (left column) and rms (right column) velocities at $x = 5.18, 11.96, 27.1$, and 33.86 from top to bottom for the CSM, the DSM, and no model. Those figures reflect the DSM results with a finer grid resolution ($590 \times 100 \times 110$) by Wu *et al.* (2006) and the experimental data by Buice and Eaton (1997). The CSM predicts almost the same streamwise mean velocity as the fine DSM at each x location. At $x = 27.1$ the DSM and no model under-predict the mean velocity profiles at $y = 0$, while the CSM agrees with the experimental data at $y = 0$. On the other hand, the CSM gives some over-predictions near an upper wall at $x = 27.1$ and 33.86 in comparison with the DSM and no model. Overall, the streamwise mean and rms velocities of the CSM agree well with those of the fine DSM and the experiment.

Figure 9 shows the profiles of Smagorinsky constant $C_s = \sqrt{C}$ for the CSM at each x location. At the centerline of the inlet, the C_s is about 0.9. As moving downstream, the C_s increases, and at the shear layer region of $x = 33.86$ the maximum C_s gives approximately 1.4, which is close to a well-known value 1.5 in a mixing layer.

Figure 10 shows the skin friction profiles for the CSM, DSM, no model, fine DSM, and experimental data. The CSM under-predicts the skin friction from the inlet to $x = 40$ on an upper wall in comparison with the DSM and fine DSM, while the CSM gives a good prediction of the skin friction on a lower wall. Overall, the CSM predicts the skin friction similar to the DSM.

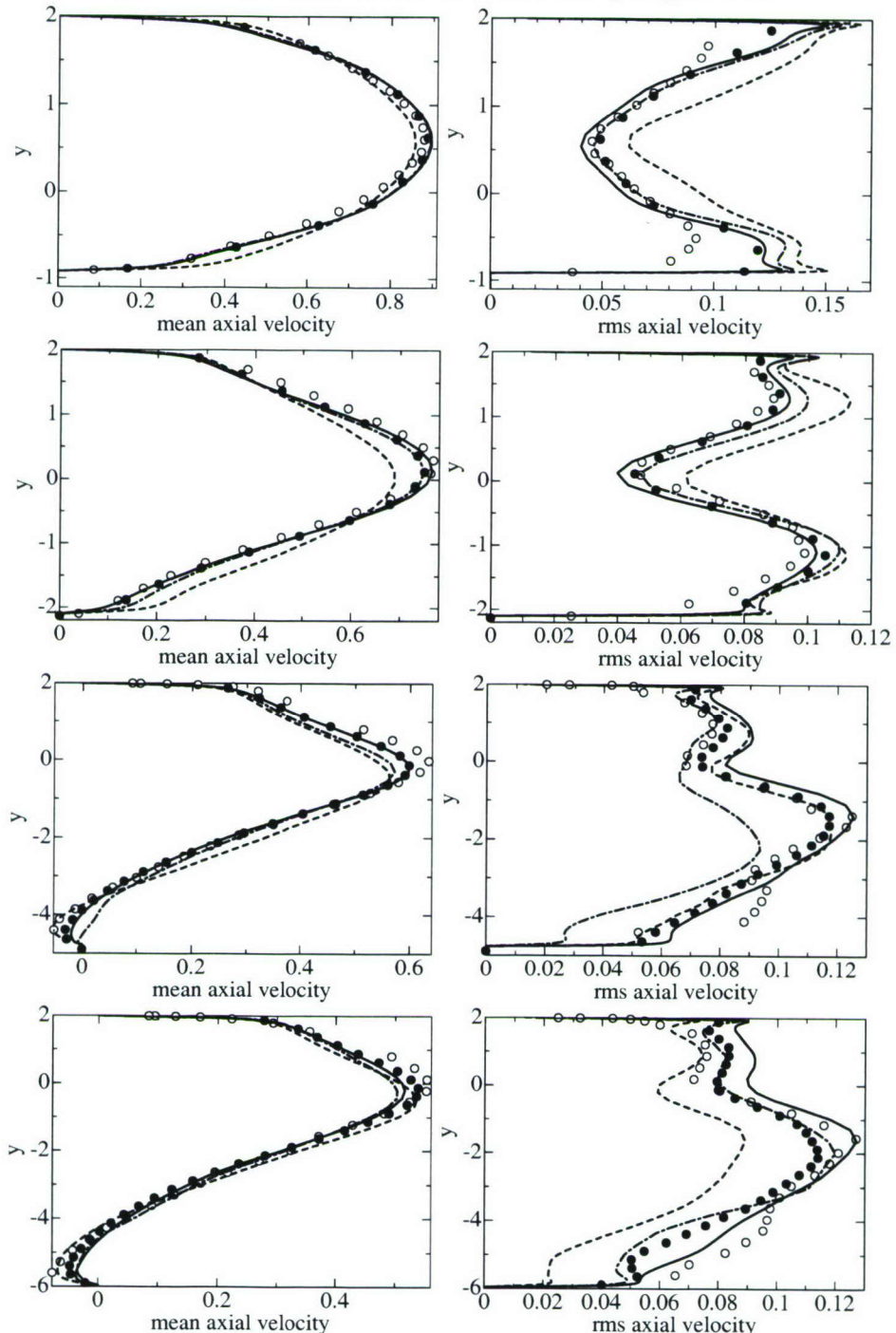


FIGURE 8. Streamwise profiles of mean (left column) and rms (right column) velocities at $x = 5.18, 11.96, 27.1$, and 33.86 from top to bottom. —, CSM; - - -, DSM; - - - - -, no model; ●, fine DSM; ○, experimental data by Buice and Eaton (1997).

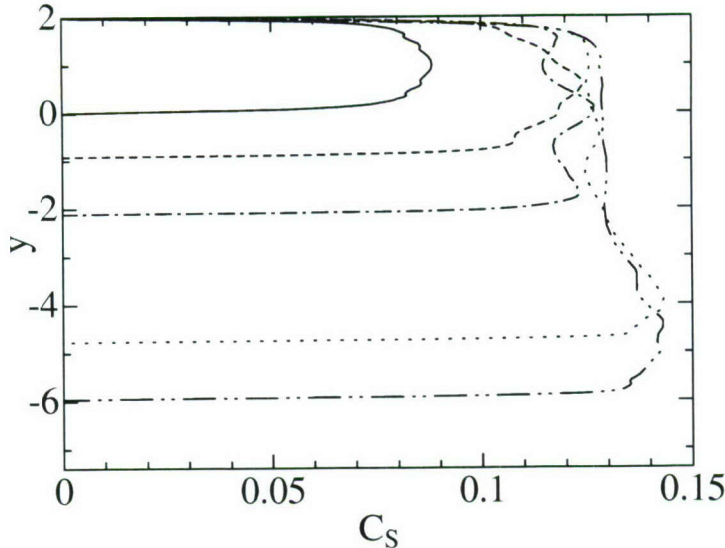


FIGURE 9. Profiles of Smagorinsky constant $C_s = \sqrt{C}$ for the CSM. —, $x = -5$; - - -, 5.18; - - - - , 11.96; ·····, 27.1; - - - - - , 33.86.

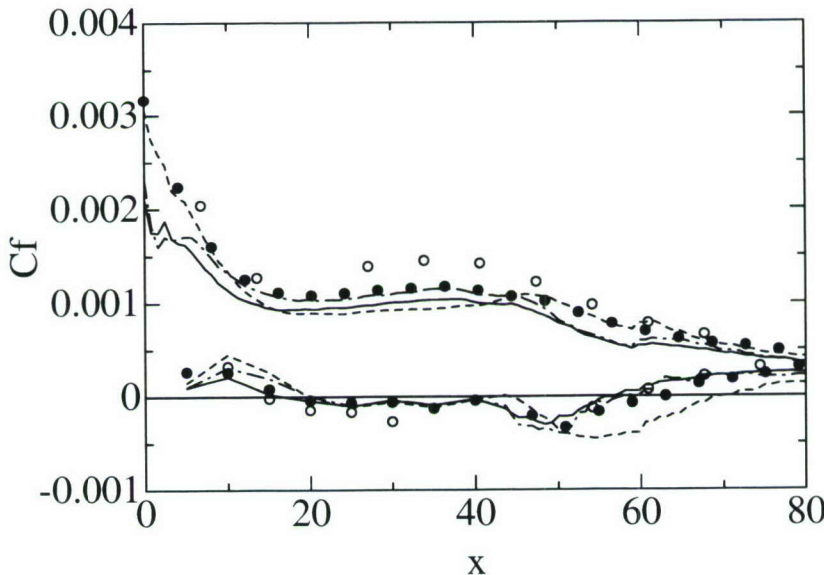


FIGURE 10. Skin friction profiles. —, CSM; - - - - , DSM; - - -, no model; •, fine DSM; ○, experimental data by Buice and Eaton (1997).

5. Conclusions

A local SGS model based on coherent structures has been applied to a backward-facing step flow and an asymmetric plane diffuser. A structured and an unstructured code was used for the backstep and diffuser flows, respectively. The performance of the local coherent structure model for both configurations is almost the same as the dynamic Smagorinsky model using an average in homogeneous directions. The coherent structure model is inexpensive and efficient in comparison with the dynamic model, and is nu-

merically stable without averaging. The present model will be suitable for the complex geometry without any homogeneous directions.

In the future, the local coherent structure model will be applied to a complex geometry without any homogeneous directions.

6. Acknowledgments

HK is deeply grateful to Prof. P. Moin for providing the research opportunity as a senior visiting fellow at the Center for Turbulence Research and also thanks Dr. D. You for his valuable comments and for improving the presentation of this manuscript.

REFERENCES

AKSELVOLL, K. & MOIN, P. 1995 Large eddy simulation of turbulent confined coannular jets and turbulent flow over a backward facing step. *Rep. TF-63, Thermosciences Division, Dept. of Mech. Eng., Stanford University*.

BUICE, C. U., & EATON, J. K. 1997 Experimental investigation of flow through an asymmetric plane diffuser. *Ph.D. Thesis, Dept. of Mech. Eng., Stanford University*.

GERMANO, M., PIOMELLI, U., MOIN, P., & CABOT, W. H. 1991 A dynamic subgrid-scale eddy viscosity model. *Phys. Fluids A* **3**, 1760–1765.

HAM, F. & IACCARINO, G. 2004 Energy conservation in collocated discretization schemes on unstructured meshes. In *Annual Research Briefs-2004*, pp. 3–14. Stanford, CA: Center for Turbulence Research.

KASAGI, N. & MATSUNAGA, A. 1995 Three-dimensional particle-tracking velocimetry measurement of turbulences statistics and energy budget in a backward-facing step flow. *Int. J. Heat and Fluid Flow* **16**, 477–485.

KOBAYASHI, H. 2005 The subgrid-scale models based on coherent structures for rotating homogeneous turbulence and turbulent channel flow. *Phys. Fluids* **17**, 045104.

LE, H., MOIN, P., & KIM, J. 1997 Direct numerical simulation of turbulent flow over a backward-facing step. *J. Fluid Mech.* **330**, 349–374.

LILLY, D. K. 1992 A proposed modification of the germano subgrid-scale closure method. *Phys. Fluids A* **4**, 633–635.

MIYAUCHI, T. & TANAHASHI, M. 2001 Coherent fine scale structure in turbulence. In *IUTAM Symposium on Geometry and Statistics of Turbulence*, edited by T. Kambe et al. (Kluwer, Netherlands), 67–76.

OBI, S., AOKI, K., & MASUDA, S. 1993 Experimental and computational study of turbulent separating flow in an asymmetric plane diffuser. In *Ninth Symp. Turbulent Shear Flows, Kyoto, Japan August 16–19*.

PIERCE, C. D. 2001 Progress-variable approach for large-eddy simulation of turbulent combustion. *Ph.D. Thesis, Dept. of Mech. Eng., Stanford University*.

SCHLÜTER, J., WU, X., & PITSCH, H. 2005 Large-eddy simulation of a separated plane diffuser. *AIAA paper*, (AIAA 2005-0672), January 2005.

SMAGORINSKY, J. 1963 General circulation experiments with the primitive equations. I. The basic experiment. *Mon. Weather Rev.* **91**, 99–152.

WU, X., SCHLÜTER, J., MOIN, P., PITSCH, H., IACCARINO, G., & HAM, F. 2006 Computational study on the internal layer in a diffuser. *J. Fluid Mech.* **550**, 391–412.

Computational study of aero-optical distortions by a turbulent wake

By A. Mani, M. Wang[†] AND P. Moin

1. Motivation and objectives

Optical aberrations induced by turbulent flows are a serious concern in airborne communication and imaging systems. In these applications an optical beam is required to be transmitted through a relatively long distance, over which the quality of the beam can degrade due to variations of the index of refraction along its path. For air and many fluids, the refractive index is linearly related to the density of the fluid through the Gladstone-Dale relation (see Wolf & Zizzis 1978), and therefore density fluctuations due to flow turbulence are the root cause of optical aberrations. An airborne optical beam generally encounters two distinct turbulent flow regimes: the turbulence in the vicinity of the aperture produced by the presence of solid boundaries, and atmospheric turbulence.

Aero-optics is the study of optical distortions by the near-field turbulent flows, typically involving turbulent boundary layers, mixing layers, and wakes (see Gilbert 1982). The depth of the aberrating flowfield is usually smaller than or comparable to the projecting (or imaging) aperture. When an initially planar optical wavefront passes a compressible flow, different parts of the wavefront experience different density in the medium and hence have different propagation speeds. Consequently the wavefront becomes deformed. A small initial deformation of the wavefront can lead to large errors on a distant target. The consequences of such deformations include optical beam deflection (bore-sight error) and jitter, beam spread, and loss of intensity. Wavefront distortions can also cause reductions of resolution, contrast, effective range, and sensitivity for airborne electro-optical sensors and imaging systems (Jones & Bender 2001).

Research in the area of turbulent distortions of optical waves can be traced back to the 1950s and 1960s (see, for example, Chernov 1960; Tatarski 1961) when the scattering of acoustic and electromagnetic waves due to random fluctuations of refractive index were studied, mostly in the context of atmosphere propagation. Most of the early studies are based on statistical analysis with simplifying assumptions such as homogeneous and isotropic turbulence, and therefore are not directly applicable in realistic aero-optical flowfields. Sutton (1969) characterized different regimes based on optical and flow parameters for the case of homogeneous and isotropic turbulence and developed statistical models to predict far-field optical aberrations.

It was in the late 1980s when aero-optics in the modern sense, i.e., the study of optical distortions due to near-aperture turbulence, came into consideration. Many experimental studies have been performed to develop high-speed wavefront measurement tools (e.g., Jumper & Fitzgerald 2001; Cheung & Jumper 2004), study the refractive index structures (e.g., Catrakis & Aguirre 2004; Dimotakis *et al.* 2001; Fitzgerald & Jumper 2004), develop distortion scaling laws (e.g., Gordeyev *et al.* 2003), and devise control techniques to suppress or modify optically important turbulence structures (e.g., Gordeyev *et al.* 2004; Sinha *et al.* 2004). Despite advances in wavefront sensor technology, significant limitations

[†] Present address: Department of Aerospace and Mechanical Engineering, University of Notre Dame

still exist in terms of spatial and temporal resolutions. Computational studies, when performed adequately, can allow us to probe the flow and optical fields in greater detail and hence complement experiments to further our understanding in this area.

Earlier computational approaches for aero-optics typically involved Reynolds-Averaged Navier-Stokes (RANS) calculations using a turbulence model such as the $k-\varepsilon$ model, from which crude algebraic relationships were used to obtain the root-mean-square (rms) of intensity and length scales of the index of refraction field. Smith & Truman (1990) used a more sophisticated approach, in which a model transport equation for the rms refractive index fluctuations was solved. The turbulence information was then fed into an optics model based on geometric optics, which predicts properties of the beam such as amplitude loss and spreading. Truman (1992) and Truman & Lee (1990) were among the first to perform time-accurate computational studies of aero-optical distortions. They used direct numerical simulation (DNS) of a homogeneous shear flow and turbulent channel flow to study the induced optical wavefront errors. The simulations were based on incompressible flow equations at relatively low Reynolds numbers, and the fluctuating refractive index was modeled by a passive scalar. The anisotropy of the optical phase errors due to anisotropy of the flow was noted in their work.

Because of its ability to resolve large-scale motions at a reasonable computational cost, Large-Eddy Simulation (LES) has recently been used for aero-optics. Childs (1993) carried out LES of a compressible turbulent mixing layer and performed ray tracing through it. Jones & Bender (2001) used LES to study aero-optical distortions in a fuselage/turret configuration. They used ray tracing to obtain the wavefront error and represented it in terms of Zernike polynomials. Also, they studied instantaneous far-field intensity patterns using the Fraunhofer approximation. Tromeur *et al.* (2003) used LES to study aero-optics of a supersonic boundary layer. Sinha *et al.* (2004) used experiments and LES to investigate control of flowfields to mitigate the distortion of a laser beam passing through a cavity shear layer. In these works the major contribution to optical distortions was assumed to be from the large resolved scales of the flow. The grid resolutions were poor in the cases involving complex geometries, and the numerical schemes employed were either total variation diminishing (TVD) or upwinding techniques that are highly dissipative. This can severely impact the effectiveness of the subgrid scale (SGS) model and artificially damp the small resolved scales of the flow (see Mittal & Moin 1997), which can be important.

The present study is concerned with the numerical simulation of a compressible turbulent wake and its aero-optical effects. We consider the propagation of an optical beam through the flow over a circular cylinder at Reynolds number of 3900 and freestream Mach number of 0.4. The time-dependent refractive-index (density) field is computed using LES, and the time series of distorted optical wavefronts and far-field intensity are obtained using a combination of ray tracing and Fourier optics. An important distinction between the present study and the previous studies is that the numerical scheme is based on a non-dissipative staggered-mesh formulation, which leads to more accurate representations of a wide range of optically important flow scales.

2. Accomplishments

2.1. Flow simulation

The compressible flow over a circular cylinder at $Re_D = 3900$ and $M = 0.4$ is computed by LES, using a sixth-order, energy conservative, compact finite difference scheme de-

	C_d	$-C_{p_b}$	St	θ_{sep}	U_{min}
Experiments†	0.99 ± 0.05	0.88 ± 0.05	0.215 ± 0.005	86 ± 2.5	-0.24 ± 0.1
LES‡	1.00	0.95	0.203	85.8	-0.32
LES¶	1.00	0.93	0.207	86.9	-0.35
LES	1.04	0.94	0.210	88.0	-0.37
LES††	0.97	0.85	0.213	88.2	-0.31
Present, $M = 0.2$	0.99	0.86	0.206	86.3	-0.33
Present, $M = 0.4$	1.18	1.08	0.202	87.1	-0.26

TABLE 1. Comparison of global flow statistics for flow over a circular cylinder at $Re = 3900$. The parameters from left to right are drag coefficient, base pressure coefficient, Strohal number, separation angle, and minimum averaged streamwise velocity.

† see Kravchenko & Moin (1998)

‡ Beaudan & Moin (1994)

¶ Mittal & Moin (1997)

|| Kravchenko & Moin (1998)

†† Rizzetta *et al.* (2003)

veloped by Nagarajan *et al.* (2003). The LES code, originally written for a C -mesh, has been modified for a generalized O -mesh to enhance grid smoothness and hence numerical stability. The numerical scheme uses implicit time advancement near the wall and third-order Runge-Kutta away from the wall. The dynamic SGS model for compressible flow by Moin *et al.* (1991) with modification of Lilly (1992) is used to account for the effect of the SGS on the flow.

The computational domain has a radius of approximately $20D$ (D = cylinder diameter) and a width of πD in the spanwise direction. The discretization of the code is based on a generalized curvilinear coordinate formulation. The mesh size is $288 \times 200 \times 48$ in the wall normal, azimuthal, and spanwise directions, respectively. A sponge layer is applied at the outer boundary to make it non-reflecting. The total integration time was over 70 shedding cycles. From the last 14 shedding cycles of the simulation, approximately 800 snapshots of the density field were saved for aero-optical study.

The literature includes several numerical and experimental investigations of incompressible flow over a cylinder at Reynolds number of 3900, which are used to help validate our results. Because all those studies are in the incompressible regime, we performed a Mach 0.2 simulation for validation and a Mach 0.4 simulation for aero-optical study. The validation is appropriate, because at Mach 0.2 the compressibility effect on flow statistics is expected to be relatively small.

Table 2.1 compares the major statistics of our simulations with the previously published ones. For the case of Mach 0.2 the global statistics are consistent with other studies. At Mach 0.4 there is a small difference in the drag coefficient, which is attributed to the effect of compressibility. Figure 1 shows the energy spectra of the vertical velocity in the wake centerline five diameters behind the cylinder. As shown in the figure, the present simulation successfully captures the details of the experimental spectrum, including very high frequency components. The two spectral peaks (at the vortex shedding frequency and its third harmonic) are captured very accurately. Contours of the instantaneous vorticity magnitude in a spanwise cut at a given time are shown in Fig. 2. The two separated shear layers and the development of the Karman vortex street are clearly seen and are in qualitative agreement with experimental observations.

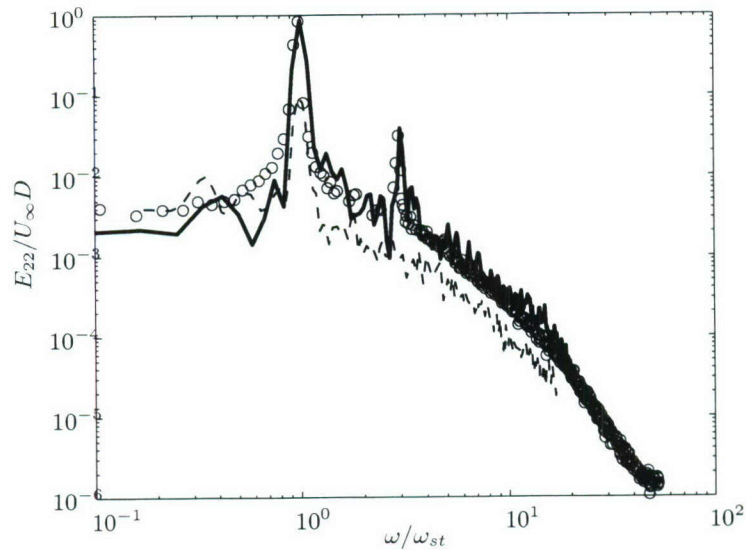


FIGURE 1. Energy spectra of vertical velocity as a function of non-dimensional frequency. —, Present LES ($M = 0.2$); - - - , LES of Kravchenko & Moin (1998); \circ , Experiment (Ong & Wallace 1999).

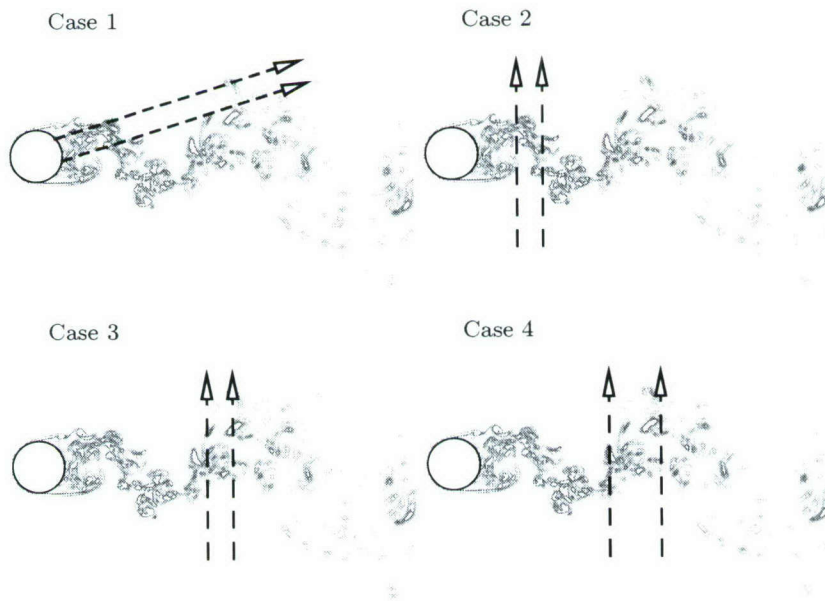


FIGURE 2. Schematics of optical propagation for four different cases. Arrows represent directions of optical propagation. The distance between the two arrows corresponds to the diameter of the optical aperture. The contours represent instantaneous vorticity magnitude in a spanwise plane.

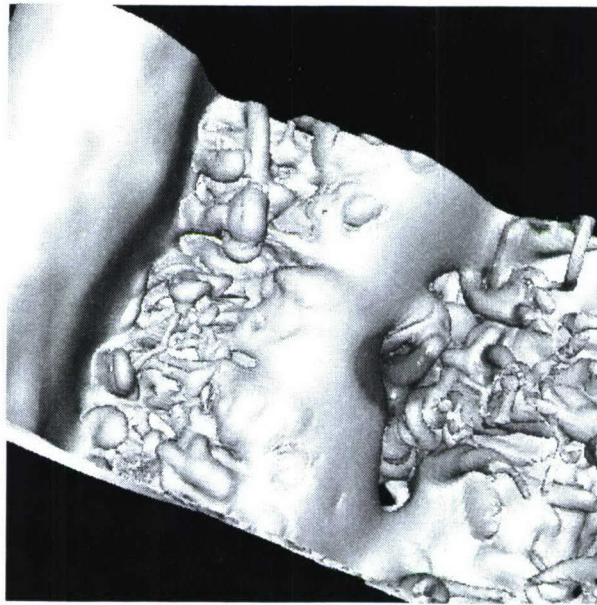


FIGURE 3. Instantaneous isosurfaces of density for $\rho = 0.98\rho_\infty$. The dark zone schematically represents the optical beam.

2.2. Optical computation

For optical analysis, four different cases are considered as shown schematically in Fig. 2. In the first case, an optical beam is emitted from the surface of the cylinder at an angle of approximately 17° with respect to the direction of downstream flow. For better numerical accuracy, the initial intensity of the beam is assumed to be a Gaussian profile that decays to $1/e^2$ times the maximum value at a distance of $0.15D$ from the optical axis. In our computations the optical intensity is truncated at $0.35D$ away from the axis where the intensity is less than 0.01% of the peak intensity. In the second case the optical beam of the same aperture diameter is shot vertically through the near wake behind the cylinder. The axis of the beam is $1.5D$ downstream from the cylinder axis. In the third case the beam is moved further downstream to $3.5D$ from the cylinder axis. Finally, in the fourth case the size of the optical aperture is doubled to $0.6D$ with its optical axis remaining in the same position as in Case 3. Figure 3 shows a snapshot of the fluctuating density field in the cylinder wake with an optical beam (corresponding to Case 3) marked as a dark spot.

A combination of ray tracing with Fourier optics, which has been used in previous computations (see, for example, Jones & Bender 2001), is an accurate tool to compute optical wave propagation in the parameter range of interest. In this method the domain of beam propagation is divided into two parts: the small near field in which ray tracing can be applied accurately, and the far field in which the density is assumed spatially uniform and Fourier optics can be applied. Spline interpolations are used to obtain the value of the density and its gradients along the ray path. Once ray tracing yields the distorted wavefront after passing the turbulence region, Fourier optics is used to find the far-field intensity pattern for given the optical wavelength and distance of propagation. The

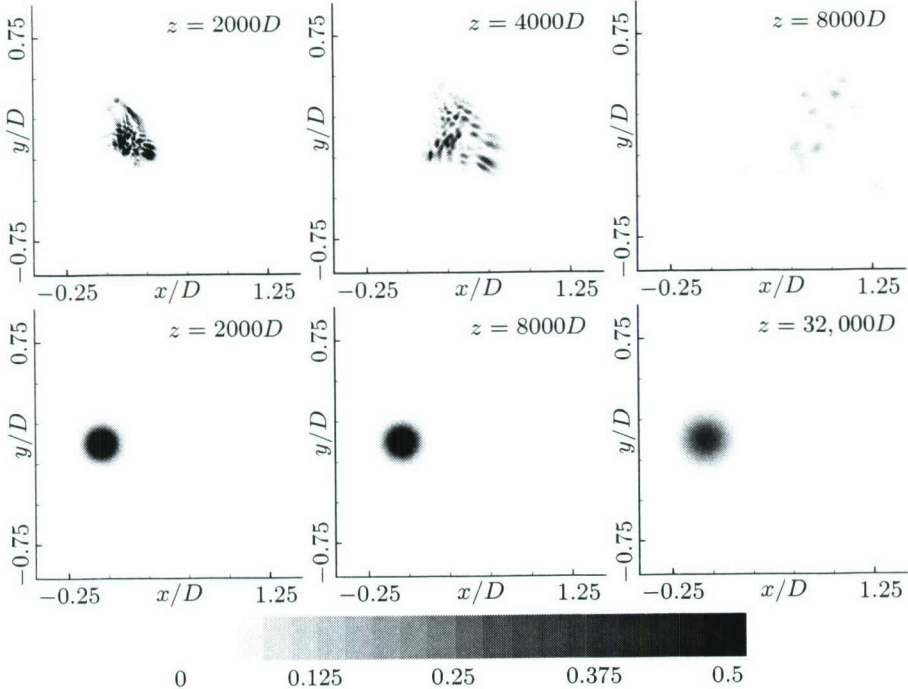


FIGURE 4. Instantaneous far-field intensity patterns for an aberrated beam corresponding to Case 1 (top) and a non-aberrated beam (bottom) at different distances of propagation. The optical wavelength is $2.5 \times 10^{-6}D$. The intensity levels are normalized by the peak intensity at the aperture where a Gaussian profile is assumed.

Fraunhofer approximation (see Saleh & Teich 1991) is used if the distance of propagation is sufficiently large; otherwise our Fourier optics is based on the exact solution of wave equation.

In the optical calculation the near field is taken to be within $20D$, while the far-field distance varies from 10^3D to infinity. The optical wavelengths considered vary from $2.5 \times 10^{-6}D$ to $4 \times 10^{-5}D$. We assume a linear relation between the index of refraction and density (see Wolf & Zizzis 1978) in the non-dimensional form: $n - 1 = 2.8 \times 10^{-4} \times \rho/\rho_\infty$, where ρ and ρ_∞ are the instantaneous and freestream densities, respectively. In general, the constant in the relation depends on the reference density ρ_∞ , which is based on air under atmospheric conditions in this study. Depending on the optical wavelength, 256 to 2048 Fourier modes in each direction in the plane perpendicular to the beam are used for far-field computations.

2.2.1. Instantaneous results

Figure 4 shows the spatial evolution of the far-field intensity of a distorted beam in Case 1 and contrasts it with that of an undistorted one, for an optical wavelength of $2.5 \times 10^{-6}D$. The distorted beam shows a highly irregular and speckled intensity pattern, as described by Zeldovich *et al.* (1995). After a sufficient distance of transmission, the distortion leads to a significant loss of intensity. The beam starts to diverge at $4000D$. In contrast, the undistorted beam remains focused for a distance of up to approximately $32,000D$. In other words, the effective range of the optical beam is reduced by one order

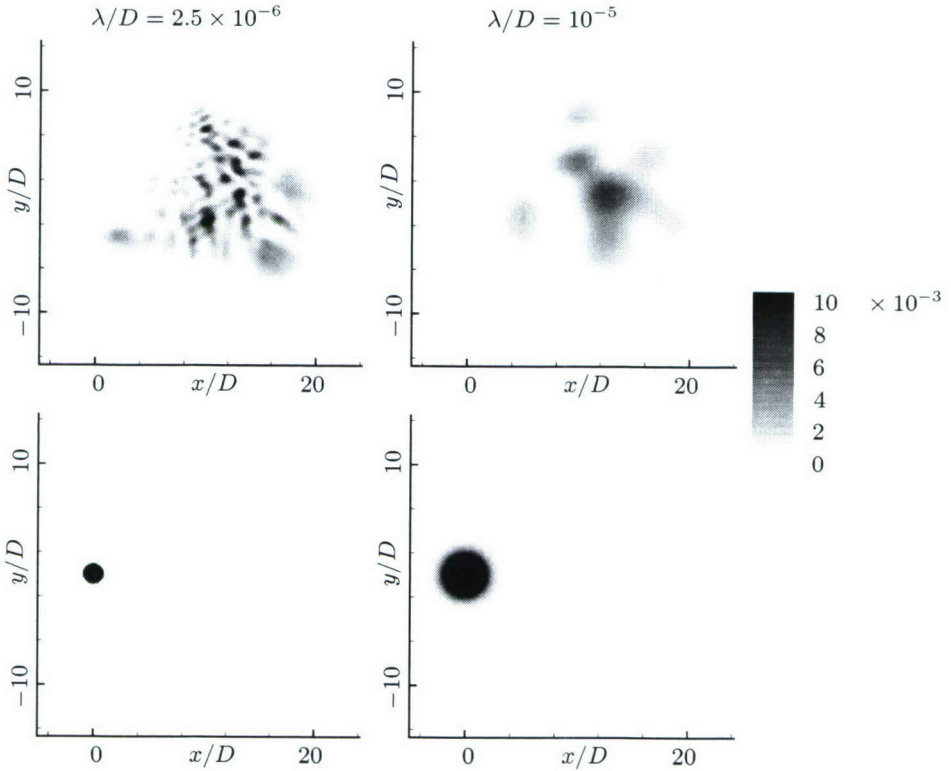


FIGURE 5. Instantaneous far-field intensity patterns for Case 1 for two different optical wavelengths (top) in comparison to undistorted beam patterns (bottom). The propagation distance of the beam is $10^5 D$, where the Fraunhofer approximation holds. The intensity levels are normalized by the peak intensity at the aperture.

of magnitude due to turbulence-induced distortions. Figure 5 shows the far-field intensity patterns for the same beam configuration with two different optical wavelengths. For the shorter wavelength beam (left) the interference patterns show smaller-scale oscillations, while the global structure of the patterns is nearly the same for both wavelengths. The speckled pattern appears at optical wavelengths smaller than $10^{-5} D$ and as expected, from diffraction theory, the speckle size was found to be approximately proportional to the wavelength.

Figure 6 shows the effect of optical aperture diameter on the instantaneous intensity pattern by comparing distortions in cases 3 and 4 induced by the same instantaneous flowfield. By changing the aperture, while the qualitative spread of the beam is not changed, the speckle sizes and the interference pattern are changed significantly.

The above results illustrate that aero-optical distortions are strongly dependent on parameters such as the optical wavelength, distance of propagation, and aperture diameter. In a related study, Mani *et al.* (2006) derived several analytical relations between the spread of a distorted beam and these parameters, as well as the statistics of the flow. For statistical study of optical distortions, those relations can help reduce the computational effort by providing algebraic descriptions. However, in this study, we present more gen-

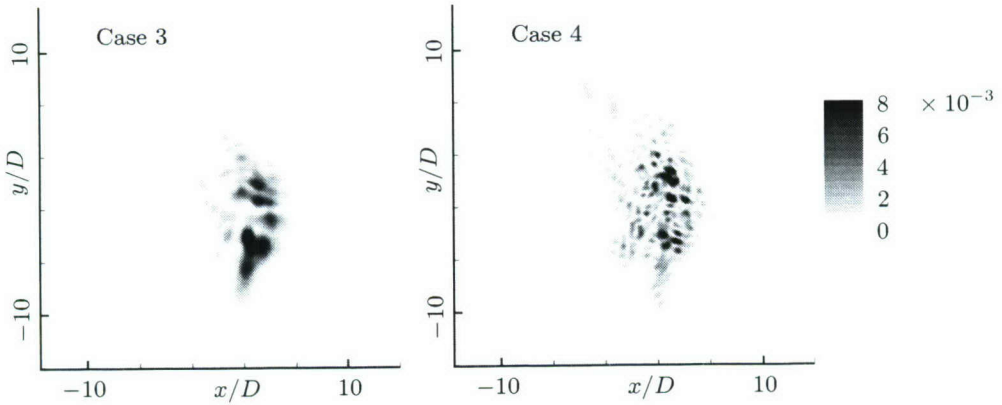


FIGURE 6. Comparison of instantaneous far-field intensity patterns for cases 3 and 4 where the only difference is the diameter of the optical aperture. The propagation distance of the beams is $10^5 D$ and the optical wavelength is $2.5 \times 10^{-6} D$.

eral statistics of optical distortions by examining the time averaged intensity pattern. We limit ourselves to the case of the Fraunhofer limit for distance of propagation in order to reduce the parameter space by one dimension. A detailed description, including different distances of propagation and the effect of distortion on the range of optical beams, is given in Mani *et al.* (2006).

2.2.2. Time averaged statistics

Figure 7 shows time averaged intensities for three wavelengths in the far field for Case 1 and compares them against the intensities of undistorted beams. As expected, for all the wavelengths studied, the undistorted beams provide higher intensities in the far field. It can be seen that for the case of undistorted beams, diffraction causes the longer wavelength beams to spread more. As a result, when there is no distortion, for shorter wavelength beams we have higher intensity, which translates to better performance of the optical device. In contrast, for the case of distorted beams the effect of the optical wavelength on the peak intensity is not as strong and is not monotone with the wavelength. In fact, there is an optimal wavelength that leads to a maximum time averaged peak intensity.

Figure 8 compares the time averaged intensity for the four different cases. The plots also provide the statistics of the tilt corrected patterns, where the tilt error is removed at every time step. From the plots it can be concluded that the tilting effect is significant, but not necessarily dominant, compared to the spreading effect. In general as the beam is moved further downstream, the aero-optical distortions decrease due to the decay of the turbulence. A comparison of cases 3 and 4 shows that the time averaged intensity pattern without tilt removal is almost unchanged, even though the aperture size is changed. This is in contrast to the case of undistorted beams for which larger aperture size leads to better focus properties. This is most likely due to the fact that the aero-optical effect dominates the diffraction effect in this regime. Furthermore, the improvement of the beam quality by tilt removal is less prominent in Case 4 compared to Case 3. Since tilt removal acts as a high-pass filter with filter size of the order of aperture diameter, this observation suggests that the optically important structures at this particular location

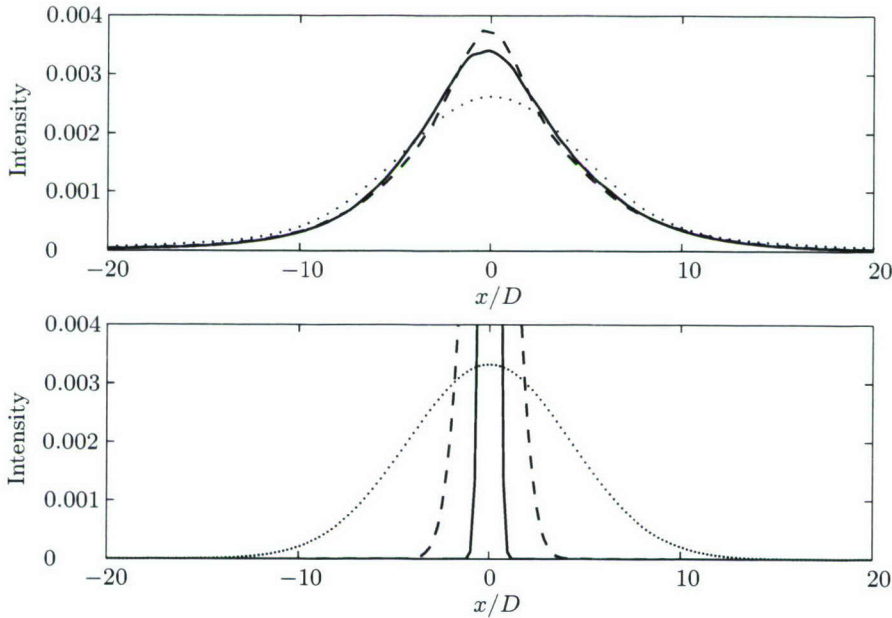


FIGURE 7. Time averaged and tilt removed intensities for different optical wavelengths (top) in comparison with those of undistorted beams (bottom). To obtain a 1-D plot, the 2-D intensity patterns are integrated in the y direction shown in Fig. 4, which is the homogeneous direction of the flow. The plots correspond to Case 1 at a distance of $10^5 D$. —, $\lambda/D = 2.5 \times 10^{-6}$; - - -, $\lambda/D = 10^{-5}$; - · - · -, $\lambda/D = 4 \times 10^{-5}$.

are dominated by length scales smaller than or comparable to the aperture size in Case 3 (for more information, see Siegenthaler *et al.* 2005).

2.3. Grid convergence

A grid convergence study was conducted to ensure that the unresolved scales in the LES are optically unimportant. The resolution was doubled in every direction to a grid of $575 \times 400 \times 96$ in the wall normal, azimuthal, and spanwise directions, respectively. Since aero-optical distortions are due to density fluctuations, we compare density spectrum from the coarse mesh simulation with that from the fine mesh simulation. It can be seen that increasing grid resolution improves the capturing of small-scale fluctuations of density. However, the aero-optical effect of the additional small-scale fluctuations appears to be negligible compared to the effect of larger scales, as shown in Fig. 10, which compares the time averaged intensities from the two simulations. This indicates that the coarser mesh simulation has satisfactory resolution in terms of capturing the important aero-optical effects.

3. Conclusion

In summary, a high-resolution LES of compressible flow past a circular cylinder at $Re_D = 3900$ and $M = 0.4$ has been performed, and the flow statistics have been validated

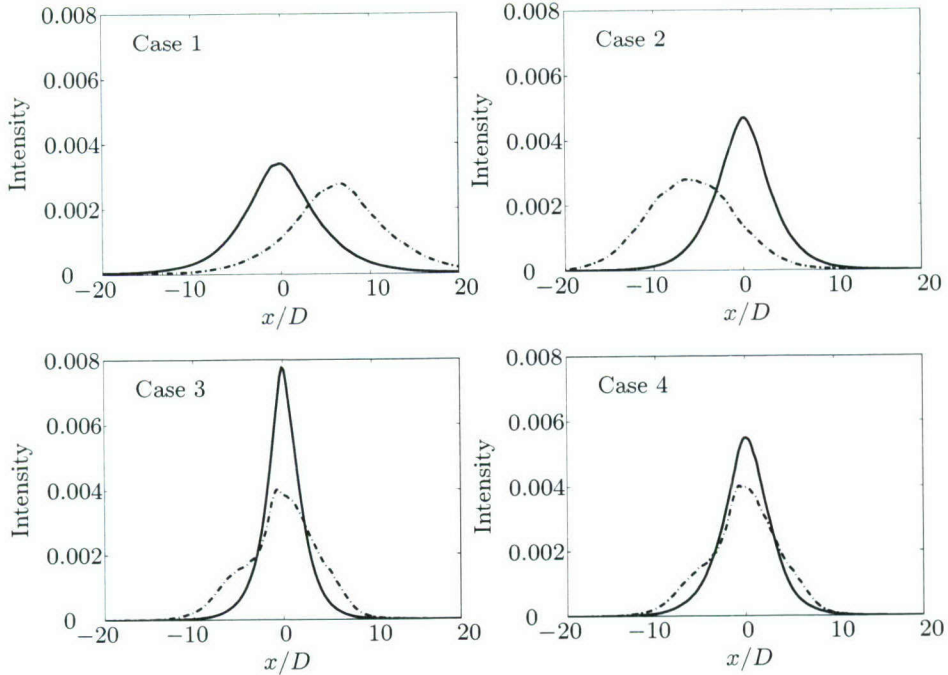


FIGURE 8. Time averaged intensity for optical wavelength of $2.5 \times 10^{-6}D$ for the four cases shown in Fig. 2. The 2-D intensity patterns are integrated in one direction (see Fig. 7 caption). —, tilt removed; - - -, original.

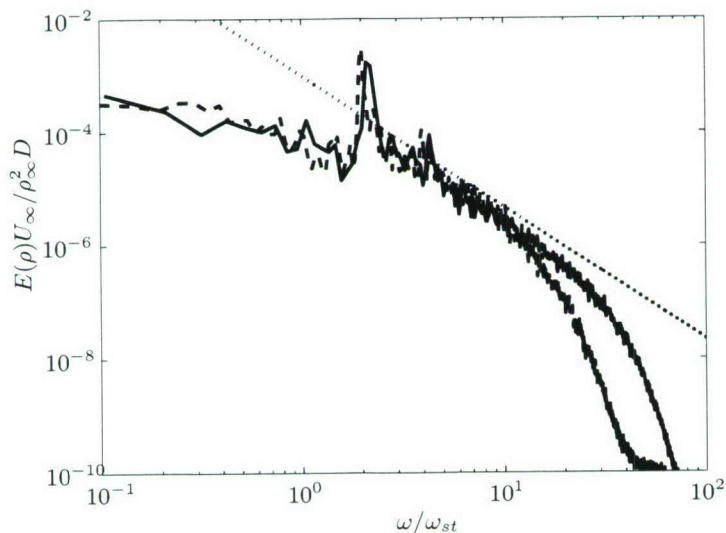


FIGURE 9. Density spectra at $5D$ downstream of the cylinder for the coarse and fine mesh simulations. - - -, Coarse mesh simulation; —, Fine mesh simulation; - - - - -, $-7/3$ law.

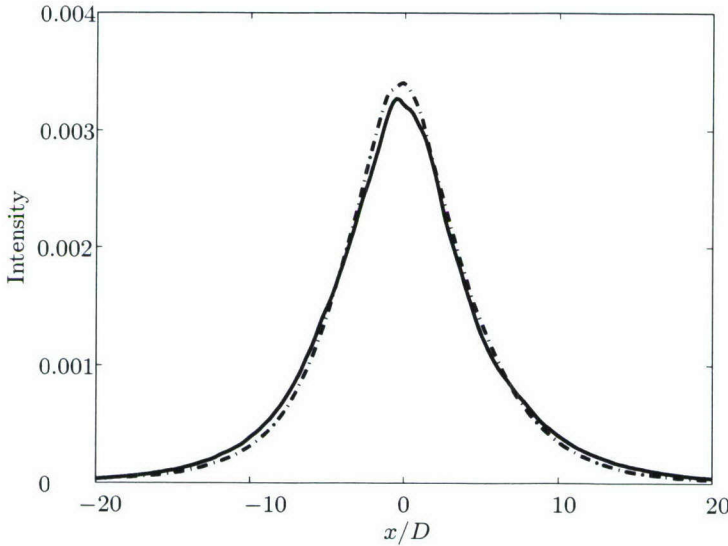


FIGURE 10. Comparison of time averaged far field intensities for $\lambda/D = 2.5 \times 10^{-6}$ and propagation distance of $10^5 D$ for the coarse mesh (---) and fine mesh (—) simulations.

against previous experimental and numerical results. Using the space-time history of the refractive index (density) field from LES, instantaneous and statistical descriptions of the flow-induced optical aberrations have been studied for different optical wavelengths and propagation distances.

Our results show that the turbulent wake flow can significantly degrade the performance of optical beams. Depending on the wavelength, the maximum irradiance of the optical beam can be reduced by one or two orders of magnitude. Also, turbulence can severely limit the effective range of an optical beam. Unlike the undistorted case where shorter wavelengths are desirable for greater depth of focus, for an aberrated beam there is an optimal wavelength for the highest peak intensity.

Acknowledgment

This work was supported by the Air Force Office of Scientific Research under grant Nos. F49-620-03-1-0132 and FA9550-06-1-0147. Computer time was provided by NASA at NASA Ames Research Center.

REFERENCES

BEAUDAN, P. & MOIN, P. 1994 Numerical experiments on the flow past a circular cylinder at sub-critical Reynolds number. *Tech. Rep. TF-62*. Department of Mechanical Engineering, Stanford University, Stanford, California.

CATRAKIS, H. J. & AGUIRRE, R. C. 2004 New interfacial fluid thickness approach in aero-optics with applications to compressible turbulence. *AIAA J.* **42**, 1973–1981.

CHERNOV, L. A. 1960 *Wave Propagation in a Random Medium*. New York, NY: McGraw-Hill.

CHEUNG, K. & JUMPER, E. J. 2004 High temporal bandwidth optical wavefront sensor technologies. Proceedings of 2004 AFOSR Contractors' Meeting in Turbulence and Rotating Flows, Denver, Colorado, Aug. 4–5, 2004.

CHILDS, R. E. 1993 Prediction and control of turbulent aero-optical distortion using large eddy simulation. AIAA Paper 93-2670.

DIMOTAKIS, P. E., CATRAKIS, H. J. & FOURGUETTE, D. C. 2001 Flow structure and optical beam propagation in high-Reynolds number gas-phase shear layer and jets. *J. Fluid Mech.* **433**, 105–134.

FITZGERALD, E. J. & JUMPER, E. J. 2004 The optical distortion mechanism in a nearly incompressible free shear layer. *J. Fluid Mech.* **512**, 153–189.

GILBERT, K. G. 1982 Overview of aero-optics. In *Progress in Astronautics and Aero-nautics: Aero-Optical Phenomena*, Vol. 80, 1–9.

GORDEYEV, S., JUMPER, E. J., NG, T. T. & CAIN, A. B. 2003 Aero-optical characteristics of compressible, subsonic turbulent boundary layers. AIAA Paper 2003-3606.

GORDEYEV, S., JUMPER, E. J., NG, T. T. & CAIN, A. B. 2004 Optical disturbances caused by transonic separated boundary layer behind a 20-degree ramp: physics and control. AIAA Paper 2004-0472.

JONES, M. I. & BENDER, E. E. 2001 CFD-based computer simulation of optical turbulence through aircraft flowfields and wakes. AIAA Paper 2001-2798.

JUMPER, E. J. & FITZGERALD, E. J. 2001 Recent advances in aero-optics. *Progress in Aerospace Sciences* **37**, 299–339.

KRAVCHENKO, A. G. & MOIN, P. 1998 B-spline methods and zonal grids for numerical simulations of turbulent flows. *Tech. Rep.* TF-73. Department of Mechanical Engineering, Stanford University, Stanford, California.

LILLY, D. K. 1992 A proposed modification of the Germano subgrid-scale closure method. *Phys. Fluids A* **4**, 633–635.

MANI, A., WANG, M. & MOIN, P. 2006 Statistical description of free-space propagation for highly aberrated optical beams. *J. Opt. Soc. Am. A* **23**, 3027–3035.

MITTAL, R. & MOIN, P. 1997 Suitability of upwind-biased finite-difference schemes for large-eddy simulation of turbulent flows. *AIAA J.* **35**, 1415–1417.

MOIN, P., SQUIRES, K., CABOT, W. & LEE, S. 1991 A dynamic subgrid-scale model for compressible turbulence and scalar transport. *Phys. Fluids A* **3**, 2746–2757.

NAGARAJAN, S., LELE, S. K. & FERZIGER, J. H. 2003 A robust high-order compact method for large eddy simulation. *J. Comput. Phys.* **191**, 392–419.

ONG, L. & WALLACE, J. 1999 The velocity field of the turbulent very near wake of a circular cylinder. *Experiments in Fluids* **20**, 441–453.

RIZZETTA, D. P., VISBAL, M. R. & BLAISDELL, G. A. 2003 A time-implicit high-order compact differencing and filtering scheme for large-eddy simulation. *Int. J. Numer. Methods Fluids* **42**, 665–693.

SALEH, B. E. A. & TEICH, M. C. 1991 *Fundamentals of Photonics*, 121–122. John Wiley & Sons, Inc.

SIEGENTHALER, J., GORDEYEV, S. & JUMPER, E. 2005 Shear layers and aperture effects for aero-optics. AIAA Paper 2005-4772.

SINHA, N., ARUNAJATESAN, S., SEINER, J. M. & UKEILEY, L. S. 2004 Large-eddy simulations of aero-optic flow fields and control application. AIAA Paper 2004-2448.

SMITH, R. & TRUMAN, C. 1990 Prediction of optical phase degradation using a turbulent

transport equation for the variance of index-of-refraction fluctuations. AIAA Paper 90-0250.

SUTTON, G. W. 1969 Effect of turbulence fluctuations in an optically active fluid medium. *AIAA J.* **7**, 1737-1743.

TATARSKI, V. I. 1961 *Wave Propagation in a Turbulent Medium*. New York, NY: McGraw-Hill.

TROMEUR, E., GARNIER, E., SAGAUT, P. & BASDEVANT, C. 2003 Large eddy simulations of aero-optical effects in a turbulent boundary layer. *Journal of Turbulence* **4** (005).

TRUMAN, C. R. 1992 The influence of turbulent structure on optical phase distortion through turbulent shear flows. AIAA Paper 92-2817.

TRUMAN, C. R. & LEE, M. J. 1990 Effects of organized turbulence structures on the phase distortion in a coherent optical beam propagating through a turbulent shear flow. *Phys. fluids A* **2**, 851-857.

WOLF, W. & ZIZZIS, G. J. 1978 *The Infrared Handbook*, pp. 16-24.

ZELDOVICH, B. Y., MAMAEV, A. V. & SHKUNOV, V. V. 1995 *Speckle-wave Interactions in Application to Holography and Nonlinear Optics*. Boca Raton, FL: CRC Press.

Simulation of the incompressible flow through a jet engine fuel nozzle rig

By X. Wu, G. Iaccarino, F. Ham AND P. Moin

1. Motivation and objectives

Swirling flow discharged from an injector nozzle is important for flame stabilization in the jet engine combustion process. Inclusion of the details of the swirl-generating device, i.e., the realistic injector nozzle geometry, in combustor numerical simulation is necessary because the complicated, spatially developing swirl pattern produced by a nozzle is difficult to emulate faithfully using indirect means. An indirect approach of swirl generation for large-eddy simulation was developed by Pierce & Moin (1998). Brankovic *et al.* (2000) reported comparison of laser velocimetry measurements with unstructured Reynolds-Averaged (RANS) predictions of incompressible swirling flow through a jet engine fuel nozzle rig. The actual hardware studied was a low-emission fuel nozzle and swirler combination, representative of current production engines. Their unstructured mesh has a total of 2.55 million hexahedral elements covering a 180° periodic sector of the injector, and was generated by simplifying a CAD model. The computations of Brankovic *et al.* were performed using the National Combustion Code (NCC). They found that quantitative accuracy was not achieved by the calculation. In particular, Brankovic *et al.* pointed out that the central recirculation zone measured from their own laser velocimetry experiments is both larger in extent, and has higher reverse flow than could be predicted using their computational approach. Other recent calculations of swirling flow in jet engine combustor with the full injector configuration were reported by Grinstein *et al.* (2002) and Roux *et al.* (2005).

Mahesh *et al.* (2004) developed an unstructured fractional-step algorithm for LES of incompressible flow in complex geometries. Their fractional-step method uses collocated grids and is formulated with combined usages of cell center based Cartesian velocity and face center based face normal velocity; pressure is stored at cell center. Discrete kinetic energy conservation is achieved by proper handling of the convection and pressure-gradient terms. Integrated global contribution of the convective term to discrete kinetic energy is zero if values at the face center are calculated as a simple arithmetic mean of the values at the two cell centers that have that particular face in common. Although pressure gradient term is globally non-conservative in the equation of discrete kinetic energy, its effect can be reduced through a least-square minimization procedure. Mahesh *et al.* applied their algorithm to the flow in one sector of a jet engine combustor. The predicted mass flow splits through various injector nozzle components compare very well with measurements. No detailed comparisons of the combustor flow velocity profiles were reported in their study.

We present LES results of incompressible, non-reacting flow in a fuel nozzle rig using the method of Mahesh *et al.* (2004). Smagorinsky subgrid-scale model was used together with a slightly modified implementation of the Germano dynamic procedure tailored for unstructured grids. Details on the model implementation and filtering procedure are as in Mahesh *et al.* The geometry is from Pratt and Whitney, and is substantially similar

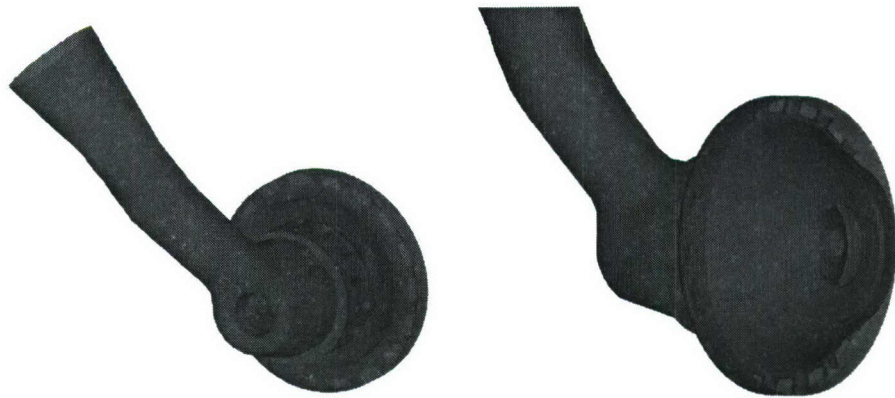


FIGURE 1. Computational model of the Pratt Whitney fuel nozzle rig. Left: side-end view; right: side-front view.

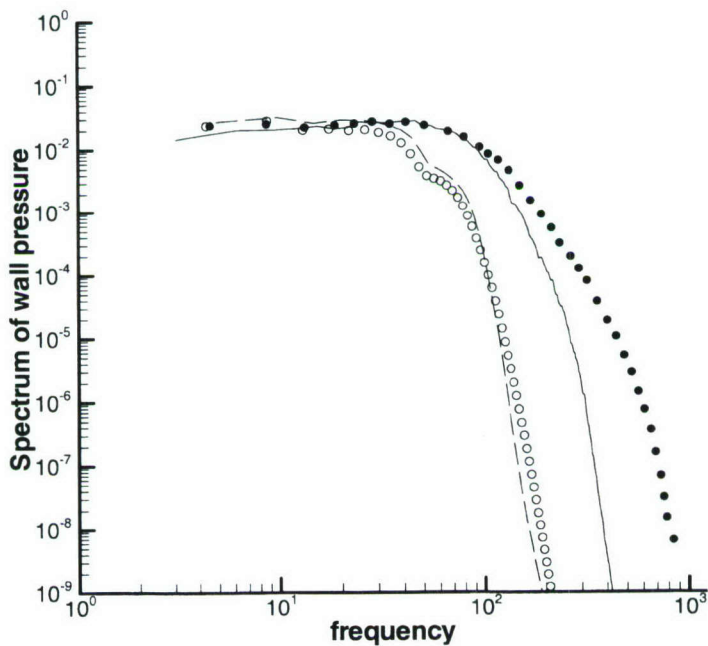


FIGURE 2. Frequency spectrum for wall pressure fluctuations in a planar channel flow. • DNS of Choi & Moin (1990) with a spectral code; ○ coarse LES of Wang with a structured finite difference code (unpublished); solid line: present fine LES; dashed line: present coarse LES.

to that of Brankovic *et al.* (2000) with the exception that the present rig does not have purge holes and their associated intake, see Fig. 1 and the Fig. 1b of Brankovic *et al.* (2000). Validation experimental data for the present nozzle rig flow are also supplied by Pratt and Whitney.

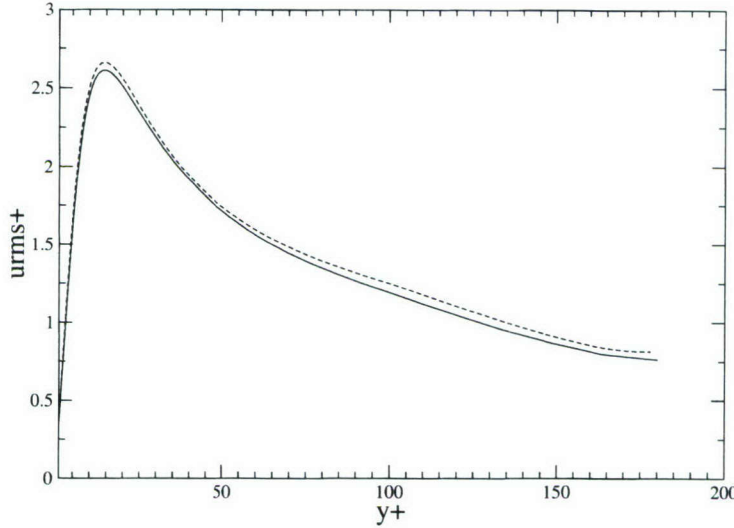


FIGURE 3. Streamwise turbulence intensity in a planar channel flow. Solid line: present fine LES; dashed line: DNS of Moser *et al.* (1999).

2. Validation in simple flows

Prior to computing the flow through injector nozzle, the present unstructured LES computer program (CDP2.1) was first applied to fully developed turbulent planar channel flow for the purpose of validation. Flow conditions and geometrical specifications used in our simulation are identical to those used in the direct numerical simulation (DNS) of Choi & Moin (1990) with a spectral method. In particular, the Reynolds number based on channel half-height and friction velocity is 180. Two mesh sizes were used in the present simulations, (32x64x32) and (128x128x128). The coarse mesh size has a resolution of 72 wall units in the streamwise direction, and 24 wall units in the spanwise direction. These are the same as those used by Meng Wang in a previous channel calculation at the Center for Turbulence Research with a structured second-order finite volume LES code. The fine mesh has the same size as in Choi & Moin. Figure 2 compares the present channel fluctuating wall-pressure spectrum with previous computations. For the calculation of power spectra estimation, a long history of pressure samples was saved at selected locations at every time step. Notations related to power spectrum computation and related post-processing procedures follow strictly those described in Choi & Moin (1990). From Fig. 2 it is clear that at the coarse resolution, our wall pressure spectra results agree well with the results computed previously using a structured LES code by Meng Wang, indicating the reliability of the present code from one perspective. The figure also shows that at the fine resolution our wall pressure spectra agree with the DNS data of Choi & Moin (1990) in the lower frequency range, but there is an earlier drop-off at the high frequency range. This is to be expected because the DNS of Choi & Moin was performed using a spectral code, while the present approach is unstructured second-order finite volume. Figure 3 compares the streamwise turbulence intensity obtained from the

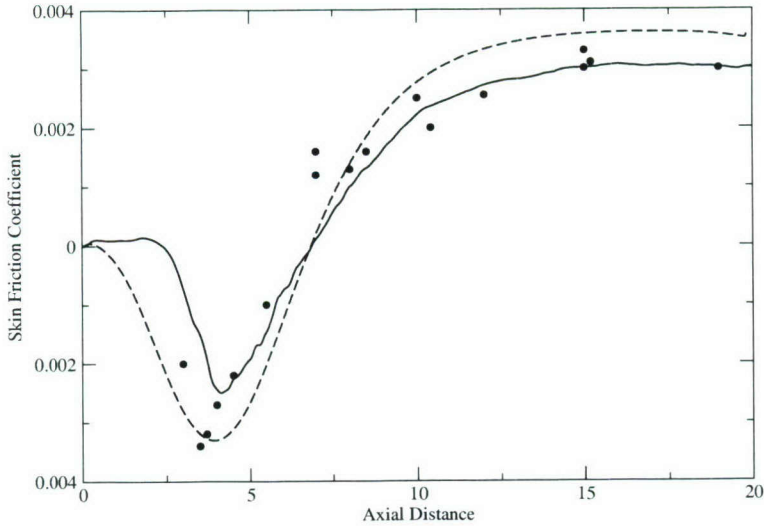


FIGURE 4. Skin friction coefficient in the flow over a backward facing step. • Jovic & Driver (1994); solid line: present LES; dashed line: present RANS.

present LES with that from the DNS of Moser *et al.* (1999). Although not shown here, mean velocity and other second order turbulence statistics from our computation also agree very well with existing DNS channel flow data.

The present computer program was also validated using turbulent flow over a backward-facing step. The flow conditions and geometrical specifications are identical to those reported by Le, Moin & Kim (1997). In particular, the Reynolds number is 5100 based on step height and inlet freestream velocity. The computational domain consists of a streamwise length of 30 step heights, including an inlet section of 10 step heights prior to the sudden expansion, vertical dimension is 6 step heights, and the spanwise width is 4 step heights. Both LES and RANS computations were performed with the same code CDP2.1. For the RANS computation, the V2F turbulence model of Durbin (1995) was implemented into the unstructured LES solver. At the upstream inlet, LES used the zero-pressure gradient flat-plate boundary layer velocity fields obtained from another independent computation. That auxillary computation uses DNS to simulate a spatially developing flat-plate boundary layer through the laminar, transitional and turbulent regimes, covering a range of momentum thickness Reynolds number from 80 to 1000. The boundary layer transitions because of imposed weak, migrating freestream perturbations at the inlet. The time-dependent velocity fields at the station of momentum thickness Reynolds number 700 were saved and subsequently used as inlet conditions for the backward-facing step LES. RANS inflow conditions are from the statistics of Le *et al.*. At the upper boundary, slip wall boundary conditions were applied. Figure 4 compares the predicted skin friction coefficient with the experimental data of Jovic & Driver (1994). The skin friction obtained from the present LES exhibits interesting similarities to the DNS skin friction results of Le *et al.* in the following three respects. Near the step corner, there is region ($0 < x < 2$) with very weak positive skin friction, indicating the existence of a minor secondary recirculation zone. Secondly, the negative peaks attained

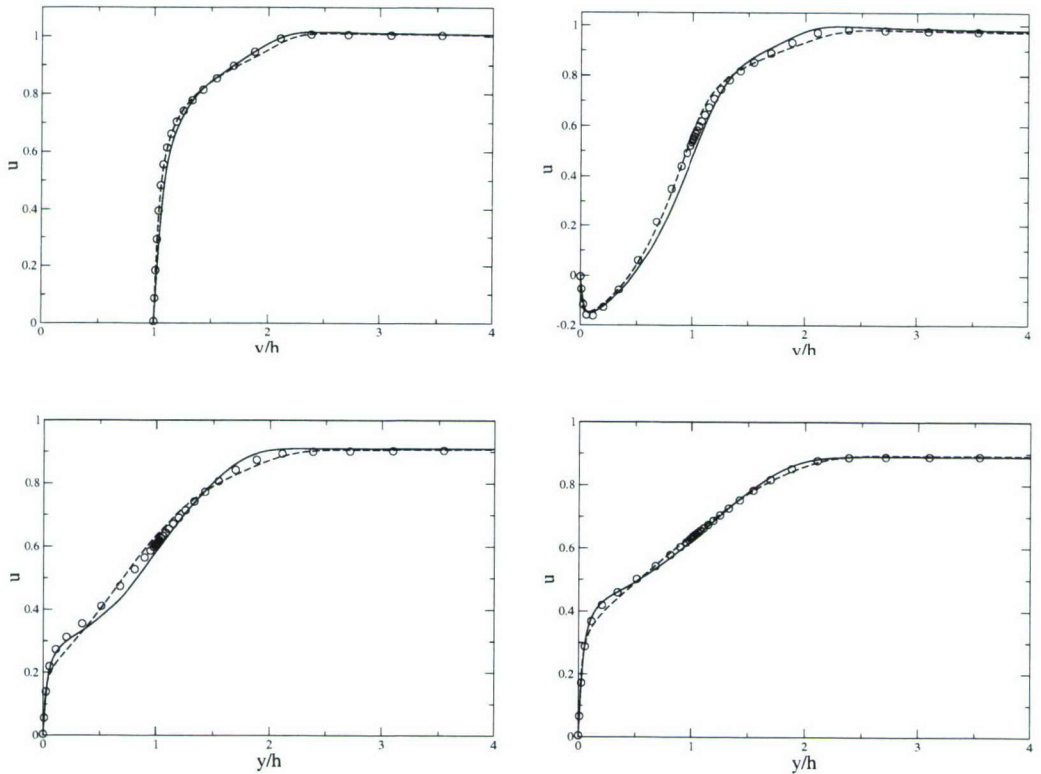


FIGURE 5. Mean streamwise velocity in the flow over a backward facing step. \circ DNS of Le *et al.* (1997); solid line: present LES; dashed line: present RANS. Upper left: $x = -3$; upper right: $x = 4$; lower left: $x = 10$; lower right: $x = 15$.

in the present LES and in previous DNS are not as deep as that of Jovic & Driver (1994). Further downstream, there is good agreement between the LES and DNS results with the experimental data. Mean streamwise velocity profiles at four different x stations are shown in Fig. 5. Both RANS and LES results show relatively good agreement with the DNS. The minor differences between the RANS and LES velocity profiles are mostly due to the slight discrepancy at the inlet.

3. Results of nozzle rig flow

Figure 1 shows the fuel injector nozzle rig model used in the present LES. Three types of air intakes can be seen from the end view. The central pipe with a small guide vane is the inlet for the core flow. The slots distributed along the circumference with a radius furthest away from the pipe axis are the tangential entries for guide flow. The slots distributed along the circumference with an intermediate radius (closer to the pipe axis) are the tangential entries for outer flow. From the side-front view, the outlets into the combustor chamber for the core flow, outer flow, and guide flow can be clearly seen. Note the axial position ranges for the three outlets are not the same, i.e., they are staggered. Figure 6 shows cross-sections of the computational domain. The $z = 0$ plane indicates

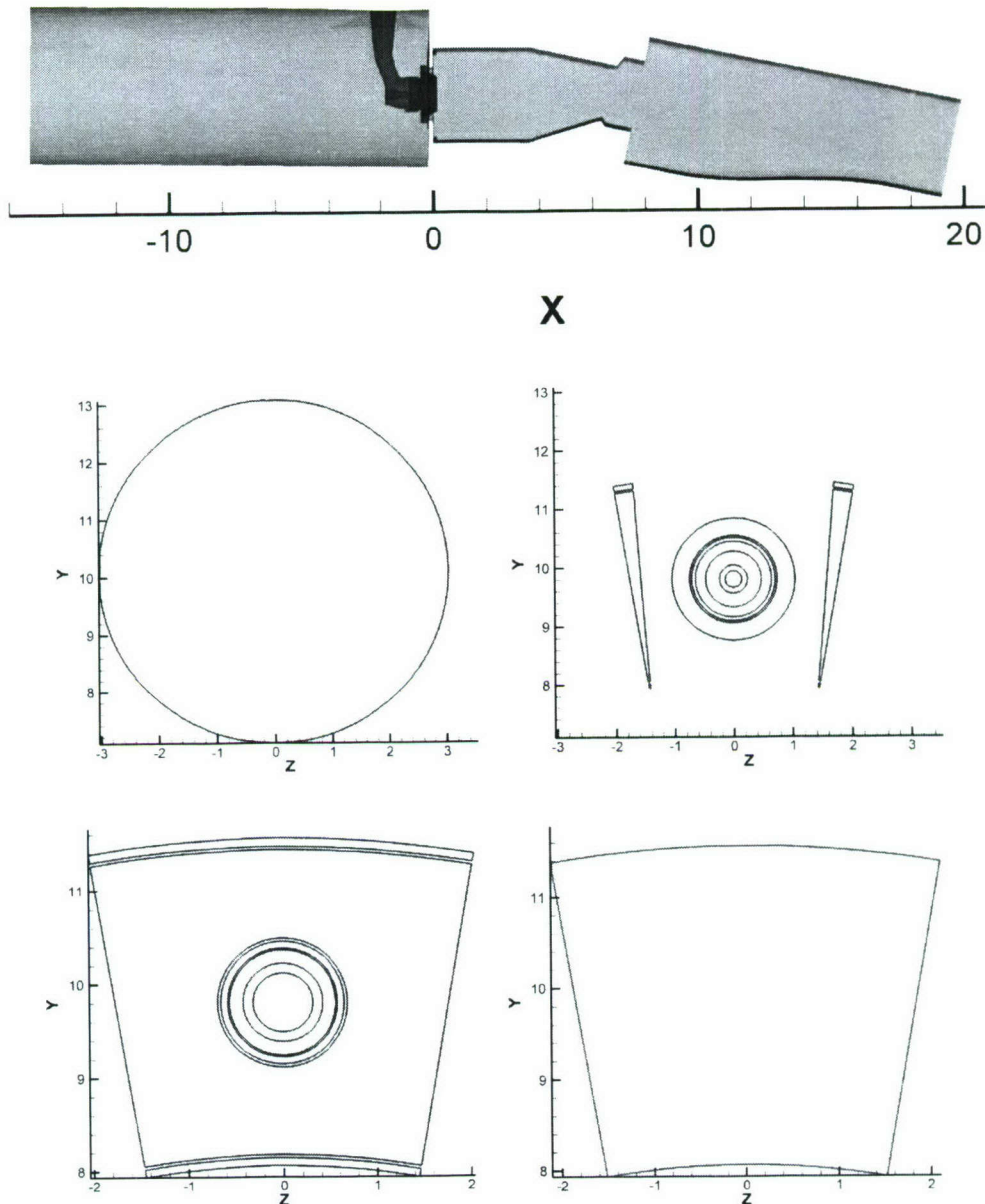


FIGURE 6. Computational domain of the present nozzle rig flow. Upper: $z = 0$ plane; middle left: $x = -4$ plane; middle right: $x = 0$ plane; lower left: $x = 0.01$ plane; lower right: $x = 2$ plane.

that axial coordinate x covers a range of $-15.5 < x < 20$, approximately. At $x = -4$, the cross-section of the computational domain is a full 360° circular pipe. Downstream of the nozzle at $x = 2$, the cross-section becomes a circular sector. As indicated in the figure, the nozzle axis is located at $y = 9.8$ and $z = 0$.

At the far upstream uniform inlet velocity was prescribed as 29.134 in/sec using ex-

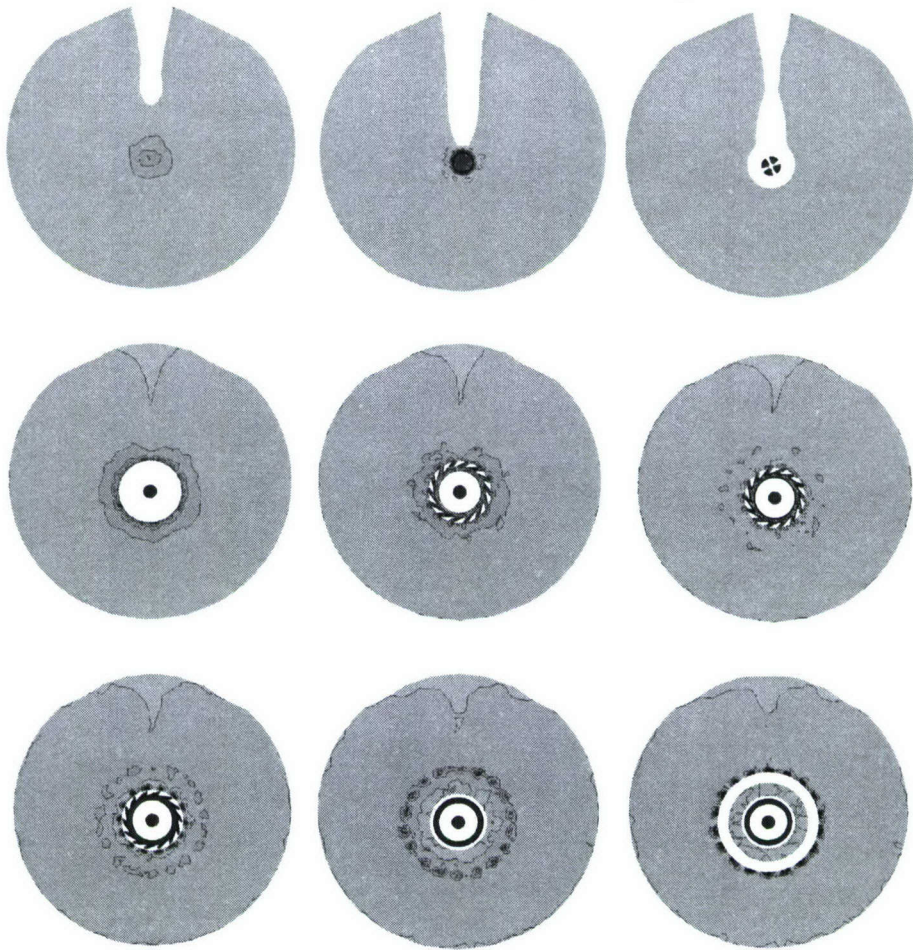


FIGURE 7. Contours of instantaneous axial velocity inside nozzle, light colors represent low axial speed. From top left to lower right (row major) the locations for the cross-sections are: $x = -2.1, -1.8, -1.55, -0.9, -0.8, -0.7, -0.6, -0.5, -0.45$, respectively.

perimental specifications. The Reynolds number based on inflow speed and unit length (1 inch) is 1246. Except for the inlet and outlet all the other boundary surfaces of the geometry are solid wall on which no-slip conditions were applied. A total of six calculations were performed with mesh sizes ranging from 3.6 to 8 million cells; they yielded similar and consistent results. Mesh shape and density in the region close to nozzle outlet were varied in the six cases. The maximum CFL number was set at 4.5 and the corresponding time step is approximately 7.0×10^{-7} seconds. It was found that 2×10^5 time steps are needed to converge the mean flow statistics.

The process of swirl generation by nozzle injector is complicated and can be appreciated by examining the velocity fields over a series of cross-sections perpendicular to the x -direction. Figure 7 shows the axial velocity contours over nine yz -planes up to $x = -0.45$. White space in the first three planes represents slices of the fuel stem hardware. The high-speed contours near the pipe axis in the plane of $x = -1.8$ is the core flow. The four small fan-like structures at $x = -1.55$ are due to the effect of guide vane inside the core

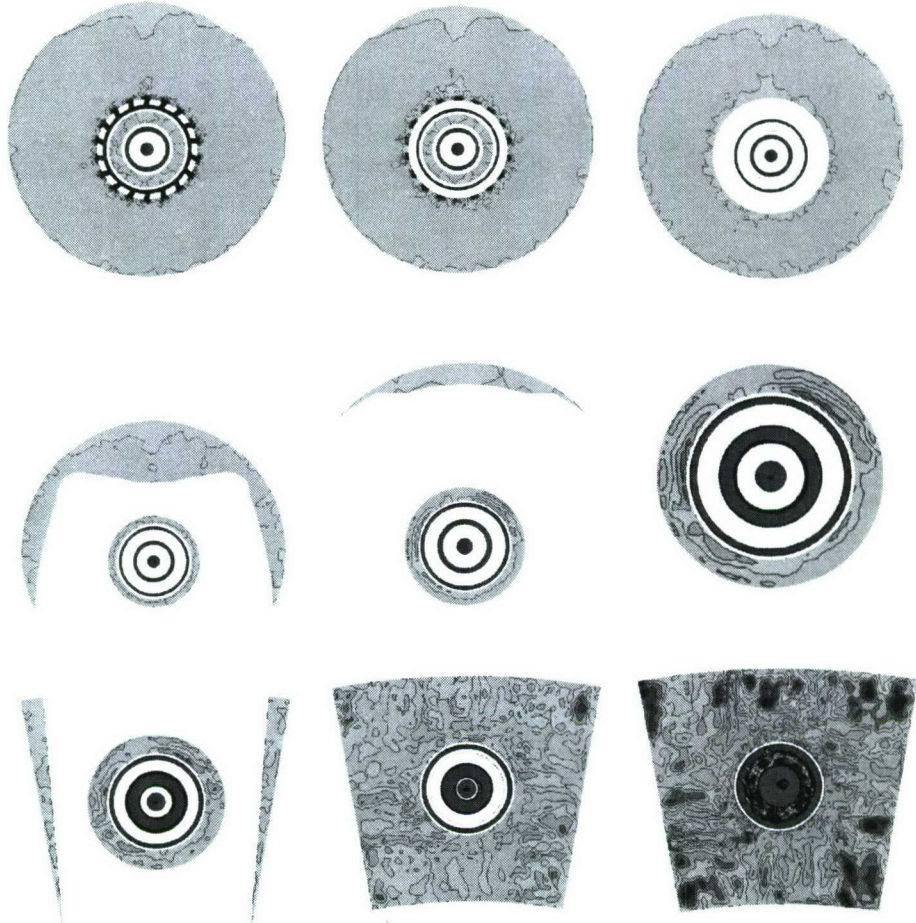


FIGURE 8. Contours of instantaneous axial velocity inside nozzle, light colors represent low axial speed. From top left to lower right (row major) the locations for the cross-sections are: $x = -0.4, -0.35, -0.20, -0.15, -0.10, -0.05, 0.00, 0.05, 0.15$, respectively.

flow intake. The tangential outer flow intakes are clearly visible on the three planes of $x = -0.8, -0.7$ and -0.6 . Also visible over these planes is the velocity wake behind the fuel stem. At the last two cross-sections the guide flow entries start to affect the flow, as indicated by the sparsely connected outer ring-like structures in the velocity contours. The actual guide flow entry slots are shown in the cross-section of $x = -0.4$ in Fig. 8. Over the yz -plane of $x = -0.2$ there are four isolated flow streams: core stream, outer stream, guide stream as well as the flow occupying the remainder of the container pipe. At the station of $x = -0.1$ the upstream container pipe has nearly ended, see also Fig. 6. Therefore almost all the inlet fluid mass now squeezes through the narrow passages near the nozzle axis. These ring-like flow streams merge further downstream inside the combustion chamber. Unlike the upstream pipe which covers a full 360° range, the downstream combustor spans only a small angular section, see the yz -plane of $x = 0.05$ and 0.15 .

Convergence of numerical solutions in complex swirling flows is more difficult than in the two simple canonical flows used for the validation study. We found that the mean

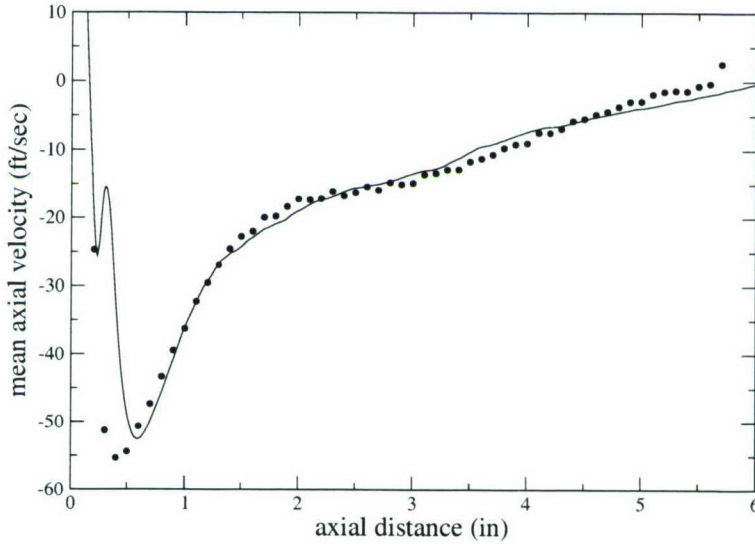


FIGURE 9. Mean axial velocity along the injector geometric centerline. • Pratt Whitney experiment; solid line: present LES.

centerline axial velocity can be used as a good indicator for monitoring convergence of LES solutions in the present nozzle rig swirling flow. For example, when a new simulation is initiated by interpolating converged solutions from an existing case with different mesh shape or mesh density, it takes another 2×10^5 time steps for the mean centerline axial velocity to reach statistically steady state. The predicted mean axial velocity along the injector geometric centerline in Fig. 9 is seen to agree with the Pratt Whitney experimental data over a significant portion of the axial distance with the exception of $0.2 < x < 0.6$. The present comparison represents a substantial improvement from that shown in the Fig. 12 of Brankovic *et al.* (2000). Note the geometries in these two studies are slightly different and the current experimental data set is close but not the same as those in Brankovic *et al.* The predicted secondary negative peak of mean axial velocity at $x \approx 0.2$ was found to be very persistent through a series of test simulations with significant changes in mesh density and composition (tetrahedral versus textural), especially in the region immediately downstream of the $x = 0$ plane. Inspection of the instantaneous and mean velocity contours over the symmetry plane of $y = 9.8$ reveals a tiny region centered at approximately $x = 0.2$ with slightly stronger negative flow compared to the region immediately downstream from $0.2 < x < 0.3$. Beyond $x = 0.3$ is the main central recirculation zone where the primary negative peak is located. The tiny patch centered at $x = 0.2$ likely arises from the interaction between the core swirling flow and the outer swirling flow, and the main central recirculation zone is due to the combined effects of all the three swirling streams. Mixing between the core and outer swirling streams occurs upstream of the guide flow outlet. Recall that the three outlets are staggered in axial position ranges. The calculated mean axial and radial velocities over the symmetry plane $y = 9.8$ as a function of distance from the injector centerline are compared with experimental data in Fig. 10. The comparison is overall satisfactory.

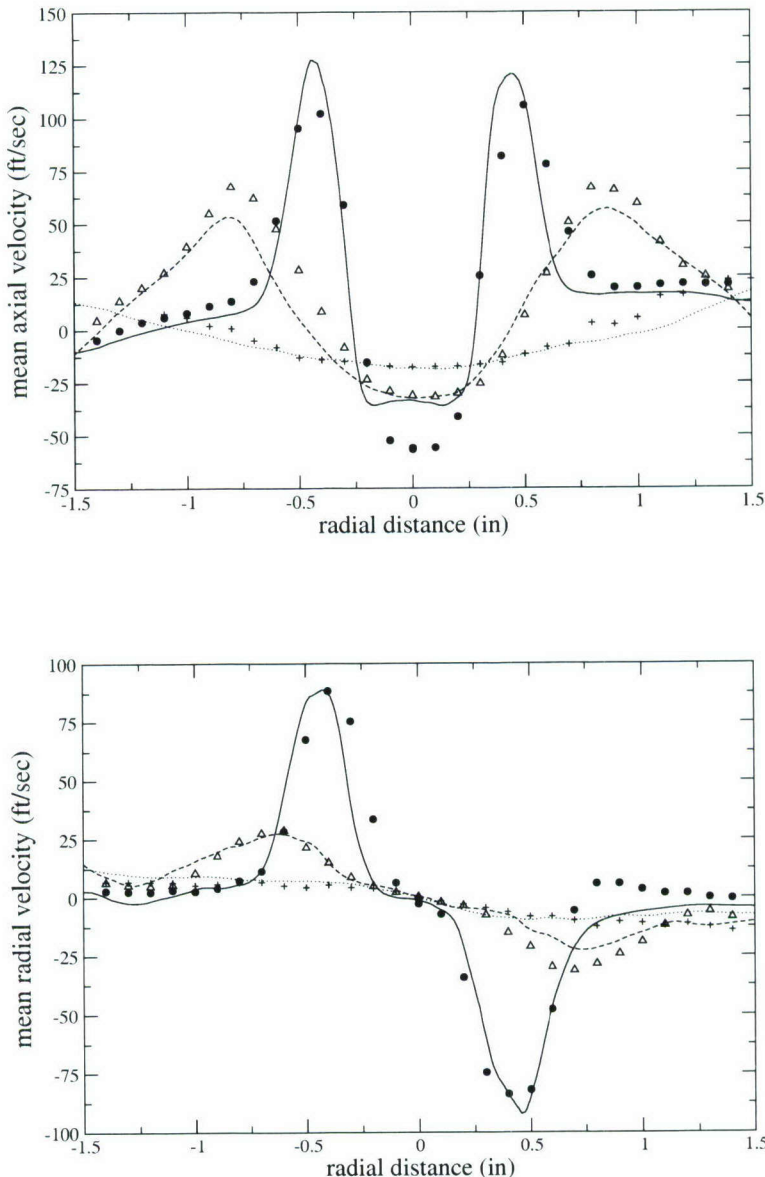


FIGURE 10. Mean velocities as a function of radial distance over the symmetry plane of $y = 9.8$.
 Upper: axial velocity; lower: radial velocity. • solid line $x = 0.4$; \triangle dashed line $x = 1.1$; + dotted line $x = 2.1$. Symbols are experimental data and lines are present LES.

The underprediction of the primary negative peak at $x = 0.4$ is directly related to the discrepancy shown in Fig. 9. Swirling vortex is generated near the nozzle as a result of the interaction of the three jet streams. This is visualized in Fig. 11 using surfaces of

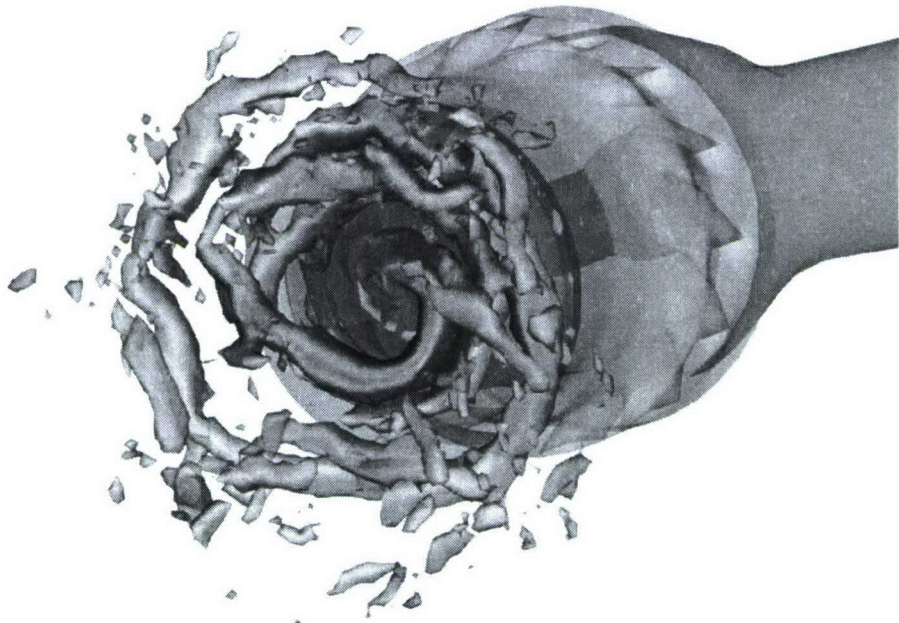


FIGURE 11. Visualization of swirling vortex near the injector using the second-invariant of the velocity gradient tensor.

the second invariant of the velocity gradient tensor. The darkened region in the figure represents higher axial speed.

4. Conclusions

Inclusion of the swirl-generating device geometry is an integral part of jet engine combustor fluid flow simulation. In this work we have applied an unstructured, energy-conserving LES approach to the computation of non-reacting flow in a realistic fuel injector nozzle. Validation results obtained for channel and backward facing step flows are in good agreement with existing DNS and experimental data. LES results for the complex nozzle rig flow demonstrated marked improvement over previous RANS results with respect to comparison with experimental measurements. The effects of the injector nozzle components are revealed through visualization of the velocity fields over a sequence of cross-sections perpendicular to the nozzle axis. Additionally, the axial velocity along the injector centerline was found to be a good indicator of solution convergence in the present swirling flow. When a new simulation is initiated using interpolated solutions from an existing converged case with different mesh shape or density, it takes nearly the same number of time steps to converge the new solution as required in the original simulation with zero initial velocity field.

Acknowledgments

Discussions with Sourabh Apte, George Constantinescu, Krishnan Mahesh, Cliff Wall, and Meng Wang are acknowledged. This work is supported by the Advanced Simulation

and Computing program of the United States Department of Energy. We are thankful to Pratt and Whitney for kindly supplying the fuel nozzle rig geometry and validation experimental data. The simulations were performed on the IBM terascale parallel machine at the San Diego Supercomputing Center.

REFERENCES

BRANKOVIC, A., MCKINNEY, R., QUYANG, H., PORTER, L., KENNEDY, J., MADABHUSHI, R. & COLKET, M. 2000, Comparison of measurements and predictions of flow in a gas turbine engine fuel nozzle. *AIAA Paper 2000-0331*.

CHOI, H. & MOIN, P. 1990, On the space-time characteristics of wall-pressure fluctuations. *Phys. Fluids*, **2**, 1450-1460.

DURBIN, P.A. 1995, Separated flow computations with the $k - \epsilon - v^2$ model. *AIAA J.* **33**, 659-664.

GRINSTEIN, F.F., YOUNG, T.R., GUTMARK, E.J., LI, G., HSIAO, G. & MONGIA, H.C. 2002, Flow dynamics in a swirl combustor. *J. Turbulence* **3**, article 30.

JOVIC, S. & DRIVER, D.M. 1995, Reynolds number effects on the skin friction in separated flows behind a backward facing step. *Exps. Fluids* **18**, 464-467.

LE, H., MOIN, P. & KIM, J. 1997, Direct numerical simulation of turbulent flow over a backward-facing step. *J. Fluid Mech.*, **330**, 349-374.

MAHESH, K., CONSTANTINESCU, G. & MOIN, P. 2004, A numerical method for large eddy simulation in complex geometries. *J. Comp. Phys.* **197**, 215-240.

MOSER, R.D., KIM, J. & MANSOUR, M.N. 1999, DNS of turbulent channel flow up to $Re_\tau = 590$. *Phys. Fluids*, **11**, 943-945.

PIERCE, C.D. & MOIN, P. 1998, Method for generating equilibrium swirling inflow conditions. *AIAA J.*, **36**, 1325-1327.

ROUX, S., LARTIGUE, G., POINSOT, T., MEIER, U. & BERAT, C. 2005, Studies of mean and unsteady flow in a swirled combustor using experiments, acoustic analysis and large eddy simulations. *Combust. Flame*, **141**, 40-54.

On the optimization of artificial neural networks for application to the approximation of chemical systems

By M. Ihme, A. L. Marsden AND H. Pitsch

1. Motivation and objectives

An artificial neural network (ANN) is a computational model for storing and retrieving acquired knowledge. ANNs consist of dense interconnected computing units that are simple models for complex neurons in biological systems. The knowledge is acquired during a learning process and is stored in the synaptic weights of the inter-nodal connections. The main advantage of neural networks is their ability to represent complex input/output relationships. They are well suited for use in data classification, function approximation, and signal processing, among others.

The performance, or fitness, of an ANN is often measured according to an error between target and actual output, training time, complexity of the ANN, or in terms of other properties important for the user. Although the elemental building blocks of a neural network, i.e., neurons, nodal connections, and the transfer functions of nodes are in themselves relatively simple, the various combinations can result in different topologies with similar or vastly different fitness characteristics. Therefore, the *a priori* design of a neural network with near-optimal fitness is not a trivial task and is usually guided by heuristics or trial-and-error. The architecture or topological structure of an ANN can be characterized by the arrangement of the layers and neurons, the nodal connectivity, and the nodal transfer functions. In this work, the class of multi-layer perceptrons (MLPs) is considered, which consists of an input layer with N_I input channels, N_L hidden layers, and an output layer with N_O output channels. The number of neurons in each hidden layer is denoted by \underline{N}_N . Nodes in the first $N_L - 1$ hidden layers are characterized by a non-linear behavior; nodes in the last hidden layer are linear (Haykin 1994).

A multi-layer perceptron is shown in Fig. 1(a). Information in this 2-3-2-1 network propagates uni-directionally from the input to the output channel. Each neuron includes a threshold which is indicated by a vertical arrow in Fig. 1(a). The significance of the threshold is explained in Section 2. In the case of a symmetric network, in which all neurons in a particular layer are connected to the same nodes, the nodal connectivity matrix can be contracted to a layer connectivity matrix $\underline{\underline{L}}$. The matrix entry L_{ij} indicates the connectivity between layer j and layer i . The layer connectivity matrix corresponding to the ANN of Fig. 1(a) is shown in Fig. 1(b).

A particular topology of an ANN, to be denoted by \mathcal{A} , can formally be written as

$$\mathcal{A} = \mathcal{A}(N_L, \underline{N}_N, \underline{\underline{L}}, \underline{\psi} | N_I, N_O, Y, J), \quad (1.1)$$

in which $\underline{\psi}$ is the vector of transfer functions for all nodes, Y is the approximated function, and J is a cost function characterizing the performance of the network. The last four arguments in Eq. (1.1) are constrained by the problem and the desired performance of the network. The design parameters N_L , \underline{N}_N , $\underline{\underline{L}}$, and $\underline{\psi}$ determine the topology of the neural

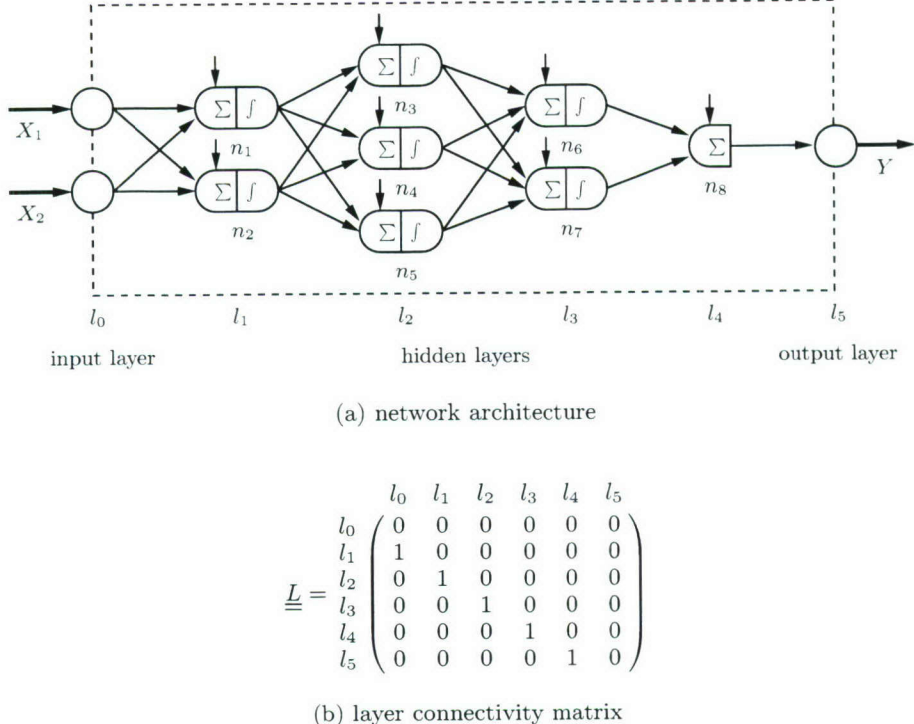


FIGURE 1. Multi-layer perceptron: (a) architecture of the MLP consisting of one input layer with two input channels X_1 and X_2 , 4 hidden layers with, respectively, 2, 3, 2, and 1 neurons in each layer. The neurons in the hidden layers are denoted by n_i , with $i = 1, \dots, 8$; (b) corresponding layer connectivity matrix.

network and have to be chosen in such a way that the ANN has an optimal performance characteristic. While small networks with only a few connections and synaptic weights are often limited in their capability to perform a certain task, large ANNs with many non-linear nodes can result in poor generalizability, long training time, and computationally expensive knowledge retrieval (Yao 1999).

Over recent years considerable research has been conducted on the evolution of topological structures of networks using evolutionary algorithms (Koza & Rice 1991; Bornholdt & Graudenz 1992; Tang *et al.* 1995; Angeline *et al.* 1994; Miller *et al.* 1989; Husken *et al.* 2005; and references in Yao 1999). However, very little work has been carried out on evolving node-specific transfer functions or the simultaneous evolution of both nodal arrangement and transfer functions (Liu & Yao 1996; Hwang *et al.* 1997). This shortcoming is addressed in the present work by proposing a methodology that can be used to simultaneously optimize the nodal arrangement, connectivity, and transfer functions of a neural network using a generalized pattern search (GPS) method developed by Torczon (1997). The GPS method is complemented by a surrogate management framework (SMF), developed by Serafini (1998) and Booker *et al.* (1999), in order to increase the efficiency of pattern search methods for computationally expensive problems. In this method, the expensive cost function is approximated by a surrogate function based on Kriging (Koehler & Owen 1996). The GPS algorithm is a derivative-free method and provides robust con-

vergence properties. This method has been used previously by Booker *et al.* (1999) for rotorblade optimization and by Marsden *et al.* (2004) for trailing-edge airfoil optimization. Recently, Audet & Dennis (2000) extended the GPS method to problems with mixed design variables with bound constraints. This method, the so-called generalized mixed variable pattern search (GMVPS), was employed in the work of Kokkolaras *et al.* (2000) to design a thermal insulation system. Here, GMVPS will be used to optimize the nodal connectivities and transfer function types of each neuron.

The main objective of this work is to use automatically generated neural networks for to approximate non-linear functions, e.g., those encountered in representing chemically reactive systems (Christo *et al.* 1996a,b; Blasco *et al.* 1999a,b, 2000; Chen *et al.* 2000; Flemming *et al.* 2005). Chemical kinetic reaction mechanisms are often comprised of thousands of chemical reactions among hundreds of species. In numerical simulations of combustion systems, for example, the direct solution of transport equations for all these species is usually not feasible, partly because of the large range of chemical time scales. To reduce the number of independent species, dimensional reduction methods have been developed, in which a part of the chemical species are projected onto lower dimensional manifolds, parameterized by the remaining species. For instance, in the case of the steady flamelet model (Peters 1984), all chemical and thermodynamic quantities are represented using only two scalars. In the case of turbulent combustion and in cases where radiation and pollutant formation are important, accurate predictions might require the number of independent scalars to grow to five or even more (Peters 2000). The functional relation between chemical species and independent scalars is usually stored in conventional tables. The size of the chemistry table increases with the number of parameters and imposes a drastic restriction on the resolution for more than three independent parameters. ANNs, in contrast, have the potential to accurately approximate complex functions using modest amount of memory. Motivated by the chemistry application, test examples are performed using functions that closely resemble the chemical characteristics of combustion systems. Nevertheless, the proposed method for the optimization of the network architecture is general in nature and applicable to other problems of interest.

The remainder of the paper is organized as follows. Section 2 discusses the ANN model and describes the training process. The GPS and GMVPS methods are presented in Section 3. These algorithms are then applied in the optimization of neural networks. In the first step, only the number of neurons per layer are optimized and the connectivity matrix and type of transfer function are fixed. This optimization problem is solved using the surrogate management framework with standard generalized pattern search. In the following, an example of the approximation of a reactive system is presented in which the nodal arrangement, transfer function, and connectivity are parameters and optimal networks are generated using the GMVPS method. The performance of the automatically generated network is compared with results obtained using a conventional tabulation technique. The paper finishes with a discussion.

2. Artificial neural network

The general structure of an MLP is shown in Fig. 1(a). This particular network consists of $N_I = 2$ input channels and $N_O = 1$ output channels and $\mathcal{A} : \mathbb{R}^{N_I} \rightarrow \mathbb{R}^{N_O}$. Note that the input nodes do not represent neurons in the conventional sense. Here they merely perform the task of normalizing the input data so that the input signal feed into the network is in the interval $[-1, 1]^{N_I}$. The output y_i of each neuron i in the hidden layers

is computed according to

$$y_i = \psi_i \left(\sum_{j=0}^{N_C} C_{ij} \omega_{ij} x_{ij} \right), \quad (2.1)$$

where x_{ij} is the input signal and N_C denotes the number of connections in the network. The element C_{ij} is unity if neurons i and j are connected and zero otherwise. The synaptic weights are denoted by ω_{ij} . Each neuron includes a threshold ω_{i0} , which is connected to a constant input signal $x_{i0} = -1$. The effect of the threshold is to lower the net input on the transfer function (Haykin 1994). A sigmoidal function

$$\psi(s) = a_1 \tanh(b_1 s), \quad (T1)$$

cyclometric function

$$\psi(s) = a_2 \operatorname{atan}(b_2 s), \quad (T2)$$

a linear function

$$\psi(s) = s \quad (T3)$$

or other monotonic functions are commonly used as transfer functions. The parameters a and b in the transfer functions (T1) and (T2) are adjustable by the user. Transfer functions (T1) and (T2) will be used in Section 4.

The synaptic weights in the network are adjusted during the training process, which in itself represents an optimization problem and can be written as

$$\min_{\omega \in \mathbb{R}^{N_\omega}} E(\omega). \quad (2.2)$$

In the above problem, $E : \mathbb{R}^{N_O \times N_t} \rightarrow \mathbb{R}$ is the error between the actual and desired output of the network, which can be written as

$$E = \frac{1}{2 N_t} \sum_{j=1}^{N_t} e^t(j) \quad \text{with} \quad e^t(j) = \sum_{i=1}^{N_O} [Y_i(j) - Y_i^t(j)]^2 \quad (2.3)$$

and $Y_i^t(j)$ represents the j^{th} training sample of the output signal i . The number of training samples is denoted by N_t . The learning process, in which the weights are iteratively adjusted, is guided by the knowledge of the desired input/output examples and is called supervised learning. A Levenberg-Marquardt algorithm (Hagan *et al.* 1996) has been used for the optimization of the synaptic weights. This algorithm is a trust region Gauss-Newton method and its fast convergence makes it suitable for training neural networks.

The main advantage of ANNs is their generalizability, meaning their accurate performance on new data. In this respect ANNs are different from tabulation methods in which discrete values of a particular function of interest are memorized and stored in a table. A good generalization of a particular ANN is dependent on the complexity of the function, the architecture of the network, and the size and information content of the training set. Networks with only a few hidden neurons and synaptic weights are restricted in the approximation of complex functions, resulting in poor generalizability characterized by so-called under-fitting. On the other hand, a network that is too complex, meaning that there are considerably more synaptic weights than training samples, can result in possible over-fitting and non-smooth function approximation.

The appropriate size of the training set is crucial for the design of an optimal network, and is usually determined by two factors. First, the *a priori* knowledge of the function to be approximated allows for an assessment of the complexity and shape of the function.

Based on this information, the minimum size of the training set required for the description of the functional shape can be determined. A second constraint on N_t is imposed by the size of the network and the number of synaptic weights. The size of the training set for a fixed architecture with N_ω synaptic weights is given by

$$N_t \geq \alpha N_\omega . \quad (2.4)$$

The value of α is chosen based on experience and analysis and typically ranges from approximately 30 for noisy training data down to 2–5 for the approximation of analytical functions. The lower bound is chosen to avoid the possible occurrence of over-fitting, which can occur if N_t is significantly smaller than αN_ω .

The generalization potential of a trained ANN is assessed using test samples. These samples are used after training to evaluate the ability of the ANN to approximate untrained samples. In this process, the performance of the ANN can be evaluated by means of the following cost function

$$J(\mathcal{A}) = \log_{10} \left(\sqrt{\frac{1}{N_s} \sum_{j=1}^{N_s} (e^s(j))^2} \right) , \quad (2.5)$$

where N_s is the number of test samples. The evaluation of the cost function requires that the synaptic weights in \mathcal{A} are fully adjusted during a preceding training process. In order to allow for an objective comparison of the fitness between different network architectures, e^s is normalized to the interval $[0, 1]$ so that $J(\mathcal{A})$ represents a relative error.

The resulting optimization problem may be formulated as

$$\begin{aligned} & \min_{N_L, \underline{N}_N, \underline{C}, \underline{\psi}} J(\mathcal{A}) \\ \text{subject to} \quad & N_L = N_L^{\max} , \\ & N_{N,i} \in \{0, 1, \dots, N_N^{\max}\}, \quad i = 1, 2, \dots, N_{L-1} , \\ & N_{N,N_L} = 1 , \\ & \underline{L} \in \mathcal{L}, \quad \underline{\psi} \in \mathcal{P} , \end{aligned}$$

where \mathcal{P} is the finite list of transfer functions and \mathcal{L} denotes the finite set of possible layer connectivity matrices. The continuous variables are N_L and \underline{N}_N and the categorical ones are \underline{L} and $\underline{\psi}$.

3. GPS method and GMVPS algorithm

The GMVPS method is an extension of the GPS method (Torczon 1997), and has been developed by Audet & Dennis (2000) to handle mixed variable problems with bound constraints. In the present case, the optimization of a network architecture can be represented as a mixed variable problem in which the number of hidden layers and neurons are (continuous) integer-valued parameters and the transfer functions and connectivity matrix are of categorical type. Categorical variables must take on values from a predefined list or discrete set of elements. Optimization in this mixed variable space is performed to find a network architecture with optimal fitness, subject to certain constraints. In this context note that the pattern search method does not guarantee that the solution is a

global minimum. The limit point of the sequence of iterations, however, corresponds to a local optimal solution, which is defined with respect to a set of neighbors. The neighborhood is specified by the user and accounts for the variation of continuous and categorical variables. A rigorous definition of local optimality for a mixed variable problem is given by Audet & Dennis (2000).

The pattern search algorithm is a derivative-free mesh-based method. The algorithm generates a sequence of iterates, whose cost function is non-increasing (Audet & Dennis 2000). All points at which the cost function is evaluated are restricted to lie on a mesh. The algorithm proceeds in two stages: a search and a poll step. The search step allows for a mesh-restricted local and global exploration of the parameter space. In this step a finite number of search points are evaluated with the objective of identifying a region with a reduced cost function. For instance, random sampling of the parameter space using Latin hypercube sampling (LHS) (McKay *et al.* 1979) or a genetic algorithm can be employed. A considerable cost reduction of the search step can be achieved by employing a less expensive surrogate function. The surrogate function is often an approximation of the cost function. The shape of the function is continuously updated by incorporating all previously evaluated points of the cost function. This surrogate function is then used to identify a new point with a potentially lower cost function. However, the surrogate function can be used only in the continuous parameter space. For categorical variables, the above-mentioned techniques have to be employed.

In the present work, Kriging approximation is employed as the surrogate function. Kriging is a statistical method and is based on the use of spatial correlation functions. Its multi-dimensional extension makes this method attractive for optimization problems with several parameters. A summary of the Kriging approximation is given by Marsden *et al.* (2004). Details of implementation are described by Lophaven *et al.* (2002).

In the case of an unsuccessful search step, a poll step in the neighborhood of the incumbent point with the lowest cost function is executed. All continuous-valued points are restricted to lie on a mesh that is constrained to the parameter space. For a mixed variable problem, the mesh M at iteration k is defined to be the direct product of the categorical variable space Ω^c and the lattice in the continuous variable space

$$M_k = \Omega^c \times \left\{ \underline{\eta}_k + \Delta_k \underline{\underline{D}} \underline{\underline{\zeta}} : \underline{\underline{\zeta}} \in \mathbb{N}^{N^D} \right\}, \quad (3.1)$$

where $\Delta_k > 0$ is the mesh size parameter and $\underline{\underline{D}}$ is an $N^c \times N^D$ matrix whose columns form a positive spanning set. If $\underline{\underline{I}}$ denotes the identity matrix and $\underline{\underline{1}}$ is the vector of ones, then $\underline{\underline{D}}$ is typically chosen as $\underline{\underline{D}} = [\underline{\underline{I}}, -\underline{\underline{1}}]$ or $\underline{\underline{D}} = [\underline{\underline{I}}, -\underline{\underline{I}}]$ (Audet & Dennis 2000).

The poll step consists of a local search in the mesh neighborhood around the current best point and, in the case that the categorical variable space is not empty, also in the set of the categorical neighbors. Polling is conducted in three steps (Audet & Dennis 2000):

- polling with respect to the continuous variables and fixed categorical parameters,
- polling in the neighborhood of categorical variables and fixed continuous parameters,
- extended polling around the neighborhood of points whose cost function is close to the incumbent value.

The continuous poll step is an evaluation of adjacent mesh points forming a positive spanning set. This step is augmented with the evaluation of points in the discrete neighborhood. If these poll steps are unsuccessful extended polling is performed. Extended polling around promising points is triggered when the previous poll steps are unsuccess-

ful. A promising point ζ for the extended polling is defined as

$$J(\eta_k) < J(\zeta) \leq (1 + \xi)J(\eta_k), \quad (3.2)$$

where $\xi > 0$ is the poll trigger. If $J(\zeta)$ is close to $J(\eta_k)$ of the current best point, polling around the continuous neighborhood of ζ is performed with the expectation of finding a better point. If a point ζ^* is found with $J(\eta_k) < J(\zeta^*) < J(\zeta)$, extended polling around this point is continued. This continues until either a new incumbent is found or until all points in the extended poll set are inferior to the incumbent. If all poll steps are unsuccessful, the mesh is refined and a new iteration, starting with a search step, is performed. More details on the algorithm and convergence proofs can be found in Audet & Dennis (2000) and Abramson (2004).

4. Results

In this section, different aspects of network optimization are explored, including optimization of the nodal arrangement, type of transfer function, and connectivity.

In Section 4.1 the nodal arrangement of the ANN is optimized using the standard GPS together with surrogate approximation. In this case, the hidden layers and neurons of the network are free parameters. In Section 4.2, the optimization method is applied to the approximation of chemical systems with optimal ANNs. In this application the transfer function type and connectivity matrix are added as optimization parameters, and the network dependence on N_L , \underline{N}_N , and \underline{C} is optimized subject to the cost function constraint. The nodal transfer function and the connectivity are parameters of categorical type and therefore require that the GMVPS method be applied. Results for two different optimization processes are discussed.

4.1. Optimal nodal arrangement

In this section, the GPS method is applied to optimize the number of neurons in a fully connected MLP. The number of neurons in the first hidden layer is a free parameter and its bounds are $0 \leq N_{N,1} \leq 32 = N_N^{\max}$. A hyperbolic tangent function with $a = 1.075$ and $b = 2$ is used as the transfer function. The number of test samples and training samples are equal and set to 350 so that the coefficient α in Eq. (2.4) is $\alpha \geq 2.7$. It can be expected that in the limit of small $N_{N,1}$, the network suffers from under-fitting and over-fitting might be observable for large $N_{N,1}$ due to small α -values. For the training of the individual networks during the GPS optimization, at most 200 iterations in the Levenberg-Marquardt algorithm are used.

To demonstrate the use of this method, a network with a scalar output, dependent on two input channels, is optimized. Mimicking a chemical reaction rate dependent on two input channels, the following analytical function is used:

$$Y = \exp \left\{ - \sum_{i=1}^{N_1=2} \frac{(X_i - X_i^0)^2}{\sigma_i} \right\}, \quad (4.1)$$

with $X^0 = (0.5, 0.5)^\top$, $\sigma = (0.01, 0.1)^\top$, and $\underline{X} \in [0, 1]^2$.

The evolution of the optimization algorithm is shown in Fig. 2. The surrogate function (solid line) is determined by the surrogate points (circles) and comprises all locations at which the cost function has previously been evaluated. Points evaluated during the search step, obtained from the minimization of the surrogate function, are denoted by square symbols. Locations that are evaluated during the poll step are denoted by diamonds

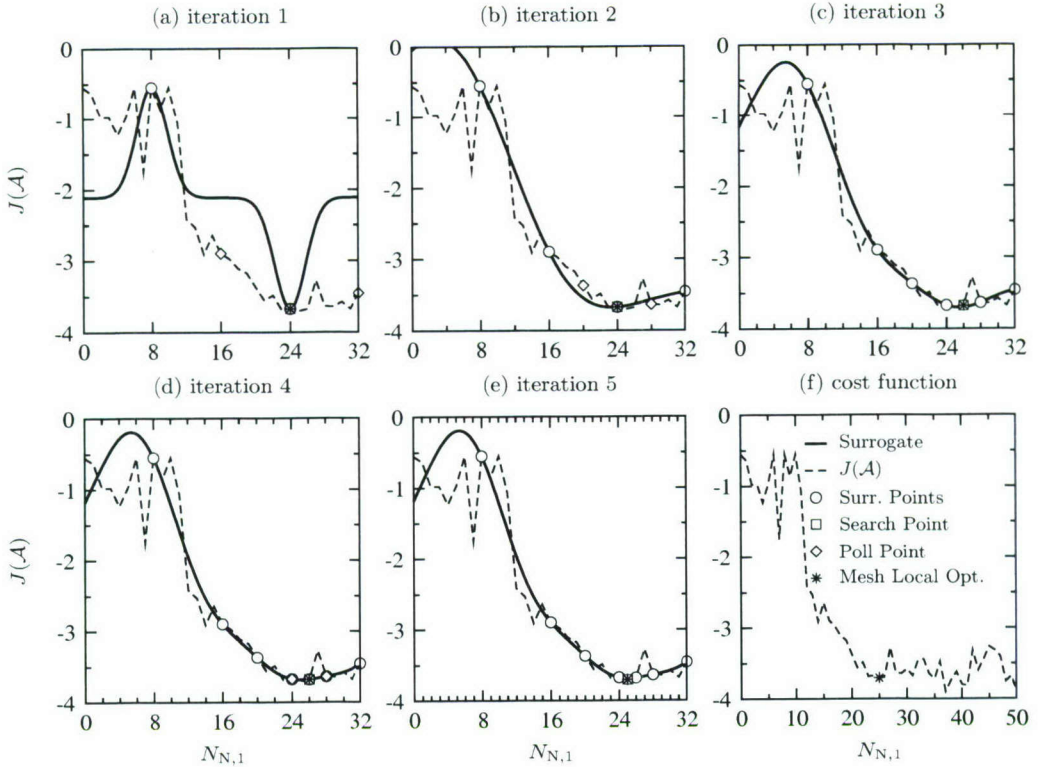


FIGURE 2. Evolution of the GPS optimization for a network with one non-linear hidden layer.

and the current best value for $N_{N,1}$ resulting in the best ANN performance is indicated by a star. In the first iteration (Fig. 2(a)) the minimum of the surrogate, evaluated during the search step, corresponds to the current best point. The search step is declared unsuccessful and polling around the previous optimal location is performed. The poll step does not result in a reduction of the cost function. The mesh size is reduced to $\Delta = 4$ in the succeeding iteration and the surrogate is updated (Fig. 2(b)). Neither the search nor the poll step are successful in the second iteration and the mesh size is further reduced to $\Delta = 2$ (Fig. 2(c)). The minimum of the newly updated surrogate function is computed and the cost function is evaluated, resulting in a reduction of $J(\mathcal{A})$ and therefore a better ANN structure. Both search and poll steps in the fourth iteration (Fig. 2(d)) are not successful and the mesh size is reduced to $\Delta = 1$ in iteration 5. From the updated surrogate function the search step determines a new minimum of the surrogate function for $N_{N,1} = 25$. The cost function for this location is evaluated, resulting in further improvement of the network fitness. The GMVPS algorithm identifies the mesh local optimizer at $N_{N,1} = 25$.

The GPS algorithm requires only eight function evaluations for the optimization of this particular network with one non-linear hidden layer. A function evaluation comprises both the training phase and fitness evaluation during the test process. It is also interesting to point out that two search steps (iterations 3 and 5) lead to reductions in the cost function and all poll steps were unsuccessful.

Figure 2(e) shows that the function evaluations are mainly clustered around the mesh local optimizer. This accumulation of points in the Kriging function can lead to a degra-

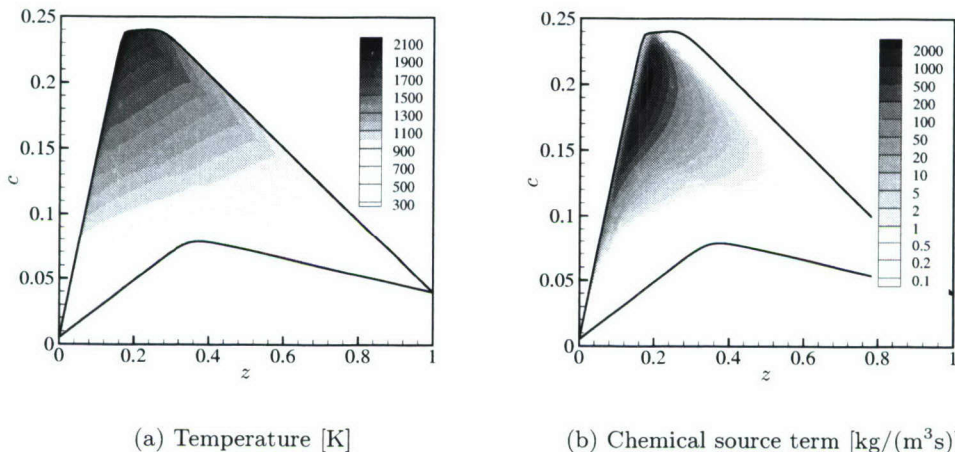


FIGURE 3. Solution of the steady laminar flamelet equations as a function of mixture fraction z and progress variable c ; (a) temperature and (b) chemical source term.

dation of the surrogate function (Marsden *et al.* 2004). This can be prevented by including space-filling points, which necessarily do not correspond to optimal points.

The evolution of the cost function for $0 \leq N_{N,1} \leq 50$ is shown in Fig. 2(f). For small $N_{N,1}$ the network suffers from under-fitting, resulting in poor generalization. By increasing the number of neurons and hence synaptic weights, $J(\mathcal{A})$ decreases and stays approximately constant for $N_{N,1} \geq 35$. A further increase in the number of synaptic weights results only in marginal improvement of the fitness. This can mainly be attributed to the limited complexity of the network structure (one hidden non-linear layer) and possible over-fitting for large $N_{N,1}$.

4.2. Chemistry example

In this section, optimal neural networks for the approximation of a chemical system are generated. In this application, all three optimization strategies, namely optimal nodal arrangement, transfer functions, and connectivity, are combined.

The chemical process under consideration describes methane/air combustion. The GRI 2.11 chemical mechanism (Bowman *et al.* 1997) containing 277 elementary chemical reactions among 49 species is used.

The steady laminar flamelet equations (Peters 1984) are often employed to describe the reaction-diffusion balance in non-premixed flames. The solutions to these equations provide temperature and mass fractions of all species in terms of two parameters. The mixture fraction z and the reaction progress variable c are used for this parameterization. Figure 3 shows the temperature and the chemical production rate of c , which can be viewed as a measure of the heat release. In the following, network optimization for the approximation of these two quantities as functions of these parameters is performed. The solid lines represent the system boundary; flame states outside this boundary are unaccessible. Note that the chemical source term is very localized around $z \approx 0.2$ and $0.15 \leq c \leq 0.23$.

The number of samples used during the training phase and testing process is 500. Sample data are obtained by applying an acceptance-rejection method (Rubinstein 1981);

Quantity	Neurons	Transfer Function	\underline{L}	$J(\mathcal{A})$
Temperature	6-7-4-7-1	(T2)-(T2)-(T2)-(T2)-(T3)	$\begin{pmatrix} 0 & 0 & 0 & 0 & 0 & 0 & 0 \\ 1 & 0 & 0 & 0 & 0 & 0 & 0 \\ 1 & 1 & 0 & 0 & 0 & 0 & 0 \\ 1 & 0 & 1 & 0 & 0 & 0 & 0 \\ 1 & 0 & 0 & 1 & 0 & 0 & 0 \\ 1 & 0 & 0 & 0 & 1 & 0 & 0 \\ 0 & 0 & 0 & 0 & 0 & 1 & 0 \\ 0 & 0 & 0 & 0 & 0 & 0 & 0 \\ 1 & 0 & 0 & 0 & 0 & 0 & 0 \\ 0 & 1 & 0 & 0 & 0 & 0 & 0 \\ 0 & 0 & 1 & 0 & 0 & 0 & 0 \\ 0 & 0 & 0 & 1 & 0 & 0 & 0 \\ 0 & 0 & 0 & 0 & 1 & 0 & 0 \end{pmatrix}$	-2.780
Chem. Source Term	2-2-8-8-1	(T2)-(T2)-(T2)-(T2)-(T3)	$\begin{pmatrix} 0 & 0 & 0 & 0 & 0 & 0 & 0 \\ 1 & 0 & 0 & 0 & 0 & 0 & 0 \\ 1 & 0 & 0 & 0 & 0 & 0 & 0 \\ 0 & 0 & 0 & 0 & 0 & 0 & 0 \\ 0 & 0 & 0 & 0 & 0 & 0 & 0 \\ 1 & 0 & 0 & 0 & 0 & 0 & 0 \\ 0 & 1 & 0 & 0 & 0 & 0 & 0 \\ 0 & 0 & 1 & 0 & 0 & 0 & 0 \\ 0 & 0 & 0 & 1 & 0 & 0 & 0 \\ 0 & 0 & 0 & 0 & 1 & 0 & 0 \end{pmatrix}$	-3.124

TABLE 1. Optimal network architecture for the approximation of temperature and chemical source term. The transfer function and connectivity matrix are free categorical parameters.

this results in higher sampling density in regions where the functional value Y is large. This method consequently results in a better resolution of the important regions with high chemical source term and temperature.

By considering the optimization of the nodal transfer function and the connectivity in the network design, the categorical neighborhood requires an extension in order to identify a network with optimal fitness in the joint continuous and categorical space. In this example, the categorical neighborhood for the transfer function includes the following combinations: (i) The transfer functions for the neurons in all layers are identical, either of type (T1) or (T2); (ii) Except for the neurons in one layer, the transfer function for the neurons is identical. The set of neighbors for the connectivity contains the following combinations: (a) fully connected feed-forward network; (b) fully connected feed-forward network with $L_{i0} = 1$ where i represents any hidden layer; (c) fully connected feed-forward network with $L_{i0} = 1$ for all i hidden layers. The poll trigger is set to $\xi = 0.05$ and the maximum number of neurons per layer and the number of non-linear hidden layers are set to 8 and 5, respectively.

The optimal network for the approximation of the temperature consists of a 6-7-4-7-1 ANN. All neurons employ a cyclometric transfer function. The connectivity resembles a fully connected feed-forward network in which all neurons are also directly connected to the input layer. The cost function of this network is $J(\mathcal{A}) = -2.780$. The regression analysis for the network is shown in Fig. 4(a).

The network for the approximation of the chemical source term is considerably different from that of the temperature. This is mainly attributed to the different shapes of the functions for temperature and chemical source term. The architecture of the optimal network consists of a 2-2-8-8-1 fully connected feed-forward network. The cost function for this network is $J(\mathcal{A}) = -3.124$ and the regression analysis for this network is shown in Fig. 4(b). Both network characteristics are summarized in Table 1.

It is interesting to compare the network performance with a conventional tabulation technique. Here, a particular chemistry table will be denoted by \mathcal{T} and the parameter space of z and c will be discretized using a Cartesian and equidistant grid. The function to be tabulated is linearly interpolated to grid points. The performance for the tabulation of temperature and chemical source term with increasing resolution is presented in Table 2.

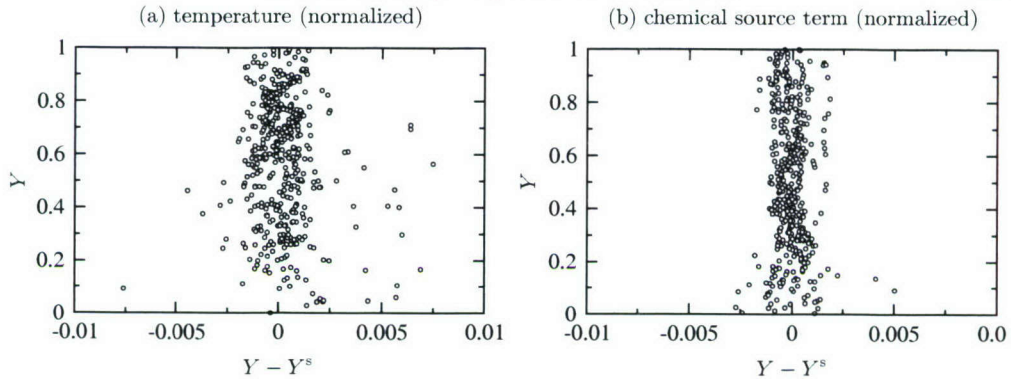


FIGURE 4. Regression analysis for approximation of (a) temperature and (b) chemical source with optimal network architecture. Note that the temperature and chemical source term are here shown in non-dimensional form.

Table size $N_z \times N_c$	Cost Function $J(T)$	
	Temperature	Chemical source term
100 \times 100	-2.240	-1.677
200 \times 200	-2.580	-2.193
300 \times 300	-2.773	-2.492
400 \times 400	-2.871	-2.621
500 \times 500	-2.974	-2.791

TABLE 2. Comparison of the performance for the representation of temperature and chemical source term using conventional tabulation technique.

In order to allow for an objective comparison between the methods, the same set of test samples is used. Generally it can be observed that the performance of the tabulation method increases monotonically with finer resolution. The resolution required for an accurate chemistry representation grows rapidly and may impose a rather restrictive bound when the number of parameters is larger than three. It is interesting to point out that for an equivalent representation of the temperature using the optimal ANN described above, a table with about 300×300 grid points in z and c direction would be required. By comparing the fitness of the ANN and tabulation for the representation of the chemical source term (Tables 1 and 2), it can be concluded that more than 500×500 grid points are required for a table to achieve an accuracy comparable with the network approximation.

5. Discussion

Optimization of an ANN has been successfully carried out using standard pattern search methods in conjunction with a surrogate function and generalized mixed variable pattern search. These methods offer extensive flexibility in implementation and freedom in choice of parameters. Using a model problem, optimization for the number of neurons,

the transfer function, and the connectivity was explored. It was demonstrated that the use of categorical variables for the transfer function and connectivity resulted in identification of better performing ANNs compared with a trial-and-error approach.

Based on experience from the model problem, an ANN was optimized to model the chemistry of methane/air combustion for prediction of temperature and chemical source term. Regression analysis for the optimal ANN demonstrates satisfactory prediction of both quantities. It is interesting to note that the optimal ANNs for prediction of these two quantities are very different, which indicates that there are underlying discrepancies in the behavior of each of these two quantities. Network performance is compared with the conventional tabulation method. It is shown that the chemistry tabulation requires considerably more memory in order to obtain equivalent accuracy.

Acknowledgments

The authors gratefully acknowledge funding by the United States Department of Energy within the Advanced Simulation and Computing (ASC) program. Helpful discussions with Masoud Aryanpour and Andrew M. Bradley are gratefully acknowledged. The authors also wish to thank Mark Abramson and John E. Dennis, Jr. for guidance on the optimization methodology.

REFERENCES

ABRAMSON, M. 2004 Mixed variable optimization of a load-bearing thermal insulation system using a filter pattern search algorithm. *Optimization and Engineering* **5** (2), 157–177.

ANGELINE, P., SAUNDERS, G. & POLLACK, J. 1994 Evolutionary algorithm that constructs recurrent neural networks. *IEEE Trans. Neural Networks* **5**, 54–65.

AUDET, C. & DENNIS, J. 2000 Pattern search algorithms for mixed variable programming. *SIAM Journal on Optimization* **11** (3), 573–594.

BLASCO, J., FUEYO, N., DOPAZO, C. & BALLESTER, J. 1999a Modelling the temporal evolution of a reduced combustion chemical system with an artificial neural network. *Combust. Flame* **113** (1-2), 38–52.

BLASCO, J., FUEYO, N., DOPAZO, C. & CHEN, J. 2000 A self-organizing-map approach to chemistry representation in combustion applications. *Combust. Theory Modelling* **4** (1), 61–76.

BLASCO, J., FUEYO, N., LARROZA, J., DOPAZO, C. & CHEN, Y. 1999b Single-step time-integrator of a methane-air chemical system using artificial neural networks. *Computers and Chemical Engineering* **23** (9), 1127–1133.

BOOKER, A., DENNIS, J., FRANK, P., SERAFINI, D., TORCZON, V. & TROSSET, M. 1999 A rigorous framework for optimization of expensive functions by surrogates. *Structural Optimization* **17** (1), 1–13.

BORNHOLDT, S. & GRAUDENZ, D. 1992 General asymmetric neural networks and structure design by genetic algorithms. *Neural Networks* **5** (2), 327–334.

BOWMAN, C., HANSON, R., DAVIDSON, D., GARDINER, W., LISSIANSKI, V., SMITH, G., GOLDEN, D., FRENKLACH, M. & GOLDENBERG, M. 1997 GRI-Mech 2.11. Available from <http://www.me.berkeley.edu/gri-mech/>.

CHEN, J., BLASCO, J., FUEYO, N. & DOPAZO, C. 2000 An economical strategy for

storage of chemical kinetics: Fitting *in situ* adaptive tabulation with artificial neural networks. *Proc. Comb. Institute* **28**, 115–121.

CHRISTO, F., MASRI, A. & NEBOT, E. 1996a Artificial neural network implementation of chemistry with PDF simulation of H₂/CO₂ flames. *Combust. Flame* **106** (4), 406–427.

CHRISTO, F., MASRI, A., NEBOT, E. & POPE, S. 1996b An integrated PDF/neural network approach for simulating turbulent reacting systems. *Proc. Comb. Institute* **26**, 43–48.

FLEMMING, F., SADIKI, A. & JANICKA, J. 2005 LES using artificial neural networks for chemistry representation. *Progress in Computational Fluid Dynamics* **5** (7), 375–385.

HAGAN, M., DEMUTH, H. & BEALE, M. 1996 *Neural Network Design*. Boston, Mass., USA: PWS Publishing Company.

HAYKIN, S. 1994 *Neural Networks: A Comprehensive Foundation*. Upper Saddle River, N.J.: Prentice Hall.

HUSKEN, M., JIN, Y. & SENDHOFF, B. 2005 Structure optimization of neural networks for evolutionary design optimization. *Soft Computing* **9** (1), 21–28.

HWANG, M., CHOI, J. & PARK, J. 1997 Evolutionary projection neural networks. In *Proc. IEEE Conference on Evolutionary Computation (ICEC '97)*, pp. 667–671.

KOEHLER, J. & OWEN, A. 1996 Computer experiments. In *Handbook of Statistics* (ed. S. Ghosh & C. Rao), pp. 261–308. New York: Elsevier Science.

KOKKOLARAS, M., AUDET, C. & DENNIS, JR., J. 2000 Mixed variable optimization of the number and composition of heat intercepts in a thermal insulation system. *Tech. Rep. TR00-21*. Department of Computational & Applied Mathematics, Rice University, Houston.

KOZA, J. & RICE, J. 1991 Genetic generation of both the weights and architecture for a neural network. In *Proc. IEEE Int. Joint Conf. Neural Networks (IJCNN'91 Seattle)*, pp. 397–404.

LIU, Y. & YAO, X. 1996 Evolutionary design of artificial neural networks with different nodes. In *Proc. IEEE Conference on Evolutionary Computation (ICEC '96)*, pp. 670–675.

LOPHAVEN, S., NIELSEN, H. & SØNDERGAARD, J. 2002 DACE: A MATLAB Kriging toolbox version 2.0. *Tech. Rep. IMM-TR-2002-12*. Technical University of Denmark, Copenhagen.

MARSDEN, A., WANG, M., DENNIS, JR., J. & MOIN, P. 2004 Optimal aeroacoustic shape design using the surrogate management framework. *Optimization and Engineering* **5** (2), 235–262.

MCKAY, M., BECKMAN, R. & CONOVER, W. 1979 Comparison of three methods for selecting values of input variables in the analysis of output from a computer code. *Technometrics* **21** (2), 239–245.

MILLER, G., TODD, P. & HEGDE, S. 1989 Designing neural networks using genetic algorithms. In *Proc. 3rd Int. Conf. Genetic Algorithms and Their Applications* (ed. J. Schaffer), pp. 379–384.

PETERS, N. 1984 Laminar diffusion flamelet models in non-premixed turbulent combustion. *Prog. Energy Combust. Sci.* **10** (3), 319–339.

PETERS, N. 2000 *Turbulent Combustion*. Cambridge: Cambridge University Press.

RUBINSTEIN, R. 1981 *Simulation and the Monte Carlo method*. John Wiley & Sons, Inc.

SERAFINI, D. 1998 A framework for managing models in nonlinear optimization of computationally expensive functions. PhD thesis, Rice University, Houston, Texas.

TANG, K., CHAN, C., MAN, K. & KWONG, S. 1995 Genetic structure for NN topology and weights optimization. In *Proc. 1st IEE/IEEE International Conference on Genetic Algorithms in Engineering Systems: Innovations and Applications (GALESIA '95)*, pp. 250–255.

TORCZON, V. 1997 On the convergence of pattern search algorithms. *SIAM Journal on Optimization* **7** (1), 1–25.

YAO, X. 1999 Evolving artificial neural networks. *Proc. IEEE* **87** (9), 1423–1447.

A dynamic front propagation model for large-eddy simulation of turbulent premixed combustion

By E. Knudsen, M. Herrmann AND H. Pitsch

1. Motivation and objectives

Turbulent premixed flames are particularly difficult to describe in the context of Large-Eddy Simulation (LES). Most industrially relevant premixed flames exist in either the corrugated flamelets regime or the thin reactions zones regime (Pitsch & Duchamp De Lageneste 2002). The width of the inner reaction zone of a flame in these regimes is comparable to, if not smaller than, the Kolmogorov length scale that describes the size of the smallest turbulent eddies in the flow. Flame preheat zones, which are typically much broader than reaction zones, may also, in the corrugated flamelets regime, exist on sub-Kolmogorov length scales. In LES, by definition, the smallest length scales of a flow are filtered out. As a result, in industrially relevant regimes the transitions that occur between unburned and burned states occur on subfilter scales.

The use of an explicit filtering procedure that could numerically resolve length scales on the order of LES filter widths would permit the simulation of these sharp unburned-to-burned transitions. Most LES codes, however, use implicit filtering. In implicit filtering, filter widths are assumed to correspond to the size of mesh cells. As such, wavenumbers on the order of the filter cutoff are sure to be under-resolved. In some particular cases, turbulence may spread and wrinkle a flame front to the extent that the filtered flame structure is resolvable using implicit filtering. Unfortunately, such a condition can be neither guaranteed nor enforced.

Premixed combustion models for implicitly filtered LES that use standalone progress variable or finite rate chemistry approaches will thus, it seems, always fail. These models are only as accurate as the schemes they use to evaluate gradients. But no scheme is capable of resolving the sharp subgrid transitions that occur in premixed implicit LES near flame fronts. LES models that attempt to resolve flame structure are therefore especially prone to numerical errors in the most critical regions of the flowfield.

This problem has been addressed through the development of application-specific techniques for premixed combustion. Each of the proposed techniques shifts difficulty away from the issue of resolution and toward the issue of modeling (Colin *et al.* 2000; Moureau *et al.* 2006; Pitsch 2005). To ensure success, these techniques must either implicitly or explicitly accomplish two separate tasks. First, they must accurately track the position of filtered flame fronts. Second, given a front position, they must provide an appropriate density field to a flow solver. In most cases, appropriate means resolvable. It does no good to have an accurate representation of a flame front if an unresolved density jump is repeatedly fed into a continuity equation.

For example, the dynamically thickened flame model (Legier *et al.* 2000) uses finite rate chemistry, but additionally broadens local reaction zones so that they can be resolved on LES grids. This broadening is achieved by increasing molecular diffusivities and, in a proportionate manner so as to keep the laminar flame speed constant, spreading out the influence of reaction source terms. The task of providing a resolved density field to

a flow solver is therefore explicitly accomplished by the model. This model suffers from one significant drawback, however, in that the widened flame severely attenuates local turbulence and prevents small eddies from influencing the front. This effectively decreases the velocity at which the front propagates and creates the need for a compensating model. The so-called “efficiency function” that is used acts to ensure that the flame will propagate at appropriately large speeds in the presence of turbulence. This efficiency function may therefore be viewed as the empirical introduction of a model describing the turbulent burning velocity.

Level set approaches such as the \mathcal{G} -equation, on the other hand, attempt to explicitly track flame fronts (Pitsch 2005). In these methods, a front is defined as an isocontour of a field variable. This variable is described at the relevant isocontour by a governing equation in which the front propagation velocity directly appears. Away from this isocontour, smooth gradients are prescribed for the field variable to ensure that it is well resolved. As in the thickened flame approach, the influence of subfilter turbulence on the propagation velocity must be modeled. In contrast to the thickened flame approach, however, resolved small-scale eddies are not necessarily damped out and thus do not necessarily need to be modeled. Additionally, and in further contrast, level set methods address the task of returning a density field to a flow solver using flamelet assumptions. Flamelet profiles are typically selected using local flow information and then mapped onto the flame front. In certain level set implementations such as those that use ghost fluids (Moureau *et al.* 2006), it is possible to prescribe subgrid density jumps. In more standard implementations, it will sometimes be necessary to borrow from the thickened flame model and artificially spread the density jump. In such a case the issue of turbulence attenuation is again encountered, but in level set methods dealing with this issue is relatively simple. The parameter used to describe turbulence intensity in the burning velocity model could simply be adjusted.

In summary, it is difficult to describe premixed combustion in the context of LES because premixed flame structures often exist entirely within single grid cells. Widely used approaches to premixed LES such as the thickened flame model and the \mathcal{G} -equation address this problem by treating these structures as coherent and then propagating them using a modeled turbulent burning velocity. The turbulent burning velocity is therefore one of the most significant modeling inputs in LES of premixed turbulent combustion. Traditional burning velocity models rely on a series of coefficients that have been tuned by analyzing both experimental and direct numerical simulation (DNS) data (Peters 2000; Abdel-Gayed & Bradley 1981). These coefficient-based approaches have been successfully applied in the context of RANS, where level set methods offer an alternative to the problem of reaction rate closure (Peters 2000; Herrmann 2000). In LES, however, where instantaneous flame realizations are available, it may be possible to eliminate the use of constant coefficients by employing dynamic procedures that determine coefficients automatically.

Im *et al.*, for example, proposed a dynamic level set propagation model in which a level set field variable is treated much like a scalar (Im *et al.* 1997). Subfilter contributions to front propagation are determined by evaluating a burning velocity at two different filter levels and comparing the results to differences in the magnitude of the gradient of the level set field variable at those same two levels. Im *et al.* claim that this approach can be physically interpreted as enforcing flame consumption conservation. They base this claim on work by Kerstein *et al.* demonstrating that a volume average of the magnitude of the gradient of the level set field variable is equivalent to a measure of the total front

area within that volume (Kerstein *et al.* 1988). In Kerstein *et al.*'s work, each isocontour of the level set field variable is treated as an equally valid representation of the flame front. Under this assumption, volume averaging is equivalent to averaging over multiple front realizations.

But more recent work (Peters 2000; Oberlack *et al.* 2001; Pitsch 2005) has stressed that level set governing equations are only valid at the field variable isocontour that they describe, and that traditional averaging procedures therefore cannot be used. Specifically, because the value of a level set field variable can be arbitrarily defined away from the relevant isocontour, volume averaging procedures can produce arbitrary results. In the present paper, then, a dynamic burning velocity model is proposed that only considers information directly from the 2-D front of interest. This model requires the use of a volumetric surface filter that is developed and presented in Section 2. In Section 3, the new filtering technique is applied to develop the dynamic model. Section 4 presents an evaluation of the model in the context of DNS. Brief conclusions are offered in Section 5.

2. Spatial filtering of a surface

Level set equations can be derived by setting the substantial derivative of a generic field variable equal to zero at a surface of interest. The resulting expression describes how the field variable isocontour associated with that surface evolves. In premixed LES, the derivation of an equation governing flame front behavior can be approached in a different way. A flame front can generally be defined as an isocontour of a generic progress variable c . This variable might represent, for example, a non-dimensionalized temperature. The equation governing the behavior of such a variable is

$$\frac{\partial c}{\partial t} + u_j \frac{\partial c}{\partial x_j} = \frac{1}{\rho} \frac{\partial}{\partial x_j} \left(\rho D \frac{\partial c}{\partial x_j} \right) + \frac{1}{\rho} \dot{\omega}_R, \quad (2.1)$$

where u_j is the local flow velocity in the j th direction, ρ is the fluid density, D is the diffusivity of the variable c , and where $\dot{\omega}_R$ is a source term that describes the effects of chemical reactions. To derive an equation describing the flame front associated with a particular c isosurface, information from Eq. (2.1) needs to be extracted directly from this isosurface, here arbitrarily defined as $c = c_0$. This extraction operation can be performed by multiplying Eq. (2.1) with a delta function, $\delta(c - c_0)$,

$$\delta(c - c_0) \left[\frac{\partial c}{\partial t} + u_j \frac{\partial c}{\partial x_j} \right] = \delta(c - c_0) \left[\frac{1}{\rho} \frac{\partial}{\partial x_j} \left(\rho D \frac{\partial c}{\partial x_j} \right) + \frac{1}{\rho} \dot{\omega}_R \right]. \quad (2.2)$$

This delta function does not necessarily need to be an infinitesimally thin Dirac delta. Rather, here δ will be defined as a normalized Gaussian of finite width. As long as this width is an order of magnitude smaller than the length scale associated with the inner reaction zone of a flame, multiplication with $\delta(c - c_0)$ will effectively give a null result everywhere except at the flame front. This finite width definition of δ is convenient because it eliminates the problem of dealing with the special mathematical properties of the Dirac delta.

Just as Dirac delta functions may equivalently be written as derivatives of heaviside functions, Gaussians may equivalently be written as derivatives of error functions. Since the δ function that appears in Eq. (2.2) only depends on c , the chain rule may be used to rewrite the left-hand side of Eq. (2.2). Remembering that what here will be referred to as the heaviside function H represents an error function of finite width, this procedure

gives

$$\delta(c - c_0) \left[\frac{\partial c}{\partial t} + u_j \frac{\partial c}{\partial x_j} \right] = \frac{\partial [H(c - c_0)]}{\partial t} + u_j \frac{\partial [H(c - c_0)]}{\partial x_j}. \quad (2.3)$$

To move the heaviside function on the right-hand side into the relevant derivatives, the gradient of the progress variable must first be written in terms of the front normal direction at c_0 , which here will be denoted n_j .

$$\frac{\partial c}{\partial x_j} = \frac{\nabla c}{|\nabla c|} |\nabla c| = n_j |\nabla c| \quad (2.4)$$

Use of the product rule on the diffusive term then gives

$$\frac{\partial}{\partial x_j} \left(\rho D \frac{\partial c}{\partial x_j} \right) = \rho D \frac{\partial n_j}{\partial x_j} |\nabla c| + n_j \frac{\partial}{\partial x_j} (\rho D |\nabla c|). \quad (2.5)$$

Finally, the delta function acts on $|\nabla c|$ as

$$\delta(c - c_0) |\nabla c| = |\delta(c - c_0) \nabla c| = |\nabla [H(c - c_0)]|. \quad (2.6)$$

Combining all of these elements, the right-hand side of Eq. (2.2) can now be written

$$\delta(c - c_0) \left[\frac{1}{\rho} \frac{\partial}{\partial x_j} \left(\rho D \frac{\partial c}{\partial x_j} \right) + \frac{1}{\rho} \dot{\omega}_R \right] = \quad (2.7)$$

$$D\kappa |\nabla [H(c - c_0)]| + \delta(c - c_0) \frac{1}{\rho} \left[n_j \frac{\partial}{\partial x_j} (\rho D |\nabla c|) + \dot{\omega}_R \right], \quad (2.8)$$

where κ is the divergence of the normal vector, or the curvature. The whole equation then becomes

$$\frac{\partial [H(c - c_0)]}{\partial t} + u_j \frac{\partial [H(c - c_0)]}{\partial x_j} = \quad (2.9)$$

$$D\kappa |\nabla [H(c - c_0)]| + \delta(c - c_0) \frac{1}{\rho} \left[n_j \frac{\partial}{\partial x_j} (\rho D |\nabla c|) + \dot{\omega}_R \right]. \quad (2.10)$$

This equation governs the behavior of a heaviside function located at the flame front, and in this form strongly resembles a level set equation. It differs from a level set equation, however, in that the heaviside function is meaningfully defined at all locations in the field away from the front.

A new variable can now be introduced. The variable G will be defined as

$$G = H(c - c_0), \quad (2.11)$$

where the G field away from $c = c_0$ is not arbitrary but rather obeys the rules of a heaviside function. A universally valid substitution in Eq. (2.10) gives

$$\frac{\partial G}{\partial t} + u_j \frac{\partial G}{\partial x_j} = D\kappa |\nabla G| + \frac{\rho_u}{\rho} s_{L,u} |\nabla G|, \quad (2.12)$$

where

$$\frac{\rho_u}{\rho} s_{L,u} = \frac{\rho_u}{\rho} \frac{1}{|\nabla c| \rho_u} \left[n_j \frac{\partial}{\partial x_j} (\rho D |\nabla c|) + \dot{\omega}_R \right]. \quad (2.13)$$

Here, the quantity s_L describes the laminar burning velocity of the flame, which is a function of the diffusion and source terms in the progress variable equation, as expected. The quantity ρ_u describes the density of the unburned fluid, and is introduced to ensure

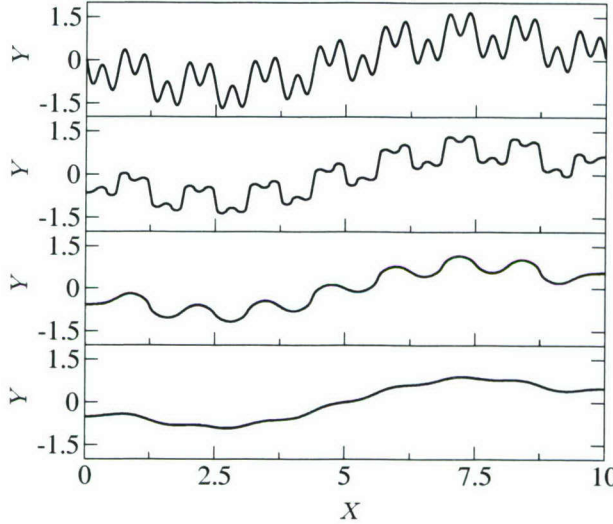


FIGURE 1. Application of Eq. (2.14) to the surface $G = 0$ defined by the field variable $G(X, Y) = 1.8 \sin\left(\frac{2\pi X}{10}\right) + \sin\left(\frac{16\pi X}{10}\right) + \sin\left(\frac{48\pi X}{10}\right) + 2Y$. The uppermost plot shows the exact level set. The three lower plots show the level set after sequential filterings. Here, $\mathcal{F}(r)$ is a box filter.

that laminar burning velocities computed in unburned reference frames, $s_{L,u}$, may be used within the equation.

Unlike level set variables, G can be volumetrically filtered because there is nothing arbitrary about its definition. Defining $\mathcal{F}(\mathbf{r})$ to be some appropriately normalized filter kernel and then applying it to the G field gives

$$\bar{G}(\mathbf{x}, t) = \int_{|\mathbf{r}| \leq \Delta} \mathcal{F}(\mathbf{r}) G(\mathbf{x} - \mathbf{r}, t) d\mathbf{r} = \int_{|\mathbf{r}| \leq \Delta} \mathcal{F}(\mathbf{r}) H(c(\mathbf{x} - \mathbf{r}, t) - c_0) d\mathbf{r}, \quad (2.14)$$

where Δ is some characteristic filter width. This filtering procedure is consistent with LES in the sense that the same filter kernel $\mathcal{F}(\mathbf{r})$ that is used to filter the Navier-Stokes equations can be used for surface filtering, even when Favre density weighting is considered. It will be assumed here that the filter kernel $\mathcal{F}(\mathbf{r})$ does not change from point to point in physical space \mathbf{x} .

Figure 1 demonstrates how the filtering operation proposed in Eq. (2.14) affects a 2-D front consisting of a variety of wavenumbers. As shown, it first removes the highest wavenumbers, as is desirable in LES. After multiple filter passes, only the lowest wavenumber mode remains.

To summarize, Eq. (2.12) governs the evolution of a heaviside function that describes the flame front. Because this equation is valid everywhere, it can be volumetrically filtered and easily manipulated. It is not numerically tractable, however, since it describes sharp jumps. A level set equation will therefore have to be introduced if simulations are to be performed.

A level set field variable \mathcal{G} associated with an unfiltered flame front can be defined as

$$\mathcal{G} = \mathcal{G}_0 \quad \forall \quad c = c_0 \quad (\text{equivalently, } \forall \quad G = G_0) \quad (2.15)$$

$$|\nabla \mathcal{G}| = 1 \quad \forall \quad c \neq c_0 \quad (\text{equivalently, } \forall \quad G \neq G_0), \quad (2.16)$$

where the definition away from the c_0 surface is arbitrary. Equation (2.15) guarantees

that the c_0 and \mathcal{G}_0 surfaces evolve in tandem. A governing equation for \mathcal{G} can be developed by following the level set derivation procedure mentioned at the beginning of this section. Taking the substantial derivative of Eq. (2.15) yields

$$\frac{D\mathcal{G}}{Dt} \Big|_{\mathcal{G}=\mathcal{G}_0} = \frac{\partial \mathcal{G}}{\partial t} \Big|_{\mathcal{G}=\mathcal{G}_0} + v_{j,\mathcal{G}_0} \frac{\partial \mathcal{G}}{\partial x_j} \Big|_{\mathcal{G}=\mathcal{G}_0} = 0, \quad (2.17)$$

where v_{j,\mathcal{G}_0} describes the combined influence of propagation and convection on the \mathcal{G}_0 front. v_{j,\mathcal{G}_0} is not arbitrary but rather is implicitly defined by Eq. (2.15). Specifically, it is what forces the \mathcal{G}_0 surface to evolve in tandem with c_0 . Since the convection and propagation speeds of c are explicitly available from Eq. (2.10) (or, equivalently, from Eq. (2.12)), however, v_{j,\mathcal{G}_0} may simply be written

$$v_{j,\mathcal{G}_0} = u_j + n_j (D\kappa + s_L) \quad (2.18)$$

where again

$$s_L = \frac{\rho_u}{\rho} s_{L,u} = \frac{\rho_u}{\rho |\nabla c| \rho_u} \frac{1}{\rho} \left[n_j \frac{\partial}{\partial x_j} (\rho D |\nabla c|) + \dot{\omega}_R \right]. \quad (2.19)$$

After substituting for v_{j,\mathcal{G}_0} at the front, the level set equation becomes

$$\frac{\partial \mathcal{G}}{\partial t} + u_j \frac{\partial \mathcal{G}}{\partial x_j} = D\kappa |\nabla \mathcal{G}| + \frac{\rho_u}{\rho} s_{L,u} |\nabla \mathcal{G}| \quad \forall \quad \mathcal{G} = \mathcal{G}_0. \quad (2.20)$$

At all locations away from the \mathcal{G}_0 surface, \mathcal{G} obeys no governing equation because it is arbitrarily defined.

Eq. (2.18) provides a critical link between Eq. (2.12) and Eq. (2.20). When G is filtered this link changes, but it does so in a completely consistent way. The filtered variable \bar{G} and its governing equation can be used to derive a level set equation at the filter level \bar{u}_j . For example, consider an unfiltered flame front described by a heaviside function such as is done in Eq. (2.11). Eq. (2.12) governs the behavior of this heaviside function. If a LES of the flame front is to be performed using a filter kernel \mathcal{F} , the corresponding filtered front can be found using Eq. (2.14). Furthermore, filtering Eq. (2.12) with the operator in Eq. (2.14) will yield an appropriate filtered governing equation. Since the \bar{G} equation is not numerically tractable, however, a level set equation describing the same surface must be developed. The corresponding level set field variable $\bar{\mathcal{G}}$ would be defined by

$$\bar{\mathcal{G}} = \mathcal{G}_0 \quad \forall \quad \bar{G} = G_0 \quad (2.21)$$

$$|\nabla \bar{\mathcal{G}}| = 1 \quad \forall \quad \bar{G} \neq G_0. \quad (2.22)$$

The governing level set equation at the front would make use of some filtered velocity $\bar{v}_{j,\bar{\mathcal{G}}_0}$. Unlike the unfiltered case, however, it is not easy to explicitly write down what this velocity should be. The unclosed terms that appear when a filter is applied to Eq. (2.12) must be modeled. They can then be used in the level set equation associated with the relevant filter level.

The results of filtering Eq. (2.12) will now be examined, and a dynamic model describing subfilter effects will be developed. The results of this model will be applicable at $\bar{G} = \mathcal{G}_0$, thus closing the problems of both filtering and numerical tractability.

3. Dynamic propagation model

With an appropriate surface filtering procedure defined, it is possible to derive a dynamic identity that describes the speed at which a turbulent front propagates. This

identity will be derived using Eq. (2.12). In many respects, it resembles Germano's identity. A particular form of the latter appears when the Navier-Stokes equations are written at two different filter levels, here denoted with respect to the velocity u_j by \bar{u}_j and $\widehat{\bar{u}}_j$.

$$\frac{\partial \bar{u}_i}{\partial t} + \frac{\partial}{\partial x_j} (\bar{u}_i \bar{u}_j) + \frac{\partial}{\partial x_j} (\bar{u}_i \bar{u}_j - \bar{u}_i \bar{u}_j) = \overline{RHS} \quad (3.1)$$

$$\frac{\partial \widehat{\bar{u}}_i}{\partial t} + \frac{\partial}{\partial x_j} (\widehat{\bar{u}}_i \widehat{\bar{u}}_j) + \frac{\partial}{\partial x_j} (\widehat{\bar{u}}_i \widehat{\bar{u}}_j - \widehat{\bar{u}}_i \widehat{\bar{u}}_j) = \widehat{\overline{RHS}}, \quad (3.2)$$

where RHS describes the pressure, diffusive, and body force terms, and where a constant density assumption has been made for simplicity. Applying the filter $\widehat{\bar{u}}_j$ to Eq. (3.1) and then subtracting Eq. (3.2) gives

$$\frac{\partial}{\partial x_j} (\widehat{\bar{u}}_i \widehat{\bar{u}}_j) - \frac{\partial}{\partial x_j} (\widehat{\bar{u}}_i \widehat{\bar{u}}_j) = \frac{\partial}{\partial x_j} (\widehat{\bar{u}}_i \widehat{\bar{u}}_j - \widehat{\bar{u}}_i \widehat{\bar{u}}_j) - \frac{\partial}{\partial x_j} (\widehat{\bar{u}}_i \widehat{\bar{u}}_j - \widehat{\bar{u}}_i \widehat{\bar{u}}_j), \quad (3.3)$$

where the fact that the right-hand sides of the Navier-Stokes equations commute with filters has been used. It has also been assumed that

$$\widehat{(\bar{u}_i)} = \widehat{\bar{u}}_i, \quad (3.4)$$

which is not necessarily true for an arbitrary filter \mathcal{F} . If all subfilter quantities are known, then Eq. (3.3), which is the spatial gradient of Germano's identity, will trivially reduce to $0 = 0$. When subfilter quantities are modeled, however, this equation does not identically hold. But employing a model that enforces this equation ensures that even when subfilter errors are made, the evolution of a doubly filtered velocity field matches the filtered evolution of a singly filtered velocity field. This condition should always be true in consistent LES procedures.

A similar analysis may be performed on a surface evolution equation. When a single filter is applied, Eq. (2.12) becomes

$$\frac{\partial \bar{G}}{\partial t} + \bar{u}_j \frac{\partial \bar{G}}{\partial x_j} + \overline{u'_j \frac{\partial G}{\partial x_j}} = D\bar{\kappa} |\nabla \bar{G}| + D\bar{\kappa}' |\nabla \bar{G}| + \frac{\rho_u}{\bar{\rho}} \bar{s}_{sgs} |\nabla \bar{G}|, \quad (3.5)$$

where $\frac{\rho_u}{\bar{\rho}} \bar{s}_{sgs} |\nabla \bar{G}|$ is the turbulent front propagation model corresponding to the filter size,

$$\frac{\rho_u}{\bar{\rho}} \bar{s}_{sgs} |\nabla \bar{G}| = \overline{\frac{\rho_u}{\rho} s_{L,u} |\nabla G|}, \quad (3.6)$$

and where primed quantities are defined as

$$\phi'(\mathbf{x}, \mathbf{r}, t) = \phi(\mathbf{x} - \mathbf{r}, t) - \bar{\phi}(\mathbf{x}, t). \quad (3.7)$$

When a second, broader filter is used, the equation becomes

$$\frac{\partial \widehat{\bar{G}}}{\partial t} + \widehat{\bar{u}}_j \frac{\partial \widehat{\bar{G}}}{\partial x_j} + \widehat{\overline{u''_j \frac{\partial G}{\partial x_j}}} = D\widehat{\bar{\kappa}} \widehat{|\nabla \bar{G}|} + D\widehat{\bar{\kappa}''} \widehat{|\nabla \bar{G}|} + \frac{\rho_u}{\bar{\rho}} \bar{s}_{sgs} \left| \nabla \widehat{\bar{G}} \right|, \quad (3.8)$$

where the double prime denotes

$$\phi''(\mathbf{x}, \mathbf{r}, t) = \phi(\mathbf{x} - \mathbf{r}, t) - \widehat{\bar{\phi}}(\mathbf{x}, t). \quad (3.9)$$

Like \bar{u}_j , $\bar{\kappa}$ is defined everywhere in the vicinity of the front, since $\kappa = \nabla \cdot \left(\frac{\nabla c}{|\nabla c|} \right)$. When

multiplied with G , however, these filtered quantities become irrelevant at all locations away from the flame front.

It is interesting to note what happens when Favre velocity filtering is used. Then, filtered velocities \bar{u}_j are defined as

$$\bar{u}_j(\mathbf{x}, t) = \frac{1}{\bar{\rho}(\mathbf{x}, t)} \int_{|\mathbf{r}| \leq \Delta} \mathcal{F}(\mathbf{r}) \rho(\mathbf{x} - \mathbf{r}, t) u_j(\mathbf{x} - \mathbf{r}, t) d\mathbf{r} \quad (3.10)$$

and fluctuating velocities as

$$u'_j(\mathbf{x}, \mathbf{r}, t) = u_j(\mathbf{x} - \mathbf{r}, t) - \frac{1}{\bar{\rho}(\mathbf{x}, t)} \int_{|\mathbf{r}| \leq \Delta} \mathcal{F}(\mathbf{r}) \rho(\mathbf{x} - \mathbf{r}, t) u_j(\mathbf{x} - \mathbf{r}, t) d\mathbf{r}. \quad (3.11)$$

Again, when these velocity fluctuations are multiplied with spatial derivatives of $G = H(c - c_0)$ in Eq. (3.5), information is retained only directly at the front. As such, the $\bar{\rho}(\mathbf{x}, t)$ term that appears in Eq. (3.11) takes on the value of the front conditioned density, $\bar{\rho}(\mathbf{x}, t) = \bar{\rho}(c_0)$, when it appears in the level set equation. In this sense, all fluctuating velocities in the equation are conditioned on the density at the front.

A simplification unique to surfaces can now be introduced. Intuition suggests that all filtered combinations of fluctuating velocities and G are approximately zero,

$$\widehat{u'_j \frac{\partial G}{\partial x_j}} \approx 0, \quad \widehat{u''_j \frac{\partial G}{\partial x_j}} \approx 0. \quad (3.12)$$

Specifically, these terms describe how high wavenumber velocity components move the filtered front. They tend to wrinkle the instantaneous front, but they act only along a 2-D surface within the filter volume. When these terms are filtered, therefore, they will on average have no effect on the mean front position. Some of the subfilter velocity fluctuations will tend to move the subfilter front location forward, and some will tend to move the front location backward. But because these fluctuations are all deviations from the local filtered velocity, when integrated along the front over the filter volume, they will all tend to cancel out. For example, if a non-propagating front were released in a flowfield of homogeneous isotropic turbulence, subfilter scale velocity fluctuations would exist. But the mean front position would remain stationary, even though the exact front becomes more and more wrinkled. These terms should therefore be unable to contribute to front propagation.

Filtering Eq. (3.5), subtracting Eq. (3.8), and manipulating produces

$$\widehat{(\bar{u}_j - \bar{u}_j) \frac{\partial \bar{G}}{\partial x_j}} = D\bar{\kappa} \widehat{|\nabla \bar{G}|} - D\bar{\kappa} \widehat{|\nabla G|} + \quad (3.13)$$

$$\widehat{(\bar{D}_{G,sgs} - \widehat{D}_{G,sgs})} + \frac{\rho_u}{\bar{\rho}} \left(\widehat{\bar{s}_{sgs} |\nabla \bar{G}|} - \widehat{\bar{s}_{sgs} |\nabla G|} \right), \quad (3.14)$$

where the filtered density at the front is taken to be independent of the filter level. Again, the term on the left-hand side describes the effect of filtered velocity fluctuations and so can be dropped. $D_{G,sgs}$ is the model used to describe subfilter curvature induced front propagation,

$$\bar{D}_{G,sgs} = D\bar{\kappa}' \widehat{|\nabla \bar{G}|}, \quad \widehat{D}_{G,sgs} = D\bar{\kappa}'' \widehat{|\nabla G|}. \quad (3.15)$$

Upon grouping all curvature related terms together into \mathcal{D} ,

$$\mathcal{D} = D\widehat{\bar{\kappa}|\nabla G|} - D\bar{\kappa}\widehat{|\nabla G|} + \widehat{(\bar{D}_{G,sgs})} - \widehat{\bar{D}_{G,sgs}} \quad (3.16)$$

the dynamic identity becomes

$$\frac{\bar{\rho}}{\rho_u} \mathcal{D} = \widehat{\bar{s}_{sgs}|\nabla \bar{G}|} - \widehat{\bar{s}_{sgs}} \left| \nabla \widehat{\bar{G}} \right|. \quad (3.17)$$

For the purposes of simplification, the remainder of this brief will consider the corrugated flamelets regime only. Diffusive effects in this regime do no significantly influence the burning velocity, resulting in $\mathcal{D} \approx 0$. In this regime, then, the identity reduces to

$$\widehat{\bar{s}_{sgs}} \left| \nabla \widehat{\bar{G}} \right| = \widehat{\bar{s}_{sgs}|\nabla \bar{G}|}. \quad (3.18)$$

LES turbulent burning velocity models usually depend much more strongly on the filtering level at which they act than on space. \bar{s}_{sgs} may therefore be drawn outside the filter integral, leaving

$$\frac{\bar{s}_{sgs}}{\widehat{\bar{s}_{sgs}}} = \frac{\widehat{|\nabla \bar{G}|}}{\left| \nabla \widehat{\bar{G}} \right|}. \quad (3.19)$$

Although this equation looks very much like a dynamic identity, the G variable will not be available in computations. Eq. (3.19) can be written in a more useful form by manipulating the filter definition. If for the purposes of demonstration the first filter level is taken to represent a completely resolved field, then

$$\widehat{|\nabla \bar{G}|} = \widehat{|\nabla G|} = \int_{r \leq 2\Delta} \mathcal{F}_{2\Delta}(\mathbf{r}) |\nabla H(c(\mathbf{x} - \mathbf{r}, t) - c_0)| d\mathbf{r} \quad (3.20)$$

$$= \int_{r \leq 2\Delta} \mathcal{F}_{2\Delta}(\mathbf{r}) \delta(c(\mathbf{x} - \mathbf{r}, t) - c_0) |\nabla c(\mathbf{x} - \mathbf{r}, t)| d\mathbf{r}. \quad (3.21)$$

It will now be assumed that $|\nabla c|$ does not strongly vary along the flame front. In the corrugated flamelets and thin reaction zones regimes this assumption is certain to hold since turbulent eddies do not penetrate the inner reaction zones of such flames. Under this assumption, $|\nabla c|$ may be treated as a constant and brought out of the integral. Additionally, a front area per filter volume may be defined as

$$a_{2\Delta} = \int_{r \leq 2\Delta} \mathcal{F}_{2\Delta}(\mathbf{r}) \delta(c(\mathbf{x} - \mathbf{r}, t) - c_0) d\mathbf{r}. \quad (3.22)$$

When \mathcal{F} is a tophat filter, $a_{2\Delta}$ describes the exact unfiltered flame area within the filter domain. When \mathcal{F} is a Gaussian, $a_{2\Delta}$ gives flame surfaces near the center of the filtering domain more weight. Using these assumptions, $\widehat{|\nabla \bar{G}|}$ may be rewritten

$$\widehat{|\nabla \bar{G}|} = |\nabla c|_{c_0} a_{2\Delta}. \quad (3.23)$$

The denominator of the right hand side of Eq. (3.19) may be written

$$\left| \nabla \widehat{\bar{G}} \right| = |\nabla c|_{c_0} \left| \int_{r \leq 2\Delta} \mathcal{F}_{2\Delta}(\mathbf{r}) \delta(c(\mathbf{x} - \mathbf{r}, t) - c_0) n_j(\mathbf{x} - \mathbf{r}, t) d\mathbf{r} \right| \quad (3.24)$$

It can be shown that the expression within the absolute value sign describes the area

density of the *filtered* flame front within the filter volume. This quantity will be defined as $\bar{a}_{2\Delta}$. Finally, since the right-hand side of Eq. (3.19) describes flame area densities within the same filter volume, the actual flame areas may be used in the identity,

$$\frac{\bar{s}_{sgs}}{\bar{s}_{sgs}} = \frac{\bar{A}_{front}}{\bar{\bar{A}}_{front}}. \quad (3.25)$$

This form of the identity agrees with Damköhler's hypothesis (Damköhler 1941),

$$\frac{s_T}{s_L} \sim \frac{A_{exact}}{A_{mean}}, \quad (3.26)$$

and enforces the condition that the mass a flame consumes should be independent of filter level.

The remainder of this brief will use a burning velocity model proposed by Peters (Pitsch 2005), (Peters 2000),

$$\frac{s_T - s_L}{u'} = -\gamma Da + \sqrt{(\gamma Da)^2 + \gamma \alpha Da}. \quad (3.27)$$

In the limits of large and small Da, respectively, this model reduces to

$$s_T = s_L + u' \frac{\alpha}{2}, \quad s_T = s_L \left(1 + (\gamma \alpha)^{\frac{1}{2}} \sqrt{\frac{D_t}{D}} \right), \quad (3.28)$$

which obey the appropriate regime scaling laws. While it is not entirely clear that the placement of the α and γ coefficients in Eq. (3.27) is ideal, it is reasonable to suggest that physically, flame mass consumption should appear in both limiting cases. Therefore, Eq. (3.25) will be used as a dynamic identity, Eq. (3.27) will be used to model s_{sgs} , and α in Eq. (3.27) will be treated as a dynamic coefficient.

4. DNS results

A direct numerical simulation (DNS) of a front propagating in forced homogeneous isotropic turbulence was performed to validate this model. The parameters describing the DNS are shown in Table 1. Turbulence was forced using the linear scheme of Rosales and Meneveau (Rosales & Meneveau 2005), and the simulation was run at a constant density. A uniform cartesian mesh was used, but in the direction of front propagation the domain length was doubled so that front statistics could be gathered for a longer period of time. The level set equation

$$\frac{\partial \mathcal{G}}{\partial t} + u_j \frac{\partial \mathcal{G}}{\partial x_j} = s_L |\nabla \mathcal{G}| \quad \forall \quad \mathcal{G} = \mathcal{G}_0 \quad (4.1)$$

was solved to describe front evolution. As there are no diffusive terms in this equation, the front effectively propagates with a Damköhler number of infinity, and thus resides in the corrugated flamelets regime. A re-initialization procedure was performed after every three time steps to force the level set field variable away from the front to conform to a distance function. Reinitialization was accomplished by first using an iterative marker method to estimate the distance to the front, and subsequently solving a PDE in psuedo-time to improve the accuracy of this estimate. The third order WENO scheme of Peng *et al.* (Peng *et al.* 1999) was used for the PDE step.

Statistics involving the front itself were computed using information from only one

Simulation Constants	Turbulence Parameters
Mesh Size = $256 \times 128 \times 128$	$Re_\lambda = 39$
$\Delta x = 1.0 \cdot 10^{-3} \text{ m}$	$Re_t = 101$
$\nu = 1.87 \cdot 10^{-5} \text{ m}^2 \cdot \text{s}^{-1}$	Integral length scale, $l_t = 7.7 \cdot 10^{-3} \text{ m}$
$\rho = 1.16 \text{ kg} \cdot \text{m}^{-3}$	Eddy turnover time, $\tau = 0.20 \text{ s}$
Burning velocity, $s_L = 0.06 \text{ m} \cdot \text{s}^{-1}$	Komogorov scale, $\eta = 5.0 \cdot 10^{-4} \text{ m}$
Forcing Coefficient, $A = 2.4$	Largest eddy size, $l = 16.0 \cdot 10^{-3} \text{ m}$

TABLE 1. DNS Parameters

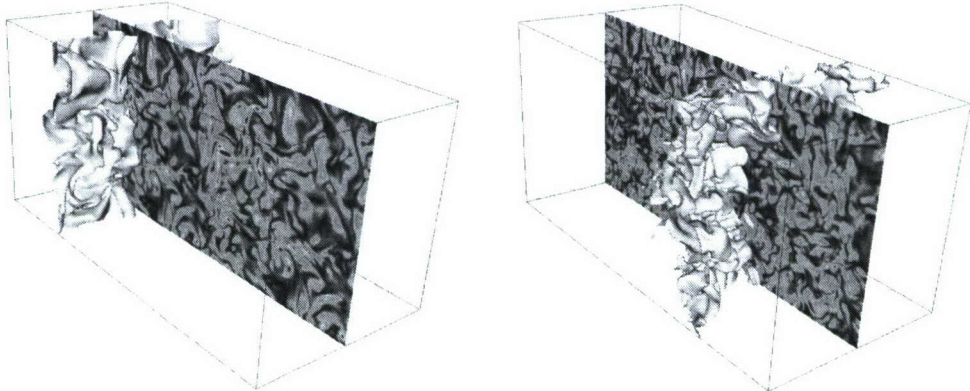


FIGURE 2. Snapshots from a DNS of front propagation. The level set is the wrinkled surface, and the cut plane shows vorticity magnitude. The left image shows an early time in the simulation, while the right image shows the fully developed front.

isocontour of the level set field variable. Neumann boundary conditions were prescribed for the level set at each end of the domain in the propagation direction. The front, however, never comes so near these boundaries that their treatment influences behavior. The front was not allowed to propagate periodically in this direction because the re-initialization procedure would create artificial fronts at the domain boundary. Periodic boundary conditions were prescribed for the level set in the other two directions.

A parallel, structured code that is second order in both time and space was used to compute the flow. Although the code was run using an implicit solver, the CFL number was limited to 0.5 to ensure that all structures were time resolved. Because the linear forcing scheme used here adds energy to the flow at all wavenumbers, the turbulent flowfield was initialized within a 128^3 cube, and then copied to an adjacent cube. This prevented the generation of wavenumbers smaller than the inverse of the box size. Periodic boundary conditions were used in every direction for the velocity field. Figure 2 shows two instantaneous realizations of the flowfield and front.

Figure 3 shows mean front displacement as a function of time, computed both directly from the DNS and from a variety of models. If no turbulent burning velocity model is used, front displacement is severely under-predicted, as expected. The static turbulent burning velocity model of Eq. (3.27), however, somewhat over-predicts front displacement. This over-prediction primarily develops at early times as the front, which is initially flat, transitions to a wrinkled surface under the influence of turbulence. In

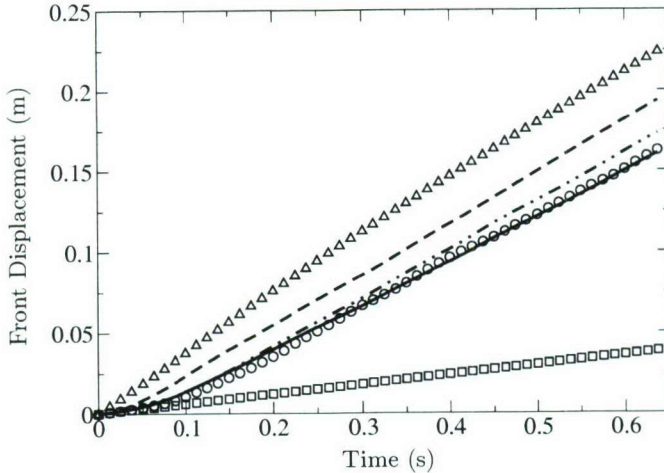


FIGURE 3. Front displacement from initial location as a function of time, using: \circ : Mean front position from DNS; \square : Laminar burning velocity; \triangle : Static turbulent burning velocity model (Eq. (3.27)); --- : $s_L \frac{A_{\text{unfiltered}}}{A_{\text{flat}}}$, with area ratio from DNS; --- : Dynamic model computed using unfiltered and singly filtered fields, $\text{---}\cdot\text{---}$: Dynamic model computed using quadruply filtered and completely filtered fields

contrast, the dynamic model accurately predicts this transition. The solid line, for example, uses unfiltered fields to describe a first filter level, and completely filtered fields to describe a second. Applying Eq. (3.25) in this context consists of multiplying the laminar burning velocity by the area of the fully resolved front and then dividing the result by the width and height of the domain, which represents the area of the completely filtered front. The results are in excellent agreement with the DNS data.

The dynamic model produces results that are somewhat less accurate when filter levels that are very closely spaced are used. For example, when unfiltered and singly filtered fields are used in Eq. (3.25), front displacement is mildly over-predicted. This error does not signify a problem with the modeling approach as much as it highlights the difficulty of describing how velocity fluctuations, u' , change with very small changes in filter wavenumber. If the fluctuations are relatively small to begin with, as they are when a singly filtered field is used, all errors made in predicting u' will strongly affect the solution of Eq. (3.25). Similar conclusions were arrived at by Im *et al.* in the context of scalar isosurfaces (Im *et al.* 1997).

Difficulties in predicting filtered velocity fluctuations are alleviated to a certain extent when the test filters selected span a wider range of wavenumbers. The $\text{---}\cdot\text{---}$ line in Fig. 3 shows that dynamic model predictions considerably improve when quadruply filtered and completely filtered fields are used as test levels.

Figure 4 shows speeds and area ratios from both the DNS and the models as a function of time. The front propagation speed that the static turbulent burning velocity model predicts varies smoothly in time, because it depends only on averaged velocity fluctuations that are a function of the amount of kinetic energy in the domain. The actual front propagation velocity, however, oscillates at relatively high frequency. The dynamic model, regardless of the filters used, appropriately captures this high frequency behavior, which appears through the surface area of the front. Specifically, even in the dynamic case that uses unfiltered and singly filtered fields, the area ratio of the fronts that is plotted using the right vertical axis qualitatively matches the plot of the DNS front propagation

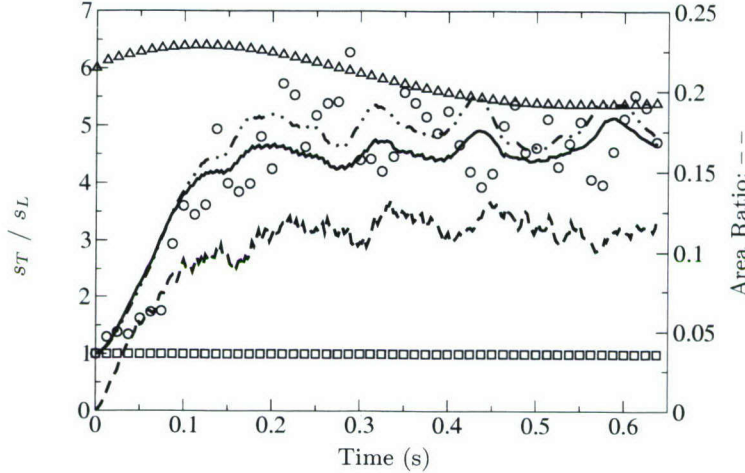


FIGURE 4. Front speed and area ratio as a function of time: \circ : s_T directly from DNS data; \square : Laminar; \triangle : Static s_T model (Eq. (3.27)); $—$: $\frac{s_T}{s_L} = \frac{A_{unfiltered}}{A_{flat}}$, with area ratio from DNS; $--$: Area ratio of unfiltered and singly filtered fronts (right vertical axis), $- \cdot -$: s_T from dynamic model, computed using quadruply filtered and completely filtered fields

speed. The errors in the model are therefore due to the scaling of this area ratio, which again is a function of subfilter velocity fluctuations.

Finally, since the model's sensitivity to u' has been emphasized, it is appropriate to describe how this quantity is computed in the DNS. The most critical requirement for this computation is that there be a match between the filtering procedure used on the front area and the procedure used on the velocity field. At a minimum, this means that the filtering kernel \mathcal{F} that is computationally applied to the front should be the same as that applied to the velocity field. Experience showed, however, that this alone was not enough. Attempts to extract differences in u' from turbulent viscosities computed at two filter levels, or from model turbulence spectra mapped onto the velocity fields, proved insufficient. Rather, the energy of the velocity fields at each filter level had to be computed. A difference in the velocity fluctuations associated with different filters could then be formed,

$$\widehat{\overline{u'}} - \overline{u'} = \sqrt{\frac{2}{3}\widehat{\overline{k}}} - \sqrt{\frac{2}{3}\overline{k}}, \quad (4.2)$$

where \overline{k} is the kinetic energy associated with the velocity field \overline{u}_j . Even when an arbitrary means of computing $\overline{u'}$ was used, this technique accurately described how velocity fluctuations varied with the filter used.

5. Conclusions

Most computationally tractable methods of simulating turbulent premixed combustion require information regarding the speed of flame front propagation. In this brief, a dynamic model for calculating this speed was presented. First, a consistent flame front filtering approach for LES was developed. This approach is useful because it both works in conjunction with standard LES filtering techniques and because it uses information from just a single 2-D surface. Next, this filtering approach was used to derive a dynamic identity that is compatible with a level set equation. When enforced, this identity en-

sures that evolving a flame front and then filtering the result yields the same answer that evolving a filtered front does. This dynamic identity, in its simplest form, may physically be viewed as an enforcement of flame mass consumption conservation. A DNS was performed to validate the proposed dynamic model. Results showed that the model predicts the speed of a propagating turbulent front with considerably more accuracy than a static burning velocity model.

6. Acknowledgements

Support from the United States Department of Defense NDSEG Fellowship Program, and from the United States Air Force Office of Scientific Research (AFOSR), is gratefully acknowledged.

REFERENCES

ABDEL-GAYED R. G., AND BRADLEY D. 1981. A two-eddy theory of premixed turbulent flame propagation. *Philosophical Transactions of the Royal Society of London A* vol. **301**, no. **1457**, 1–25.

COLIN O., DUCROS F., VEYNANTE D., AND POINSOT T. 2000. A thickened flame model for large eddy simulations of turbulent premixed combustion. *Phys. Fluids* **12**, 1843–1862.

DAMKÖHLER G. 1941. Der Einfluß der Turbulenz auf die Flammengeschwindigkeit in Gasgemischen. *Z. Elektrochem.* **46**, 601–652, English Translation NASA Tech. Mem. 1112.

HERRMANN M. 2000. Numerische simulation vorgemischter und teilweise vorgemischter turbulenter flammen. *Dissertation*, RWTH Aachen.

IM H. G., LUND T. S. AND FERZIGER J. H. 1997. Large eddy simulation of turbulent front propagation with dynamic subgrid models. *Phys. Fluids* **9**, 3826–3833.

KERSTEIN A. R., ASHURST W. T. AND WILLIAMS F. A. 1988. Field equation for interface propagation in an unsteady homogeneous flow field. *Phys. Review A* **37** no. **7**, 2728–2731.

LEGIER J. P., POINSOT T., AND VEYNANTE D. 2000. Dynamically thickened flame LES model for premixed and non-premixed turbulent combustion. *Proc. 2000 CTR Summer Program, Stanford University*.

MOUREAU V., MINOT P., BERAT C., AND PITSCH H. 2006. A ghost-fluid method for large-eddy simulation of premixed combustion in complex geometries. *J. Computational Physics*, *in Press*.

OBERLACK M., WENZEL H. AND PETERS N. 2001. On symmetries and averaging of the G-equation for premixed combustion. *Combust. Theory Modelling*, **5**, 363–383.

PENG D., MERRIMAN B., OSHER S., ZHAO H., AND KANG M. 1999. A PDE-Based fast local level set method. *J. Computational Physics*, **155**, 410–438.

PETERS N. 2000. Turbulent combustion. Cambridge University Press.

PITSCH H. AND DUCHAMP DE LAGENESTE L. 2002. Large-eddy simulation of premixed turbulent combustion using a level set approach. *Proc. Combustion Institute* **29**, 2001–2008.

PITSCH H. 2005. A consistent level set formulation for large-eddy simulation of premixed turbulent combustion. *Combust. Flame*, **143**, 587–598.

ROSALES C. AND MENEVEAU C. 2005. Linear forcing in numerical simulations of isotropic turbulence: physical space implementations and convergence properties. *Phys. Fluids* **17**, 1–8.

Consistent and accurate state evaluations in variable-density flow simulations

By L. Shunn AND F. Ham

1. Motivation and objectives

For the case of low-Mach number combustion where acoustic effects are considered unimportant, the variable-density equations for reacting flows can realize substantial efficiency gains relative to fully compressible formulations. In variable-density formulations, pressure and density are formally decoupled by defining the density through an equation-of-state (EOS) in terms of one or more transported scalars: $\rho = \rho(\phi_1, \phi_2, \dots)$. The EOS may be given by an analytic expression, or as is common for complex reactive systems, it may be precomputed and tabulated as a function of the scalars.

When the variable-density equations are discretized and solved numerically, it is common to use a fractional-step formulation where a constant-coefficient Poisson equation for pressure is derived through a constraint on the divergence of ρu_i coming from the continuity equation. The resulting equation for pressure has the time derivative of the density as a source term, and is solved and used to correct the velocity field and enforce mass conservation discretely. For density ratios of approximately three or greater, instabilities are commonly encountered and resolved by largely ad hoc techniques whose effect on the solution cannot easily be quantified. For example, Pierce & Moin (2001, 2004) characterized the problem as “spurious heat release” related to inconsistencies between the mass and scalar transport, and resolved the instabilities by spatially filtering the computed $\partial\rho/\partial t$ source term several times. While this will not alter the mass in the simulation (assuming a conservative filter), it does have the effect of moving mass around in a way not called for by the governing equations. Forkel & Janicka (2000) performed temporal filtering of the density to stabilize their calculations. This introduces an additional complexity and hysteresis to the state equation whose effect is also difficult to quantify.

Other authors have reformulated the numerical method to solve a variable-coefficient Poisson system derived through a constraint on the velocity divergence coming from the energy equation. While these approaches stably support much higher density ratios, it appears necessary to relax the conservation properties of the scheme (Nicoud 2000), or allow the state to wander somewhat from the state equation (Pember *et al.* 1998).

In the present study the instability problem is resolved by recognizing that nonlinearities in the state equation can introduce a multi-scale resolution problem not supported by the grid. This problem can be largely resolved by simply evaluating the density (and other tabulated source terms) using an accurate subgrid representation.

2. Consistent state evaluations

2.1. Numerical method

The simulations presented in this brief are performed using a collocated, unstructured version of the algorithm of Pierce & Moin (2001). The algorithm employs a temporally-

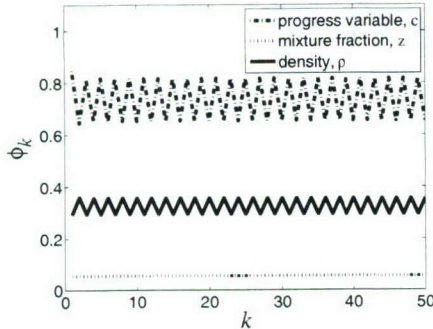


FIGURE 1. Scalars versus inner-iterations at a single spatial location in a non-convergent combustion simulation.

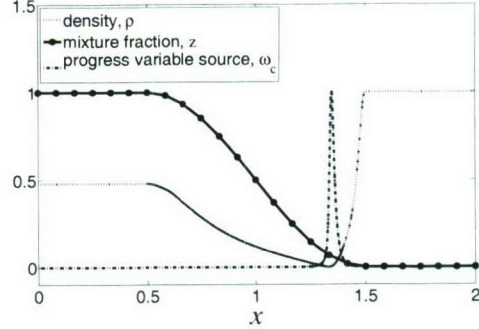


FIGURE 2. Mixture fraction, density, and product source term.

staggered variable arrangement in which velocity components are staggered in time with respect to density and other scalar variables. The velocity and scalars are implicitly advanced in time, and an iterative approach is used at each time level to repair linearization errors and enhance stability. The overall algorithm was implemented in the computer code CDP using unstructured node-based finite volume operators. Details of CDP's node-base operators are described elsewhere in this volume (Ham *et al.* 2006).

The salient features of the iteration process at each time step are as follows:

1. The scalar equation(s) are advanced in time. This yields $(\rho\phi)^{k+1}$, from which a provisional estimate for ϕ^{k+1} is obtained by $\hat{\phi} = (\rho\phi)^{k+1}/\rho^k$.
2. The momentum equation is advanced to obtain provisional velocities: \hat{u}_i .
3. The provisional scalar values are used to evaluate the density from the EOS: $\rho^{k+1} = f(\hat{\phi})$.
4. The updated density is used to correct the scalar(s) to ensure primary conservation: $\phi^{k+1} = (\rho\phi)^{k+1}/\rho^{k+1}$.
5. A Poisson equation is solved for pressure corrections that satisfy the continuity equation, and the pressure and velocity fields are adjusted accordingly.
6. The process is repeated from step 1 and continued until convergence.

Linear stability analysis indicates that the above iterative approach is second-order accurate when at least two inner-iterations are employed (Pierce & Moin 2001). Additional iterations may improve the stability of the scheme, but do not increase the order of accuracy. When the scheme is applied to real combustion problems, however, it is generally not iterated to convergence. Normally, a fixed number of inner-iterations are performed (typically 3–5) and then the time step is considered to be “converged.” Formal verification of the second-order behavior of the algorithm requires convergence of the system at each time step. For many of the combustion problems investigated, however, rigorous convergence of the scheme was not possible. For example, Fig. 1 shows the values of three scalar quantities sampled from one spatial location in a combustion simulation at successive inner-iterations of a single time step. In this example the density is obtained as a function of two transported scalars: the mixture fraction, z , and a reaction progress-variable, c . Clearly, the system is non-convergent irrespective of the number of inner-iterations used, presenting a serious impediment to verification.

2.2. Source of instabilities

These instabilities can be reproduced and their sources understood by studying much simpler problems. Consider, for example, the 1-D problem depicted in Fig. 2, which shows the mixture fraction, z , as a function of the spatial coordinate, x . Also shown are the density and product source term, ω_c , which are consistent with non-premixed methane chemistry at slightly elevated pressures. An example computational grid is denoted by the solid symbols along the mixture fraction curve. Note that although the mixture fraction transition in the figure is reasonably resolved, the highly non-linear behavior of the density and source term would be grossly under-represented on this grid. Instabilities can develop as the under-resolved, non-linear features of the EOS are transported through the grid.

Consider the case of convective scalar transport (no diffusion) with the density given as a continuous function of one scalar, i.e.,

$$\frac{\partial \rho \phi}{\partial t} + \frac{\partial \rho u_i \phi}{\partial x_i} = 0, \quad \rho = \rho(\phi). \quad (2.1)$$

Together with continuity,

$$\frac{\partial \rho}{\partial t} + \frac{\partial \rho u_i}{\partial x_i} = 0, \quad (2.2)$$

these equations are equivalent to passive scalar advection and a divergence-free velocity field, i.e.,

$$\frac{\partial \phi}{\partial t} + u_i \frac{\partial \phi}{\partial x_i} = 0, \quad \frac{\partial u_i}{\partial x_i} = 0. \quad (2.3)$$

This continuous equivalence is exploited in some numerical approaches for multi-phase flow, such as the level set method, where Eq. 2.3 is discretized and solved. For the case of turbulent combustion, however, discrete conservation is considered important, so it is preferable to discretize and solve the conservative form of both scalar transport and continuity. Due to discretization errors, this equivalence is not realized discretely and manifests itself in some non-physical divergence in the velocity field.

One way to reduce this non-physical divergence can be seen by considering the leading truncation error associated with the second-order approximations normally used in discretizing Eqs. 2.1 and 2.2. Consider the 1-D case inside a control volume of size Δx . The volume integration of density associated with the time derivative in the continuity equation is

$$\frac{1}{\Delta x} \int_{-\Delta x/2}^{\Delta x/2} \rho(\phi) dx = \rho(\phi_0) + \frac{\Delta x^2}{24} \left[\left. \frac{\partial \rho}{\partial \phi} \right|_{\phi_0} \left. \frac{\partial^2 \phi}{\partial x^2} \right|_0 + \left. \frac{\partial^2 \rho}{\partial \phi^2} \right|_{\phi_0} \left(\left. \frac{\partial \phi}{\partial x} \right|_0 \right)^2 \right] + O(\Delta x^4) \quad (2.4)$$

and the volume integration of density times the scalar associated with the time derivative in the scalar transport equation is

$$\begin{aligned} \frac{1}{\Delta x} \int_{-\Delta x/2}^{\Delta x/2} \rho(\phi) \phi dx &= \rho(\phi_0) \phi_0 + \\ &\quad \frac{\Delta x^2}{24} \left[\left. \rho(\phi_0) \frac{\partial^2 \phi}{\partial x^2} \right|_0 + 2 \left. \frac{\partial \rho}{\partial \phi} \right|_{\phi_0} \left(\left. \frac{\partial \phi}{\partial x} \right|_0 \right)^2 \right] + \end{aligned} \quad (2.5)$$

$$\phi_0 \frac{\partial \rho}{\partial \phi} \left. \frac{\partial^2 \phi}{\partial x^2} \right|_0 + \phi_0 \frac{\partial^2 \rho}{\partial \phi^2} \left. \left(\frac{\partial \phi}{\partial x} \right)_0^2 \right] + O(\Delta x^4).$$

By introducing a higher-order reconstruction of density in the control volume, it is clear that the truncation errors associated with both of these approximations can be reduced. For example, introducing a more accurate approximation for the density in the control volume, $\hat{\rho}$:

$$\hat{\rho} = \rho(\phi_0) + \frac{\Delta x^2}{24} \left[\frac{\partial \rho}{\partial \phi} \left. \frac{\partial^2 \phi}{\partial x^2} \right|_0 + \frac{\partial^2 \rho}{\partial \phi^2} \left. \left(\frac{\partial \phi}{\partial x} \right)_0^2 \right] \quad (2.6)$$

removes all of the second-order error in Eq. 2.4 and two of the four second-order terms in Eq. 2.5. Numerical experiments indicate that the removal of the curvature term involving $\partial^2 \rho / \partial \phi^2$ is particularly important, as this term is normally dominant.

The extension of this more accurate approximation of the density to multiple dimensions and unstructured grids is presented in the next section.

2.3. Tetrahedral quadrature

The purpose of this section is to develop a family of optimized quadrature rules that can be used to efficiently evaluate volume-averaged state quantities in reactive simulations. Determining quadrature points for volume integration has been the subject of many studies; see the reviews of Cools & Rabinowitz (1993) and Cools (1999) for details. Accurate and efficient quadrature points can be generated by the recursive application of 1-D Gaussian quadrature, referred to as the product Gaussian rule (see Stroud 1971). When the product Gaussian rule is applied to tetrahedra, however, it results in an unpleasant asymmetry (and presumably inefficiency), clustering the points near one of the vertices.

The product Gaussian rule implicitly assumes an underlying structured hexagonal grid for the point locations. This grid samples a hexagonal space more or less uniformly. For tetrahedra, however, the structured hexagonal grid is inappropriate. A more natural grid for tetrahedra is that obtained by the hexagonal close-packed structure. Hexagonal close-packing is the arrangement obtained by packing spheres of equal size in the most efficient manner, such that each sphere (not on the boundary) touches its 12 nearest neighbors. In the present study we describe a method for developing quadrature points for tetrahedra based on parameterizing the point locations in terms of an underlying hexagonal close-packed grid, and then optimizing the precise point locations and weights to reduce the truncation error in the quadrature approximation. Such an approach results in a family of symmetric rules for tetrahedral integration where the number of integration points progresses as $n_p = 1, 4, 10, 20, 35, 56$, etc.

The integration of the function $f(x)$ over the tetrahedron Ω with volume V_Ω is defined

$$\int_{\Omega} f(x) dV = V_\Omega \left(\sum_{i=1}^{n_p} w_i f(x_i) + O(\delta^p) \right), \quad (2.7)$$

where δ is a length scale associated with the tetrahedron (e.g., the longest edge length), and p is the order of the integration. The integration points (or quadrature points) x_i are defined in terms of the four vertices of the tetrahedron X_1, X_2, X_3, X_4 as

$$x_i = \sum_{j=1}^4 a_{i,j} X_j. \quad (2.8)$$

An integration scheme of this sort should have the following desirable properties (adapted from Vavasis 1998):

1. The scheme is optimal in some sense, e.g., minimizing truncation error.
2. It is symmetric, i.e., the scheme is independent of vertex ordering or the rule is invariant under affine maps of the tetrahedron to itself.
3. The weights are all positive: $w_i \geq 0$.
4. The quadrature points are all interior to the tetrahedron: $a_{i,j} \geq 0$.

The following integration schemes were developed by parametrizing the integration point locations in terms of the vectors of the unit equilateral tetrahedron scaled by δ

$$\begin{aligned} X_1 &= \delta \left(-\frac{1}{2}, -\frac{\sqrt{3}}{2}, -\frac{\sqrt{6}}{12} \right) \\ X_2 &= \delta \left(\frac{1}{2}, -\frac{\sqrt{3}}{2}, -\frac{\sqrt{6}}{12} \right) \\ X_3 &= \delta \left(0, \frac{\sqrt{3}}{3}, -\frac{\sqrt{6}}{12} \right) \\ X_4 &= \delta \left(0, 0, \frac{\sqrt{6}}{4} \right) \end{aligned}$$

and comparing the Taylor series expansion at the points to the exact integration of the Taylor series over the tetrahedron. The coefficients of successive powers of δ produce a series of non-linear equations that can be set equal to zero to solve for the positions and weights. When it was not possible to completely eliminate the truncation error at the highest level, then the error can be minimized in a least-squares sense, assuming the partial derivatives are all of equal magnitude. When more than one solution is found satisfying all four of the previously mentioned criteria, then the solution is considered to be the one with minimum least-squares truncation error.

The parameterization of the points exploits the tetrahedral symmetry by arranging the points as close-packed spheres and writing the sphere locations as linear combinations of the above vectors. Once the optimal solutions have been obtained, the point locations and weights are assembled and stored in a computer library for efficient implementation in numerical applications. The optimized rules are shown in Fig. 3, and their properties are summarized in Table 1.

3. Results

3.1. 1-D example problem

The 1-D combustion problem shown schematically in Fig. 4 has been designed to demonstrate the impact of EOS evaluations on a flow simulation. Here an initial transition from fuel ($z = 1$) to oxidizer ($z = 0$) is imposed and allowed to evolve subject to diffusive mixing. A constant reference-frame velocity u_{RF} can be supplied to translate the entire system through the computational grid.

For this problem, a polynomial state-relationship of the form

$$\rho = 2z + (1 - z)^{18} \quad (3.1)$$

is used to describe the density. This EOS exhibits strong non-linear behavior in the region

TABLE 1. Tetrahedral quadrature rules.

Rule	Points	Order of Accuracy
------	--------	-------------------

1	1	$O(\delta^2)$
2	4	$O(\delta^3)$
3	10	$O(\delta^4)$
4	20	$O(\delta^6)$
5	35	$O(\delta^7)$
6	56	$O(\delta^9)$

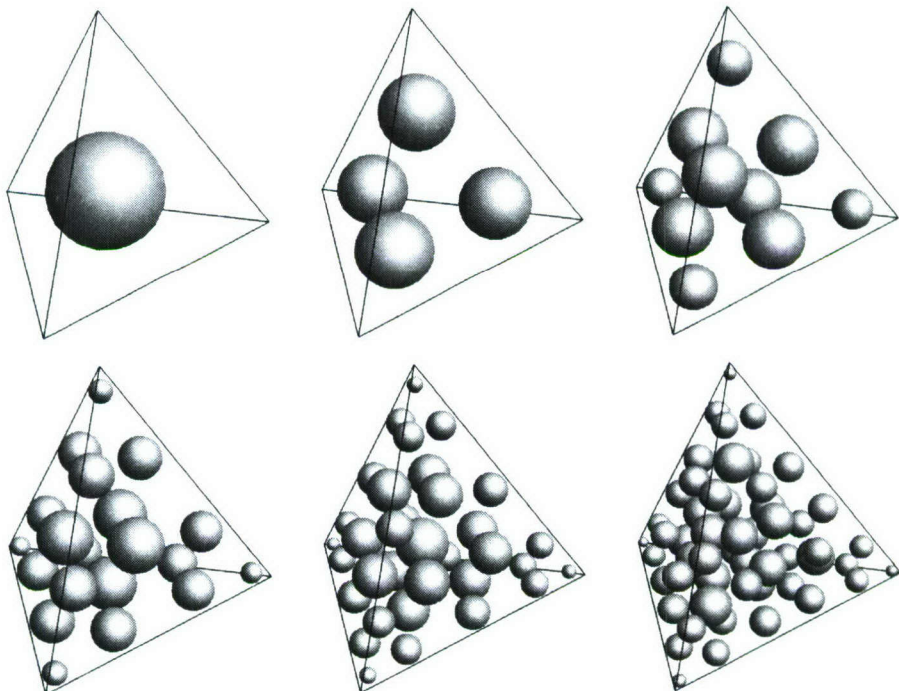


FIGURE 3. Tetrahedral integration quadrature point locations and weights. Top row (left to right): 1-, 4-, and 10-point rules. Bottom row (left to right): 20-, 35-, and 56-point rules.

$z \leq 0.2$ (see Fig. 5), and is indicative of the general behavior expected in non-premixed combustion systems. In particular, the density minimum around $z \approx 0.12$ suggests a region of reaction and heat release caused by the mixing of relatively dense fuel at $z = 1$ with moderately dense (preheated) air at $z = 0$.

As the fuel front in Fig. 4 diffuses, the low-density reactive region broadens and forces mass out of the right-hand side of the domain. The velocity at the exit, u_{out} , can be used

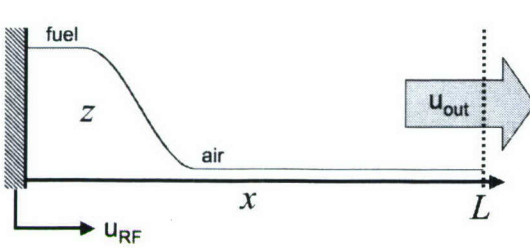


FIGURE 4. 1-D combustion problem.

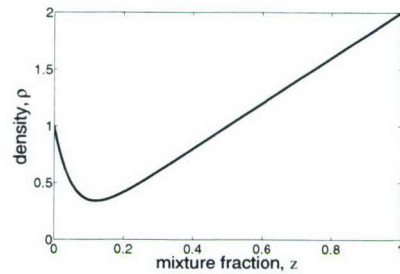


FIGURE 5. Model reactive EOS.

to monitor the global rate-of-change of mass in the system:

$$(u_{out} - u_{RF}) = \frac{-1}{\rho_{x=L}} \frac{d}{dt} \int_0^L \rho dx. \quad (3.2)$$

Here the outlet velocity is used to gauge the effectiveness of the density evaluations.

The 1-D diffusion problem was solved numerically using two different EOS-evaluation methods. In the first method, the mean density at a node is computed by simply evaluating the EOS using the mean mixture fraction value for that node. This method is referred to as “node evaluations.” In the second approach, the independent function (z in this case) is reconstructed linearly and continuously in the polyhedral region around each grid node. Each polyhedral control volume is then tessellated into tetrahedral subvolumes involving a combination of nodes, vertices, edges, and faces. A quadrature rule is applied within each subvolume to accurately integrate the state equation in space and construct an appropriate approximation to the density. This evaluation technique is referred to as “tetrahedral integration” (TI). 128 points in x were used in all of the simulations, and the most accurate (56-point) quadrature rule was applied in the TI evaluations.

Figs. 6 and 7 show numerical solutions to the 1-D diffusion problem with reference-frame velocities of $u_{RF} = 0$ and $u_{RF} = 0.2$, respectively. Solutions using node evaluations and the TI method are compared in each figure. Three cases, denoted as (a), (b), and (c), were run for each EOS-evaluation technique. In case (a), the EOS (Eq. 3.1) was evaluated analytically to compute the density. In cases (b) and (c), the EOS was interpolated linearly from a grid of uniformly-spaced points in mixture-fraction space. Case (b) used 101 points in z ($\Delta z = 0.01$), and case (c) used 51 points in z ($\Delta z = 0.02$). Cases (b) and (c) are of practical interest due to the widespread use of tabulated state-relationships in industrial computations. Interpolation of the EOS at these z -resolutions is not unreasonable. The maximum and average errors in the density for case (b) are $\epsilon_{max} = 3.5 \times 10^{-3}$ and $\epsilon_{avg} = 1.5 \times 10^{-4}$. For case (c) the errors are approximately four times larger: $\epsilon_{max} = 1.3 \times 10^{-2}$ and $\epsilon_{avg} = 6.0 \times 10^{-4}$.

At the beginning of the simulation, the outlet velocity starts from some initial value dictated by the rate of diffusion and decays smoothly as the mixture fraction gradient decreases. This behavior is captured very well with both EOS-evaluation techniques when the analytic EOS is used to compute the density, as indicated in case (a) shown in Figs. 6 and 7. When linear interpolation is used to evaluate the EOS, however, interpolation errors cause unphysical oscillations in the velocity. These errors are clearly shown in cases (b) and (c) of Figs. 6 and 7. The node-based EOS evaluations are particularly susceptible to these errors.

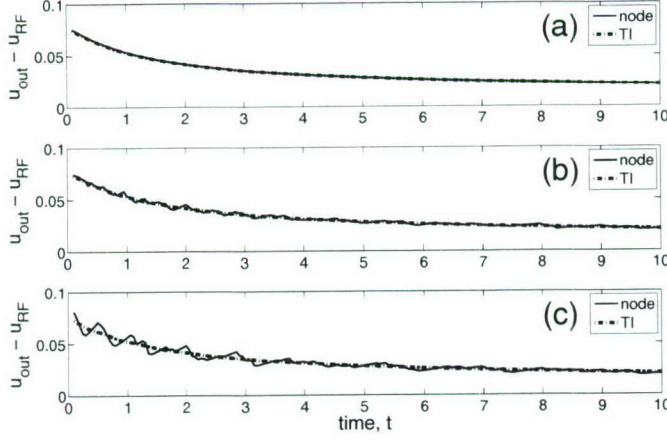


FIGURE 6. 1-D combustion problem with reference-frame velocity $u_{RF} = 0.0$. (a) analytic EOS evaluation, (b) linear interpolation $\Delta z = 0.01$, (c) linear interpolation $\Delta z = 0.02$.

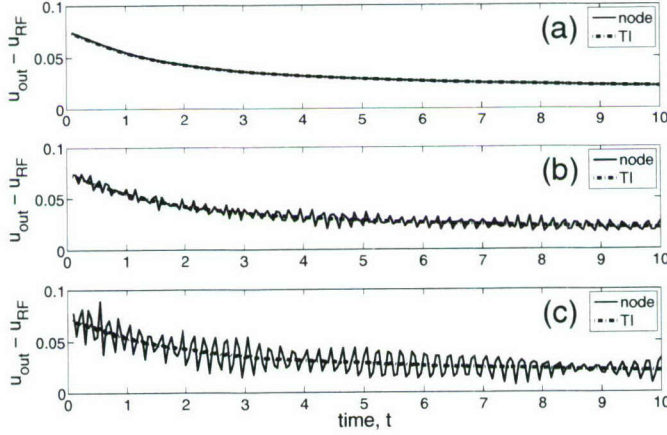


FIGURE 7. 1-D combustion problem with reference-frame velocity $u_{RF} = 0.2$. (a) analytic EOS evaluation, (b) linear interpolation $\Delta z = 0.01$, (c) linear interpolation $\Delta z = 0.02$.

To examine the cause of the unphysical oscillations, consider the evolution of the stoichiometric mixture fraction value, z_{st} . This value indicates the ratio of fuel to air that leads to chemical reactions, and can be loosely identified in this example as the density minimum in Fig. 5. As the flow evolves, the location of z_{st} (and the corresponding non-linear density region) moves through the computational grid under the effects of diffusion and reference-frame translation. When the EOS is under-resolved on the computational grid, this can lead to subtle errors in the instantaneous density field. These errors, when summed globally, lead to fluctuations with respect to time in the total amount of mass contained within the computational domain. In pressure projection methods, any erroneous mass is instantaneously removed from the system by adjusting the pressure and velocity to “correct” the global mass-balance of the system. As a consequence, spurious

density fluctuations give rise to spurious velocity and pressure fluctuations. The velocity and density in turn influence the evolution of the scalar field in a highly non-linear manner, further compounding the errors. The end result is that small errors in the EOS evaluation can amplify and lead to very large errors in the velocity and scalar fields.

Another way to explain these errors is to consider the implications of the piecewise-linear EOS used in cases (b) and (c). This representation is characterized by discontinuous first derivatives and undefined second derivatives of the density in mixture-fraction space. Examination of Eqs. 2.4 and 2.5 shows that these derivative terms are important for accurate approximation of the density. Neglecting these terms, as is done with node evaluations, can lead to large discrepancies in the numerical results.

The TI method is more resistant to this type of error because the TI-evaluated density reflects a subgrid average over the control volume, including features of the EOS that are not resolved on the computational grid. Small oscillations are still observed in the TI results, but the errors remain small and do not overwhelm the physics as in the case of the node evaluations.

3.2. 2-D example problem

In more complex systems, EOS-evaluation errors can lead to significant errors in the time evolution of the flow, including the development of spurious flow structures and unphysical mixing. This is demonstrated through the 2-D problem shown in Fig. 8. The initial configuration is similar to the classical Rayleigh-Taylor mixing problem, however, the density is given by the “reactive” EOS used in the previous example (Eq. 3.1). As the initial disturbance evolves under the influence of gravity, the low-density region around z_{st} is confined to a thin region around the fuel-oxidizer interface. Discretely representing these highly complex mixing patterns is a challenging computational problem.

Fig. 8 compares the time evolution of the 2-D mixing problem using node-based density evaluations and the TI method. Simulation results on four different grids are presented to show the effects of grid refinement on the solution and to give a point of comparison to judge the physicality of the coarse-grid solutions. For each EOS-evaluation method, the coarsest solution is shown in the left-most column of the figure matrix, and time increases from top to bottom. The most accurate (56-point) quadrature rule was applied for all evaluations in the TI computations. A non-dimensional viscosity of $\mu = 8.0 \times 10^{-4}$ was used in all cases, while the mixture fraction diffusivity was set to zero.

After only a short integration time, distinct differences emerge between the two EOS-evaluation methods. These differences are particularly pronounced on the coarser grids shown in Fig. 8. In the case of the node-based evaluations, the interface develops unphysical corrugations that numerically amplify as the solution progresses. After some time, the flowfield is contaminated with spurious flow structures evolving from an unphysical mixing-history. The coarse-grid results for the TI method, while still unresolved on the computational grid, tend to better preserve the characteristics and appearance of the resolved solutions. The difference between the two methods is clearly noticeable in Fig. 9, which shows the long-time evolution of the flowfield on a 50×150 grid. The different evaluation techniques are shown side-by-side with a more resolved solution for comparison purposes.

3.3. Adaptive tetrahedral integration

The hierarchical nature of the quadrature rules shown in Fig. 3 lends itself naturally to an adaptive EOS-evaluation procedure. Such an adaptive approach should efficiently focus additional quadrature work only where it is needed and apply lower-order methods

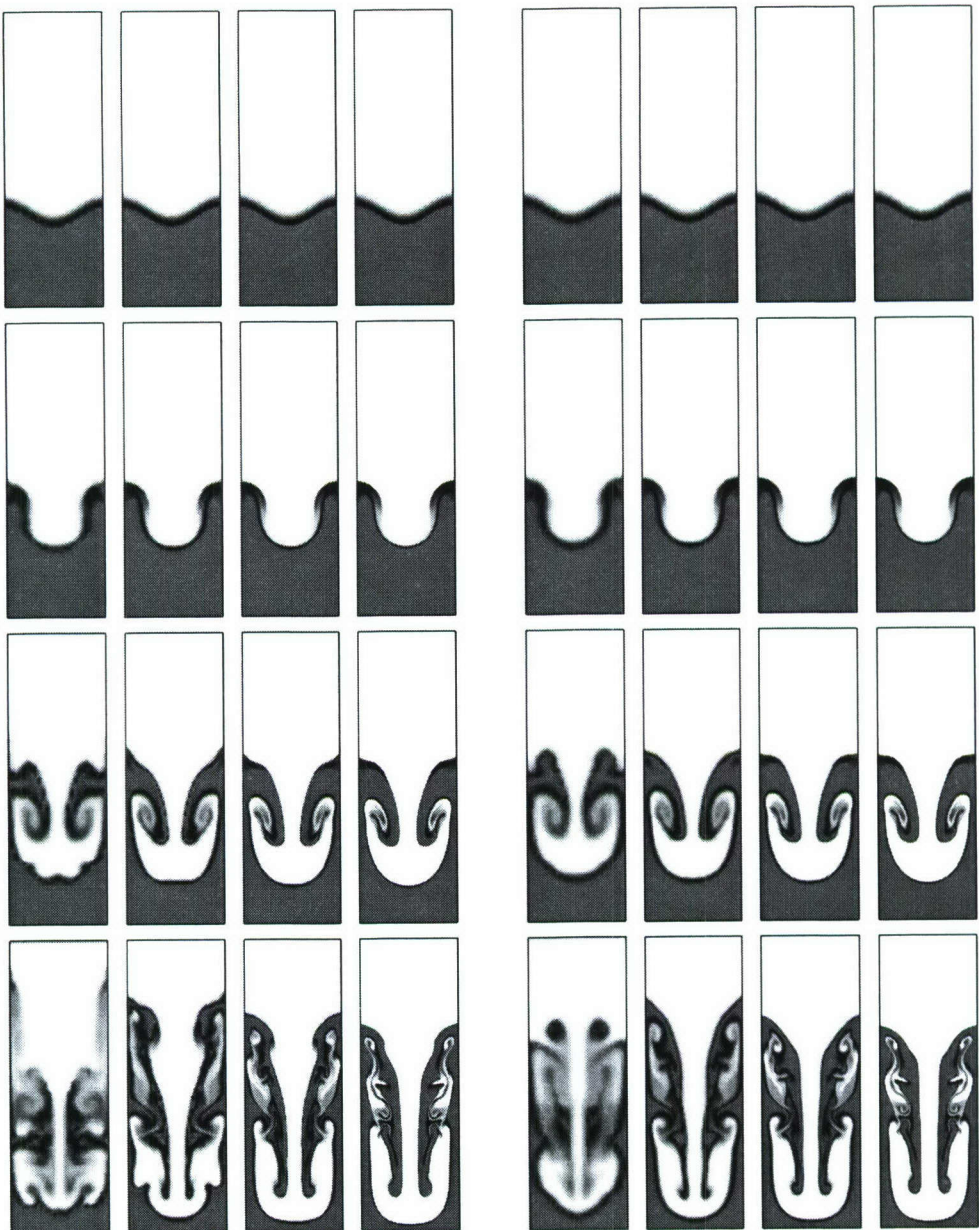


FIGURE 8. 2-D Rayleigh-Taylor instability. The left figures use node EOS-evaluations, and the right figures use TI 56-point EOS-evaluations. (top to bottom) $t = 0$, $t = 1.56$, $t = 3.08$, $t = 4.64$. (left to right) 25×75 , 50×150 , 100×300 , 200×600 grids.

in regions that do not demand special treatment. One implementation strategy would be to adaptively select the quadrature rule based on the local spatial gradient of the scalar field. A computational cell that spans a large region of scalar-space would, for example, select a high-order, multi-point quadrature rule, whereas a cell with relatively homogeneous composition might only require a one-point evaluation. The minimum and



FIGURE 9. 2-D Rayleigh-Taylor instability at $t = 5.2$. (left to right) Node evaluations on 50×150 grid, TI 56-point evaluations on 50×150 grid, TI 56-point evaluations on 100×300 grid.

maximum values of the scalars at the vertices of tetrahedral subvolumes is a natural choice for gradient estimation in such a method.

The adaptive method described above has been applied to the 2-D Rayleigh-Taylor mixing problem (see Fig. 10). The criterion for rule selection in this example required at least one quadrature point per Δz of 0.005. The time evolution of the solution is shown in Fig. 10. The upper figures show the evolution of the density, and the lower figures show the number of quadrature points used per subvolume. It is clearly seen that the bulk of the EOS-evaluation work is concentrated in the thin interface region of the solution. Fig. 11 compares the solution using the adaptive procedure with that obtained by universally applying the 56-point quadrature rule. The solutions are virtually indistinguishable.

The total execution time of the simulations was monitored for the 100×300 grid case, and the results are presented in Table 2. In all of the simulations, a sufficient number of inner-iterations was performed at each time level to converge the maximum density difference $|\rho^{k+1} - \rho^k|$ to less than 1.0×10^{-6} . Using TI with the 56-point quadrature rule incurred an increase of approximately 20% in the total execution time compared to node-based density evaluations. The adaptive TI method was the least computationally expensive approach. In this case, the extra EOS-evaluation work was offset by a decrease in the number of inner-iterations per time step and multi-grid cycles per Poisson-solve required to achieve the given levels of density and pressure convergence, respectively.

4. Summary

A method for consistent and accurate EOS evaluations in variable-density flow simulations has been developed and implemented. Various example problems were studied that

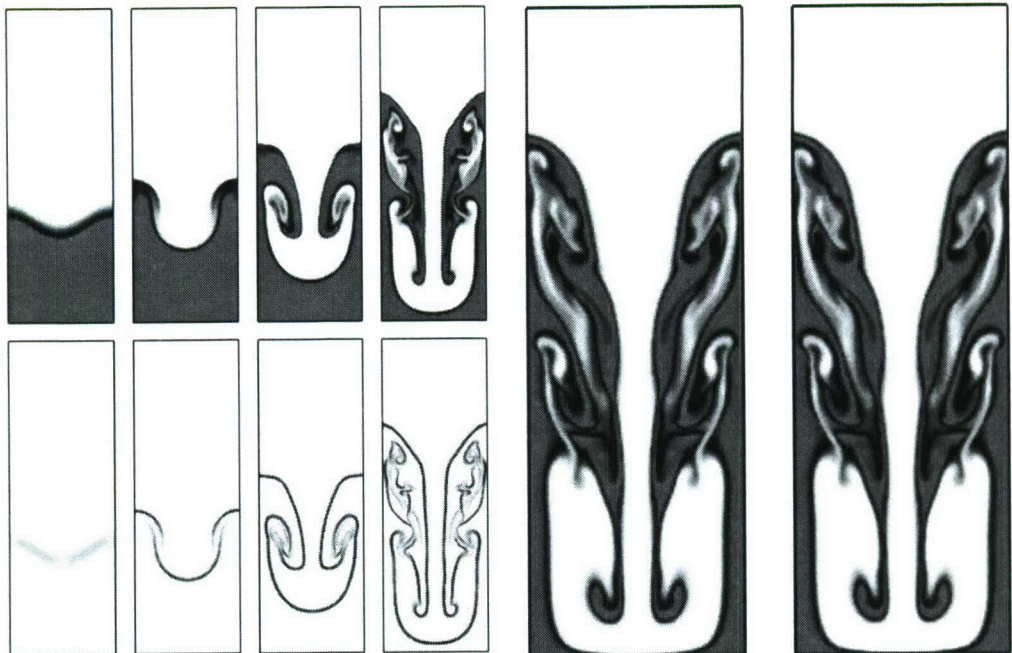


FIGURE 10. 2-D Rayleigh-Taylor instability on 100×300 grid using adaptive TI evaluations. Density on top, number of quadrature points per subvolume on bottom. (left to right) $t = 0$, $t = 1.56$, $t = 3.08$, $t = 4.64$.

FIGURE 11. 2-D Rayleigh-Taylor instability on 100×300 grid at $t = 5.2$. (left to right) TI adaptive, TI 56-point.

TABLE 2. Execution time of simulations.

Method	Time Steps	Total Time (min)	Average no. of Inner-Iterations	MG Cycles per Iteration
node	1120	180	40.1	12.3
TI 56-point	1120	211	34.1	9.05
TI adaptive	1120	178	34.5	9.00

demonstrate that under-resolving the EOS can lead to numerical instabilities and unphysical flow features. A hierarchy of symmetric quadrature rules for tetrahedral volume integration was developed and used to efficiently integrate the EOS in fluid dynamics simulations. The new method, termed tetrahedral integration (TI), was shown to reduce EOS-evaluation errors, mitigate many of the undesirable numerical artifacts that result from other techniques, and produce a more physical evolution of the flowfield. The extra cost of the TI method is offset by better convergence and stability properties of the numerical solution.

Acknowledgments

This work was supported by the U.S. Department of Energy through the Advanced Simulation and Computing (ASC) program.

REFERENCES

COOLS, R. 1999 Monomial cubature rules since “Stroud”: a compilation — part 2. *J. Comput. Appl. Math.* **112**, 21–27.

COOLS, R. & RABINOWITZ, P. 1993 Monomial cubature rules since “Stroud”: a compilation. *J. Comput. Appl. Math.* **48**, 309–326.

FORKEL, H. & JANICKA, J. 2000 Large-eddy simulation of a turbulent hydrogen diffusion flame. *Flow, Turb. Comb.* **65**, 163–175.

HAM, F., MATTSSON, K. & IACCARINO, G. 2006 Accurate and stable finite volume operators for unstructured flow solvers. *Annual Research Briefs 2006* Center for Turbulence Research, Stanford University, NASA Ames.

NICOUUD, F. 2000 Conservative high-order finite-difference schemes for low-Mach number flows. *J. Comput. Phys.* **158**, 71–97.

PEMBER, R. B., HOWELL, L. H., BELL, J. B., COLELLA, P., CRUTCHFIELD, C. Y., FIVELAND, W. A. & JESSEE, J. P. 1998 An adaptive projection method for unsteady, low-Mach number combustion. *Comb. Sci. Tech.* **140** (1-6), 123–168.

PIERCE, C. D. & MOIN, P. 2001 Progress-variable approach for large-eddy simulation of turbulent combustion. PhD thesis, Stanford University.

PIERCE, C. D. & MOIN, P. 2004 Progress-variable approach for large-eddy simulation of non-premixed turbulent combustion. *J. Fluid Mech.* **504**, 73–97.

STROUD, A. H. 1971 *Approximate calculation of multiple integrals*. Englewood Cliffs, NJ: Prentice-Hall.

VAVASIS, S. A. 1998 Quadrature over tetrahedra.
<http://www.cs.cornell.edu/home/vavasis/quad.html>. Accessed June 2006.

Scalar gradient and small-scale structure in turbulent premixed combustion

By S. H. Kim AND H. Pitsch

1. Motivation and objectives

The scalar gradient is a key quantity in describing and modeling turbulent mixing and combustion. In studies of scalar fields for non-reacting flows, it has been shown that the gradient of a passive scalar tends to align with the most compressive strain and that its magnitude is highly intermittent (Ashurst *et al.* 1987; Brethouwer *et al.* 2003; Warhaft 2000). As compared with the non-reacting case, the statistical characteristics of the gradient of a reactive scalar are not well understood due to the complexity in non-linear turbulence/chemistry interaction. In chemically reacting flows, chemical reactions, the rate of which is influenced by turbulence, can have leading-order effects on the scalar gradient evolution, and the interaction of the scalar and turbulence fields can be strongly affected by thermal expansion due to heat release (Swaminathan & Grout 2006).

The characteristics of the scalar gradient in turbulent premixed flames are quite different from those in conserved scalar mixing. The evolution of scalar gradient fields for high Damköhler number (Da) flames (Damköhler 1940) is governed by strong coupling of diffusion and chemical reactions in relatively thin flame fronts, while, in non-reacting flows, turbulent straining is the unique mechanism of generating small-scale scalar variations. For the corrugated flamelet regime, where the thickness of the flame front is smaller than all turbulence length scales, the laminar flamelet theory well describes the structure of local flame fronts (Peters 2000), and the scalar gradient in turbulent flames is expected to be similar to that in corresponding laminar flames. However, the small-scale structure inside flame fronts is not fully understood for the moderate and low Da regime, such as the thin reaction zones regime or the broken reaction zones regime (Peters 2000), where the scale separation is not strictly valid.

The scalar gradient and flame broadening have been a subject of experimental and computational studies of premixed flames, especially with high turbulence intensity. While increasing turbulence intensity is generally expected to result in flame broadening, there has been controversy in the literature whether turbulence makes flame fronts thinner or thicker. The thickening of flame fronts has been reported by O'Young & Bilger (1997) and Chen & Mansour (1998), while the increase of the scalar gradient has been observed in other experiments (Buchsman *et al.* 1996; Soika *et al.* 1998) and direct numerical simulations (DNS) (Swaminathan & Bilger 2001). The importance of the Markstein number in flame thickening in the thin reaction zones regime has been proposed on the basis of the laminar flamelet theory (de Goey *et al.* 2005), while Law *et al.* (1994) and Sung *et al.* (1996) reported the insensitivity of the flame thickness to the flame stretch in their analysis of strained laminar flames. In general, large-scale turbulence contributes to flame thinning via a straining velocity field, while small-scale turbulence thickens flame fronts. The thickening process may depend on the relative importance of the effects of the large- and small-scale turbulence (de Goey *et al.* 2005). The curvature of flame fronts (Soika *et al.* 1998; Renou *et al.* 1998) and thermal expansion due to heat release are

also expected to have significant effects on the local turbulent velocity field and flame thickening/thinning processes. However, detailed physical mechanisms for flame thickening/thinning, and their relative importance have not been fully understood.

In this paper, we investigate the scalar gradient and the small-scale structure of turbulent premixed flames with emphasis on flame thickening/thinning. The Lagrangian equation for the evolution of the scalar gradient following an isoscalar surface is presented, which is useful in studying physical mechanisms for the scalar gradient evolution in propagating reaction front problems. The terms in the Lagrangian form of the scalar gradient equation are analyzed using DNS data for statistically 1-D planar flames with high intensity turbulence. Emphasized in this paper are the following: detailed mechanisms for flame thickening/thinning, the alignment of flame normal with turbulent strain, and the effects of heat release on these processes.

2. The equation for scalar gradients on isoscalar surfaces

In turbulent premixed flames, relatively thin reaction fronts propagate into turbulent medium, and the scalar gradient maintains itself due to the balance between diffusion and reactions. In this reaction front propagating problem, the Lagrangian-type equation is useful in studying the evolution of the local instantaneous reaction front structure. Of particular interest here is the time evolution of the scalar gradient following the flame surface.

The equation for a scalar ϕ can be written as

$$\frac{D\phi}{Dt} = (\mathbf{n} \cdot \mathbf{u}_\phi) |\nabla\phi| = \Omega_\phi, \quad (2.1)$$

where \mathbf{u}_ϕ is the velocity of the iso-surface relative to the fluid. $\frac{Dg}{Dt} = \frac{\partial g}{\partial t} + \mathbf{U} \cdot \nabla g$ is the Stokes derivative, where \mathbf{U} is the fluid velocity. The normal vector \mathbf{n} is defined as

$$\mathbf{n} = -\frac{\nabla\phi}{|\nabla\phi|}. \quad (2.2)$$

For a reacting scalar obeying Fickian diffusion, $\Omega_\phi = 1/\rho \nabla \cdot (\rho D \nabla\phi) + \omega_\phi$, where D is the molecular diffusivity, ω_ϕ is the chemical reaction rate, and ρ is the density. The displacement speed can be written as

$$u_\phi = \frac{1}{\rho |\nabla\phi|} [\nabla \cdot (\rho D \nabla\phi) + \omega_\phi]. \quad (2.3)$$

Taking the gradient of eqrefphieq and the inner product with $-\mathbf{n}$, we obtain

$$\frac{Dg}{Dt} = -\frac{1}{g} \nabla\phi \cdot \mathbf{S} \cdot \nabla\phi - \mathbf{n} \cdot \nabla\Omega_\phi, \quad (2.4)$$

where $|\nabla\phi| \equiv g$. \mathbf{S} is a strain rate tensor defined by $1/2(\nabla\mathbf{U} + \nabla\mathbf{U}^T)$. The equation for the evolution of g following the iso- ϕ surface can be written as

$$\frac{D_\phi g}{Dt} = -g \mathbf{n} \cdot \mathbf{S} \cdot \mathbf{n} - g \mathbf{n} \cdot \nabla u_\phi, \quad (2.5)$$

where $\frac{D_\phi g}{Dt} = \frac{\partial g}{\partial t} + (\mathbf{U} + \mathbf{u}_\phi) \cdot \nabla g$. This equation can be rewritten as

$$\rho \frac{D_\phi g}{Dt} = -\rho g \mathbf{n} \cdot \hat{\mathbf{S}} \cdot \mathbf{n} - [\rho g \nabla \cdot \mathbf{U} - g u_\phi \mathbf{n} \cdot \nabla \rho] - g \mathbf{n} \cdot \nabla \rho u_\phi, \quad (2.6)$$

where $\hat{\mathbf{S}} = \mathbf{S} - (\nabla \cdot \mathbf{U})\mathbf{I}$. \mathbf{I} is the identity matrix. From the continuity equation, we have

$$\frac{D_\phi \rho}{Dt} = -\rho \nabla \cdot \mathbf{U} + u_\phi \mathbf{n} \cdot \nabla \rho. \quad (2.7)$$

The equation for the normalized increase of the norm of the scalar gradient can therefore be written as

$$\frac{1}{g} \frac{D_\phi g}{Dt} = -\mathbf{n} \cdot \hat{\mathbf{S}} \cdot \mathbf{n} + \frac{1}{\rho} \frac{D_\phi \rho}{Dt} - \frac{1}{\rho} \mathbf{n} \cdot \nabla \rho u_\phi. \quad (2.8)$$

Note that each term on the right-hand side (r.h.s.) of the above equation vanishes in an unstretched laminar premixed flame. Decomposing the diffusion term in the displacement speed into the components normal and tangential to the isosurface, the displacement speed can be written as

$$u_\phi = -D\kappa + u_\phi^n, \quad (2.9)$$

where

$$u_\phi^n = \frac{1}{\rho |\nabla \phi|} \left[\frac{\partial}{\partial n} \left(\rho D \frac{\partial \phi}{\partial n} \right) + \rho \omega_\phi \right]. \quad (2.10)$$

$\kappa = \nabla \cdot \mathbf{n}$ is the mean curvature. κ is positive when an iso-scalar surface is convex toward the unburned side. n denotes the coordinate along the normal direction \mathbf{n} . With this decomposition, (2.8) can be rewritten as

$$\frac{1}{g} \frac{D_\phi g}{Dt} = -\mathbf{n} \cdot \hat{\mathbf{S}} \cdot \mathbf{n} + \frac{1}{\rho} \frac{D_\phi \rho}{Dt} - \frac{1}{\rho} \mathbf{n} \cdot [-\nabla(\rho D\kappa) + \nabla(\rho u_\phi^n)]. \quad (2.11)$$

By taking conditional averaging we obtain

$$\begin{aligned} \left\langle \frac{1}{g} \frac{D_\phi g}{Dt} \middle| \phi = \varphi \right\rangle &= \left\langle -\mathbf{n} \cdot \hat{\mathbf{S}} \cdot \mathbf{n} \middle| \phi = \varphi \right\rangle + \left\langle \frac{1}{\rho} \frac{D_\phi \rho}{Dt} \middle| \phi = \varphi \right\rangle \\ &\quad + \left\langle \frac{1}{\rho} \mathbf{n} \cdot \nabla(\rho D\kappa) \middle| \phi = \varphi \right\rangle - \left\langle \frac{1}{\rho} \mathbf{n} \cdot \nabla \rho u_\phi^n \middle| \phi = \varphi \right\rangle, \end{aligned} \quad (2.12)$$

where the angular brackets denote ensemble averaging conditioned on the quantity on the right side of the vertical bar.

It is worthwhile to review the physical meaning of the first term on the r.h.s. of (2.8). We have

$$\mathbf{n} \cdot \mathbf{S} \cdot \mathbf{n} = \mathbf{n} \cdot \nabla(\mathbf{U} \cdot \mathbf{n}) = \frac{\partial U_n}{\partial n}. \quad (2.13)$$

The first term on the r.h.s. of (2.8) is thus the dilatation on the tangential plane of an iso- ϕ surface, the so-called tangential strain rate:

$$-\mathbf{n} \cdot \hat{\mathbf{S}} \cdot \mathbf{n} = \nabla_T \cdot \mathbf{U}_T, \quad (2.14)$$

where ∇_T and \mathbf{U}_T are the gradient operator and the velocity projected on the tangential plane, respectively. This represents the increase of surface area due to turbulent stretching (Chung & Law 1986; Candel & Poinsot 1990). For non-reacting scalar mixing in incompressible flows, the scalar gradient is aligned with the most compressive strain. Then, the average tangential strain is positive, and the area of a non-propagating surface increases (Batchelor 1954; Cocke 1963). For a propagating surface, the evolution of the surface area is also influenced by the curvature of the surface (Pope 1988; Chung & Law 1986; Candel & Poinsot 1990). The alignment characteristics are represented by the eigen-decomposition of the rate-of-strain tensor \mathbf{S} . Using the eigen-decomposition, the

tangential strain rate can be written as

$$-\mathbf{n} \cdot \hat{\mathbf{S}} \cdot \mathbf{n} = -[(\alpha_1 - \Delta)\psi_1^2 + (\alpha_2 - \Delta)\psi_2^2 + (\alpha_3 - \Delta)\psi_3^2]. \quad (2.15)$$

α_i is the eigenvalue of the strain rate tensor \mathbf{S} , which satisfies $\alpha_1 \geq \alpha_2 \geq \alpha_3$ and $\alpha_1 + \alpha_2 + \alpha_3 = \Delta$. $\psi_i = \mathbf{n} \cdot \mathbf{e}_i$, where \mathbf{e}_i is the eigenvector corresponding to α_i . The eigenvectors of $\hat{\mathbf{S}}$ are the same as those of \mathbf{S} . Hereafter, the tangential strain rate term is denoted by T_{ts} .

The second term on the r.h.s. of (2.8) represents the effects of the time evolution of the density along the trajectory of the iso-surface. In flames with unity Lewis number, this term represents compressibility effects and thus is negligible for low Mach number flows. This term also represents the effects of differential diffusion. In flames with non-unity Lewis number, the iso-surface of the progress variable can propagate with different speed from that of the density, even for the low Mach number limit. Hereafter, this term is denoted by T_ρ .

The last term of (2.8) represents the effects of variations of the mass flux along the normal to the iso-surfaces. In stationary laminar flames, we obtain

$$0 = -\mathbf{n} \cdot \hat{\mathbf{S}} \cdot \mathbf{n} - \frac{1}{\rho} \mathbf{n} \cdot \nabla \rho u_\phi. \quad (2.16)$$

This means that the mass flux through an isosurface varies in a straining velocity field. The variation can be estimated as

$$\frac{|\delta(\rho u_\phi)|}{\rho_u s_L} \sim \frac{l_F}{s_L} \frac{\rho |\hat{\mathbf{S}}|}{\rho_u} \sim \text{Ka}, \quad (2.17)$$

where Ka is the Karlovitz number (Peters 2000), ρ_u is the density of the unburned gas, and s_L is the laminar flame speed. In the laminar flamelet regime with $\text{Ka} \ll 1$, the variation will be negligible. In a highly strained flame with high Ka, the variation of the mass flux can be significant. In turbulent flames with moderate and low Da, e.g., those in the thin reaction zone regime, the small-scale wrinkling of flame fronts is significant such that the radius of curvature is of the order of thickness of an unstretched laminar flame. In that case, the radius of curvature can have significant variations for different iso-surfaces, which results in variations of the propagation speed. The curvature variation term, the third term on the r.h.s. of (2.11), emphasizes the role of the small-scale turbulence in turbulent mixing and flame thickening. The term involving u_ϕ^n represents the tendency to return to the unstretched laminar flame structure. Hereafter, the term involving κ and that involving u_ϕ^n are referred as the curvature variation term T_κ and the normal mass flux variation term T_n , respectively.

3. Direct numerical simulations

The compressible Navier-Stokes equations are solved:

$$\frac{\partial \rho}{\partial t} + \frac{\partial \rho u_j}{\partial x_j} = 0 \quad (3.1)$$

$$\frac{\partial \rho u_i}{\partial t} + \frac{\partial}{\partial x_j} (\rho u_i u_j) = -\frac{\partial p}{\partial x_i} + \frac{\partial \tau_{ij}}{\partial x_j} + \rho f_i \quad (3.2)$$

$$\frac{\partial \rho e}{\partial t} + \frac{\partial}{\partial x_j} [(\rho e + p) u_j] = \frac{\partial u_j \tau_{ij}}{\partial x_i} + \frac{\partial}{\partial x_j} \left(\lambda \frac{\partial T}{\partial x_j} \right) + \rho Q \omega_\phi \quad (3.3)$$

	u'/s_L	l/l_F	Da	Ka	Re_λ
PF1	13.8	3.9	0.28	14	95
PF2	19.5	2.75	0.14	28	95

TABLE 1. Characteristics of the simulated premixed flames (u' : r.m.s. initial turbulent velocity, l : initial integral length scale, S_L : laminar flame speed, l_F : flame thickness based on the maximum temperature gradient, $Da = S_L/(u'l_F)$, $Ka = D_u^2/(S_L l_K)^2$, l_K : Kolmogorov length scale, D_u : unburned mixture diffusivity, Re_λ : Reynolds number based on the Taylor scale).

$$\frac{\partial \rho \phi}{\partial t} + \frac{\partial}{\partial x_j} (\rho u_j \phi) = \frac{\partial}{\partial x_j} (\rho D \frac{\partial \phi}{\partial x_j}) + \rho \omega_\phi, \quad (3.4)$$

where

$$\rho e = \frac{1}{2} \rho u_j u_j + \frac{p}{\gamma - 1} \quad (3.5)$$

$$\tau_{ij} = \mu \left(\frac{\partial u_i}{\partial x_j} + \frac{\partial u_j}{\partial x_i} - \frac{2}{3} \delta_{ij} \frac{\partial u_k}{\partial x_k} \right). \quad (3.6)$$

p is pressure, e is the total internal energy, ω_ϕ is the chemical reaction rate of the scalar ϕ , Q is a heat release parameter. The thermal conductivity λ and the diffusion coefficient D are given as

$$\lambda = \mu c_p / Pr \text{ and } D = \mu / (\rho Sc), \quad (3.7)$$

where c_p is the specific heat at constant pressure. The dynamic viscosity μ is given as

$$\mu = \mu_u (T/T_u)^{0.7}. \quad (3.8)$$

The Prandtl number Pr and the Schmidt number Sc are set to 0.7. The gas mixture is assumed to be a perfect gas with a specific heat ratio of $\gamma=1.4$. The Mach number based on the root mean square (r.m.s.) velocity fluctuations is below 0.1 for all the cases studied here. The equations are integrated using a low-storage fourth-order Runge-Kutta method with a sixth order compact finite difference scheme for spatial discretization (Kennedy *et al.* 2000; Lele 1992).

The simulated flames are statistically 1-D premixed flames propagating in decaying homogeneous turbulence. The reaction rate is given by

$$\omega_{Y_R} = A Y_R \exp \left(-\frac{T_a}{T} \right), \quad (3.9)$$

where Y_R is the mass fraction of the deficient species in the reactant. The activation temperature T_a is set to be $4T_b$, where T_b is the burned gas temperature. The heat release parameter Q is chosen such that the density ratio between unburned and burned gas, γ , is equal to 6. The reaction progress variable is defined here as $C = 1 - Y_R/Y_{R,u}$, where the subscript u denotes the unburned side.

A non-reflecting boundary condition is used for the x_1 direction, while the x_2 and x_3 directions are periodic (Poinsot & Lele 1992). The equations are solved on $512 \times 256 \times 256$ grid points. Initial turbulence is homogeneous and isotropic. The characteristics of the premixed flames are shown in Table 1. The initial turbulence intensity u'/s_L is larger than 10, while the length scale ratio l/l_F is approximately 3–4. The laminar flame thickness l_F is based on the maximum temperature gradient. The initial Da for the cases PF1 and PF2 are 0.14 and 0.28, respectively.

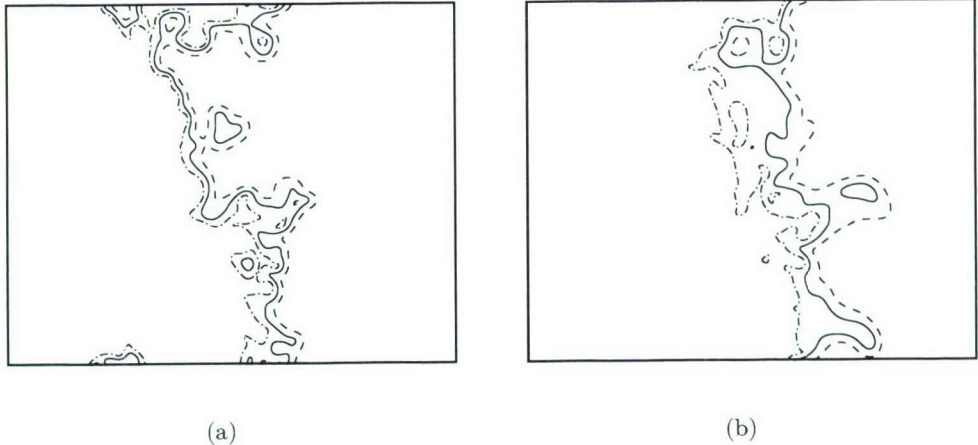


FIGURE 1. Instantaneous fields of the reaction progress variable C for (a) PF1 and (b) PF2 (dashed dotted line: $C = 0.1$, solid line: $C = 0.5$, dashed line: $C = 0.9$).

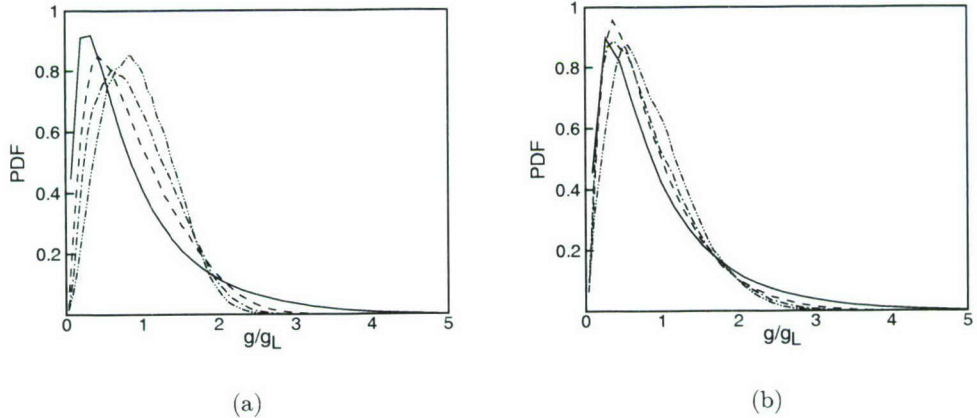


FIGURE 2. PDFs of the normalized scalar gradient conditioned on $C = \zeta$ for (a) PF1 and (b) PF2 (solid line: $\zeta = 0.03$, dashed line: $\zeta = 0.08$, dashed dotted line: $\zeta = 0.13$, dashed dotted line: $\zeta = 0.18$).

4. Results and discussion

4.1. Characteristics of flame and scalar gradient field

Figure 1 shows the instantaneous C -field for PF1 and PF2 at $\tau \approx 4.5$, where τ is the time normalized by the initial eddy turnover time l/u' . There is significant small-scale wrinkling as well as large-scale wrinkling for both cases. In the region with large curvature, where the small-scale turbulence is intense, the preheat zone is thickened. Variations of the curvature along the flame normal are also evident near this region. For PF2, flame thickening is more evident while, in some regions, thin flame fronts are also observed.

Figure 2(a) shows the conditional probability density function (PDF) of different nor-

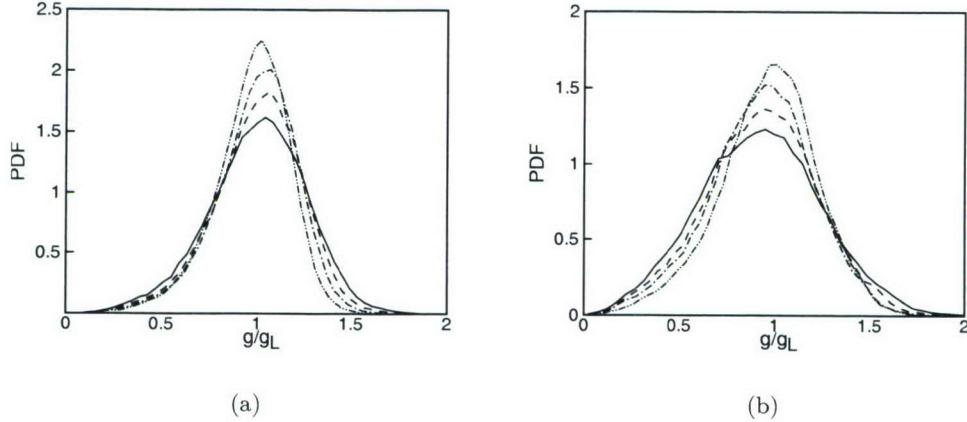


FIGURE 3. PDFs of the normalized scalar gradient conditioned on $C = \zeta$ for (a) PF1 and (b) PF2 (solid line: $\zeta = 0.43$, dashed line: $\zeta = 0.48$, dashed dotted line: $\zeta = 0.53$, dashed dotted line: $\zeta = 0.58$).

malized scalar gradients for $C < 0.2$ for PF1. For low values of C , the PDF is skewed with the peak at $g/g_L < 1$. While the preheat zone is thickened on average, the local scalar gradient can be significantly higher than the corresponding laminar flame value g_L . The conditional PDF for PF2 is shown in Fig. 2(b). For the lower Da case, the shift of the peak of PDF toward the higher g/g_L occurs more slowly with increasing C , which indicates that the flame is more broadened at these values, and has a wider distribution than that for PF1. The conditional PDFs for $0.45 < C < 0.65$ are shown in Fig. 3. For $0.45 < C < 0.65$, the PDF peaks around $g/g_L \sim 1$. The variance of the PDF becomes smaller as C increases. The conditional average of g is similar to the corresponding laminar value g_L .

4.2. Balance of terms in the scalar gradient equation

The terms in the scalar gradient equation are evaluated and shown in Fig. 4. The terms are averaged over the whole domain with the condition that $C = \zeta$, where ζ is the sample space variable of C . The balance of the terms for PF1 at $\tau \approx 2.5$ are shown in Fig. 4(a). On average, the local flame fronts are being thickened in the preheat zone. The conditional average of the normalized Lagrangian time derivative of g , $\langle 1/gDg/Dt|_\phi|\zeta \rangle$, is almost zero for $C > 0.5$, which indicates that there is no significant variation of the average flame thickness in the reaction zone. For PF1, there is a significant change in flame thickening processes in the preheat zone and the reaction zone. The balance of the terms for PF2 at $\tau \approx 2.5$ are shown in Fig. 4(b). For the lower Da case, the reaction zone as well as the preheat zone are being thickened. The conditional average $\langle 1/gD_\phi g/Dt|\zeta \rangle$ shows almost linear dependence on ζ , which indicates decreasing strength of the thickening processes with increasing ζ . The balance of the terms at a later time $\tau \approx 4.5$ for PF1 is shown in Fig. 4(c). The dependence of the average time derivative of g on ζ is qualitatively the same as that in Fig. 4(b), but the magnitude of each term is decreased due to decaying turbulence. As shown in Fig. 4(d), for PF2, the strength of the thickening process in the reaction zone is reduced more rapidly than that in the preheat zone. The terms on the r.h.s. of (2.11) show the same qualitative behavior for all plots shown in Fig. 4. The

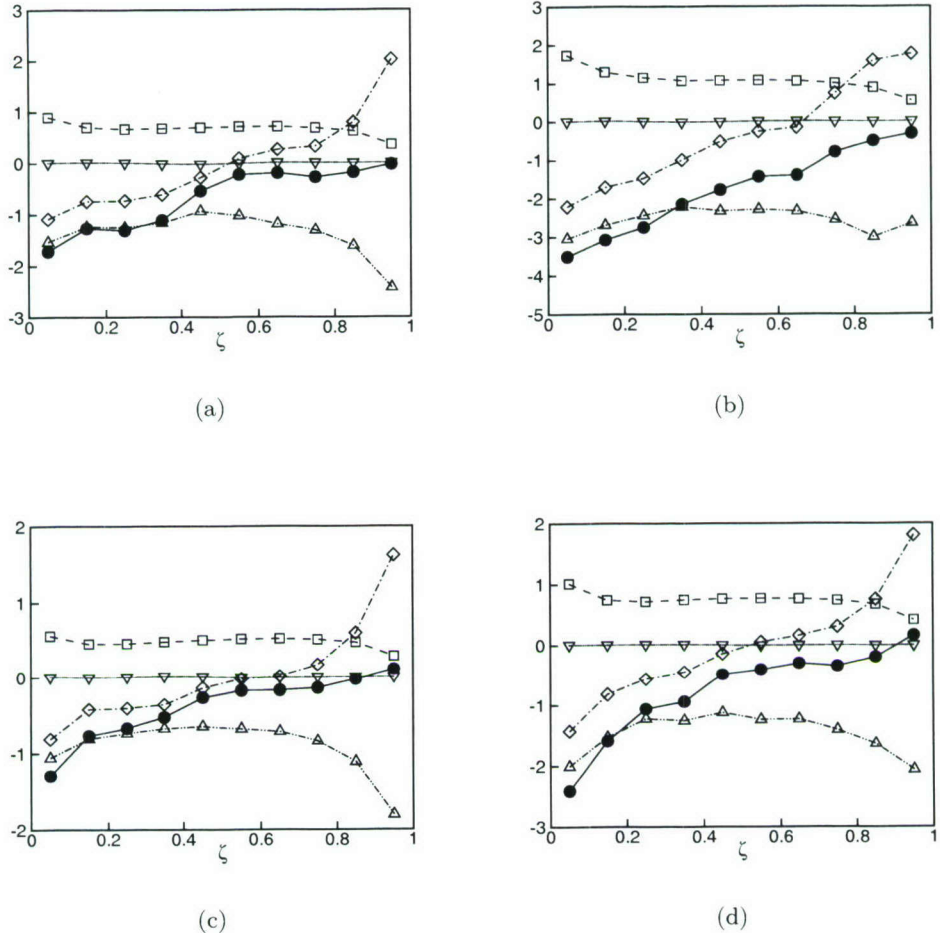


FIGURE 4. Balance of terms for (a) PF1 at $\tau = 2.5$, (b) PF1 at $\tau \approx 4.5$, (c) PF2 at $\tau \approx 2.5$ and (d) PF1 at $\tau \approx 4.5$ (squares: tangential strain rate term $\langle T_{ts} | \zeta \rangle$, upside down triangles: Lagrangian time derivative of the density $\langle T_{\rho} | \zeta \rangle$, diamonds: normal mass flux variation term $\langle T_n | \zeta \rangle$, triangles: curvature variation term $\langle T_{\kappa} | \zeta \rangle$, filled circles: $\langle 1/gD_{\phi}g/Dt | \zeta \rangle$; terms are normalized by the flame time scale t_F).

tangential strain rate term T_{ts} , which represents the turbulent stretching of the isoscalar surface, is a primary source of the scalar gradient generation. The curvature variations tend to thicken the flame fronts throughout. The major sink term in the scalar gradient equation is the curvature variation term T_{κ} in Fig. 4. The density variation term T_{ρ} is negligible in the present unity Lewis number flames. In the preheat zone, T_{ts} is balanced primarily with the normal mass flux variation term T_n , and the average time derivative $\langle 1/gD_{\phi}g/Dt | \zeta \rangle$ is almost equal to the curvature variation term T_{κ} . On the other hand, for $0.5 < C < 0.8$ with significant reaction rates, T_n does not contribute to flame thickening in the present flames. $\langle T_n | \zeta \rangle$ increases with ζ , and is balanced primarily with $\langle T_{\kappa} | \zeta \rangle$ for $\zeta \approx 1$.

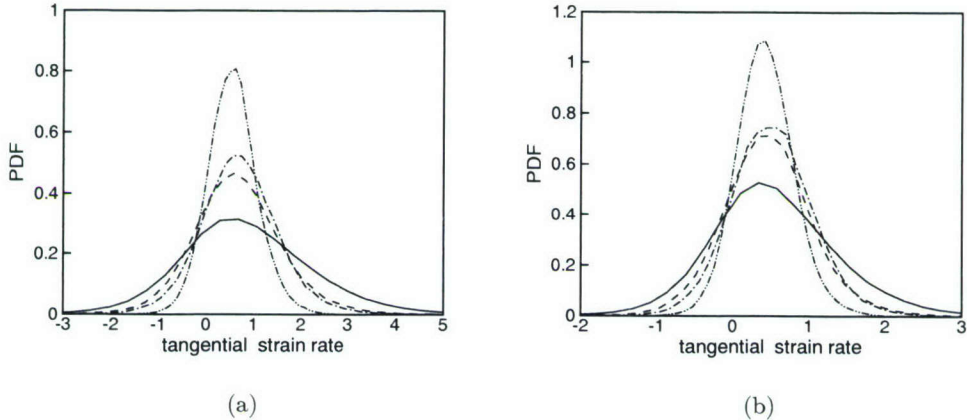


FIGURE 5. PDFs of the tangential strain rate term T_{ts} conditioned on $C = \zeta$ at (a) $\tau \approx 2.5$ and (b) $\tau \approx 4.5$ (solid line: $\zeta = 0.03$, dashed line: $\zeta = 0.28$, dashed dotted line: $\zeta = 0.53$, dashed dotted dotted line: $\zeta = 0.93$; PF1).

4.3. Tangential strain rate term and alignment characteristics

Figure 5(a) shows the PDFs of the tangential strain rate term T_{ts} conditioned on $C = \zeta$ for PF1 at $\tau \approx 2.5$. The PDF is close to Gaussian with the peak at the positive value. As shown in Fig. 4, the conditional average $\langle T_{ts} | \zeta \rangle$ is positive for the whole range of ζ . This is consistent with the conjecture of Batchelor (1952). The positivity of the average stretching rate has been rigorously proven in an incompressible and isotropic field (Cocke 1969). Note that the variance becomes smaller with increasing ζ . This suggests the intensity of the small-scale turbulence becomes weaker when going to the burned side, as expected. The PDFs of T_{ts} at a later time $\tau \approx 4.5$ are shown in Fig. 5(b). While the level of the variance is reduced, the decreasing rate of the variance with ζ is similar to that at $\tau \approx 2.5$.

Figure 6 shows the joint PDF of the curvature κ and the tangential strain rate term T_{ts} for PF1 at $\tau \approx 4.5$. For the ensemble with $0.4 < C < 0.8$, T_{ts} has a negative correlation with the κ . The negative correlation has been observed previously in DNS (Chakraborty & Cant 2005) and in experiments (Soika *et al.* 1998). The correlation for the ensemble with $0.05 < C < 0.15$ is much weaker than that with $0.4 < C < 0.8$.

The correlation of the tangential strain rate and the curvature can be explained by the following decomposition of the tangential strain rate:

$$T_{ts} = -\mathbf{n} \cdot \check{\mathbf{S}} \cdot \mathbf{n} + \frac{2}{3} \Delta \mathbf{I}, \quad (4.1)$$

where

$$\check{\mathbf{S}} = \mathbf{S} - \frac{1}{3} \Delta \mathbf{I}. \quad (4.2)$$

In the first term on the r.h.s. of (4.1), the first-order effects of the dilatation is removed in the sense that the trace of the tensor $\check{\mathbf{S}}$ vanishes. The joint PDF of the curvature κ and the dilatation Δ is shown in Fig. 7. The dilatation shows a strong negative correlation with the curvature for the ensemble with $0.4 < C < 0.8$ in Fig. 7(b). The correlation becomes weaker for low values of C in Fig. 7(a). For the ensemble with $0.4 < C < 0.8$,

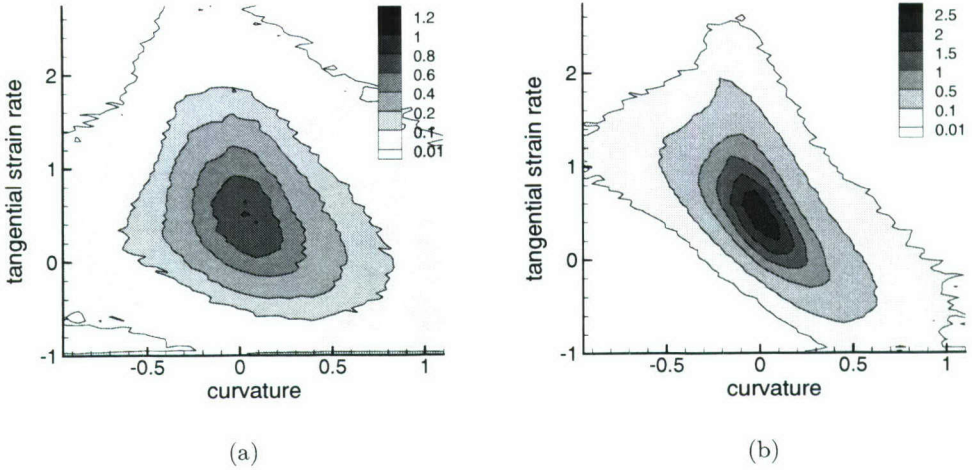


FIGURE 6. The joint PDFs of the curvature and the tangential strain rate term for (a) the ensemble with $0.05 < C < 0.15$ and (b) the ensemble with $0.4 < C < 0.8$ (PF1, $\tau \approx 4.5$).

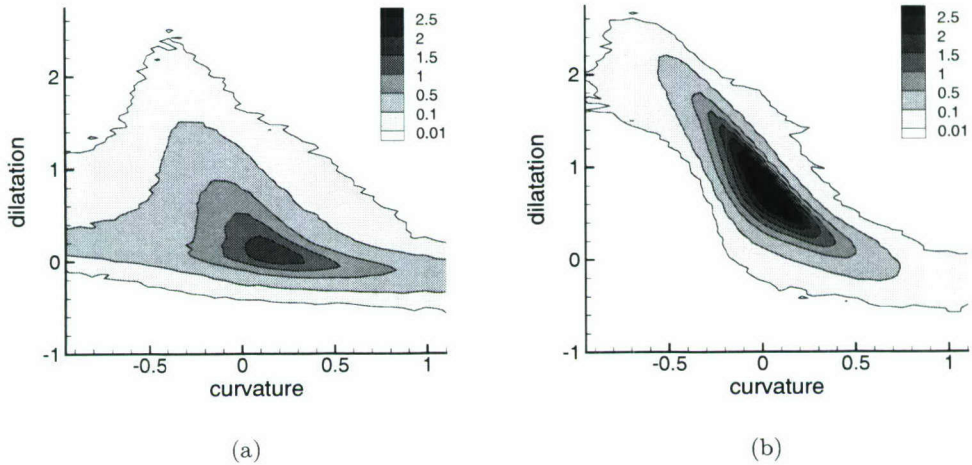


FIGURE 7. The joint PDFs of the curvature and the tangential strain rate term for (a) the ensemble with $0.05 < C < 0.15$ and (b) the ensemble with $0.4 < C < 0.8$ (PF1, $\tau \approx 4.5$).

the slope of the conditional dilatation as a function of the curvature is steeper than that of the tangential strain rate by a factor of approximately 1.5, as indicated in (4.1). The conditional dilatation is known to be important in the structure of turbulent premixed flames (Swaminathan *et al.* 1997). In a flame with unity Lewis number and low Mach

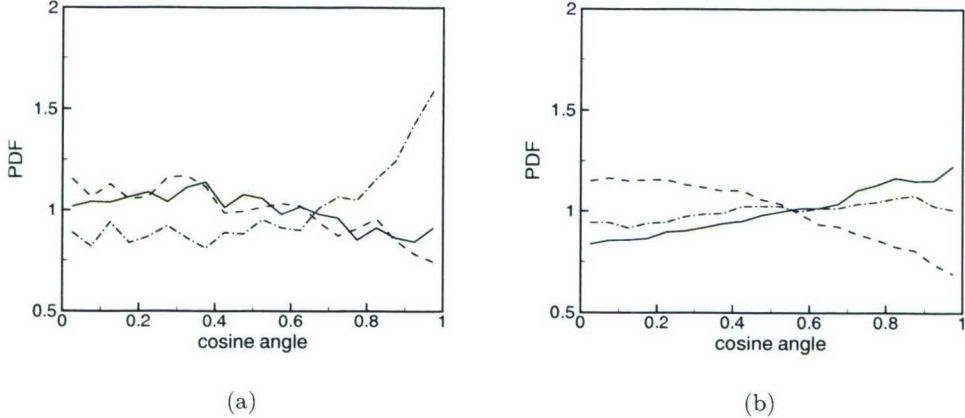


FIGURE 8. PDFs of the cosine angle, ψ_i , between the flame normal \mathbf{n} and the principal axis of the strain tensor, conditioned on (a) $\kappa = -0.5$ and (b) $\kappa = 0$, for the ensemble with $0.4 < C < 0.8$ (dashed dotted line: ψ_1 , dashed line: ψ_2 , solid line: ψ_3 ; PF1; $\tau \approx 4.5$).

number, the dilatation can be written as

$$\Delta = \frac{\beta}{\rho_u} (\nabla \cdot \rho D \nabla C + \rho \omega_C) = \beta g \frac{\rho u_C}{\rho_u} = \beta g \frac{1}{\rho_u} (\rho u_C^n - \rho D \kappa), \quad (4.3)$$

where $\beta = (T_b - T_u)/T_u$. (4.3) shows that the dilatation is closely related to the propagation property of the flame front. The dependence of the tangential strain rate on the curvature is mainly determined by the curvature dependence of the displacement speed, while the correlation with the scalar gradient can be of significance. As in the above equation, the displacement speed u_C has a negative correlation with the curvature κ .

In Figs. 6 and 7, the tangential strain rate is more scattered than the dilatation especially for the negative curvature, and the conditional average $\langle T_{ts} | \zeta \rangle$ is lower than $\langle \Delta | \zeta \rangle$ for large $|\kappa|$. These can be explained by investigating the alignment characteristics of the flame normal \mathbf{n} with the principal axis of the strain. Figure 8 shows the PDF of the cosine angle, ψ_i , between the iso-surface normal vector \mathbf{n} and the eigenvector of the strain rate tensor \mathbf{e}_i , conditioned on the curvature κ . PDF is evaluated for the ensemble with $0.4 < C < 0.8$. For $\kappa = -0.5$, which is normalized by s_L/D_u , the normal vector \mathbf{n} is more aligned with the most extensive strain. Considering that the eigenvectors of $\tilde{\mathbf{S}}$ are the same as those of \mathbf{S} and that the trace of $\tilde{\mathbf{S}}$ is equal to zero, the term, $-\mathbf{n} \cdot \tilde{\mathbf{S}} \cdot \mathbf{n}$, becomes negative, and therefore contributes in the opposite direction to the dilatation term. Turbulent fluctuations of this term are responsible for the weaker correlation between T_{ts} and κ . In Fig. 8, \mathbf{n} has no evident preferential alignment for very low values of $|\kappa|$, while the PDF for ψ_3 is slightly higher than those for ψ_2 and ψ_3 near $\psi_i = 1$. Overall, the term $-\mathbf{n} \cdot \tilde{\mathbf{S}} \cdot \mathbf{n}$ tends to reduce the scalar gradient for large $|\kappa|$ in the present flame.

To further investigate the alignment characteristics, the PDFs of ψ_i conditioned on $C = \zeta$ are shown in Fig. 9. For low and high values of ζ , the scalar gradient is more aligned with the most compressive strain, but the degree of the alignment is not as strong as in conserved scalar mixing (Ashurst *et al.* 1987). No preferential alignment of the scalar gradient is observed in the middle of the flame front, while the PDF of ψ_i is

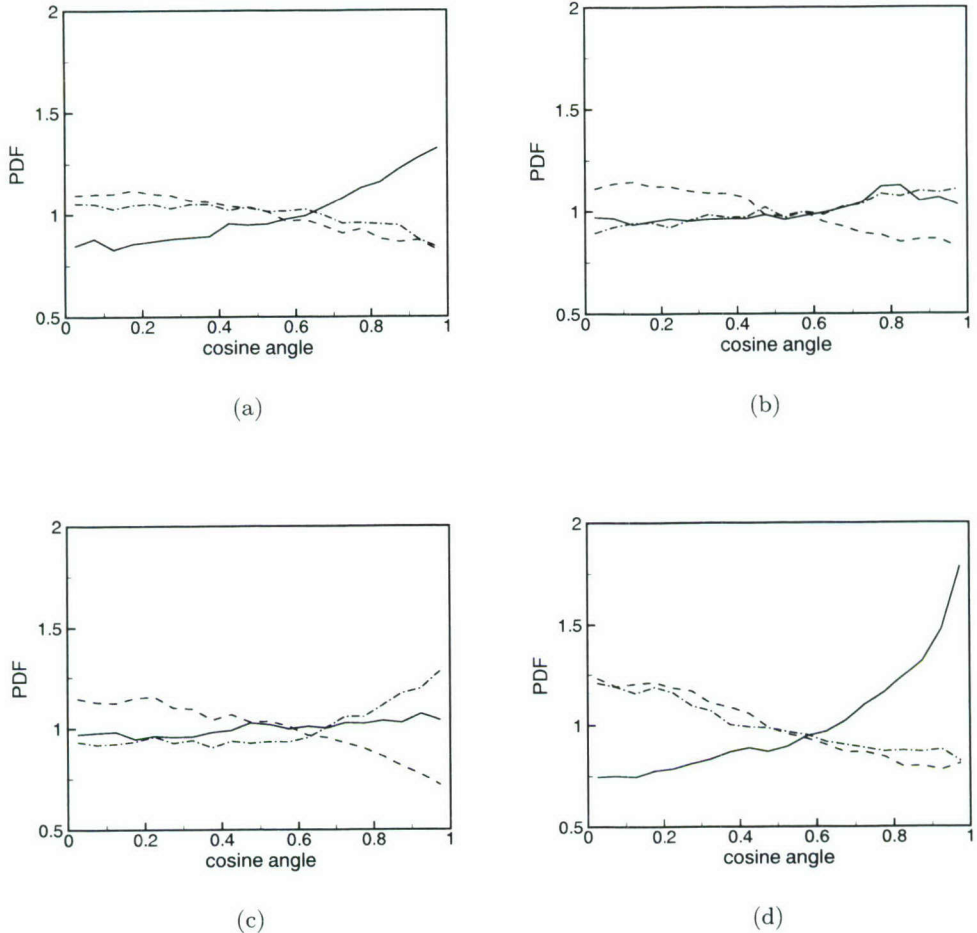


FIGURE 9. Alignment characteristics on iso-scalar surfaces with (a) $C = 0.05$, (b) $C = 0.25$, (c) $C = 0.55$, and (d) $C = 0.95$ (dashed dotted line: ψ_1 , dashed line: ψ_2 , solid line: ψ_3 ; PF1; $\tau \approx 4.5$).

slightly higher than others in Fig. 9(c). For $\zeta = 0.6$, the dilatational velocity induced by the heat release is largest.

As shown in Figs. 8 and 9, the alignment characteristics in premixed flames are significantly different from those in non-reacting flows, due to the heat release effects and the different origin of the generation mechanism of the scalar gradient. In their study of the alignment characteristics in turbulent premixed flames with high Da, Swaminathan & Grout (2006) found that the scalar gradient in high Da premixed flames aligns with the most extensive strain in contrast to non-reacting scalars. This is because in high Da flames the velocity field induced by heat release is dominant over the turbulent velocity field. The dilatational velocity is mostly in the flame normal direction in high Da flames. In non-reacting flows, the preferential alignment of the scalar gradient with the most compressive strain has been reported (Ashurst *et al.* 1987; Warhaft 2000). The present

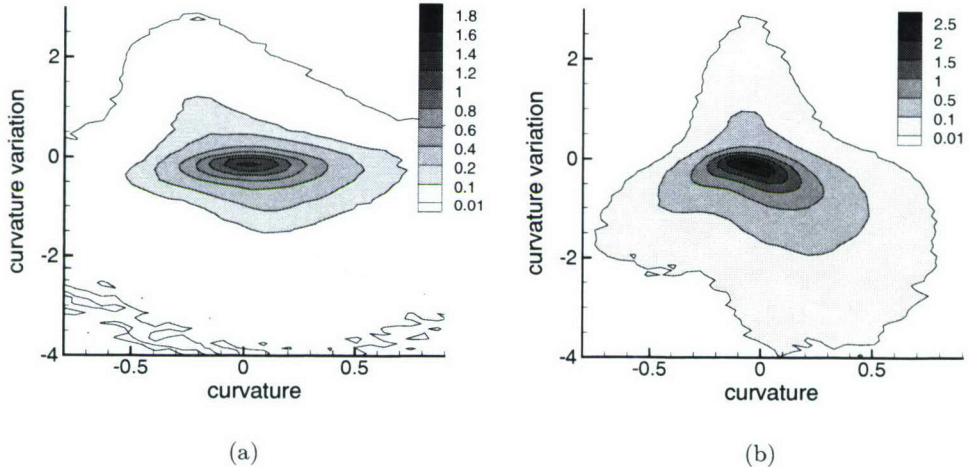


FIGURE 10. The joint PDFs of the curvature and the curvature variation term for (a) the ensemble with $0.05 < C < 0.15$ and (b) the ensemble with $0.4 < C < 0.8$ (PF1, $\tau \approx 4.5$).

results show that the alignment of the scalar gradient with the most extensive strain rate becomes less evident with decreasing Da. Alignment characteristics are determined by the relative importance of the dilatation and the turbulence. Since the dilatation is of the order of β/τ_c , where τ_c is the chemical time scale, and the strain rate is of the order of the small-scale turbulent time scales, the relative importance of the dilatation can be estimated by the parameter β/Ka . The dependence of the alignment characteristics on ζ is primarily due to that of the dilatation on ζ . In addition, due to the correlation between the dilatation and the curvature, the alignment characteristics in premixed flames show stronger dependence on the curvature than in non-reacting scalars.

The dependence of the tangential strain rate on the curvature is a direct consequence of the heat release effects in premixed flames. The relationship between the dilatation and the displacement speed is primarily responsible for this dependency. In reaction front propagation with no heat release, such dependence of the tangential strain rate on the curvature will not be observed. It is expected that, in the front with no heat release, the tangential strain rate has a maximum near $\kappa = 0$ and decreases with increasing $|\kappa|$.

4.4. Effects of the tangential strain rate and the curvature on the mass flux variation term

Figure 10 shows the joint PDF of the curvature κ and the curvature variation term T_κ for PF1. T_κ has a negative correlation with the $|\kappa|$ for the ensemble with $0.4 < C < 0.8$. This implies that smaller-scale wrinkling is more responsible for flame thickening. T_κ always has a negative value when $|\kappa|$ is large. For low values of $|\kappa|$, T_κ can be positive, while it is much more probable for T_κ to be negative. For large $|\kappa|$, the wrinkling is of the order of the flame thickness and significant variations of the curvature across flame fronts occur. T_κ then plays a key role in the thickening of flame fronts. Significant scattering in the joint PDF means the importance of small-scale turbulence that can locally make high curvature and associated curvature variation near the iso-surface with small curvature. As shown in Fig. 11(b), T_κ has essentially no correlation with the curvature for the

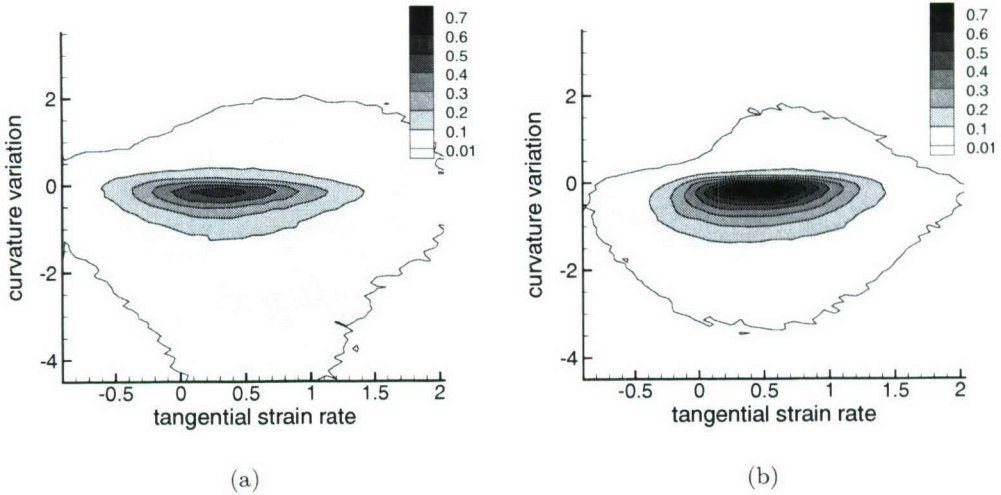


FIGURE 11. The joint PDFs of the tangential strain rate and the curvature variation term for (a) the ensemble with $0.05 < C < 0.15$ and (b) the ensemble with $0.4 < C < 0.8$ (PF1, $\tau \approx 4.5$).

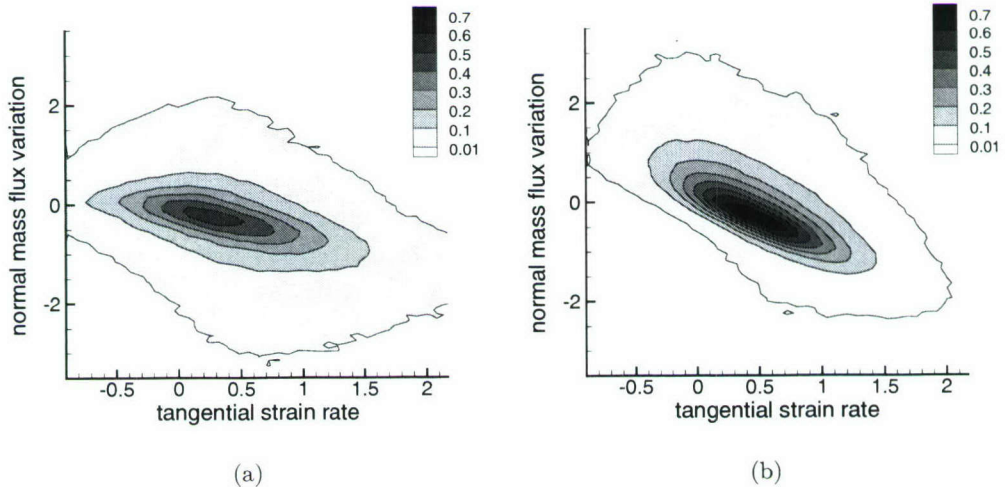


FIGURE 12. The joint PDFs of the tangential strain rate and the normal mass flux variation term for (a) the ensemble with $0.05 < C < 0.15$ and (b) the ensemble with $0.4 < C < 0.8$ (PF1, $\tau \approx 4.5$).

ensemble with $0.5 < C < 0.15$. The response of the reaction fronts to wrinkling is different for different iso-surfaces, while the curvature variations contribute to reduce the scalar gradient for all ranges of C . The curvature variation term has no correlation with the tangential strain rate term in Fig. 11.

Figure 12 shows the joint PDF of the tangential strain rate term T_{ts} and the normal mass flux variation term T_n for PF1. T_n has a negative correlation with T_{ts} for both

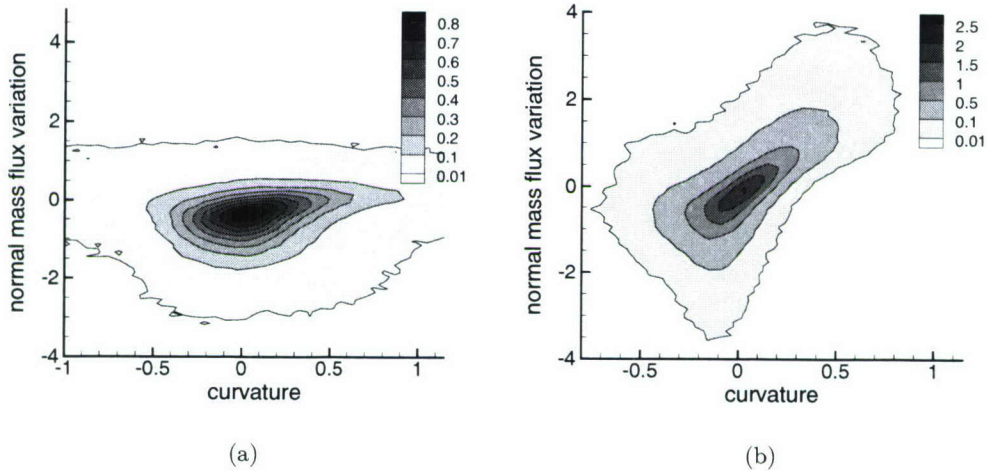


FIGURE 13. The joint PDFs of the curvature and the normal mass flux variation term for (a) the ensemble with $0.05 < C < 0.15$ and (b) the ensemble with $0.4 < C < 0.8$ (PF1, $\tau \approx 4.5$).

ensemble with $0.05 < C < 0.15$ and that with $0.4 < C < 0.8$. This correlation is determined by the response of the unstretched flame to the straining velocity field. For the preheat zone with no reaction, the normal mass flux term has the contribution only from diffusion normal to the iso-surface, and the positive tangential strain rate enhances the normal diffusion, which reduces the scalar gradient. The same argument applies to the reaction zone, since the reaction rate on an iso-surface does not change for unity Lewis number. In Fig. 12(b), T_κ has a negative correlation with the tangential strain rate. This can be explained by (2.16).

Figure 13 shows the joint PDF of the curvature κ and the normal mass flux variation term T_n . For the ensemble with $0.4 < C < 0.8$, T_n has a positive correlation with the κ , but the correlation is weaker than that between the tangential strain rate T_{ts} and the normal mass flux T_n . This correlation does not indicate the direct influence of κ on the normal mass flux variations, but comes from the correlation between κ and T_{ts} . The correlation between κ and T_n for the ensemble with $0.4 < C < 0.8$ is weaker than that with $0.4 < C < 0.8$.

5. Conclusion

The scalar gradient and the small-scale structure of turbulent premixed flames with high turbulence intensity are investigated using DNS data for statistically 1-D planar flames. The evolution equation for the scalar gradient following an iso-scalar surface is presented. In the Lagrangian form of the scalar gradient equation, which is useful in propagating reaction front problems, the evolution of the scalar gradient on an iso-scalar surface is governed by the tangential strain rate, the Lagrangian time derivative of the density, and the mass flux variations along the normal to the iso-scalar surface. The mass flux variation term is decomposed into the normal and the tangential components to investigate the effects of the curvature.

The major sink term in the scalar gradient equation is shown to be the curvature

variation term, while the tangential strain rate term is a major source term. In the preheat zone, the average of the tangential strain rate term conditioned on the progress variable is balanced with that of the normal mass flux variation term, and the conditional average Lagrangian time derivative of the scalar gradient is approximately equal to the conditional average curvature variation term. In the reaction zone, the curvature variation term is primarily balanced with the tangential strain rate term. It is observed that the thickening process in the reaction zone is much weaker than that in the preheat zone. In one of our simulated flames, a sudden drop of the strength of flame thickening in the reaction zone was observed.

The statistics of each term in the scalar gradient equation are investigated. The tangential strain rate and the curvature are found to have a negative correlation. It is shown that the negative correlation is due to the relation between the dilatation and the displacement speed of an iso-scalar surface. This implies that the heat release effects are of significant importance in the evolution of the scalar gradient in premixed flames. The dependence of the dilatation on the curvature is also shown to affect the alignment characteristics of the flame normal with the principal axis of the strain. The curvature variation term is found to have a negative correlation with the magnitude of the curvature, which suggests that smaller-scale wrinkling is more responsible for flame thickening.

REFERENCES

ASHURST, W. M. T., KERSTEIN, A. R., KERR, R. M. & GIBSON, C. H. 1987 Alignment of vorticity and scalar gradient with strain rate in simulated Navier-Stokes turbulence. *Phys. Fluids* **30**, 2343–2353.

BATCHELOR, G. K. 1952 The effect of homogeneous turbulence on material lines and surfaces. *Proc. Royal Soc. London* **A213**, 349–366.

BRETHOUWER, G., HUNT, J. C. R. & NIEUWSTADT, F. T. M. 2003 Micro-structure and Lagrangian statistics of the scalar field with a mean gradient in isotropic turbulence. *J. Fluid Mech.* **474**, 193–225.

CANDEL, S. M. & POINSOT, T. J. 1990 Flame stretch and the balance equation for flame area. *Combust. Sci. Tech.* **70**, 1–15.

CHEN, Y. C. & MANSOUR, M. S. 1998 Investigation of flame broadening in turbulent premixed flames in the thin-reaction-zones regime. *Proc. Combust. Inst.* **28**, 811–818.

CHAKRABORTY, N. & CANT, R. S. 2005 Effects of strain rate and curvature on surface density function transport in turbulent premixed flames in the thin reaction zone regime. *Phys. Fluids* **17**, 065108.

CHUNG, S. H. & LAW, C. K. 1984 An invariant derivation of flame stretch. *Comb. Flame* **55**, 123–125.

COCKE, W. J. 1969 Turbulent hydrodynamic line stretching: consequences of isotropy. *Phys. Fluids* **12**, 2488–2492.

DAMKÖHLER, G. 1940 Der einfluß der Turbulenz auf die Flammengeschwindigkeit in Gasgemischen. *Z. Electrochem* **46**, 601–652.

DE GOEY, L. P. H., PLESSING, T., HERRMANN, R. T. E. & PETERS, N. 2005 Analysis of the flame thickness of turbulent flamelets in the thin reaction zones regime. *Proc. Combust. Inst.* **30**, 859–866.

GIBSON, C. H. 1968 Fine structure of scalar fields mixed by turbulence. I. Zero-gradient points and minimal gradient surfaces. *Phys. Fluids* **11**, 2305–2315.

KENNEDY, C. A., CARPENTER, M. H. & LEWIS, R. M. 2000 Low-storage, explicit Runge-Kutta schemes for the compressible Navier-Stokes equations. *Appl. Nume. Math.* **35**, 177–219.

LAW, C. K., SUNG, C. J., YU, G. & AXELBAUM, R. L. 1994 On the structural sensitivity of purely strained planar premixed flames to strain rate variations. *Comb. Flame* **98**, 139–154.

LELE, S. K. 1992 Compact finite difference schemes with spectral-like resolution. *J. Comp. Phys.* **103**, 16–42.

O'YOUNG, F & BILGER, R. W. 1997 Scalar gradient and related quantities in turbulent premixed flames. *Comb. Flame* **109**, 682–700.

PETERS, N., TERHOEVEN, P., CHEN, J. H. & ECHEKKI, T. 1998 Statistics of flame displacement speeds from 2D unsteady methane-air flames. *Proc. Combust. Inst.* **28** 833–839.

PETERS, N. 2000 *Turbulent Combustion*, Cambridge University Press.

POINSOT, T. J. AND LELE, S. K. 1992 Boundary conditions for direct numerical simulations of compressible viscous flows. *J. Comp. Phys.* **101**, 104–129.

POPE, S. B. 1988 The evolution of surfaces in turbulence. *Int. J. Eng. Sci.* **28**, 445–469.

RENOU, B., BOUKHALFA, A., PUECHBERTY, D. & TRINITÉ, M. 1998 Effects of stretch on the local structure of freely propagating premixed low-turbulent flames with various Lewis numbers. *Proc. Combust. Inst.* **27**, 841–847.

SOIKA, A., DINKELACKER, F & LEIPERTZ, A. 1998 Measurement of the resolved flame structure of turbulent premixed flames with constant Reynolds number and varied stoichiometry. *Proc. Combust. Inst.* **27**, 785–792.

SUNG, C. J., LIU, J. B. & LAW, C. K. 1996 On the scalar structure of nonequidiffusive premixed flames in counterflow. *Comb. Flame* **106**, 168–183.

SWAMINATHAN, N., BILGER, R. W. & RUETSCH, G. R. 1997 Interdependence of the instantaneous flame front structure and the overall scalar flux in turbulent premixed flames. *Combust. Sci. Tech.* **128**, 73–97.

SWAMINATHAN, N. & BILGER, R. W. 2001 Scalar dissipation, diffusion and dilatation in turbulent H₂-air premixed flames with complex chemistry. *Combust. Theory Modelling* **3**, 429–446.

SWAMINATHAN, N. & GROUT, R. W. 2006 Interaction of turbulence and scalar fields in premixed flames. *Phys. Fluids* **18**, 045102.

WARHAFT, Z. 2000 Passive scalars in turbulent flows. *Annu. Rev. Fluid Mech.* **32**, 203–240.

A balanced force refined level set grid method for two-phase flows on unstructured flow solver grids

By M. Herrmann

1. Motivation and objectives

In liquid/gas flows, surface tension forces often play an important role. For example, during the atomization of liquid jets by coaxial fast-moving gas streams, the details of the formation of small-scale drops from aerodynamically stretched out ligaments is governed by capillary forces (Marmottant & Villermaux 2004). From a numerical point of view, surface tension poses a unique challenge since it is a singular force, active only at the location of the phase interface. In addition, the situation is further complicated by the fact that material properties, like density and viscosity, exhibit a discontinuity at the same location. One of the prerequisites for correctly treating surface tension forces is therefore the ability to locate the position of the phase interface accurately. To this end, several phase interface tracking schemes exist for fixed grid flow solvers, among them the marker method (Tryggvason *et al.* 2001), the Volume-of-Fluid (VoF) method (Gueyffier *et al.* 1999), and the level set method (Sussman *et al.* 1994). Here we will use a variant of the level set method, termed Refined Level Set Grid method (Herrmann 2004, 2005), to ensure good fluid volume conservation properties.

Different strategies exist to discretize the surface tension force once the location of the phase interface is known. The most commonly used method is due to Brackbill *et al.* (1992) called Continuum Surface Force (CSF). Here, the ideally singular surface tension force is spread into a narrow band surrounding the phase interface by the use of regularized delta functions. These can take the form of a discrete derivative of a Heaviside scalar, i.e., the volume fraction, in VoF methods, or spread out delta functions, like the popular cosine approximation due to Peskin (1977) in level set methods. Especially in level set methods, the use of spread out delta functions can be problematic, since convergence under grid refinement is only guaranteed for certain, not commonly employed delta function approximations (Engquist *et al.* 2005). An alternative to the CSF method is the Ghost Fluid Method (GFM) proposed in Fedkiw *et al.* (1999) that aims to apply the jump conditions and surface tension force as singular source terms within the context of finite difference schemes.

Both the CSF and the GFM method, however, are prone to generating unphysical flows, so-called spurious currents, near the location of the phase interface when surface tension forces are present. In the canonical test cases of an equilibrium column and an equilibrium sphere, these velocity errors can grow unbounded very fast, if they are not artificially damped by introducing viscosity. The amplitude of the spurious currents when damped by viscosity is of the order of $u \sim 0.01\sigma/\mu$ for VoF and level set methods and $u \sim 10^{-5}\sigma/\mu$ for marker methods (Scardovelli & Zaleski 1999), where σ is the surface tension coefficient and μ is the viscosity. Thus, numerical simulations are limited by a critical Laplace number, $La = \sigma\rho R/\mu^2$, where ρ is the density and R is a characteristic phase interface radius of curvature, since for large La , i.e., large σ , spurious currents start to dominate the physical flow (Scardovelli & Zaleski 1999).

The reason for the occurrence of spurious currents is twofold. The major reason is a discrete imbalance between the surface tension force and the associated pressure jump across the phase interface (Francois *et al.* 2006). The second source of error is due to errors associated with evaluating phase interface curvature. To address the former source of error, Young *et al.* (2002) proposed a modification to the procedure of Kim & Choi (2000) to regain discrete consistency. However, they were using the CSF method with smeared out delta functions in a level set context and, hence, the exact discrete balance was not achieved. Francois *et al.* (2006) proposed a so-called “balanced force algorithm” for VoF schemes on structured Cartesian meshes that discretely balances the surface tension force and the associated pressure jump across the interface. In that paper, the discrete evaluation of the delta function as the derivative of the volume fraction scalar naturally results in the discrete balance when following a similar approach to the one proposed in Young *et al.* (2002). The approach by Francois *et al.* (2006) eliminates spurious currents up to machine precision zero, if the interface curvature is prescribed exactly.

Different strategies exist to increase the accuracy of curvature evaluation. For VoF methods, the height-function approach (Sussman 2003) allows second-order converging curvature calculation. However, the required stencil sizes are large and thus problematic for interfaces close to each other. For level set methods, curvature at the node location can be calculated with high-order accuracy, however, the phase interface curvature is approximated to first order at most, due to the fact that nodal location and phase interface position typically do not coincide.

In this paper, we will extend the balanced force algorithm of Francois *et al.* (2006) and Young *et al.* (2002) to unstructured flow solver grids using the RLSG level set method to track the phase interface. To achieve second-order converging curvature evaluation, an interface projected curvature evaluation method is proposed. The performance of the balanced force RLSG method is demonstrated analyzing equilibrium columns and spheres on structured and unstructured flow solver grids. Finally, to demonstrate the capability of the new method in complex flows, a Rayleigh-Taylor instability is presented.

2. Governing equations

The equations governing the motion of an unsteady, incompressible, immiscible, two-fluid system are the Navier-Stokes equations,

$$\frac{\partial \mathbf{u}}{\partial t} + \mathbf{u} \cdot \nabla \mathbf{u} = -\frac{1}{\rho} \nabla p + \frac{1}{\rho} \nabla \cdot (\mu (\nabla \mathbf{u} + \nabla^T \mathbf{u})) + \mathbf{g} + \frac{1}{\rho} \mathbf{T}_\sigma, \quad (2.1)$$

where \mathbf{u} is the velocity, ρ the density, p the pressure, μ the dynamic viscosity, \mathbf{g} the gravitational acceleration, and \mathbf{T}_σ the surface tension force which is non-zero only at the location of the phase interface \mathbf{x}_f . Furthermore, the continuity equation results in a divergence-free constraint on the velocity field,

$$\nabla \cdot \mathbf{u} = 0. \quad (2.2)$$

The phase interface location \mathbf{x}_f between the two fluids is described by a level set scalar G , with

$$G(\mathbf{x}_f, t) = 0 \quad (2.3)$$

at the interface, $G(\mathbf{x}, t) > 0$ in fluid 1, and $G(\mathbf{x}, t) < 0$ in fluid 2. Differentiating Eq. (2.3)

with respect to time yields the level set equation,

$$\frac{\partial G}{\partial t} + \mathbf{u} \cdot \nabla G = 0. \quad (2.4)$$

Assuming ρ and μ are constant within each fluid, density and viscosity at any point \mathbf{x} can be calculated from

$$\rho(\mathbf{x}) = H(G)\rho_1 + (1 - H(G))\rho_2 \quad (2.5)$$

$$\mu(\mathbf{x}) = H(G)\mu_1 + (1 - H(G))\mu_2, \quad (2.6)$$

where indices 1 and 2 denote values in fluid 1, respectively 2, and H is the Heaviside function. From Eq. (2.3) it follows that

$$\delta(\mathbf{x} - \mathbf{x}_f) = \delta(G)|\nabla G| \quad (2.7)$$

with δ the Dirac delta function. Furthermore, the interface normal vector \mathbf{n} and the interface curvature κ can be expressed in terms of the level set scalar as

$$\mathbf{n} = \frac{\nabla G}{|\nabla G|}, \quad \kappa = \nabla \cdot \mathbf{n}. \quad (2.8)$$

Using Eqs. (2.7) and (2.8), the surface tension force \mathbf{T}_σ can thus be expressed as

$$\mathbf{T}_\sigma(\mathbf{x}) = \sigma\kappa\delta(\mathbf{x} - \mathbf{x}_f)\mathbf{n} = \sigma\kappa\delta(G)|\nabla G|\mathbf{n} = \sigma\kappa\delta(G)\nabla G, \quad (2.9)$$

with σ the surface tension coefficient.

3. Numerical method

In this section, we first briefly summarize the RLSG method used to solve the level set equation and discuss how the RLSG level set solution is coupled to structured and unstructured flow solver grids. Next, the level set-based balanced force algorithm for unstructured flow solver grids is presented and the performance of the resulting method is illustrated using the canonical test cases of equilibrium columns and spheres prescribing curvature exactly. Then, the method to calculate second-order converging interfacial curvatures is outlined. Finally, results are presented for curvature evaluation of columns and spheres on structured and unstructured flow solver grids.

3.1. Refined Level Set Grid method

In the RLSG method, all level set-related equations are evaluated on a separate, equidistant Cartesian grid using a dual-narrow band methodology for efficiency. This so-called G -grid is overlaid onto the flow solver grid, which can be either structured or unstructured. Details on the method when used in conjunction with a structured, equidistant Cartesian flow solver grid and its performance in generic test cases can be found in Herrmann (2006, 2005). To a certain extent the RLSG method is similar to the recently proposed Narrow-Band Locally Refined Level Set (NBLR-LS) approach by Gomez *et al.* (2005). However, the latter is limited to Cartesian grids, whereas the former can deal with arbitrary unstructured flow solver meshes. In the following, we will discuss only recent modifications to the RLSG method not contained in the aforementioned publications.

3.1.1. Re-initialization

For reasons of numerical accuracy, one would like to maintain G away from the interface $G = 0$ as smooth a field as possible. Sussman *et al.* (1994) proposed defining the level

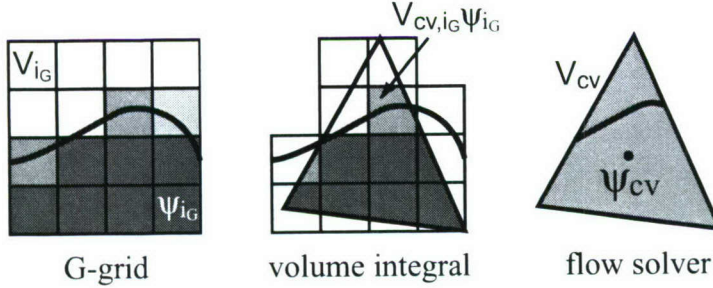


FIGURE 1. Volume integration for unstructured flow solver grid cells.

set scalar away from the interface to be a signed distance function, i.e., $|\nabla G| = 1$. Since solution of Eq. (2.4) will not maintain this property, a re-initialization procedure has to be applied to force $G \neq 0$ back to $|\nabla G| = 1$. Several different strategies exist to achieve this, the one used in this work is based on the PDE-based re-initialization by Sussman *et al.* (1994) using the modified signed function due to Peng *et al.* (1999). Unfortunately, it is well known that repeated application of the PDE-based re-initialization will inadvertently move the $G = 0$ isosurface and hence will not conserve fluid volume and thus fluid mass. It is therefore desirable to limit the application of the re-initialization procedure to situations where the divergence from G being a signed distance function would adversely impact numerical accuracy by using an appropriate trigger criterion.

Here we will use a slight modification to the criterion proposed by Gomez *et al.* (2005). The PDE-based re-initialization procedure is applied only if

$$\max(|\nabla G|) > \alpha_{\max} \text{ or } \min(|\nabla G|) < \alpha_{\min}, \quad (3.1)$$

evaluated inside the transport band \mathcal{T} -band (see Herrmann (2005, 2006) for definition of the individual bands). Also, Eq. (3.1) is used as a convergence criterion for the pseudo-time iteration of the re-initialization, while still limiting the maximum number of iteration steps to $n_{\max} = Cd_{\mathcal{N}}/h_G$, where $d_{\mathcal{N}}$ is the width of the re-initialization band (\mathcal{N} -band), C is the CFL-number, and h_G is the grid cell size of the G -grid. In the results presented in this paper we use $\alpha_{\max} = 2$ and $\alpha_{\min} = 10^{-4}$, resulting in typically 1-2 pseudo-time iteration steps until convergence is reached, should re-initialization be triggered.

3.1.2. Coupling to flow solver

In the Navier-Stokes equation, the position of the phase interface influences two different terms. The first term is due to Eqs. (2.5) and (2.6), since $H(G)$ is a function of the position of the phase interface. For finite volume formulations, the volume fraction ψ_{cv} of control volume cv is defined as

$$\psi_{cv} = 1/V_{cv} \int_{V_{cv}} H(G) dV, \quad (3.2)$$

with V_{cv} the volume of the control volume cv . In the RLSG method, the above integral is evaluated on the G -grid as

$$1/V_{cv} \int_{V_{cv}} H(G) dV = \frac{\sum_{i_G} V_{cv,i_G} \psi_{i_G}}{\sum_{i_G} V_{cv,i_G}}, \quad (3.3)$$

where V_{cv,i_G} is the joined intersection volume of the G -grid cell i_G and the flow solver control volume cv (see Fig. 1), and the G -grid volume fraction ψ_{i_G} is calculated using an

analytical formula developed by van der Pijl *et al.* (2005),

$$\psi_{i_G} = f(G_{i_G}, \nabla G_{i_G}). \quad (3.4)$$

The joined intersection volumes V_{cv,i_G} are calculated using CHIMPS (Alonso *et al.* 2006), employing a Sutherland-Hodgman clipping procedure (Sutherland & Hodgman 1974) to calculate the intersection volume between a Cartesian grid cell and convex tetra-, penta-, and hexahedra.

The second term that is a function of the interface position is the surface tension force term, Eq. (2.9). This term could be calculated first on the G -grid, using a smeared out version of the delta function δ_ϵ , and then volume averaged to the flow solver grid,

$$\mathbf{T}_{\sigma_{cv}} = 1/V_{cv} \sum_{i_G} V_{cv,i_G} \mathbf{T}_{\sigma_{i_G}} = \frac{\sum_{i_G} V_{cv,i_G} \sigma \kappa_{i_G} \delta_\epsilon(G_{i_G})(\nabla G)_{i_G}}{\sum_{i_G} V_{cv,i_G}}. \quad (3.5)$$

However, as will be seen later, this formulation is inconsistent with the balanced force algorithm. Instead, only the interface curvature is transferred from the G -grid to the flow solver grid,

$$\kappa_{cv} = \frac{\sum_{i_G} V_{cv,i_G} \delta_{i_G} \kappa_{i_G}}{\sum_{i_G} V_{cv,i_G} \delta_{i_G}}, \quad (3.6)$$

where $\delta_{i_G} = 0$ if $\psi_{i_G} = 0$ or $\psi_{i_G} = 1$, and $\delta_{i_G} = 1$ otherwise. The use of δ_{i_G} ensures that κ is treated as a surface quantity and not a volume quantity.

In order to couple the level set equation, Eq. (2.4), to the Navier-Stokes equation, \mathbf{u}_{i_G} has to be calculated from \mathbf{u}_{cv} . Again the CHIMPS infrastructure is used and either tri-linear or C1, isotropic tri-cubic interpolation (Lekien & Marsden 2005) is employed. It should be pointed out that strictly speaking neither one of these velocity interpolations can maintain a smooth curvature field under G -grid refinement. To achieve this property, k_{int} is defined as

$$k_{int} = \nabla \cdot (\nabla(\mathbf{u}_{int} \cdot \mathbf{n})), \quad (3.7)$$

where \mathbf{u}_{int} is the interpolated velocity onto the G -grid and \mathbf{n} is the interface normal vector, would have to be continuous when switching between neighboring interpolation cells. Clearly, for tri-linear interpolation, this is not the case and even the isotropic tri-cubic interpolation of Lekien & Marsden (2005) does not guarantee this property, since neither ∂_{xx} nor ∂_{yy} nor ∂_{zz} are kept continuous between neighboring interpolation cells. Constructing an interpolation scheme that fulfills the above condition will be part of future work.

To achieve second-order in time, the level set equation is solved staggered in time with respect to the Navier-Stokes equation.

3.2. Balanced force algorithm

The solution method of the Navier-Stokes equations is based on the fractional-step method for collocated variables on unstructured grids described in Mahesh *et al.* (2004). In the following, outlined is only the part of the algorithm that ensures discrete balance between surface tension forces and pressure gradient forces. It is based on the balanced force method for Volume of Fluid methods on collocated Cartesian grids (Francois *et al.* 2006).

For simplicity, we will omit the viscous term in the following discussion. The term is fully implemented and solved for in flux form, with the viscosity at the cell face calculated by the harmonic mean of the centroid viscosities of the two control volumes cv and nbr

sharing the face,

$$\mu_f = \frac{2\mu_{cv}\mu_{nbr}}{\mu_{cv} + \mu_{nbr}}. \quad (3.8)$$

The cell centroid values are calculated by

$$\mu_{cv} = \psi_{cv}\mu_1 + (1 - \psi_{cv})\mu_2. \quad (3.9)$$

The algorithm then reads

$$V_{cv} \frac{u_{i,cv}^* - u_{i,cv}^n}{\Delta t} + \sum_f u_f^{n+1/2} \frac{u_{i,cv}^{n+1/2} + u_{i,nbr}^{n+1/2}}{2} A_f = V_{cv}g + V_{cv}F_{i,cv}^{n+1/2} \quad (3.10)$$

$$\frac{u_{i,cv}^{n+1} - u_{i,cv}^*}{\Delta t} = -\frac{1}{\rho_{cv}^{n+1/2}} \frac{\partial p^{n+1/2}}{\partial x_i}, \quad (3.11)$$

where A_f is the face area, u_f the face normal velocity, $F_{i,cv}$ the density weighted surface tension force defined below, and superscripts denote time levels.

To define the force $F_{i,cv}^{n+1/2}$ at the control volume centroid, we first need to define the surface tension force at the cell face,

$$T_{\sigma_f}^{n+1/2} = \sigma \kappa_f^{n+1/2} (\nabla \psi)_f^{n+1/2}. \quad (3.12)$$

Here, the face curvature is calculated from the centroid curvature, Eq. (3.6),

$$\kappa_f^{n+1/2} = \frac{\alpha_{cv}^{n+1/2} \kappa_{cv}^{n+1/2} + \alpha_{nbr}^{n+1/2} \kappa_{nbr}^{n+1/2}}{\alpha_{cv}^{n+1/2} + \alpha_{nbr}^{n+1/2}} \quad (3.13)$$

with

$$\alpha_{cv}^{n+1/2} = \begin{cases} 1 & : 0 < \psi_{cv}^{n+1/2} < 1 \\ 0 & : \text{otherwise} \end{cases} \quad (3.14)$$

and

$$(\nabla \psi)_f^{n+1/2} = (\psi_{nbr}^{n+1/2} - \psi_{cv}^{n+1/2})/|\mathbf{s}_{cv,nbr}|. \quad (3.15)$$

Here, $\mathbf{s}_{cv,nbr}$ is the vector connecting the cv and nbr control volume centroids. Then, $F^{n+1/2}$ at the face becomes

$$F_f^{n+1/2} = T_{\sigma_f}^{n+1/2} / \rho_f^{n+1/2}, \quad (3.16)$$

with $\rho_f^{n+1/2} = (\rho_{cv}^{n+1/2} + \rho_{nbr}^{n+1/2})/2$ and the centroid densities calculated from

$$\rho_{cv}^{n+1/2} = \psi_{cv}^{n+1/2} \rho_1 + (1 - \psi_{cv}^{n+1/2}) \rho_2. \quad (3.17)$$

Finally, $F_f^{n+1/2}$ defined at the cell face needs to be transferred to the control volume centroid. It is crucial that for this, one uses exactly the same operation that is used for transferring $(\partial p/\partial n)_f$ to $(\partial p/\partial x_i)_{cv}$ in the pressure corrector step. Here we use the face-area weighted least-squares method of Mahesh *et al.* (2004) by minimizing

$$\epsilon_{cv} = \sum_f \left(F_{i,cv}^{n+1/2} n_{i,f} - F_f^{n+1/2} \right)^2 A_f. \quad (3.18)$$

After solving Eq. (3.10) to obtain $u_{i,cv}^*$, the cell face normal velocities u_f^* are calculated,

$$u_f^* = \frac{1}{2} (u_{i,cv}^* + u_{i,nbr}^*) n_{i,f} - \frac{1}{2} \Delta t \left(F_{i,cv}^{n+1/2} + F_{i,nbr}^{n+1/2} \right) n_{i,f} + \Delta t F_f^{n+1/2}. \quad (3.19)$$

This is essentially a modification of the procedure by Kim & Choi (2000), first proposed by Young *et al.* (2002). To correct the face intermediate face velocities u_f^* to be divergence free, we then solve the following variable coefficient Poisson system,

$$\sum_f \frac{1}{\rho_f^{n+1/2}} \frac{\partial p^{n+1/2}}{\partial n} A_f = \frac{1}{\Delta t} \sum_f u_f^* A_f, \quad (3.20)$$

and then apply the correction

$$u_f^{n+1} = u_f^* - \Delta t P_f, \quad (3.21)$$

with

$$P_f = \frac{1}{\rho_f^{n+1/2}} (\nabla p^{n+1/2})_f = \frac{1}{\rho_f^{n+1/2}} \frac{p_{nbr}^{n+1/2} - p_{cv}^{n+1/2}}{|\mathbf{s}_{cv,nbr}|}. \quad (3.22)$$

Next, the centroid-based density weighted pressure gradient P_{cv} is calculated from the face-based density weighted gradient P_f using the same face-area weighted least-squares method employed in calculating F_f (see Eq. 3.18),

$$\epsilon_{cv} = \sum_f (P_{i,cv} n_{i,f} - P_f)^2 A_f. \quad (3.23)$$

Finally, the control volume centroid velocity is corrected (cf. Eq. 3.11),

$$u_{i,cv}^{n+1} = u_{i,cv}^* - \Delta t P_{i,cv}, \quad (3.24)$$

concluding the flow solver time step.

3.3. Exact curvature equilibrium inviscid column and sphere

To illustrate the performance of the balanced force algorithm, we analyze the canonical test cases of the equilibrium inviscid column and sphere. In this case, the surface tension forces should exactly balance the pressure jump across the phase interface, resulting in the column and sphere remaining perfectly at rest. We employ the test case parameters suggested by Williams *et al.* (1999) and used by Francois *et al.* (2006): a column (or sphere), of radius $R = 2$ is placed at the center of an 8x8(x8) domain. The surface tension coefficient σ is set to 73, resulting in a theoretical pressure jump across the interface of $\Delta p^{ex} = 36.5$ for the column and $\Delta p^{ex} = 73$ for the sphere. The density inside the column/sphere is set to $\rho_1 = 1$ and the density outside the column/sphere ρ_2 is varied. Equidistant Cartesian and unstructured prism and tetrahedral flow solver grids are tested. The flow solver grid is characterized by the characteristic grid size h , whereas the equidistant Cartesian G -grid size is denoted by h_G .

The error in pressure is measured in two different ways (Francois *et al.* 2006),

$$E(\Delta p_{max}) = \max(p_{cv}) - \min(p_{cv}) - \Delta p^{ex} \quad (3.25)$$

$$E(\Delta p_{part}) = \overline{p_{cv}}|_{r \leq R/2} - \overline{p_{cv}}|_{r \geq 3R/2} - \Delta p^{ex}, \quad (3.26)$$

where the bar indicates an arithmetic average over all control volumes fulfilling the given condition.

Table 1 summarizes the errors in velocity, pressure, and kinetic energy E_{kin} for the column after a single time step of size $\Delta t = 10^{-6}$ for varying density ratios if the exact curvature of the column is used for κ_{cv} in Eq. (3.6). As can be seen, both on the Cartesian and the unstructured prism flow solver grid, errors are machine precision zero, even for extremely large density ratios.

ρ_1/ρ_2	$L_\infty(u)$	E_{kin}	$E(\Delta p_{max})$	$E(\Delta p_{part})$	ρ_1/ρ_2	$L_\infty(u)$	E_{kin}	$E(\Delta p_{max})$	$E(\Delta p_{part})$
1	6.76e-20	6.86e-40	4.14e-16	3.41e-15	1	1.82e-16	1.06e-32	1.82e-16	4.58e-13
10^3	3.59e-17	6.28e-35	9.90e-14	9.21e-13	10^3	2.55e-16	7.84e-36	2.55e-16	1.97e-15
10^5	9.93e-19	2.26e-40	3.16e-16	1.58e-15	10^5	5.43e-16	8.43e-38	5.43e-16	2.29e-15
10^{10}	9.77e-19	1.74e-40	7.30e-16	1.19e-15	10^{10}	3.93e-18	3.39e-39	3.93e-18	7.40e-15

TABLE 1. Errors in velocity and pressure after single time step for varying density ratio in the inviscid, equilibrium column test case using exact curvature and $h = h_G = 0.2$; Cartesian flow solver grid (left) and prism flow solver grid (right).

ρ_1/ρ_2	$L_\infty(u)$	E_{kin}	$E(\Delta p_{max})$	$E(\Delta p_{part})$	ρ_1/ρ_2	$L_\infty(u)$	E_{kin}	$E(\Delta p_{max})$	$E(\Delta p_{part})$
1	5.49e-17	6.95e-34	6.57e-14	1.19e-12	1	3.31e-16	8.20e-33	1.31e-11	1.25e-14
10^3	1.15e-17	1.40e-36	1.15e-14	9.41e-14	10^3	1.07e-15	5.96e-35	4.81e-14	1.50e-15
10^5	1.21e-16	3.30e-39	5.30e-15	1.38e-14	10^5	2.58e-15	2.76e-36	1.42e-14	1.02e-15
10^{10}	5.47e-16	8.24e-36	3.54e-13	2.74e-13	10^{10}	9.95e-11	2.73e-35	2.40e-15	5.60e-16

TABLE 2. Errors in velocity and pressure after single time step for varying density ratio in the inviscid, equilibrium sphere test case using exact curvature and $h = h_G = 0.2$; Cartesian flow solver grid (left) and tetrahedral flow solver grid (right).

Table 2 summarizes the same quantities in the sphere test case. Again, both on the Cartesian and the tetrahedral flow solver grid, machine precision zero errors are achieved for varying density ratios, if the exact curvature is employed.

Thus, provided that the exact curvature is known, the balanced force algorithm results in machine zero spurious currents, even in the inviscid case. However, the exact curvature is rarely known, instead it has to be evaluated and is prone to errors. These curvature errors are then the sole source of error for spurious currents.

3.4. Curvature evaluation

As noted in the previous section, only curvature errors result in spurious currents when employing the balanced force algorithm. Hence the task of minimizing spurious currents is equivalent to increasing the accuracy of curvature evaluation. In standard level set methods (Sethian 1999), curvature is evaluated at G -node locations by discretizing Eq. (2.8),

$$\kappa = \frac{G_{,xx}^2 (G_{,y}^2 + G_{,z}^2) + G_{,yy} (G_{,x}^2 + G_{,z}^2) + G_{,zz} (G_{,x}^2 G_{,y}^2)}{(G_{,x}^2 + G_{,y}^2 + G_{,z}^2)^{3/2}} - 2 \frac{G_{,xy} G_{,x} G_{,y} + G_{,xz} G_{,x} G_{,z} + G_{,yz} G_{,y} G_{,z}}{(G_{,x}^2 + G_{,y}^2 + G_{,z}^2)^{3/2}}, \quad (3.27)$$

typically using a 27-point stencil. It is important to point out that this approach approximates the curvature of the G -isosurface that passes through the nodal point itself. It is therefore, at best, only a first-order approximation to the curvature of the phase

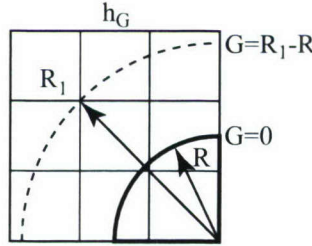


FIGURE 2. Inherent phase interface curvature error when evaluating curvature at nodes. Curvature is determined to be $\kappa = 1/R_1 = 1/(R + O(h_G))$ instead of $\kappa = 1/R$.

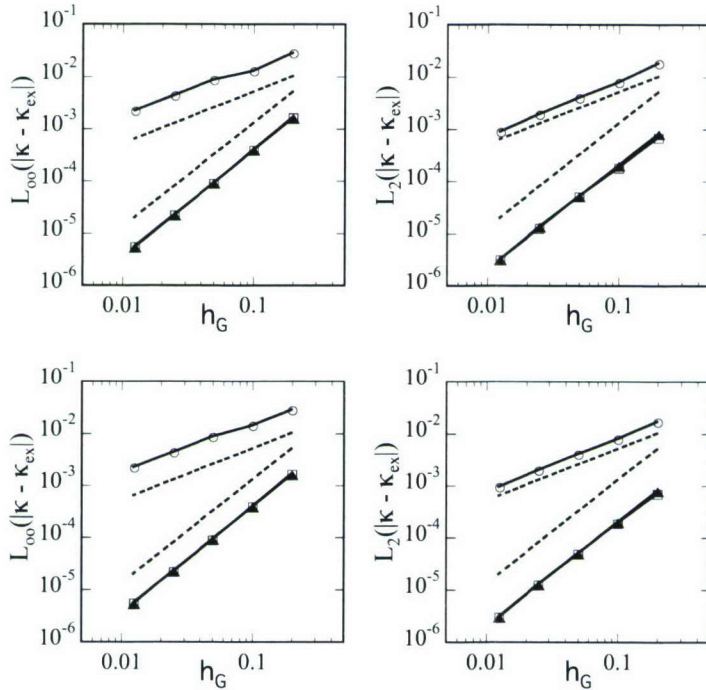


FIGURE 3. Initial column curvature errors under G -grid refinement; flow solver grid $h = 0.2$; Cartesian flow solver grid (top), prism flow solver grid (bottom); nodal curvature (circles), direct front curvature (squares), Chopp front curvature (triangles), first- and second-order convergence (dashed lines).

interface, which can be a distance h_G away from nodes directly adjacent to the interface (see Fig. 2). Figures 3 and 4 demonstrate this first-order convergence rate under G -grid refinement for both the column and the sphere test case using either Cartesian flow solver grids (column and sphere), unstructured prism grids (column), or tetrahedral grids (sphere) with $h = 0.2$.

Since the root cause of the first-order convergence rate is the fact that curvature is not calculated at the interface itself, different approaches can be taken to overcome this problem. Introducing a polynomial representation of the interface in terms of interface-based coordinates is a viable approach in two dimensions, but becomes cumbersome in three dimensions. Here, we will follow an alternative approach using the fact that a

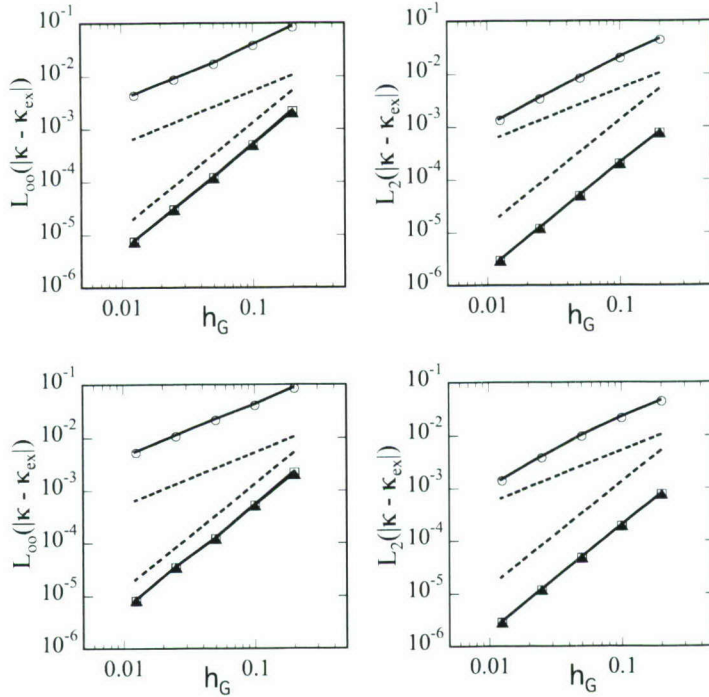


FIGURE 4. Initial sphere curvature errors under G-grid refinement; flow solver grid $h = 0.2$; Cartesian flow solver grid (top), prism flow solver grid (bottom); nodal curvature (circles), direct front curvature (squares), Chopp front curvature (triangles), first- and second-order convergence (dashed lines).

quantity defined only on the interface itself, like curvature, can be distributed to the whole computational domain in a meaningful way by solving

$$\nabla \kappa \cdot \nabla G = 0. \quad (3.28)$$

This effectively sets κ constant in the front normal direction. Note that due to Eq. (3.6), Eq. (3.28) needs to be solved only for G -nodes adjacent to the interface. The problem is therefore similar to determining the initially accepted values in the Fast Marching Method (Adalsteinsson & Sethian 1999). For this purpose, Chopp (2001) developed a Newton's method that determines the nearest point on the interface (called "base-point" in the following) for a given node in two dimensions. The method relies on approximating the level set scalar within each computational cell close to the interface by a bi-cubic spline. For this purpose, G need not be a distance function. We have extended Chopp's method to three dimensions using C1, isotropic tri-cubic interpolations (Lekien & Marsden 2005). We typically find the base-point within 2–4 Newton iterations. However, the algorithm can find base-points that lay outside of the considered G -grid cell for which the tri-cubic interpolation is valid. In this case, the base-point is rejected, unless none of the alternative eight G -cells the node belongs to yields a valid base-point. Once the base-point coordinates have been determined, the base-point's curvature is calculated by tri-linear interpolation using the surrounding nodal curvature values. Using Eq. (3.28), the nodal curvature is then set equal to its base-point's curvature.

The resulting curvature errors under G -grid refinement using Chopp's method are

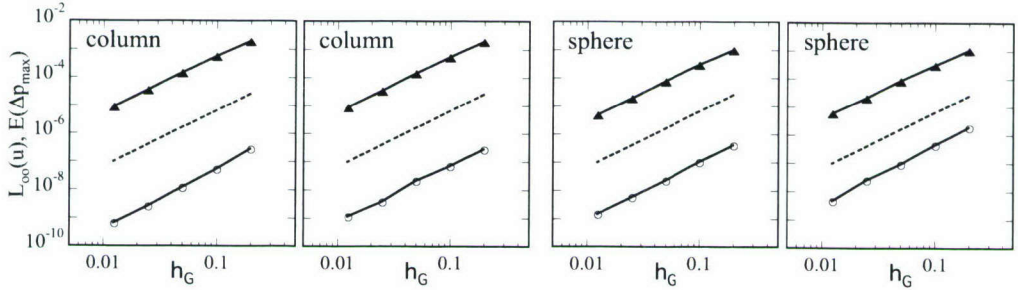


FIGURE 5. Equilibrium inviscid column and sphere velocity (circle) and pressure (triangle) errors after 1 time step under G-grid refinement; flow solver grid $h = 0.2$, density ratio $\rho_1/\rho_2 = 10^3$; from left and right: column Cartesian flow solver grid, column prism flow solver grid, sphere Cartesian flow solver grid, and sphere tetrahedral flow solver grid; dashed lines mark second-order convergence.

shown in Figs. 3 and 4. They show second-order convergence, and even on coarse grids, Chopp's method yields more than one order of magnitude better curvature estimates than the nodal-based evaluation. The drawback of Chopp's method is that for complex interface geometries in three dimensions, the Newton algorithm does not always converge. The method thus lacks the stability required for complex interface geometries typically found in liquid/gas flows. Thus, the following method is proposed as an alternative.

Assuming that G is smooth in the vicinity of the phase interface, the base-point \mathbf{x}_B for a given node \mathbf{x}_G close to the interface can be explicitly calculated from

$$\mathbf{x}_B = \mathbf{x}_G - d\mathbf{n} = \mathbf{x}_G - \frac{G}{|\nabla G|} \frac{\nabla G}{|\nabla G|}, \quad (3.29)$$

where all gradients are calculated using central differences. This approach is termed *direct front curvature* in the following. It gives good base-point estimates only for nodes close to the interface. However, due to the way Eq. (3.6) is evaluated, κ needs to be calculated only on nodes close to the interface, making the direct front curvature method viable. As before, once base-points have been determined, their curvature is again calculated using tri-linear interpolation from the surrounding nodal curvature values. Then, according to Eq. (3.28), the curvature values of nodes are set to their respective base-points' curvature values. Figures 3 and 4 also include the curvature errors calculated by the direct method. As can be seen, they are virtually indistinguishable from the values obtained using Chopp's method yielding second-order convergence.

Comparing the obtained curvature errors to those calculated by Francois *et al.* (2006), both Chopp's and the direct method give curvature errors an approximate factor of 5 lower than the 7x3 stencil height function method employed in that paper. While a height function approach could be employed in the RLSG method as well, since volume fractions ψ are readily available, the effective G -stencil needed would be 9x5x5 (cf. Eq. 3.2), as compared to 4x4x4 in the direct front curvature method. Smaller stencil sizes are especially important for complex interface geometries, since both the height function and all level set curvature methods are based on the assumption that all ψ and G values in the stencil relate to one continuous interface segment only. Auxiliary, non-contiguous, interface segments inside the stencil can introduce significant errors. Hence, smaller stencil sizes are preferred to limit these errors.

In the following, we will employ the direct front curvature method to calculate nodal

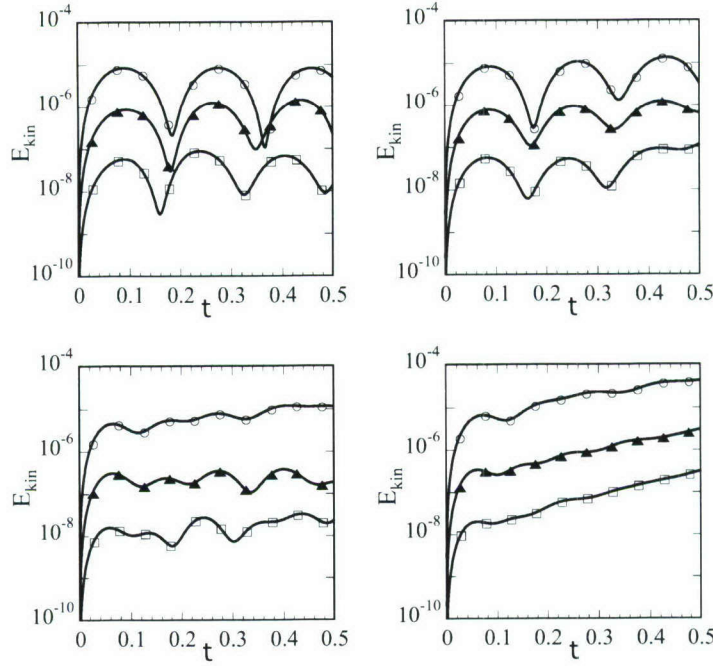


FIGURE 6. Temporal evolution of kinetic energy for equilibrium inviscid column (top) and sphere (bottom) for 500 time steps under G -grid refinement: $h_G = 0.4$ (circle), $h_G = 0.2$ (triangle), $h_G = 0.1$ (box); flow solver grid $h = 0.4$, density ratio $\rho_1/\rho_2 = 10^3$; Cartesian flow solver grids (top left and bottom left), prism flow solver grid (top right), and tetrahedral flow solver grid (bottom right).

curvature values on the G -grid. Figure 5 shows the errors in velocity and pressure after a single time step of size $\Delta t = 10^{-6}$, using $\rho_1 = 1$ and $\rho_2 = 10^{-3}$ and refining the resolution h_G of the G -grid. As expected, due to the balanced force algorithm, errors in curvature evaluation result in errors in velocity and pressure, showing the same second-order convergence behavior (cf. Figs. 3 and 4).

4. Results

4.1. Long-time evolution of the equilibrium inviscid column and sphere

As shown in the previous section, errors in curvature evaluation result in spurious currents that are small, but non-zero. Thus, the long-time behavior of the equilibrium column and sphere is of interest, since errors might accumulate and result in large erroneous velocities.

Figure 6 shows the temporal evolution of the kinetic energy in the computational domain for both the inviscid column and sphere on Cartesian and unstructured flow solver grids. The flow solver characteristic grid size is $h = 0.4$ in all simulations, $\rho_1 = 1$, $\rho_2 = 10^{-3}$, $\sigma = 73$, and the fixed time step size is $\Delta t = 10^{-3}$. As observed by Francois *et al.* (2006), the column seems to enter an oscillatory mode that appears quite stable on a Cartesian flow solver grid (top left), but shows a slight growth on the prism flow solver grid (top right). The inviscid sphere results, on the other hand, do not exhibit such a clear periodic behavior. In the Cartesian flow solver grid case, different periods seem to be superposed, and the unstructured tetrahedral grid shows an increase in kinetic energy

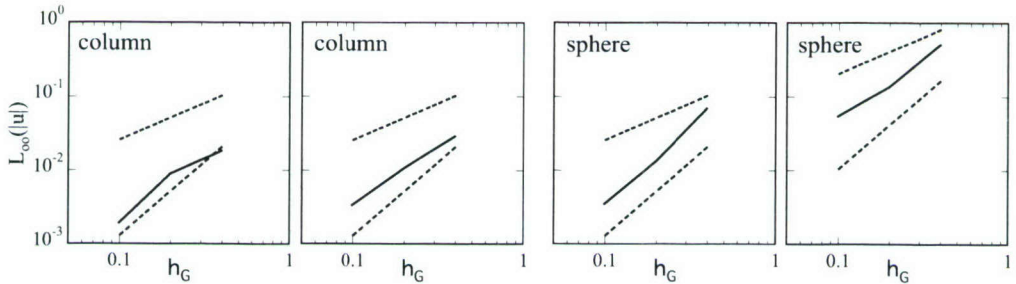


FIGURE 7. Equilibrium inviscid column and sphere maximum velocity error during 500 time steps under G -grid refinement; flow solver grid $h = 0.4$, density ratio $\rho_1/\rho_2 = 10^3$; from left to right: column Cartesian flow solver grid, column prism flow solver grid, sphere Cartesian flow solver grid, and sphere tetrahedral flow solver grid; dashed lines mark second-order convergence.

without reaching a periodic state. This is due to the fact that the unstructured grid lacks the symmetry of the Cartesian grids of the flow solver and the G -grid. This symmetry seems to initiate a periodic oscillation instead of a constant growth in spurious currents and is thus beneficial in this particular test case, but not indicative of the method's performance in a more general setting. In the general case, one can expect a growth of the kinetic energy along the lines of the unstructured grid results, necessitating at later times the use of viscous dissipation to control the spurious currents. However, the balanced force method exhibits very low levels of spurious currents and indeed, this level can be made even smaller if the G -grid is refined to increase the accuracy of the interface curvature evaluation. Figure 7 shows the convergence rates for the maximum velocity error under G -grid refinement, using a flow solver resolution of $h = 0.4$. Close to second-order convergence can be observed both on structured and unstructured flow solver grids.

4.2. Rayleigh-Taylor instability

To demonstrate the performance of the proposed method, the complex flow of a Rayleigh-Taylor instability is computed. This is a common test problem performed by a variety of different methods (Bell & Marcus 1992; Puckett *et al.* 1997; Popinet & Zaleski 1999; Gomez *et al.* 2005). A heavy fluid, $\rho_1 = 1.225$, $\mu_1 = 0.00313$, is placed above a light fluid, $\rho_2 = 0.1694$, $\mu_2 = 0.00313$, inside a domain of size 1×4 . The interface between the two fluids is placed in the middle of the domain and is perturbed by a cosine wave of amplitude 0.05. The gravity constant is set to $g = 9.81$. We set the time step size constant to $\Delta t = 2.5 \cdot 10^{-4}$ and simulate up to $t = 0.9$. Figure 8 shows the interface shape at different instances in time for a Cartesian flow solver grid of $h = 1/512$ and a G -grid of $h_G = 1/512$. As will be demonstrated below, this grid resolution ensures grid converged results and thus will be used as a reference solution in the following.

Figures 9–11 show the interface shape for different flow solver and G -grid resolutions. Using the coarsest flow solver grid of $h = 1/64$ presented in Fig. 9, one can already notice deviations from the reference solution at early times. While the stem and bubble shape is well captured, the fine scale geometry of the side arms is not well maintained. Up to $t = 0.8$, there appears almost no difference between the results using $h_G \geq 1/128$. This indicates that the deviations from the reference solution are due to errors in the flow representation and not due to errors in the interface tracking scheme. However, at $t = 0.9$, the very fine connecting bridge at the side arms can only be maintained by

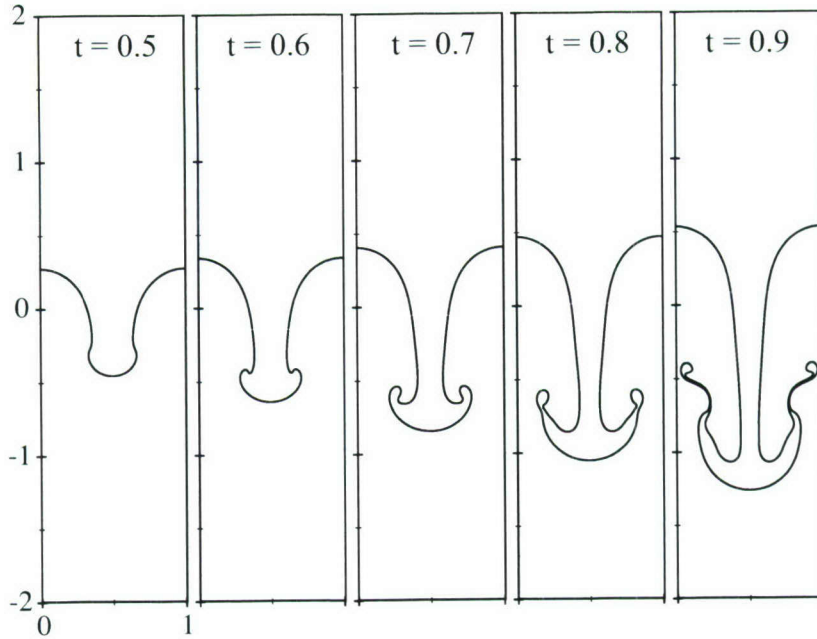


FIGURE 8. Rayleigh-Taylor instability interface shapes for reference solution, $h = h_G = 1/512$.

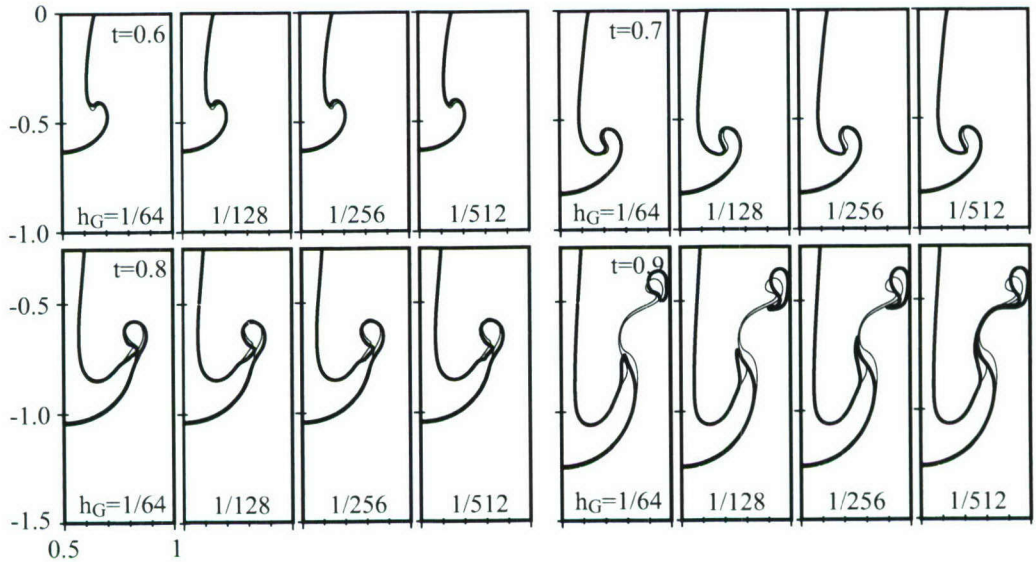


FIGURE 9. Rayleigh-Taylor instability interface shapes under G -grid refinement $h_G = 1/64$, $1/128$, $1/256$, and $1/512$ (left to right in each group) at $t = 0.6$, 0.7 , 0.8 , and 0.9 (top left to bottom right) and flow solver grid $h = 1/64$. Thin line denotes reference solution.

$h_G = 1/512$. Note that except for the difference in the details of the connecting bridge, the larger scale geometric features are consistent between different G -grid resolution with $h_G \geq 1/128$.

At a flow solver grid of $h = 1/128$ presented in Fig. 10, virtually no difference can

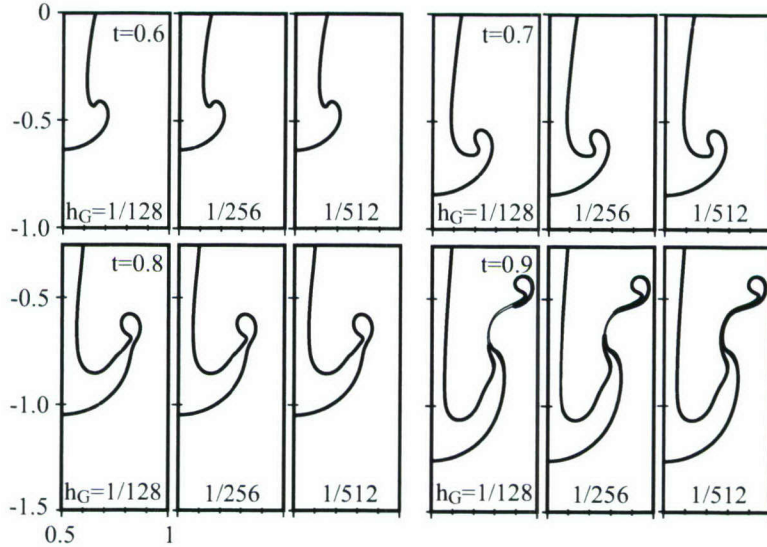


FIGURE 10. Rayleigh-Taylor instability interface shapes under G -grid refinement $h_G = 1/128$, $1/256$, and $1/512$ (left to right in each group) at $t = 0.6, 0.7, 0.8$, and 0.9 (top left to bottom right) and flow solver grid $h = 1/128$. Thin line denotes reference solution.

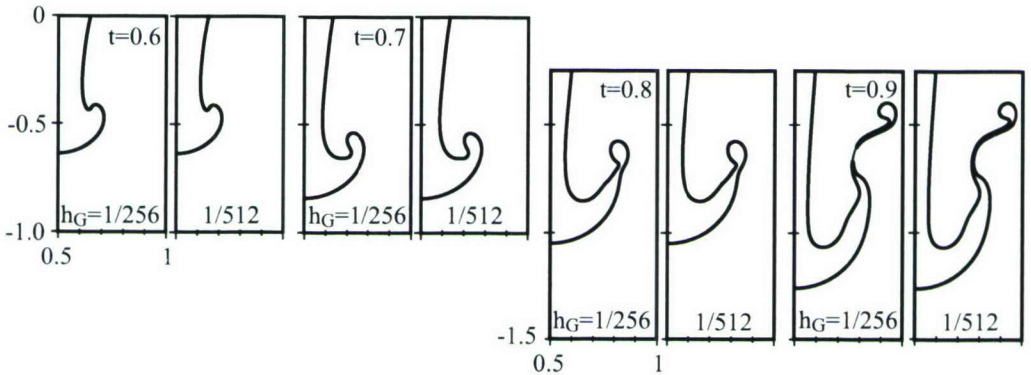


FIGURE 11. Rayleigh-Taylor instability interface shapes under G -grid refinement $h_G = 1/256$ and $1/512$ (left to right in each group) at $t = 0.6, 0.7, 0.8$, and 0.9 (left to right) and flow solver grid $h = 1/256$. Thin line denotes reference solution.

be discerned between the reference solution and G -grid resolutions of $h_G \geq 1/128$ up to $t = 0.8$. At $t = 0.9$, however, the thin connecting bridge is only supported by $h_G = 1/512$. Comparing the results at $t = 0.9$ of $h = 1/128$ to those of $h = 1/64$ (cf. Fig. 9), the finer grid flow solver results capture the shape of the interface significantly better. This indicates that the flowfield is well resolved by the $h = 1/128$ grid.

This observation is further substantiated by refining the flow solver grid further to $h = 1/256$, presented in Fig. 11. Virtually no difference to the reference solution can be discerned, with the exception of $h_G = 1/256$ at $t = 0.9$, where again the complete fine connecting bridge is not supported by that G -grid resolution. Nonetheless, those parts of the bridge that can be maintained by the grid are in excellent agreement with the reference solution.

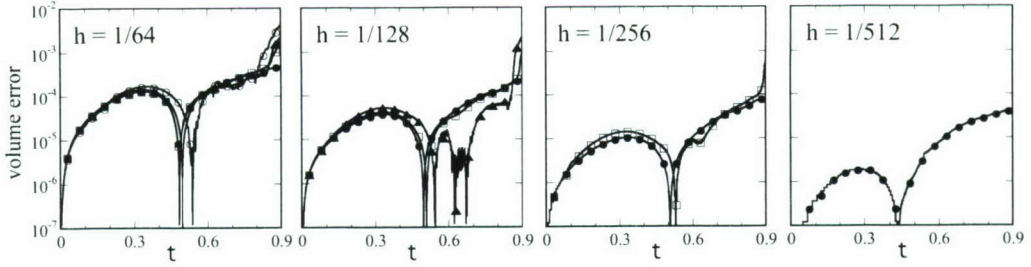


FIGURE 12. Rayleigh-Taylor instability normalized volume error, $h = 1/64$, $h = 1/128$, $h = 1/256$, and $h = 1/512$ (from left to right) for $h_G = 1/64$ (open circle), $h_G = 1/128$ (filled triangle), $h_G = 1/256$ (open box), and $h_G = 1/512$ (filled circle).

To ascertain the volume/mass conservation properties of the method, Fig. 12 depicts the normalized volume error, defined as

$$E_V(t) = \frac{|\sum_{cv} \psi_{cv}(t)V_{cv} - \sum_{cv} \psi_{cv}(t=0)V_{cv}|}{\sum_{cv} \psi_{cv}(t=0)V_{cv}}. \quad (4.1)$$

Except for $h_G = 1/512$, all solutions show an increase in error at late times. This is due to the disappearance of the thin connecting bridge. Also, at constant flow solver grid size h and G -grid refinement, the volume errors converge to a non-zero value. Furthermore, the converged error decreases when increasing the flow solver grid resolution. This indicates the source of this error: because \mathbf{u}_{i_G} is used to solve the level set transport equation (Eq. 2.4), \mathbf{u} is not discretely divergence free. An improved interpolation scheme to determine \mathbf{u}_{i_G} could therefore eliminate this error and will be investigated in the future. Nonetheless, the observed volume errors on fine G -grids are very small and well within acceptable limits.

5. Conclusion and future work

A balanced force RLSG method has been presented for structured and unstructured flow solver grids. The method ensures machine precision zero spurious currents for arbitrary density ratios if the curvature can be evaluated exactly. Spurious current magnitude is directly related to errors in the evaluation of the interface curvature. To minimize spurious currents in actual applications, a robust second-order converging curvature evaluation scheme has been presented that significantly reduces spurious currents compared to the traditional first-order converging curvature evaluation schemes. The performance and good volume conservation properties of the RLSG method have been demonstrated using the Rayleigh-Taylor instability.

Future work will focus on enhancing the velocity interpolation scheme from the currently employed tri-linear or tri-cubic interpolation. Furthermore, subgrid models for surface tension-induced subgrid velocities are necessary when extremely refining the G -grid. Finally, the employed methods will be used to study the primary atomization of liquid jets and sheets to help develop a LES-type model for primary atomization.

Acknowledgments

The author would like to thank Olivier Desjardins, Dokyun Kim, Guillaume Blanquart, and Frank Ham for many fruitful discussions. The work was supported by the Department of Energy's ASC program.

REFERENCES

ADALSTEINSSON, D. & SETHIAN, J. A. 1999 The fast construction of extension velocities in level set methods. *J. Comput. Phys.* **148**, 2–22.

ALONSO, J. J., HAHN, S., HAM, F., HERRMANN, M., IACCARINO., G., KALITZIN, G., LEGRESLEY, P., MATTSSON, K., MEDIC, G., MOIN, P., PITSCH, H., SCHLUTER, J., SVARD, M., DER WEIDE, E. V., YOU, D., & WU, X. 2006 CHIMPS: A high-performance scalable module for multi-physics simulation. In *42nd AIAA/ASME/SAE/ASEE Joint Propulsion Conference & Exhibit*, AIAA-Paper 2006-5274.

BELL, J. B. & MARCUS, D. L. 1992 A second-order projection method for variable-density flows. *J. Comput. Phys.* **101**, 334–348.

BRACKBILL, J. U., KOTHE, D. B., & ZEMACH, C. 1992 A continuum method for modeling surface tension. *J. Comput. Phys.* **100**, 335–354.

CHOPP, D. L. 2001 Some improvements of the fast marching method. *SIAM J. Sci. Comput.* **23**, 230–244.

ENGQUIST, B., TORNBERG, A.-K., & TSAI, R. 2005 Discretization of dirac delta functions in level set methods. *J. Comput. Phys.* **207** (207), 28–51.

FEDKIW, R., ASLAM, T., MERRIMAN, B., & OSHER, S. 1999 A non-oscillatory Eulerian approach to interfaces in multimaterial flows (the ghost fluid method). *J. Comput. Phys.* **152**, 457–492.

FRANCOIS, M. M., CUMMINS, S. J., DENDY, E. D., KOTHE, D. B., SICILIAN, J. M., & WILLIAMS, M. W. 2006 A balanced-force algorithm for continuous and sharp interfacial surface tension models within a volume tracking framework. *J. Comput. Phys.* **213**, 141–173.

GOMEZ, P., HERNANDEZ, J., & LOPEZ, J. 2005 On the reinitialization procedure in a narrow-band locally refined level set method for interfacial flows. *Int. J. Numer. Meth. Eng.* **63** (10), 1478–1512.

GUEYFFIER, D., LI, J., NADIM, A., SCARDOVELLI, S., & ZALESKI, S. 1999 Volume of Fluid interface tracking with smoothed surface stress methods for three-dimensional flows. *J. Comput. Phys.* **152**, 423–456.

HERRMANN, M. 2004 On mass conservation and desingularization of the level set/vortex sheet method. In *Annual Research Briefs-2004*. Stanford, CA: Center for Turbulence Research.

HERRMANN, M. 2005 Refined level set grid method for tracking interfaces. In *Annual Research Briefs-2005*, 3–18. Center for Turbulence Research.

HERRMANN, M. 2006 Simulating two-phase flows using the refined level set grid method. In *ILASS Americas 19th Annual Conference on Liquid Atomization and Spray Systems*. ILASS Americas.

KIM, D. & CHOI, H. 2000 A second-order time-accurate finite volume method for unsteady incompressible flow on hybrid unstructured grids. *J. Comput. Phys.* **162** (2), 411–428.

LEKIEN, F. & MARSDEN, J. 2005 Tricubic interpolation in three dimensions. *Int. J. Numer. Meth. Engng.* **63**, 455–471.

MAHESH, K., CONSTANTINESCU, G., & MOIN, P. 2004 A numerical method for large-eddy simulation in complex geometries. *J. Comput. Phys.* **197** (1), 215–240.

MARMOTTANT, P. & VILLERMAUX, E. 2004 On spray formation. *J. Fluid Mech.* **498**, 73–111.

PENG, D., MERRIMAN, B., OSHER, S., ZHAO, H., & KANG, M. 1999 A PDE-based fast local level set method. *J. Comput. Phys.* **155**, 410–438.

PESKIN, C. S. 1977 Numerical analysis of blood flow in the heart. *J. Comput. Phys.* **25**, 220–252.

VAN DER PIJL, S. P., SEGAL, A., & VUIK, C. 2005 A mass-conserving level-set method for modelling of multi-phase flows. *Int. J. Numer. Meth. Fluids* **47**, 339–361.

POPINET, S. & ZALESKI, S. 1999 A front-tracking algorithm for accurate representation of surface tension. *Int. J. Numer. Meth. Fluids* **30**, 775–793.

PUCKETT, E. G., ALMGREN, A. S., BELL, J. B., MARCUS, D. L., & RIDER, W. J. 1997 A high-order projection method for tracking fluid interfaces in variable density incompressible flows. *J. Comput. Phys.* **130**, 269–282.

SCARDOVELLI, R. & ZALESKI, S. 1999 Direct numerical simulation of free-surface and interfacial flow. *Annu. Rev. Fluid Mech.* **31**, 567–603.

SETHIAN, J. A. 1999 *Level Set Methods and Fast Marching Methods*, 2nd edn. Cambridge, UK: Cambridge University Press.

SUSSMAN, M. 2003 A second order coupled level set and volume-of-fluid method for computing growth and collapse of vapor bubbles. *J. Comput. Phys.* **187** (1), 110–136.

SUSSMAN, M., SMEREKA, P., & OSHER, S. 1994 A level set method for computing solutions to incompressible two-phase flow. *J. Comput. Phys.* **114**, 146.

SUTHERLAND, I. E. & HODGMAN, G. W. 1974 Reentrant polygon clipping. *Comm. ACM* **17** (1), 32–42.

TRYGGVASON, G., BUNNER, B., ESMAEELI, A., JURIC, D., AL-RAWAHI, N., TAUBER, W., HAN, J., NAS, S., & JAN, Y.-J. 2001 A front-tracking method for the computations of multiphase flow. *J. Comput. Phys.* **169**, 708–759.

WILLIAMS, M. W., KOTHE, D. B., & PUCKETT, E. G. 1999 Convergence and accuracy of continuum surface tension models. In *Fluid Dynamics at Interfaces* (ed. W. Shyy & R. Narayanan), pp. 294–305. Cambridge: Cambridge University Press.

YOUNG, Y.-N., HAM, F. E., HERRMANN, M., & MANSOUR, N. 2002 Interaction between turbulent flow and free surfaces. In *Annual Research Briefs-2002* (ed. P. Bradshaw), 301–312. Stanford, CA: Center for Turbulence Research.

Toward two-phase simulation of the primary breakup of a round liquid jet by a coaxial flow of gas

By D. Kim, O. Desjardins, M. Herrmann AND P. Moin

1. Motivation and objectives

Two-phase flows are very common in nature and technical processes such as ocean waves, tire splash, and combustion devices. Among them, the atomization of liquid jets or sheets by gas streams has received much attention due to its direct applicability to the design of combustion chambers. However, it is challenging to model such a phenomenon because of its complex nature. In a combustion chamber, fuel is typically injected as a liquid and atomized subsequently to enhance evaporation. Combustion then occurs in the gaseous phase. Atomization involves a sudden jump in the density across the interface, surface tension force on the interface, topological changes of the interface, and phase transition. Moreover, atomization of the liquid jet usually occurs in a turbulent environment.

The atomization of a liquid jet can be considered as two subsequent processes, i.e., primary atomization followed by secondary atomization. The primary atomization is the initial breakup of the liquid jet into large and small liquid structures close to the injection nozzle. It involves complex interface topology of large coherent liquid structures. The secondary atomization is the subsequent breakup into smaller drops forming sprays. For the secondary atomization, a number of breakup models for liquid drops have been proposed and validated (Reitz 1987; Tanner 1997; Apte *et al.* 2003). Using these breakup models, there have been several attempts to simulate a liquid jet injected into a chamber by representing the liquid core by a collection of liquid drops. However, the results are easily changed by the initial drop size distribution, which is unknown without appropriate primary atomization modelling. Although primary atomization is necessary to simulate the whole atomization process, modelling still remains a major unresolved problem. It is, therefore, crucial to develop a feasible high-fidelity computational tool for simulation of the whole primary and secondary atomization process.

In this study, we conduct numerical simulations to investigate the breakup mechanism of a liquid jet surrounded by a coaxial flow of gas. A Refined Level Set Grid (RLSG) method (Herrmann 2004; 2005; 2006) coupled to a Lagrangian spray model (Apte *et al.* 2003) is used to capture the whole breakup process of the liquid jet. In the near field of the liquid jet, where the primary breakup occurs, motion and topological changes of the liquid jet are described by the RLSG method. In this region, a liquid jet consists of the core and ligaments, which subsequently break into drops of various sizes. The drops generated by the primary breakup are transferred to a Lagrangian spray model in order to describe the secondary breakup process.

2. Numerical methods

2.1. Governing equations

The Navier-Stokes equations for incompressible, immiscible, two-phase flow are described as

$$\rho \frac{\partial \mathbf{u}}{\partial t} + \rho \mathbf{u} \cdot \nabla \mathbf{u} = -\nabla p + \nabla \cdot \tau + \mathbf{T}_\sigma \quad (2.1)$$

$$\nabla \cdot \mathbf{u} = 0, \quad (2.2)$$

where ρ is the density, p is the pressure, τ is the viscous stress tensor, and \mathbf{T}_σ is the surface tension force.

A level set method is applied to track the location of the phase interface. The location and time evolution of the phase interface are described by the level set equation:

$$\frac{\partial G}{\partial t} + \mathbf{u} \cdot \nabla G = 0, \quad (2.3)$$

where the isosurface $G = 0$ defines the location of the interface, $G > 0$ in the liquid, and $G < 0$ in the gas phase. In the computational domain, G is set to be a signed distance function to the interface:

$$|\nabla G| = 1. \quad (2.4)$$

The interface normal vector \mathbf{n} and the interface curvature κ can be calculated as

$$\mathbf{n} = \frac{\nabla G}{|\nabla G|}, \quad (2.5)$$

$$\kappa = \nabla \cdot \mathbf{n}. \quad (2.6)$$

In this paper, we used the RLSG method to solve the coupled level set equations (2.3, 2.4). The level set transport equation (2.3) is solved on a separate refined G-grid using fifth-order WENO scheme (Jiang & Peng 2000) with a third-order TVD Runge-Kutta time discretization (Shu & Osher 1989). It is coupled to the flow solver through \mathbf{u} . The velocity \mathbf{u} on the fine G-grid is obtained by trilinear interpolation from the flow solver grid. Reinitialization (2.4) is solved by an iterative procedure using a fifth-order WENO scheme and a first-order pseudo-time integration (Sussmann *et al.* 1994; Peng *et al.* 1999). The numerical details about the RLSG method are described in Herrmann (2005; 2006).

In order to solve the flow-field, an unstructured grid solver is used based on a balanced force finite volume formulation of the variable density Navier-Stokes equations (Mahesh *et al.* 2004; Ham & Iaccarino 2004; Herrmann 2006). The Navier-Stokes equations (2.1) are coupled to the level set equation (2.3) through the density, viscosity, and surface tension force. The density ρ and the viscosity μ in a cell i are defined as volume averaged quantities:

$$\rho_i = \psi_i \rho_l + (1 - \psi_i) \rho_g \quad (2.7)$$

$$\mu_i = \psi_i \mu_l + (1 - \psi_i) \mu_g, \quad (2.8)$$

where the subscript l denotes quantities in the liquid and the subscript g denotes those in the gas phase. The flow solver volume fraction ψ is defined as

$$\psi_i = \frac{1}{V_i} \int_{V_i} H(G) dV, \quad (2.9)$$

where H is the Heaviside function and V_i is the control volume of the flow solver grid cell. In the RLSG method, this integral is calculated on the G-grid as

$$\frac{1}{V_i} \int_{V_i} H(G) dV = \frac{\sum_{i_G} \psi_{i_G} V_{i,i_G}}{\sum_{i_G} V_{i,i_G}} \quad (2.10)$$

where V_{i,i_G} is the joined intersection volume of the G-grid cell i_G and the flow solver control volume V_i , and the G-grid volume fraction ψ_{i_G} is calculated using an analytical formula developed by van der Pijl *et al.* (2005),

$$\psi_{i_G} = f(G_{i_G}, \mathbf{n}_{i_G}). \quad (2.11)$$

The surface tension force \mathbf{T}_σ is calculated as

$$\mathbf{T}_{\sigma,i} = \int_{V_i} \sigma \kappa \nabla \psi d\mathbf{x}, \quad (2.12)$$

where σ is the surface tension force coefficient. The curvature κ is transferred from the G-grid to the flow solver grid,

$$\kappa = \frac{\sum_{i_G} V_{i,i_G} \delta_{i_G} \kappa_{i_G}}{\sum_{i_G} V_{i,i_G} \delta_{i_G}}, \quad (2.13)$$

where $\delta_{i_G} = 0$ if $\psi_{i_G} = 0$ or $\psi_{i_G} = 1$, and $\delta_{i_G} = 1$ otherwise. Details of the balanced force algorithm and curvature are described in Herrmann (2006).

2.2. Coupling to flow solver

In this work, the RLSG method has been coded in a separate solver called LIT (Level set Interface Tracker). All communication between the level set solver and the flow solver is handled by a coupling software, named CHIMPS (Coupler for High-performance Integrated Multi-Physics Simulations, Alonso *et al.* 2006). CHIMPS is used for all interpolation of velocity vectors from the flow solver grid to the G-grid and all volume integration from the G-grid to the flow solver grid. The advantage of this approach is that any flow solver can be coupled to LIT. In this study, LIT has been coupled to CDP, a fully unstructured, LES flow solver (Ham & Iaccarino 2004; Mahesh *et al.* 2005; Herrmann 2006).

2.3. Drop transfer

A vast number of atomized drops can be generated in the atomization process of liquid jets. Thus, it becomes prohibitively expensive to resolve every drop by the level set scalar. Instead, Lagrangian spray models are more adequate to describe small scale liquid drops having simple geometry. In this study, broken small liquid drops are identified, removed from the level set representation, and inserted as liquid drops into a Lagrangian spray model if they satisfy the two criteria presented below.

In order to identify the broken-off drops, special care must be taken because broken liquid structures can span different blocks on different processors. The drop identification algorithm with multi-block domain decomposition is fully explained in Herrmann (2005).

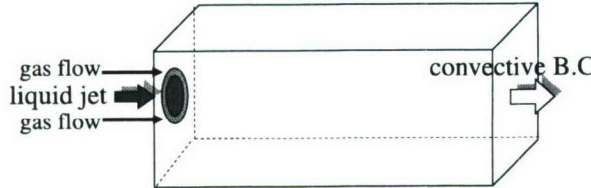


FIGURE 1. Computational domain of a round liquid jet surrounded by a coaxial flow of gas.

Using this algorithm, the volume of a broken drop and its center of mass can be easily calculated.

As previously mentioned, there are two criteria for drop transfer. The first one states that the drop volume V_D has to be smaller than the volume criterion for a Lagrangian spray model,

$$V_D \leq V_{D_{max}}, \quad (2.14)$$

with $V_{D_{max}}$ proportional to the volume of the local flow solver grid cell volume V_i . Since the RLSG method can provide subgrid resolution with respect to the flow solver grid, broken-off liquid structures whose volumes are less than V_i are still resolved, can be identified and are candidates for Lagrangian spray tracking. The second criterion is a shape criterion. Although a broken-off liquid structure might satisfy the above volume criterion, it should not be transferred to the Lagrangian spray model if its shape is not spherical, for example, if it is a thin ligament. The spherical shape criterion is defined as

$$r_{max} < 2r_{sphere}, \quad (2.15)$$

where r_{max} is the maximum distance between the center of mass and the surface of the drop and r_{sphere} is the radius of a sphere such that $4/3\pi r_{sphere}^3 = V_D$. If both criteria are satisfied, the liquid drop is removed from the level set tracked representation and inserted into the Lagrangian spray model, preserving its mass, center of mass, and momentum.

3. Results

When a liquid jet flows in a faster coaxial gas stream, different atomization regimes are observed depending on Weber numbers and the velocity difference between the liquid and gas (Farago & Chigier 1992; Zaleski *et al.* 1996). At low gas velocity, a liquid jet wanders in the gas stream, inducing bags and rims. For higher gas velocities, the liquid jet is no longer deformed as a whole, but it is peeled off at its surface forming ligaments. These ligaments are broken into small liquid droplets. The typical droplet size decreases with the velocity difference (Yatsuyanagi *et al.* 1994; Lasheras *et al.* 1998). The drop size distribution shows an exponential tail characteristic of broad size statistics and is very important for industrial applications.

Recently, Marmottant and Villermiaux (2004) performed various experiments on the atomization of a liquid jet when a gas stream flows coaxial to its surface. Their experimental findings suggest that two successive instabilities are responsible for the disintegration of the liquid jet into dispersed droplets. First, a Kelvin-Helmholtz type instability triggers axisymmetric modulations on the liquid by shear between the slow liquid and the fast gas stream. Then, these axisymmetric waves undergo transverse azimuthal modulations when the gas velocity goes beyond a critical velocity. This azimuthal secondary instabil-

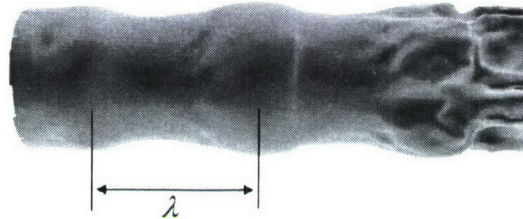


FIGURE 2. Axisymmetric modulation on the liquid surface at the initial stage of the breakup.

ity of the axisymmetric waves was explained by the Rayleigh-Taylor instability in their study (Marmottant & Villermaux 2004). At azimuthal wave crests, liquid ligaments are produced, elongated by the gas stream, and finally broken into droplets.

In this section, we investigate these two instabilities responsible for the droplet formation from a round liquid jet and examine the statistical property of the resulting droplets for different G-grid resolutions.

3.1. Computational details

A round liquid jet surrounded by a coaxial flow of gas is simulated as shown in Fig. 1. The liquid jet is injected at the center with the nozzle diameter D . The surrounding gas flows coaxially with the annular gap thickness h . The gap thickness h is $0.3D$. In this paper, the jet parameters are determined following the experiment of Marmottant & Villermaux (2004). However, the density ratio of the liquid and gas is limited to 5. The Reynolds and Weber numbers of the gas based on the gap thickness h are $Re_g = u_g h / \nu_g = 3770$ and $We_g = \rho_g h u_g^2 / \sigma = 34$, respectively, which are the same values in the experiment. The Reynolds and Weber numbers of the liquid are $Re_l = u_l D / \nu_l = 295$ and $We_l = \rho_l D u_l^2 / \sigma = 0.6$, respectively, based on the liquid jet velocity and D . The momentum ratio used is $\rho_l u_l^2 / \rho_g u_g^2 = 190$. An error function is used for the velocity profile of the gas and the liquid at inlets. The inlet boundary-layer thickness of the gas δ_g is $0.096D$; that of the liquid δ_l is determined by

$$\delta_l = \sqrt{\frac{\mu_l \rho_g}{\mu_g \rho_l}} \delta_g. \quad (3.1)$$

The boundary-layer thickness used in this study is larger than that in the experiment of Marmottant & Villermaux (2004) due to the available grid resolution.

The size of the computational domain used is $-2.5 < x/D < 2.5$, $-2.5 < y/D < 2.5$, and $0 < z/D < 8$. Slip boundary conditions are used except at the jet inlet and exit boundary, and convective boundary conditions are used for the exit boundary. Uniform Cartesian meshes are used for the flow solver and level set solver grids. The grid size for the flow solver is $\Delta x/D = 0.02$. For the level set solver, we used two different G-grids: $\Delta_G/D = 0.02$ and $\Delta_G/D = 0.01$. The velocity profiles of the gas and the liquid at the inlet are used for the initial velocity field along the jet direction.

3.2. Kelvin-Helmholtz instability

Figure 2 shows the axisymmetric modulation on the liquid jet at the initial stage. Two fluids having different velocities are inherently unstable, producing an instability of the Kelvin-Helmholtz type. From the stability analysis by Villermaux (1998), the selected

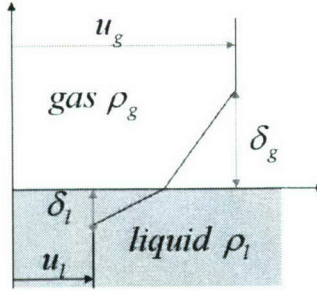


FIGURE 3. Linear velocity profile used in the Kelvin-Helmholtz stability analysis.

wavelength and frequency at the maximum growth rate are expressed as a function of the density ratio and gas boundary-layer thickness δ_g when a linear velocity profile is assumed (Fig. 3):

$$\lambda_{kh} = \frac{2\pi}{0.8} F\left(\frac{\rho_l}{\rho_g}\right) \delta_g, \quad (3.2)$$

where $F(\rho_l/\rho_g)$ is

$$F\left(\frac{\rho_l}{\rho_g}\right) = \frac{5}{6} - \frac{1}{6(\rho_l/\rho_g)} + \frac{\sqrt{5 + 13(\rho_l/\rho_g) - 37(\rho_l/\rho_g)^2 + 27(\rho_l/\rho_g)^3}}{6\sqrt{2}(\rho_l/\rho_g)}. \quad (3.3)$$

The group velocity of the most amplified wavenumber is well estimated by a convection velocity u_c as

$$u_c = \frac{\sqrt{\rho_1}u_1 + \sqrt{\rho_2}u_2}{\sqrt{\rho_1} + \sqrt{\rho_2}}. \quad (3.4)$$

Thus, the period of the surface modulation T_{kh} is given by

$$T_{kh} = \frac{1}{f_{kh}} = \frac{u_c}{\lambda_{kh}}. \quad (3.5)$$

From the computational result, the wavelength is measured as the mean distance between the highest point of the primary waves and the frequency is measured by calculating the mean velocity of the wave crests. Table 1 shows the wavelength and period divided by those obtained from the stability analysis, respectively. Experimental values from Marmottant & Villermaux (2004) are much smaller than those from the stability analysis since the velocity profile is not linear in the experiments and the effective linear boundary-layer thickness used in the stability analysis is much larger than the experiment as mentioned in Marmottant & Villermaux (2004). However, the boundary-layer thickness used in this study is 4 times larger than the experiment. Therefore, our results are much closer to the stability analysis than the experiment.

3.3. *Raleigh-Taylor instability*

After the onset of shear instability causing axisymmetric waves, transverse azimuthal modulations appear as shown in Fig. 4. Several mechanisms have been suggested to explain these modulations. Villermaux and Clanet (2002) have proposed that transient

Table 1. Comparison of the wavelength and period of the primary modulation.

	Experiments (Marmottant <i>et al.</i> 2004)	Present study	Stability analysis
Wavelength λ/λ_{kh}	0.29	0.83	1.0
Period T/T_{kh}	0.33	0.85	1.0

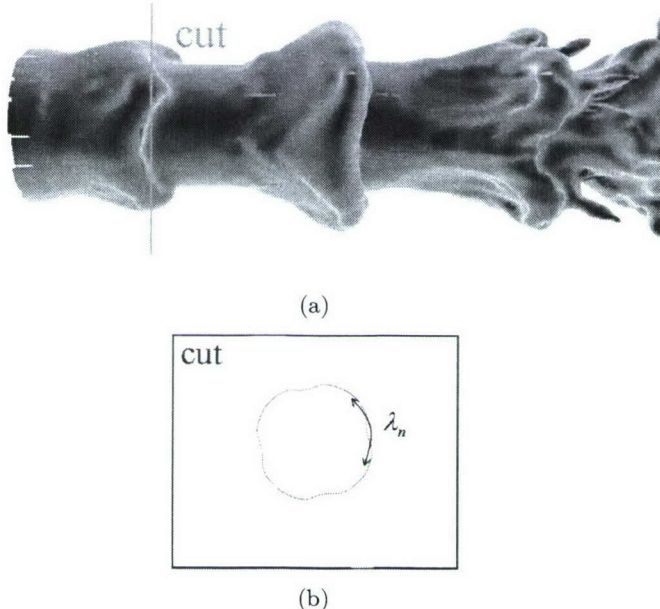


FIGURE 4. (a) Transverse azimuthal modulations on the liquid surface; (b) liquid interface in the cutting plane.

acceleration in the direction normal to the liquid at the rims triggers a Rayleigh-Taylor instability, which produces the azimuthal perturbation.

The most amplified wavenumber k_m can be calculated by (Chandrasekhar 1961)

$$k_m = \left[\frac{(\rho_2 - \rho_1)g}{3\sigma} \right]^{1/2}, \quad (3.6)$$

where g is the maximum acceleration of the primary wave expressed as

$$g = a \left(2\pi \frac{u_c - u_1}{\lambda_{kh}} \right)^2, \quad (3.7)$$

with a the amplitude of the primary wave. By this stability analysis, the theoretical wavelength for our simulated condition is approximately $0.72D$, which means four crests are triggered on the primary wave rims. As shown in Fig. 4(b), our computational result is consistent with the stability analysis showing exactly four crests.

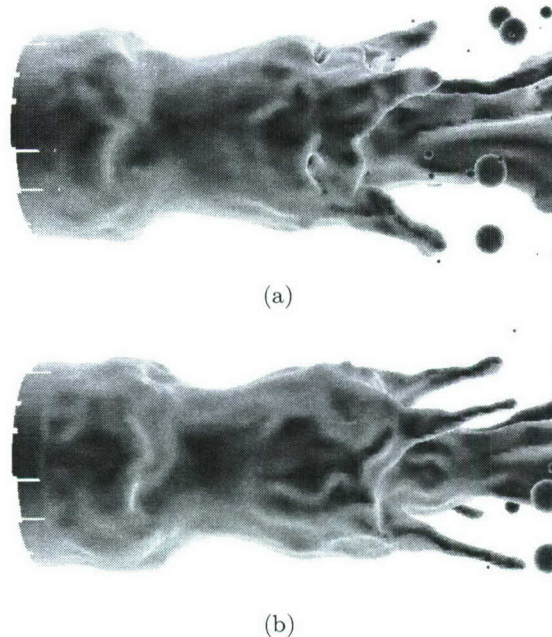


FIGURE 5. (a) Development of the ligaments; (b) further elongation of the ligaments.

3.4. Ligament development and breakup

The transverse azimuthal modulations grow in amplitude producing small ligaments at the wave crests. These are elongated further by the gas stream and their diameter decreases as shown in Fig. 5. The ligaments are finally pinched off, usually at their base, and broken into liquid droplets. When the ligaments are detached, a capillary instability grows in a very short time and breaks them into several droplets of different sizes (Fig. 6). These droplets are automatically transferred to the Lagrangian spray model through our drop transfer algorithm (Fig. 6(b)).

3.5. Drop formation

Several drops are formed from the detached ligaments. In natural spray formation, drops, such as rain drops and fuel droplets, have a broad range of sizes. The statistical drop size distribution has been known to show an exponential tail shape.

In the computational simulations, level set tracked liquid droplets smaller than the G-grid resolution cannot be resolved correctly. Thus, drop size distributions at small scales of the order of the G-grid resolution can be expected to be dependent on the grid resolution and should be considered a numerical artifact. It is, therefore, important to determine a converged drop diameter d_c , i.e., the drop size above which the drop size distribution is statistically converged and grid-independent.

Figure 7 shows the drop size distribution with two different G-grid resolutions. The flow solver grid resolution is fixed to $\Delta x/D = 0.02$. As shown in Fig. 7, the peaks in the number of drops show a large difference between the two grids. However, the drop size distributions at larger diameters have a similar shape. Thus, we can consider the converged drop diameter to be approximately $d_c = 0.04D$. In terms of the G-grid resolution $\Delta_G = 0.02$, the converged drop diameter d_c thus corresponds to $d_c = 2\Delta_G$. Any drops produced with a diameter smaller than d_c ought to be considered a numerical

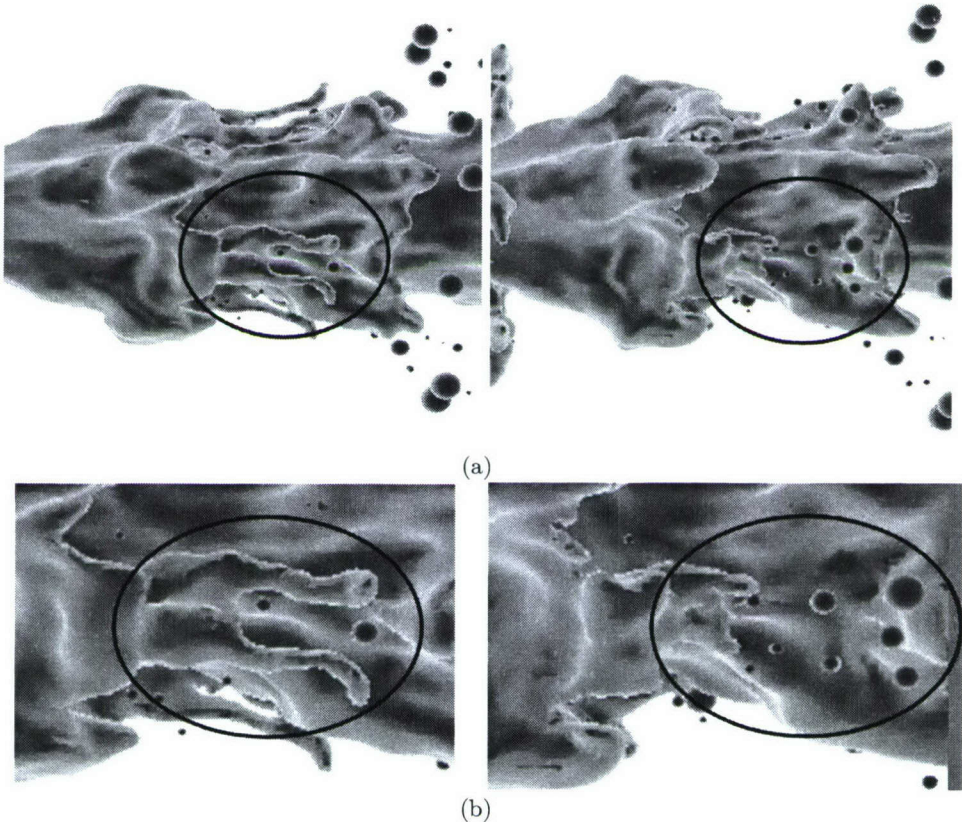


FIGURE 6. (a) Formation of the droplet from the ligaments; (b) zoom on the ligament-breakup region: liquid jet structures such as ligaments are tracked by the level set method and shaded spherical objects are Lagrangian sprays.

artifact and cannot be trusted. Therefore, the concept of a converged drop diameter provides an important and useful reference for computational simulations.

4. Conclusions and future work

The atomization of a liquid jet surrounded by a coaxial flow of gas was numerically simulated using a Refined Level Set Grid (RLSG) method with a Lagrangian spray model. The characteristics of the underlying breakup mechanism have been examined to show the validity of the simulation. Our results are consistent with the experimentally observed physical mechanisms and the corresponding stability analysis. The drop-size distribution of the resulting spray after breakup exhibits grid-independent results for drops resolved by at least two G-grid cells per diameter. This proves the applicability of our method for simulations of the atomization process of liquid jets.

In this work, the density ratio between the gas and liquid was limited to 5. Future work will focus on the atomization of coaxially atomized liquid jets with higher density ratio and thin boundary-layer thickness using the same parameters as the experiments of Marmottant & Villermaux (2004).

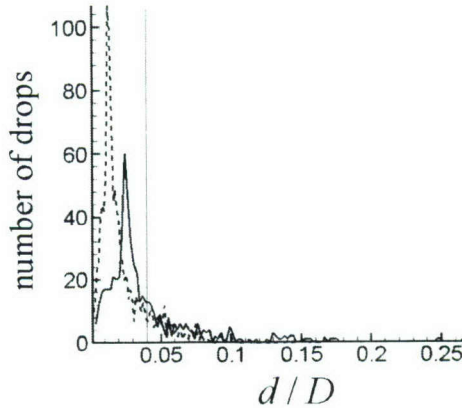


FIGURE 7. Drop size distribution with two different G-grid sizes: —, $\Delta_G = 0.02$; ---, $\Delta_G = 0.01$.

Acknowledgments

The work presented in this paper was supported by the Department of Energy's ASC program. The authors also would like to thank F. Ham and S. Apte.

REFERENCES

ALONSO, J. J., HAHN, S., HAM, F., HERRMANN, M., IACCARINO, G., KALITZIN, G., LEGRESLEY, P., MATTSSON, K., MEDIC, G., MOIN, P., PITSCH, H., SCHLÜTER, J., SVÄRD, M., VAN DER WEIDE, E., YOU, D. & WU, X. 2006 CHIMPS: A high-performance scalable module for multi-physics simulations. *AIAA Paper 2006-5274*.

APTE, S. V., GOROKHOVSKI, M. & MOIN, P. 2003 LES of atomizing spray with stochastic modeling of secondary breakup *Int. J. Mult. Flow* **29**, 1503–1522.

CHANDRASEKHAR, S. 1961 Hydrodynamic and hydromagnetic stability. *Dover*.

FARAGÓ, Z. & CHIGIER, N. 1992 Morphological classification of disintegration of round liquid jets in a coaxial air stream. *Atom. Sprays* **2**, 137–153.

HAM, F. & IACCARINO, G. 2004 Energy conservation in collocated discretization schemes on unstructured meshes. *Annu. Res. Briefs 2004*, Center for Turbulence Research, 3–14.

HERRMANN, M. 2004 On mass conservation and desingularization of the Level Set/Vortex Sheet method. *Annual Research Briefs 2004*, Center for Turbulence Research, 15–30.

HERRMANN, M. 2005 Refined Level Set Grid method for tracking interfaces. *Annual Research Briefs 2005*, Center for Turbulence Research, 3–18.

HERRMANN, M. 2006 A balanced force refined level set grid method for two-phase flows on unstructured flow solver grids. *Annual Research Briefs 2006*, Center for Turbulence Research.

JIANG, G.-S. & PENG, D. 2000 Weighted ENO schemes for Hamilton-Jacobi equations. *SIAM J. Sci. Comp.* **21**, 2126–2143.

LASHERAS, J., VILLERMAUX, E. & HOPFINGER, E. 1998 Breakup and atomization of a round water jet by a high-speed annular jet. *J. Fluid Mech.* **357**, 351–379.

MAHESH, K., CONSTANTINESCU, G. & MOIN, P. 2004 A numerical method for large eddy simulation in complex geometries. *J. Comput. Phys.* **197**, 215–240.

MARMOTTANT, P. & VILLERMAUX, E. 2004 On spray formation *J. Fluid Mech.* **498**, 73–111.

PENG, D., MERRIMAN, B., OSHER, S., ZHAO, H. & KANG, M. 1999 A PDE-based fast local level set method. *J. Comput. Phys.* **155**, 410–438.

SHU, C.-W. & OSHER, S. 1989 Efficient implementation of essentially non-oscillatory shock-capturing schemes. *J. Comput. Phys.* **77**, 439–471.

VILLERMAUX, E. 1998 On the role of viscosity in shear instabilities. *Phys. Fluids* **10**, 368–373.

VAN DER PIKL, S. P., SEGAL, A. & VUIK, C. 2005 A mass-conserving level-set method for modelling of multi-phase flows. *Int. J. Numer. Meth. Fluids* **47**, 339–361.

YATSUYANAGI, N., SAKAMOTO, H. & SATO, K. 1994 Atomization characteristics of liquid jets injected into a high-velocity flow field. *Atom. Sprays* **4**, 451–471.

ZALESKI, S., LI, J., SCARDOVELLI, R. & ZANETTI, G. 1996 Direct simulation of multiphase flows with density variations. In *Colloque IUTAM on Variable Density Low Speed Turbulent Flows, Marseille 8–10 Juillet 1996* (ed. L. Fulachier & F. Anselmet). Kluwer.

Stable and high-order accurate finite difference schemes on singular grids

By M. Svärd AND E. van der Weide

1. Motivation and objectives

The use of finite difference methods on curvilinear grids is an established computational method and the technique has been thoroughly analyzed with respect to accuracy and stability. However, coordinate mappings are usually assumed to be smooth and topology conserving, such that a smooth mapping to a square grid exists. For practical applications it is not always possible to construct grids with these properties and singularities are sometimes present in the metric coefficients. Yet, it is desirable to have a robust computational method on such grids and obtain high-quality solutions.

In particular, we will study the grid shown in Figure 1, which we will refer to as the circle segment. The circle segment can be viewed as the mapping from a Cartesian grid where one side is collapsed into a point.

We will use a certain kind of finite difference schemes satisfying a summation-by-parts (SBP) rule. In combination with the Simultaneous Approximation Term technique (SAT), these schemes can be proven stable using energy estimates. The SAT technique use penalty terms to impose the boundary conditions weakly. (For SBP-SAT theory see Carpenter et al. 1994; Carpenter & Nordström 1999; Kreiss & Scherer 1974; Mattsson et al. 2006; Nordström & Carpenter 1999; Strand 1994; Svärd 2004; Svärd & Mattsson 2005; Svärd & Nordström 2006.) For such schemes, we will propose two different ways to recover design order accuracy despite singularities in the grid. The first is designed for SBP-SAT schemes and can be used at boundaries where boundary conditions are supplied. The other can be applied to any boundary and any stable finite difference scheme.

2. Summation-by-parts discretization

Before studying singular grid transformations, we introduce the basic concepts of SBP-SAT schemes. Discretize $0 \leq x \leq 1$ using $N+1$ evenly distributed grid points with spacing h . Introduce the scalar grid function $v(t) = (v_0(t), \dots, v_N(t))^T$. Then the first derivative is approximated by $P^{-1}Qv$, where P is a positive definite (symmetric) matrix. P is used to define a discrete l_2 equivalent norm, $\|v\|_P^2 = v^T P v$. In our particular schemes P is diagonal, which is a necessary requirement for stability on curvilinear grids. (See Svärd 2004.) Q is skew-symmetric almost everywhere and $Q + Q^T = \text{diag}(-1, 0, \dots, 0, 1) = B$. In two space dimensions, we use a subscript x or y to distinguish between operators in the respective directions.

As a model problem for the non-linear two-dimensional Euler equations, we consider,

$$u_t + a(x, y)u_x + b(x, y)u_y = 0, \quad 0 \leq x, y \leq 1, \quad t \geq 0, \quad (2.1)$$

where $a(x, y), b(x, y) > 0$. The equation is subject to the following boundary conditions,

$$u(0, y, t) = g_1(y, t), \quad u(x, 0, t) = g_2(x, t).$$

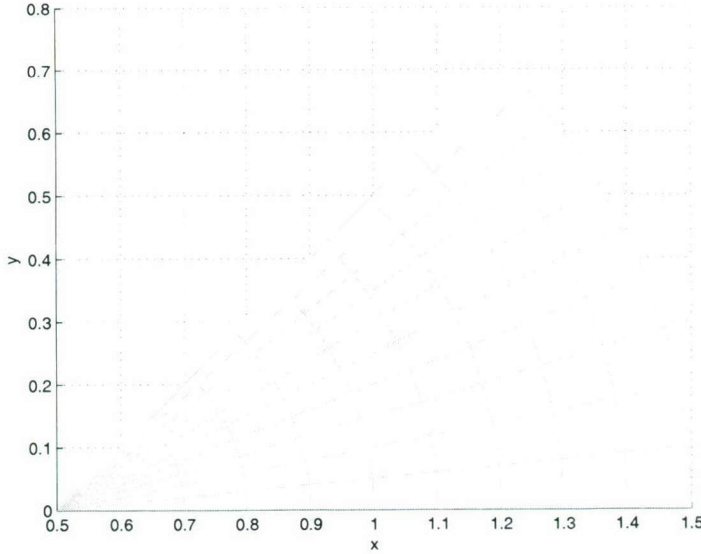


FIGURE 1. A grid with a collapsed side.

We discretize the equation using N points in the x -direction and M in the y -direction. We denote the grid sizes by $h_x = 1/N$ and $h_y = 1/M$. Let $v_{ij}(t)$ be the approximate solution of $u(x_i, y_j, t)$ and v be the vector $v = (v_{00}, v_{20}, \dots, v_{NM})$. Define $a_{ij} = a(x_i, y_j)$ and $b_{ij} = b(x_i, y_j)$ and distribute a_{ij} and b_{ij} on the diagonal of a matrix in the same way v_{ij} was distributed. Denote the resulting matrices A and B . The discretization of (2.1) can be written.

$$\begin{aligned} v_t + A(I \otimes D_x)v + B(D_y \otimes I)v = \\ \tau_1(I \otimes P^{-1}E_{0x})(v - G_1) + \tau_2(P^{-1}E_{0y} \otimes I)(v - G_2) \end{aligned} \quad (2.2)$$

where $E_{0y}v = (v_{0,0}, \dots, v_{N,0})^T$, $E_{0x} = (v_{0,0}, 0, \dots, v_{0,1}, 0, \dots, v_{0,M}, 0, \dots)^T$. The symbol \otimes denotes the Kronecker product. Moreover, G_1 and G_2 are vectors with $(G_1)_{0j} = g_1(y_j, t)$ and $(G_2)_{i0} = g_2(x_i, t)$ and 0 elsewhere.

To prove stability, we freeze the coefficients in A and B (and denote the respective scalars by a and b) and apply the energy method by multiplying by $v^T(P_y \otimes P_x)$,

$$\begin{aligned} (\|v\|_{P_{xy}}^2)_t + av^T(P_y \otimes B_x)v + bv^T(B_y \otimes P_x)v = \\ 2\tau_1(P_y \otimes E_{0x})(v - G_1) + 2\tau_2(E_{0y} \otimes P_x)(v - G_2) \end{aligned} \quad (2.3)$$

In (2.3) we have introduced the norm $\|v\|_{P_{xy}}^2 = v^T(P_y \otimes P_x)v$. Assuming homogeneous data, $\tau_1 \leq -a/2$ and $\tau_2 \leq b/2$ guarantees stability.

In this article, we will use two different schemes. The first is the commonly used central second-order stencil with a first order boundary closure. We will refer to this scheme as the 2-1 method. The other is the standard central difference fourth-order accurate scheme with a specific second-order boundary closure that enforces the SBP property. This scheme is called the 4-2 method. In both cases the norm P is diagonal and the precise form of operators (P and Q) can be found in Strand (1994).

2.1. Grid singularities

Consider,

$$u_t + au_x + bu_y = 0. \quad (2.4)$$

Assume $0 \leq a \leq 1$ and $b = -\sqrt{1 - a^2}$. The exact solution is, $u(x, t) = \sin(ax + by - t)$. Introduce $x = x(\xi, \eta)$, $y = y(\xi, \eta)$. Then (2.4) can be written as,

$$u_t + a(\xi_x u_\xi + \eta_x u_\eta) + b(\xi_y u_\xi + \eta_y u_\eta) = 0 \quad (2.5)$$

We define $J = (x_\xi y_\eta - x_\eta y_\xi)$ and obtain,

$$J\xi_x = y_\eta, \quad J\xi_y = -x_\eta, \quad J\eta_x = -y_\xi, \quad J\eta_y = x_\xi, \quad J = (\xi_x \eta_y - \xi_y \eta_x)^{-1}.$$

In the circle segment (Figure 1) we have ξ and η being the polar coordinates r and θ with the transformation $(x, y) = (r \cos(\theta) + 0.5, r \sin(\theta))$, $r = [0, 1]$, $\theta = [0, \pi/4]$. In this case, $\frac{\partial r}{\partial x} \sim 1$, $\frac{\partial r}{\partial y} \sim 1$, $\frac{\partial \theta}{\partial x} \sim \frac{1}{r}$, $\frac{\partial \theta}{\partial y} \sim \frac{1}{r}$. We rewrite equation (2.5),

$$u_t + \hat{a}u_\xi + \hat{b}u_\eta = 0, \quad \hat{a} = a\xi_x + b\xi_y, \quad \hat{b} = a\eta_x + b\eta_y. \quad (2.6)$$

Equation (2.6) is now a variable coefficient problem in ξ, η -space and we wish to employ the same discretization technique as for (2.1). However, \hat{a} and \hat{b} may now be singular.

We will study the effect of the following approximation. *At the singular point, approximate the indefinite metric coefficients with the coefficients of non-singular neighbors.* This is a first-order approximation of the metrics and the truncation error of the approximation of the equation reduces to first order at that point.

For the circle segment (Figure 1), we note that the transformation from the square makes $x = 0.5, y = 0$ a multi-valued point, since all the points on that side collapse to one. Let $(x(i, j), y(i, j))$, $i = 0..N, j = 0..M$ be a grid point. Then $(x(0, j), y(0, j)) = (x(0, k), y(0, k))$ for any valid combination j, k . With that notation, we choose,

$$y_\eta(x(0, j), y(0, j)) = y_\eta(x(1, j), y(1, j)), \quad x_\eta(x(0, j), y(0, j)) = x_\eta(x(1, j), y(1, j)).$$

3. Analysis

To study the basic mechanisms of singular coordinate transformations, we consider the one-dimensional problem,

$$u_t + u_x = 0, \quad t \geq 0, \quad 0 \leq x \leq \infty. \quad (3.1)$$

Introduce a coordinate transformation $x = x(\xi)$ such that,

$$u_t + \xi_x u_\xi = 0, \quad t \geq 0, \quad \xi_1 \leq \xi \leq \xi_2. \quad (3.2)$$

Let $x = \xi^2/2$ such that $x_\xi = \xi$. Furthermore, $\xi_x = x_\xi^{-1} = \frac{1}{\xi}$. This motivates the study of the following problem,

$$u_t + \frac{1}{x}u_x = 0, \quad t \geq 0, \quad 0 \leq x \leq \infty. \quad (3.3)$$

In this case the coefficient in front of u_x becomes singular as $x \rightarrow 0$. However, in the circle segment case it is the coefficient in front of the u_η that becomes singular as $r \rightarrow 0$. This fact suggests that also the following model problem is relevant to analyze.

$$u_t + \frac{1}{y}u_x = 0, \quad t \geq 0, \quad 0 \leq x, y \leq \infty. \quad (3.4)$$

We will also study,

$$u_t + au_x = 0, \quad t \geq 0, \quad 0 \leq x \leq \infty, \quad a > 0, \quad (3.5)$$

which will give us insight in the properties of the penalty imposition of boundary conditions. Equation (3.5) will be referred to as Model Problem 1, since it is the simplest to analyze. Moreover, (3.3) is denoted Model Problem 2 and (3.4) Model Problem 3.

3.1. Model problem 1

Consider (3.5) and assume that $u \rightarrow 0$ sufficiently fast as $x \rightarrow \infty$. We use the exact solution $u(x, t) = \sin(ax - t)$ to provide initial and boundary data. We discretize using the SBP-SAT methodology.

$$v_t + aP^{-1}Qv = \tau P^{-1}E_0(v - g) \quad (3.6)$$

where $E_0 = \text{diag}(1, 0, \dots, 0)$. Assuming homogeneous data, the energy estimate becomes,

$$(\|v\|_P^2)_t - av_0^2 + av_0^2 = 2\tau v_0^2. \quad (3.7)$$

For $\tau \leq -a/2$ the scheme is stable. The 2-1 scheme can be proven to have a globally second-order convergence rate and the 4-2 third order. (See Gustafsson 1975, 1981; Svärd & Nordström 2006.) We define the convergence rate, $q = |\log(e_1/e_2)/\log(h_1/h_2)|$ where e_1 and e_2 are the errors (in an appropriate norm) on two different grids with grid sizes h_1 and h_2 . The numerical solution using the two different schemes are computed using the standard fourth-order explicit Runge-Kutta scheme in time, with a time step small enough for the temporal errors to be negligible. (Correct convergence rates have been shown for these schemes.) Our proposed remedy, for the coordinate singularity was to make a first-order approximation of the metric coefficients, i.e. to lower the accuracy of the approximation of the partial differential equations at that point. To model that, we add an order 1 error (a constant c) to the equations at the boundary point. The stability properties are not changed by the addition of a lower order term. According to classical theory Gustafsson (1975, 1981), the resulting order of accuracy should be 1. We will now analyze this case in detail. Let u be the exact solution and define the error $e_k(t) = u(x_k, t) - v_k(t)$ and the vector $e = (e_1, e_2, \dots)^T$. Then the error equation is,

$$e_t + aP^{-1}Qe = \tau P^{-1}E_0(e - 0) + T,$$

where T is the truncation-error vector with the constant c at the boundary point included. Hence, $T = (\mathcal{O}(1), \mathcal{O}(h^2), \dots)^T$. Next, we split the truncation error into two parts, $T = T_i + T_b$, where, $T_i = (\mathcal{O}(1), 0, \dots)^T$, $T_b = (0, \mathcal{O}(h^2), \dots)^T$. Correspondingly, we let $e = e_i + e_b$ and split the problem into,

$$(e_i)_t + aP^{-1}Qe_i = \tau P^{-1}E_0(e_i - 0) + T_i, \quad (3.8)$$

$$(e_b)_t + aP^{-1}Qe_b = \tau P^{-1}E_0(e_b - 0) + T_b, \quad (3.9)$$

Note that, e_i and e_b are in general non-zero everywhere since there is usually a strong coupling between the interior and the boundary. It follows directly from the energy estimate of (3.8) that e_i is of order T_i , i.e. second-order in this case. Let $(P^{-1})_{00} = (hp)^{-1}$ where p is a constant. ($p = 1/2$ for the 2-1 scheme and $p = 17/48$ for the 4-2 scheme.)

N	$\tau = -a$				$\tau = -a/h$			
	l_2 -error	q_2	l_∞ -error	q_∞	l_2 -error	q_2	l_∞ -error	q_∞
10	0.0025	-	0.0071	-	9.8062e-04	-	0.0029	-
20	0.0010	1.3219	0.0035	1.0205	2.2634e-04	2.1152	7.7750e-04	1.8991
40	4.2519e-04	1.2338	0.0016	1.1293	5.1196e-05	2.1444	1.8462e-04	2.0743
80	2.0653e-04	1.0418	7.7984e-04	1.0368	1.2834e-05	1.9961	4.7078e-05	1.9714
160	1.0075e-04	1.0356	3.9445e-04	0.9833	3.1810e-06	2.0124	1.2239e-05	1.9436
320	4.9906e-05	1.0135	1.9911e-04	0.9863	7.9385e-07	2.0025	3.0348e-06	2.0118

TABLE 1. Errors and convergence rates at $t = 0.1$ for the 2-1 discretization of the advection equation with $a = 1$ and zeroth-order boundary error.

For e_b we proceed by Laplace transforming (3.9).

$$s(\hat{e}_b)_i + a \frac{(\hat{e}_b)_{i+1} - (\hat{e}_b)_{i-1}}{2h} = (\hat{T}_b)_i = 0, \quad i \geq 1 \quad (3.10)$$

$$s(\hat{e}_b)_0 + a \frac{(\hat{e}_b)_1 - (\hat{e}_b)_0}{h} = \tau \frac{(\hat{e}_b)_0}{ph} + (\hat{T}_b)_0, \quad (3.11)$$

We make the following ansatz, $(\hat{e}_b)_i = \sigma \kappa^i$ and define $\tilde{s} = sh/a$. At the left boundary all κ with $|\kappa| < 1$ for $Re \tilde{s} > 0$ should be supplied with boundary conditions. If σ is bounded for $Re \tilde{s} \geq 0$ the scheme is stable. (See Gustafsson et al. 1995.) We use the ansatz in (3.10) and obtain $\kappa = -\frac{\tilde{s}}{a} \pm \sqrt{\frac{\tilde{s}^2}{a^2} + 1}$. It can be shown that $\kappa_1 = -\frac{\tilde{s}}{a} + \sqrt{\frac{\tilde{s}^2}{a^2} + 1} < 1$, for $Re \tilde{s} > 0$. We use the definition that the square root denotes the value with positive real part. (In this case $\sigma_2 = 0$ corresponding to κ_2 due to the fall-off condition of u . Otherwise, it is bounded by the right boundary condition.) We insert $(\hat{e}_b)_i = \sigma_1 \kappa_1^i$ in (3.11), and use the expression for κ_1 ,

$$\sigma_1 \left(\sqrt{\frac{\tilde{s}^2}{a^2} + 1} - 1 - \frac{\tau}{ap} \right) = \frac{h(T_b)_0}{a}.$$

Denote the resolvent $R = \left(\sqrt{\frac{\tilde{s}^2}{a^2} + 1} - 1 - \frac{\tau}{ap} \right)$. For $Re \tilde{s} \geq 0$ we have that $Re \sqrt{\frac{\tilde{s}^2}{a^2} + 1} \geq 0$. Hence, $\sigma_1 \neq 0$ if $-1 - \frac{\tau}{ap} > 0$, i.e. $\tau < -a/2$. This is in full agreement with the stability analysis using the energy estimate. Choosing $\tau = \text{constant} < -a/2$ implies that R is of order 1 and $\sigma_1 \sim \frac{h(T_b)_0}{a}$. If $(T_b)_0$ is of order h we have $\sigma_1 \sim h^2$. Hence, $\hat{e}_b \sim h^2$. Transforming back using Parseval's relation, we obtain that e_b is second-order accurate. This is the classical result that a scheme is allowed to be closed with 1 order less accuracy at the boundary without degrading the global accuracy. (See Gustafsson 1975, 1981 and also Svärd & Nordström 2006.)

In our example, $(T_b)_0 \sim 1$ implying that \hat{e}_b and consequently e_b is $\mathcal{O}(h)$. In Table 2 this case is computed, corroborating the expected first-order convergence rate. We use $c = 0.1$ as the order 1 error, $a = 1$, $\tau = -a$.

Next, we consider the case $\tau = -a/(h^p) < -a$. Now, $R \sim 1/(h^p)$ and $\sigma \sim h^{p+1}(T_b)_0$. In our case with zeroth-order boundary closure and $p = 1$ we recover second-order global accuracy, see Table 1. Of course, there is little to gain by choosing a larger p since the global order of accuracy is also limited by the interior accuracy. To show that these conclusions carry over to high-order finite difference methods, we compute a similar

τ	$-a$	$-a$	$-a/h$	$-a/h$
N	l_2 -error	q_2	l_2 -error	q_2
10	1.0220e-04	-	5.1669e-05	-
20	2.7002e-05	1.9203	9.0017e-06	2.5210
40	7.0084e-06	1.9459	1.3840e-06	2.7014
80	1.7607e-06	1.9929	1.7674e-07	2.9691
160	4.3989e-07	2.0009	2.2384e-08	2.9811
320	1.0973e-07	2.0032	2.8176e-09	2.9899

TABLE 2. Errors and convergence rates at $t = 0.1$ for the 4-2 discretization of the advection equation with $a = 1$ and first-order boundary error. Different scalings of the penalty parameter, τ .

example using the 4-2 scheme. For the 4-2 scheme, we add, $0.1h$ to the first point in the scheme, i.e. a first-order error, and compute the solution with different scalings of the penalty term, see Table 2. As expected the convergence rate drops to 2 with $\tau = -a$. Third-order convergence is recovered for $\tau = -a/h$.

3.2. Model problem 2

The previous example shows a fundamental phenomenon that order of accuracy may be increased via a stronger enforcement of the penalty boundary conditions. However, we assumed that $a(x) = a$ and we may only claim that the analysis holds for a case where $a(x)$ is smooth. But, in the coordinate transformation case the $a(x)$ becomes singular. Hence, we continue our analysis and consider Model Problem 2 (3.3) and observe that $u(x, t) = \sin(\frac{x^2}{2} - t)$ is the solution. Obviously, (3.3) is singular at $x = 0$. Let $x_i = ih$ and $a(x_i) = 1/x_i$ for $i = 1, \dots, N$ and $a(x_0) = 1/x_1$, which is a first-order approximation. Define $A = \text{diag}(a(x_0), a(x_1), \dots, a(x_N))$. We discretize (3.3) as,

$$v_t + AP^{-1}Qv = \tau P^{-1}E_0(v - g) \quad (3.12)$$

Since A^{-1} and P are diagonal and positive definite, we can define a norm $\|v\|^2 = v^T A^{-1} P v$. Then we use the energy method with homogenous data and arrive at,

$$\|v\|_t^2 - v_0^2 + v_N^2 = 2\tau a^{-1}(x_0)v_0^2 \quad (3.13)$$

The scheme is stable if $\tau \leq -1/(2a^{-1}(x_0))$. Since $a^{-1}(x_0) = x_1 = h$ we have, $\tau \leq -1/(2h)$. This stability limit is easily verified in computations and is valid for both the 2-1 method and 4-2 method. In the 2-1 case the first-order closure of A is sufficient for globally second-order convergence. However, in the 4-2 case the convergence drops from third to second order, see Table 3. Note also that the stability limit of τ is dependent on the strength of the singularity. In this case $a(x) = 1/x$ implies that $\tau \sim 1/h$. But, if $a(x) = 1/\sqrt{x}$ we would obtain $\tau \sim 1/\sqrt{h}$, and so on.

Next, we consider the possibility to raise the order of accuracy at the boundary by increasing the strength of τ as a function of h . Again, we consider the boundary portion of the error equation for the quarter-space problem. (The interior can readily be shown to give the correct convergence rate via the energy estimate.)

$$(e_i)_t + \frac{1}{x_i} \frac{e_{i+1} - e_{i-1}}{2h} = 0, \quad i > 1, \quad (e_0)_t + \frac{1}{x_1} \frac{e_1 - e_0}{h} = \frac{\tau}{ph} e_0 + T_0, \quad i = 0, \quad (3.14)$$

τ	$-1/h$	$-1/h$	$-1/h^2$	$-1/h^2$
N	l_2 -error	q	l_2 -error	q
10	0.0025	-	2.7040e-04	-
20	6.1073e-04	2.0333	3.9040e-05	2.7921
40	1.4964e-04	2.0290	4.7133e-06	3.0501
80	3.7125e-05	2.0110	6.2343e-07	2.9184

TABLE 3. Errors and convergence rates at $t = 0.1$ for the 4-2 scheme with $a = 1/x$ and first-order approximation of metrics at $x = 0$.

Laplace transform the first equation in (3.14) results in $\kappa(i) = -\tilde{s}x_i \pm \sqrt{(\tilde{s}x_i)^2 + 1}$. Again, $|\kappa_1| = |-\tilde{s}x_i + \sqrt{(\tilde{s}x_i)^2 + 1}| < 1$ and $\operatorname{Re} \sqrt{(\tilde{s}x_i)^2 + 1} > 0$, since $x_i > 0$. We note that according to our approximation $x_0 = x_1 = h$. Laplace transforming equation (3.14) and using the explicit expression for κ_1 yield,

$$\sigma\left(\frac{\sqrt{(\tilde{s}h)^2 + 1} - 1}{h} - \frac{\tau}{p}\right) = h\hat{T}_0, \quad i = 0, \quad t \geq 0$$

For stability, we demand that the resolvent, $R = \left(\frac{\sqrt{(\tilde{s}h)^2 + 1} - 1}{h} - \frac{\tau}{p}\right) > 0$, for $\operatorname{Re} \tilde{s} \geq 0, h \geq 0$. Since $\operatorname{Re} \sqrt{(\tilde{s}h)^2 + 1} \geq 0$ we must require that, $-\frac{1}{h} - \frac{\tau}{p} > 0$ and obtain $\tau < -p/h = -1/(2h)$. With $\tau \sim 1/h$ we have $R \sim 1$ and $\sigma \sim h\hat{T}_0$. Using Parseval's relation, we also obtain that $e_b \sim h\hat{T}_0$.

As in the constant coefficient case we may choose $\tau \sim 1/h^p$ to obtain $e_b \sim h^{p+1}\hat{T}_0$. With $\tau = -1$ the scheme is unstable as predicted by theory and the results $\tau = -1/h$ and $\tau = -1/h^2$ are displayed in Table 3. The results supports the theoretical derivations.

3.3. Model problem 3

The polar singularity was modelled by, $u_t + \frac{1}{y}u_x = 0$, $0 \leq x, y \leq 1$. This equation is discretized as outlined in (2.2). We choose $A = \operatorname{diag}(a(y_0), \dots, a(y_M))$, where $a(y_0) = 1/y_1$ and $a(y_i) = 1/y_i$, $i = 1..M$. That is, we commit a first-order error along the line $y = 0$. We need boundary conditions at $x = 0$ and choose $\tau_1 = -a(y_i)$ at y_i in (2.2). Further, $\tau_2 = 0$ in (2.2). We use the exact solution $u = \sin(yx - t)$ to provide boundary and intitial data. We do not need to redo a similar analysis but only interpret this case from the results of the constant coefficient. For each $y \neq 0$ the equation is approximated to design order. If we assume that the 4-2 is employed, we have third-order global convergence. In other words, for $N \times M - 1$ points the error is $\mathcal{O}(h_x^3)$. For $y = 0$ we approximate $1/y$ by $1/y_1 = 1/h_y$ and we commit a first-order error on N points. We assume that $h_x \sim h_y \sim h$. Then the overall l_2 -error, e_{l_2} , is computed as,

$$e_{l_2}^2 = h^2 \sum_{i=1}^N \sum_{j=1}^M e_{ij}^2 \sim h^2 (N(M-1)(h^3)^2 + N(h)^2) \sim h^2(h^4 + h) \sim h^3$$

or, $e_{l_2} \sim h^{1.5}$. The computational results are displayed in Table 4 and the convergence rate is 1.5 as predicted. As mentioned above, we need not supply any boundary condition at $y = 0$. However, at any boundary we may enforce the exact solution, if known, as a

N	error	q
10	0.0195	-
20	0.0067	1.5412
40	0.0023	1.5425
80	8.1073e-04	1.5043

TABLE 4. Errors and convergence rates at $t = 0.1$ for the 4-2 scheme with $a = 1/y$ and first-order approximation of $1/y$ at $y = 0$.

N	error	q
10	0.0011	-
20	1.9677e-04	2.4829
40	3.4801e-05	2.4993
80	6.1540e-06	2.4995

TABLE 5. Errors and convergence rates at $t = 0.1$ for the 4-2 method with $a = 1/y$ and first-order approximation of $1/y$ at $y = 0$. A penalty term enforce the exact solution along the slip boundary $y = 0$.

boundary condition. In this case we know the exact solution and we choose $\tau_2 = -a(y_0)$. As the previous analysis suggests, we should gain one order of accuracy at $y = 0$ (and globally.) We note that Table 5 supports that conclusion.

3.4. Advection equation on the circle segment

We will compute the solution to the advection equation with the 4-2 method on the circle segment shown in Figure 1. The grid spacing is equidistant meaning $\Delta r = \text{constant}$ and $\Delta\phi = \text{constant}$ with $N + 1$ points in both directions, implying that $h_\xi = h_\eta = 1/N$. (The general coordinate ξ corresponds to r and η to θ .) We use the scheme (2.2) for the equation (2.6) with $a = 0.9$ and $b = -\sqrt{1 - a^2}$ and compute two different cases:

(a) $(\tau_1)_j = -\hat{a}(x_0, x_j)$ and $(\tau_2)_i = \hat{b}(x_i, y_N)$. (A local penalty parameter is computed at each gridpoint.)

(b) $(\tau_1)_j = -\hat{a}(x_0, x_j)/h_\xi$ and $(\tau_2)_i = \hat{b}(x_i, y_N)$.

In the first case, we commit an $\mathcal{O}(h)$ error along the line $\xi = 0$. The penalty strength at $\xi = 0$ is the marginal scaling for stability. Hence, this case corresponds to Model Problem 3 without the extra penalty term at $y = 0$. We would expect the l_2 convergence rate to be 1.5 and the l_∞ convergence rate to be 1, which is the case in Table 6.

The second case corresponds to Model Problem 3 with the additional penalty at $y = 0$ in the sense that the penalty is unnecessary strong for pure stability purposes. However, the effect is an increased convergence rate by one order in both l_2 and l_∞ , which is observed in Table 7.

3.5. Grid singularity at outflow boundary.

So far, we have only considered the case of a grid with boundary condition at the singularity. To study the case of a grid singularity at an outflow we consider Model Problem

N	l_2 -error	q_2	l_∞ -error	q_∞
10	0.0068	-	0.0292	-
20	0.0024	1.5025	0.0142	1.0401
40	8.5049e-04	1.4967	0.0071	1.000
80	3.0001e-04	1.5033	0.0036	0.9798

TABLE 6. Errors and convergence rates on the circle segment grid at $t = 0.1$ for the 4-2 method with $(\tau_1)_j = -\hat{a}(x_0, x_j)$.

N	l_2 -error	q_2	l_∞ -error	q_∞
10	0.0012	-	0.0057	-
20	2.2791e-04	2.3965	0.0016	1.8329
40	4.2458e-05	2.4244	4.5839e-04	1.8034
80	7.7408e-06	2.4555	1.2366e-04	1.8902

TABLE 7. Errors and convergence rates on the circle segment grid at $t = 0.1$ for the 4-2 method with $(\tau_1)_j = -\hat{a}(x_0, x_j)/h_\xi$.

2, modified to a left-going wave problem.

$$u_t - a(x)u_x = 0, \quad a(x) = \frac{1}{x}, \quad u(1, t) = g(t), \quad 0 \leq x \leq 1 \quad (3.15)$$

The idea is to try to increase the accuracy of the approximated metric coefficient at the left boundary. The naive approach is to extrapolate to higher order using the ansatz, $a(x_0) \approx \alpha a(x_1) + \beta a(x_2)$, and Taylor expand.

$$\begin{aligned} a(x_0) \approx & \alpha(a(x_0) + a'(x_0)(x_1 - x_0) + a''(x_0)\frac{(x_1 - x_0)^2}{2}) \\ & + \beta(a(x_0) + a'(x_0)(x_2 - x_0) + a''(x_0)\frac{(x_2 - x_0)^2}{2}). \end{aligned} \quad (3.16)$$

We have to interpret the derivatives as limits as $x_0 \rightarrow 0$. Then we obtain the conditions,

$$\alpha + \beta = 1, \quad \alpha h + 2h\beta = 0, \quad \alpha = 2, \beta = -1. \quad (3.17)$$

This is the same solution we would obtain if we had fit a linear polynomial between x_1 and x_2 and extrapolated to x_0 . The Taylor expansions, however, gives insight in the errors committed. The convergence rates obtained using this kind of extrapolation is shown in Table 8. p is the order of the extrapolation polynomial, i.e. $p = 0$ is the previously used simple extrapolation from a close neighbor. $p = 1$ the linear extrapolation derived above, and $p = 2$ a second-order polynomial. As is clearly seen, trying to extrapolate to higher order does not raise the accuracy. To explain these results, we consider the first error term of (3.16).

$$e = \alpha a''(x_0)\frac{(x_1 - x_0)^2}{2} + \beta a''(x_0)\frac{(x_2 - x_0)^2}{2}. \quad (3.18)$$

Let x_0 approach 0 and compute the limit, $e = \alpha \frac{1}{h} + \beta \frac{1}{2h}$. We conclude that the error at x_0 is a term $a(x_0 + h)$, i.e. a first order error, which explains the results in Table 8. Of

p	0		1		1		2	
	N	l_2 -error	q	l_2 -error	q	l_2 -error	q	
11	0.0024	-		0.0016	-	0.0013	-	
21	5.6173e-04	2.0951	3.7609e-04	2.0889	3.0830e-04	2.0761		
41	1.3472e-04	2.0599	8.9812e-05	2.0661	7.3485e-05	2.0688		
81	3.3056e-05	2.0270	2.2041e-05	2.0267	1.8035e-05	2.0267		

TABLE 8. Eq (3.15) approximated with the 4-2 scheme. Extrapolation of $-1/x$ to $x = 0$ with polynomial order p .

N	l_2 -error	q_2
11	2.9288e-04	-
21	3.5629e-05	3.0392
41	3.7477e-06	3.2490
81	4.4241e-07	3.0825

TABLE 9. Eq (3.15) approximated with the 4-2 scheme. $-1/h^2$ approximating $-1/x$ at $x = 0$.

\sqrt{N}	l_2 -error	q_2	l_∞ -error	q_∞
11	0.0024	-	0.0136	-
21	8.3055e-04	1.5309	0.0068	1.000
41	2.8687e-04	1.5337	0.0034	1.000
81	1.0012e-04	1.5187	0.0017	1.000
161	3.5161e-05	1.5097	8.4251e-04	1.0128

TABLE 10. Circle segment with outflow at singular point ($a = -1, b = 0$). Zeroth-order interpolation of y_η, x_η to $x = 0.5, y = 0$.

course, extrapolation only gives smaller leading error term with higher polynomial order if the extrapolated function is sufficiently smooth, which was not the case above. This leads us to extrapolate the smooth inverse of $1/x$.

That is, we approximate $x_0 = 0$ to second order accuracy, i.e. $x_0 \equiv x' = h^2$, such that $1/x_0$ is approximated by $1/x' = 1/h^2$ which is a second-order approximation and the entire scheme should recover third-order accuracy. Indeed, this is confirmed in Table 9. Again, the numerical scheme becomes more stiff. Applying the same idea to the circle segment suggest that y_η and x_η should be extrapolated to second-order accuracy. In our example the functions are linear and we use a linear extrapolation to a point $\mathcal{O}(\Delta r^2)$ away from the singularity. The results are displayed in Table 10 and 11. As is seen we get the predicted convergence rate 2 in l_∞ . We have confirmed that the maximum errors occur at the singular point and get an approximate convergence rate of 2.5 in l_2 .

\sqrt{N}	l_2 -error	q_2	l_∞ -error	q_∞
11	3.8502e-04	-	0.0022	-
21	7.2143e-05	2.4160	5.8375e-04	1.9141
41	1.3120e-05	2.4591	1.4845e-04	1.9754
81	2.7956e-06	2.2305	3.7411e-5	1.9884

TABLE 11. Circle segment with outflow at singular point ($a = -1, b = 0$). Linear interpolation of y_η, x_η to a point h^2 away from $x = 0.5, y = 0$.

3.6. Time step limits

Both the proposed remedies for the grid singularity introduces a stiffness to the problem, if compared to the same problem on a non-singular grid. However, if we accept the choice of a singular grid transformation and still want to compute a solution, the time step restriction is unavoidable. Consider,

$$u_t + a(x)u_x = 0 \quad (3.19)$$

Then the CFL constraint is $\Delta t < c \cdot a(x)/h$ where c is a constant depending on the choice of numerical scheme. As an example, we use model problem 1 where $a(x) = 1/x$. The more accurate we want to approximate $a(0)$, the more stiff the problem becomes.

4. The Euler equations

We will demonstrate the robustness of the proposed techniques using the Euler equations of gas dynamics. We will consider an analytical vortex solution that enables us to measure the error. Since the flows will be subsonic there will be boundary conditions both at inflows and at outflows but not on all variables. Hence, we will use the technique where the metric coefficients are approximated (and not the remedy utilizing stronger penalties). The computations will be carried out with the multi-block SBP-SAT finite difference code SUmb. The Euler equations are stated on conservative form and since the previous analysis was carried out on primitive form, we will briefly discuss the differences with respect to the metric approximations. The Euler equations in a Cartesian system can be stated as,

$$u_t + F_x + G_y = 0 \quad (4.1)$$

where u are the conservative variables and F, G are the fluxes. Applying a coordinate transformation results in,

$$(Ju)_t + (J\xi_x F + J\xi_y G)_\xi + (J\eta_x F + J\eta_y G)_\eta = 0. \quad (4.2)$$

We note that $J\xi_x = y_\eta, J\xi_y = -x_\eta, J\eta_x = -y_\xi, J\eta_y = x_\xi$ are not singular but well-defined on the grids we have considered. Hence, it is only J appearing in the time derivative that is troublesome. To compute J , we use the approximations of the metric coefficients discussed at length above. We use the analytical solution as initial and boundary data. The Mach number is 0.5 and the solution is computed with the 4-2 scheme marched with a 3rd-order explicit Runge-Kutta scheme on 4 different meshes. The domain is seen in Figure 2 and the grid sizes are: 33×17 points (grid 1); 65×33 points (grid2); 129×65 points (grid 3); 257×129 points (grid 4). At $T = 0.6$ the l_2 -errors, l_∞ -errors and convergence

grid	l_∞ -error	q	l_2 -error	q
1	0.7263e-02	-	5.424e-4	-
2	0.2251e-02	1.69	2.032e-4	1.42
3	0.9573e-03	1.23	6.027e-5	1.75
4	0.4275e-03	1.16	1.921e-5	1.65

TABLE 12. l_2 -errors, l_∞ -errors and convergence rates for the Euler equations computed with the 4-2 schemes.

rates are displayed in Table 12. We note that the computational convergence rates, are close to the theoretical 1.5 in l_2 and 1 in l_∞ . Also, the computations are perfectly stable on all grids and we note that the 4-2 method is quite accurate although the formal order is degraded due to the singularity. In Figure 2 the density is shown at $T = 0.6$ for two different grids: the coarsest (grid 1) and the second finest (grid 2). We observe that on grid 3 an almost perfect solution is obtained but even the solution on the coarsest mesh is good.

5. Conclusions

We have considered fictitious singularities introduced by the mapping of a non-square computational grid to a square that results in singular metric coefficients. We approach this problem by studying one-dimensional model problems and present two ways of handling the singularity, while keeping design order of the scheme.

The first remedy is applicable to SBP-SAT schemes and requires only a crude and simple approximation of the metric coefficients (one can even choose them to be an arbitrary constant). The accuracy is recovered through a stronger enforcement of the penalty boundary conditions.

The second technique, is a sufficiently accurate extrapolation of the metric coefficients to a point that approaches the singularity sufficiently fast. This solution is generally applicable to any stable finite difference scheme. However, care has to be taken when the metric coefficients are extrapolated and naive extrapolations do not improve the accuracy. Numerical examples supports the linear analysis for both remedies.

Both methods yield a more stiff set of ordinary differential equations to solve, compared to the same problem on a non-singular grid. The additional stiffness is proportional to the strength of the singularity. We show that this is a natural CFL constraint.

Finally, we show how to interpret the results for a system of equations in conservative form. We demonstrate that the non-linear two-dimensional Euler equations computed with the 4-2 scheme is robust with the second technique and obey the same accuracy properties as the linear counterpart.

REFERENCES

Carpenter, M. H., Gottlieb, D. and Abarbanel, S. Time-stable boundary conditions for finite-difference schemes solving hyperbolic systems: Methodology and application to high-order compact schemes. *J. Comput. Phys.*, 111(2), 1994.

Carpenter, M.-H., Nordström, J. and Gottlieb, D. A Stable and Conservative Interface Treatment of Arbitrary Spatial Accuracy. *J. Comput. Phys.*, 148, 1999.

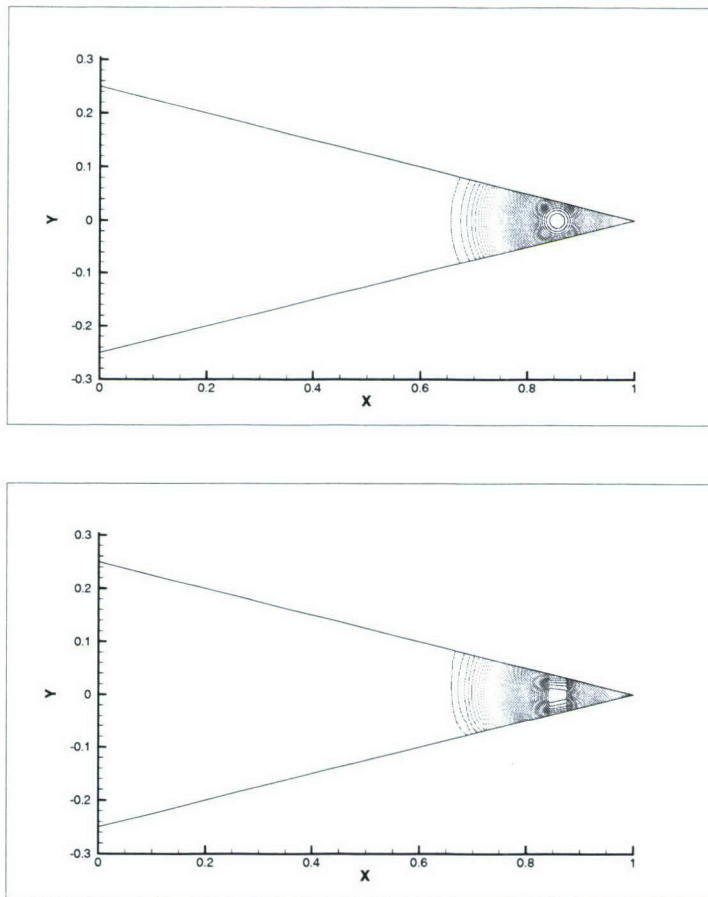


FIGURE 2. The density of the Euler vortex solution at $T = 0.6$. The top figure computed with the 4-2 method on Grid 3 and the bottom figure on Grid 1.

Gustafsson, B. The convergence rate for difference approximations to mixed initial boundary value problems. *Math. Comp.*, 29(130):396–406, Apr. 1975.

Gustafsson, B. The convergence rate for difference approximations to general mixed initial boundary value problems. *SIAM J. Numer. Anal.*, 18(2):179–190, Apr. 1981.

Gustafsson, B., Kreiss, H.-O. and Oliger, J. *Time dependent problems and difference methods*. John Wiley & Sons, Inc., 1995.

Kreiss, H.-O. and Scherer, G. Finite element and finite difference methods for hyperbolic partial differential equations. *Mathematical Aspects of Finite Elements in Partial Differential Equations.*, Academic Press, Inc., 1974.

Mattsson, K., Svärd, M., Carpenter, M. H. and Nordström, J. High-order accurate computations for unsteady aerodynamics. *in press Computers and Fluids*, 2006.

Nordström, J. and Carpenter, M. H. Boundary and interface conditions for high-order finite-difference methods applied to the Euler and Navier-Stokes equations. *J. Comput. Phys.*, 148, 1999.

Strand, B.. Summation by Parts for Finite Difference Approximations for $d/d x$. *J. Comput. Phys.*, 110, 1994.

Svärd, M. On coordinate transformation for summation-by-parts operators. *Journal of Scientific Computing*, 20(1), 2004.

Svärd, M., Mattsson, K. and Nordström, J. Steady state computations using summation-by-parts operators. *Journal of Scientific Computing*, 24(1):79–95, September 2005.

Svärd, M. and Nordström, J. On the order of accuracy for difference approximations of initial-boundary value problems. *J. Comput. Physics*, 218(1):333–352, October 2006.

Stable and compact finite difference schemes

By K. Mattsson, M. Svärd AND M. Shoeybi

1. Motivation and objectives

Compact second derivatives have long been known to have good accuracy properties for pure second derivatives. However, for many equations subject to boundary conditions, stability can not easily be proven for problems with a combination of mixed ($\partial^2/\partial x\partial y$) and pure ($\partial^2/\partial x^2, \partial^2/\partial y^2$) second derivatives, such as the compressible Navier-Stokes equations.

We remark that spatial Padé discretizations (see, for example, Lele (1992)) are often referred to as "compact schemes". The approximation of the derivative is obtained by solving a tri- or penta-diagonal system of linear equations at every time step. Hence, Padé discretizations lead to full difference stencils, similar to spectral discretizations. In this paper the term "compact" will be used exclusively for schemes with a minimal stencil width.

For the continuous problem one can derive an energy estimate for the linearized and symmetrized Navier-Stokes equations, proving boundedness of the initial-boundary value problem (see for example Nördstrom & Svärd (2005) and Carpenter *et al.* (1999)). Although the analysis is done for 2-D problems, the extension to 3-D problems is straightforward. If first-derivative difference operators that satisfy a Summation-By-Parts (SBP) formula (see Kreiss & Scherer (1974)) are employed twice for all second-derivatives (pure and mixed), yielding a non-compact stencil, and if the Simultaneous Approximation Term (SAT) method by Carpenter *et al.* (1994) is used to implement the boundary conditions, one can exactly mimic the continuous energy estimate (proving stability). There are two obvious drawbacks to this approach when compared to a compact formulation, namely:

- (1) There is no mechanism to damp the highest frequency mode (spurious oscillations).
- (2) Less accurate difference approximations of pure second-derivative terms (due to the leading order error constant) are created.

The former could partially be resolved by the addition of artificial damping, but it is difficult to tell *a priori* how much is needed. Accuracy and stability are closely linked. The two drawbacks above work together to make compact schemes more accurate than non-compact schemes, especially in regions where viscous effects are important. A property that is not addressed in this paper is computational cost. For a scalar problem on a Cartesian grid, the compact scheme is clearly less expensive, but for more realistic applications (for example the 3-D Navier-Stokes equations on a curvilinear grid), this is still an open question.

Compact second-derivative SBP operators that are stable in combination with first-derivative SBP approximations were derived in Mattsson & Nordström (2004). However, it is not clear how to obtain a stable and accurate overall scheme with the addition of mixed derivative terms.

In Section 2 we discuss the SBP property for the first- and second-derivative difference operators. A 2-D model for the Navier-Stokes equations is introduced in Section 3, and we show how to combine the SAT method and the SBP operators to obtain stable finite

difference approximations using the energy method (see for example Gustafsson *et al.* (1995)). In Section 4 the accuracy of the compact and the non-compact formulations are compared by performing numerical simulations for the both the model-problem and the 2-D Navier-Stokes equations. Conclusions are presented in Section 5.

2. Definitions

The two-dimensional schemes are constructed using 1-D SBP finite-difference operators. We begin with a short description and some definitions (for more details, see Kreiss & Scherer (1974); Strand (1994); Mattsson & Nordström (2004)).

2.1. One-dimensional problems

Let the inner product for real-valued functions $u, v \in \mathbf{L}^2[0, 1]$ be defined by $(u, v) = \int_0^1 u v dx$, and let the corresponding norm be $\|u\|^2 = (u, u)$. The domain $(0 \leq x \leq 1)$ is discretized using $N+1$ equidistant grid points,

$$x_i = i h, \quad i = 0, 1, \dots, N, \quad h = \frac{1}{N}.$$

The approximative solution at grid point x_i is denoted v_i , and the discrete solution vector is $v^T = [v_0, v_1, \dots, v_N]$. Similarly, we define an inner product for discrete real-valued vector functions $u, v \in \mathbf{R}^{N+1}$ by $(u, v)_H = u^T H v$, where $H = H^T > 0$, with the corresponding norm $\|v\|_H^2 = v^T H v$. The following vectors will be used frequently:

$$e_0 = [1, 0, \dots, 0]^T, \quad e_N = [0, \dots, 0, 1]^T. \quad (2.1)$$

Consider the hyperbolic scalar equation $u_t + u_x = 0$ (excluding the boundary condition). Multiplying by u and integration by parts (referred to as the energy method) leads to

$$\frac{d}{dt} \|u\|^2 = -(u, u_x) - (u_x, u) = -u^2|_0^1, \quad (2.2)$$

where $u^2|_0^1 \equiv u^2(x=1) - u^2(x=0)$.

DEFINITION 2.1. *A difference operator $D_1 = H^{-1}Q$ approximating $\partial/\partial x$ is a compact first-derivative SBP operator if $H = H^T$ is diagonal, $x^T H x > 0$, $x \neq 0$, and $Q + Q^T = B = \text{diag}(-1, 0, \dots, 0, 1)$.*

A semi-discretization of $u_t + u_x = 0$ is $v_t + D_1 v = 0$. Multiplying by $v^T H$ from the left and adding the transpose lead to

$$\frac{d}{dt} \|v\|_H^2 = -(v, H^{-1}Qv)_H - (H^{-1}Qv, v)_H = -v^T (Q + Q^T) v = v_0^2 - v_N^2. \quad (2.3)$$

Equation (2.3) is the discrete analog of (2.2).

For parabolic problems, we need an SBP operator for the second derivative. Consider the heat equation, $u_t = u_{xx}$. Multiplying by u and integration by parts leads to

$$\frac{d}{dt} \|u\|^2 = (u, u_{xx}) + (u_{xx}, u) = 2u u_x|_0^1 - 2\|u_x\|^2. \quad (2.4)$$

DEFINITION 2.2. *A difference operator $D_2 = H^{-1}(-M + BS)$ approximating $\partial^2/\partial x^2$ is said to be a compact second-derivative SBP operator if $H = H^T$ is diagonal, $x^T H x > 0$, $x \neq 0$, $M = M^T$ is sparse, $x^T M x \geq 0$, S includes an approximation of the first-derivative operator at the boundary and $B = \text{diag}(-1, 0, \dots, 0, 1)$.*

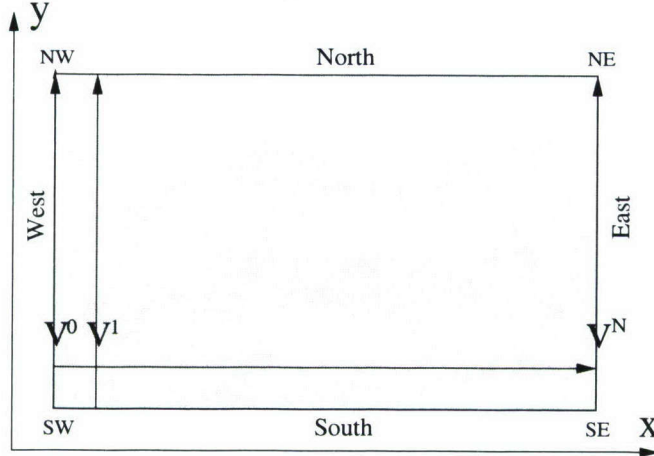


FIGURE 1. Domain 2-D

In Mattsson & Nordström (2004), high-order compact second-derivative SBP operators were constructed. A semi-discretization of $u_t = u_{xx}$ is $v_t = D_2 v$. Multiplying by $v^T H$ and adding the transpose, lead to

$$\frac{d}{dt} \|v\|_H^2 = 2v_N(Sv)_N - 2v_0(Sv)_0 - 2v^T M v. \quad (2.5)$$

Formula (2.5) is the discrete analog of (2.4).

Obtaining energy estimates for schemes utilizing both D_1 and D_2 requires that both are based on the same norm H .

2.2. Two-dimensional domains

We begin by introducing the Kronecker product

$$C \otimes D = \begin{bmatrix} c_{0,0} D & \cdots & c_{0,q-1} D \\ \vdots & & \vdots \\ c_{p-1,0} D & \cdots & c_{p-1,q-1} D \end{bmatrix},$$

where C is a $p \times q$ matrix and D is an $m \times n$ matrix. Two useful rules for the Kronecker product are $(A \otimes B)(C \otimes D) = (AC) \otimes (BD)$ and $(A \otimes B)^T = A^T \otimes B^T$.

Next, consider the domain Ω defined as $0 \leq x \leq 1$, $0 \leq y \leq 1$ with an $(N+1) \times (M+1)$ -point equidistant grid as

$$\begin{aligned} x_i &= i h_x, \quad i = 0, 1, \dots, N, \quad h_x = \frac{1}{N}, \\ y_j &= j h_y, \quad j = 0, 1, \dots, M, \quad h_y = \frac{1}{M}. \end{aligned}$$

The numerical approximation at grid point (x_i, y_j) is denoted $v_{i,j}$. We define a discrete solution vector $v^T = [v^0, v^1, \dots, v^N]$, where $v^k = [v_{k,0}, v_{k,1}, \dots, v_{k,M}]$ is the solution vector at x_k along the y direction, illustrated in Fig. 1. To simplify the notation we introduce $v_{w,e,s,n}$ to define the boundary values at the west, east, south and north boundaries (see Fig. 1). In order to distinguish whether a difference operator P is working in the x or the y direction, we will use the notations P_x and P_y . The following two-

dimensional operators will frequently be used:

$$\begin{aligned} D_x &= (D_1 \otimes I_y), & D_y &= (I_x \otimes D_1), \\ D_{2x} &= (D_2 \otimes I_y), & D_{2y} &= (I_x \otimes D_2), \\ H_x &= (H \otimes I_y), & H_y &= (I_x \otimes H), \end{aligned} \quad (2.6)$$

where D_1 , D_2 , and H are the one-dimensional operators. $I_{x,y}$ are the identity matrices of appropriate sizes in the x and y direction, respectively. We also introduce the two-dimensional norm $\bar{H} \equiv H_x H_y$.

3. Numerical method

Our main interest is the compressible Navier-Stokes equations, which can be written as:

$$u_t + (Au)_x + (Bu)_y = C_{11}u_{xx} + C_{12}u_{xy} + C_{21}u_{yx} + C_{22}u_{yy}, \quad [x, y] \in \Omega, \quad t \geq 0. \quad (3.1)$$

The non-linear equations can be stated as (3.1) but we consider (3.1) to be the linearized, symmetrized, and frozen coefficient equations. It can be shown (see Strang (1964)) that if the frozen coefficient problem is well-posed so the non-linear problem will be for smooth solutions. These equations have been studied more extensively (see for example Nördstrom & Svärd (2005)).

3.1. The continuous model problem

As a model of (3.1) we consider the two-dimensional non-linear parabolic problem

$$u_t + \left(\frac{u^2}{2}\right)_x + \left(\frac{u^2}{2}\right)_y = c_{11}u_{xx} + c_{12}u_{xy} + c_{21}u_{yx} + c_{22}u_{yy} + F, \quad [x, y] \in \Omega, \quad t \geq 0, \quad (3.2)$$

where F is a forcing function. Equation (3.2) is subject to the following boundary conditions:

$$\begin{aligned} \alpha_w u + c_{11}u_x + c_{12}u_y &= g_w & \alpha_s u + c_{21}u_x + c_{22}u_y &= g_s \\ \alpha_e u + c_{11}u_x + c_{12}u_y &= g_e & \alpha_n u + c_{21}u_x + c_{22}u_y &= g_n \end{aligned} \quad . \quad (3.3)$$

The subscripts denote (w)est, (e)ast, (s)outh and (n)orth boundaries, respectively. The main focus of this paper is to analyze the discretization of the viscous terms.

To further simplify the analysis, we will consider the linearized parabolic problem

$$u_t + au_x + bu_y = c_{11}u_{xx} + c_{12}u_{xy} + c_{21}u_{yx} + c_{22}u_{yy} + F, \quad [x, y] \in \Omega, \quad t \geq 0 \quad (3.4)$$

and assume that the boundary data are homogeneous. (The analysis holds for homogeneous data, but introduces unnecessary notation.) We wish to discretize u_{xx} and u_{yy} with the compact stencil while the mixed derivatives are approximated using D_x and D_y . The problem lies in deriving sufficient stability conditions for the resulting scheme.

We apply the energy method to (3.4), and with the use of (3.3) we obtain

$$\frac{d}{dt} \|u\|^2 = BT + DI + FO, \quad (3.5)$$

where $FO = \eta \|u\| + \frac{1}{\eta} \|F\|$ (for an arbitrary constant $\eta > 0$) and

$$DI = - \int_0^1 \int_0^1 w^T (C + C^T) w \, dx \, dy, \quad (3.6)$$

where

$$C = \begin{bmatrix} c_{11} & c_{12} \\ c_{21} & c_{22} \end{bmatrix}, \quad w = \begin{bmatrix} u_x \\ u_y \end{bmatrix}$$

denotes the contribution from the dissipative terms. Parabolicity requires that

$$x^T (C + C^T) x \geq 0. \quad (3.7)$$

The Navier-Stokes equations (3.1) satisfy the same relation (3.7) with C_{ij} instead of c_{ij} . (See Nördstrom & Svärd (2005).)

The boundary terms are given by

$$BT = \int_0^1 (a + 2\alpha_w) u_w^2 - (a + 2\alpha_e) u_e^2 dy + \int_0^1 (b + 2\alpha_s) u_s^2 - (b + 2\alpha_n) u_n^2 dx.$$

An energy estimate exists for

$$(a + 2\alpha_w) \leq 0, \quad (a + 2\alpha_e) \geq 0, \quad (b + 2\alpha_s) \leq 0, \quad (b + 2\alpha_n) \geq 0. \quad (3.8)$$

3.2. The non-compact formulation

A semi-discretization of (3.4) employing only the first-derivative SBP operator combined with the SAT method can be written as

$$\begin{aligned} v_t + a D_x v + b D_x v &= c_{11} D_x D_x v + c_{12} D_x D_y v \\ &\quad + c_{21} D_y D_x v + c_{22} D_y D_y v + SAT + F. \end{aligned} \quad (3.9)$$

The discrete version of the boundary conditions (3.3) is given by

$$\begin{aligned} L_w v &= \alpha_w v_w + c_{11} (D_x v)_w + c_{12} (D_y v)_w = g_w \\ L_e v &= \alpha_e v_e + c_{11} (D_x v)_e + c_{12} (D_y v)_e = g_e \\ L_s v &= \alpha_s v_s + c_{22} (D_y v)_s + c_{21} (D_x v)_s = g_s \\ L_n v &= \alpha_n v_n + c_{22} (D_y v)_n + c_{21} (D_x v)_n = g_n \end{aligned} \quad (3.10)$$

The penalty term in (3.9) is given by

$$SAT = \begin{aligned} &+ \tau_w H_x^{-1} e_0 \otimes (L_w v - g_w) + \tau_e H_x^{-1} e_N \otimes (L_e v - g_e) \\ &+ \tau_s H_y^{-1} (L_s v - g_s) \otimes e_0 + \tau_n H_y^{-1} s (L_n v - g_n) \otimes e_N. \end{aligned} \quad (3.11)$$

LEMMA 3.1. *The scheme (3.9) with homogeneous data has a non-growing solution, if D_1 is a compact first-derivative SBP operator, $\tau_{w,s} = 1$, $\tau_{e,n} = -1$ and (3.7), (3.8) hold.*

Proof. Let $F = g_{w,e,s,n} = 0$. Multiplying (3.9) by $v_t^T \bar{H}$ from the left and adding the transpose lead to

$$\begin{aligned} \frac{d}{dt} \|v\|_{\bar{H}}^2 &= -2c_{11} v_w^T H(D_x v)_w (1 - \tau_w) - 2c_{12} v_w^T H(D_y v)_w (1 - \tau_w) \\ &\quad + 2c_{11} v_e^T H(D_x v)_e (1 + \tau_e) + 2c_{12} v_e^T H(D_y v)_e (1 + \tau_e) \\ &\quad - 2c_{22} v_s^T H(D_y v)_s (1 - \tau_s) - 2c_{21} v_s^T H(D_x v)_s (1 - \tau_s) \\ &\quad + 2c_{22} v_n^T H(D_y v)_n (1 + \tau_n) + 2c_{21} v_n^T H(D_x v)_n (1 + \tau_n) \\ &\quad + (2\tau_w \alpha_w + a) v_w^T H v_w + (2\tau_e \alpha_e - a) v_e^T H v_e \\ &\quad + (2\tau_s \alpha_s + b) v_s^T H v_s + (2\tau_n \alpha_n - b) v_n^T H v_n + DI \end{aligned}$$

The dissipative term is given by

$$DI = - \begin{bmatrix} D_x v \\ D_y v \end{bmatrix}^T [(C + C^T) \otimes \bar{H}] w \begin{bmatrix} D_x v \\ D_y v \end{bmatrix}, \quad (3.12)$$

which exactly mimics (3.6). If $\tau_{w,s} = 1$, $\tau_{e,n} = -1$ we obtain

$$\begin{aligned} \frac{d}{dt} \|v\|_H^2 &= (2\alpha_w + a)v_w^T H v_w - \tau_e(2\alpha_e + a)v_e^T H v_e \\ &\quad + (2\alpha_s + b)v_s^T H v_s - (2\alpha_n + b)v_n^T H v_n + DI \end{aligned}.$$

This is completely analogous to (3.5). If (3.8) hold we obtain a non-growing energy. \square

3.3. The compact formulation

A semi-discretization of (3.4) using compact operators and the SAT method can be written as

$$\begin{aligned} v_t + aD_x v + bD_x v &= c_{11}D_{2x}v + c_{12}D_x D_y v \\ &\quad + c_{21}D_y D_x v + c_{22}D_{2y}v + SAT + F. \end{aligned} \quad (3.13)$$

The discrete version of the boundary conditions (3.3) are now (compare with (3.10)) given by

$$\begin{aligned} \tilde{L}_w v &= \alpha_w v_w + c_{11}(S_x v)_w + c_{12}(D_y v)_w = g_w \\ \tilde{L}_e v &= \alpha_e v_e + c_{11}(S_x v)_e + c_{12}(D_y v)_e = g_e \\ \tilde{L}_s v &= \alpha_s v_s + c_{22}(S_y v)_s + c_{21}(D_x v)_s = g_s \\ \tilde{L}_n v &= \alpha_n v_n + c_{22}(S_y v)_n + c_{21}(D_x v)_n = g_n \end{aligned}. \quad (3.14)$$

The penalty term in (3.13) is given by

$$SAT = \begin{aligned} &+ \tau_w H_x^{-1} e_0 \otimes (\tilde{L}_w v - g_w) + \tau_e H_x^{-1} e_N \otimes (\tilde{L}_e v - g_e) \\ &+ \tau_s H_y^{-1} (\tilde{L}_s v - g_s) \otimes e_0 + \tau_n H_y^{-1} s (\tilde{L}_n v - g_n) \otimes e_N \end{aligned}. \quad (3.15)$$

LEMMA 3.2. *The scheme (3.13) with homogeneous data has a non-growing solution, if D_1 is a compact first-derivative SBP operator, D_2 is a compact second-derivative SBP operator, $x^T(M - Q^T H^{-1} Q)x \geq 0$, $\tau_{w,s} = 1$, $\tau_{e,n} = -1$ and (3.7), (3.8) hold.*

Proof. Let $F = g_{w,e,s,n} = 0$. Multiplying (3.13) by $v_t^T \bar{H}$ from the left and adding the transpose lead to

$$\begin{aligned} \frac{d}{dt} \|v\|_H^2 &= -2c_{11}v_w^T H(D_x v)_w(1 - \tau_w) - 2c_{12}v_w^T H(S_y v)_w(1 - \tau_w) \\ &\quad + 2c_{11}v_e^T H(D_x v)_e(1 + \tau_e) + 2c_{12}v_e^T H(S_y v)_e(1 + \tau_e) \\ &\quad - 2c_{22}v_s^T H(D_y v)_s(1 - \tau_s) - 2c_{21}v_s^T H(S_x v)_s(1 - \tau_s) \\ &\quad + 2c_{22}v_n^T H(D_y v)_n(1 + \tau_n) + 2c_{21}v_n^T H(S_x v)_n(1 + \tau_n) \\ &\quad + (2\tau_w \alpha_w + a)v_w^T H v_w + (2\tau_e \alpha_e - a)v_e^T H v_e \\ &\quad + (2\tau_s \alpha_s + b)v_s^T H v_s + (2\tau_n \alpha_n - b)v_n^T H v_n + DI_c \end{aligned}.$$

In Lemma (3.1) it is shown that by using the first derivative twice, i.e., $(D_1)^2 = H^{-1}(-Q^T H^{-1} Q + BD_1)$ to approximate the two terms, $c_{11}u_{xx}$ and $c_{22}u_{yy}$, we obtain DI as in (3.12). The dissipative part of $(D_1)^2$ is given by $-Q^T H^{-1} Q$. If the compact second derivative $D_2 = H^{-1}(-M + BS)$ is used, the dissipative part is given by $-M$. We restate M as

$M = Q^T H^{-1} Q + (M - Q^T H^{-1} Q)$ and define the rest term $R \equiv M - Q^T H^{-1} Q$. According to the assumption, R is positive semi-definite. Then we obtain for the compact scheme the dissipative term analogous to (3.12),

$$DI_c = DI - c_{11}v^T R_x H_y v - c_{22}v^T H_x R_y v,$$

which mimics (3.6) with two small additional damping terms.

Finally, for stability of the scheme we also need to bound the boundary terms. With $\tau_{w,s} = 1$, $\tau_{e,n} = -1$ we obtain

$$\begin{aligned} \frac{d}{dt} \|v\|_{\tilde{H}}^2 &= (2\alpha_w + a)v_w^T H v_w - \tau_e(2\alpha_e + a)v_e^T H v_e \\ &\quad + (2\alpha_s + b)v_s^T H v_s - (2\alpha_n + b)v_n^T H v_n + DI_c \end{aligned}.$$

This is completely analogous to (3.5). If (3.8) hold we obtain a non-growing energy. \square

3.4. Definiteness of R

Consider a p th-order accurate discretization of the periodic problem (3.13). One can easily derive the following relations for the rest term $R^{(p)}$ (see Lemma 3.2)

$$\begin{aligned} -R^{(2)} &= -\frac{h^3}{4} D_4 \\ -R^{(4)} &= +\frac{h^5}{18} D_6 - \frac{h^7}{144} D_8 \\ -R^{(6)} &= -\frac{h^7}{80} D_8 + \frac{h^9}{600} D_{10} - \frac{h^{11}}{3600} D_{12} \\ -R^{(8)} &= +\frac{h^9}{350} D_{10} - \frac{h^{11}}{2520} D_{12} + \frac{h^{13}}{14700} D_{14} - \frac{h^{15}}{78400} D_{16}, \end{aligned} \quad (3.16)$$

where

$$D_{2n} = (D_+ D_-)^n \quad (3.17)$$

is an approximation of $\frac{d^2 v}{dx^{2n}}$; $(D_+ D_- v)_j = (v_{j+1} - 2v_j + v_{j-1})/h^2$ is the compact second-order finite difference approximation. By using Fourier analysis, it is easily shown (see, for example, Mattsson *et al.* (2004)) that $-R^{(p)}$ constitutes only dissipative terms.

We have shown that the non-compact stencil plus a dissipative term is equal to the compact scheme for a Cauchy problem. Since we have derived an energy estimate for the non-compact scheme, we conclude that the same estimate (with an additional dissipative term) will lead to stability for the compact scheme as well. However, a careful boundary closure is required in order to maintain this property for initial-boundary value problems.

Lemma (3.2) introduces a relation between the compact first- and second-derivative SBP operators via $R \equiv M - Q^T H^{-1} Q$. For the second-order accurate case we have

$$R^{(2)} = \frac{1}{h} \begin{bmatrix} \frac{1}{4} & -\frac{1}{2} & \frac{1}{4} & 0 & 0 & 0 & 0 \\ -\frac{1}{2} & \frac{5}{4} & -1 & \frac{1}{4} & 0 & 0 & 0 \\ \frac{1}{4} & -1 & \frac{3}{2} & -1 & \frac{1}{4} & 0 & 0 \\ 0 & \frac{1}{4} & -1 & \frac{3}{2} & -1 & \frac{1}{4} & 0 \\ 0 & 0 & \frac{1}{4} & -1 & \frac{3}{2} & -1 & \frac{1}{4} \\ 0 & 0 & 0 & \frac{1}{4} & -1 & \frac{5}{4} & -\frac{1}{2} \\ 0 & 0 & 0 & 0 & \frac{1}{4} & -\frac{1}{2} & \frac{1}{4} \end{bmatrix}. \quad (3.18)$$

The following Theorem can be proven (although it is not shown here).

THEOREM 3.3. *Let A be an $n \times n$ pentadiagonal symmetric matrix. Assume $\sum_{j=1}^n A_{ij} =$*

0 and $A_{ii} > 0$, $A_{i,i+1} < 0$, $A_{i,i+2} > 0$. If $-A_{2,3} \geq 2A_{2,4}$, $-A_{n,n-1} \geq 2A_{n,n-2}$ and $-A_{i,i+1} \geq 2A_{i-1,i+1} + 2A_{i,i+2}$, $i = 3 \dots n-2$, then A is positive semi-definite.

COROLLARY 3.4. *The matrix, $R^{(2)}$, given by (3.18) is positive semi-definite.*

Proof. The conditions in Theorem 3.3 can easily be verified. \square

In the fourth- and sixth-order cases it is possible to derive similar Theorems. After extensive analysis (not shown here) we conclude that the compact schemes are bounded by energy estimates, if the boundary closures are chosen properly.

4. Results

We compare the efficiency of the compact and the non-compact formulation by performing numerical simulations of the non-linear problem (3.2). Choosing $c_{11} = c_{12} = c_{21} = c_{22} = \epsilon$, we construct the analytic solution

$$u = -a \tanh \left(\frac{a((1-\alpha)x + \alpha y - ct)}{2\epsilon} \right) + c, \quad (4.1)$$

which describes a two-dimensional viscous shock. The parameter α defines the propagation angle of the shock, and a, c can be chosen arbitrarily. We solve the problems on a rectangular domain Ω . The standard explicit fourth-order Runge-Kutta method is used for time integration.

One of the leading motives (see Section 1) for using a compact formulation was to have damping on the high-frequency modes, which are often triggered by unresolved features in the solution (like a shock). In the first test we compared the compact and non-compact fourth-order discretizations with $a = 1$, $c = 2$, and $\alpha = 0.2$, allowing the viscous shock to travel out through the north-east boundary. The results are shown in Fig. 2.

In the second test we choose $a = 1$, $c = 0$ to obtain a stationary viscous shock. This means that there are no dispersive errors present in the computation, which isolates the dissipative errors. To test the efficiency in handling mildly under-resolved problems (strong shocks require additional artificial dissipation), we compared the second-order formulations for the case with $\epsilon = 0.01$. For $N < 100$, this is a slightly under-resolved problem. To obtain a solution with an $l_2(\text{error}) < 0.01$, the compact second-order formulation requires 38^2 grid points, and the non-compact 2nd-order formulation requires 94^2 grid points. This is due to the presence of high-frequency modes in the non-compact formulation. In Fig. 2 we show a comparison of the convergence history between the compact and the non-compact formulation on the mesh with 38^2 grid points. Both solutions were run to $t = 10$. The compact discretization is clearly superior.

4.1. The two-dimensional compressible Navier-Stokes

To demonstrate that the stability properties of (3.4) carry over to the 2-D Navier-Stokes equations, we will compute an analytic viscous shock solution (see Svärd & Nordström (2006)) and laminar flow over a cylinder. (In fact, the the stability properties carry over to the 3-D Navier-Stokes equations as well.)

In the first test we chose a computational domain $0 \leq x, y \leq 3$. The shock is initiated 0.25 unit lengths away from the diagonal of the box and is propagated with an angle of 45° , 0.5 length units across the grid. The Reynold number is 10, which results in a smooth profile. A convergence study is shown in Table 1. The convergence rate is calculated as

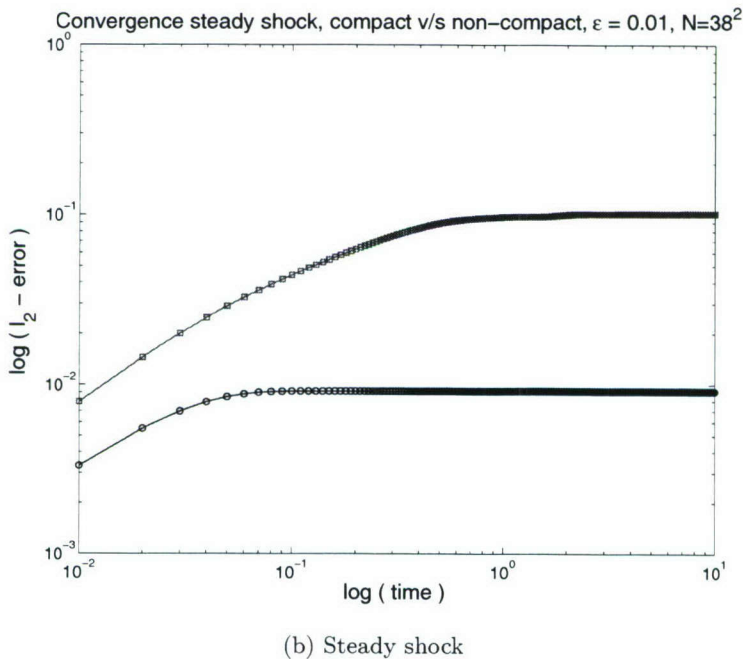
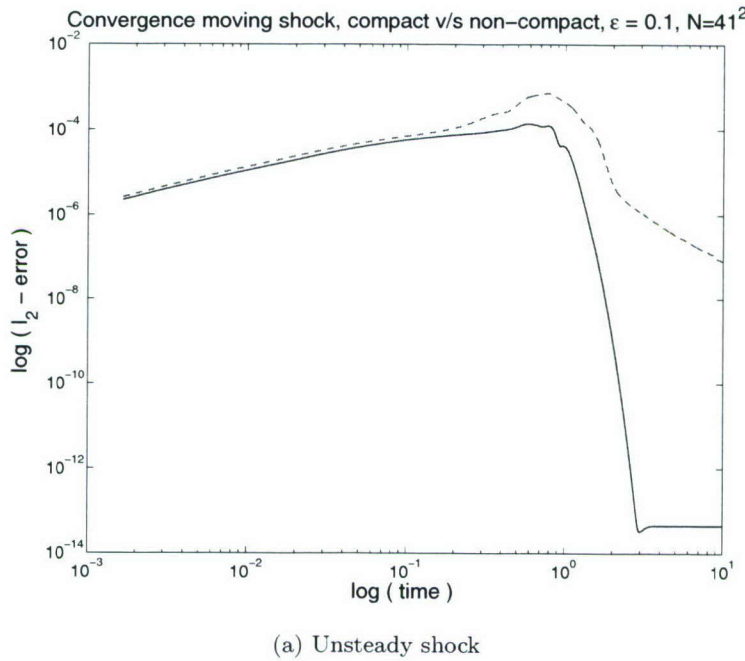


FIGURE 2. The convergence histories. The solid line (and circles) are the fourth-order compact and the dashed (and boxes) the non-compact.

N	$l_2^{(compact)}$	$q^{(compact)}$	$l_2^{(non-compact)}$	$q^{(non-compact)}$
30	-1.61		-1.43	
60	-2.28	2.22	-2.06	2.07
120	-2.89	2.14	-2.68	2.06
240	-3.50	2.10	-3.28	2.05

TABLE 1. $\log(l_2 - \text{error})$ and convergence rate, q, for the compact and non-compact stencils on Cartesian grids.

Drag Coefficient	Maximum Drag Coefficient	Maximum Lift Coefficient	Base Pressure Coefficient
1.3471	1.3569	0.3254	0.7407
Strouhal number	Separation Angle	Recirculation Bubble length	U_{min}
0.1687	118.6	1.414	-0.1778

TABLE 2. Simulation results.

$$q = \log_{10} \left(\frac{\|w - w^{(h_1)}\|_h}{\|w - w^{(h_2)}\|_h} \right) / \log_{10} \left(\frac{h_1}{h_2} \right), \quad (4.2)$$

where w is the analytic solution and $w^{(h_1)}$ the corresponding numerical solution with grid size h_1 . $\|w - w^{(h_1)}\|_h$ is the discrete $l_2 - \text{error}$.

Although the study is not shown here, the difference in accuracy between the compact and wide stencil formulations (for a steady problem) was found to be larger when the shock is not fully resolved (by increasing the Re number, using a coarse grid).

In the second test we computed the flow over a 2-D cylinder at $Re_D = 100$. An unstructured finite volume code for compressible N-S equations is used to simulate the flow. The free-stream Mach number is set to 0.1 to be able to compare the results from previous incompressible simulations. The domain is a cylinder of radius $30 \times D$. Structured grid is used near the cylinder while unstructured grid is used to capture the wake. To resolve the thin laminar boundary layer in front of the cylinder, the minimum radial grid spacing is set to 3×10^{-3} , while 260 points are used in the circumferential direction. Figure 3 shows the contour of density.

Table 2 shows the results, which are in good agreement with the results presented in Kravchenko (1998); Kwon & Choi (1995).

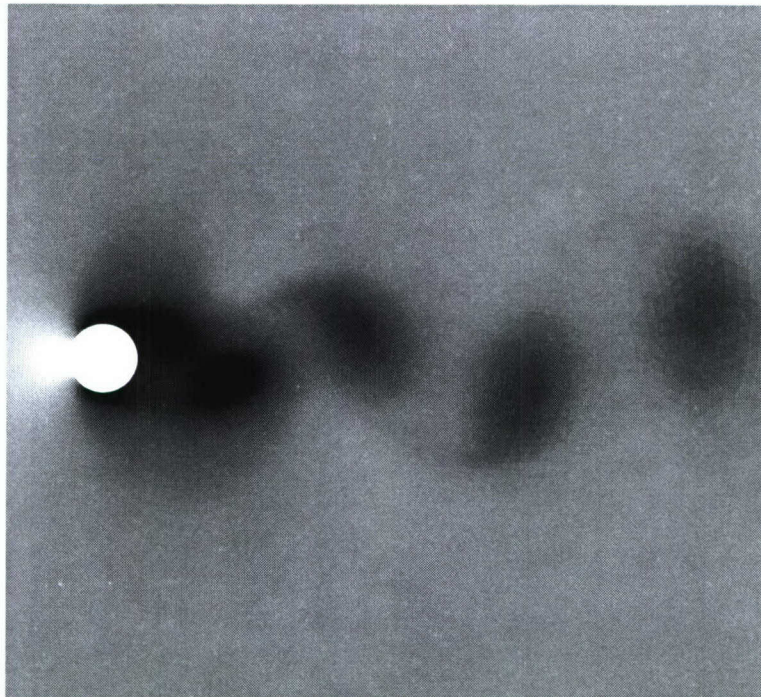


FIGURE 3. Flow over a 2-D cylinder (density), $Re_D = 100$.

5. Conclusions and future work

Our approach have been to use SBP operators and the SAT technique to enforce the boundary conditions. By using energy estimates it is proven that there are compact SBP operators that lead to stability for problems with mixed and pure second derivatives, such as the compressible Navier-Stokes equations. Numerical computations for both Burgers' equation and the two-dimensional Navier-Stokes equations corroborate the stability properties and also show that the compact schemes are more accurate than the corresponding non-compact schemes.

The next step will be to couple the compact unstructured finite volume discretization to a high-order finite difference discretization to obtain an efficient hybrid Navier-Stokes solver. This will allow us to capture the geometry using the unstructured method and also allow us to capture the wave propagation in the farfield.

Acknowledgments

This work is supported by the Advanced Simulation and Computing Program of the United States Department of Energy.

REFERENCES

CARPENTER, M. H. & NORDSTRÖM, J. & GOTTLIEB, D. 1999, A Stable and Conservative Interface Treatment of Arbitrary Spatial Accuracy. *J. Comp. Phys.* **148**, 341–365.

CARPENTER, M. H. & GOTTLIEB, D. & ABARBANEL, S. 1994, Time-stable boundary conditions for finite-difference schemes solving hyperbolic systems: Methodology and application to high-order compact schemes. *J. Comp. Phys.* **111**, 220–236.

GUSTAFSSON, B. & KREISS, H.-O. & OLIGER, J. 1995, Time dependent problems and difference methods. *Wiley, New York*.

KRAVCHENKO, A. G. 1998, B-spline methods and zonal grids for numerical simulation of turbulent flows *Ph.D. Thesis*, Department of Mechanical Engineering, Stanford University.

KREISS, H.-O. & SCHERER, G. 1974, Finite element and finite difference methods for hyperbolic partial differential equations. *Mathematical Aspects of Finite Elements in Partial Differential Equations.*, Academic Press, Inc.

KWON, K. & CHOI, H. 1994, Control of laminar vortex shedding behind a circular cylinder using splitter plates. *Phys. Fluids* **8**(2), 479–486.

LELE, S. K. 1992, Compact Finite Difference Schemes with Spectral-like Resolution. *J. Comp. Phys.* **103**, 16–42.

MATTSSON, K. & SVÄRD, M. & NORDSTRÖM, J. 2004, Stable and Accurate Artificial Dissipation. *J. Sci. Comput.* **21**, 57–79.

MATTSSON, K. & NORDSTRÖM, J. 2004, Summation by parts operators for finite difference approximations of second derivatives. *J. Comp. Phys.* **199**, 503–540.

NORDSTRÖM, J. & SVÄRD, M. 2005, Well Posed Boundary Conditions for the Navier–Stokes Equations. *SIAM J. Num. Anal.* **43**, 1231–1255.

STRAND, B. 1994, Summation by Parts for Finite Difference Approximations for d/dx . *J. Comp. Phys.* **110**, 47–67.

STRANG, G. 1964, Accurate partial difference methods II. Non-linear problems *Num. Math.* **6**, 37–46.

SVÄRD, M. & NORDSTRÖM, J. 2006, On the order of accuracy for difference approximations of initial-boundary value problems. *J. Comp. Phys.* **218**, 333–352.

Efficient wave propagation on complex domains

By K. Mattsson, F. Ham AND G. Iaccarino

1. Motivation and objectives

In many applications, such as general relativity (see, for example, Szilagyl *et al.* (2005)), seismology, and acoustics, the underlying equations are systems of second-order hyperbolic partial differential equations. However, as pointed out by Kreiss *et al.* (2002), with very few exceptions (see for example Kreiss *et al.* (2002, 2004); Shubin & Bell (1987); Bamberger *et al.* (1997); Cohen & Joly (1996)), the equations are rewritten and solved on first-order form. There are three obvious drawbacks with this approach: 1) the number of unknowns is doubled, 2) spurious oscillations due to unresolved features might be introduced, and 3) double resolution (both in time and in each of the spatial dimensions) is required to obtain the same accuracy. The reasons for solving the equations in first-order form are due to the fact that computational methods for first-order hyperbolic systems are very well developed, and they are naturally more suited for complex geometries.

For problems on complex domains it is very difficult to maintain both high-order accuracy and efficiency. To retain high-order accuracy for problems with discontinuities in the coefficients is another concern (see for example Gustafsson & Mossberg (2004) and Gustafsson & Wahlund (2004)). High-order finite difference methods are very accurate and efficient on problems that are relatively simple geometrically. In Mattsson & Nordström (2006) high-order accurate, strictly stable schemes for the wave equations on discontinuous media were constructed by combining compact Summation-By-Parts (SBP) operators (constructed in Mattsson & Nordström (2004)) with the projection method. However, on complex domains it is difficult to obtain a high quality grid that supports high-order accuracy. In Kreiss *et al.* (2002, 2004, 2006) a second-order accurate finite difference method for the wave equation on second-order form was constructed, where the geometry is handled by embedding the domain into a Cartesian grid. It is unclear if that technique can be extended to accurately handle discontinuous media.

In this paper we will show how to impose boundary and discontinuous interface conditions in a strictly stable way by combining compact second derivative SBP operators and the Simultaneous Approximation Term (SAT) method by Carpenter *et al.* (1994). To handle complex geometries we will make use of a compact and second-order accurate Laplacian operator with SBP property on unstructured grids (presented in Ham *et al.* (2006) elsewhere in this volume).

In Section 2 we introduce some definitions and discuss the SBP property for the second derivative. In Section 3 we introduce the numerical method by considering the second-order wave equation in one dimension (1-D). In Section 4 we verify the accuracy and stability properties by performing numerical computations on complex geometries using an unstructured finite volume discretization. In Section 5 we present our conclusions.

2. Definitions

Definitions are needed to describe the SBP property in detail. For clarity we consider the 1-D problem. The extension to the 3-D unstructured case is directly related to the 1-D analysis through the use of matrix notation, as will be shown in Section 4.

2.1. The energy method

Let the inner product for real valued functions $u, v \in \mathbf{L}^2[0, 1]$ be defined by $(u, v) = \int_0^1 u^T v \, dx$, and let the corresponding norm be $\|u\|^2 = (u, u)$. We also introduce a weighted norm

$$\|u\|_\omega^2 = \int_0^1 u^T u \omega(x) \, dx ,$$

where $\omega(x) \in \mathbf{L}^2[0, 1]$ is a positive function. The domain ($0 \leq x \leq 1$) is discretized using $N+1$ equidistant grid points,

$$x_i = i h, \quad i = 0, 1, \dots, N, \quad h = \frac{1}{N} .$$

The numerical approximation at grid point x_i is denoted v_i , and the discrete solution vector is $v^T = [v_0, v_1, \dots, v_N]$. We define an inner product for discrete, real valued vector-functions $u, v \in \mathbf{R}^{N+1}$ by $(u, v)_H = u^T H v$, where $H = H^T > 0$, with a corresponding norm $\|v\|_H^2 = v^T H v$.

2.2. Summation-By-Parts property

An SBP operator mimics the behavior of the corresponding continuous operator with respect to the inner product previously mentioned. Consider the wave equation $au_{tt} = (bu_x)_x$, $x \in [0, 1]$, and $a, b > 0$. Integration by parts (IBP) leads to

$$\frac{d}{dt} (\|u_t\|_a^2 + \|u_x\|_b^2) = 2buu_x|_0^1 . \quad (2.1)$$

Consider the semi-discrete approximation $AHv_{tt} = (-M + BS)v$, where A is the projection of a onto the diagonal. By multiplying the semi discrete approximation by v_t^T and by adding the transpose, we obtain

$$\frac{d}{dt} (\|v_t\|_{HA}^2 + v^T M v) = 2v_0(BSv)_0 + 2v_N(BSv)_N . \quad (2.2)$$

To obtain (2.2) requires that 1) $H > 0$ and diagonal, 2) $M = M^T \geq 0$, and 3) BS mimic the boundary derivative operator. Formula (2.2) is a discrete analog to the IBP formula (2.1) in the continuous case. The above procedure is referred to as the energy method. We introduce the following definition:

DEFINITION 2.1. A difference operator $D_2 = H^{-1}(-M + BS)$ approximating $(bu_x)_x$ is said to be a symmetric second derivative SBP operator if H is diagonal and positive definite, M is symmetric and positive semi-definite, S includes an approximation of the first derivative operator at the boundary, and $B = \text{diag}(-b_0, 0, \dots, 0, b_N)$.

3. Boundary treatment

In this method developed by Carpenter *et al.* (1994), the boundary conditions are introduced as a penalty term. When the energy method is applied, a discrete analog to the continuous energy is obtained.

Consider the 1-D wave equation on second-order form:

$$\begin{aligned} au_{tt} &= (bu_x)_x + F, \quad 1 \geq x \geq 0, \quad t \geq 0 \\ u &= f_1, \quad u_t = f_2, \quad 1 \geq x \geq 0, \quad t = 0, \end{aligned} \quad (3.1)$$

where $\sqrt{a^{-1}b} = c$ is the wave speed. For density waves $a^{-1} = \rho c^2$, and $b^{-1} = \rho$, where $\rho > 0$ is the density of the media. General boundary conditions are given by

$$\begin{aligned} L_l u &= \beta_1 u(0, t) - \beta_2 b_0 u_x(0, t) + \beta_3 u_t(0, t) = g_l(t) \\ L_r u &= \beta_1 u(1, t) + \beta_2 b_N u_x(1, t) + \beta_3 u_t(1, t) = g_r(t). \end{aligned} \quad (3.2)$$

Note that (3.2) includes the special case of Dirichlet boundary conditions (and radiation boundary conditions. See for example Tsynkov (1998) and Hagstrom (1999)).

3.1. Mixed boundary conditions

We start by considering the case where $\beta_2 \neq 0$, which includes the important case of Neumann boundary conditions ($\beta_1 = 0$, $\beta_2 = 1$, $\beta_3 = 0$). Assuming zero boundary data and forcing function F , the energy method leads to

$$\frac{d}{dt} \left(\|u_t\|_a^2 + \|u_x\|_b^2 + \frac{\beta_1}{\beta_2} u_0^2 + \frac{\beta_1}{\beta_2} u_1^2 \right) = -\frac{\beta_3}{\beta_2} (u_t^2)_0 - \frac{\beta_3}{\beta_2} (u_t^2)_1. \quad (3.3)$$

Hence, the continuous problem (3.1) and (3.2) have an energy estimate if

$$\frac{\beta_1}{\beta_2} \geq 0, \quad \frac{\beta_3}{\beta_2} \geq 0. \quad (3.4)$$

The semi-discrete boundary conditions corresponding to (3.2) can be written

$$\begin{aligned} L_l^T v &= \beta_1 v_0 + \beta_2 (BSv)_0 + \beta_3 (v_t)_0 = g_l \\ L_r^T v &= \beta_1 v_N + \beta_2 (BSv)_N + \beta_3 (v_t)_N = g_r, \end{aligned} \quad (3.5)$$

where v is the discrete solution vector, S is the boundary derivative operator in Definition 2.1, and $B = \text{diag}(-b_0, 0, \dots, 0, b_N)$.

The SAT method for the wave equation in second-order form with the boundary conditions (3.2), can be written

$$\begin{aligned} HAv_{tt} &= (-M + BS)v + \tau e_0 (L_l^T v - g_l) + \tau e_N (L_r^T v - g_r) + F \\ v &= f_1, \quad v_t = f_2, \quad t = 0. \end{aligned} \quad (3.6)$$

LEMMA 3.1. (3.6) with homogenous data has a non-growing solution if D_2 is a symmetric SBP operator, $\tau = 1/\beta_2$ and (3.4) hold.

Proof. Let $F, g_l, g_r = 0$. Multiplying (3.6) by v_t^T from the left and adding the transpose leads to

$$\begin{aligned} v_t^T H A v_{tt} + v_{tt}^T A H v_t &= -v_t^T M v - v^T M^T v_t + 2(v_t)_0 (BSv)_0 + 2(v_t)_N (BSv)_N \\ &\quad + 2\tau(v_t)_0 (\beta_1 v_1 + \beta_2 (BSv)_0 + \beta_3 (v_t)_0) \\ &\quad + 2\tau(v_t)_N (\beta_1 v_N + \beta_2 (BSv)_N + \beta_3 (v_t)_N) \end{aligned}.$$

If D_2 is a symmetric SBP operator we obtain

$$\begin{aligned} \frac{d}{dt} (\|v_t\|_{H^A}^2 + v^T M v - \tau \beta_1 v_0^2 - \tau \beta_1 v_N^2) &= +\tau \beta_3 (v_t)_0^2 + \tau \beta_3 (v_t)_N^2 \\ &\quad + 2(1 + \tau \beta_2)(v_t)_0 (BSv)_0 + 2(1 + \tau \beta_2)(v_t)_N (BSv)_N \end{aligned}$$

If $\tau = -1/\beta_2$, we obtain an energy estimate completely analogous to (3.3). If (3.4) holds, we have a non-growing energy. \square

3.2. Dirichlet boundary conditions

We now consider the case of Dirichlet boundary conditions ($\beta_1 = 1$, $\beta_2 = 0$, $\beta_3 = 0$). We introduce the following Lemma:

LEMMA 3.2. *The dissipative part M of a symmetric second-derivative SBP operator has the following property:*

$$v^T M v = h \frac{\alpha}{b_0} (BSv)_0^2 + h \frac{\alpha}{b_N} (BSv)_N^2 + v^T \tilde{M} v , \quad (3.7)$$

where \tilde{M} is symmetric and positive semi-definite, and α a positive constant, independent of h .

This was indicated in Carpenter *et al.* (1999) but never derived explicitly. With Dirichlet boundary condition ($\beta_1 = 1$, $\beta_2 = 0$, $\beta_3 = 0$) and homogenous data, the energy method leads to

$$\frac{d}{dt} (\|u_t\|_a^2 + \|u_x\|_b^2) = 0 . \quad (3.8)$$

The SAT method for the wave equation on second-order form and Dirichlet boundary conditions is given by

$$\begin{aligned} HA v_{tt} = & (-M + BS)v + \epsilon (BS)^T e_0 (v_0 - g_l) + \sigma b_0 e_0 (v_0 - g_l) + F \\ & + \epsilon (BS)^T e_N (v_N - g_r) + \sigma b_N e_N (v_N - g_r) \end{aligned} \quad (3.9)$$

$$v(0) = f_1, \quad v_t(0) = f_2 .$$

LEMMA 3.3. (3.9) with homogenous data has a non-growing solution if D_2 is a symmetric SBP operator, $\sigma \leq -\frac{1}{\alpha h}$, $\epsilon = 1$, and (3.7) hold.

Proof. Let $F, g_l, g_r = 0$. Multiplying (3.9) by v_t^T from the left and adding the transpose leads to

$$\begin{aligned} v_t^T H A v_{tt} + v_{tt}^T A H v_t = & -v_t^T M v - v^T M^T v_t + 2(v_t)_0 (BSv)_0 + 2(v_t)_N (BSv)_N \\ & + 2\epsilon (BSv_t)_0 v_0 + 2\sigma b_0 (v_t)_0 v_0 \\ & + 2\epsilon (BSv_t)_N v_N + 2\sigma b_N (v_t)_N v_N \end{aligned} .$$

If D_2 is a symmetric SBP operator, $\epsilon = 1$ and (3.7) hold, we obtain

$$\frac{d}{dt} \left(\|v_t\|_{H^A}^2 + v^T \tilde{M} v + w_0^T R_0 w_0 + w_N^T R_N w_N \right) = 0 ,$$

where $w_{0,N}^T = [v_{0,N}, (BSv)_{0,N}]$ and

$$R_0 = \begin{bmatrix} -\sigma b_0 & -1 \\ -1 & \frac{\alpha h}{b_0} \end{bmatrix}, \quad R_N = \begin{bmatrix} -\sigma b_N & -1 \\ -1 & \frac{\alpha h}{b_N} \end{bmatrix} .$$

Finally, if $\sigma \leq -\frac{1}{\alpha h}$ holds, we have a non-growing energy. \square

We introduce the penalty-strength parameter γ through

$$\sigma = -\gamma \frac{1}{\alpha h}$$

Hence a value of $\gamma < 1$, according to Lemma 3.3, will not result in an energy estimate and might lead to an unstable scheme.

3.3. Discontinuous media interface

We start by deriving the interface conditions for the continuous problem. Consider the wave equation

$$aw_{tt} = (bw_x)_x, \quad x \in [-1, 1], \quad t \geq 0,$$

where $a, b > 0$ are discontinuous at $x = 0$ and $c = \sqrt{b/a}$ is the wave propagation speed. Integration by parts leads to

$$\begin{aligned} \int_{-1}^1 aw_{tt}w_t dx &= \lim_{\epsilon \rightarrow 0} \left(\int_{-1}^{-\epsilon} (bw_x)_x w_t dx - \int_1^{\epsilon} (bw_x)_x w_t dx \right) \\ &= \lim_{\epsilon \rightarrow 0} \left(bw_x w_t|_{-1}^1 - bw_x w_t|_{-\epsilon}^{\epsilon} - \int_{-1}^{-\epsilon} bw_x w_{xt} dx + \int_1^{\epsilon} bw_x w_{xt} dx \right). \end{aligned}$$

Obtaining an energy estimate requires that w and bw_x are continuous across the interface, i.e., $\lim_{\epsilon \rightarrow 0} (bw_x w_t|_{-\epsilon}^{\epsilon}) = 0$, leading to $\frac{d}{dt} (\|w_t\|_a^2 + \|w_x\|_b^2) = bw_x w_t|_{-1}^1$. We consider the following problem

$$\begin{aligned} a_1 u_{tt} &= (b_1 u_x)_x, \quad -1 \leq x \leq 0 \\ a_2 v_{tt} &= (b_2 v_x)_x, \quad 0 \leq x \leq 1 \end{aligned}, \quad (3.10)$$

where $a_1 \neq a_2$, $b_1 \neq b_2$. Continuity at the interface ($x = 0$) means that

$$u_t = v_t, \quad b_1 u_x = b_2 v_x. \quad (3.11)$$

The first condition ($u_t = v_t$) holds if we impose $u = v$ at the interface. This will have implications for the time discretization. The discrete approximation to (3.11) is given by

$$u_N = v_0, \quad (u_t)_N = (v_t)_0, \quad (B_1 S v)_N = (B_2 S v)_0, \quad (3.12)$$

where all conditions (also $u = v$) are written out. If we use the interface conditions (3.11) and apply homogeneous Neumann conditions ($u_x = 0$) at the outer boundaries the energy method leads to

$$\frac{d}{dt} E = 0, \quad (3.13)$$

where the energy is defined as

$$E = \|u_t\|_{a_1}^2 + \|v_t\|_{a_2}^2 + \|u_x\|_{b_1}^2 + \|v_x\|_{b_2}^2. \quad (3.14)$$

We will treat the semi-discrete problem in such a way that we exactly mimic (3.13).

The SAT method for this particular problem (3.10)-(3.11) can formally be written

$$\begin{aligned} HA_1 u_{tt} &= (-M_1 + B_1 S)u & HA_2 v_{tt} &= (-M_2 + B_2 S)v \\ &+ \tau e_N(u_N - v_0) & &+ \tau e_0(v_0 - u_N) \\ &+ \beta (B_1 S)_N^T e_N(u_N - v_0) & &+ \beta (B_2 S)_0^T e_0(v_0 - u_N) \\ &+ \gamma e_N((B_1 S u)_N + (B_2 S v)_0) & &+ \gamma e_0((B_2 S v)_0 - (B_1 S u)_N) \\ &+ \sigma e_N((u_t)_N - (v_t)_0) & &+ \sigma e_0((v_t)_0 - (u_t)_N) \\ &+ SAT_l & &+ SAT_r \end{aligned} \quad (3.15)$$

utilizing the discrete conditions (3.12). Here u and v are the solution vectors corresponding to the left and right domain respectively. $SAT_{l,r}$ correspond to the outer boundaries (described in previous sections). The left and right domain is discretized using $(N+1)$ and $(M+1)$ grid points.

We can have different discretizations in the left and right domains. The only requirement for the stability analysis to hold is that we use symmetric SBP operators (see Definition 2.1) in each of the domains.

If we multiply (3.15) by $u_t^T H$ and $v_t^T H$, respectively, we obtain

$$\frac{d}{dt} E_H = 2\sigma v_t^T D v_t , \quad (3.16)$$

where the discrete energy is defined as

$$E_H = \|u_t\|_{H_{A_1}}^2 + \|v_t\|_{H_{A_2}}^2 + u^T M_1 u + v^T M_2 v + IT + BT ,$$

where IT corresponds to the interface terms, BT the boundary terms, and

$$D = \begin{bmatrix} 1 & -1 \\ -1 & 1 \end{bmatrix}$$

is a positive semi-definite matrix. The first stability requirement is that $\sigma \leq 0$.

The advantage of choosing $\sigma = 0$ is that we can obtain a compact time discretization. This is also the choice in the computations. However, by choosing $\sigma < 0$ we introduce damping, which will potentially lead to a more robust and less reflective interface treatment. We have not included that numerical study in this paper.

To have a discrete energy we must further show that E_H is positive. Certain relations need to be met to demonstrate this. We begin by recognizing the symmetry conditions

$$\gamma = -\frac{1}{2} \quad , \quad \beta = \frac{1}{2} . \quad (3.17)$$

The interface term is given by $IT = w^T R w$, where

$$R = \begin{bmatrix} -\tau & \tau & -\frac{1}{2} & \frac{1}{2} \\ \tau & -\tau & \frac{1}{2} & -\frac{1}{2} \\ -\frac{1}{2} & \frac{1}{2} & \frac{h\alpha}{b_1} & 0 \\ \frac{1}{2} & -\frac{1}{2} & 0 & \frac{h\alpha}{b_2} \end{bmatrix} , \quad w = \begin{bmatrix} u_N \\ v_0 \\ (B_1 S u)_N \\ (B_2 S v)_0 \end{bmatrix} .$$

Obtaining an energy estimate requires

$$\tau \leq -\frac{b_1 + b_2}{4h\alpha} , \quad (3.18)$$

such that R becomes positive semi-definite. Here $b_{1,2}$ denotes the local values of $b_{1,2}$ at the interface.

4. 3-D simulations on unstructured grids

By combining symmetric second-derivative SBP operators and the SAT method, to implement the boundary conditions (see for example (3.9)), we obtain an ODE system (with N unknowns)

$$\begin{aligned} v_{tt} &= Qv + G(t) \\ v(0) &= f_1 , v_t(0) = f_2 \end{aligned} , \quad (4.1)$$

for the discrete solution vector v . In Section 3 we have shown that the matrix Q have non-positive and real eigenvalues (a necessary stability condition) by utilizing the energy method. For the second-order accurate case we approximate v_{tt} using the central second-order scheme resulting in an explicit two-step method (see Mattsson & Nordström (2006) for details). The present method has been implemented for unstructured tetrahedral grids using a node-based finite-volume discretization.

4.1. Verification

In the first test we verify the accuracy and stability of the Dirichlet boundary conditions. The semi-discrete finite volume system, including Dirichlet boundary conditions, can be written:

$$\bar{H}Av_{tt} = (-\bar{M} + \bar{B}S_{i,b}) + \epsilon(\bar{B}S_{i,b})^T(v - g) + \sigma B_{i,b}(v - g), \quad (4.2)$$

where \bar{H} is the nodal volume, \bar{M} is the symmetric unstructured volume-integrated Laplacian operator described in Ham *et al.* (2006). Here $\bar{B}S_{i,b}$ is the volume-integrated gradient operator, which is based on Green-Gauss integration over the one-sided boundary nodal volumes assuming a linear variation in each associated tetrahedron. $B_{i,b}$ is the value of b at the boundary nodes. In the 1-D case we concluded (see Lemma 3.3) that σ is proportional to h^{-1} . Based on the previous structured 1-D analysis we expect that σ is proportional to $\bar{H}_{i,b}/A_{i,b}$, where $A_{i,b}$ is the area magnitude and $\bar{H}_{i,b}$ the nodal volume associated with the boundary node. The penalty parameters ϵ, σ in (4.2) are completely analogous to the ones in the 1-D case (3.9).

An energy estimate exists for the choice $\beta = 1$ and $\sigma = -\gamma\bar{H}_{i,b}/A_{i,b}$, for some γ large enough. Unlike the uniform structured 1-D case, it is more complicated to analytically derive a single sharp value for the minimum borrowing penalty, i.e., γ_{min} , that is applicable to all unstructured grids. Instead we performed a numerical study. There was a slight variation of the threshold value at which the simulations become unstable, although always close to 1, the limit in the 1-D case.

To verify the stability and accuracy of the unstructured implementation, a triply-periodic tetrahedral mesh was generated around a $2 \times 2 \times 2$ array of three cube compounds. Inspiration for this choice of geometry comes from M. C. Escher's Waterfall (see Fig. 1). Our cubes have a characteristic dimension of 0.2, and have center-to-center spacing of 0.5 in a $1 \times 1 \times 1$ box. The simulation of the wave equation in the surrounding volume requires an unstructured mesh to capture the complex polyhedral boundaries, although at any resolution the boundaries are precisely represented because all surfaces are planar. This allows us to generate a series of fine grids starting from a coarse grid by recursively applying a tetrahedral-splitting algorithm.

A grid convergence study was performed using the sequence of triply-periodic grids described previously and computing the standing wave problem $u = \sin(wct) \sin(wx)$, with the exact solution as initial condition and time-dependent Dirichlet boundary data. The convergence rate is calculated as

$$q = \log_{10} \left(\frac{\|u - v^{(N_1)}\|_h}{\|u - v^{(N_2)}\|_h} \right) / \log_{10} \left(\frac{N_1}{N_2} \right)^{1/d}, \quad (4.3)$$

where d is the dimension (here $d = 1$), u is the analytic solution, and $v^{(N_1)}$ the corresponding numerical solution with N_1 unknowns. $\|u - v^{(N_1)}\|_h$ is the discrete l_2 norm of the error. The results are presented in Table 1, where the grid sizes range from 46,680 tetrahedra up to 23,900,160 tetrahedra on the finest grid. With each grid refinement

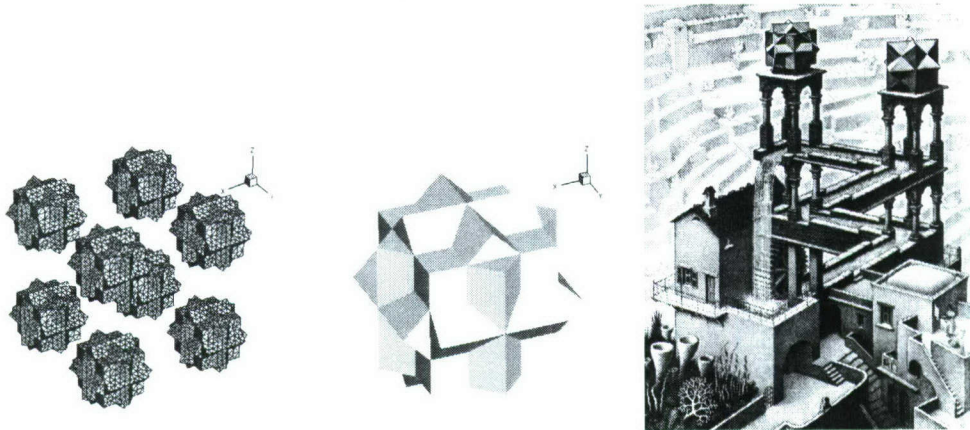


FIGURE 1. Geometrical details and inspiration for the three cube compounds.

N	$\log(l_2)$	q	Δx	$\log(l_2)$	q
46,680	-1.46	-	0.0625	-1.11	
373,440	-2.08	2.056	0.03125	-1.70	1.97
2,987,520	-2.69	2.028	0.015625	-2.31	2.07
23,900,160	-3.30	2.003	0.0078125	-2.92	2.04
			0.00390625	-3.52	2.00

TABLE 1. Unstructured grid refinement study: reduction in l_2 error with grid refinement for Dirichlet BC (left) and discontinuous interface (right).

the time step was also refined by a factor of 2 such that the temporal integration error remained small.

In the second test we verify the accuracy for the discontinuous interface. We chose an analytic solution

$$u = \cos(w_1 c_1 t) \cos(w_1 x), \quad x \in [-1, 0], \quad t \geq 0, \quad w_1 = (2n+1)\pi, \quad m, n \in \mathbf{Z}$$

$$v = \cos(w_2 c_2 t) \cos(w_2 x), \quad x \in [0, 1], \quad t \geq 0, \quad w_2 = (2m+1)\pi, \quad c_2 = c_1 \frac{w_1}{w_2},$$

and compute the solution on a square multi-block domain with $a_1 = b_1 = 1$, $a_2 = b_2 = 0.6$, $n = 1$ and $m = 2$. A convergence study is shown in Table 1.

4.2. Application

As a qualitative illustration of the method's capability, we compute the 3-D propagation of a Gaussian pulse in the volume surrounding the $2 \times 2 \times 2$ array of 3-cube compounds. For this case, we made use of the unstructured mesh to significantly extend the grid at modest cost to help reduce reflections at the far field boundary. The simulations reported below were run on the finest grid (see Table 1) produced by 3 applications of recursive tetrahedral refinement to this coarse grid.

To qualitatively investigate the effect of the Dirichlet boundary conditions, the same simulation was run with homogenous Neumann boundary conditions at the boundaries. Results from these simulations are compared in Fig. 2. The grid for this simulation

consisted of 31,126,528 tetrahedra, with constant computational time step $\Delta t = 0.00025$. Results are plotted on a plane passing through the center of 4 of the polyhedra for 3 times, $t = 0.25$, $t = 0.5$, and $t = 0.75$. The location of the center of the initial pulse is in this plane and displaced slightly toward the upper right, producing the observed diagonal symmetry. At $t = 0.75$ the coarseness of the outer grid (see Fig. 2) can be seen producing some reflections.

In the last computation we discretize the interior of the 3-cube compounds and use $a_1 = b_1 = 1$ on the outside domain and $a_2 = b_2 = .2$ on the inside. We then apply the discontinuous interface treatment to compute the 3-D propagation of the Gaussian pulse. The result from that simulation is presented in Figure 2.

5. Conclusions and future work

Time stable boundary treatments are derived for the wave equation on second-order form and on discontinuous media. We consider an unstructured Finite Volume discretization to handle complex geometries in 3-D. The methodology is based on the SBP properties of the schemes in combination with the SAT penalty technique to impose general boundary and interface conditions. The efficiency and accuracy of this method has been verified by numerical simulations.

The next step will be to couple the unstructured finite volume discretization to a high order finite difference discretization to obtain an efficient hybrid method. That will also require some effort to handle the far field boundaries using non-reflecting boundary conditions.

Acknowledgments

This work is supported by the Advanced Simulation and Computing Program of the United States Department of Energy.

REFERENCES

BAMBERGER, A. & GLOWINSKI, R. & TRAN, Q. H. 1997, A domain decomposition method for the acoustic wave equation with discontinuous coefficients and grid change. *SIAM J. Num. Anal.* **34**, 603–639.

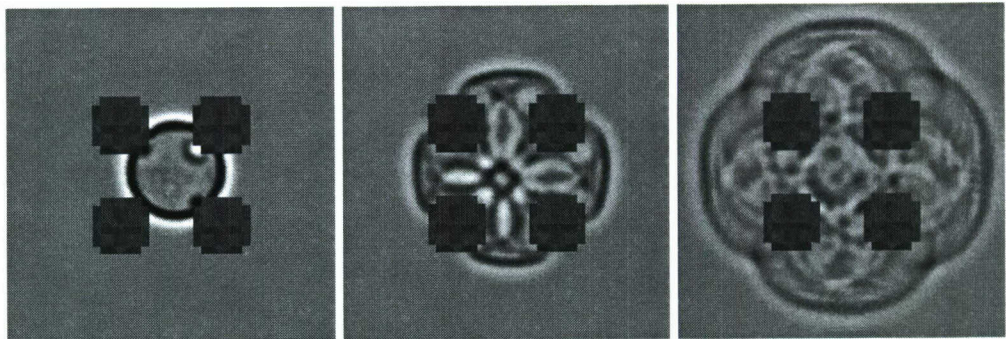
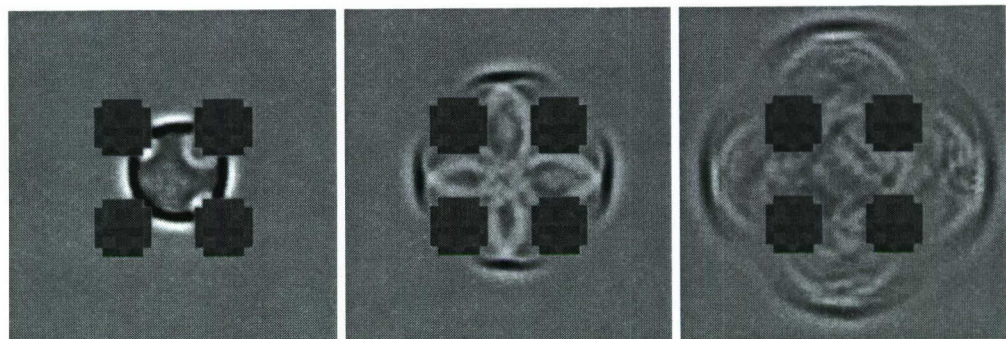
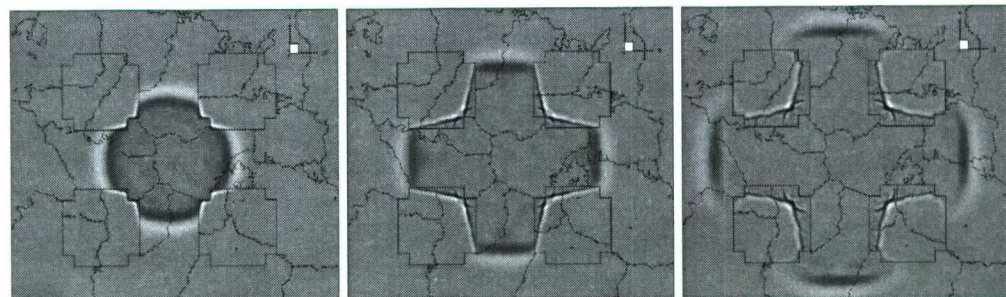
CARPENTER, M. H. & GOTTLIEB, D. & ABARBANEL, S. 1994, Time-stable boundary conditions for finite-difference schemes solving hyperbolic systems: Methodology and application to high-order compact schemes. *J. Comp. Phys.* **111**, 220–236.

CARPENTER, M. H. & NORDSTRÖM, J. & GOTTLIEB, D. 1999, A Stable and Conservative Interface Treatment of Arbitrary Spatial Accuracy. *J. Comp. Phys.* **148**, 341–365.

COHEN, G. & JOLY, P. 1996, Construction and analysis of fourth-order finite difference schemes for the acoustic wave equation in nonhomogeneous media. *SIAM J. Num. Anal.* **33**, 1266–1302.

GUSTAFSSON, V. & MOSSBERG, E. 2004, Time compact high order difference methods for wave propagation. *SIAM J. Sci. Comput.* **26**, 259–271.

GUSTAFSSON, V. & WAHLUND, P. 2004, Time compact difference methods for wave propagation in discontinuous media. *SIAM J. Sci. Comput.* **26**, 272–293.

(a) Neumann boundary conditions: $\partial\phi/\partial n = 0$ (b) Dirichlet boundary conditions: $\phi = 0$ 

(c) Discontinuous media.

FIGURE 2. Propagation of a 3D Gaussian pulse comparing different boundary and interface conditions on the $2 \times 2 \times 2$ array of 3-cube compounds.

HAGSTROM, T. 1999, Radiation boundary conditions for the numerical simulation of waves. *Acta Numerica* 8, 47–106.

HAM, F. & MATTSSON, K. & IACCARINO, G. 2006 Accurate and stable finite vol-

ume operators for unstructured flow solvers *Center for Turbulence Research Annual Research Briefs* Stanford University, Stanford, California.

KREISS, H.-O. & PETERSSON, N. A. & YSTRÖM, J. 2002, Difference approximations for the second order wave equation. *SIAM J. Num. Anal.* **40**, 1940–1967.

KREISS, H.-O. & PETERSSON, N. A. & YSTRÖM, J. 2004, Difference approximations of the Neumann problem for the second order wave equation. *SIAM J. Num. Anal.* **42**, 1292–1323.

KREISS, H.-O. & PETERSSON, N. A. 2006, A Second Order Accurate Embedded Boundary Method for the Wave Equation with Dirichlet Data. *SIAM J. Sci. Comput.* **27**, 1141–1167.

MATTSSON, K. & NORDSTRÖM, J. 2004, Summation by parts operators for finite difference approximations of second derivatives. *J. Comp. Phys.* **218**, 503–540.

MATTSSON, K. & NORDSTRÖM, J. 2006, High order finite difference methods for wave propagation in discontinuous media. *J. Comp. Phys.* **220**, 249–269.

SHUBIN, G. R. & BELL, J. B. 1987, A modified equation approach to constructing fourth order methods for acoustic wave propagation. *SIAM J. Sci. Stat. Comput.* **8**, 135–151.

SZILAGYL, B., & KREISS, H.-O. & WINICOUR, J. W. 2005, Modeling the Black Hole Excision Problem. *Physical Review D* **71**, 104035.

TSYNKOV, S. V. 1998, Numerical solution of problems on unbounded domains. A review. *Applied Numerical Mathematics* **27**, 465–532.

A stable, efficient, and adaptive hybrid method for unsteady aerodynamics

By **J. Nordström**[†], **M. Svärd**, **M. Shoeybi**, **F. Ham**, **K. Mattsson**, **G. Iaccarino**,
E. van der Weide AND **J. Gong**[‡]

1. Motivation and objectives

The generation and transportation of vortices from wingtips, rotors, and wind mills, and the generation and propagation of sound from aircraft, cars, and submarines require methods that can handle locally highly non-linear phenomena in complex geometries as well as efficient and accurate signal transportation in domains with smooth flow and geometries.

These demands require a hybrid between a finite volume method on an unstructured grid (for the non-linear phenomena and complex geometries) and a high-order finite difference method on the structured part (for the wave propagation).

There are essentially two different types of hybrid methods. The most common one employs different governing equations in different parts of the computational domain. A typical example is noise generated in an isolated part of the flow, considered as the sound source. The nonlinear phenomenon in the complex geometry is often computed by the Euler or Navier-Stokes equations. The sound propagation to the far field is considered governed by the linear wave equation with source terms from the Euler or Navier-Stokes calculation, see Lyrantzis (1994); Wells & Renaut (1997).

All coupling procedures that involve different governing equations suffer from one major problem. A stable and accurate numerical procedure does not suffice for convergence to the true solution, even if accurate data is at hand. Convergence to the true solution requires *a priori* knowledge of exactly where and how the solution shifts from being governed by one equation set to being governed by the other. This *a priori* knowledge cannot be obtained as part of the coupling procedure.

In this project we intend to develop another type of hybrid method that avoids the artificial decoupling mentioned above and uses the same governing equations (in this case the Euler or Navier-Stokes equations) in the whole computational domain, not just close to the source. The word hybrid points in this case to the use of different numerical methods in different parts of the computational domain. Examples of this type of hybrid method can be found in Burbeau & Sagaut (2005); Rylander & Bondeson (2000). In this type of coupling procedure (provided that accurate data is known), a stable and accurate numerical procedure does suffice for convergence to the true solution.

Strict stability, which prevents error growth on realistic mesh sizes, is very important for calculations over long times. We have derived and studied strictly stable unstruc-

[†] Department of Information Technology, Scientific Computing, Uppsala University, SE-751 05 Uppsala, Sweden, Department of Aeronautical and Vehicle Engineering, KTH, The Royal Institute of Technology, SE-100 44 Stockholm, Sweden, Department of Computational Physics, FOI, The Swedish Defence Research Agency, SE-164 90 Stockholm, Sweden

[‡] Department of Information Technology, Scientific Computing, Uppsala University, SE-751 05 Uppsala, Sweden

tured finite volume methods (Nordström *et al.* 2003; Svärd & Nordström 2004; Svärd *et al.* 2006) and higher-order finite difference methods (Carpenter *et al.* 1999; Nordström & Carpenter 1999, 2001; Mattsson & Nordström 2004; M. & Nordström 2006) for hyperbolic, parabolic, and incompletely parabolic problems. These methods employ so-called summation-by-parts (SBP) operators and impose the boundary conditions weakly (Nordström *et al.* 2003; Carpenter *et al.* 1994).

In (Nordström & Gong 2006) it was proven that a specific interface procedure is stable for hyperbolic systems of equations. This project will rely heavily on these results; we will apply the theoretical results to the Euler equations. In a forthcoming paper we will include the treatment of the viscous terms in the Navier-Stokes equations.

A general 3-D code (CDP) that uses the node-centered finite volume method mentioned above has been developed by the Center for Turbulence Research (CTR) at Stanford University. A 3-D multi-block code (SUmb) that uses the finite difference technique discussed above is available at the Department of Aeronautics & Astronautics at Stanford University. These codes compute approximations to the Euler or Navier-Stokes equations and are the initial building blocks for the new hybrid method. A third coupling code (CHIMPS-lite, a simplified version of CHIMPS) will administer the coupling procedure and make it possible for the two solvers to communicate in an efficient and scalable way (Alonso *et al.* 2006).

2. Analysis

The material in this section is based on Nordström & Gong (2006). To introduce our technique we will consider the hyperbolic system

$$u_t + Au_x + Bu_y = 0, \quad -1 \leq x \leq 1, 0 \leq y \leq 1 \quad (2.1)$$

with suitable initial and boundary conditions. A and B are constant symmetric matrices with k rows and columns. We will also consider a simplified computational domain that is divided into two subdomains. A so-called edge-based unstructured finite volume method will be used to discretize (2.1) on subdomain $[-1, 0] \times [0, 1]$ with an unstructured mesh, while a high-order finite difference method will be used on subdomain $[0, 1] \times [0, 1]$ with a structured mesh (see Fig. 1).

The fact that the unknowns in the finite volume and the finite difference methods are located in the nodes and can be collocated at the interface is a key ingredient in the coupling procedure presented below.

2.1. The edge-based finite volume method

In Nordström *et al.* (2003); Nordström & Gong (2006) it was shown that the semi-discrete finite volume form of (2.1) on subdomain $[-1, 0] \times [0, 1]$ can be written

$$\mathbf{u}_t + \{[(P^L)^{-1}Q_x^L] \otimes A\}\mathbf{u} + \{[(P^L)^{-1}Q_y^L] \otimes B\}\mathbf{u} = \{[(P^L)^{-1}(E_I^L)^T P_y^L] \otimes \Sigma^L\}(\mathbf{u}_I - \mathbf{v}_I) + \text{SAT}^L, \quad (2.2)$$

where SAT^L is the penalty term that imposes the outer boundary conditions weakly. The SAT technique is a penalty procedure that can be used to specify outer boundary conditions as well as treating block interfaces. \mathbf{u}_I and \mathbf{v}_I are vectors that represent \mathbf{u} and \mathbf{v} (\mathbf{v} is the discrete finite difference solution that will be presented below) on the interface respectively. E_I^L is a projection matrix that maps \mathbf{u} to \mathbf{u}_I such that $\mathbf{u}_I = (E_I^L \otimes I_k)\mathbf{u}$.

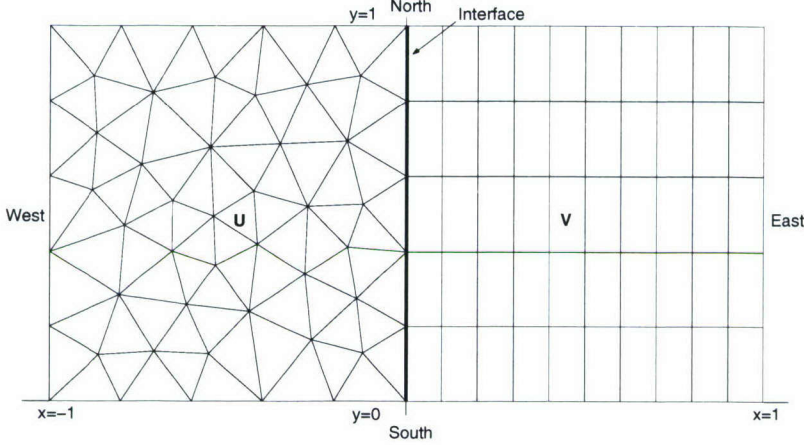


FIGURE 1. The hybrid mesh on the computational domain.

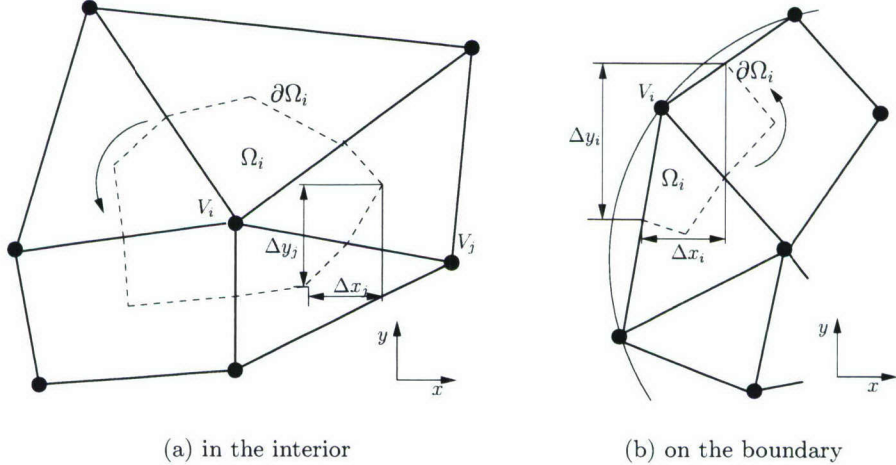


FIGURE 2. The grid (solid lines) and the dual grid (dashed lines).

The non-zero components of E_I^L have the value 1 and appear at the interface. $P_y^L \otimes \Sigma^L$ is a penalty matrix that will be determined below by stability requirements.

P^L is a positive diagonal $m \times m$ matrix with the control volumes Ω_i on the diagonal and Q_x^L and Q_y^L are almost skew symmetric $m \times m$ matrices. The matrices Q_x^L and Q_y^L have the components

$$(Q_x^L)_{ij} = \frac{\Delta y_j}{2} = -(Q_x^L)_{ji}, \quad (Q_x^L)_{ii \notin \partial\Omega} = 0, \quad (Q_x^L)_{ii \in \partial\Omega} = \frac{\Delta y_i}{2}, \quad (2.3)$$

$$(Q_y^L)_{ij} = -\frac{\Delta x_j}{2} = -(Q_y^L)_{ji}, \quad (Q_y^L)_{ii \notin \partial\Omega} = 0, \quad (Q_y^L)_{ii \in \partial\Omega} = -\frac{\Delta x_i}{2}. \quad (2.4)$$

The definition of Δx_j and Δy_j is presented in Fig. reffig:grid. Moreover, (2.3) and (2.4) imply that Q_x^L and Q_y^R satisfy

$$Q_x^L + (Q_x^L)^T = Y, \quad Q_y^L + (Q_y^L)^T = X, \quad (2.5)$$

where the non-zero elements in Y and X are Δy_i , $-\Delta x_i$ and correspond to the boundary points. For more details on the SBP properties of the finite volume scheme, see Nordström *et al.* (2003).

2.2. The high-order finite difference method

Consider the subdomain $[0, 1] \times [0, 1]$ with a structured mesh of $n \times l$ points. The finite difference approximation of u at the grid point (x_i, y_j) is a $k \times 1$ vector denoted \mathbf{v}_{ij} . We organize the solution in the global vector $\mathbf{v} = [\mathbf{v}_{11}, \dots, \mathbf{v}_{1l}, \mathbf{v}_{21}, \dots, \mathbf{v}_{2l}, \dots, \mathbf{v}_{n1}, \dots, \mathbf{v}_{nl}]^T$. \mathbf{v}_x and \mathbf{v}_y are approximations of u_x and u_y and are approximated using the high-order accurate SBP operators for the first derivative constructed in Mattsson & Nordström (2004); Kreiss & Scherer (1974); Strand (1994). The difference operators in the x and y direction on the right subdomain are denoted $(P_x^R)^{-1}Q_x^R$ and $(P_y^R)^{-1}Q_y^R$, respectively.

The semi-discrete approximation of (2.1) on subdomain $[0, 1] \times [0, 1]$ can be written,

$$\mathbf{v}_t + \{[(P_x^R)^{-1}Q_x^R] \otimes I_y^R \otimes A\} \mathbf{v} + \{I_x^R \otimes [(P_y^R)^{-1}Q_y^R] \otimes B\} \mathbf{v} = \text{SAT}^R + \{[(P_x^R \otimes P_y^R)^{-1}(E_I^R)^T] P_y^R \otimes \Sigma^R\}(\mathbf{v}_I - \mathbf{u}_I), \quad (2.6)$$

where the sizes of the identity matrices I_x^R and I_y^R are $n \times n$ and $l \times l$ respectively. SAT^R is the SAT penalty term for the outer boundary conditions. E_I^R is a projection matrix that maps \mathbf{v} to \mathbf{v}_I , that is, $\mathbf{v}_I = (E_I^R \otimes I_k)\mathbf{v}$. Σ^R is a penalty matrix that will be determined below by stability requirements.

Note that \mathbf{u}_I and \mathbf{v}_I in (2.2) and (2.6) are collocated at the interface. This is absolutely essential for the accuracy of the hybrid scheme. It will be shown that it is also necessary for stability.

Note that the operators $(P_x^R)^{-1}Q_x^R$ and $(P_y^R)^{-1}Q_y^R$ are SBP operators since matrices P_x^R and P_y^R are symmetric and positive definite and the matrices Q_x and Q_y are nearly skew-symmetric, that is,

$$Q_x^R + (Q_x^R)^T = D_x^R = \text{diag}(-1, 0, \dots, 0, 1), \quad Q_y^R + (Q_y^R)^T = D_y^R = \text{diag}(-1, 0, \dots, 0, 1), \quad (2.7)$$

where D_x^R and D_y^R are $n \times n$ and $l \times l$ matrices, respectively.

2.3. Stable interface treatment

We define the norms $N^L = P^L \otimes I_k$ and $N^R = (P_x^R \otimes P_y^R) \otimes I_k$, where $N^L = (N^L)^T > 0$ and $N^R = (N^R)^T > 0$. We also define an inner product and a norm for discrete real vector-functions $\mathbf{a}, \mathbf{b} \in \mathbf{R}^n$ by

$$(\mathbf{a}, \mathbf{b})_H = \mathbf{a}^T H \mathbf{b}, \quad \|\mathbf{a}\|_H^2 = (\mathbf{a}, \mathbf{a}), \quad H = H^T > 0. \quad (2.8)$$

We apply the energy method by multiplying (2.2) and (2.6) with $\mathbf{u}^T N^L$ and $\mathbf{v}^T N^R$ respectively. We also use (2.5), (2.7), (2.8), (2.5) and assume that the terms including \mathbf{u}_B , \mathbf{v}_E , \mathbf{v}_S , \mathbf{v}_N at the outer boundaries are precisely cancelled by the SAT terms (Carpenter *et al.* 1999; Nordström & Carpenter 1999). This yields the energy estimate

$$\frac{d}{dt} (\|u\|_{N^L}^2 + \|u\|_{N^R}^2) = [\mathbf{u}_I, \mathbf{v}_I]^T M_I [\mathbf{u}_I, \mathbf{v}_I], \quad (2.9)$$

where

$$M_I = \begin{bmatrix} -P_y^L \otimes A + P_y^L \otimes \Sigma^L + P_y^L \otimes (\Sigma^L)^T & -P_y^L \otimes \Sigma^L - P_y^R \otimes \Sigma^R \\ -P_y^L \otimes \Sigma^L - P_y^R \otimes \Sigma^R & P_y^R \otimes A + P_y^R \otimes \Sigma^R + P_y^R \otimes (\Sigma^R)^T \end{bmatrix}.$$

We need M_I to be negative semi-definite for stability. Consider a simplified case where

$$P_y^L = P_y^R = P_y, \quad \Sigma^L = (\Sigma^L)^T, \quad \Sigma^R = (\Sigma^R)^T. \quad (2.10)$$

This yields,

$$M_I = P_y \otimes \begin{bmatrix} -A + 2\Sigma^L & -\Sigma^L - \Sigma^R \\ -\Sigma^L - \Sigma^R & A + 2\Sigma^R \end{bmatrix} = P_y \otimes M.$$

To obtain stability M has to be negative semi-definite. We can diagonalize A by $X^T A X = \Lambda$, where X is an orthogonal matrix consisting of the eigenvectors of A . Moreover, consider penalty parameters Σ^L and Σ^R of the form $X^T \Sigma^L X = \Lambda^L$ and $X^T \Sigma^R X = \Lambda^R$. We denote by λ_i the i th diagonal component of Λ and similarly λ_i^L and λ_i^R for Λ^L and Λ^R . Then we obtain a negative semi-definite M if

$$\lambda_i^R = \lambda_i^L - \lambda_i, \quad \lambda_i^L \leq \frac{\lambda_i}{2}, \quad i = 1, \dots, k. \quad (2.11)$$

The first condition in (2.11) is recognized as the condition for a conservative interface treatment. The second condition in (2.11) leads to stability if conservation is guaranteed. For more details, see Nordström & Carpenter (1999).

We have proved the following proposition:

PROPOSITION 2.1. *If the conditions (2.10)-(2.11) hold, (2.9) leads to a bounded energy and (2.2), (2.6) have a stable and conservative interface treatment.*

The specific SBP operators that are based on diagonal norms are given in Mattsson & Nordström (2004); Strand (1994). When we use the second-order diagonal norm $P_y^R = \text{diag}[1/2, 1, \dots, 1, 1/2]/h$ on the right subdomain, we do not need to change the control volumes on the left domain, since $P_y^L = P_y^R$. But the standard fourth- and sixth-order diagonal norms are

$$\frac{1}{h} \begin{bmatrix} \frac{17}{48} & & & & & \\ & \frac{59}{48} & & & & \\ & & \frac{43}{48} & & & \\ & & & \frac{49}{48} & & \\ & & & & 1 & \\ & & & & & \ddots \end{bmatrix}, \frac{1}{h} \begin{bmatrix} \frac{13649}{43200} & & & & & \\ & \frac{12013}{8640} & & & & \\ & & \frac{2711}{4320} & & & \\ & & & \frac{5359}{4320} & & \\ & & & & \frac{7877}{8640} & \\ & & & & & \frac{43801}{43200} \\ & & & & & 1 \\ & & & & & & \ddots \end{bmatrix}, \quad (2.12)$$

respectively. In both cases we need to modify the control volume for the finite volume method at the points on the interface to guarantee $P_y^L = P_y^R$. The old dual grid for the points at the interface consists of the lines between the center of the triangles and the midpoints of the edges. In order to match P_y^L and P_y^R , the new lines will connect the center of the triangles and the points at the interface that correspond to the P_y^R (see Fig. 3).

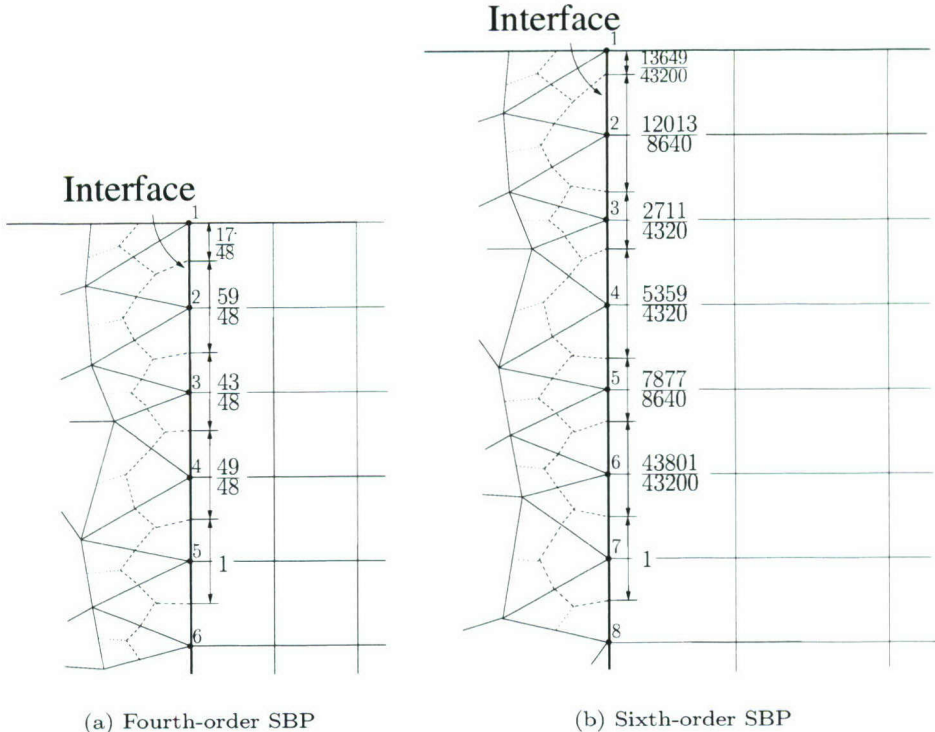


FIGURE 3. The modified control volumes for the points on the interface.

2.4. The coupling code, CHIMPS-lite

A general 3-D code (CDP) that uses the node-centered finite volume method previously mentioned has been developed by the Center for Turbulence Research (CTR) at Stanford University. Also available at the Department of Mechanical Engineering at Stanford University is a 3-D multi-block code (SUmb) based on high order finite difference methods.

These two codes compute approximations to the Euler or Navier-Stokes equations and are the initial building blocks for the new hybrid method. The codes are node-based and use SBP operators and penalty techniques for imposing the boundary and interface conditions weakly. This numerical technique enables coupling of the two codes by sending the value of the dependent variables in the nodes located on the interface to the other code while simultaneously receiving the colocated data at the interface from the other code. Each code provides boundary data to the other code.

A third coupling code (CHIMPS-lite) administers the coupling procedure and makes it possible for the two solvers to communicate in an efficient and scalable way. CHIMPS-lite is a simplified version of CHIMPS (Alonso *et al.* 2006) designed specifically for interfaces with colocated nodes where no interpolation is required. In an initial setup phase, both codes register their interface nodes with CHIMPS-lite, and the parallel communication pattern is built. Using this communication pattern, CHIMPS-lite then facilitates the exchange of interface data at each stage in the Runge-Kutta scheme. The development of coupling software like CHIMPS and CHIMPS-lite is an essential new ingredient that will

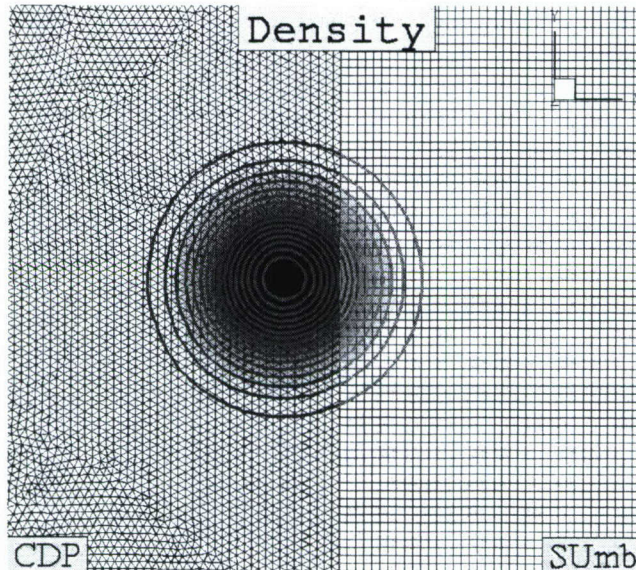


FIGURE 4. Transport of a vortex across an interface for the Euler equations.

take the coupling idea from theoretical concept to practical tool for fluid flow investigations.

3. Results

We consider this project as work in progress; only a few preliminary results currently exist. Fig. 4 presents a calculation using the unstructured finite volume code CDP coupled to the high order finite difference code SUmb. The calculation is fourth order accurate and shows the transport of a vortex across an interface for the Euler equations. Other similar results have been produced. The results indicate that the procedure is stable and useful.

4. Future work

Future work involves verifying the computational procedure against exact solutions to ensure that it converges at the correct rate. We also intend to apply the method to a high-lift device problem with complex geometry and high accuracy requirements. These results will be presented at the 2007 SIAM Conference on Computational Science and Engineering, in Costa Mesa, California.

Viscous terms will then be included and verified in the same manner. A stable and accurate operational hybrid method for the Navier-Stokes equations will allow for the analysis of very demanding fluid flow problems involving complex geometries and wave propagation effects that are not possible to address today.

REFERENCES

ALONSO, J. J., HAHN, S., HAM, F., HERRMANN, M., IACCARINO, G., KALITZIN, G., LEGRESLEY, P., MATTSSON, K., MEDIC, G., MOIN, P., PITSCHE, H., SCHLUTER,

J., SVÄRD, M., VAN DER WEIDE, E., YOU, D. & WU, X. 2006 Chimps: A high-performance scalable module for multi-physics simulations. *AIAA paper* **2006-5274**.

BURBEAU, A. & SAGAUT, P. 2005 A dynamic p-adaptive discontinuous Galerkin method for viscous flows with shocks. *Computers and Fluids* **34**, 401–417.

CARPENTER, M. H., GOTTLIEB, D. & ABARBANEL, S. 1994 Time-stable boundary conditions for finite-difference schemes solving hyperbolic systems: Methodology and application to high-order compact schemes. *J. Comput. Phys.* **111**(2).

CARPENTER, M. H., NORDSTRÖM, J. & GOTTLIEB, D. 1999 A stable and conservative interface treatment of arbitrary spatial accuracy. *J. Comput. Phys.* **148**, 341–365.

KREISS, H.-O. & SCHERER, G. 1974 Finite element and finite difference methods for hyperbolic partial differential equations. In *Mathematical Aspects of Finite Elements in Partial Differential Equations*. Academic Press Inc.

LYRINTZIS, A. 1994 Review: The use of Kirchhoff's method in computational aeroacoustics. *Journal of Fluids Engineering* **116**, 665–676.

M., S. & NORDSTRÖM, J. 2006 On the order of accuracy for difference approximations of initial-boundary value problems. *J. Comput. Phys.* **218**, 333–352.

MATTSSON, K. & NORDSTRÖM, J. 2004 Summation by parts operators for finite difference approximations of second derivatives. *J. Comput. Phys.* **199**, 503–540.

NORDSTRÖM, J. & CARPENTER, M. H. 1999 Boundary and interface conditions for high order finite difference methods applied to the Euler and Navier-Stokes equations. *J. Comput. Phys.* **148**, 621–645.

NORDSTRÖM, J. & CARPENTER, M. H. 2001 High-order finite difference methods, multidimensional linear problems and curvilinear coordinates. *J. Comput. Phys.* **173**, 149–174.

NORDSTRÖM, J., FORSBERG, K., ADAMSSON, C. & ELIASSON, P. 2003 Finite volume methods, unstructured meshes and strict stability. *Applied Numerical Mathematics* **45**, 453–473.

NORDSTRÖM, J. & GONG, J. 2006 A stable hybrid method for hyperbolic problems. *J. Comput. Phys.* **212**, 436–453.

RYLANDER, T. & BONDESON, A. 2000 Stable FEM-FDTD hybrid method for Maxwell's equations. *Comput. Phys. Comm* **125**, 75–82.

STRAND, B. 1994 Summation by parts for finite difference approximations for d/dx . *J. Comput. Phys.* **110**, 47–67.

SVÄRD, M., GONG, J. & NORDSTRÖM, J. 2006 Strictly stable artificial dissipation for finite volume schemes. *Applied Numerical Mathematics* **56**, 1481–1490.

SVÄRD, M. & NORDSTRÖM, J. 2004 Stability of finite volume approximations for the Laplacian operator on quadrilateral and triangular grids. *Applied Numerical Mathematics* **51**, 101–125.

WELLS, V. L. & RENAUT, R. A. 1997 Computing aerodynamically generated noise. *Annu. Rev. Fluid Mech.* **29**, 161–199.

Accurate and stable finite volume operators for unstructured flow solvers

By F. Ham, K. Mattsson AND G. Iaccarino

1. Motivation and objectives

The development of unstructured numerical methods for complex geometries remains a pacing issue in the application of Large Eddy Simulation (LES) to flows of engineering interest. Techniques such as LES place strict and often conflicting demands on numerical methods because of both the long integration times involved and the broad spectral content of the solution. The developer must strike the right balance between accuracy, stability, and conservation, all the time paying careful attention to the overall cost of solving the resulting systems. This paper describes the decisions (and compromises) made in the development of CDP†, an unstructured finite volume flow solver developed as part of Stanford's DOE-funded ASC Alliance program to perform LES in complex geometries.

2. Numerical method

2.1. *SBP/SAT as a framework for development*

As one starts to analyze existing finite volume operators or develop new operators suitable for unstructured LES, it is important to have a systematic framework for this endeavor. Historically in the context of LES and Direct Numerical Simulation (DNS), the concept of kinetic energy conservation has served this role. Operators or discretizations that discretely conserve kinetic energy (in the incompressible, inviscid limit) have been shown to produce more accurate turbulence simulations. Discrete kinetic energy conservation also provides a stability proof for the discretization, and it can guide the choice of operators in higher-order methods (Morinishi *et al.* 1998) and unstructured grids (Perot 2000; Mahesh *et al.* 2004; Ham & Iaccarino 2004). In these more complex cases, however, the discrete manipulations required can become cumbersome.

One of the most promising alternatives for developing provably stable and accurate discretizations with minimal dissipation is to discretize the equations using the so-called summation-by-parts (SBP) operators (Kreiss & Scherer 1974) and impose boundary conditions weakly using a penalty procedure called simultaneous approximation term (SAT) (Carpenter *et al.* 1994). The combination of these techniques (SBP and SAT) can produce discretizations where strict stability can be proven using a technique referred to as “the energy method”. For time-dependent problems involving long-time integration, strict stability provides a more complete and appropriate statement of stability than traditional Lax-Richtmyer stability (Lax & Richtmyer 1956) because, on realistic meshes, strictly stable schemes do not allow non-physical solution growth in time (Carpenter *et al.* 1993). In many ways, the energy method is similar to kinetic energy conservation;

† CDP is named after Charles David Pierce (1969–2002)



FIGURE 1. Details of an asymmetric channel mesh using all unstructured primitives.

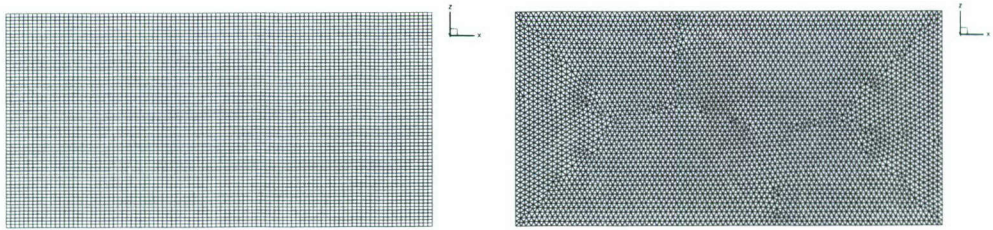


FIGURE 2. Comparisons of near-wall asymmetric channel mesh: (left) $y = -1$; (right) $y = 1$.

however, it represents a more complete and broadly applicable framework for developing discretizations that naturally includes boundary conditions and can be extended to systems of equations where kinetic energy conservation is an inappropriate goal.

The development of CDP's operators and boundary closures described in this brief summarizes our progress to date in applying the SBP/SAT methodology to the finite volume method for general polyhedral grids.

2.2. Nodal vs. cell-centered discretizations

Before describing the operators, we briefly address the decision to use the nodes for collocation of the unknowns. Early implementations of the LES unstructured solver (Mahesh *et al.* 2004; Ham & Iaccarino 2004) were based on a cell-centered control volume (CV) approach. For high-quality hex-dominant meshes, this CV approach proved very efficient and accurate, with results documented in a variety of simulations in moderately complex geometry (Mahesh *et al.* 2004; Wu *et al.* 2006). Truly complex geometries, however, commonly involve regions of tetrahedral elements where CV discretizations are known to be inaccurate if simple averages are used to preserve operator symmetries. In Ham *et al.* (2006), we reported the results of a one-to-one comparison of the two methods using the inviscid Taylor vortex problem on a variety of grids, and concluded that, with few exceptions, the nodal discretization was significantly more accurate, displaying consistent second order rates of error reduction.

More recently we have compared the performance of the two methods on identical grids for simulating turbulent flow in a plane channel using purposely asymmetric meshes. One such asymmetric channel suitable for the $Re_\tau = 180$ simulation is shown in Fig. 1.

On the bottom half of the channel ($y < 0$) the mesh consists of regular hexahedra with

	structured side	unstructured side
Δy^+ at wall	0.17	0.18
Δz^+	18	23 – 27
Δx^+	24	23 – 27
CV count	294912	348929

TABLE 1. Details for asymmetric-mesh turbulent channel grid spacings, $Re_\tau = 180$, domain size: $4\pi \times 2 \times 2\pi$. For the unstructured region a range is provided because the resolution depends on the triangle orientation.

near-wall stretching. On the top half, however, we triangulate the top wall and extrude the tris to produce a boundary layer of prisms with a similar near-wall stretching. These prisms then transition to tets, then a final transition layer of pyramids to join to the lower hex mesh. The mesh supports periodic boundary conditions in both streamwise (x) and spanwise (z) directions. Fig. 2 compares the meshes at the two walls. Mesh spacing details are provided in Table 1. All simulations were run with no subgrid scale (SGS) model.

Fig. 3 compares the computed mean velocity profiles for the CV and node-based cases. The CV case exhibits a substantial asymmetry in the mean, with the peak velocity significantly higher and shifted toward the unstructured half of the calculation. It appears the unstructured side of the grid is destroying the boundary layer flow structures responsible for momentum transfer. The node-based result shows much less mesh sensitivity, producing a nearly symmetric mean that compares much more favorably with the resolved DNS result of Moser *et al.* (1999) (over-predicted slightly, as is expected with the relatively coarse mesh spacing and no SGS model).

This particular calculation dramatically illustrates the benefit of the node-based formulation for unstructured boundary layers, and was one several issues that motivated us to modify CDP's discretization to a node-based formulation. Another significant motivation was that node-based SBP operators with SAT boundary closures support stable and accurate coupling to other SBP/SAT solvers, including coupling with higher-order finite difference (see, for example, Nordström *et al.* (2006) elsewhere in this volume).

Although worth noting, we do not consider the increased efficiency on simplex grids a primary motivation. While the number of unknowns is significantly reduced on tetrahedral grids, LES-suitable grids normally minimize the number of tets for reasons of solution quality, and so this savings is never realized in actual computations. In addition, because the node-based operators are generally more costly to compute than CV-based operators, they are pre-computed and stored, making the node-based version more memory intensive than previous CV-based versions, despite the reduced number of unknowns in some cases.

2.3. SBP/SAT definitions

Here we briefly define SBP (an internal property of the operators) and SAT (a method to apply boundary conditions) using scalar convection-diffusion. The passive transport of scalar ϕ in an incompressible velocity field is governed by the following equation:

$$\phi_t + (u \cdot \nabla)\phi = \alpha \nabla^2 \phi. \quad (2.1)$$

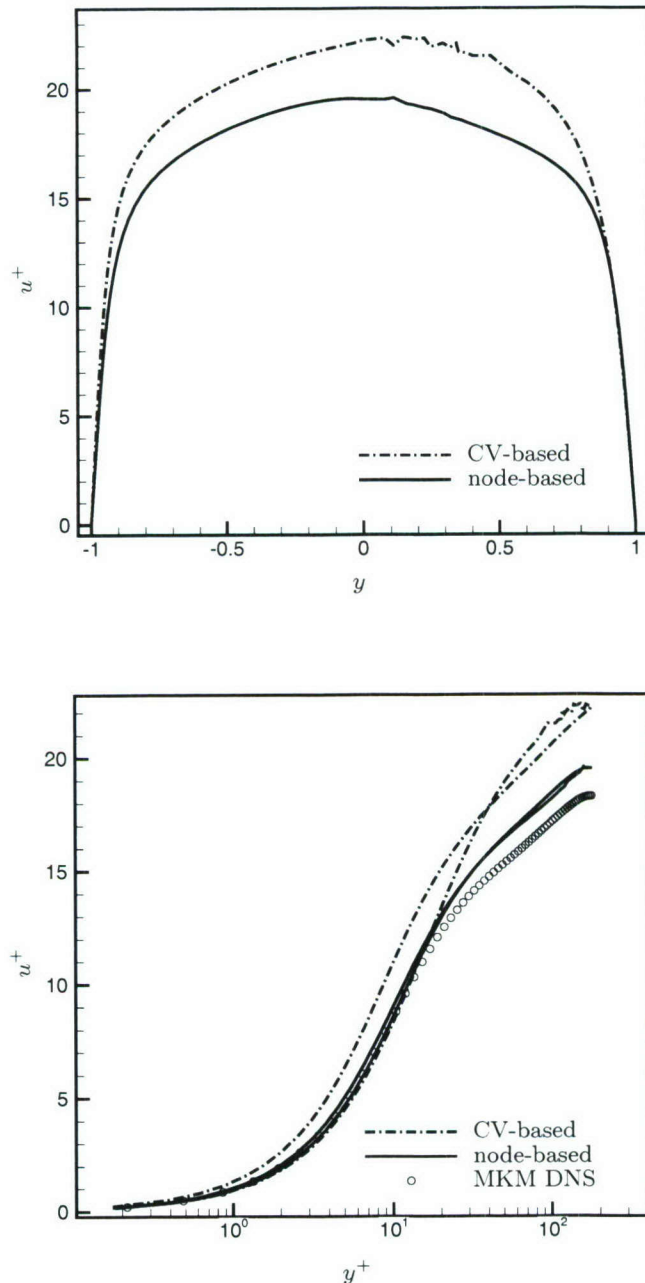


FIGURE 3. Comparisons of computed mean velocity profiles for asymmetric-mesh turbulent channel showing substantial mesh-induced asymmetry in the CV-based formulation. The bumpy region between $0 < y < 0.5$ corresponds to the tetrahedral region where averaging in the two homogenous directions is not available because nodes are not at identical y locations.

A SBP/SAT semi-discretization of this equation, including boundary conditions, will have the following matrix form:

$$V\phi_t + (Q + B)\phi = \alpha(L + S)\phi + \text{penalty terms}, \quad (2.2)$$

where V is the diagonal matrix of nodal volumes, $V^{-1}(Q + B)$ is the convective operator split into internal and boundary parts, and $V^{-1}(L + S)$ is the Laplacian operator split into internal and boundary parts. We note that Eq. 2.2 is solved at all nodes in the domain, including those on the boundary.

Application of the energy method to Eq. 2.2 involves multiplying by ϕ^T and adding the transpose to produce the following discrete equation for the time evolution of scalar energy:

$$\phi^T V \phi_t + \phi^T V^T \phi_t \equiv \frac{d}{dt} \|\phi\|_V^2 = -\phi^T (Q + Q^T) \phi + \phi^T (L + L^T) \phi + \text{other terms}. \quad (2.3)$$

For simplicity we have omitted the details of the boundary penalties, lumping all boundary-related terms into “*other terms*”. Eq. 2.3 is called an energy estimate if all terms on the right-hand side involving the unknown ϕ can be bounded (typically ≤ 0). Clearly the first two terms can be bounded for any ϕ if matrices Q and L have certain properties. This is in fact the essence of SBP operators: it is an internal property of the operators that produces these desired properties. Specifically, the convective operator $V^{-1}(Q + B)$ is called an SBP operator if the internal part Q is skew-symmetric (i.e., $Q + Q^T \equiv 0$), and the Laplacian operator $V^{-1}(L + S)$ is called an SBP operator if $L + L^T$ is negative semi-definite. SBP operators thus simplify the derivation of energy estimates by isolating the work required to the boundary and interface terms. For these remaining terms (lumped in *other terms*), the SAT method can be used; examples are provided in the following subsection.

2.4. CDP’s operators

This subsection describes the details of the discrete finite volume operators used to develop the internal discretization and boundary conditions in CDP. The operators are developed for a node-based discretization on general polyhedral meshes, where both grid coordinates and the unknowns are collocated at nodes. Figure 4 provides some geometrical details used for operator construction.

2.4.1. Nodal volumes and volume integration

The node-based volumes required for integrating the time derivative and any source terms are computed by tessellating each cell into “sub-tets”, each defined by a node, an edge, a face, and a cell as shown in Fig. 4. The volume of the sub-tet is then added to the volume associated with node “P”. In the current version of CDP, the volume or mass matrix is thus diagonal (lumped-mass approximation). Row “P” of the volume integration operator V has a single diagonal entry equal to the sum of its associated sub-tet volumes $V_{t'}$:

$$\begin{aligned} V_P \phi &\approx \int_P \phi dV \\ &= \sum_{t' \in T'_P} V_{t'} \phi_{P_t}, \end{aligned} \quad (2.4)$$

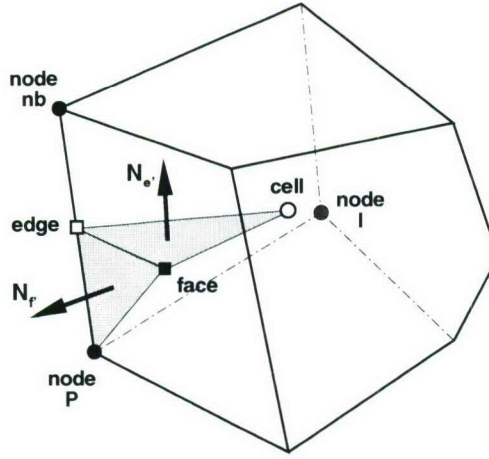


FIGURE 4. Geometrical details for 3-D node-based meshes. Unknowns are stored at nodes (e.g., P and edge-based neighbor nb). Edge centers are located at the midpoint between nodes, face centers are located at the simple average of their surrounding nodes, and cell centers are defined by the simple average of their surrounding nodes. $N_{e'}$ is a sub-edge normal, associated with an internal or boundary edge. $N_{f'}$ is a sub-face normal associated with boundary faces only. N is used to indicate normals with area magnitude.

where t' represents a sub-tet, and T'_P the set of all sub-tets associated with node “ P ”.

To further simplify the construction of these volumes and the operators in general, we choose the simple average of surrounding nodes to define face and cell centers. Unlike CV-based formulations, where face and cell centers are defined at the centroids or centers of mass, this same definition for the node-based mesh has no obvious benefit. The choice of simple average for center locations ensures that interpolations based on simple averages of nodal data will be limited and linearly exact. For meshes built from simplex elements (tris/tets), the simple average is of course equivalent to the center of mass.

2.4.2. Convective operator

CDP’s convective operator including SAT penalty treatment was presented in Ham *et al.* (2006), but is described here for completeness. For row “ P ” of the convective operator:

$$(Q_P + B_P) \phi \approx \int_P \frac{\partial u_i \phi}{\partial x_i} dV = \oint_P \phi u_i \hat{n}_i dA \quad (2.5)$$

$$= \sum_{e' \in E'_P} U_{e'} \frac{\phi_P + \phi_{nb}}{2} A_{e'} + \sum_{f' \in F'_P} U_{f'} \phi_P A_{f'}, \quad (2.6)$$

where e' represents a sub-edge, E'_P the set of all sub-edges associated with node P , f' represents a boundary sub-face, and F'_P the set of all boundary sub-faces associated with node P . $U_{e'}$ and $U_{f'}$ are sub-edge and sub-face velocity components in the outward-normal direction. Clearly the internal part of the operator is skew-symmetric by construction.

2.4.3. Laplacian operator

The discretization of the Laplacian operator is particularly challenging for unstructured finite volume methods because it is difficult to simultaneously achieve accuracy and stability on general unstructured grids. In the case of the Laplacian operator, stability can be translated into the SBP requirement that the symmetric part of the internal operator $L + L^T$ be negative semi-definite, and that the SAT closure yields an energy estimate.

These stability requirements are normally met by construction in the finite element method (FEM), however FEM Laplacian operators are rarely used in FVM. Even CV-FEM (Schneider & Raw 1987), a popular hybrid of the two, only uses FEM basis functions to compute gradients at integration points around the nodal control volume, and the resulting operator will not guarantee the desired stability properties. The typical reasons FEM Laplacian operators are not used routinely in FVM are:

- Inconsistencies between the FEM “lumped mass” volume and the FVM volume on certain grids (although, for node-based FVM they are equivalent on structured orthogonal grids and arbitrary simplex grids)
- The perception that FEM operators have greater complexity (involve more neighbors), and are thus more expensive. While this is true on structured orthogonal grids where FVM reduces to the finite difference method, on general unstructured grids the complexity of FVM is similar to or even greater than FEM.
- FVM has the additional constraint that the Laplacian must discretely be the divergence of a gradient, i.e., the discrete operators must mimic the identity:

$$\nabla^2 \equiv \nabla \cdot \nabla. \quad (2.7)$$

This final discrete requirement allows the viscous terms in FVM to be formulated in terms of a discretely conserved flux involving face-normal gradients, and also allows the use of the Poisson solve to discretely project the divergence out of the predicted velocity field when fractional-step time advancement is used. This discrete decomposition is not always clear in the case of FEM Laplacians.

In CDP, the volume-integrated Laplacian operator is constructed using divergence theorem and the sub-edge concept presented in Fig. 4. For row “ P ” of the Laplacian operator:

$$(L_P + S_P) \phi \approx \int_P \frac{\partial^2 \phi}{\partial x_i \partial x_i} dV = \oint_P \frac{\partial \phi}{\partial x_i} \hat{n}_i dA \quad (2.8)$$

$$= \sum_{e' \in E'_P} \frac{\partial \phi}{\partial x_i} \Big|_{e'} \hat{n}_{i,e'} A_{e'} + \sum_{f' \in F'_P} \frac{\partial \phi}{\partial x_i} \Big|_{f'} \hat{n}_{i,f'} A_{f'} \quad (2.9)$$

$$= \sum_{e' \in E'_P} S_{e'} \phi + \sum_{f' \in F'_P} S_{f'} \phi, \quad (2.10)$$

where e' represents a sub-edge, E'_P the set of all sub-edges associated with node P , f' represents a boundary sub-face, and F'_P the set of all boundary sub-faces associated with node P . $\hat{n}_{e'}$ the sub-edge outward unit normal (outward with respect to P), $A_{e'}$ the sub-edge area, $S_{e'}$ and $S_{f'}$ are the sub-edge and sub-face normal-derivative-times-area operators, respectively. The required gradient for each sub-edge is determined by solving the following 3×3 system for the unknown gradient components:

$$\left. \frac{\partial \phi}{\partial x_i} \right|_{e'} (x_{i,nb} - x_{i,P}) = \phi_{nb} - \phi_P \quad (2.11)$$

$$\left. \frac{\partial \phi}{\partial x_i} \right|_{e'} \left(\frac{1}{N_{nof}} \sum x_{i,nof} - \frac{1}{2}(x_{i,nb} + x_{i,P}) \right) = \frac{1}{N_{nof}} \sum \phi_{nof} - \frac{1}{2}(\phi_{nb} + \phi_P) \quad (2.12)$$

$$\left. \frac{\partial \phi}{\partial x_i} \right|_{e'} \left(\frac{1}{N_{noc}} \sum x_{i,noc} - \frac{1}{2}(x_{i,nb} + x_{i,P}) \right) = \frac{1}{N_{noc}} \sum \phi_{noc} - \frac{1}{2}(\phi_{nb} + \phi_P), \quad (2.13)$$

where P and nb represent the two nodes associated with the edge of this sub-edge, nof the N_{nof} nodes of the face associated with the sub-edge (these will of course include P and nb) and noc the N_{noc} nodes of the cell associated with this sub-edge (these will also include P and nb).

It is important to note that the sub-edges are not combined into a single edge normal and edge area prior to dotting with an edge-based gradient. This combination of normals to a single edge normal may simplify the construction of the operator, but it is not done in CDP. As such, in addition to being compact and linearly exact (which, for a Laplacian, means returning zero in a linear field), the resulting operator has two important properties:

- In the limit of Cartesian structured meshes, the standard symmetric second-order finite difference Laplacian is recovered (involving only node P and the 6 neighbors that share an edge with P).
- For the case of simplex elements, the standard symmetric FEM Laplacian using linear basis functions is recovered.

The first of these properties is well known, and would have resulted even if we had combined the sub-edge normals into a single edge. The equivalence with linear FEM on simplex grids and resulting symmetry, however, is less well known and requires this sub-edge construction.

Part of the stability requirement for the Laplacian operator is the SBP property that $L + L^T$ be negative semi-definite. For both the limiting cases previously described, it is well known that this is true. On general polyhedra, however, we do not have a proof. But numerical experiments using a variety of polyhedral meshes indicate that the operator is negative semi-definite except for the case of extreme element deformation.

The boundary part of the Laplacian operator is a summation over sub-faces, and will be non-zero at boundary nodes only. The three required components of the gradient at each sub-face are determined by solving a similar 3×3 system, involving the two equations:

$$\left. \frac{\partial \phi}{\partial x_i} \right|_{f'} (x_{i,nb} - x_{i,P}) = \phi_{nb} - \phi_P \quad (2.14)$$

$$\left. \frac{\partial \phi}{\partial x_i} \right|_{f'} \left(\frac{1}{N_{nof}} \sum x_{i,nof} - x_{i,P} \right) = \frac{1}{N_{nof}} \sum \phi_{nof} - \phi_P \quad (2.15)$$

and one of:

$$\left. \frac{\partial \phi}{\partial x_i} \right|_{f'} (x_{i,I} - x_{i,P}) = \phi_I - \phi_P \quad (2.16)$$

$$\left. \frac{\partial \phi}{\partial x_i} \right|_{f'} \left(\frac{1}{N_{noc}} \sum x_{i,noc} - x_{i,P} \right) = \frac{1}{N_{noc}} \sum \phi_{noc} - \phi_P, \quad (2.17)$$

with the first of these being preferred. Nodes P and nb are on the edge associated with the boundary sub-face, nof are the N_{nof} nodes of the face associated with the sub-face, I (for Internal) is/are the node(s) along the edge(s) of P not part of the boundary face, but still part of the internal cell that contains the boundary face, and noc are the N_{noc} nodes associated with the internal cell that contains the boundary face. For clarity, node I is labeled in Fig. 4. Although the last equation is never used for grids composed of convex unstructured primitives (tet, pyramid, prism, hex), it is included here because on certain non-convex or polyhedral meshes (e.g., meshes with hanging nodes on boundary faces), the edges associated with node I can be coplanar with the boundary face.

While there are no restrictions on the complexity of $S_{f'}$ with regard to stability, here we have made the practical decision to define it in a way that simplifies the parallel implementation. In CDP the domain is decomposed such that the cells (elements) are uniquely divided among the processors, however nodes, edges, and faces that lie on inter-processor boundaries are multiply defined. By expressing the $S_{f'}$ operator as a global sum of locally available information (the cell and boundary face that completely define the gradient are entirely present on only one processor), this also makes the transpose of $S_{f'}$ (required by the SAT penalty – see §2.6) a global sum of locally available information.

In addition, this local definition of $S_{f'}$ makes it straightforward to include only those sub-faces that participate in a particular Dirichlet or Neumann boundary condition. For example, a single node can have sub-faces associated with an adiabatic boundary and sub-faces associated with an isothermal wall, each requiring a separate boundary treatment.

2.5. Gradient operator

While the gradient operator is not required in the discretization of scalar transport, it is required for the incompressible Navier-Stokes equations, so we include a brief description here. CDP's gradient operator uses Green-Gauss theorem to approximate the integral of the gradient over the volume as follows:

$$\begin{aligned} G_{i,P} \phi &\approx \int_P \frac{\partial \phi}{\partial x_i} dV = \oint_P \phi n_i dA \\ &= \sum_{e' \in E'_P} \frac{\phi_e + \phi_f + \phi_c}{3} \hat{n}_{i,e'} A_{e'} + \sum_{f' \in F'_P} \frac{\phi_P + \phi_e + \phi_f}{3} \hat{n}_{i,f'} A_{f'} \\ &= \sum_{e' \in E'_P} \frac{\phi_e + \phi_f + \phi_c}{3} N_{i,e'} + \sum_{f' \in F'_P} \frac{\phi_P + \phi_e + \phi_f}{3} N_{i,f'}, \end{aligned} \quad (2.18)$$

where ϕ_e , ϕ_f , and ϕ_c are computed from simple averages of the nodes associated with the edge, face, and cell defining the sub-edge or boundary sub-face, and $N_{e'}$ and $N_{f'}$ the sub-edge and sub-face normals with area magnitude. Note that the second part of the gradient operator is non-zero for boundary nodes only.

Interestingly, on simplex grids this operator is exactly equivalent to the standard skew-symmetric edge-based gradient operator and to the gradient operator resulting from FEM with linear basis functions. The operator is also skew-symmetric on structured orthogonal hex grids, and is linearly exact and generally more accurate than the edge-based operators on general polyhedral meshes, although not exactly skew-symmetric.

2.6. Scalar transport with SAT penalties

Using the previously described operators, it is now possible to illustrate how SAT penalties are added to produce a strictly stable finite volume discretization for scalar transport:

$$\begin{aligned}
 V_P \phi_t + \sum_{e' \in E'_P} U_{e'} \frac{\phi_P + \phi_{nb}}{2} A_{e'} + \sum_{f' \in F'_P} U_{f'} \phi_P A_{f'} = \\
 \alpha \sum_{e' \in E'_P} S_{e'} \phi + \alpha \sum_{f' \in F'_P} S_{f'} \phi + \\
 \sigma_1 \sum_{f' \in F'_P} U_{f'}^-(\phi_P - g_P) A_{f'} - \sigma_2 \alpha \sum_{f' \in F'_P} S_{f'}^T(\phi - g), \quad (2.19)
 \end{aligned}$$

where the potentially time-dependent Dirichlet boundary data g has been introduced on the rhs using penalty parameters σ_1 for the advection term, and σ_2 for the diffusion. $S_{f'}^T$ is the transpose of the sub-face normal-derivative-times-area operator, which introduces penalty terms into all nodes associated with the $S_{f'}$ operator, including those not directly on the boundary.

Application of the energy method to this system leads to an energy estimate for penalty parameters $\sigma_1 > 1/2$ and $\sigma_2 = 1$.

2.7. Incompressible Navier-Stokes

It is also possible to develop a finite volume discretization of the incompressible Navier-Stokes equations using the CDP operators with good accuracy and stability properties. For this case, however, we cannot make the claim of strict stability on arbitrary unstructured meshes, and present the discretization as a work in progress.

Following the collocated fraction-step methods developed in Zang *et al.* (1994); Kim & Choi (2000); Mahesh *et al.* (2004), CDP's incompressible flow algorithm proceeds as follows:

1. Extrapolate the divergence-free edge-based (not sub-edge; see step 5 below) velocity field to the midpoint of the current time step. Set the boundary sub-face velocities to the normal component of the known boundary velocity g_i :

$$U_e^{n+1/2} = \frac{3}{2} U_e^n - \frac{1}{2} U_e^{n-1} \equiv U_e \quad U_{f'}^{n+1/2} = \frac{1}{2} (g_{i,f'}^n + g_{i,f'}^{n+1}) \hat{n}_{i,f'} \equiv U_{f'}. \quad (2.20)$$

2. Build momentum equation for velocity predictor \hat{u}_i :

$$\begin{aligned}
 V_P \frac{\hat{u}_i - u_i^n}{\Delta t} + \sum_{e' \in E'_P} U_{e'} \frac{\hat{u}_{i,P} + \hat{u}_{i,nb} + u_{i,P}^n + u_{i,nb}^n}{4} A_{e'} + \sum_{f' \in F'_P} U_{f'} (\hat{u}_{i,P} + u_{i,P}^n) A_{f'} - \\
 \frac{\nu}{2} \sum_{e' \in E'_P} S_{e'} (\hat{u}_i + u_i^n) - \frac{\nu}{2} \sum_{f' \in F'_P} S_{f'} (\hat{u}_i + u_i^n) + G_{i,P} p^{n-1/2} = \\
 \sigma_1 \frac{1}{2} \sum_{f' \in F'_P} U_{f'}^-(\hat{u}_{i,P} + u_{i,P}^n - g_i^{n+1} - g_i^n) A_{f'} - \\
 \sigma_2 \frac{\nu}{2} \sum_{f' \in F'_P} S_{f'}^T (\hat{u}_i + u_i^n - g_i^{n+1} - g_i^n). \quad (2.21)
 \end{aligned}$$

3. Modify the matrix to project wall velocities to $\hat{u}_i = 0$. Solve for \hat{u}_i .
4. Remove old pressure gradient from all velocities (including any projected walls):

$$V_P \frac{u_i^* - \hat{u}_i}{\Delta t} = G_{i,P} p^{n-1/2}. \quad (2.22)$$

5. Interpolate u_i^* to the edges and take the edge-normal component. It is important to produce a single edge-based velocity component here to preserve the skew-symmetry of the convective operator. We consider two possibilities for interpolating to the edge, either a simple average of the two nodes associated with the edge:

$$U_e^* = \frac{1}{2 A_e} (u_{i,P}^* + u_{i,nb}^*) \sum_{e' \in e} \hat{n}_{i,e'} A_{e'}, \quad (2.23)$$

where the edge area is defined $A_e = \sum_{e' \in e} A_{e'}$. A more accurate alternative on bad grids is the following:

$$U_e^* = \frac{1}{A_e} \sum_{e' \in e} \frac{u_{i,e}^* + u_{i,f}^* + u_{i,c}^*}{3} \hat{n}_{i,e'} A_{e'}. \quad (2.24)$$

6. Solve the following Poisson equation for the new pressure at the midpoint of the time interval:

$$\sum_{e' \in E_P} S_{e'} p^{n+1/2} = \sum_{e \in E_P} \frac{U_e^* A_e}{\Delta t} + \sum_{f' \in F'_P} \frac{U_{f'}^{n+1} A_{f'}}{\Delta t}. \quad (2.25)$$

7. Correct the edge-based velocity components and node-based velocity vectors using the new pressure:

$$A_e \frac{U_e^{n+1} - U_e^*}{\Delta t} = - \sum_{e' \in e} S_{e'} p^{n+1/2} \quad (2.26)$$

$$V_P \frac{u_i^{n+1} - u_i^*}{\Delta t} = -G_{i,P} p^{n+1/2}. \quad (2.27)$$

8. Project wall velocities: $u_i^{n+1} = 0$.

We note that in the previous discretization, wall boundary conditions were projected ($u_i = 0$), rather than weakly enforced with a viscous penalty and $g_i = 0$. Projection was found necessary to get accurate near-wall behavior in turbulent boundary layers.

3. Results

3.1. Heat equation

To test the accuracy of the Laplacian operator and SAT boundary closure, we first solve the time-dependent heat equation on both periodic and non-periodic meshes using the manufactured solution:

$$\phi = \sin(x) \sin(y) \sin(z) \cos(t) \quad (3.1)$$

Fig. 3.1 shows the spatial convergence study on a sequence of nested tetrahedral meshes $-\pi \leq x_i \leq \pi$. The convergence is second order in l_2 both with and without boundary

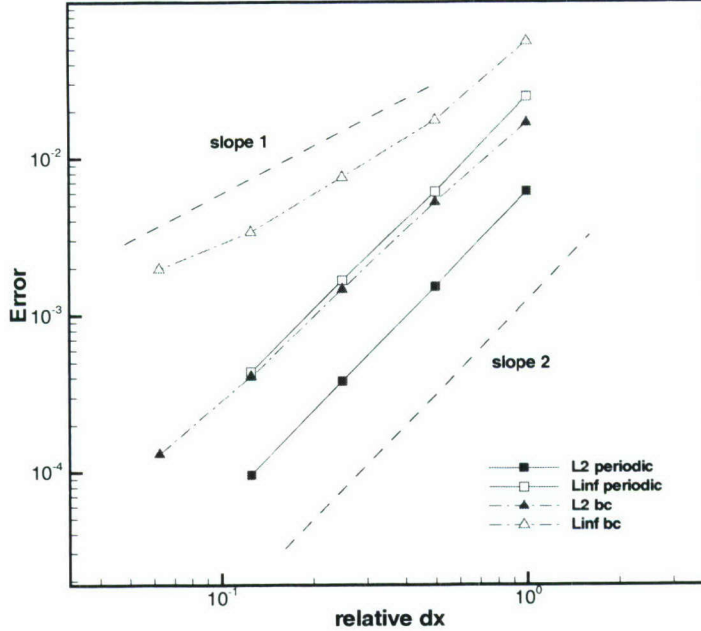


FIGURE 5. Spatial mesh refinement study for heat equation with manufactured solution on irregular tetrahedral grids.

conditions. l_∞ errors are second order with periodic boundaries, and first order with the Dirichlet boundary conditions and SAT boundary closure.

3.2. Advection Taylor vortices

The advecting Taylor vortex problem is an exact solution of the incompressible Navier-Stokes equations. Here we write the solution as:

$$u(x, y, t) = U - \cos(\pi(x - x_0 - Ut)) \sin(\pi(y - y_0 - Vt)) e^{-\frac{2\pi^2 t}{\nu}} \quad (3.2)$$

$$v(x, y, t) = V + \sin(\pi(x - x_0 - Ut)) \cos(\pi(y - y_0 - Vt)) e^{-\frac{2\pi^2 t}{\nu}} \quad (3.3)$$

$$p(x, y, t) = \frac{1}{4} (\cos(2\pi(x - x_0 - Ut)) + \cos(2\pi(y - y_0 - Vt))) e^{-\frac{4\pi^2 t}{\nu}}. \quad (3.4)$$

To break grid symmetries and make the problem more challenging, this solution includes an initial displacement of the vortices (x_0, y_0) and a constant advection speed (U, V) . For $\sqrt{U^2 + V^2} < 1$ this leads to time-dependent boundary conditions with regions of inflow and outflow. Using the discretization of the incompressible Navier-Stokes equations described in the previous section, several mesh convergence studies were performed and are reported in Figs. 6 through 10. All studies were performed with $\nu = 0.01$, $(U, V) = (0.25, 0.15)$, and errors computed at $t = 1$ for velocity, and $t = 1 - \Delta t/2$ for pressure (because pressure is stored at the midpoint of the time step).

Figure 9 (left) shows an interesting result where the pressure error is seen to fall off to first order on randomly perturbed quad meshes when the fine meshes are unrelated to the coarse meshes, apart from being a factor of 2 finer in both directions. This first-order convergence rate occurs on both periodic and Dirichlet boundary condition (bc) cases, indicating that it is not due to the bc's, but rather the inaccuracy of the internal

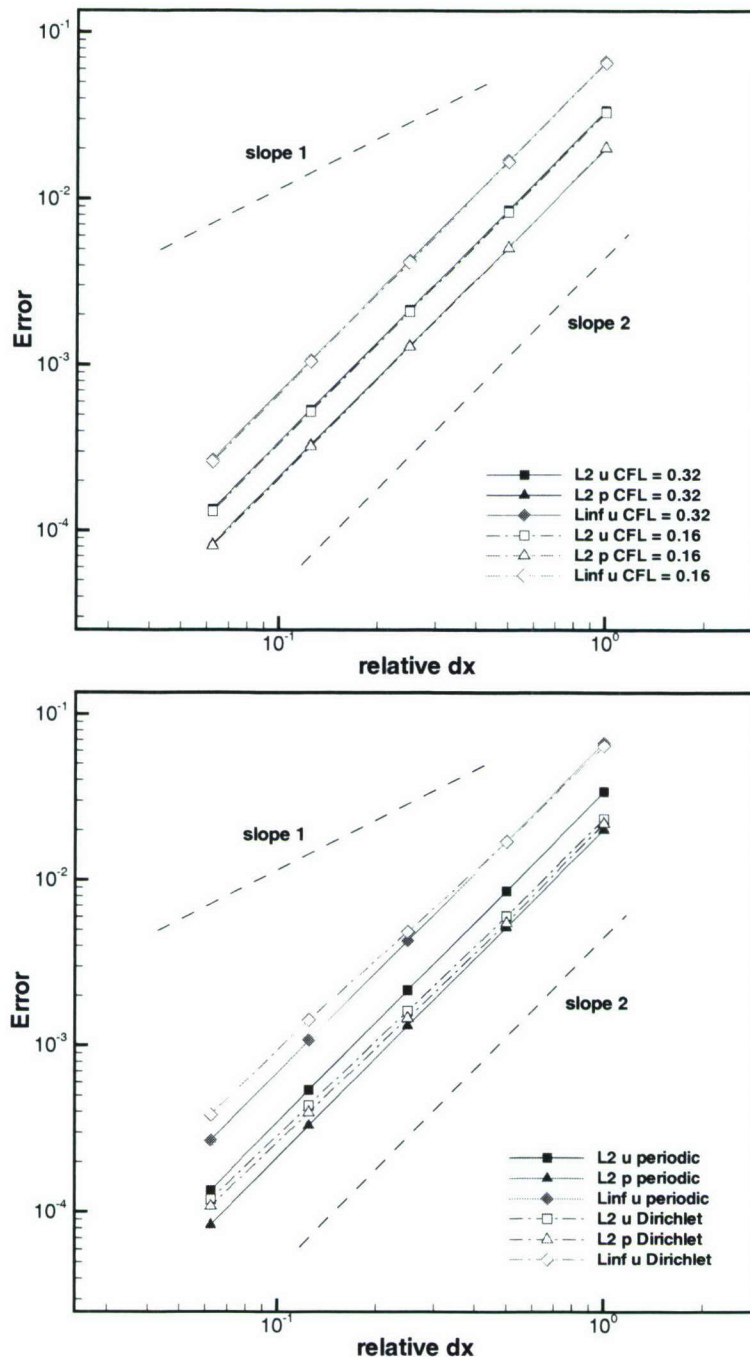


FIGURE 6. Advection Taylor vortex problem on uniform Cartesian grids: (top) changing time step size to confirm observed error is spatially dominated: periodic boundary conditions with $CFL = 0.32$ (solid) and $CFL = 0.16$ (dashed); (bottom) effect of Dirichlet boundary conditions imposed using the SAT approach.

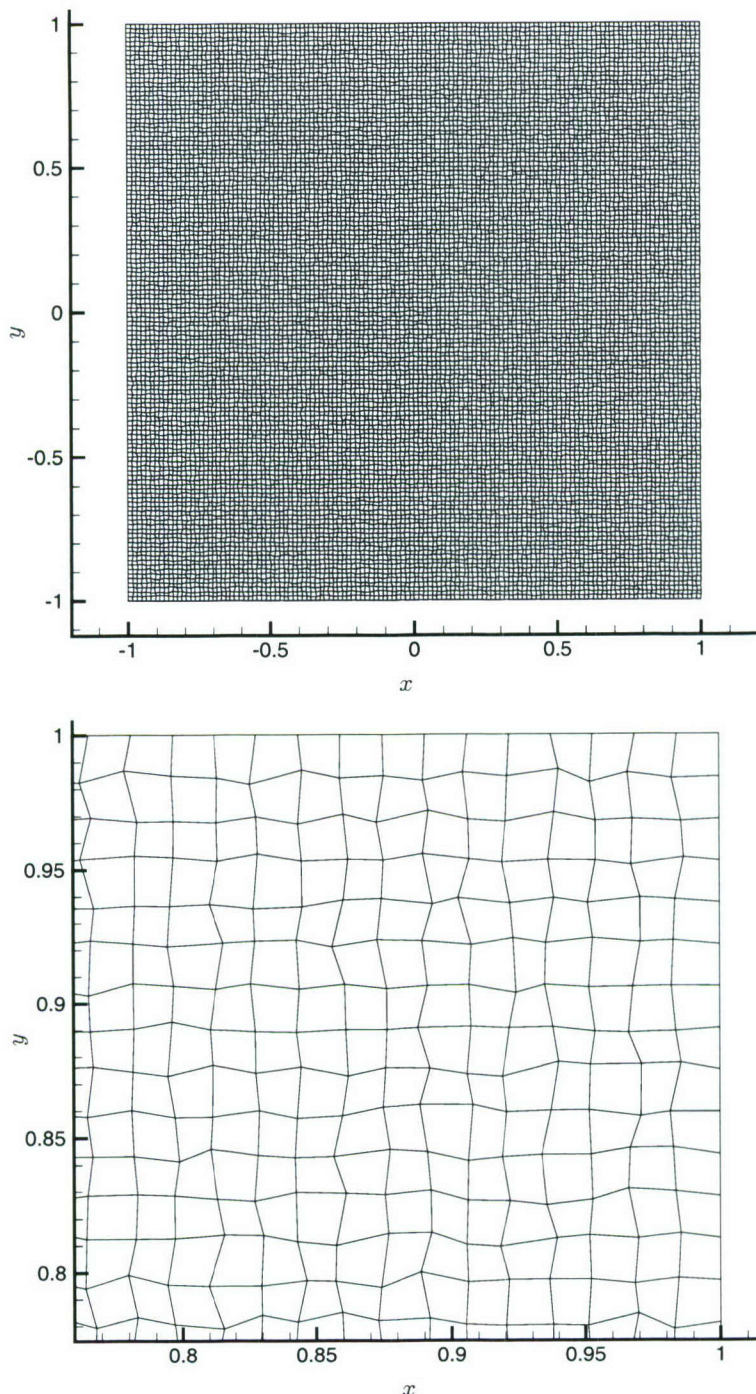


FIGURE 7. Randomly skewed quadrilateral mesh used for convecting Taylor vortex problem: (top) full mesh; (bottom) detail.

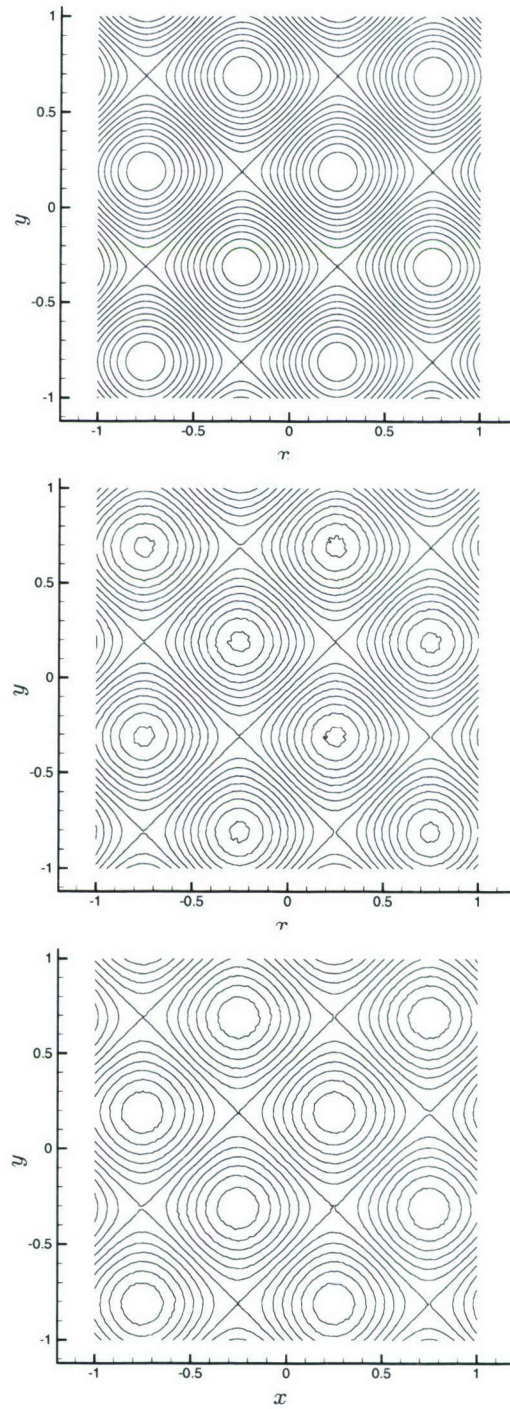


FIGURE 8. Contours of computed pressure at $t = 0, 0.5$, and 1.0 for convecting Taylor vortex problem on the skewed quadrilateral mesh shown in Fig. 7. For this case, vortices are advected in the positive x direction with $U = 1$, $V = 0$, viscosity is $\nu = 0.01$, Dirichlet boundary conditions on all boundaries.

Laplacian operator on irregular quad meshes. When nested homothetic refinement of the parent grid is used (a coarse grid is perturbed and then successively refined), the pressure recovers its second order behavior.

4. Conclusions

SBP operators and SAT boundary closures have been described for the finite volume method applied to arbitrary polyhedral meshes. The operators use a node-based (cell-vertex) formulation, where the unknowns are collocated with the nodes. The operators produce a strictly stable discretization for scalar advection diffusion. When applied to the heat equation and incompressible Navier-Stokes equations, manufactured and analytic solutions have been used to show consistent second order convergence in l_2 errors on a variety of unstructured grids.

The incompressible flow solver described in this brief is being successfully applied to an increasing range of flow problems in complex geometry. In addition, the operators as described readily support the stable and accurate discretization of other partial differential equations, including the linear wave equation (Mattsson *et al.* 2006) and a formulation for variable density reacting flows (Shunn & Ham 2006; Medic *et al.* 2006a,b). The development of a stable and accurate discretization for compressible flows on unstructured grids is currently in process.

Acknowledgments

We thank the U.S. Department of Energy for support of this work under the ASC Alliance program.

REFERENCES

CARPENTER, M. H., GOTTLIEB, D. & ABARBANEL, S. 1993 The stability of numerical boundary treatments for compact high-order finite difference schemes. *J. Comput. Phys.* **108**(2).

CARPENTER, M. H., GOTTLIEB, D. & ABARBANEL, S. 1994 Time-stable boundary conditions for finite-difference schemes solving hyperbolic systems: Methodology and application to high-order compact schemes. *J. Comput. Phys.* **111**(2).

HAM, F. & IACCARINO, G. 2004 Energy conservation in collocated discretization schemes on unstructured meshes. Annual Research Briefs 2004. Center for Turbulence Research, Stanford University / NASA Ames.

HAM, F., MATTSSON, K., IACCARINO, G. & MOIN, P. 2006 Towards time-stable and accurate les on unstructured grids. In *Complex Effects in Large Eddy Simulation, Lecture Notes in Computational Science and Engineering* 56, pp. 235–249. Springer.

KIM, D. & CHOI, H. 2000 A second-order time-accurate finite volume method for unsteady incompressible flow on hybrid unstructured grids. *J. Comput. Phys.* **162**, 411–428.

KREISS, H.-O. & SCHERER, G. 1974 Finite element and finite difference methods for hyperbolic partial differential equations. In *Mathematical Aspects of Finite Elements in Partial Differential Equations*. Academic Press Inc.

LAX, P. & RICHTMYER, R. 1956 Survey of the stability of linear finite difference equations. *Comm. on Pure and Applied Math.* **IX**.

MAHESH, K., CONSTANTINESCU, G. & MOIN, P. 2004 A numerical method for large-eddy simulation in complex geometries. *J. Comput. Phys.* **197**, 215–240.

MATTSSON, K., HAM, F. & IACCARINO, G. 2006 Efficient wave propagation on complex domains. Annual Research Briefs 2006. Center for Turbulence Research, Stanford University.

MEDIC, G., KALITZIN, G., YOU, D., HERRMANN, M., HAM, F., VAN DER WEIDE, E., PITSCH, H. & ALONSO, J. 2006a Integrated rans/les computations of turbulent flow through a turbofan jet engine. Annual Research Briefs 2006. Center for Turbulence Research, Stanford University.

MEDIC, G., YOU, D. & KALITZIN, G. 2006b An approach for coupling RANS and LES in integrated computations of jet engines. Annual Research Briefs 2006. Center for Turbulence Research, Stanford University.

MORINISHI, Y., LUND, T. S., VASILYEV, O. V. & MOIN, P. 1998 Fully conservative higher order finite difference schemes for incompressible flow. *J. Comput. Phys.* **143**, 90–124.

MOSER, R. D., KIM, J. & MANSOUR, N. N. 1999 Dns of turbulent channel flow up to $re_{\tau}=590$. *Phys. Fluids* **11**, 943–945.

NORDSTRÖM, J., SVÄRD, M., SHOEYBI, M., HAM, F., MATTSSON, K., IACCARINO, G., VAN DER WEIDE, E. & GONG, J. 2006 A stable, efficient and adaptive hybrid method for unsteady aerodynamics. Annual Research Briefs 2006. Center for Turbulence Research, Stanford University.

PEROT, B. 2000 Conservation properties of unstructured staggered mesh schemes. *J. Comput. Phys.* **159**, 58–89.

SCHNEIDER, G. E. & RAW, M. J. 1987 Control volume finite element method for heat transfer and fluid flow using collocated variables: Part i. computational procedure. *Numerical Heat Transfer* **11**, 363–390.

SHUNN, L. & HAM, F. 2006 Consistent and accurate state evaluations in variable-density flow simulations. Annual Research Briefs 2006. Center for Turbulence Research, Stanford University.

WU, X., SCHLUTER, J., MOIN, P., PITSCH, H., IACCARINO, G. & HAM, F. 2006 Computational study on the internal layer in a diffuser. *J. Fluid Mech.* **550**, 391–412.

ZANG, Y., STREET, R. L. & KOSEFF, J. R. 1994 A non-staggered grid, fractional step method for time-dependent incompressible Navier-Stokes equations in curvilinear coordinates. *J. Comput. Phys.* **114**, 18–33.

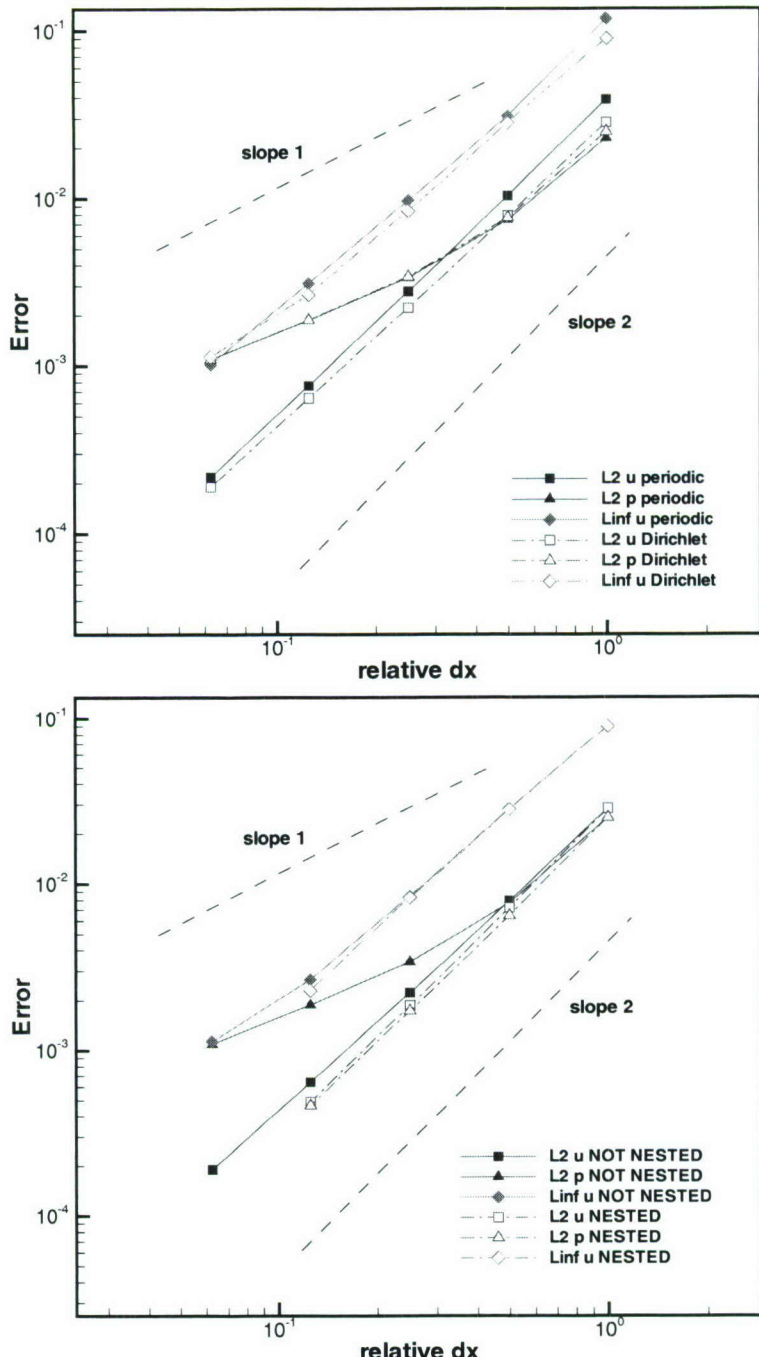


FIGURE 9. Advection Taylor vortex problem on skewed quadrilateral meshes: (top) randomly skewed meshes where fine meshes are unrelated to coarse meshes, apart from being a factor of 2 finer; (bottom) nested (homothetically refined) quads starting from the same coarse grid.

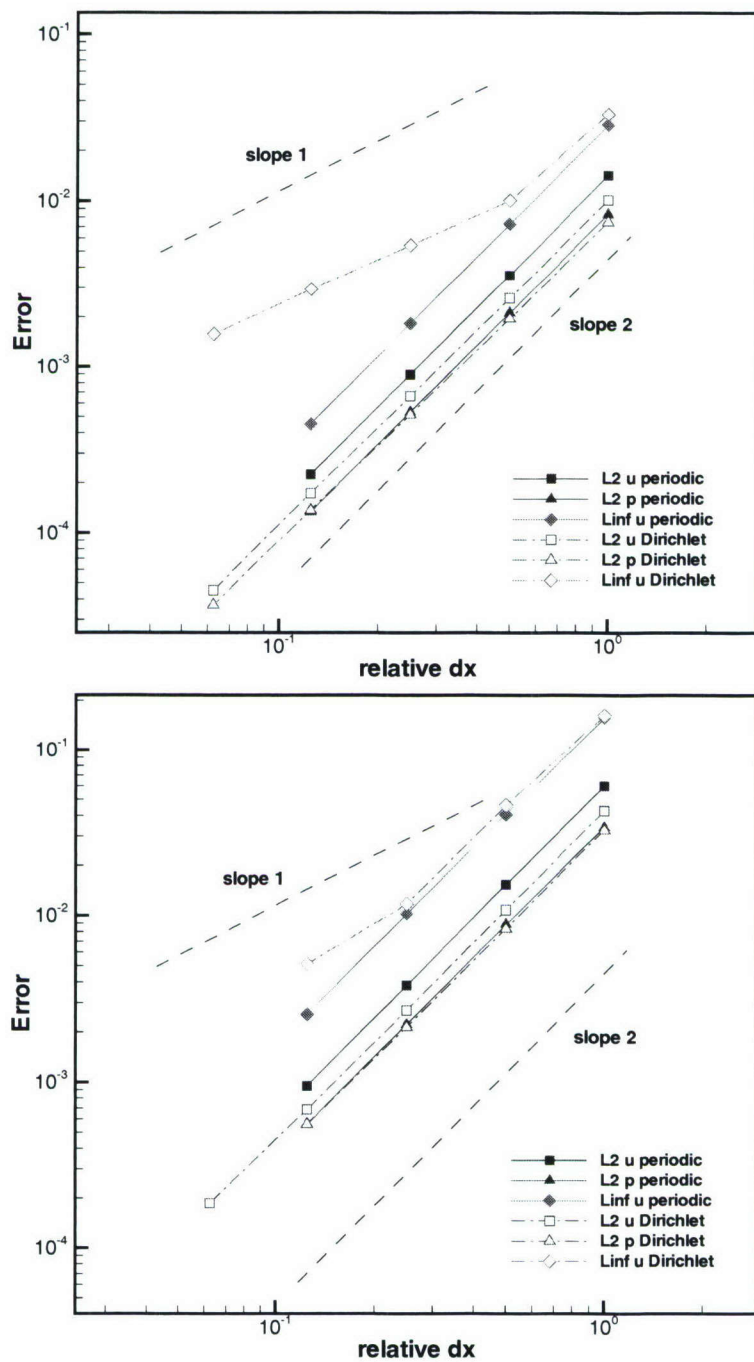


FIGURE 10. Advecting Taylor vortex problem on simplex grids: tris (top) and tets (bottom)

Coupled high-fidelity URANS simulation for helicopter applications

By S. Hahn, K. Duraisamy[†], G. Iaccarino,
S. Nagarajan, J. Sitaraman[†], X. Wu,
J. J. Alonso, J. D. Baeder[‡], S. K. Lele, P. Moin AND F. Schmitz[‡]

1. Motivation and objectives

Transonic flows on the advancing side of a helicopter rotor and blade-wake/blade-vortex interactions (BWI, BVI) are the major sources of helicopter noise. Both phenomena should be accurately predicted for a successful improvement of state-of-the-art helicopter design. To account for the former, a fully compressible CFD solver is essential in computing the flow around rotor blades. In most compressible flow solvers, however, the artificial dissipation formulated for shock capturing may lead to an erroneous dissipation of the wake or tip vortices and their subsequent spreading. Furthermore, the typical operating Reynolds number is very high, which makes the application of LES to helicopter rotor flow infeasible.

This article summarizes our technical efforts toward the development of high-fidelity CFD tools for rotorcraft applications as part of the DARPA Helicopter Quieting project. The key ideas in our strategy to overcome the difficulties previously stated are:

- (1) Coupling fully compressible and incompressible CFD solvers for near-blade and wake regions, respectively;
- (2) Incorporation of the low-dissipation algorithm (Mahesh *et al.* 2004; Ham & Iaccarino 2004) into the incompressible URANS solver for the wake region, in order to minimize the dissipation of vortical structures;
- (3) Using the most advanced four-equation v^2-f turbulence model (Durbin 1995) for improved predictive performance.

This combination will resolve both compressibility and wake effects with solvers best suited for each purpose. We use the multi-block, structured SUmb code (Van der Weide *et al.* 2006) and the unstructured CDP solver (Ham & Iaccarino 2004) for compressible and incompressible flow solvers, respectively. These two codes have been successfully applied to the full gas turbine simulation (Medic *et al.* 2007). Note that the initial setup of the necessary computational frameworks such as a moving-mesh capability, coupling strategy, and validation cases is already reported in Hahn *et al.* (2005). As a continuing work, this article will mainly focus on more challenging validation cases.

This paper is organized as follows: Section 2 briefly describes new aspects of the revised coupling software. Section 3 introduces the technique of anisotropic adaptive mesh refinement. Validations for the UH-60A and HART-II cases are provided in Sections 4 and 5, respectively, followed by the rotational correction on the v^2-f model in Section 6.

[†] Research fellow, University of Maryland.

[‡] Professor, University of Maryland.

2. Revision of coupling software

In order to facilitate the coupling procedure, it is more advantageous to have a separate coupling module that exclusively performs complicated searches, interpolations, and data transfer in an automated manner. For this purpose, we developed an initial version of coupling software, named CHIMPS (Coupler for High-performance Integrated Multi-Physics Simulations), through a collaboration with the ASC project in 2005 (Schlüter *et al.* 2005). We completely revised CHIMPS in 2006. The main objective of this revision is to provide more direct control of coupling procedures by specifying the frequency and nature of the data exchange between the applications. Furthermore, more functionalities are introduced to handle a wider class of applications within a coupled simulation (for example, particle-based simulations in addition to grid-based approaches) and to support various kinds of code-to-code data exchange (for example, spatially integrated data in addition to simply interpolated ones). This redesign not only provides more comprehensible, user-friendly, and organized API routines but also demonstrates efficient performance. On the other hand, along with the existing Python API, the CHIMPS library now supports a Fortran API to expedite the debugging of large-scale integrated simulations. C API may be also added in the near future. We examined the performance of the revised software for various applications, including simple interpolations, internal- and external-flow computations, and particle-based simulations. All test cases yielded successful results both in accuracy and scalability. This revised CHIMPS was also successfully applied to all the validation cases presented below. For detailed information on the revised CHIMPS (including users' manual), see Alonso *et al.* (2006).

3. Anisotropic adaptive mesh refinement (AAMR)

One of the objectives of the present research in rotorcraft aerodynamics is to develop a computational approach that enables the accurate representation of the development of wake vortices and their interactions. Adaptive Mesh Refinement (AMR) allows efficient clustering of cells in the specific regions of interest. It is therefore a possible candidate to achieve the required high resolution in the vortical regions without affecting the grid elsewhere. The present implementation is an extension of the classical AMR technique to include anisotropic refinement, since mesh resolution in the wake is only required in the vortex core, where large gradients are expected. Along the vortex axis, the grid resolution can be relaxed quite dramatically, unless strong interactions between the vortices cause breakdown. The meshes are built (and refined) using a tool developed for the immersed boundary technique (Iaccarino & Ham 2005); any orthogonal coordinate basis can be used to take advantage of the quasi-circularity of the vortices in a rotorcraft wake. As illustrated in figure 1 for a hovering case, the grid alignment between the vortex and the azimuthal direction allows full advantage to be taken of the anisotropy. In comparison, the Cartesian grid with the same resolution requirement contains typically 50% more grid cells. Once the grid is generated, it is converted into an unstructured polyhedral mesh.

One of the difficulties in the application of AMR schemes is the definition of the *region of interest* (i.e. where to apply refinement). Typically a scalar quantity (marker) is defined and all the cells above a threshold value are split. In the present work, the use of anisotropic AMR introduces an additional difficulty: the refinement marker must be a vector. Our choice for a marker quantity is illustrated in figure 2. Due to the specific nature of the refinement requirement in this application, we have chosen a vortex-related

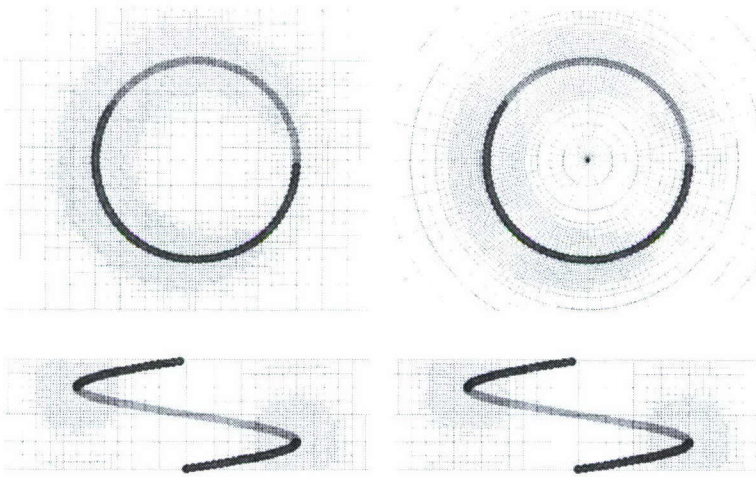


FIGURE 1. Example of grid refinement on helical vortices. The adapted mesh can be generated either in a Cartesian (left) or cylindrical (right) coordinate system.

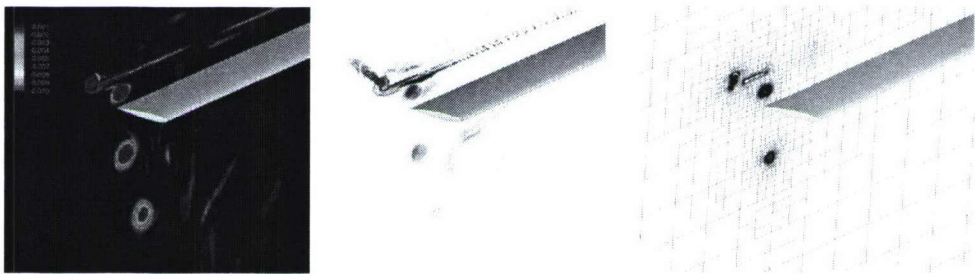


FIGURE 2. Detection criteria to perform anisotropic grid refinement. The helicity is used to select the cells to be refined (left) and the vorticity vector to identify the vortex direction (middle). The corresponding adapted grid is also illustrated (right).

parametrization. The first observation is that, although we require a vector quantity, we first rely on the *classical* scalar detection and calculate a direction vector afterward. Helicity (the dot product of velocity and vorticity vectors) is used as a scalar marker in the present study, which is presented in the leftmost plot of figure 2. It allows vortex cores to be sharply detected and *filters out* the vorticity generated in the boundary layer and shed in the near wake. The vorticity vector is then used to identify the vortex axis. An example of the grid generated for a rotor in hover is also presented in figure 2.

The final and most complicated step in applying this technology to rotorcraft wakes is to embed the refinement procedure within the solution loop, as the vortices move within the domain of interest. The current implementation is based on a loose coupling between grid generator and flow solver. The mesh is regenerated at specific checkpoints during the calculations, usually every 100 time steps. Simple linear interpolation is used to transfer the solution between grids. To illustrate the application of dynamic AMR, three different grid systems and corresponding solutions are illustrated for the problem of a translating vortex dipole in figure 3. The grid is generated using the detection scheme previously described. The marker is then spread over a larger area by applying a

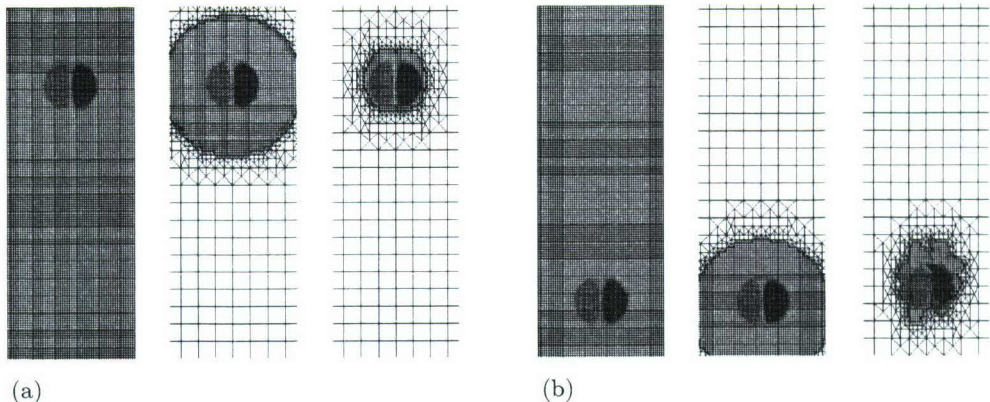


FIGURE 3. Translation of a vortex dipole: (a) at $t = 0$; (b) at a later time. Results from uniform (left) and two different adapted meshes (middle and right) are compared.

smoothing procedure: this allows a good solution accuracy to be retained as the vortex moves with the lapse of time. Two adaptive grids with different amounts of smoothing are shown in figure 3, along with a uniform grid as a reference. From figure 3, it appears that the amount of smoothing has a considerable effect on the preservation of vortices. In particular, the grid obtained by spreading the marker on a large area yields a solution almost comparable to that obtained from a fully uniform mesh. Note that the amount of smoothing applied to the marker is a function of the speed of vortices.

4. Validation on the forward flight: UH-60A

In the present study, the ability to handle the fluid–structure interaction is devised by coupling a structural analysis code, the University of Maryland Rotorcraft Comprehensive Analysis Code (UMARC), with the SUmb/CDP/CHIMPS flow analysis platform. The calculations are performed in a loosely coupled fashion (i.e. data exchange between CFD and CSD happens every revolution) to ensure stable convergence of aeroelastic motion, aerodynamic loading, and vehicle trim. Figure 4 shows grid topology used for the near- (SUmb) and off-body (CDP) meshes in this simulation. The total number of grid points for this simulation is approximately 6 million.

The fluid–structure analysis has been performed on a few forward-flight conditions for the UH-60A rotor where measured data are available from flight tests by Bousman *et al.* (1994). Results obtained for two critical steady-flight conditions are presented in this report: (1) high-speed forward flight (critical for high vibration); (2) high-altitude stall (critical for torsional loading and push-rod load).

The high-speed forward-flight condition is dominated by two critical flow phenomena that determine the phase and magnitude of the aerodynamic loading (Sitaraman *et al.* 2005). The first effect is the generation of large nose-down pitching moments in the advancing-blade phase because of the incidence of high transonic Mach numbers. These high nose-down pitching moments cause a large elastic torsional response that determines the phase and magnitude of the sectional aerodynamic lift as well (i.e. causes blades to be negatively loaded in the advancing-blade phase). Another dominant physical phenomenon is the blade–wake interaction, again on the advancing-blade phase. Blades with negative tip loading generate strong inboard wake sheets in contrast to strong rolled-up

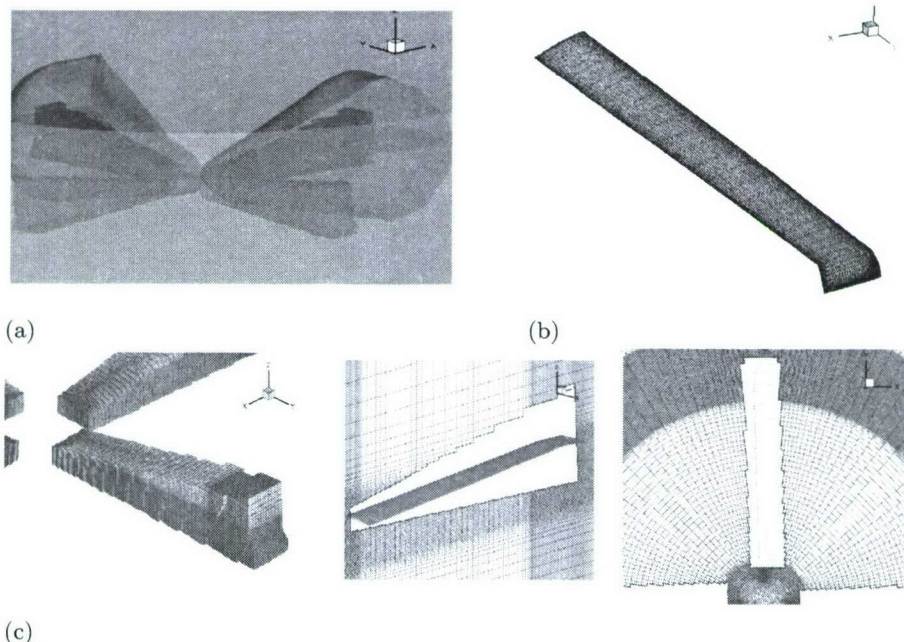


FIGURE 4. Grid topology in the SUmb-CDP coupling for the UH-60A case: (a) domain configuration (dark and light regions for inner CDP holes and SUmb domains, respectively); (b) surface mesh on the blade; (c) off-body CDP meshes and inner holes.

tip vortices. These inboard wake sheets interact with the following blade and, due to their proximity and strength, cause appreciable impulsive perturbations in the sectional aerodynamic lift. This impulsive lift is the main contributor to fixed-frame vibrations at this flight condition.

Figure 5 shows time histories of aerodynamic loading obtained from the coupled aeroelastic simulation and the comparison with flight-test data. From the phase and magnitude of the normal force and pitching moment, it is evident that the coupled aeroelastic simulation accurately resolves the transonic effects in the advancing-blade phase. The evidence of impulsive loading is also found in the advancing-blade phase, suggesting the appropriate resolution for the phenomenon of blade-wake interaction as well. Overall, we obtained a good correlation between the flight-test data and computed aerodynamic loading for the entire rotor disk; this is also clear in contours of the normal force and its azimuthal derivative presented in figure 6.

For the high-altitude stall condition, the significant physical phenomena are the dynamic stall events in the retreating-blade phase, which are highly aeroelastic in nature. A high pitch-angle variation for generating large thrust at a high-altitude operating condition causes the first stall event (named trim stall). The trim stall event creates negative pitching moments, which cause an elastic torsional response that subsequently causes the flow to reattach and stall again (named torsion stall; Sitaraman & Baeder 2006). Therefore, a fully consistent fluid-structure coupling is absolutely necessary to obtain the correct phase and magnitude of the stall events. Present calculations show a good correlation with test data at this flight condition (figure 7), both in the phase and magnitude of the stall events: this is most evident in the time histories of pitching moment

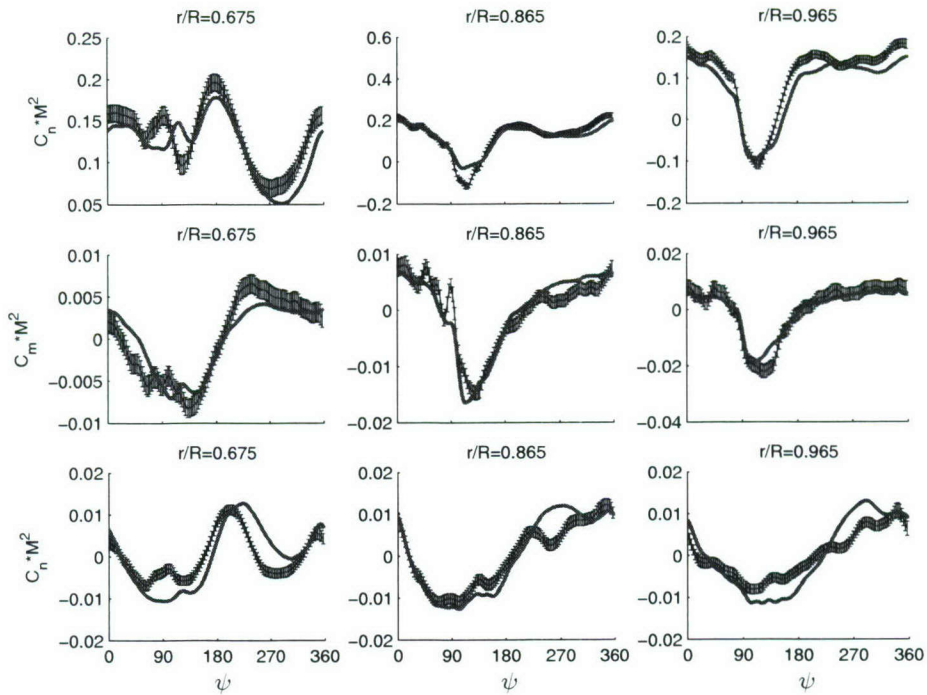


FIGURE 5. Time histories of the normal force (top), pitching moment (middle), and chord force (bottom) for the UH-60A high-speed forward-flight condition (8534). Solid lines and error bars represent simulation results and experimental data, respectively.

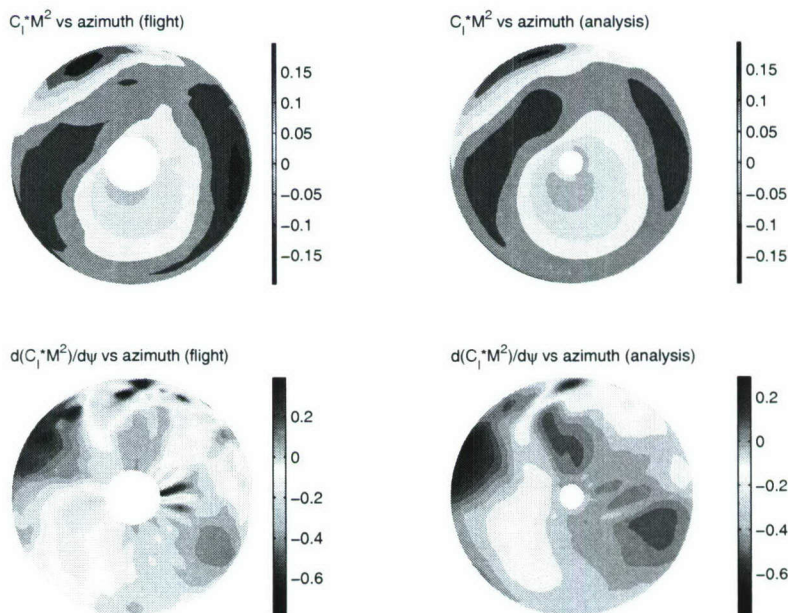


FIGURE 6. Contours of the normal force (top) and its azimuthal derivative (bottom) for the UH-60A high-speed forward-flight condition (8534). Experimental data and simulation results are shown on the left and right, respectively.

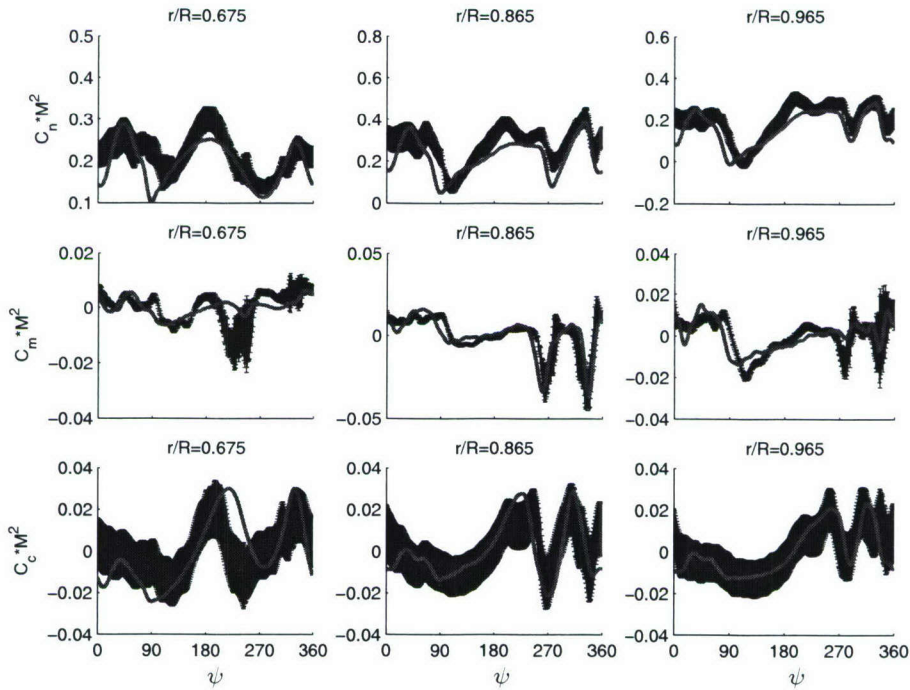


FIGURE 7. Time histories of the normal force (top), pitching moment (middle), and chord force (bottom) for the UH-60A high-altitude stall condition (9017). Solid lines and error bars represent simulation results and experimental data, respectively.

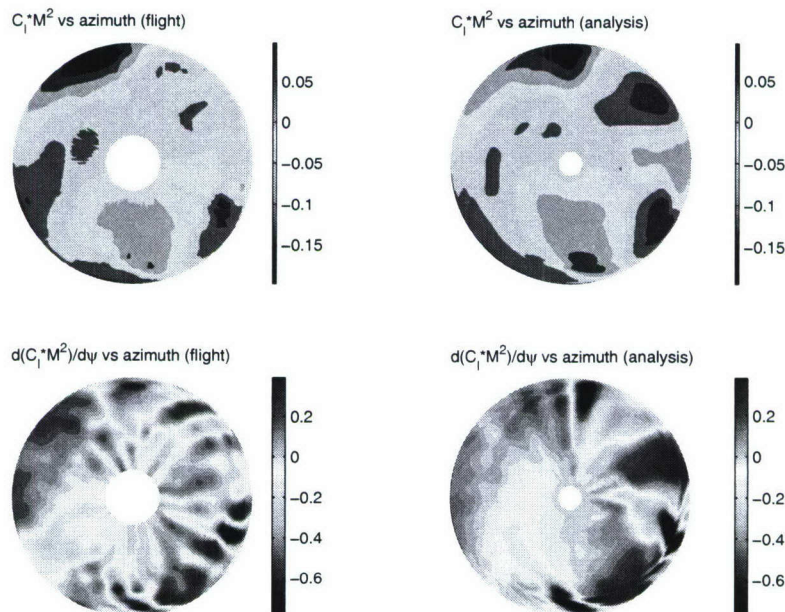


FIGURE 8. Contours of the normal force (top) and its azimuthal derivative (bottom) for the UH-60A high-altitude forward-flight condition (9017). Experimental data and simulation results are shown on the left and right, respectively.

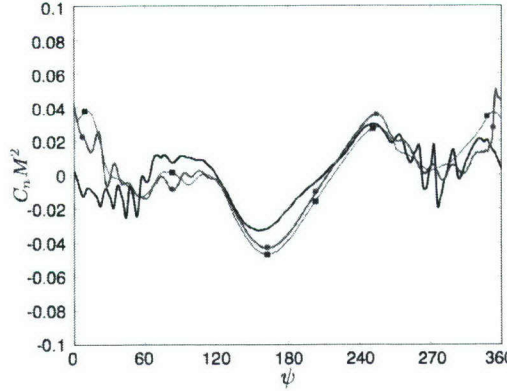


FIGURE 9. Time histories of the normal force at $r/R = 0.87$ for the HART-II baseline case: —●—, 3-mesh coupling (20 million cells in total); —■—, 2-mesh coupling (6 million cells in total); ——, experimental data.

and chord force. The contour plot of aerodynamic loading on the entire rotor disk, shown in figure 8, also exhibits a good agreement with the experiment, both in the location and magnitude of the stall events.

5. Validation on the descent flight: HART-II

The descent-flight condition for helicopters is dominated by blade–vortex interaction events that cause mid- to high-frequency impulses in aerodynamic loading and contribute significantly to the mid-frequency noise spectrum.

The SUmb/CDP/CHIMPS flow analysis has been conducted for a descent-flight operating condition, chosen from the HART-II wind-tunnel tests by Yu *et al.* (2002). Prescribed blade motions are used for this case in order to calibrate the resolution requirements for the flow analysis. Similarly to the UH-60A case, we initially coupled a single SUmb and a single CDP (without any mesh adaptation) for the near- and cylindrically shaped off-body regions, respectively, with approximately 6 million mesh elements in total. In this case, the wake effects could not be sufficiently accounted for. Consequently, we have devised a coupling of a single SUmb and two different instances of CDP (i.e. 3-mesh coupling), which capture the rotor-disk and wake regions, respectively. Since the near wake at this flight condition is populated by strong tip vortices, the conventional mesh generation would require an extremely large grid number. Therefore, we have applied the AAMR technique (described in Section 3) to the CDP domain for the wake region, where the CDP grids are pre-adapted based on the free-wake solution. Figure 9 shows the comparison of airload histories for the two different mesh systems. A significant improvement is noted in the aerodynamic loading with the 3-mesh coupling: the BVI events are evident on both the advancing and retreating sides. In the case of the 2-mesh coupling, the vortex/wake system is diffused quite significantly and the associated BVI events are completely smoothed out. Therefore, this simulation does provide proof-of-concept demonstration for the benefit of AAMR in predicting blade–vortex interactions. Nevertheless, it is to be noted that the mesh resolution for the 3-mesh coupling is still unsatisfactory for precisely accounting for the wake structure. The BVI events captured by the 3-mesh coupling are still much weaker than those demonstrated by the experi-

ment, which leaves room for improvement. A finer mesh system with similar topology will be applied in the near future.

6. Turbulence-model improvement for dynamic stall using LES database

Linear eddy-viscosity models have an inherent limitation in the correct representation of influence from system rotation or streamline curvature. Pettersson Reif *et al.* (1999) suggested a rotational correction for the v^2-f model, where the eddy-viscosity coefficient is modified to mimic the second-moment closure in the case of isotropic turbulence that is subject to system rotation. This correction introduces a new eddy-viscosity coefficient, C_μ^* , which is represented as a function of non-dimensional strain- and rotation-rate tensors, η_1 and η_2 , viz.

$$C_\mu^* = C_\mu \frac{1 + \alpha_2|\eta_3| + \alpha_3|\eta_3|}{1 + \alpha_4|\eta_3|} \left(\sqrt{\frac{1 + \alpha_5\eta_1}{1 + \alpha_5\eta_2}} + \alpha_1\sqrt{\eta_2} + \alpha_1\sqrt{\eta_2}\sqrt{|\eta_3| - \eta_3} \right)^{-1}, \quad (6.1)$$

where C_μ is the uncorrected eddy-viscosity coefficient, $\eta_1 = S_{ik}^* S_{ik}^*$, $\eta_2 = \Omega_{ik}^* \Omega_{ik}^*$, $S_{ik}^* = \frac{1}{2}T(\partial U_i / \partial x_k + \partial U_k / \partial x_i)$, $\Omega_{ik}^* = \frac{1}{2}T(\partial U_i / \partial x_k - \partial U_k / \partial x_i + 4.5\epsilon_{ikim}\Omega_m^f)$, ϵ_{ikim} and Ω_m^f are the permutation symbol and angular velocity for system rotation, $T = \min[\max(k/\epsilon, 6\sqrt{\nu/\epsilon}), \alpha k/\sqrt{3}C_\mu S v^2]$, $S = \sqrt{2S_{ik} S_{ik}}$, $S_{ik} = S_{ik}^*/T$, $\alpha_1 = 0.055\sqrt{f_1}$, $\alpha_2 = \frac{1}{2}f_1$, $\alpha_3 = \frac{1}{4}f_1$, $\alpha_4 = \frac{1}{5}\sqrt{f_1}$, $\alpha_5 = \frac{1}{40}$, and $f_1 = \sqrt{v^2/0.367k}$. Finally, the eddy viscosity is computed as follows:

$$\nu_t = C_\mu^* \bar{v^2} T. \quad (6.2)$$

On the other hand, further analysis on homogeneous rotating turbulence shows that a constraint should be devised on C_μ^* in order to limit the turbulent production to levels attained by the original second-moment closure. In the present study, effects of this constraint are tested simply by introducing a limiter to C_μ^* as follows:

$$C_\mu^* = C_\mu \min \left[\frac{1 + \alpha_2|\eta_3| + \alpha_3|\eta_3|}{1 + \alpha_4|\eta_3|} \left(\sqrt{\frac{1 + \alpha_5\eta_1}{1 + \alpha_5\eta_2}} + \alpha_1\sqrt{\eta_2} + \alpha_1\sqrt{\eta_2}\sqrt{|\eta_3| - \eta_3} \right)^{-1}, 1.06 \right]. \quad (6.3)$$

This variant was shown to provide an improved predictive performance for the laminarization near the core of wing-tip vortex in a static 3D airfoil (Duraisamy & Iaccarino 2005). In order to examine its performance in highly non-equilibrium wall-bounded flows, the correction is further applied to a 2D dynamic stall in the present study. For a precise assessment of accuracy, a flow over a pitching NACA0012 airfoil is computed using both LES and URANS.

The Reynolds and Mach numbers chosen are $Re = u_\infty c / \nu_\infty = 1.3 \times 10^5$ and $M = u_\infty / a_\infty = 0.3$, where u_∞ , ν_∞ , and a_∞ are velocity, kinematic viscosity, and speed of sound at the free stream, and c is the chord length. A NACA0012 airfoil is pitching about the leading edge and the pitching condition is $\alpha(t) = \alpha_0 + \Delta\alpha \sin(\omega t)$, $\alpha_0 = 10^\circ$, $\Delta\alpha = 5^\circ$, $\beta = \omega c / 2u_\infty = 0.5$, where $\alpha(t)$ is the angle of attack, ω is the pitching frequency, and β is the reduced frequency. Note that the static airfoil at this mean angle of attack has a small separation bubble near the leading edge, with transition in the separated shear layer. A fully compressible LES code, based on the sixth-order compact scheme and staggered arrangement of conserved variables (Nagarajan *et al.* 2003), and SUmb are

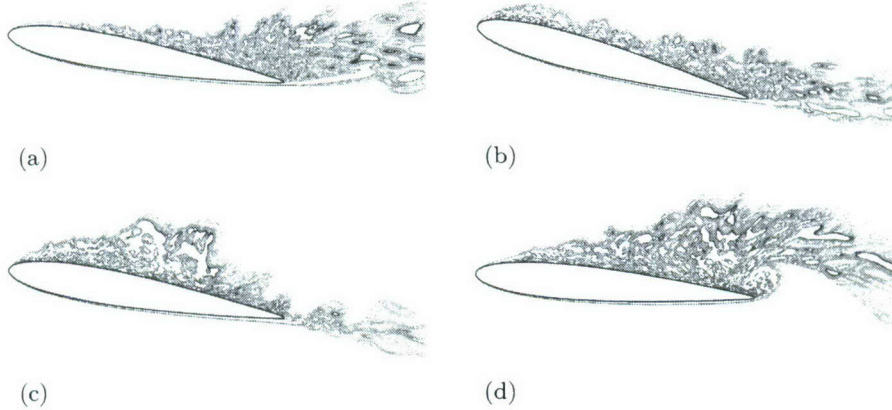


FIGURE 10. Contours of the spanwise vorticity from LES: (a) $t = nT$ (middle of upstroke); (b) $t = nT + \frac{1}{4}T$ (highest incidence); (c) $t = nT + \frac{1}{2}T$ (middle of downstroke); (d) $t = nT + \frac{3}{4}T$ (lowest incidence). T denotes the pitching period.

used for the present LES and URANS, respectively. For both LES and URANS, an O-mesh system with 480×300 points in the chordwise and normal directions, respectively, is used. The domain extends approximately $20c$ from the airfoil in each direction. For the 3D LES simulations, a rather small spanwise domain of $0.1c$ is used along with 128 grid points near the wall. This spanwise resolution is decreased away from the wall using a zonal approach. For URANS, three different variants of the v^2-f model, the original uncorrected version together with the corrections (6.1) and (6.3), are considered. For all the computed cases, the simulation is initialized with the flowfield from the static-airfoil calculation at the mean angle of attack. For URANS, 1200 time steps per pitching period guarantee the time accuracy for the uncorrected version and (6.1), whereas 4800 time steps per pitching period are necessary for (6.3). On the other hand, 30,000 time steps per pitching period are used for LES.

Figure 10 shows contours of the spanwise vorticity from LES at four different time instants. This figure clearly shows the evolution of a dynamic-stall vortex (DSV) and its detachment. Formation of a large DSV is found around the mid-chord location during the downstroke (figure 10c) and it moves closer to the trailing edge at the instant of lowest incidence (figure 10d). When the DSV is in the vicinity of the upper airfoil surface, it induces a suction peak on the airfoil, leading to high lift. Figure 11 shows a comparison of the surface pressure distribution among the LES and three URANS simulations at four different time instants. The uncorrected v^2-f model substantially underpredicts the suction peak throughout the DSV formation and detachment process. The rotational correction without the limiter, (6.1), introduces a certain amount of improvement over the uncorrected one, but it is still grossly inaccurate both in the strength and phase of the DSV. On the other hand, the rotational correction with the limiter, (6.3), shows a significant enhancement in the overall accuracy. It reproduces the amplitude of the suction peak quite closely, although it is still wider than that predicted by LES. Figure 12 shows time histories of lift and drag coefficients from the LES and URANS simulations. The superiority of the rotational correction with the limiter is especially prominent during the later stage of downstroke and earlier stage of upstroke (i.e. near the valleys of lift and drag coefficients), where the recovery from stall (decreasing drag coefficient) is predicted

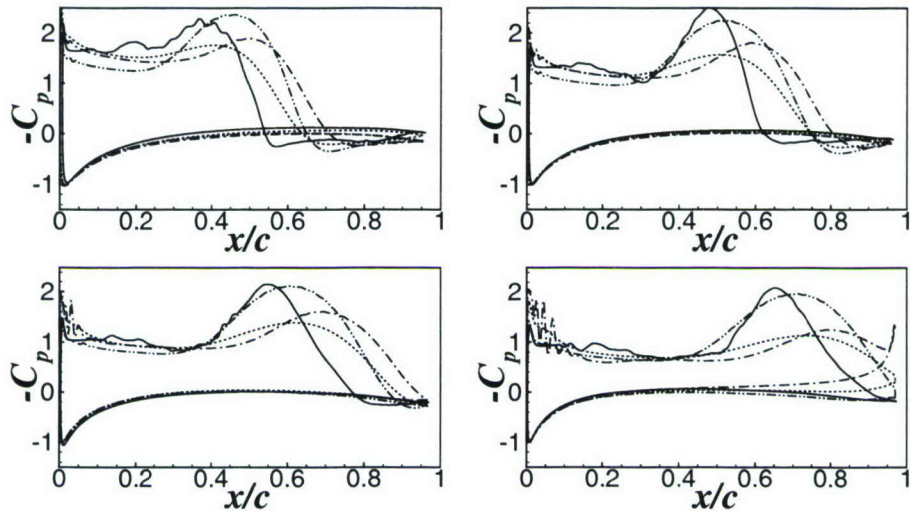


FIGURE 11. Pressure coefficient on the airfoil surface at four different time instants: —, LES (phase-averaged data); - - -, uncorrected v^2-f ; - · - -, rotational correction without the limiter; - · · - -, rotational correction with the limiter.

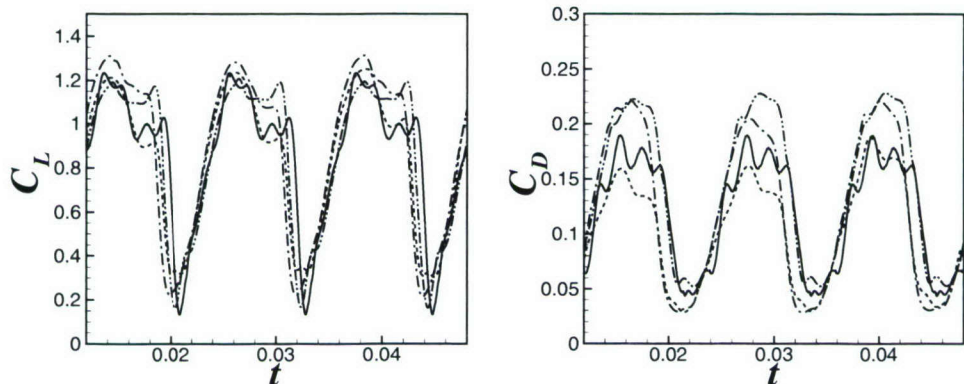


FIGURE 12. Time histories of lift (left) and drag (right) coefficients: —, LES (phase-averaged data); - - -, uncorrected v^2-f ; - · - -, rotational correction without the limiter; - · · - -, rotational correction with the limiter.

more accurately than the other v^2-f variants. However, the maximum values of lift and drag still deviate considerably from the LES values. A proper modification of the limiter near the solid surface will be explored in a future study.

Acknowledgments

This work is supported by the Defense Advanced Research Projects Agency (DARPA) of the United States Department of Defense.

REFERENCES

ALONSO, J. J., HAHN, S., HAM, F., HERRMANN, M., IACCARINO, G., KALITZIN, G.,

LEGRESLEY, P., MATTSSON, K., MEDIC, G., MOIN, P., PITSCHE, H., SCHLÜTER, J., SVÄRD, M., VAN DER WEIDE, E., YOU, D. & WU, X. 2006 CHIMPS: A high-performance scalable module for multi-physics simulations. *AIAA Paper 2006-5274*.

BOUSMAN, G., KUFELD, R. M., BALOUGH, D., CROSS, J. L., STUDEBAKER, K. F. & JENNISON, C. D. 1994 Flight testing the UH-60A airloads aircraft. *Proc. of the 50th Annual Forum of the American Helicopter Society*, Washington, D. C., May, 1994.

DURAISAMY, K. & IACCARINO, G. 2005 Modeling vortical flows using linear eddy viscosity closures. *B. Am. Phys. Soc.*, **50**.

DURBIN, P. A. 1995 Separated flow computations with the $k-\epsilon-v^2$ model. *AIAA J.* **33**, 659–664.

HAHN, S., ALONSO, J., BAEDER, J. D., DURAISAMY, K., IACCARINO, G., LELE, S., MOIN, P., SCHMITZ, F., SHOEYBI, M. & WU, X. 2005 Progress on hybrid unsteady simulation of helicopter rotor flow. *Annu. Res. Briefs 2005*, Center for Turbulence Research, 121–138.

HAM, F. & IACCARINO, G. 2004 Energy conservation in collocated discretization schemes on unstructured meshes. *Annu. Res. Briefs 2004*, Center for Turbulence Research, 3–14.

IACCARINO, G. & HAM, F. 2005 Automatic mesh generation for LES in complex geometries. *Annu. Res. Briefs 2005*, Center for Turbulence Research, 15–26.

MAHESH, K., CONSTANTINESCU, G. & MOIN, P. 2004 A numerical method for large eddy simulation in complex geometries. *J. Comput. Phys.* **197**, 215–240.

MEDIC, G., YOU, D., KALITZIN, G., PITSCHE, H., VAN DER WEIDE, E. & ALONSO, J. J. 2007 Integrated computations of an entire jet engine. *Proc. of the ASME/IGTI Turbo Expo*, GT2007-27094.

NAGARAJAN, S., LELE, S. K. & FERZIGER, J. H. 2003 A robust high-order compact method for large eddy simulation. *J. Comput. Phys.* **191**, 392–419.

PETTERSSON REIF, B. A., DURBIN, P. A. & OOI, A. 1999 Modelling rotational effects in eddy-viscosity closures. *Int. J. Heat Fluid Flow* **20**, 563–573.

SCHLÜTER, J. U., WU, X., VAN DER WEIDE, E., HAHN, S., HERRMANN, M., ALONSO, J. J. & PITSCHE, H. 2005 A Python approach to multi-code simulations: CHIMPS. *Annu. Res. Briefs 2005*, Center for Turbulence Research.

SITARAMAN, J. & BAEDER, J. D. 2006 Evaluation of wake prediction methodologies used in CFD based rotor airload calculations. *AIAA Paper 2006-3472*.

SITARAMAN, J., DATTA, A., BAEDER, J. D. & CHOPRA, I. 2005 Coupled CFD/CSD prediction of rotor aerodynamic and structural dynamic loads for three critical flight conditions. *Proc. of the 31st European Rotorcraft Forum*, Firenze, Italy, September 13–15, 2005.

VAN DER WEIDE, E., KALITZIN, G., SCHLÜTER, J. & ALONSO, J. J. 2006 Unsteady turbomachinery computations using massively parallel platforms. *AIAA Paper 2006-421*.

YU, Y. H., TUNG, C., VAN DER WALL, B., PAUSDER, H., BURLEY, C., BROOKS, T., BEAUMIER, P., YVES, D., MERCKER, E. & PENGEL, K. 2002 The HART-II test: rotor wakes and aeroacoustics with higher harmonic pitch control (HHC) inputs - the joint German/French/Dutch/US project. *Proc. of the AHS 58th Forum*, Montreal, Canada, June 2002.

Integrated RANS/LES computations of turbulent flow through a turbofan jet engine

By **G. Medic, G. Kalitzin, D. You, M. Herrmann, F. Ham, E. van der Weide, H. Pitsch AND J. Alonso**

1. Motivation and objectives

The interaction between different components of a jet engine represents a very important aspect of the engine design process. Sudden mass flow-rate changes induced by flow separation and pressure waves, interaction of the unsteady wakes originating from the fan blades with the low-pressure compressor, high temperature streaks interacting with the first stages of the turbine are all complex unsteady phenomena that cannot be simply accounted for through boundary conditions of a single component simulation. Only simulations that integrate multiple engine components can describe these flow features accurately.

Today's use of Computational Fluid Dynamics (CFD) in gas turbine design is usually limited to component simulations. The demand on the models to represent the large variety of physical phenomena encountered in the flow path of a gas turbine mandates the use of a specialized and optimized approach for each component. The flow-field in the turbomachinery portions of the domain is characterized by both high Reynolds numbers and high Mach numbers. The prediction of the flow requires the precise description of the turbulent boundary layers around the rotor and stator blades, including tip gaps and leakage flows. A number of flow solvers that have been developed to deal with this kind of problem have been in use in industry for many years. These flow solvers are typically based on the Reynolds-Averaged Navier-Stokes (RANS) approach. Here, the unsteady flow-field is ensemble-averaged, removing all the details of the small scale turbulence; a turbulence model becomes necessary to represent the effects of turbulence on the mean flow.

The flow in the combustor, on the other hand, is characterized by multi-phase flow, intense mixing, and chemical reactions. The prediction of turbulent mixing is greatly improved using flow solvers based on Large-Eddy Simulations (LES). While the use of LES increases the computational cost, LES has been the only predictive tool able to simulate consistently these complex flows. LES resolves the large-scale turbulent motions in time and space, and only the influence of the smallest scales, which are usually more universal and hence, easier to represent, has to be modeled (Ferziger, 1996, and Sagaut, 2002). Since the energy-containing part of the turbulent scales is resolved, a more accurate description of scalar mixing is achieved, leading to improved predictions of the combustion process, as shown in Raman & Pitsch (2005). LES flow solvers have been shown in the past to be able to model simple flames and are currently being adapted for use in gas turbine combustors, e.g., Poinsot *et al.* (2001) and Constantinescu *et al.* (2003).

In order to compute the flow in the entire jet engine, one needs to couple RANS and LES solvers. We have developed a software environment that allows a simulation of multi-component effects by executing multiple solvers simultaneously. Each of these solvers computes a portion of a given flow domain and exchanges flow data at the interfaces with

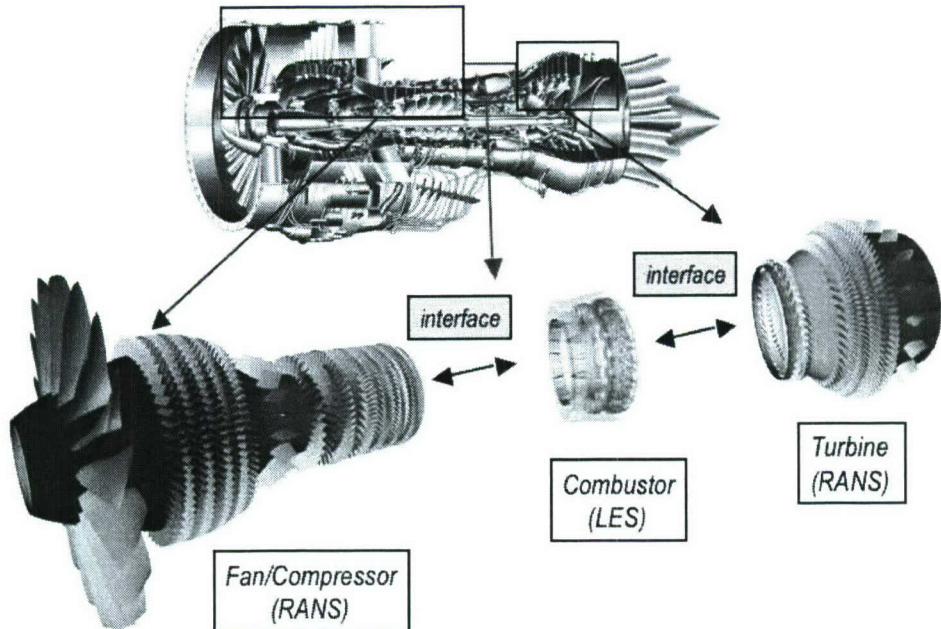


FIGURE 1. Decomposition of the engine for flow simulations.

its peer solvers (see figure 1). The approach to couple two or more existing flow solvers has the distinct advantage of building upon the experience and validation that has been put into the individual codes during their development. It provides the possibility of running simulations in different domains at different time steps, and provides a higher degree of flexibility. We will demonstrate this approach in a simulation of a 20° sector of the entire gas turbine jet engine, encompassing the fan, low- and high-pressure compressor, combustor, high- and low-pressure turbine, and the exit nozzle. We will show that such a simulation can deliver important insight into the physics of interaction between different engine components within a manageable turnover time, which is necessary to be useful in the design process of an engine.

2. Flow solvers

For the integrated computations presented here, we use flow solvers that are well-suited and tested for the individual components: a RANS flow solver for the turbomachinery parts and an LES flow solver for the combustor. These solvers were further adapted for efficient use on massively parallel platforms of up to several thousand CPUs, which are needed for these integrated computations of an entire jet engine.

2.1. RANS flow solver

The RANS flow solver used in the computations is the SUmb code developed at the Aerospace Computing Lab (ACL) at Stanford. The flow solver computes the unsteady

Reynolds-Averaged Navier-Stokes equations using a cell-centered discretization on arbitrary multi-block meshes (see Yao *et al.*, 2000). The solution procedure is based on efficient explicit modified Runge-Kutta methods with several convergence acceleration techniques such as multi-grid, residual averaging, and local time-stepping. These techniques, multi-grid in particular, provide excellent numerical convergence and fast solution turnaround. The turbulent viscosity is computed from a $k - \omega$ two-equation turbulence model and adaptive wall functions are employed to compute the boundary conditions. The dual time-stepping technique of Jameson (1991), Alonso *et al.* (1995), and Belov *et al.* (1996) is used for time-accurate simulations that account for the relative motion of moving parts as well as other sources of flow unsteadiness.

2.2. LES flow solver

The LES flow solver used for the current study is the CDP code developed at the Center for Turbulence Research (CTR) at Stanford. The numerical algorithms and their implementation are described in detail in Mahesh *et al.* (2006). Here we summarize the main features of the methodology. The filtered Navier-Stokes equations are solved in an unstructured grid system using a Smagorinsky-type subgrid-scale (SGS) model of Germano *et al.* (1991). The integration method used to solve the governing equations is based on a fully implicit fractional-step method. All terms, including cross-derivative diffusion terms, are advanced in time using the Crank-Nicholson method.

The Cartesian components of momentum, density, and pressure are stored at the nodes of the computational elements. Once density is obtained from a flamelet library, the continuity equation can be imposed as a constraint on the momentum field, with the time-derivative of density as a source term. This constraint is enforced by the pressure, in a manner analogous to the enforcement of the incompressibility constraint for constant density flows. The computational approach is to first advance the mixture fraction and the progress variable. The flamelet library yields the density, whose time-derivative is then computed. The momentum is predicted using the convective, viscous, and pressure-gradient at first. The predicted value of the momentum is then projected such that the continuity equation is satisfied.

2.3. Boundary conditions

The definition of the boundary conditions requires special attention, especially for LES. Because a part of the turbulent spectrum is resolved in the LES, the challenge is to regenerate and preserve the turbulence at the boundaries.

At the LES inflow boundary, the challenge is to prescribe transient turbulent velocity profiles from ensemble-averaged RANS data. Turbulent fluctuations at the inflow of the combustor have to be constructed using an additional LES computation. The fluctuations can be precomputed and stored in a database, as shown in Schluter *et al.* (2004), or computed on the fly from an auxiliary duct computation as in Medic *et al.* (2006).

For the RANS solver, inlet and exit boundary conditions are applied using the time-averaged solution from the LES, as suggested in Kim *et al.* (2004). Turbulence variables (such as k and ω) can also be computed on the fly from a quasi-2D RANS computation of an auxiliary duct at the turbine inflow. For more details, see Medic *et al.* (2006).

3. CHIMPS: Multi-solver coupling

Previous approaches to couple solvers were based on a pure MPI approach; for more details see Shankaran *et al.* (2001), Schluter *et al.* (2003a), Schluter *et al.* (2003b), and

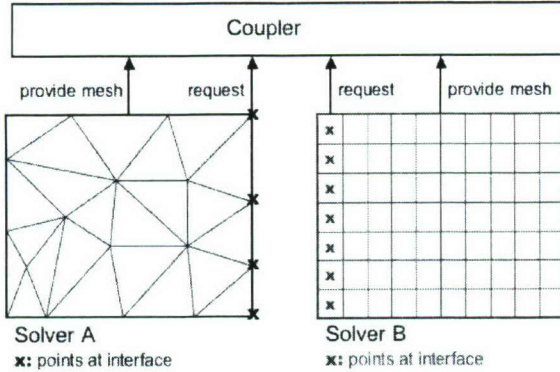


FIGURE 2. CHIMPS approach: solvers communicate location of their interface points and their mesh and solution to the coupler. The coupler determines how to provide information to the solver at the interface nodes.

Schlüter *et al.* (2005). In that approach, MPI is used to let different solvers communicate directly with each other. The disadvantage of this approach is that the implementation is tedious and error prone since each MPI command in one solver requires a corresponding MPI command in the other solver. Furthermore, the search and interpolation routines have to be implemented in each solver separately.

A more effective approach consists in implementing all the coupling routines (communication, search, and interpolation) in a separate software module that performs these tasks: Coupler for **H**igh-**P**erformance **I**ntegrated **M**ulti-**P**hysics **S**imulations (CHIMPS) (for the latest update see Alonso *et al.*, 2006). The solvers are now communicating with the coupler software only (figure 2) and the coupler performs all searches and interpolations. In this latest version, the coupler supports both a script language such as Python and standard programming languages like Fortran90.

4. Full-engine simulations

In this section we present an integrated multi-component simulation of a Pratt & Whitney aircraft engine. This simulation simultaneously computes the flow in the fan/compressor, the combustor, and the turbine, and each of the components exchanges flow data with its neighbors. The goal of this simulation is to demonstrate the ability to perform complex, multi-physics, multi-code simulation on a real-world problem. The domain consists of a 20° sector of all the components; in view of the full-engine simulation, this is the smallest sector that can be chosen since it contains one fuel injector. The initial solution for the integrated simulation is provided by a combination of the component simulations.

Note that the blade counts in turbomachinery are normally such that no sector periodicity occurs. This is done to avoid instabilities caused by resonance between two components. As a consequence, the true unsteady simulation can only be done for the entire wheel, unless simplifying assumptions are made. The currently accepted practice is to rescale the blade counts of the turbomachinery stages such that sector periodicity is obtained. To preserve the same flow blockage, the pitch of the blades is adjusted according to common industry practice.

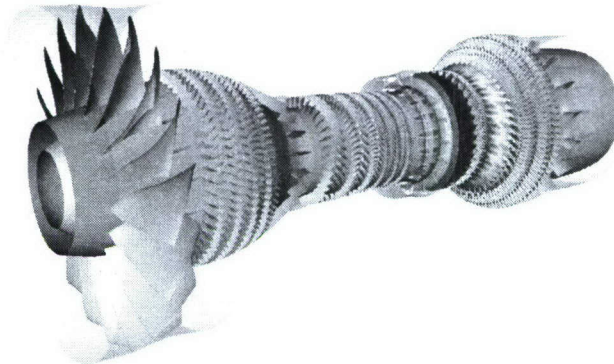


FIGURE 3. Simulation of the entire engine: axial velocity.

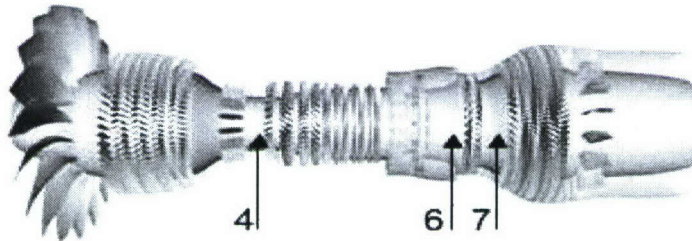


FIGURE 4. Flow stations.

4.1. *Operating conditions*

The operating conditions for the engine correspond to cruise conditions; these define the boundary conditions for the engine: fan inlet conditions, turbine outlet conditions, and fuel inlet conditions. Boundary conditions are also specified at the interfaces, however here they are computed using the data from the neighboring component.

For the fan inlet, the total temperature, total pressure, and the flow directions are imposed. At the outlet of the compressor, the static pressure is imposed. The combustor receives at the inlet the flow vector $[u, v, w]$. The fuel mass flow rate is defined corresponding to the cruise operating conditions. The actual outlet of the combustor domain is far downstream in order to minimize the effect of the domain boundary and the convective outflow condition. The turbine inlet receives the total pressure, the total temperature and the flow directions from the combustor; the quantities that are transferred are time-averaged on the fly as the computation proceeds. At the turbine outlet, we specify the static pressure.

The communication between the components is handled by the coupling software CHIMPS. Since the turbomachinery meshes of each sector may not necessarily coincide with the sector mesh of the neighboring domain, the interface donor cells are searched over the entire circumference of the engine. A fast search method has been developed to minimize the time spent on the sector searches. Vector components of exchanged flow

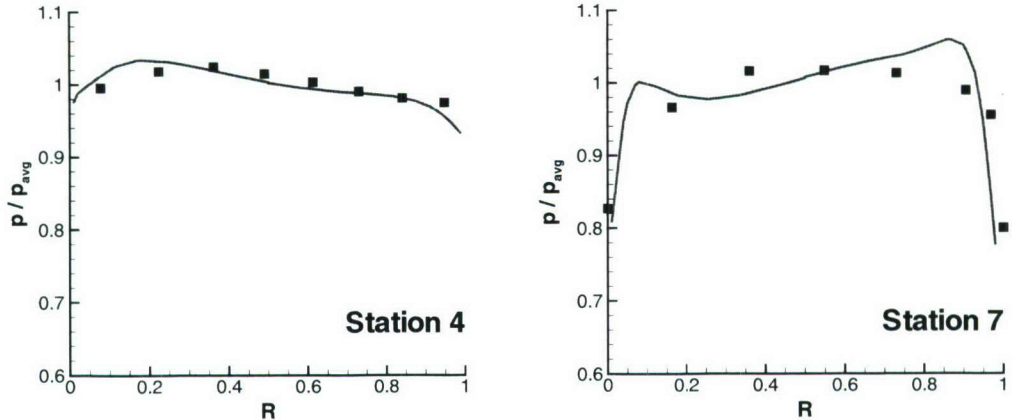


FIGURE 5. Total pressure, circumferentially averaged profiles.

variables are automatically rotated dependent on the azimuthal offset of the neighboring domains.

4.2. Computational cost

The computational domain includes the fan, the low- and the high-pressure compressor, the combustor, the high- and low-pressure turbine, and the exit nozzle, as shown in figure 3. We considered two sets of grids for the compressor: a finer grid consisting of approximately 57 million cells for the entire fan/compressor and a coarser grid consisting of approximately 8 million cells. The combustor grid contains 3 million cells and the fine grid for the turbine consists of approximately 15 million cells, whereas the coarser grid for the turbine consists of about 3 million cells. The time step has been chosen to assure that in the turbomachinery components we use at least 30 time steps for a blade passing in a blade row with the highest count and the highest rotational speed. This translates to about 11,500 time steps needed for a full wheel revolution of the slower low-pressure components and 3700 time steps for the faster rotating high-pressure components. In addition, estimates for the number of time steps needed for a flow-through time range from 10,000 time steps for the high-pressure spool core of the engine, to about 20,000 for the entire engine.

We have performed multiple simulations on a DOE ALC Xeon Linux cluster. The simulations typically run for 1500 time steps in 24 hours of wall-clock time on 700 processors, for the entire engine using the coarser grid for the fan/compressor and the turbine. The fan/compressor was run on 480 processors, the combustor on 80 processors, and the turbine on 140 processors. To obtain the same amount of time steps for the entire engine on the finer grid, approximately 4,000 processors are needed. A flow-through time for the entire engine can then be computed within 14 days of uninterrupted running.

An important component of these computations is the parallel I/O, which, depending on the desired frequency and extent of output data, can take up to 50 % of the run time (when saving output at every single time step). Here, we have chosen to save the output every 10 time steps.

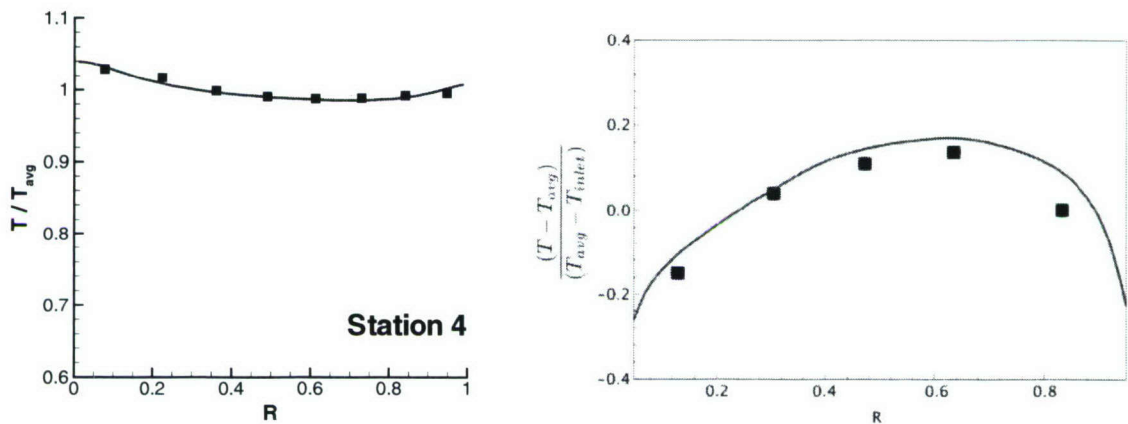


FIGURE 6. Total temperature, circumferentially averaged profiles.

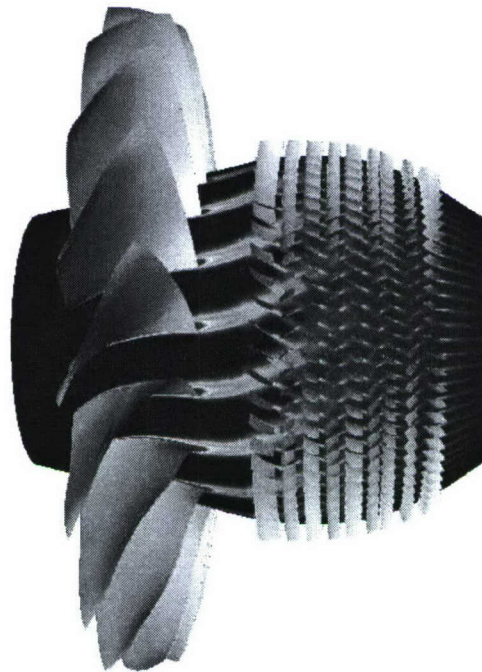


FIGURE 7. Fan/low-pressure compressor interaction: turbulent kinetic energy, mid-span.

4.3. Results

First, the fidelity of the integrated simulation at 7,500 time-steps is examined by comparing the results at several axial locations (see figure 4) to existing data provided by Pratt & Whitney. Circumferentially averaged radial profiles of total pressure and total temperature are shown in figures 5 and 6, respectively. The results agree reasonably well with the data. However, the predictions are somewhat less accurate near the hub and the casing.

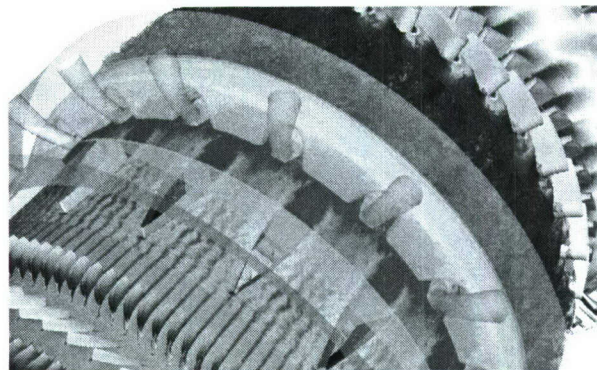


FIGURE 8. Compressor/combustor interface: axial velocity, mid-span.

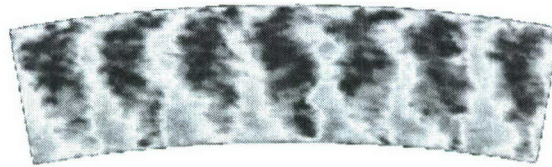


FIGURE 9. Compressor/combustor interface: axial velocity at the interface.

Next, we focus on the solution in the vicinity of the component interfaces and investigate three specific interaction phenomena. The first is the interaction of the wakes from the fan blades with the low-pressure compressor. The second concerns the influence of the wakes from the high-pressure compressor on the diffuser and the flow in the combustor, and the third one concerns the propagation of unsteady hot streaks from the combustor into the turbine.

Details of the wakes from the fan blades are illustrated by the contours of kinetic energy of turbulence presented for the mid-span radial plane and shown in figure 7. These wakes are propagating almost all the way through the low-pressure compressor, which effects the efficiency and flow capacity in the low-pressure compressor. That is the subject of a more detailed study, contrasting these quantities from the integrated and the standalone component computations which is currently under way.

The axial velocity contours at the compressor/combustor interface plotted in the mid-span radial plane are shown in figure 8. The wakes from the last row of vanes in the high pressure compressor are propagating into the diffuser, as can be seen from the contours of the instantaneous axial velocity in figure 9. We are currently examining the effect of these wakes on the stability (and possibly separation) of the flow in the diffuser, as well as its effect on the flow splits and the flow in the combustor chamber.

Figure 10 presents an isosurface of mean temperature in the combustor and turbine, indicating the high temperature streaks propagating through the combustor/turbine interface and into the turbine, i.e., the time-averages of the flow variables from the combus-

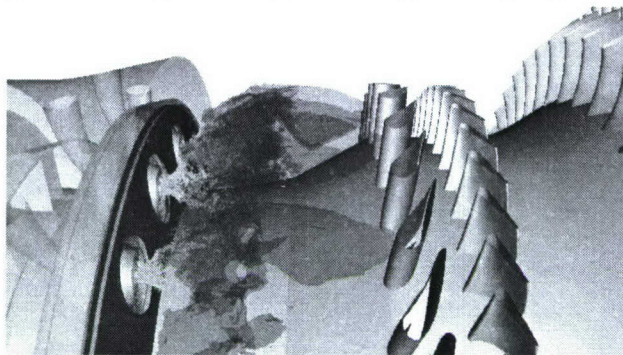


FIGURE 10. Combustor/turbine interface: isosurface of mean temperature.

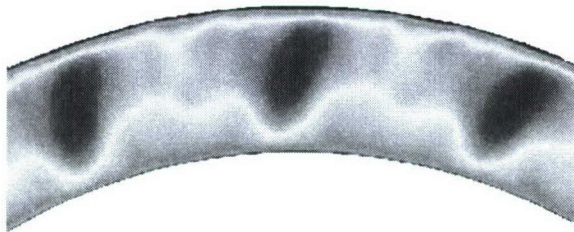


FIGURE 11. Combustor/turbine interface: mean temperature.

tor computation are passed to the turbine (total pressure, total temperature, and flow angles). At the turbine inflow there is a strong variation of temperature and axial velocity in the circumferential direction. The circumferential variation of the temperature at the combustor/turbine interface is illustrated in figures 11 and 12; we have observed a 10% variation of temperature at mid-span.

5. Conclusions

A new approach to simulate multi-component effects is proposed. In this approach, existing solvers are adapted for use in integrated simulations and a new software module has been developed to allow the coupling of multiple solvers. The advantage of using this module is that it is written in a general fashion and solvers can easily be adapted to communicate with other solvers. The software module performs many of the required coupling tasks, such as searches, interpolations, and process-to-process communication.

We demonstrated this approach in a simulation of the entire flow path of a Pratt & Whitney jet engine. The results are promising and we were able to show that the computational cost of such simulations is not prohibitive. The importance of interactions of the fan with the low-pressure compressor, the high-pressure compressor with the combustor-inlet diffuser, and the combustor with the high-pressure turbine are discussed. More details and a quantitative characterization of these interactions will be provided in future publications.

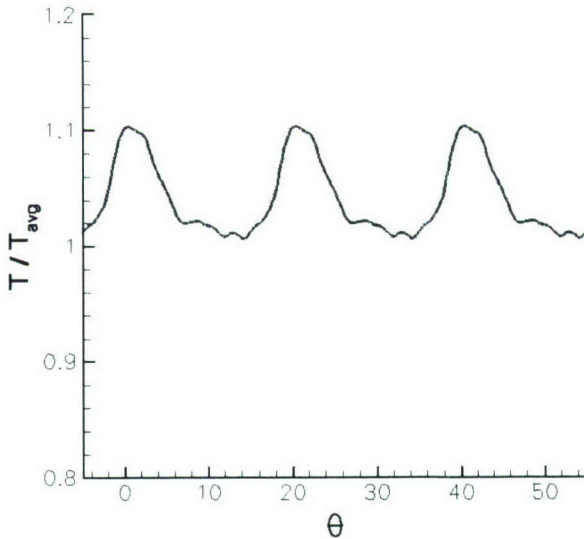


FIGURE 12. Combustor/turbine interface: circumferential variation of mean temperature at mid-span.

Acknowledgements

We thank the U.S. Department of Energy for the support under the ASC program and DARPA under the Helicopter Quieting program.

We also thank Pratt & Whitney for providing the engine geometry, computational meshes, helpful comments and discussions.

Furthermore, many more people at Stanford University have been involved in this work than could be mentioned in the list of authors. We would like to thank S. Hahn, J. Schlüter, X. Wu, K. Mattsson, M. Svard, G. Iaccarino, and P. Moin for their help.

REFERENCES

Alonso, J. J., Martinelli, L., and Jameson, A., 1995. "Multigrid Unsteady Navier-Stokes Calculations with Aeroelastic Applications." *AIAA Paper*, AIAA 95-0048.

Alonso, J.J., et al., 2006. "CHIMPS: A high-performance scalable module for multi-physics simulations." *AIAA Paper*, AIAA-2006-5274.

Belov, A., Martinelli, L., and Jameson, A., 1996. "Three-Dimensional Computations of Time-Dependent Incompressible Flows with an Implicit Multigrid-Driven Algorithm on Parallel Computers." *Proceedings of the 15th International Conference on Numerical Methods in Fluid Dynamics*, Monterey, CA.

Constantinescu, G., Mahesh, K., Apte, S., Iaccarino, G., Ham, F., and Moin, P., 2003. "A new paradigm for simulation of turbulent combustion in realistic gas turbine combustors using LES." *ASME Turbo Expo 2003*, GT2003-38356.

Ferziger, J. H., 1996. *New Tools in Turbulence Modelling*. Vol. New Tools in Turbulence Modelling of *Les édition physique*, Chapter 2 Large eddy simulation: an introduction and perspective, Springer, 29–47.

Germano, M., Piomelli, U., Moin, P., and Cabot, W., 1991. "A dynamic subgrid-scale eddy viscosity model." *Phys. Fluids*, Vol. A, No. 3 (7), 1760–1765.

Jameson, A., 1991. "Time Dependent Calculations Using Multigrid, with Applications to Unsteady Flows Past Airfoils and Wings." *AIAA paper*, AIAA Paper 91-1596.

Kim, S., Schlüter, J., Wu, X., Alonso, J. J., and Pitsch, H., 2004. "Integrated simulations for multi-component analysis of gas turbines: RANS boundary conditions." *AIAA Paper*, AIAA 2004-3415.

Mahesh, K., Constantinescu, G., Apte, S., Iaccarino, G., Ham, F., and Moin, P., 2006. "Large-eddy simulation of reacting turbulent flows in complex geometries." *Journal of Applied Mechanics*, Vol. 73, 374-381.

Medic, G., You, D. and Kalitzin, G., 2006. "An approach for coupling RANS and LES in integrated computations of jet engines." CTR Annual Research Briefs.

Poinsot, T., Schlüter, J., Lartigue, G., Selle, L., Krebs, W., and Hoffmann, S., 2001. "Using large eddy simulations to understand combustion instabilities in gas turbines." *IUTAM Symposium on Turbulent Mixing and Combustion*, Kingston, Canada, 1–8.

Raman, V. and Pitsch, H., 2005. "Large-eddy simulation of a bluff-body stabilized flame using a recursive refinement procedure." *Comb. Flame*, Vol. 142, 329–347.

Sagaut, P., 2002. *Large eddy simulation for incompressible flows*. Springer, Berlin, 2nd ed.

Schlüter, J. U., Shankaran, S., Kim, S., Pitsch, H., Alonso, J. J., and Moin, P., 2003. "Integration of RANS and LES flow solvers for simultaneous flow computations." *AIAA Paper*, AIAA 2003-0085.

Schlüter, J. U., Shankaran, S., Kim, S., Pitsch, H., Alonso, J. J., and Moin, P., 2003. "Towards multi-component analysis of gas turbines by CFD: integration of RANS and LES flow solvers." *ASME Turbo Expo 2003*, GT2003-38350.

Schlüter, J. U., Pitsch, H., and Moin, P., 2004. "Large Eddy Simulation inflow conditions for coupling with Reynolds-averaged Flow Solvers." *AIAA Journal*, Vol. 42, No. 3, 478–484.

Schlüter, J. U., Wu, X., Kim, S., Alonso, J. J., and Pitsch, H., 2005. "A Framework for Coupling Reynolds-Averaged with Large Eddy Simulations for Gas Turbine Applications." *Journal of Fluids Engineering*, Vol. 127, No. 4, 806–815.

Shankaran, S., Liou, M.-F., Liu, N.-S., and Alonso, J. J., 2001. "A multi-code-coupling interface for combustor/turbomachinery simulations." *AIAA Paper*, AIAA 2001-0974.

Yao, J., Jameson, A., Alonso, J. J., and Liu, F., 2000. "Development and validation of a massively parallel flow solver for turbomachinery flows." *AIAA Paper*, AIAA-00-0882.

An approach for coupling RANS and LES in integrated computations of jet engines

By G. Medic, D. You AND G. Kalitzin

1. Motivation and objectives

Large-scale computations of the flow in an entire jet engine can be carried out by using different simulation techniques for each component of the engine. The flow in the combustor is characterized by multi-phase flow, intense mixing and chemical reactions, and the prediction of turbulent combustion is greatly improved by using LES, as discussed in Pitsch (2006). The flow in the compressor and turbine is computed using the unsteady RANS framework since the high Reynolds numbers make the cost of resolving the boundary layers with LES prohibitive (see Chapman, 1979). For such integrated computations to be successful, a proper coupling of the flow variables is needed at the interfaces between the RANS and LES solvers.

A fully coupled solution requires that all flow variables must be exchanged at the interface. When some engine components are computed with LES and others with RANS, approximations will have to be made to couple instantaneous and averaged variables. To simplify the problem, in this paper we consider only the one-way coupling of the velocity and turbulence variables. One-way coupling means that information is passed only downstream; the variables at the inlet of the downstream domain are computed from the variables at the outlet of the upstream domain.

For the RANS/LES interface, turbulent fluctuations need to be added to the velocity from an upstream RANS computation. This was previously investigated in Schlüter *et al.* (2004). It has been suggested that the LES flow solver has to reconstruct the resolved turbulence according to the statistical data delivered by the RANS flow solver, in particular, according to the turbulent kinetic energy k when RANS is computed with a two-equation turbulence model that includes a transport equation for k . It is further proposed that one could use fluctuations computed from an auxiliary, *a priori* LES of a periodic channel and scale them with the turbulent kinetic energy from the upstream RANS computation. In that study, virtual body forces were used inside the channel to drive the flow to the desired mean flow velocity, as in Pierce & Moin (1998).

Although an accurate turbulence description needs to take into account the convection from upstream, in this paper it is suggested that turbulence production at the compressor/combustor and combustor/turbine interfaces is dominated by strong mean velocity gradients in the wakes and boundary layers. At the compressor/combustor interface, the wakes of the upstream compressor blades create significant mean shear and the local production of turbulence dominates. Thus, only the mean velocity is passed to the LES inlet from RANS and turbulence fluctuations equilibrated with the mean velocity profile are computed using a recycling technique from an LES of an auxiliary annular duct. This is explained in detail in Section 2.

For the LES/RANS interface, such as the combustor/turbine interface, a simple time average of the velocity provides a mean velocity at the inlet of the RANS domain. This velocity distribution is again highly non-uniform, which allows to describe turbulence at

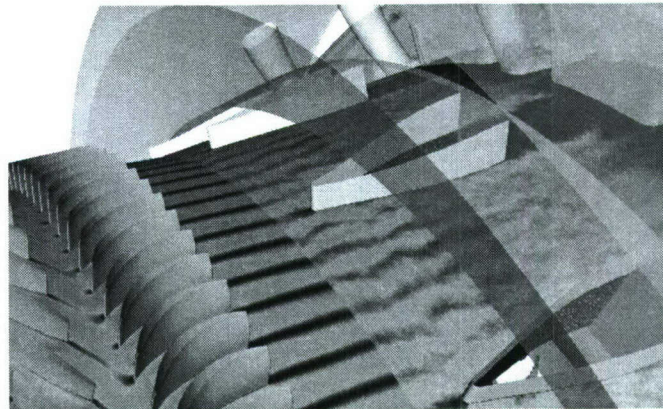


FIGURE 1. Compressor and combustor: RANS and LES axial velocity, mid-passage.

the inlet with the local turbulence generation from the mean velocity. Analogous to the treatment for the RANS/LES interface, we propose here to use an auxiliary duct in which the RANS turbulence model equations are solved for the transferred mean velocity. The advantages of the proposed approach are discussed in Section 3.

2. RANS/LES interface

The region of the compressor exit and combustor inlet is shown in figure 1. The flow in the compressor is computed with unsteady RANS using the $k-\omega$ model of Wilcox (1998) and the flow in the combustor is computed with LES. The last blade row of the compressor is a row of stators and does not rotate. The blade row upstream is a row of rotors that rotate counter-clockwise (by an observer looking downstream).

The axial velocity and turbulent kinetic energy in a cross-section at the compressor exit are shown in figures 2 and 3, respectively. The mean flow is highly complex, with the wakes originating from the last stage of the compressor. These wakes are unsteady due to the rotation of the rotors in the compressor. Larger values of turbulent kinetic energy are in the regions with strong velocity gradients. The large values of k near the hub might be spurious; they are highly dependent on the quality of the grid. This illustrates the fact k from the $k-\omega$ model usually fails to accurately represent the true turbulent kinetic energy in complex flows.

The flowfield in the downstream LES domain is highly dependent on the conditions at the inlet. To generate an inflow profile for the LES in the combustor, the mean velocity at the combustor inlet is set equal to the RANS velocity at the compressor exit and appropriate fluctuations need to be added. Instead of using the turbulent kinetic energy k from RANS to scale the fluctuations from a periodic channel, as in Schluter *et al.* (2004), we propose to generate turbulent fluctuations equilibrated with the mean velocity profile, that is relatively accurately predicted with RANS, by using a recycling technique inspired by Lund *et al.* (1998).

Here we compute the fluctuations on the fly in an auxiliary annular duct. The cross-section of the duct corresponds to the combustor inlet, and the length of the duct is chosen to correspond to the distance between the last compressor blade row and the combustor inlet. Convective boundary conditions are imposed at the exit of the duct and a no-slip condition is applied at the top and bottom cylindrical walls. When the integrated

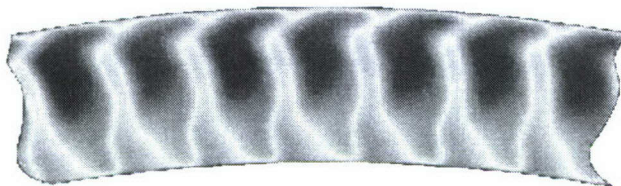


FIGURE 2. Compressor/combustor interface: axial velocity from RANS.

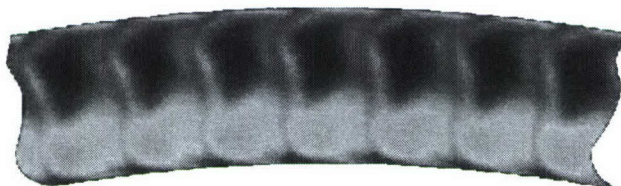


FIGURE 3. Compressor/combustor interface: turbulent kinetic energy from RANS.

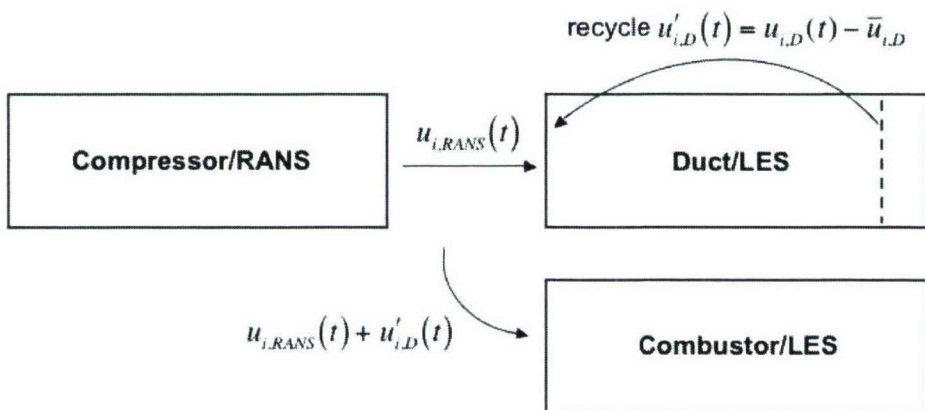


FIGURE 4. Compressor/combustor interface: RANS \rightarrow LES.

computations are performed for a 20° sector of the engine, periodicity is assumed in the circumferential direction for the duct as well. At the duct inlet the mean velocity from the compressor/combustor interface is imposed. By using the viscosity of the flow in the combustor, the Reynolds number of the duct LES corresponds to the Reynolds number at the combustor inlet.

As previously mentioned, the fluctuations are computed with a recycling technique. A cross-section upstream of the duct exit is chosen, as shown schematically in figure 4. The mean velocity at this cross-section is computed by time-averaging the velocity: $\bar{u}_{i,D} = 1/T \int u_{i,D}(t) dt$. The fluctuations $u'_{i,D} = u_{i,D} - \bar{u}_{i,D}$ are then added to the mean flow at the inlet of the duct. The LES in the duct is computed until converged rms values at the inlet are obtained.

The recycling technique can be refined to account for pressure gradients, curvature, and flow structures in the duct. Contour plots of the axial velocity in a mid-plane between the bottom and top walls are presented in figure 5. As shown, the mean velocity diffuses when propagating downstream. In the recycling procedure, this evolution of the wakes in the streamwise direction can be accounted for with a scaling of the circumferential spreading of the wakes. A similarity analysis in the far wake implies that the thickness of the wake spreads proportionally to the square root of streamwise coordinate ($\delta \sim x^{1/2}$). With such a scaling, the recycled fluctuations correspond better to the mean velocity at the inflow of the LES domain. Otherwise, the thickness of the wake increases as the recycling progresses.

Contour plots for the instantaneous axial velocity and the mean axial velocity are shown for the duct inlet in figures 6 and 7, respectively. The corresponding u_{RMS} velocity and turbulent kinetic energy from the LES are shown in figures 8 and 9. Both turbulent quantities have larger values in the shear regions. The large values of turbulent kinetic energy, observed with the RANS turbulent kinetic energy near the hub (figure 3), are not present as convection from upstream is neglected.

The LES in the auxiliary duct is computed on the fly, in parallel with the computations in the compressor and the combustor. This allows to take into account the unsteadiness of the mean flow. Finally, after the fluctuations are generated in the auxiliary duct, they are superimposed with the mean velocity at the compressor/combustor interface as presented in figure 4.

2.1. Validation: recycling for plane channel flow

The recycling technique used here has been validated for plane channel flow at $Re_\tau = 180$. The Reynolds number is based on channel half-height, δ , and friction velocity, u_τ . A mesh of $64 \times 64 \times 64$ grid points in the streamwise, wall-normal, and spanwise directions, respectively, is employed in the computational domain size of $4\pi\delta \times 2\delta \times \frac{4}{3}\pi\delta$. Periodic boundary conditions are imposed in the spanwise direction and a no-slip condition is applied at the top and bottom walls. The dynamic subgrid-scale (SGS) model of Germano *et al.* (1991) is employed.

First, periodic channel flow is computed by also imposing periodic boundary conditions in the streamwise direction. The mean velocity profile is in good agreement with the DNS of Kim *et al.* (1987), as shown in figure 10.

In the recycled channel case, convective outlet boundary conditions are employed at the outlet of the channel. The velocity at the inflow is computed every time step by superposing the mean velocity profile (from the periodic channel case) with the fluctuations computed at the channel exit. The simulation is initiated with the mean velocity profile superimposed with random fluctuations and the simulation is continued until con-

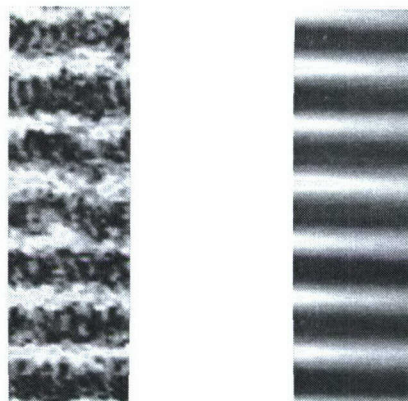


FIGURE 5. Auxilliary duct: the instantaneous (left) and mean (right) axial velocity, mid-plane, top view.

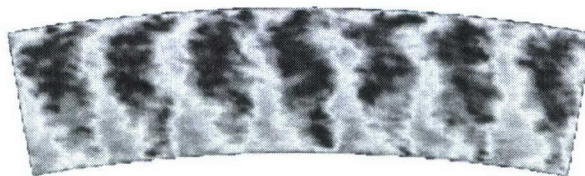


FIGURE 6. Compressor/combustor interface: instantaneous axial velocity.

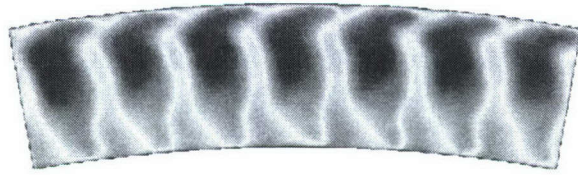


FIGURE 7. Compressor/combustor interface: mean axial velocity.

verged rms velocities are obtained. As shown in figure 11, the rms velocity fluctuations obtained from the recycled simulation compare well with those from the periodic channel simulation and the DNS of Kim *et al.* (1987).

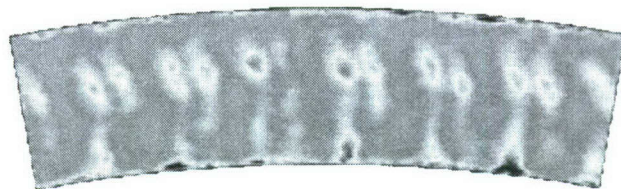
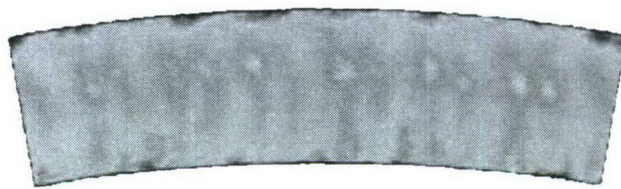
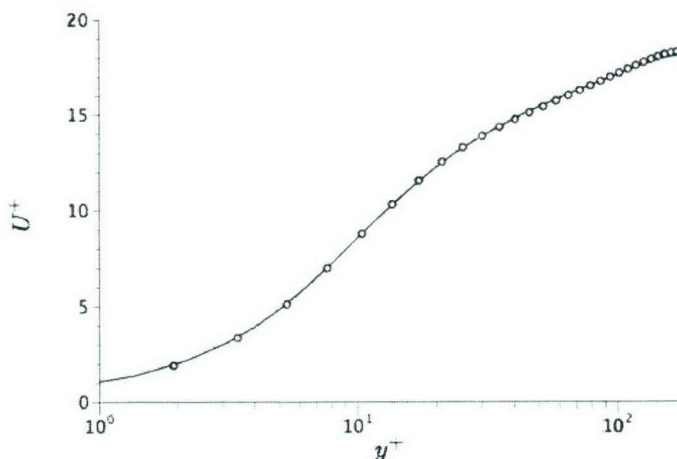
FIGURE 8. Compressor/combustor interface: u_{RMS} .

FIGURE 9. Compressor/combustor interface: turbulent kinetic energy.

FIGURE 10. Mean streamwise velocity profiles in wall units at $Re_\tau = 180$. —, periodic LES; \circ , DNS of Kim *et al.* (1987).

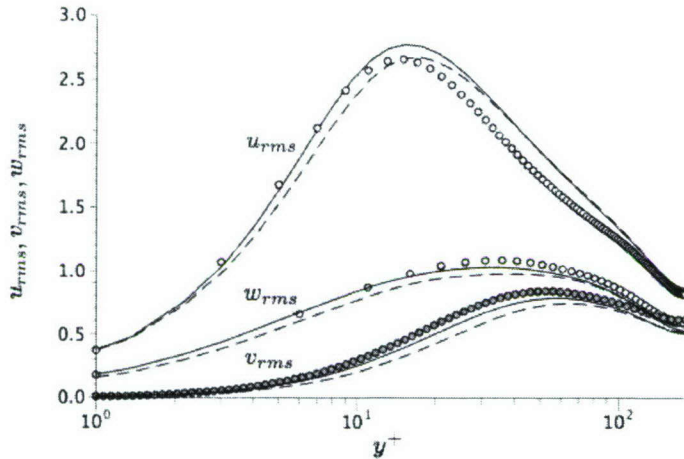


FIGURE 11. Profiles of rms velocity fluctuations in wall units at $Re_\tau = 180$. ---, recycling LES; —, periodic LES; \circ , DNS of Kim *et al.* (1987).

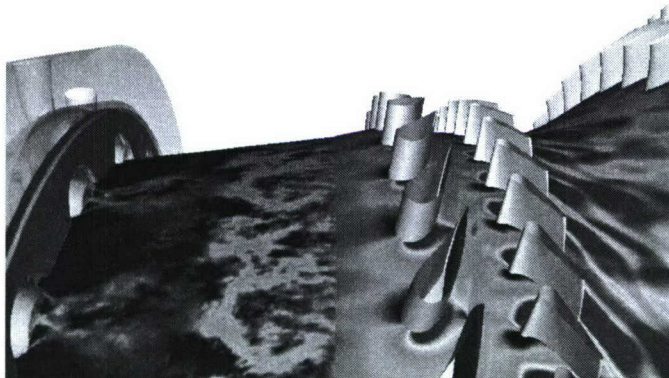


FIGURE 12. Combustor and turbine: LES and RANS axial velocity, mid-passage.

3. LES/RANS interface

At the combustor/turbine interface (from LES to RANS, see figure 12), inflow conditions are needed for the RANS turbulence variables. Here we use the $k-\omega$ turbulence model in the turbine; k and ω need to be specified at the turbine inflow. An obvious suggestion would be to compute k and ω directly from the instantaneous velocity field at the combustor exit. The disadvantage of this strategy is explained in the following subsection.

3.1. Periodic channel flow

In order to examine in detail how well the RANS turbulence variables can be reconstructed from LES, we return to the periodic channel flow at $Re_\tau = 180$ discussed previously. The LES has a sufficient near-wall resolution and it was run for approximately 100 flow-through times. This permits a long time integration of the equation resulting in a statistically well-converged solution.

The Reynolds number is somewhat low for a RANS computation, but the inconsistency between the LES statistics and the RANS turbulence variables are representative. Figure

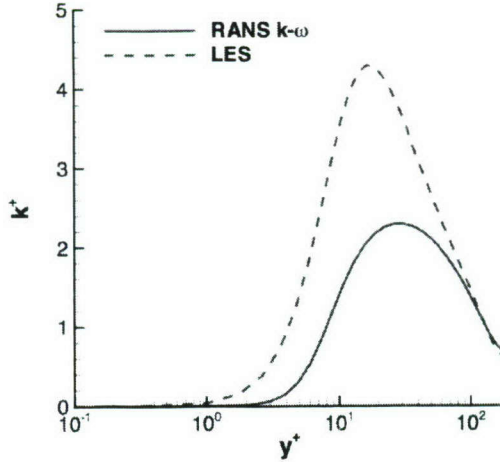


FIGURE 13. Channel flow at $Re_\tau = 180$, LES vs. RANS k - ω model, turbulent kinetic energy k .

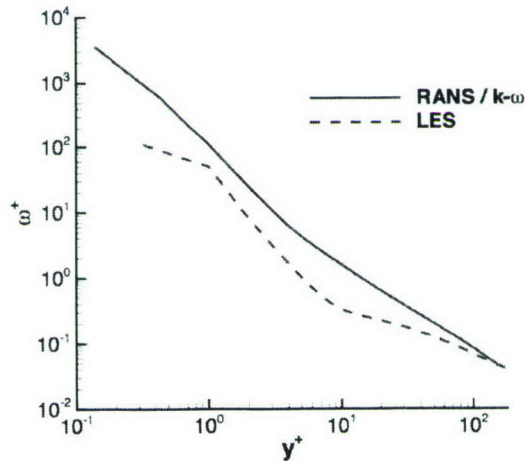


FIGURE 14. Channel flow at $Re_\tau = 180$, LES vs. RANS k - ω model, specific dissipation rate ω computed using $\varepsilon = \nu \frac{\partial u'_i}{\partial x_k} \frac{\partial u'_i}{\partial x_k}$.

13 compares k from the k - ω model with $k = 1/2\bar{u}'_i\bar{u}'_i$ from LES. The near-wall peak is practically absent for the k - ω turbulent kinetic energy.

The specific dissipation rate $\omega = \varepsilon/(C_\mu k)$ is compared to ω from the LES, computed using two different approaches. A first approach consists of computing the turbulence dissipation using its definition (for DNS): $\varepsilon = \nu \frac{\partial u'_i}{\partial x_k} \frac{\partial u'_i}{\partial x_k}$. The resulting ω is compared to that of the k - ω model in figure 14. The trend of increasing ω when approaching the wall is relatively well captured, but there are significant discrepancies in the buffer and the logarithmic layer. Therefore, we also examined a second approach where ε is computed using the assumption that the dissipation rate equals production: $\varepsilon = -\bar{u}'_i\bar{u}'_k \partial \bar{u}_i / \partial x_k$. The resulting ω is compared to that of the k - ω model in figure 15. As expected, the

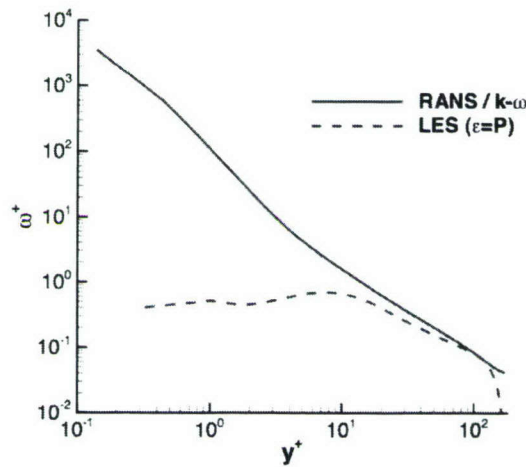


FIGURE 15. Channel flow at $Re_\tau = 180$, LES vs. RANS k - ω model, specific dissipation rate ω computed using $\varepsilon = P$.

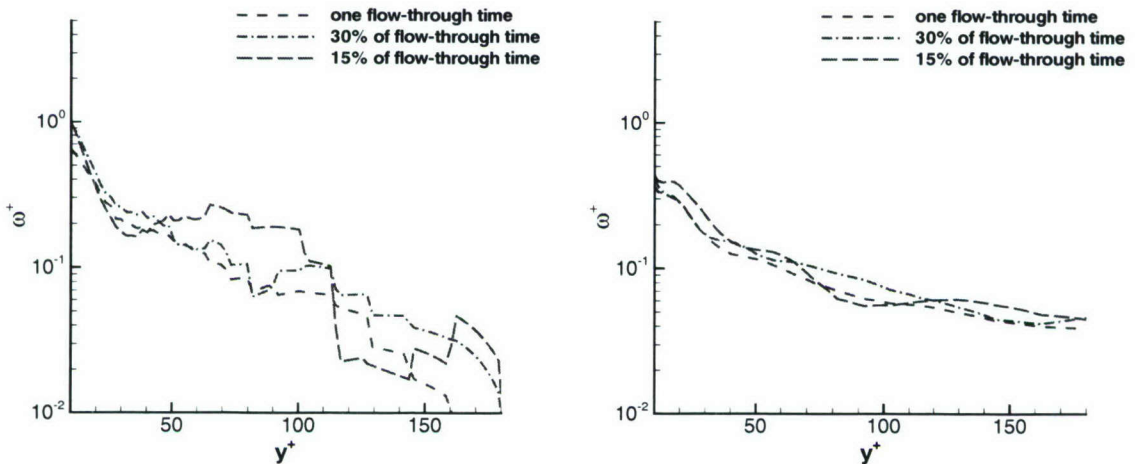


FIGURE 16. Channel flow at $Re_\tau = 180$, LES, specific dissipation rate ω in the logarithmic layer, computed using $\varepsilon = \nu \frac{\partial u'_1}{\partial x_k} \frac{\partial u'_1}{\partial x_k}$ (left) and $\varepsilon = P$ (right) with the statistics for ε and k over very short time windows.

agreement is best in the logarithmic layer where the used assumption holds. However, below $y^+ = 20$ this approach for computing ε yields a bad prediction for ω : the near-wall increase is completely absent. Such near-wall behavior may lead to numerical instabilities in the near-wall region.

The convergence of the statistics for ε is presented for the logarithmic layer in figure 16, where ω for both approaches are plotted for computations with averaging over different time windows (from one flow-through time to only 15 % of one flow-through time). It becomes apparent that for short time windows, the values of ω are strongly oscillating, thus further reducing the numerical stability when used with the k - ω model.

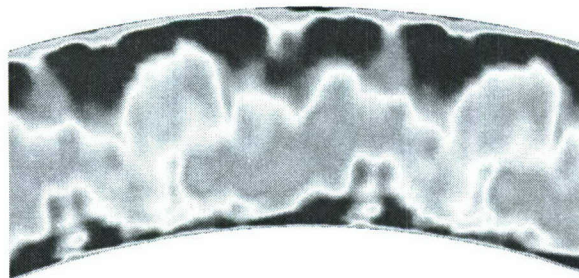


FIGURE 17. Combustor/turbine interface: mean axial velocity.

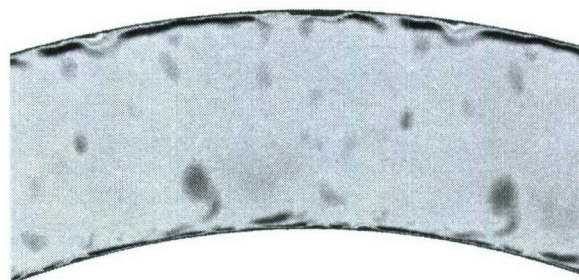


FIGURE 18. Combustor/turbine interface: ν_t from the auxilliary duct.

This is especially important as the mean flow in jet engines has unsteady features with relatively small time scales (up to one flow-through time). Thus, the use of weakly averaged statistics of ε is questionable; our experience with the engine computations showed that these approaches for computing ω lead to severe numerical instabilities. Note that in the jet engine computations the grid resolution in certain regions for both LES and RANS is not comparable to the one used for this simple flow.

Furthermore, to complicate matters, if one is to employ a more complex RANS turbulence model, such as the four-equation v^2-f model of Durbin (1995), it becomes practically impossible to reconstruct turbulence variables from the LES, i.e., the variables f or v^2 have no clear physical counterpart in complex flows. It is therefore clear that reconstructing the RANS turbulence variables directly from the LES is unfeasible in a general case.

3.2. Combustor/turbine interface

The aforementioned arguments lead to a conclusion that k and ω at the turbine inlet should instead be computed from the mean flow velocity field, shown for the combustor/turbine interface in figure 17. The mean velocity is a first-order moment that converges significantly faster than the rms velocities (second-order moments) and a smaller averaging window can be employed. As was the case with the compressor/combustor interface, convection of turbulence will be ignored.

Analogous to the proposed auxiliary annular duct used to compute the inflow fluctuations for the LES domain, we propose here to use an auxiliary duct in which the RANS turbulence model equations are solved for the mean velocity field transferred at

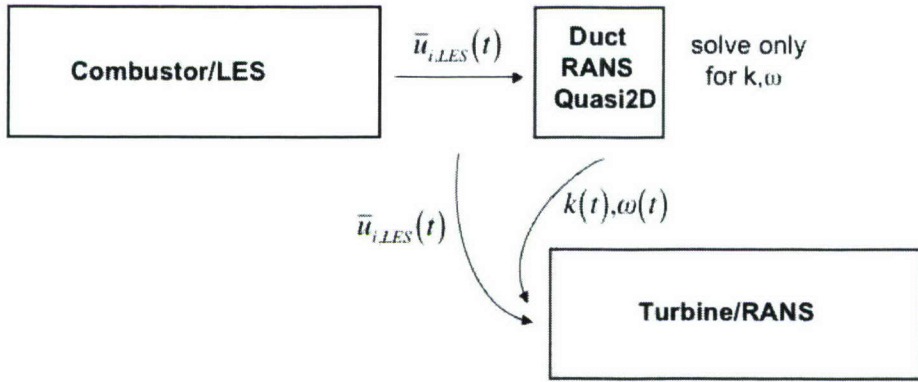


FIGURE 19. Combustor/turbine interface: LES → RANS.

the turbine inflow (see figure 19). The duct is quasi two-dimensional with a cross-section identical to the combustor/turbine interface and a single cell in the streamwise direction. The mean velocity from the combustor outlet is passed to the duct and the equations for k and ω are iterated until convergence for a frozen mean flow is achieved. Finally, the mean velocity from the combustor and k and ω from the duct are passed to the turbine inlet.

The underlying assumption of this approach is that, again, local effects dominate turbulence production over convection effects, especially near walls. This produces an inflow boundary condition for the RANS domain that is consistent with the RANS turbulence model used. Most importantly, the turbulent eddy-viscosity remains consistent with the transferred mean velocity, as shown in figures 17 and 18.

4. Conclusions

An approach to couple the LES and RANS computational frameworks is proposed. The approach consists in the generation of turbulence inflow conditions in auxiliary ducts in parallel with the main computation. We have demonstrated this approach in a simulation of a 20° sector of an entire jet engine, with LES used for the combustor and RANS for the turbomachinery parts.

In the case of compressor/combustor interface, an auxiliary LES computation is carried out in a three-dimensional duct with the turbulent fluctuations generated using a recycling technique. Because k from RANS is not accurate enough for these complex flows, instead of using the turbulent kinetic energy k from RANS to scale the fluctuations from a periodic channel, we proposed to generate turbulent fluctuations equilibrated with the mean velocity profile that is relatively accurately predicted with RANS.

For the combustor/turbine interface, an auxiliary RANS computation is carried out in a quasi-2D duct. The turbulence variables for the RANS model, specifically the k - ω model, are computed from the duct simulation with a frozen mean flow. This technique obviates numerical instabilities observed when k and ω were computed directly from the instantaneous velocity field at the combustor exit using weakly averaged statistics from LES.

Acknowledgements

We thank the U.S. Department of Energy for the support under the ASC program. We also thank Pratt & Whitney for providing the engine geometry, helpful comments and discussions.

REFERENCES

Chapman, D.R., 1979. "Computational aerodynamics development and outlook." *AIAA Journal*, Vol. 17, 1293–1313.

Durbin, P. A., 1995. "Separated flow computations with the $k-\varepsilon-v^2$ model." *AIAA Journal*, Vol. 33, 659–664.

Germano, M., Piomelli, U., Moin, P., and Cabot, W., 1991. "A dynamic subgrid-scale eddy viscosity model." *Phys. Fluids*, Vol. A, No. 3 (7), 1760–1765.

Kim, J., Moin, P., and Moser, R., 1987. "Turbulence statistics in fully developed channel flow at low Reynolds number." *Journal of Fluid Mechanics*, Vol. 177, 133–166.

Lund, T. S., Wu, X., and Squires, T. S., 1998. "Generation of turbulent inflow data for spatially-developing boundary layer simulations." *Journal of Computational Physics*, Vol. 140, 233–258.

Pierce, C.D., and Moin, P., 1998. "Method for generating equilibrium swirling inflow conditions." *AIAA Journal*, Vol. 36, No. 7, 1325–1327.

Pitsch, H., 2006. "Large eddy simulation of turbulent combustion." *Annual Review of Fluid Mechanics*, Vol. 38, 453–482.

Schlüter, J. U., Pitsch, H., and Moin, P., 2004. "Large Eddy Simulation inflow conditions for coupling with Reynolds-averaged Flow Solvers." *AIAA Journal*, Vol. 42, No. 3, 478–484.

Wilcox, D. C., 1998. *Turbulence Modeling for CFD*. 2nd edition, DCW Industries, Inc., La Canada, CA.

Low frequency sound sources in high-speed turbulent jets

By D. J. Bodony† AND S. K. Lele

1. Motivation and objectives

A gap exists in the understanding of the sources of jet noise and their dependence on external conditions, such as those determined by the nozzle and the environment farther upstream. The influence of nozzle chevrons on the radiated sound is, for example, still characterized parametrically based on a series of experimental studies (Saiyed *et al.* 2003). Further development of an understanding of the “sound sources” in a high-Reynolds-number jet, however, is slowed for two primary reasons: (i) the lack of a universally agreed-upon acoustic theory, and (ii) the difficulty in making experimental measurements suggested by the acoustic theories. The current theories, most notably those of Lighthill (1952), Lilley (1974), Tam & Auriault (1999), and Goldstein (2003) are similar in their arbitrary, but exact, rearrangement of the Navier-Stokes equations (with new variables in the case of Goldstein and a proposed source term by Tam & Auriault), and in the functional form of the identified source term. The acoustic source is of the general form

$$\{\text{linear combination of } \partial_t \text{ and } \partial_{x_i}\} S_j(\mathbf{x}, t),$$

where the source S_j itself may involve additional differentiation. Measurements of S_j are quite difficult and, currently, only point-measurements of related quantities have been obtained (Panda & Seasholtz 2002; Panda *et al.* 2004). It presently appears that the major practical difference between the dominant theories is in their sensitivity to numerical errors (Freund *et al.* 2005).

Large-eddy and direct numerical computational studies of jet noise offer an alternative to experimental measurements but suffer from the resource requirements imposed by the near-nozzle turbulent annular shear layers for jets at realistic Reynolds numbers. An accurate calculation does not yet exist that includes the nozzle geometry (see, e.g., Andersson *et al.* (2003) and Uzun & Hussaini (2006)) so most studies have concentrated on the portion of the jet immediately downstream of the nozzle exit plane (Freund 2001; Bogey *et al.* 2003; Bodony & Lele 2004, 2005). (A review of the use of large-eddy simulations (LES) for jet noise prediction is given in Bodony & Lele (2006).) The direct numerical simulation (DNS) of Freund (2001) continues to be the only calculation of its type; post-processing of the DNS data has been useful in evaluating key assumptions (e.g., Khavaran *et al.* (2002)). However, the high cost, low Reynolds number, and single jet operating point of the DNS calculation are limiting.

To complement the DNS calculation of Freund and to develop and expand the capabilities of LES for jet noise prediction, a series of numerical simulations were conducted by the authors for jets at six operating conditions with Mach numbers ranging from 0.4 to 2.0 of both heated and unheated jets. Details of the calculations are available in Bodony

† Present address: Department of Aerospace Engineering, University of Illinois at Urbana-Champaign

& Lele (2005). Due to resolution limitations the far-field sound of the simulations is limited to those frequencies with $St = fD_j/U_j \leq 1.2$; near-field frequencies are limited to $St \leq 1.5$.

This paper is concerned with those jets originally presented in Bodony & Lele (2005) having $M_j \geq 0.9$, which includes two unheated jets and one heated jet. Additional analysis is performed on the databases generated by the space-time histories of the jets to investigate characteristics of the sound generation. To do so we adopt Lighthill's acoustic analogy (Lighthill 1952) and explore its ability to predict the sound of the jets as compared to the sound directly captured in the compressible LES calculations. Effects of jet Mach number and temperature on the radiated sound, in the context of Lighthill's theory, are discussed.

1.1. Objectives

Using the LES databases described in Bodony & Lele (2005) the objectives of this work are to critically examine the ability of Lighthill's acoustic analogy to predict the acoustic spectra of hot and cold high-speed jets. To accomplish this we first present a comparison of the Lighthill-predicted sound spectra to the directly computed sound spectra from the compressible LES calculations. We then examine in more detail the components of the Lighthill spectra.

2. Sound predictions using Lighthill's theory

2.1. Previous work

Lighthill's theory has been used previously in numerical noise prediction. For a plane (2-D) jet Bastin *et al.* (1997) found that the monopole source form $S = \partial_{x_i} \partial_{x_j} T_{ij}$, where

$$T_{ij} = \rho u_i u_j + [(p - p_\infty) - a_\infty^2 (\rho - \rho_\infty)] \delta_{ij} - \tau_{ij} \quad (2.1)$$

is the Lighthill stress tensor, yielded inferior sound predictions relative to the alternative far-field expression involving \tilde{T}_{ij} or its counterpart in the frequency domain, which are in appropriate quadrupole forms. In his round jet Freund (2001) found using the identity

$$S = \frac{\partial^2}{\partial t^2} (\rho - \rho_\infty) - a_\infty^2 \frac{\partial^2}{\partial x_j \partial x_j} (\rho - \rho_\infty), \quad (2.2)$$

that noise predictions using Lighthill's theory compared well with the instantaneous pressure time history. Later Freund (2002) showed that the Lighthill-predicted noise spectrum at $\Theta = 30^\circ$ compared well with the DNS data and with the data of Stromberg *et al.* (1980). Freund also discussed the relative roles of the “shear noise,” “self noise,” and “entropy” terms embedded in T_{ij} .

2.2. Frequency domain considerations

In this section we use the space-time databases generated from the simulations to demonstrate the feasibility of using LES in combination with Lighthill's theory to predict jet noise and to extend the predictions to heated jets.

The calculation of the far-field sound using Lighthill's theory begins by considering the integral form of the time-Fourier-transformed version of Eq. 2.2,

$$\widehat{\rho - \rho_\infty}(\mathbf{x}; \omega) := \widehat{\rho}(\mathbf{x}; \omega) = \frac{1}{4\pi a_\infty^2} \int_{\mathcal{R}^3} \frac{e^{i\omega R/a_\infty}}{R} \hat{S}(\mathbf{y}; \omega) d\mathbf{y}, \quad (2.3)$$

where $R = |\mathbf{x} - \mathbf{y}|$ and \hat{S} is the transformed monopole source. The advantage of using the frequency-domain form of Eq. 2.3 and not its time-domain analog is in avoiding the interpolation needed for the evaluation of S at the retarded time $t - R/a_\infty$. An alternative form that follows from integrating Eq. 2.3 by parts twice (and assuming the boundary terms vanish for a surface taken to infinity) is

$$\hat{\rho}'(\mathbf{x}; \omega) = \frac{1}{4\pi a_\infty^2} \int_{\mathcal{R}^3} \frac{\partial^2}{\partial y_i \partial y_j} \left\{ \frac{e^{i\omega R/a_\infty}}{R} \right\} \hat{T}_{ij}(\mathbf{y}; \omega) d\mathbf{y} \quad (2.4)$$

where the quadrupole Fourier amplitude \hat{T}_{ij} now appears explicitly.

In view of Eq. 2.1 the resultant density Fourier amplitudes can be considered as the sum of the components

$$\hat{\rho}'_{\text{tot}} = \hat{\rho}'_{\text{mom}} + \hat{\rho}'_{\text{ent}} + \hat{\rho}'_{\text{vis}},$$

where

$$\hat{\rho}'_{\text{mom}}(\mathbf{x}; \omega) = \frac{1}{4\pi a_\infty^2} \int_{\mathcal{R}^3} \frac{\partial^2}{\partial y_i \partial y_j} \left\{ \frac{e^{i\omega R/a_\infty}}{R} \right\} \hat{\rho} u_i u_j(\mathbf{y}; \omega) d\mathbf{y}, \quad (2.5)$$

$$\hat{\rho}'_{\text{ent}}(\mathbf{x}; \omega) = \frac{1}{4\pi a_\infty^2} \int_{\mathcal{R}^3} \frac{\partial^2}{\partial y_i \partial y_j} \left\{ \frac{e^{i\omega R/a_\infty}}{R} \right\} \left(\hat{p}' - a_\infty^2 \hat{\rho}' \right) (\mathbf{y}; \omega) d\mathbf{y}, \quad (2.6)$$

and

$$\hat{\rho}'_{\text{vis}}(\mathbf{x}; \omega) = \frac{-1}{4\pi a_\infty^2} \int_{\mathcal{R}^3} \frac{\partial^2}{\partial y_i \partial y_j} \left\{ \frac{e^{i\omega R/a_\infty}}{R} \right\} \hat{\tau}_{ij}(\mathbf{y}; \omega) d\mathbf{y}. \quad (2.7)$$

Freund (2003) found that the viscous stress contribution to \hat{T}_{ij} was negligible; hence, we take $\hat{\rho}'_{\text{vis}} \equiv 0$. We also do not consider the the contribution of the subgrid scale (SGS) stresses to the Lighthill-determined acoustic spectra and focus solely on the sound due to the resolved field.

3. Observations

Application of the integral form of Lighthill's analogy (Eq. 2.4), for the Mach 0.9 unheated jet is shown for the two observer angles of 30° and 90° at a distance of $30D_j$ in fig. 1. The Kirchhoff surface predictions for the same jet at the corresponding angles are also shown for comparison. There is reasonable agreement at both angles within the statistical uncertainty due to the limited LES data record length. The peak SPL (sound pressure level) and the corresponding peak frequency are captured in the Lighthill integrations. (Freund (2003), for the 30° prediction, saw similar agreement with his DNS database.) Similar spectral shapes are seen in both prediction methods at each angle.

In fig. 2 the Lighthill and Kirchhoff surface predictions are repeated for the Mach 2 unheated jet. As with the near-sonic cold jet the two sound predictions are similar for a wide range of Strouhal numbers. The peak SPL and Strouhal number are captured as is the spectral shape for all frequencies. At 30° the Lighthill-predicted spectrum is 2 dB below the Kirchhoff spectrum for $0.4 \leq St \leq 1.0$. As $St \rightarrow 1.5$, the predictions begin to differ due to grid resolution limitations with the Lighthill prediction being the higher. Our Kirchhoff surface data are not reliable beyond $St = 1.2$ for this jet.

The Mach 1 heated jet results are shown in fig. 3 where, again, the two methods yield similar predictions over a range of frequencies. For both angles the Lighthill prediction

shows an over prediction for $St < 0.2$, although the Kirchhoff surface data shows increased oscillations in SPL at these frequencies, indicative of the limited statistical sample. The peak frequency appears to be closer to $St = 0.2$ at this operating condition for each angle.

For each jet the contributions to the total spectrum by the momentum term (Eq. 2.5) and the so-called entropy term (Eq. 2.6) are presented next. The decomposition due to Lilley (1974) of

$$p - p_\infty - a_\infty^2(\rho - \rho_\infty) := p' - a_\infty^2\rho' = \underbrace{-\frac{\gamma - 1}{2}\rho u_k u_k}_{\text{term I}} + \underbrace{a_\infty^2 \int \frac{\partial}{\partial x_k} \left[\rho u_k \left(\frac{h_\infty - h_s}{h_\infty} \right) \right] dt}_{\text{term II}}, \quad (3.1)$$

with h_∞ and h_s being the freestream and static enthalpies, is used to further examine the spectra. Such a decomposition was also used by Freund (2003) for his Mach 0.9 jet. Note that term II involves an integral over time but may be related to the local total energy via the energy equation.

Figure 4 shows the decomposition for the unheated Mach 0.9 jet. At 30° and at 90° the momentum contribution dominates the overall spectrum; for the shallower angle it over-contributes by approximately 2 dB (as also found by Freund (2003)). The $p' - a_\infty^2\rho'$ contribution is a relatively small portion in an overall SPL sense, approximately 10 dB below the momentum term's level. However, for frequencies $St < 1$ at $\Theta = 30^\circ$, there is some cancellation between $\rho u_i u_j$ and $p' - a_\infty^2\rho'$. It is interesting to note that at low frequencies, at 30° , the entropic (term II) contribution to $p' - a_\infty^2\rho'$ is minimal but increases with increasing frequency. At 90° the momentum term dominates at all frequencies and shows very little, if any, correlation with $p' - a_\infty^2\rho'$ for the available range of frequencies. At 30° there is significant interplay between the entropy components term I and term II, especially at higher frequencies.

For the Mach 2 cold jet (fig. 5) at 30° the Lighthill-predicted spectra are of a different nature than for the Mach 0.9 cold jet; at 90° the high-speed jet spectra is qualitatively the same as for the lower speed jet. Figure 5(a) shows that (i) there is much greater $(\rho u_i u_j) - (p' - a_\infty^2\rho')$ cancellation at all frequencies, and (ii) the peak frequency of the individual spectra near $St = 1$ does not correspond to the peak frequency of the total spectrum's peak of $St = 0.3$. (There does, however, appear to be a weak local maximum near $St = 0.3$ for the individual spectra.) Below $St = 0.4$ the momentum stress term is approximately 3 dB greater than the total SPL, indicating cancellation. For this range of frequencies ($St < 0.4$) we find that term I \gg term II for the entropy contribution; at higher frequencies they are of comparable magnitude. At $St = 0.4$ and above, the $\rho u_i u_j$ and $(p' - a_\infty^2\rho')\delta_{ij}$ contributions become increasingly anticorrelated to yield a total SPL that is much less than the individual SPLs. Conversely, for $St \geq 0.4$, the term I and term II portions of $p' - a_\infty^2\rho'$ show constructive interference.

Turning to the 90° spectrum in fig. 5(b) we find that it is the momentum stress that is the dominant source of the radiated noise. The so-called entropy term contributes very little at all frequencies. The spectral peak occurs near $St = 0.3$ for all individual spectra and for the total spectrum.

When the Mach 1 heated jet, with $T_j/T_\infty = 2.3$, is considered as in fig. 6, we find a picture that differs in some important aspects from the unheated jet at the same velocity. At 30° the heated jet's component spectra show a St peak well beyond the peak frequency of the total spectrum, although there is a minor local maximum near $St = 0.2$

in the individual spectra. Over all frequencies the $\rho u_i u_j$ and $p' - a_\infty^2 \rho'$ contributions are closely correlated, especially at higher frequencies; it is now the term II component that is most important. Indeed, $-[(\gamma - 1)/2]\rho u_k u_k$ seems to play a very small role. At 90° the momentum and term II components combine constructively for the total SPL for $St < 0.4$ but add destructively for higher frequencies. At both angles the decay of the total SPL with increasing St shows a different functional form than do the individual spectra.

4. Discussion

The aforementioned observations highlight additional aspects of the Lighthill-predicted sound spectra that are worth discussing in greater detail. The first is the difference in the 30° individual component spectra and the total spectrum for the high-speed jets as shown in figures 5(a) and 6(a). The second is the amount of cancellation that occurs for the high-speed jets between the momentum and entropic contributions.

4.1. High-speed jet spectra at $\Theta = 30^\circ$ and 90°

The Mach 2.0 unheated and Mach 1.0 heated jets exhibit qualitatively different spectra at 30° for the *individual* components of \hat{T}_{ij} compared to its sum, in contrast to the Mach 0.9 cold jet as found here (fig. 4) and earlier by Freund (2003). To examine the cause consider the further decomposition of the momentum term $\rho u_i u_j$ into

$$\rho u_i u_j = \bar{\rho} \bar{u}_i \bar{u}_j + \underbrace{\bar{\rho}(\bar{u}_i u'_j + u'_i \bar{u}_j)}_{L_1} + \underbrace{\rho' \bar{u}_i \bar{u}_j}_{L_2} + \underbrace{\rho'(\bar{u}_i u'_j + u'_i \bar{u}_j)}_{Q_1} + \underbrace{\bar{\rho} u'_i u'_j}_{Q_2} + \underbrace{\rho' u'_i u'_j}_{C} \quad (4.1)$$

where an overbar denotes a time-averaged quantity with corresponding fluctuation denoted by the prime. The terms L_1 and L_2 are linear in the fluctuations; Q_1 and Q_2 are quadratic in the fluctuations; and C is cubic. The very first term, $\bar{\rho} \bar{u}_i \bar{u}_j$, has only a mean component and does not radiate sound; it is not considered further. The spectra for the five remaining terms are plotted in fig. 7 for the Mach 2 cold jet and in fig. 8 for the Mach 1 heated jet. From the figures it is apparent that the subcomponents of $\rho u_i u_j$ are qualitatively similar to the overall $\rho u_i u_j$ spectrum.

For the Mach 2.0 cold jet in the 30° direction, the cubic term is of the least importance at all frequencies. The linear term $L_2 = \rho' \bar{u}_i \bar{u}_j$ is of the most importance for $St \geq 0.5$ while L_1 dominates for $St < 0.5$. At 90° the linear term L_2 becomes of the least importance at all frequencies while the two terms $L_1 = \bar{\rho}(\bar{u}_i u'_j + u'_i \bar{u}_j)$ and $Q_2 = \rho'(\bar{u}_i u'_j + u'_i \bar{u}_j)$ contribute most to the overall spectrum, with the latter term dominating for $St < 0.5$. It is notable that the linear term L_2 swaps dominance completely with the pair (L_1, Q_2) when the observer angle is changed.

For the Mach 1.0 heated jet (fig. 8) we find the linear term L_2 dominates at all frequencies, with the quadratic term Q_2 being within 5 dB over the spectrum. The linear term L_1 is confined to $St \leq 0.1$, while the terms Q_1 and C are 8–10 dB and 10–15 dB, respectively, below the L_2 contribution. At 90° the linear term L_2 is far below the overall spectrum and does not appear on the scale of fig. 8(b). For all frequencies the Q_1 quadratic term accounts for the majority of the overall $\rho u_i u_j$ spectrum, while the spectra of L_1 and C are similar but does not appear to contribute to the total.

Historically those terms proportional to \bar{u}_i , i.e., those that include the mean velocity, have been associated with the notion of “shear noise” (Goldstein 1976), where the sound is generated by the interaction of fluctuations with the mean flow. Another interpretation

is that the sound is redistributed by the mean flow through refraction. For the case of $L_2 = \rho' \bar{u}_i \bar{u}_j$ for the 30° observer the significant cancellation that occurs with the term $(p' - a_\infty^2 \rho')$ suggests that neither of these two interpretations are appropriate; if they were appropriate one would not expect such a large portion of the available energy to be non-radiating.

The linearity of L_2 in the density fluctuations implies that the portion of the far-field density spectrum due to L_2 will be proportional to $\omega^4 S_{\rho\rho}$ in the Fraunhofer limit, where $S_{\rho\rho}$ is the spectrum of ρ' ,

$$S_{\rho\rho} = \int \langle \rho'(t) \rho'(t + \tau) \rangle \exp\{i\omega\tau\} d\tau.$$

For weakly compressible turbulence it is expected that $\rho'/\bar{\rho} \sim (u'/\bar{a})^2$ and, similarly, $p'/\bar{p} \sim (u'/\bar{a})^2$. Thus $S_{\rho\rho} \sim S_{uu} S_{uu}$ functionally so that the density and pressure fluctuation spectra are, to leading order in u'/\bar{a} , quadratic in the velocity spectra. For the 30° observer, then, the term $\rho' \bar{u}_x \bar{u}_x$ dominates the six terms of L_2 and has a frequency dependence that is functionally similar to Q_2 , the term quadratic in the velocity fluctuations. Near-field temporal spectra of ρ' and u'_x (not shown, but available in Bodony (2004)) demonstrate that this is indeed the case.

Finally, we note that for the Mach 0.9 unheated jet, the lower mean shear and consequently lower fluctuation root-mean-square (rms) values are not able to produce meaningful levels of ρ' (Bodony & Lele 2005) to be of consequence in the sound radiated to the far-field.

The dominance of the L_2 term for the 30° observer for both the Mach 2.0 cold and Mach 1.0 hot jets then explains the strong correlation of $\rho u_i u_j$ with $(p' - a_\infty^2 \rho') \delta_{ij}$. Because $\bar{u}_x \sim a_\infty$ in the sound generating portion of the jet (Bodony & Lele 2005) and because $\rho u_i u_j \approx \rho' \bar{u}_x \bar{u}_x \delta_{ij}$, we have the leading two terms canceling, leaving $p' \delta_{ij}$ and the remaining terms of $\rho u_i u_j$, all of which are of lower magnitude.

At 90° the relevance of the L_2 is lowered as the radial mean velocity component \bar{u}_r is very small relative to \bar{u}_x and a_∞ in the radiating portion of the jet. The terms $L_1 \approx \bar{\rho} \bar{u}_x u'_r$, $Q_1 \approx \bar{\rho} \bar{u}_x u'_r$, and $Q_2 = \bar{\rho} u'_i u'_j$ thus remain possible contributors to the overall sound radiation. For the heated jet, with its low value of mean density in the sound-generating region, $L_{1,\text{hot}} < L_{1,\text{cold}}$ given that the velocity fluctuation levels are very similar in magnitude between the cold and hot jets. For the cold jet at 90° we thus expect $L_1 > Q_1, Q_2$, which is observed for $St \geq 0.5$ while at lower frequencies $Q_2 > L_1$. For the heated jet at 90° the observation angle and low mean density imply that $Q_2 > Q_1, L_1$.

We note that the ordering arguments are made based on order-of-magnitude estimates and do not consider the frequency dependence of the fluctuations, other than the ω^2 contribution coming from the Green's function.

4.2. On Lilley's decomposition of T_{ij}

From observations of the unheated jets at 90° it appears that both constituents of the $p' - a_\infty^2 \rho'$ term, namely term I and term II as defined in Eq. 3.1, are of approximately equal magnitude and combine to form the "entropic" contribution to the SPL. For the heated jet, however, it is the enthalpy fluctuation term that takes precedence. This and the fact that, for the unheated jets at least, some cancellation occurs between the $\rho u_i u_j$ and $[(\gamma-1)/2] \rho u_k u_k$ terms suggest that it may be more useful to prefer the decomposition

(Lilley 1974) of

$$T_{ij} = \underbrace{\rho u_i u_j - \frac{\gamma - 1}{2} \rho u_k u_k \delta_{ij}}_{\text{momentum stress}} + \underbrace{a_\infty^2 \int \frac{\partial}{\partial x_k} \left[\rho u_k \left(\frac{h_\infty - h_s}{h_\infty} \right) \right] \delta_{ij} dt}_{\text{enthalpy flux}} - \underbrace{\tau_{ij}}_{\text{viscous stress}} \quad (4.2)$$

to better describe the roles of the various stresses to the sound spectra. The presence of the integral in time implies a non-local dependence of the sound field on the enthalpy fluxes. However, through the energy equation it is possible to write

$$\int \frac{\partial}{\partial x_k} \left[\rho u_k \left(\frac{h_\infty - h_s}{h_\infty} \right) \right] dt$$

as $\rho(E/h_\infty - 1)$, where E is the total energy per unit mass, so that the appearance of the time integral is not unphysical. In using Eq. 4.2 the independence in modeling of the momentum and enthalpy fluctuations may be helpful. This conclusion is further borne out by the relative roles played by the momentum and “entropy” terms for the hot Mach 1 jet.

At 30° the data suggest that Lilley’s decomposition may also be beneficial. It was discussed previously that the leading terms of $\rho u_i u_j$ and $(p' - a_\infty^2 \rho') \delta_{ij}$ almost completely cancel for the high-speed jets considered in this study. In Lilley’s rearrangement of T_{ij} this cancellation occurs naturally within the momentum stress term, leaving the enthalpy flux contribution and the remaining momentum stress terms. As the arguments made in determining the canceling are general, we would expect this conclusion to hold for other, high-speed jets with $U_j \geq a_\infty$ up to those jets with $M_j > 2.5$ where Mach wave radiation becomes important.

5. Conclusions

Based upon the investigation of the space-time databases provided by three large-eddy simulations of high-speed turbulent jets, the accuracy of Lighthill’s acoustic analogy has been examined. It was found that the Lighthill predictions agreed very well with the directly computed radiated sound for jets of Mach numbers 0.9 (cold), 1.0 (hot), and 2.0 (cold). Investigation of the sound spectra showed that the momentum contribution due to $\rho u_i u_j$ was dominant at 90° but its overall effect was dependent on cancellation with the so-called entropy component $p - p_\infty - a_\infty^2(\rho - \rho_\infty)$ at 30° . In the cold Mach 0.9 jet the momentum stress was the determining factor for the sound spectra; at higher jet velocities this contribution was tempered by the $-[(\gamma - 1)/2]\rho u_k u_k \delta_{ij}$ portion of the entropy term for the cold jet and by the “enthalpy flux” term for the heated jet. Modeling of the sound sources is believed to be made easier by considering the combined term $\rho u_i u_j - [(\gamma - 1)/2]\rho u_k u_k \delta_{ij}$ separate from the enthalpy flux, due to Lilley (1974), as the latter term is more important for heated jets. At 30° it does not appear that considering the momentum and entropic portions of T_{ij} , in its original Lighthill (1952), is entirely beneficial, as the leading order contributions from these two terms cancel. That high-speed jets are quieter when heated (keeping the jet velocity constant) appears to be due to a reduced sound-generating volume and a reduced convective jet Mach number.

6. Acknowledgements

This work was partially funded by the Aeroacoustics Research Consortium and by the Center for Turbulence Research. Computer resources were provided by the Department of Defense through contract AFOSR F49620-01-1-0138. The authors thank Professor J. Freund of the University of Illinois at Urbana-Champaign for access to his data. An earlier, limited version of this article appeared as AIAA paper AIAA-2005-3041 and was presented at the AIAA/CEAS Aeroacoustics Conference and Exhibit in Monterey, California, 22–25 May 2005.

REFERENCES

ANDERSSON, N., ERIKSSON, L.-E. & DAVIDSON, L. 2003 Large-Eddy Simulation of a Mach 0.75 Jet. AIAA Paper 2003-3312, Presented at the 9th AIAA/CEAS Aeroacoustics Conference and Exhibit, Hilton Head, S.C., 12–14 May.

BASTIN, F., LAFON, P. & CANDEL, S. 1997 Computation of jet mixing noise due to coherent structures: plane jet case. *J. Fluid Mech.* **335**, 261–304.

BODONY, D. J. 2004 Aeroacoustics of Turbulent Free Shear Flows. PhD thesis, Stanford University, Stanford, California.

BODONY, D. J. & LELE, S. K. 2004 Jet noise prediction of cold and hot subsonic jets using large-eddy simulation. AIAA Paper 2004-3022, Presented at the 10th AIAA/CEAS Aeroacoustics Conference, Manchester, U.K., May 10–12.

BODONY, D. J. & LELE, S. K. 2005 On using large-eddy simulation for the prediction of noise from cold and heated turbulent jets. *Phys. Fluids* **17** (085103).

BODONY, D. J. & LELE, S. K. 2006 Review of the current status of jet noise predictions using large-eddy simulation (invited). AIAA Paper 2006-0468, Presented at the 44th Aerospace Sciences Meeting and Exhibit, Reno, NV.

BOGEY, C., BAILLY, C. & JUVÉ, D. 2003 Noise investigation of a high subsonic, moderate Reynolds number jet using a compressible LES. *Theor. Comp. Fluid. Dyn.* **16**, 273–297.

FREUND, J. B. 2001 Noise sources in a low-Reynolds-number turbulent jet at Mach 0.9. *J. Fluid Mech.* **438**, 277–305.

FREUND, J. B. 2002 Turbulent jet noise: Shear noise, self-noise, and entropic contributions. AIAA Paper 2002-2423, Presented at the 8th AIAA/CEAS Aeroacoustics Conference & Exhibit, Breckenridge, C.O., 17–19 June.

FREUND, J. B. 2003 Noise-source turbulence statistics and the noise from a Mach 0.9 jet. *Phys. Fluids* **15** (6), 1788–1799.

FREUND, J. B., SAMANTA, A., WEI, M. & LELE, S. K. 2005 The robustness of acoustic analogies. AIAA Paper 2005-2940, Presented at the 11th AIAA/CEAS Aeroacoustics Conference and Exhibit, Monterey, CA, 23–25 May.

GOLDSTEIN, M. E. 1976 *Aeroacoustics*. New York, N. Y.: McGraw-Hill.

GOLDSTEIN, M. E. 2003 A generalized acoustic analogy. *J. Fluid Mech.* **488**, 315–333.

KHAVARAN, A., BRIDGES, J. & FREUND, J. B. 2002 A Parametric Study of Fine-Scale Turbulence Mixing Noise. AIAA Paper 2002-2419, Presented at the 8th AIAA/CEAS Aeroacoustics Conference, June 17–19, 2002, Breckenridge, Colorado.

LIGHTHILL, M. J. 1952 On sound generated aerodynamically I. General theory. *Proc. R. Soc. London A* **211**, 564–587.

LILLEY, G. M. 1974 On the noise from jets. *Tech. Rep. AGARD CP-131*.

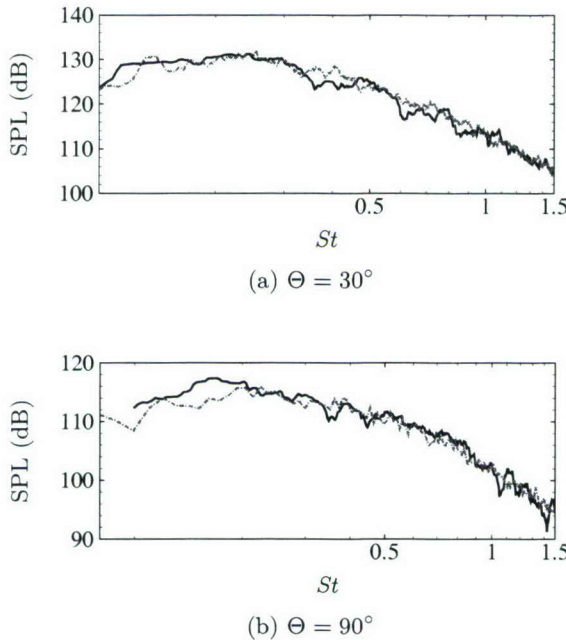


FIGURE 1. Narrowband spectra at $\mathcal{R} = 30D_j$ for the Mach 0.9 unheated jet M09TR086.
 Legend: —, Lighthill (total), - - -, Kirchhoff Surface.

PANDA, J. & SEASHOLTZ, R. G. 2002 Experimental investigation of density fluctuations in high-speed jets and correlation with generated noise. *J. Fluid Mech.* **450**, 97–130.

PANDA, J., SEASHOLTZ, R. G., ELAM, K. A., MIELKE, A. F. & ECK, D. G. 2004 Effect of heating on turbulent density fluctuations and noise generation from high speed jets. AIAA Paper 2004-3016, Presented at the 10th AIAA/CEAS Aeroacoustics Conference & Exhibit, Manchester, U.K., 10–12 May.

SAIYED, N. H., MIKKELSEN, K. L. & BRIDGES, J. E. 2003 Acoustics and Thrust of Quiet Separate-Flow High-Bypass-Ratio Nozzles. *AIAA J.* **41** (3), 372–378.

STROMBERG, J. L., MCLAUGHLIN, D. K. & TROUTT, T. R. 1980 Flow field and acoustic properties of a Mach number 0.9 jet at a low Reynolds number. *J. Sound Vib.* **72**, 159–176.

TAM, C. K. W. & AURIAULT, L. 1999 Jet Mixing Noise from Fine-Scale Turbulence. *AIAA J.* **37** (2), 145–153.

UZUN, A. & HUSSAINI, M. 2006 High Frequency Noise Generation in the Near-Nozzle Region of a Jet. AIAA Paper 2006-2499, Presented at the 12th AIAA/CEAS Aeroacoustics Conference and Exhibit, Cambridge, MA.

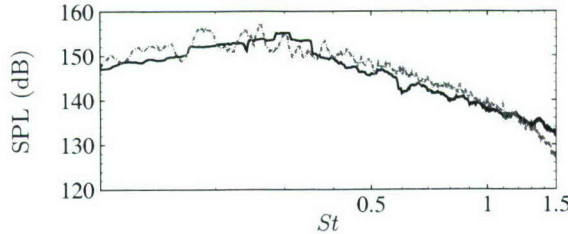
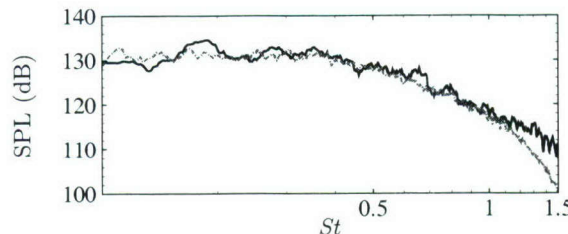
(a) $\Theta = 30^\circ$ (b) $\Theta = 90^\circ$

FIGURE 2. Narrowband spectra at $\mathcal{R} = 30D_j$ for the Mach 2.0 unheated jet M15TR056.
 Legend: —, Lighthill (total), - · -, Kirchhoff Surface.

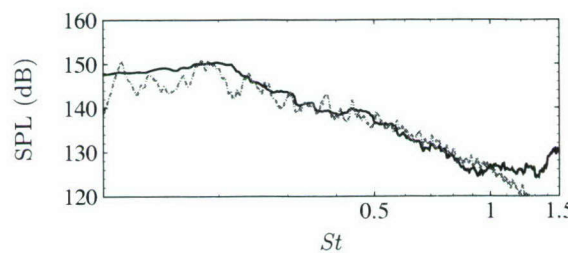
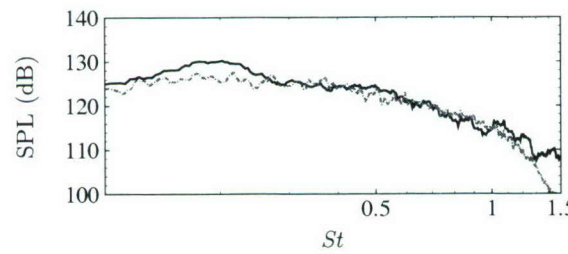
(a) $\Theta = 30^\circ$ (b) $\Theta = 90^\circ$

FIGURE 3. Narrowband spectra at $\mathcal{R} = 30D_j$ for the Mach 1.0 heated jet M15TR230. Legend:
 —, Lighthill (total), - · -, Kirchhoff Surface.

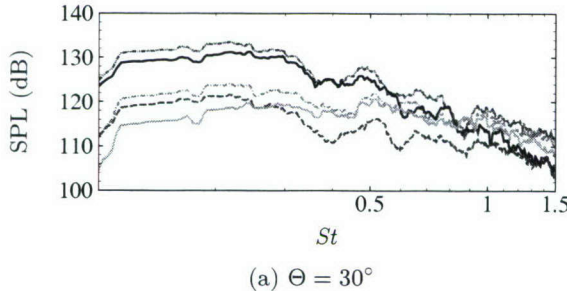
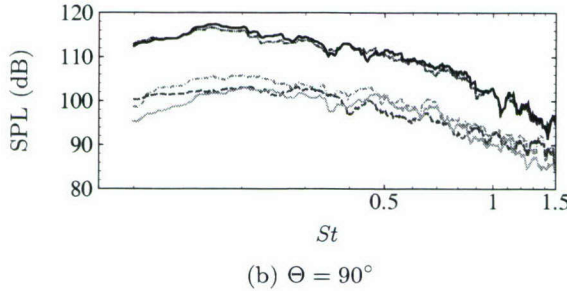
(a) $\Theta = 30^\circ$ (b) $\Theta = 90^\circ$

FIGURE 4. Narrowband spectra at $\mathcal{R} = 30D_j$ for the Mach 0.9 unheated jet M09TR086. Legend: —, total, - · - · -, $\rho u_i u_j$, - - - -, $p' - a_\infty^2 \rho'$, - - -, entropy (term I), · · · · -, entropy (term II).

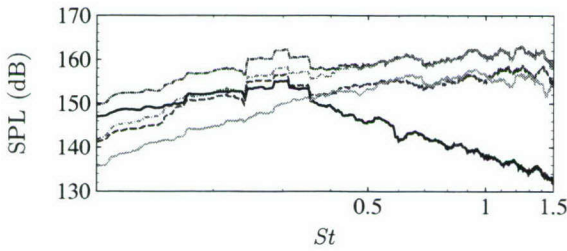
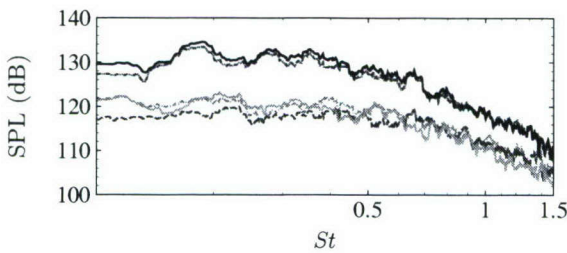
(a) $\Theta = 30^\circ$ (b) $\Theta = 90^\circ$

FIGURE 5. Narrowband spectra at $\mathcal{R} = 30D_j$ for the Mach 2.0 unheated jet M15TR056. Legend: —, total, - · - · -, $\rho u_i u_j$, - - - -, $p' - a_\infty^2 \rho'$, - - -, entropy (term I), · · · · -, entropy (term II).

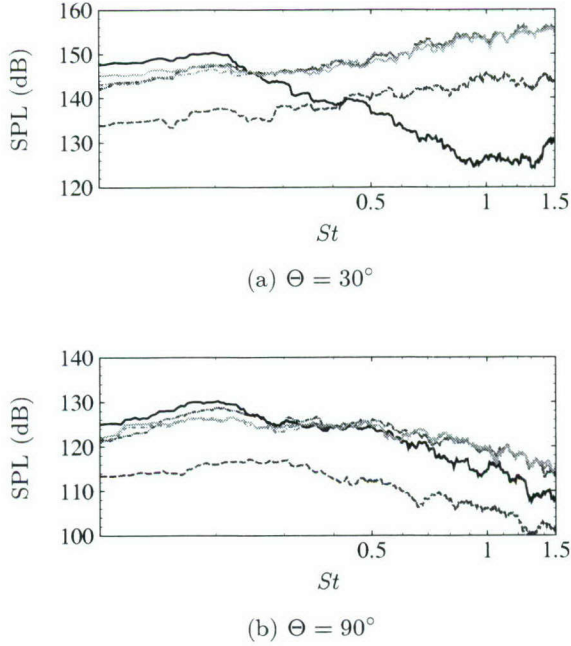


FIGURE 6. Narrowband spectra at $\mathcal{R} = 30D_j$ for the Mach 1.0 heated jet M15TR230. Legend: —, total, - · -, $\rho u_i u_j$, - · · -, $p' - a_\infty^2 \rho'$, ---, entropy (term I), · · ·, entropy (term II).

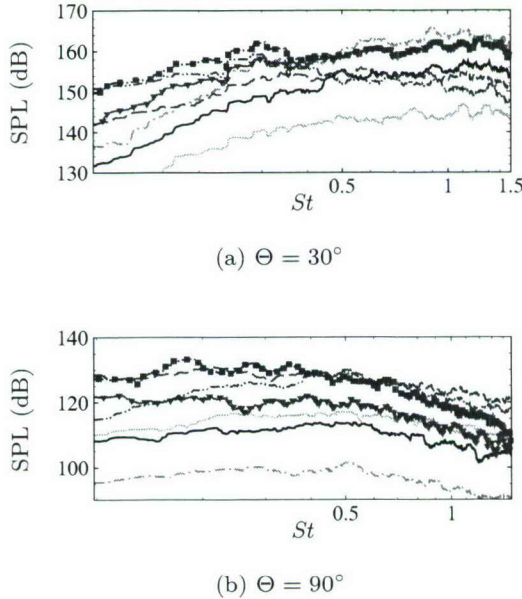


FIGURE 7. Component spectra contributing to the spectrum of $\rho u_i u_j$ for the jet M15TR056. Legend: - · · -, L_1 ; - · -, L_2 ; —, Q_1 ; - - -, Q_2 ; · · ·, C ; - ▼ -, $p' - a_\infty^2 \rho'$; - ■ -, $\rho u_i u_j$ spectrum.

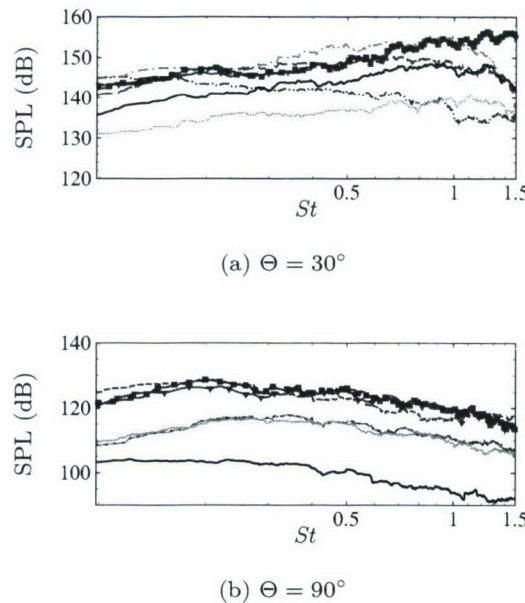


FIGURE 8. Component spectra contributing to the spectrum of $\rho u_i u_j$ for the jet M15TR230. Legend: $- \cdots, L_1$; $- \cdot -, L_2$; $-$, Q_1 ; $- \cdots, Q_2$; \cdots, C ; $- \blacktriangledown -, p' - a_\infty^2 \rho'$; $- \blacksquare -, \rho u_i u_j$ spectrum. Note the curve for L_2 in (b) lies below the figure scale.

Improved near-wall accuracy for solutions of the Helmholtz equation using the boundary element method

By Y. Khalighi AND D. J. Bodony

1. Motivation and objectives

The propagation of flow-generated sound in the presence of surfaces often depends on the scattering properties of those surfaces. In the low Mach number limit and in the context of a linear acoustic theory such as that of Lighthill (1952) the process of noise prediction is divided into two steps: (i) the calculation of the sound sources generated by the flow, and (ii) the propagation of the sound. The latter stage accounts for the traveling of acoustic waves in the medium as well as the scattering of the sound due to solid objects. The propagative behavior of the environment can be fully described by the acoustic Green's function tailored to that environment's specific geometry. In the frequency domain, the Green's function is the fundamental solution of the Helmholtz equation with appropriate boundary conditions on the solid surfaces as well as a far-field radiation condition for exterior problems (Crighton 1975).

The Boundary Element Method (BEM) can be ideally employed for Helmholtz equation. It has a few inherent advantages over Finite Element and Finite Volume techniques, including the ease of applying infinite domains in exterior problems, not being subject to dissipation and dispersion error, and not requiring a volume mesh (Worbel & Aliabadi 2002).

In the BEM, the Helmholtz equation is cast into an integral equation using Green's second theorem. After surface discretization, the first step in the BEM is to numerically solve a boundary integral equation on the solid surface. In the next step the solution at any point in the volume, i.e., any point off the surface, can be calculated by a boundary quadrature formula using the results from the first step. In both steps the integral kernels exhibit singularities, or nearly so, and special attention must be paid in the evaluation of these integrals. Even if the surface solution obtained in the first step is accurate, the numerical evaluation of the surface quadrature can be inaccurate for points located within a distance of a few elements from the solid surface. The source of this inaccuracy is numerical integration of a kernel that is close to its singular point. In this work, using an asymptotic expansion of the singular kernel we present a new approach to circumvent this problem and recover the desirable order of accuracy in the vicinity of the surface.

The evaluation of the broadband noise due to the turbulent flow past an airfoil trailing edge at low Mach number is one application requiring accuracy in the Green's function obtained by quadrature. It is known that the noise generation is concentrated very close to the trailing edge (Amiet 1976; Wang & Moin 2000) where the influence of the airfoil on the sound propagation is significant. However, because of the low Mach number the acoustic wavelength is much higher than the flow scales and, as a result, the size of BEM surface mesh can be large compared to flow scales. Consequently, the major source region

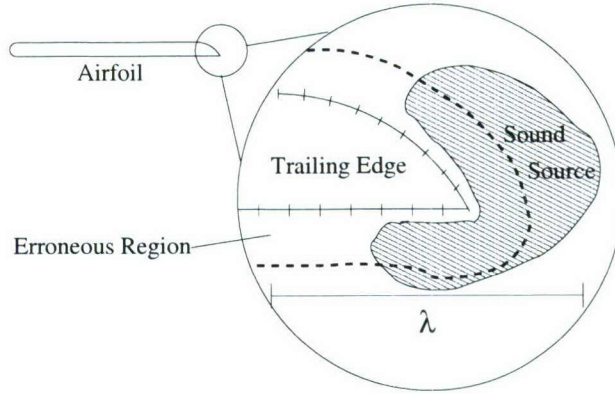


FIGURE 1. Schematic of sound source region in the vicinity of the solid surface.

can be at a distance of a few BEM surface elements and may be subject to errors due to the quadrature (see Fig. 1).

2. Basic concepts in BEM [†]

2.1. Helmholtz equation, fundamental solutions, and boundary conditions

The Helmholtz equation for a time-harmonic signal of frequency ω can be written as

$$(\nabla^2 + k^2)\phi(\mathbf{x}) = 0 \quad \mathbf{x} \in \Omega, \quad (2.1)$$

where $k = \omega/C$ is the wavenumber and C is the constant speed of sound. Since the Helmholtz equation is presented in the frequency space ϕ is, in general, complex-valued. The fundamental solutions of the Helmholtz equation (with a source term in the form of $-\delta(\mathbf{x} - \mathbf{x}_0)$) in two and three dimensions are, respectively,

$$G(\mathbf{x}, \mathbf{x}_0) = -\frac{i}{4} H_0^{(1)}(k|\mathbf{x} - \mathbf{x}_0|) \quad (2.2)$$

$$G(\mathbf{x}, \mathbf{x}_0) = -\frac{e^{ik|\mathbf{x} - \mathbf{x}_0|}}{4\pi|\mathbf{x} - \mathbf{x}_0|}, \quad (2.3)$$

where $H_0^{(1)}$ is the Hankel function of the first kind of the order zero. In the present work the derivations and results are based on an analysis of the 2-D problem but the same methodology can be applied to 3-D problems, though additional difficulties arise.

For *interior problems*, three standard boundary conditions—Dirichlet, Neumann, and Robin—can be applied on the boundary surfaces Γ_D , Γ_N , and Γ_R , respectively, where $\Gamma = \Gamma_D \cup \Gamma_N \cup \Gamma_R$ entirely bounds Ω . For *exterior problems*, in addition to previous boundary condition types for the interior surfaces, the Sommerfeld radiation condition should be satisfied far from the object. The Sommerfeld radiation condition can be written as

$$\lim_{r \rightarrow \infty} r \left(\frac{\partial \phi}{\partial r} + ik\phi \right) = 0 \quad (2.4)$$

and represents the propagation of sound without reflection away from the body.

[†] Additional details can be found in Worbel & Aliabadi (2002) and Brebbia *et al.* (1984).

2.2. Formulation of Direct BEM Equations

Direct boundary integral equations can be derived by applying the second Green's identity to the solution of Helmholtz equation $\phi(\mathbf{x})$ and its fundamental solution $G(\mathbf{x}, \mathbf{x}_0)$. By taking the source point \mathbf{x}_0 on the boundary Γ_x , the Helmholtz equation reduces to an integral equation on the boundary, viz,

$$c(\mathbf{x}_0)\phi(\mathbf{x}_0) = \int_{\Gamma_x} \frac{\partial\phi(\mathbf{x})}{\partial n} G(\mathbf{x}_0, \mathbf{x}) ds - \int_{\Gamma_x} \phi(\mathbf{x}) \frac{\partial G(\mathbf{x}_0, \mathbf{x})}{\partial n} ds. \quad (2.5)$$

In this expression $c(\mathbf{x}_0)$ is a geometry-dependent parameter. It varies between zero and unity and equals 1/2 if the point is on a smooth part of the boundary; at edges it is related to the angle of the joining surfaces.

If the source point \mathbf{x}_0 is inside the domain Ω , but not on the surface Γ_x , the value of ϕ at that point can be written in terms of an integral over the surface as

$$\phi(\mathbf{x}_0) = \int_{\Gamma_x} \frac{\partial\phi(\mathbf{x})}{\partial n} G(\mathbf{x}_0, \mathbf{x}) ds - \int_{\Gamma_x} \phi(\mathbf{x}) \frac{\partial G(\mathbf{x}_0, \mathbf{x})}{\partial n} ds. \quad (2.6)$$

Equations 2.5 and 2.6 are the basis of the direct BEM. The method can be described as a two-step approach. In the first step, (2.5) is discretized on the surface and the integral equation is numerically *solved* for the unknowns. The type of unknown depends on the boundary condition applied on the surface, for example, on Γ_D with Dirichlet boundary condition ϕ is described and the equation is solved for $\frac{\partial\phi}{\partial n}$. In the second step the solution at any point inside the volume can be numerically *integrated* using expression (2.6).

The kernel of integrals in (2.5) and (2.6) are the free space Green's function of the Helmholtz equation and its derivative. As can be seen from (2.2) and (2.3), G and $\frac{\partial G}{\partial n}$ have singular behavior as \mathbf{x}_0 approaches \mathbf{x} . Since in (2.5) point \mathbf{x}_0 lies on the boundary Γ_x , the kernel is singular at $\mathbf{x} = \mathbf{x}_0$. Despite the singularity these integrals exist in the sense of their Cauchy principal value and are discussed in detail in the literature (for example see Worbel & Aliabadi (2002) and Brebbia *et al.* (1984)).

Obviously, the singularity of the kernels does not take place in (2.6) as \mathbf{x}_0 does not lie on the surface. However, \mathbf{x}_0 can be very close to the surface and this causes numerical issues, which is the central focus of the current work.

3. Numerical issues in the calculation of the boundary integral

In this work we set the desirable order of accuracy as second order. We assume the boundary solution is available with at least this order of accuracy and will focus on the accuracy of the numerical quadrature for points \mathbf{x}_0 not on the surface. Assuming the boundary is discretized and represented by N linear elements, (2.6) can be written as

$$\phi(\mathbf{x}_0) = \sum_{i=1}^N \left(\int_{\Gamma_i} \frac{\partial\phi(\mathbf{x})}{\partial n} G(\mathbf{x}_0, \mathbf{x}) ds - \int_{\Gamma_i} \phi(\mathbf{x}) \frac{\partial G(\mathbf{x}_0, \mathbf{x})}{\partial n} ds \right). \quad (3.1)$$

A simple, piecewise constant representation of ϕ and $\frac{\partial\phi}{\partial n}$ is sufficient for rectangular integration, thus second order of accuracy. This can be written as

$$\phi(\mathbf{x}_0) \approx \sum_{i=1}^N \left(\frac{\partial\phi(\mathbf{x}_i)}{\partial n} G(\mathbf{x}_0, \mathbf{x}_i) S_i - \phi(\mathbf{x}_i) \frac{\partial G(\mathbf{x}_0, \mathbf{x}_i)}{\partial n} S_i \right), \quad (3.2)$$

where \mathbf{x}_i and S_i are center and area of element i , respectively. In this representation the solution is approximated by N *point* monopoles and dipoles. We call this *point-wise representation*.

An alternative representation at the same order of approximation is to represent the integral by summation of *distributed* single- and double-layer acoustic potentials as

$$\begin{aligned}\phi(\mathbf{x}_0) &\approx \sum_{i=1}^N \left(K_i \frac{\partial \phi(\mathbf{x}_i)}{\partial n} - H_i \phi(\mathbf{x}_i) \right) \\ K_i &= \int_{\Gamma_i} G(\mathbf{x}_0, \mathbf{x}) ds \\ H_i &= \int_{\Gamma_i} \frac{\partial G(\mathbf{x}_0, \mathbf{x})}{\partial n} ds.\end{aligned}\quad (3.3)$$

This is a *distributed representation* of the integral. The analytical expressions for H_i and K_i are not known and are not likely to exist because of the complexity of G and $\frac{\partial G}{\partial n}$ as it can be seen from (2.2) and (2.3). However, an analytical solution exists for the fundamental solution of the 2-D Laplace operator (Worbel & Aliabadi 2002).

In order to compare the accuracy of pointwise and distributed representations, a simple 2-D Laplace equation is studied. Let ψ be defined as:

$$\psi(x, y) = x \quad -1 \leq x \leq 1, \quad -1 \leq y \leq 1. \quad (3.4)$$

The boundary of the domain is discretized into N equal elements and the exact solution is applied on the center of each element. The solution inside the domain is then calculated using different integral representations. We tested the distributed expression with 40 elements and the pointwise expression with 40, 80, and 160 elements. The results are shown in Fig. 2. Clearly, the accuracy of the pointwise expression is reduced close to the boundaries. This could be expected since the leading error term in the pointwise representation scales with h/R (where h is the size of element and $R = |\mathbf{x}_0 - \mathbf{x}_i|$ as shown in Fig. 3) and that term becomes significant when \mathbf{x}_0 is in the vicinity region of any element. The error of the pointwise representation can be reduced by using a more accurate numerical integration, such as subdividing the closest element to smaller elements or using quadratures of higher order. Note that the error will arise as the point gets close enough to the element. As is shown in Fig. 2, the distributed formulation with 40 elements is more accurate than the pointwise expression with 160 elements in an L_∞ sense.

This observation can be problematic in acoustic applications where major sound sources are close, in terms of the acoustic wavelength, to the boundaries (see trailing edge example in Fig. 1). Here, an erroneous acoustics Green's function unphysically amplifies the noise sources close to the wall. This situation is likely to occur in the turbulent flow simulation past a solid surface where the wall normal resolution is very high ($y^+ \approx 1$). It is very expensive to use BEM elements with sizes on the order of wall units. On the other hand, an exact distributed integral formulation is not possible because of the complexity of the Green's function. An intermediate formulation, which is described in the next section, uses the asymptotic behavior of the solution in the vicinity of the near-wall elements.

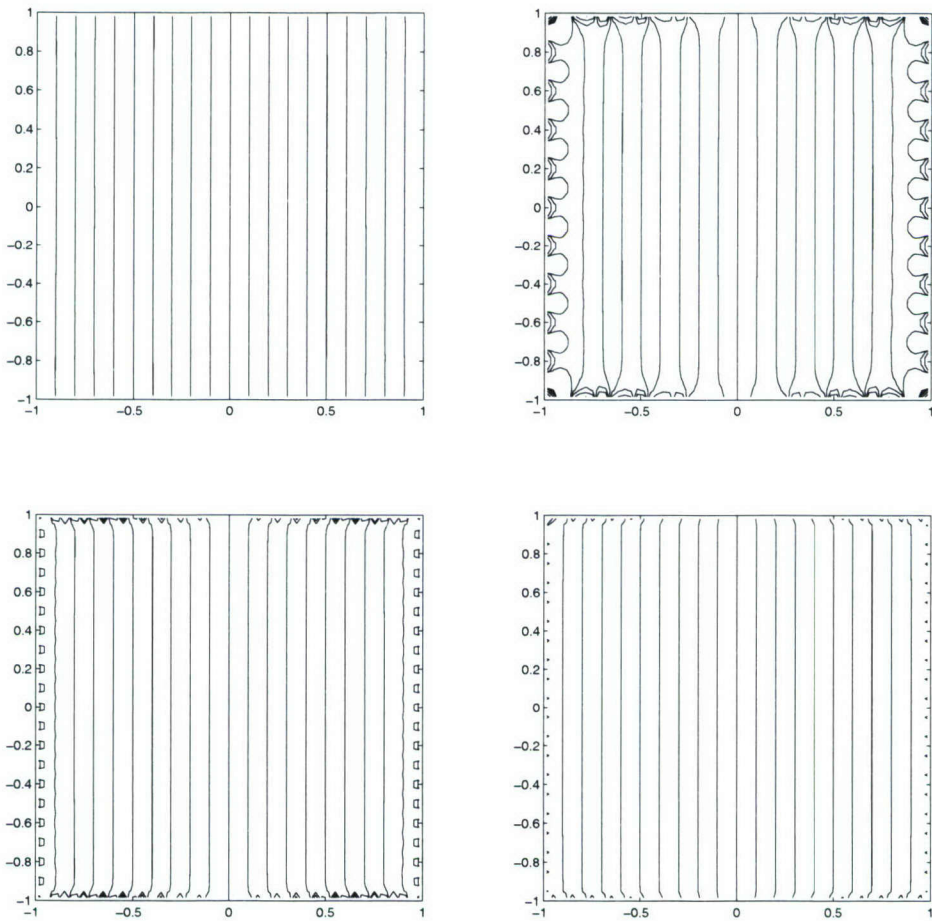


FIGURE 2. Contour levels of solution to the Laplace equation. Top left: distributed representation $N = 40$, top right: pointwise representation $N = 40$, bottom left: pointwise representation $N = 80$, bottom right: pointwise representation $N = 160$.

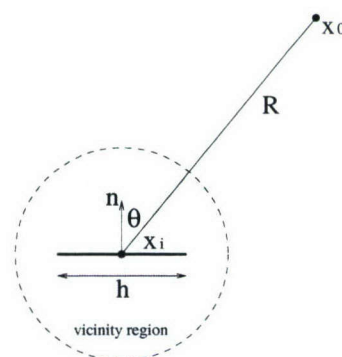


FIGURE 3. A 2-D BEM element.

4. Asymptotic expansion for 2-D BEM element

In BEM the size of boundary elements should be sufficient to resolve the wavelength $\lambda = 2\pi/k$ of the sound, implying that $h \ll \lambda$ as required by the simple elements used here. In the vicinity region of the element where R is comparable to, or smaller than, the size of element h , we have $kR \ll 1$. This observation suggests that the Helmholtz equation in this region can be approximated by the Laplace equation and that the distributed expression in its analytical form can be applied for the corresponding element. This can be verified from the asymptotic behavior of the free space Green's function for the 2-D Helmholtz equation (2.2).

From Abramowitz & Stegun (1964) the Hankel function has the following asymptotic behavior, for $|z| \ll 1$,

$$H_0^{(1)}(z) \sim \frac{2i}{\pi} \ln(z), \quad (4.1)$$

which results in the fundamental solution of the form

$$G^*(R) \sim \frac{1}{2\pi} \ln(kR) \quad (4.2)$$

$$\frac{\partial G^*(R)}{\partial R} \sim \frac{1}{2\pi R}, \quad (4.3)$$

which has the same form as the free space Green's function for the 2-D Laplace equation. Thus H_i and K_i defined in (3.4) can be approximated for the region at the vicinity of the element using the analytical expression of distributed representation. However, for points far from the element the pointwise distribution is sufficient; see Fig. 2. As a result, these two formulations can be blended using a transition function to provide a globally accurate, economical approximation for H_i and K_i . This asymptotic approximation can be written as

$$K_i \approx T(R/h)G(\mathbf{x}_0, \mathbf{x}_i)h + (1 - T(R/h))K_i^V \quad (4.4)$$

$$H_i \approx T(R/h)\frac{\partial G(\mathbf{x}_0, \mathbf{x}_i)}{\partial n}h + (1 - T(R/h))H_i^V. \quad (4.5)$$

The analytical expressions for K_i^V and H_i^V are available in Appendix A. $T(\eta)$ is a transition function defined as

$$T(\eta) = 0.5(1 + \tanh(10(\eta/\alpha - 1))). \quad (4.6)$$

T and T' both vanish at $\eta = 0$. It has a smooth transition centered at $\eta = \alpha$ and becomes unity with zero derivative at sufficiently large η . Based on experience, $\alpha = 2$ provides sufficiently accurate results.

5. A test case

As a validation test case we calculate the solution for the scattering of a planar wave of wavelength $\lambda/D = 0.44$ off a solid circular cylinder, as shown in Fig. 4. The solution on the surface is calculated using second-order BEM and the solution of a point at distance d from the cylinder is calculated using the asymptotic approximation formulation of (4.4) and (4.5). The calculation is done for three different resolutions of $N = 100, 200$, and 400 elements. An analytical solution exists in the form of infinite series and is available in Appendix B. We truncate the infinite series by neglecting all terms smaller than 10^{-12} in magnitude.

The result for absolute value of the solution $|\phi|$ is shown in Fig. 5. There is desirable

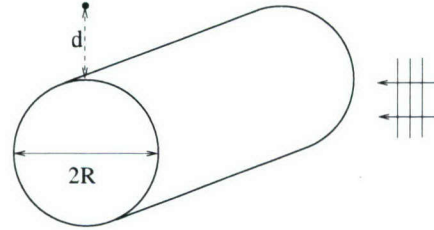


FIGURE 4. Schematic of the scattering from cylinder.

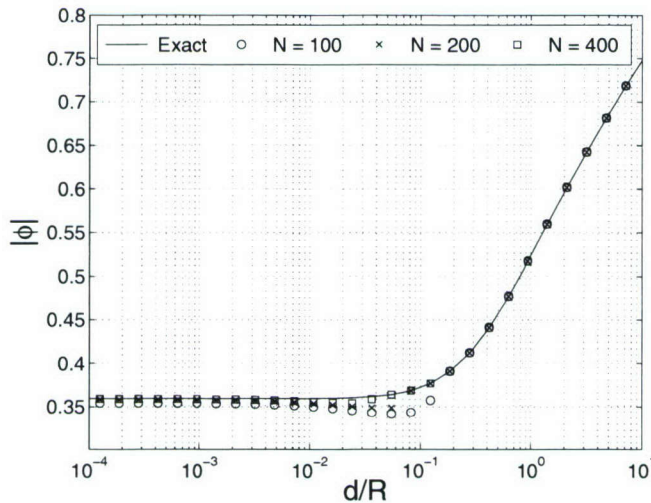


FIGURE 5. Comparison of BEM result and exact solution as the point approaches the solid surface.

agreement between the exact solution and the BEM result in the both far-field and the vicinity regions. The maximum error occurs in the transition point, as could be expected.

To assess the order of accuracy of the scheme, $(N/100)^2 |\phi_{\text{BEM}} - \phi_{\text{exact}}|$ is plotted in Fig. 6. There it can be seen that the error curves for both asymptotic branches converge, which shows the second order of accuracy for the far-field solution and for the solution in the vicinity of the surface. Slightly better than first-order accuracy is observed in the transition region.

6. Possible extensions to 3-D problems

A key point for the implementation of 2-D asymptotic approximation is the ability to carry out the integrals analytically. Unfortunately, this is not the case in 3-D, even for very simple triangular surface elements. This problem can be remedied by making another approximation to calculate integrals in the vicinity region.

When the observer point is very close to the element, the shape of the element has very little effect. In other words, the observer does not see the edges. This suggests replacing the closest element with an element of the same area but a simpler geometry (e.g., a circle). This method provides acceptable results (not shown) when the point is very close

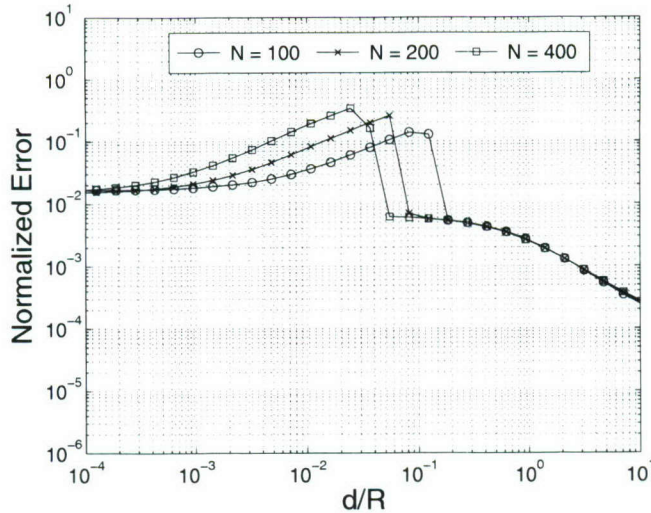


FIGURE 6. Plot of normalized error with N^2 to demonstrate the second order of accuracy.

to surface; however, it can be rather erroneous when the point is in the vicinity of the edges or far from the element.

Another technique that can be applied to both 2-D and 3-D problems is using the continuity of the solution and extrapolating the solution from the closest element. This can be written as

$$\phi \sim \phi_{\text{boundary}} - \frac{\partial \phi_{\text{boundary}}}{\partial n} d_n, \quad (6.1)$$

where d_n is normal distance between the point and the closest element. This method is very easy to implement for both 2-D and 3-D cases, but is not as accurate as using distributed representation for the vicinity region. We continue to work on the 3-D problem.

7. Summary

We have developed a new approach to accurately and efficiently calculate the boundary integrals that appear in the BEM formulation in two dimensions. It is first shown that pointwise representation of the integral can be very inaccurate close to the boundaries. Based on this observation we devised a method using the asymptotic expansion of the solution in the vicinity of elements. A simple test case was presented to show applicability of the method.

Appendix A. Analytical expressions for K_i^V and H_i^V

$$\begin{aligned} K_i^V &= \int_{\text{element}} G^* dl \\ &= \frac{1}{4\pi} \left(b \ln(k^2(b^2 + d^2)) - a \ln(k^2(a^2 + d^2)) + 2d \tan^{-1} \left(\frac{4dh}{4R^2 - h^2} \right) - 2h \right) \end{aligned} \quad (\text{A } 1)$$

$$\begin{aligned}
 H_i^V &= \int_{\text{element}} \frac{\partial G^*}{\partial n} dl \\
 &= \frac{1}{2\pi} \tan^{-1} \left(\frac{4dh}{4R^2 - h^2} \right)
 \end{aligned} \tag{A 2}$$

where G^* is defined in (4.2) and a , b , and d are related to the geometry via

$$\begin{aligned}
 d &= R \cos \theta \\
 a &= \sqrt{R^2 + h^2/4 - Rh \sin \theta} \\
 b &= \sqrt{R^2 + h^2/4 + Rh \sin \theta}.
 \end{aligned} \tag{A 3}$$

Appendix B. Exact solution of scattering from a rigid cylinder

Assume a solid cylinder with radius a is subject to a planar incident wave of wavenumber k traveling normal to the generator of the cylinder,

$$\phi_i(r, \theta) = e^{ikr \cos \theta}, \tag{B 1}$$

where r is the polar distance from the axis and θ is measured from the direction of k .

By decomposing the solution into incident and scattered parts and separation of variables, the solution can be written as infinite series

$$\phi(r, \theta) = \phi_i + \sum_{m=0}^{\infty} A_m \cos(m\theta) H_m^{(1)}(kr), \tag{B 2}$$

where the A_m can be calculated from

$$A_m = -2i^m \left(1 + i \frac{Y_{m-1}(ka) - Y_{m+1}(ka)}{J_{m-1}(ka) - J_{m+1}(ka)} \right)^{-1} \quad m \neq 0 \tag{B 3}$$

$$A_0 = - \left(1 + i \frac{Y_1(ka)}{J_1(ka)} \right)^{-1}. \tag{B 4}$$

Acknowledgment

The work presented in this paper was supported by the Office of Naval Research.

REFERENCES

ABRAMOWITZ, M. & STEGUN, I. A. 1964 *Handbook of Mathematical Functions with Formulas, Graphs, and Mathematical Tables*. New York: Dover.

AMIET, R. K. 1976 Noise due to turbulent flow past a trailing edge. *Journal of Sound Vibration* **47**, 387–393.

BREBBIA, C. A., TELLES, J. C. F. & WROBEL, L. C. 1984 *Boundary element techniques, Theory and application in engineering*. Berlin: Springer-Verlag.

CRIGHTON, D. G. 1975 Basic principles of aerodynamic noise generation. *Progress in Aerospace Sciences* **16**, 31–96.

LIGHTHILL, M. J. 1952 On Sound Generated Aerodynamically. I. General Theory. *Royal Society of London Proceedings Series A* **211**, 564–587.

WANG, M. & MOIN, P. 2000 Computation of trailing-edge flow and noise using large-eddy simulation. *AIAA J.* **38**, 2201–2209.

WORBEL, L. C. & ALIABADI, F. 2002 *The Boundary Element Method, Volume 1: Application in Therm-Fluids and Acoustics*. New York: John Wiley & Sons, Inc.

Evaluation of active control of a laminar separation bubble based on linear stability theory

By O. Marxen, R. B. Kotapati[†] AND D. You

1. Motivation and objectives

Control of laminar separation using zero-net-mass-flux (ZNMF) devices for airfoils operating at low to medium Reynolds numbers is a common approach in laboratory experiments, in both numerical (e.g., Fasel & Postl 2006; Rist & Augustin 2006) and experimental (e.g., Bons *et al.* 2001) setups. However, ongoing physical processes in such flows can be diverse, spanning from convective-type (Kelvin-Helmholtz) instability (Rist & Augustin 2006) to vortex-wall interaction (Simens & Jimenez 2006).

Here, an interpretation of a flow situation investigated numerically during the CTR summer program (Kotapati *et al.* 2006) in terms of local linear stability theory based on the Orr-Sommerfeld equation is presented. Such an instability corresponds to the convective-type Kelvin-Helmholtz instability for laminar separation bubbles (LSB). In contrast to Rist & Augustin (2006), the present flow possesses an actual ZNMF actuator geometry for forcing, and investigates a wider range of forcing frequencies.

Results obtained from numerical simulations mentioned above shall be post-processed and analysed with respect to unsteady disturbance evolution in the flow. First, stability characteristics of the different mean flows resulting from different forcing frequencies are evaluated theoretically; numerical data are then Fourier-analyzed in time and are compared to theoretical results. Based on such a comparison, a discussion of similarities and differences between numerical and theoretical results then allows us to conclude on physical mechanism in operation. This is expected to help to improve the efficiency of active flow-control devices in the future.

2. Flow configuration and mean flows

A configuration shall be considered that was studied numerically during the 2006 CTR summer program (Kotapati *et al.* 2006). Data from respective simulations (cases 2.2–2.5) in that reference shall be analyzed here with respect to their stability properties and disturbance evolution, leading to a deeper understanding of physical processes taking place in the controlled flowfields. A brief overview of the setup and the mean flow shall be given in this section. Note that the simulations are 2-D only. Nevertheless, in the following the term *transition* will be used, indicating saturation of the dominant disturbance, even though no true (3-D) turbulent state is reached.

2.1. Overview

The general setup is given by a finite flat plate with an elliptic nose placed in a channel with slip walls, subject to a uniform incoming freestream at the channel inlet. In the rear part of the plate, steady blowing and suction is applied on the upper (slip) wall of the

[†] Mechanical and Aerospace Engineering, The George Washington University, Washington, DC 20052, USA

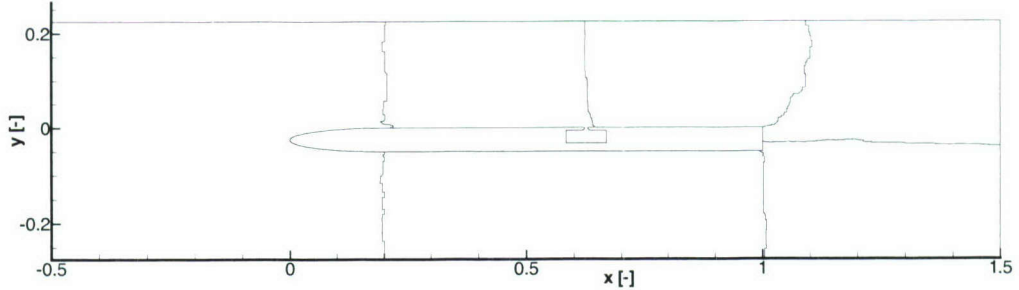


FIGURE 1. Configuration used for numerical simulations.

case	forcing frequency f_J
2.1	-
2.2	1.5
2.3	3.0
2.4	6.0
2.5	9.0

TABLE 1. Overview of simulation cases with respect to their forcing frequency.

channel in the interval $0.2 < x/c < 0.8$, which induces an adverse pressure gradient at the top wall of the flat plate and in turn leads to separation of the laminar boundary layer on that plate.

All quantities are non-dimensionalized with the inlet velocity of the channel and the chord of the plate. This amounts to a Reynolds number of 60,000. The wall-normal origin of the coordinate system lies on the top wall of the flat plate while the streamwise origin corresponds to the start of the plate, i.e., the (elliptic) nose. The flat part of the finite plate starts at $x/c=0.2$. In the following, we focus solely on the region around the separation bubble, which is located in the flat section downstream of the elliptic leading edge and upstream of the end of the plate, namely $0.2 < x/c < 1.0$.

A ZNMF actuator is centered at $x/c=0.625$. This actuator is used to diminish boundary-layer separation downstream of its location by forcing at different frequencies, but with a fixed amplitude. Four different non-dimensional frequencies were applied in the four different cases 2.2–2.5 (see Table 1). Case 2.1 refers to an undisturbed flow and will not be further considered.

The flow is computed by means of the second-order finite-volume based code CDP (Ham & Iaccarino 2004), which has been developed at the Center for Turbulence Research at Stanford University. For details of these simulations, refer to Kotapati *et al.* (2006). Only a very brief overview of the results with respect to the mean flow is provided in the next section. The mean flow for each case will be used as a base flow for subsequent stability calculations.

2.2. Mean flows

Figures 2 and 3 show boundary-layer parameters for all simulations with forcing. Those were computed from streamwise mean-flow velocity profiles up to a wall-normal distance of $y=0.0347$. Within this distance from the plate, changes in the potential flow, which introduce an error into the computation of displacement and momentum thicknesses, re-

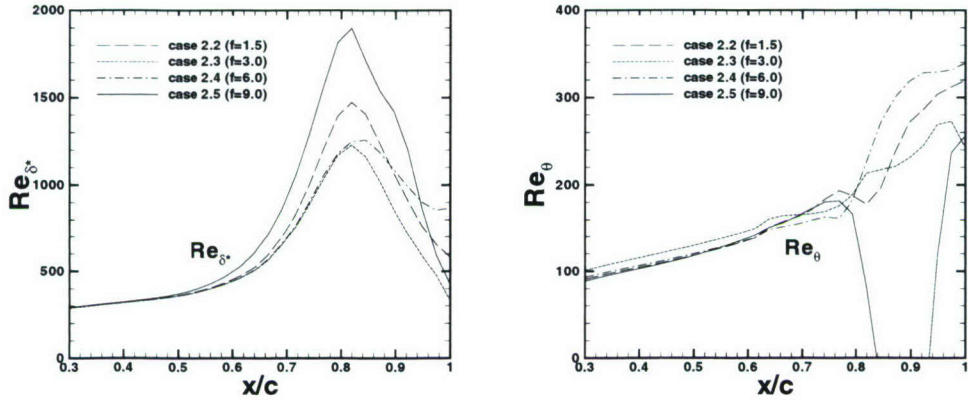


FIGURE 2. Reynolds numbers based on the displacement thickness δ_* (left) and the momentum thickness θ (right) for cases 2.2–2.5.

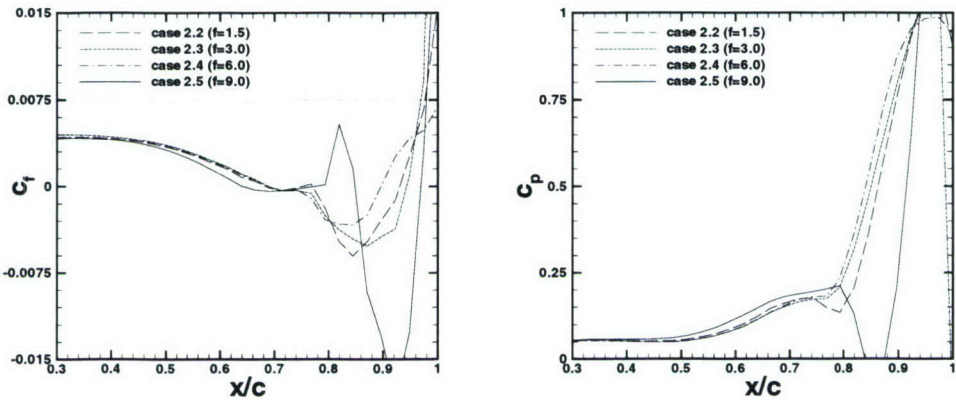


FIGURE 3. Skin-friction (left) and wall-pressure (right) coefficients for cases 2.2–2.5. The pressure is chosen such that it is the same for all cases at $x/c=0.3$.

main fairly small. Typical features of laminar separation bubbles can be observed when looking at these time-averaged quantities. For instance, the larger the bubble, the larger is its displacement thickness (see Fig. 2, left). The Reynolds number based on the momentum thickness θ (Fig. 2, right) strongly changes only when the flow transitions, so this quantity gives a rough idea of the transition location. The mean flow in case 2.5 (forcing frequency $f=9$) is somewhat similar to the undisturbed case (not shown here). Instead, case 2.5 will be referred to as essentially uncontrolled.

Forcing at the three lower frequencies ($f \leq 6$), cases 2.2–2.4 respectively, considerably reduces the size of the separation region. This is visible via the skin-friction coefficient c_f (Fig. 3, left), whose changes in sign from positive to negative and vice versa mark the separation and reattachment location, respectively. When compared to the essentially uncontrolled case 2.5 it is obvious that this reduction takes place from both sides, i.e., not only does the reattachment location move upstream, the separation location also

moves downstream. This is due to a feedback effect, namely disturbance input causes earlier transition downstream that in turn changes the mean flow, i.e., causes a mean flow deformation, via the pressure at the location of forcing or even upstream of it. Such a feedback effect of the mean flow deformation has also been reported by Marxen (2005).

This change in pressure due to forcing is clearly observable in Fig. 3 (right): the pressure increase is delayed upstream of transition, or more precisely disturbance input causes a weaker pressure increase upstream of separation, again in accordance with findings of Marxen (2005). Note that, for example, at $x/c=0.6$ the wall-pressure coefficient c_p possesses a larger value in case 2.3 or 2.4 than in case 2.5. Instead, on the downstream side, an earlier pressure increase takes place inside the separation bubble in cases 2.3 and 2.4 compared to case 2.5.

However, cases 2.2–2.4 possess essentially the same separation location, while slightly differing in mean reattachment location. This suggests that the reattachment processes are slightly different in these three cases, and that the upstream effect of the mean flow deformation does not always cause a simultaneous movement of both separation and reattachment location. On the other hand, when considering the pressure coefficient c_p (Fig. 3, right) it becomes clear that, for example, the pressure in case 2.2 is slightly higher upstream of separation at $x/c=0.6$ compared to case 2.4. This is in accordance with the fact that a slightly larger separation bubble has developed in case 2.2 with corresponding influence on the pressure distribution (the previously mentioned effect of the mean flow deformation).

In terms of size of separation bubbles, we would order them by increasing size (starting with the smallest) in the following way, based on the pressure distribution c_p and displacement Re_{δ^+} : case 2.4 ($f=6$), 2.3 ($f=3$), 2.2 ($f=1.5$), and 2.5 ($f=9$). The length of the separation bubble (computed from the skin-friction coefficient c_f) does not perfectly fit with this order, but a reason for that will be suggested below.

3. Linear stability theory: results for the different base flows and the effect of mean flow deformation

The development of perturbations introduced into a laminar flow via a ZNMF actuator is characterized by disturbance growth that will eventually lead to transition. For a sufficiently small disturbance level, the initial behavior of these perturbations is linear, i.e., can be treated by a set of linear equations, in contrast to the non-linear Navier-Stokes equations. Here, we will focus on a certain class of disturbances, specifically wave-like perturbations with exponential growth in x (spatial model).

A theoretical approach according to Schlichting (1979) is employed to describe the behavior of small disturbances: so-called Linear Stability Theory (LST) based on the Orr-Sommerfeld equation. Only a short overview of LST shall be given; more elaborate treatments can be found in Schmid & Henningson (2001) and Boiko *et al.* (2002). Decomposition of the flowfield into a known 2-D parallel steady base flow $u_B=u_B(y)$ (parallel-flow assumption) and small disturbance quantities $s'=p', u', v'$, and linearizing with respect to these disturbances leads to a system of linear partial differential equations. Submitting a normal-mode ansatz for the perturbations:

$$s' = \check{s}' \cdot e^{i(\alpha x - \omega t)} + \text{conjugate complex}, \quad \check{s}' = \check{s}'(y) \in \mathbf{C}, \quad (3.1)$$

into the equations to obtain a separation of variables yields the Orr-Sommerfeld equation:

$$(\alpha u_B - \omega) \left(\frac{\partial^2 \check{v}'}{\partial y^2} - \alpha^2 \check{v}' \right) - \alpha \frac{\partial^2 u_B}{\partial y^2} \check{v}' = -\frac{i}{Re} \left(\alpha^4 \check{v}' - 2\alpha_{eff}^2 \frac{\partial^2 \check{v}'}{\partial y^2} + \frac{\partial^4 \check{v}'}{\partial y^4} \right), \quad (3.2)$$

with complex α , $\Re(\alpha)$ being the streamwise wavenumber and $\Im(\alpha)$ the streamwise amplification rate, and with complex ω , $\Re(\omega)$ being the circular frequency and $\Im(\omega)$ the temporal amplification rate.

The ordinary differential equation (3.2) is supplemented by homogeneous boundary conditions at the wall ($y=0$) and in the free-stream $y \gg \delta_{99}$ in which case an eigenvalue problem for the perturbation quantities is obtained, if either α or ω is assigned. We adopt the spatial approach by prescribing $\Re(\omega)$, setting $\Im(\omega)=0$ and obtain a complex disturbance spectrum α .

Due to the parallel-flow assumption, the only information required to determine stability or instability of a laminar flow is the streamwise base-flow velocity u_B at a certain streamwise location. For that reason, LST can be classified as a theory describing *local* instability. Note that for the present definition, we have an unstable flow for a given disturbance frequency $\Re(\omega)=\beta=2\pi f$, if $\Im(\alpha(u_B, \beta)) < 0$, while $\Im(\alpha(u_B, \beta)) > 0$ means that the flow is stable.

Here, a solution to the Orr-Sommerfeld equation is obtained numerically by means of an iterative shooting method (Müller 1995). Only the non-zero discrete eigenvalue corresponding to strongest amplification will be considered. Starting values for the iteration procedure are obtained from a direct solution of the temporal approach ($\Re(\alpha)$ prescribed, $\Im(\alpha)=0$), by making use of a conversion procedure based on a formula by Gaster (1962).

Application of linear stability theory to laminar separation bubbles has shown favorable agreement between theoretical results and DNS (e.g., Marxen *et al.* 2003; Marxen 2005) despite the strong non-parallelity of the base-flow profile. In most cases, only one unstable eigenmode is reported.

Velocity profiles with an inflection point are known to possess particularly large growth rates (Schlichting 1979). Profiles at separation and inside the LSB resemble free shear layers by showing such an inflection point, and thus exhibit very strong growth of small wave-like perturbations. The dominant role of the inflection point with regard to the instability in a LSB suggests this instability be attributed to the Kelvin-Helmholtz (i.e., free-shear-layer) type; this is frequently done in literature (Pauley *et al.* 1990; Watmuff 1999; Spalart & Strelets 2000; Yang & Voke 2001).

Stability diagrams for all considered base flows (cases 2.2–2.5) are computed based on linear stability theory. Results are given in Figs. 4 and 5. It can be seen that the controlled flow (cases 2.2–2.4) is more stable than the essentially uncontrolled flow (case 2.5): the amplified region (contained within the thick black line) is much smaller than in the controlled case. Such a stabilizing effect of small disturbances on the mean flow even upstream of transition was also described in Marxen (2005). Furthermore, the most unstable frequency, which roughly corresponds to $f=6$ in case 2.5, is lowered to $f \approx 4.5$ in cases 2.2–2.4. A shift in most unstable frequency was predicted in Marxen (2005) as an effect of the mean flow deformation.

4. Comparison of LST results with numerical simulation data

To allow for a comparison between numerical and theoretical results, numerical results are Fourier-analyzed in time using available discrete time steps $l=1$ to $l=L_{per}$

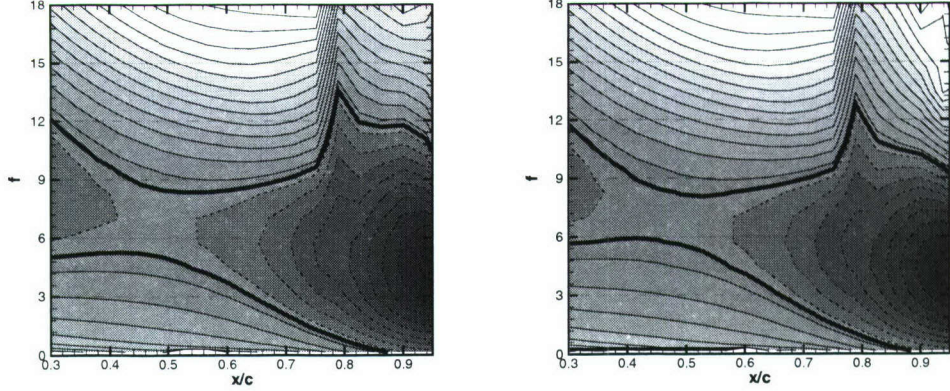


FIGURE 4. Stability diagram for cases 2.2 (left) and 2.3 (right): contours of the imaginary part of the smallest non-zero eigenvalue α_i computed from the Orr-Sommerfeld equation. The thick black line gives the contour $\alpha_i=0$, while dashed lines indicate negative α_i corresponding to an amplified disturbance.

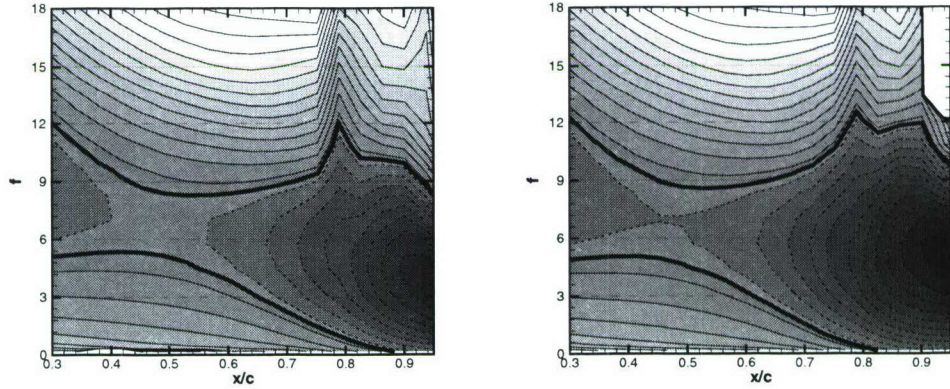


FIGURE 5. Stability diagram for cases 2.4 (left) and 2.5 (right). The legends are the same as in Fig. 4.

($L_{per}=20 \dots 25$) – with the forcing frequency being the respective fundamental frequency β_0^{pp} for such an analysis. The corresponding inverse operation is Fourier synthesis, with $\beta_0^{pp}=1.5$ (case 2.2), $\beta_0^{pp}=3$ (case 2.3), $\beta_0^{pp}=6$ (case 2.4), $\beta_0^{pp}=9$ (case 2.4):

$$u(x, y, l) = \sum_{h=0}^H A_u^{(f=h\beta_0^{pp})}(x, y) \cos(h\beta_0^{pp}\Delta t l + \Phi^{(h)}(x, y)), \quad H \leq L_{per}/2 \quad (4.1)$$

First, we compare disturbance amplification, i.e., the downstream evolution of the disturbance amplitude. For data from numerical simulations, wall-normal maxima of the amplitudes of the streamwise disturbance velocity are computed:

$$A_{u,max}^{(f=h\beta_0^{pp})}(x) = \max \left\{ A_u^{(f=h\beta_0^{pp})}(x = const, y) \right\} \quad (4.2)$$

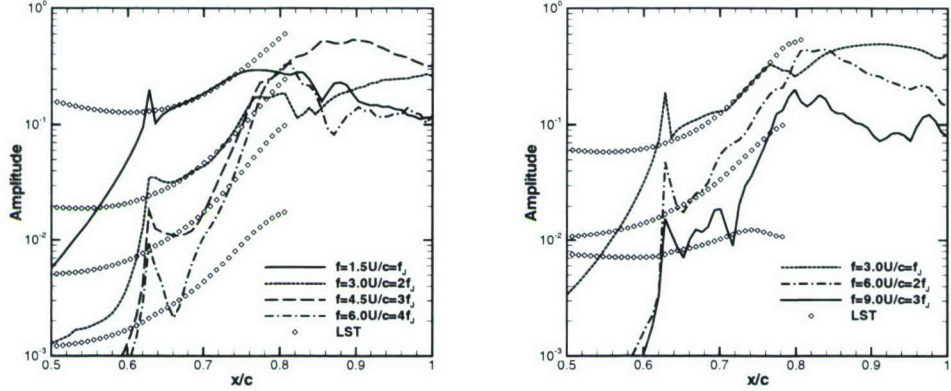


FIGURE 6. Disturbance amplification based on the streamwise disturbance velocity $A_{u,max}(x/c)$ for cases 2.2 (left) and 2.3 (right) in comparison with results from LST: $A_{LST}(x/c)$ (symbols).

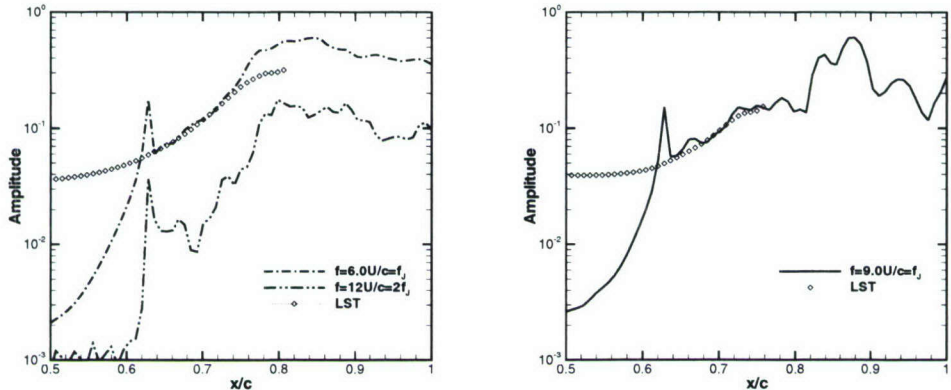


FIGURE 7. Disturbance amplification based on the streamwise disturbance velocity $A_{u,max}(x/c)$ for cases 2.4 (left) and 2.5 (right) in comparison with results from LST: $A_{LST}(x/c)$ (symbols).

These are plotted in Figs. 6 and 7. In contrast, theoretical amplification rates α_i are integrated in a downstream direction according to $A_{LST}(x/c) = A_0 \exp(-\int \alpha_i(x/c) dx)$, all based on the respective underlying mean flow of the respective case. Since LST leaves A_0 undetermined, A_0 is chosen in an arbitrary manner for each single curve independently so that they best fit respective numerical simulation data. In all four cases the strongest peak in amplitude is visible at the position of the ZNMF actuator $x/c=0.625$ for the respective forcing frequency, for example for $f=3$ in case 2.3 (Fig. 6, right).

Furthermore, in all cases, slightly downstream of the actuator location we find a region where the observed amplification agrees well with LST for the *forced* disturbance. However, only in case 2.4 ($f=6$) does this disturbance also dominate the flow downstream (in the sense that it remains the largest disturbance downstream of the position of the first deviation between LST and the numerical simulation).

In case 2.2, the disturbance with $f=4.5$ becomes dominating downstream, and this

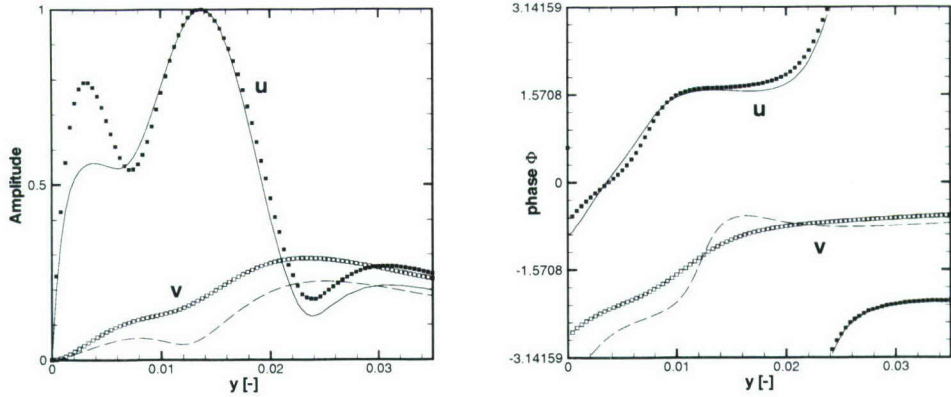


FIGURE 8. Wall-normal amplitude functions (left) and phase functions (right) for the streamwise and wall-normal disturbance velocity (amplitudes normalized by the respective maximum of the streamwise-velocity amplitude) for case 2.2, $f=1.5=f_J$ in comparison with results from LST (symbols) at a position $x/c=0.75$.

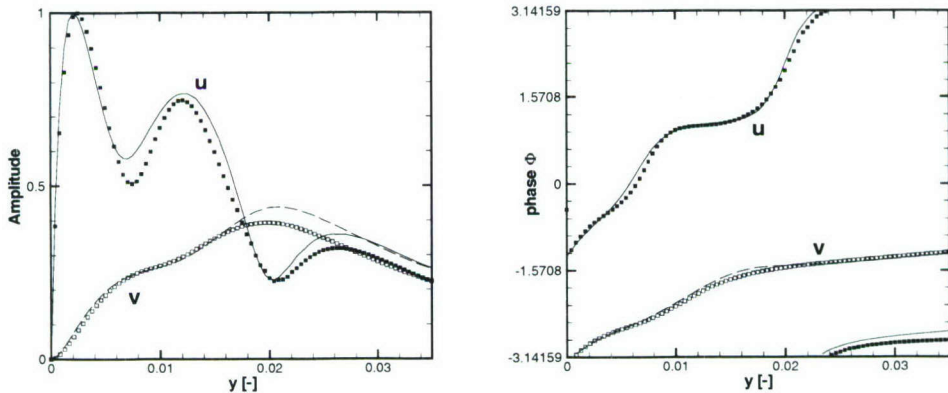


FIGURE 9. Wall-normal amplitude functions (left) and phase functions (right) for the streamwise and wall-normal disturbance velocity (amplitudes normalized by the respective maximum of the streamwise-velocity amplitude) for case 2.3, $f=3=f_J$ in comparison with results from LST (symbols) at a position $x/c=0.75$.

disturbance is amplified stronger than suggested by LST (Fig. 6, left). In principal, the same is observable in case 2.3, where the disturbance with $f=6$ overtakes the one with $f=3$ at $x/c=0.8$ (Fig. 6, right), even though they quickly reverse order again downstream. This latter event is associated with vortex pairing, as can be seen from visualizations.

Streamwise wavenumbers computed from streamwise derivatives of the phases of the Fourier-analyzed simulation data show reasonable agreement with LST results for all four cases as well (not shown). Good agreement of numerical results with LST in all cases for the forced disturbance within a certain region downstream of actuation is confirmed by reviewing wall-normal distributions of amplitude and phase functions (see Figs. 8–11).

It appears that the lower the frequency, the more pronounced is the maximum in

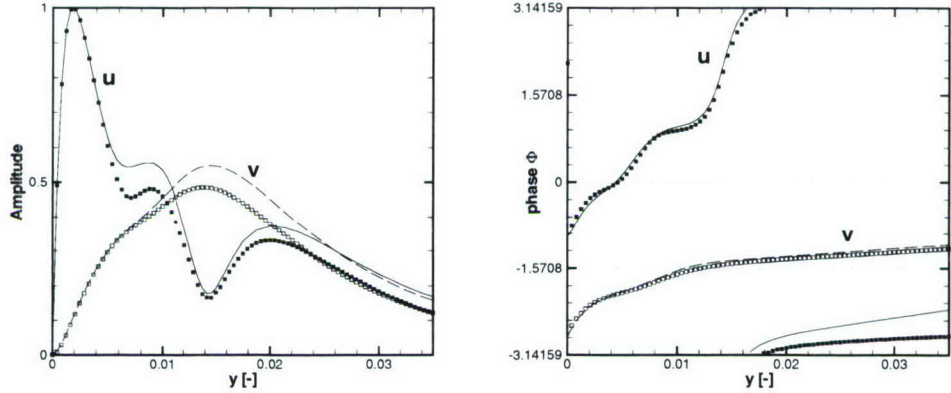


FIGURE 10. Wall-normal amplitude functions (left) and phase functions (right) for the streamwise and wall-normal disturbance velocity (amplitudes normalized by the respective maximum of the streamwise-velocity amplitude) for case 2.4, $f=6=f_J$ in comparison with results from LST (symbols) at a position $x/c=0.70$.

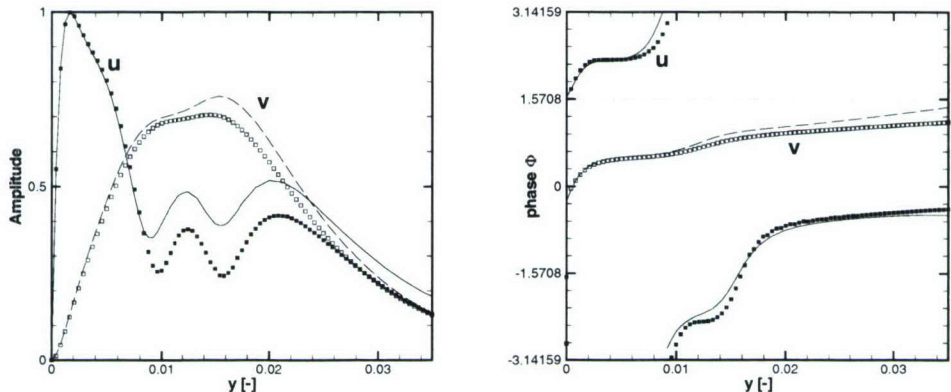


FIGURE 11. Wall-normal amplitude functions (left) and phase functions (right) for the streamwise and wall-normal disturbance velocity (amplitudes normalized by the respective maximum of the streamwise-velocity amplitude) for case 2.5, $f=9=f_J$ in comparison with results from LST (symbols) at a position $x/c=0.70$.

u -amplitude away from the wall. However, keep in mind that the base flows are also different in all cases and that not the same x locations are compared ($x/c=0.75$ in cases 2.2 and 2.3, and $x/c=0.7$ in cases 2.4 and 2.5).

5. Discussion

The origin of higher harmonics (particularly visible in both cases 2.2 and 2.3, Fig. 6) is non-linear generation around the location of forcing via the ZNMF actuator. Their downstream growth is not due to a linear instability (note the poor agreement between LST and numerical results) but might be caused by continuous non-linear generation,

a secondary instability in the presence of a large fundamental disturbance, an absolute instability inside the bubble, or a global instability. Which of these possibilities is true remains unclear, but at least non-linear generation cannot explain why these initially higher harmonics finally overtake the generating one, suggesting that one of the other possibilities, i.e., instabilities, might be involved. Clarification of this issue is beyond the scope of this paper and remains a subject of further exploration in the future.

In case 2.4 we see disturbance growth of the forced perturbation in agreement with LST; this disturbance governs the flow downstream, i.e., it saturates, leading to vortex roll-up associated with gain of amplitude of higher harmonics, without letting them actually overtake, followed by vortex shedding. A similar behavior was observed in several earlier studies of transition in LSBs (e.g., Marxen 2005) and active control of LSBs (e.g., Rist & Augustin 2006). However, final disturbance growth slightly before saturation is larger compared to LST, which was not observed in the cited studies; a specific reason for this strong growth remains unclear.

Case 2.5 was denoted before as essentially uncontrolled, and from spectra given in Kotapati *et al.* (2006) it can be deduced that disturbances with frequencies lower than the forcing frequency play a significant role. These are not computable from the present data of just one forcing period. For that reason, no further conclusions about the transition process can be derived from Fig. 7. Still, we can once more observe good agreement between numerical data and LST shortly downstream of forcing, even in this case.

Disturbance saturation for the respective forcing frequency in cases 2.2 and 2.3 can be observed from the sudden drop in amplification and from deviation from good agreement with LST (Fig. 6). However, disturbances of higher frequencies in these cases grow beyond that level of saturation, unlike in case 2.4. Obviously, in cases 2.2 and 2.3 the saturation of the forced disturbance does not mark the end of the transition process, note that cases 2.2–2.4 show first saturation at roughly the same streamwise location $x/c=0.76$, while only case 2.4 shows an increase in Re_θ directly thereafter (even though it is soon followed by case 2.3). Moreover and more importantly, the saturation in case 2.2 does not equal quick reattachment as it does in case 2.4 (the case with the earliest reattachment). A possible explanation is that in cases 2.2 and 2.3, the forced perturbation is not able to fully transition the flow and thus the resulting (only slightly) increased mixing is not able to reattach the flow immediately. Instead, in these cases the transition process continues until it finishes with the saturation of a higher harmonic disturbance with $f=4.5$ (case 2.2) or $f=6$ (case 2.3).

In case 2.3 this continuation of the transition process is finished within a short distance, and thus both the pressure distribution and the height of the bubble in this case is quite similar to case 2.4. Also, Re_θ increases almost as early (as noted above). However, the skin-friction distribution of both cases is quite different in the rear part. This is believed to be due to the vortex-pairing mentioned earlier, which takes place in case 2.3 only: the resulting fairly large vortex that is shed from the bubble induces a large reverse-flow velocity close to the wall and causes a larger negative skin friction in the mean at the position of its formation.

So far, the influence of the finite dimension of the plate (which ends at $x/c=1$) was not considered; however, it could play a role with respect to the processes that remain unclear (as previously mentioned). At least in case 2.4 it is quite likely that the wake is forced by the vortices shed from the separation bubble and therefore locks on to this shedding frequency $f=6$ as stated in Kotapati *et al.* (2006), i.e., the wake is influenced by the bubble but not vice versa. The same seems true for case 2.3, where vortex pairing

occurs in the bubble and a vortex with frequency $f=3$ is shed, which again is observed as the dominating frequency in the wake. In contrast, it remains unclear what happens in the wake and whether there is interaction in cases 2.2 and 2.5.

6. Conclusions

Four different cases of a laminar separation bubble being forced at different frequencies by means of a ZNMF actuator were considered with respect to disturbance growth occurring in the respective flow. Linear instability of the resulting mean flows were evaluated based on the Orr-Sommerfeld equation, so-called local linear stability theory (LST). This led to a deeper understanding of some occurring instability processes.

Our research indicates that a larger separation bubble corresponds to a larger region of instability and a higher most-amplified frequency. A feedback effect of the mean flow deformation, i.e., a change of the mean flow caused through disturbance input even upstream of transition, could be observed in accordance with reports in Marxen (2005).

When comparing Fourier-analyzed numerical results with theoretical eigensolutions, a region of good agreement both with respect to eigenvalues (amplification rates) and eigenfunctions (wall-normal amplitude and phase functions) was found in all cases. This emphasizes that in *all* cases the ZNMF actuator triggered an instability mode in the flow.

However, the triggered instability mode was not the cause for transition in every case, nor for reattachment. Only in the case where control was most effective (case 2.4), where the forcing frequency is close to the integrally most amplified frequency of the resulting mean flow, does the triggered perturbation lead to transition and reattachment. Such a behavior is in agreement with similar studies of active flow control, e.g., Rist & Augustin (2006). Since this case also corresponds to the smallest separation bubble, it appears best for efficient flow control to select a forcing frequency close to the most amplified disturbance as computed by LST.

On the other hand, the disturbance behavior could not solely be explained in all cases by linear stability theory in the region close to transition. Instead, indications for other instabilities to be active were found and discussed, but future work is required to fully understand ongoing processes.

At least in cases 2.3 and 2.4, the cases with the second-smallest and smallest separation bubbles (based on c_p and Re_θ), the presence of a wake downstream of separation does not seem to play a role. This is due to the fact that the separation bubble dynamics are largely governed by the forced perturbation with respect to the vortex-shedding frequency, and rather this wake is just forced by the perturbations convecting downstream from the bubble. This suggests that both problems (i.e., separation bubble and wake dynamics) are decoupled and can be studied independently of each other in these cases.

Present results indicate that it would be beneficial to place the actuator further upstream, since in all cases the flow is at least neutrally stable as early as $x/c=0.5$ for frequencies ≥ 3 . This is even more true if the most amplified frequency according to LST is selected. A drawback of LST is that it cannot predict the most amplified frequency of the *controlled* flow *a priori*. However at least an estimation can be derived from a stability analysis of the uncontrolled flow, and then a slightly lower frequency should be selected.

7. Future work

A deeper understanding of flow dynamics for the present case of laminar-separation control was gained with the help of linear stability theory. However, several questions were also raised. The following list provides an overview of possible future research on the present setup:

- The choice of the actuator length might be suboptimal (note the large drop in amplitude at the end of the slot in Figs. 6 and 7), and therefore the receptivity of the boundary layer with respect to the actuator should be investigated (varying actuator dimensions, positions, and jet exit momentum),
- The influence of the wake on the separation bubble should be clarified by simulations with a semi-infinite plate,
- Subharmonic vortex-pairing is not observed in case 2.4 (in contrast to case 2.3), a possible reason for this is the absence of a (large) subharmonic disturbance in case 2.4: a simulation with forcing at $f=6$ with some added smaller perturbation at $f=3$ could clarify the influence of subharmonic background noise on vortex pairing,
- To clarify growth of disturbances with growth rates exceeding those from LST, the flow should be investigated with respect to occurrence of (local) absolute instability, global instability, and secondary (local and global) instability.

REFERENCES

BOIKO, A. V., GREK, G. R., DOVGAL, A. V. & KOZLOV, V. V. 2002 *The Origin of Turbulence in Near-Wall Flows*, 1st edn. Springer, Berlin, Heidelberg, New York.

BONS, J. P., SONDERGAARD, R. & RIVIR, R. B. 2001 Turbine separation control using pulsed vortex generator jets. *J. Turbomachinery* **123** (2), 198–206.

FASEL, H. F. & POSTL, D. 2006 Interaction of separation and transition in boundary layers: direct numerical simulations. In *Sixth IUTAM Symposium on Laminar-Turbulent Transition* (ed. R. Govindarajan), *Fluid Mechanics and its applications*, vol. 78, pp. 71–88. Proc. of the 6th IUTAM Symposium on Laminar-Turbulent Transition, Bangalore, India, Dec. 13–17, 2004, Springer, Berlin, New York.

GASTER, M. 1962 A note on the relation between temporally-increasing and spatially-increasing disturbances in hydrodynamic stability. *J. Fluid Mech.* **14**, 222–224.

HAM, F. & IACCARINO, G. 2004 Energy conservation in collocated discretization schemes on unstructured meshes. In *Annual Research Briefs 2004*, pp. 3–14. Center for Turbulence Research, Stanford University.

KOTAPATI, R., MITTAL, R., MARXEN, O., YOU, D., KITSIOS, V., OOI, A. & SORIA, J. 2006 Harnessing resonant interactions for active control of separated flows. In *Proceedings of the 2006 Summer Program*, pp. 445–456. Center for Turbulence Research, Stanford University.

MARXEN, O. 2005 Numerical studies of physical effects related to the controlled transition process in laminar separation bubbles. Dissertation, Universität Stuttgart.

MARXEN, O., LANG, M., RIST, U. & WAGNER, S. 2003 A combined experimental/numerical study of unsteady phenomena in a laminar separation bubble. *Flow, Turbulence and Combustion* **71**, 133–146.

MÜLLER, W. 1995 Numerische Untersuchung räumlicher Umschlagvorgänge in dreidimensionalen Grenzschichtströmungen. Dissertation, Universität Stuttgart.

PAULEY, L. L., MOIN, P. & REYNOLDS, W. C. 1990 The structure of two-dimensional separation. *J. Fluid Mech.* **220**, 397–411.

RIST, U. & AUGUSTIN, K. 2006 Control of Laminar Separation Bubbles Using Instability Waves. *AIAA J.* **44** (10), 2217–2223.

SCHLICHTING, H. 1979 *Boundary-Layer Theory*. McGraw-Hill, New York.

SCHMID, P. J. & HENNINGSON, D. S. 2001 *Stability and Transition in Shear Flows*, 1st edn. Springer, Berlin, New York.

SIMENS, M. P. & JIMENEZ, J. 2006 Alternatives to Kelvin-Helmholtz instabilities to control separation bubbles. In *Power for Land Sea and Air, ASME*. Proceedings of ASME Turbo Expo 2006, Barcelona, Spain, May 8–11, 2006.

SPALART, P. R. & STRELETS, M. K. 2000 Mechanisms of transition and heat transfer in a separation bubble. *J. Fluid Mech.* **403**, 329–349.

WATMUFF, J. H. 1999 Evolution of a wave packet into vortex loops in a laminar separation bubble. *J. Fluid Mech.* **397**, 119–169.

YANG, Z. & VOKE, P. R. 2001 Large-eddy simulation of boundary-layer separation and transition at a change of surface curvature. *J. Fluid Mech.* **439**, 305–333.

Large-eddy simulation of flow separation over an airfoil with synthetic jet control

By D. You AND P. Moin

1. Motivation and objectives

The performance of an airplane wing has a significant impact on issues such as runway distance, approach speed, climb rate, payload capacity, and operation range, but also on the community noise and emission level as an efficient lift system also reduces thrust requirements (see Woodward & Lean 1993; Thibert *et al.* 1995). The performance of an airplane wing is often degraded by flow separation. Flow separation on an airfoil surface is related to the aerodynamic design of the airfoil profile. However, non-aerodynamic constraints such as material property, manufacturability, and stealth capability in military applications often conflict with the aerodynamic constraints, and either passive or active flow control is required to overcome the difficulty. Passive control devices, for example, vortex generators (Jirasek 2004), have proven to be quite effective in delaying flow separation under some conditions. However, they can introduce a drag penalty when the flow does not separate. Over the past several decades various active flow control concepts have been proposed and evaluated to improve the efficiency and stability of lift systems by controlling flow separation. Many of these techniques involve continuous blowing or suction, which can produce effective control but is difficult to apply in real applications.

In recent years, control devices involving zero-net-mass-flux oscillatory jets or synthetic jets have shown good feasibility for industrial applications and effectiveness in controlling flow separation (e.g., Glezer & Amitay 2002; Rumsey *et al.* 2004; Wygnanski 2004). The application of synthetic jets to flow separation control is based on their ability to stabilize the boundary layer by adding/removing momentum to/from the boundary layer with the formation of vortical structures. The vortical structures in turn promote boundary layer mixing and hence momentum exchange between the outer and inner parts of the boundary layer. The control performance of the synthetic jets greatly relies on parameters such as the amplitude, frequency, and location of the actuation. Therefore an extensive parametric study is necessary for optimizing the control parameters.

For numerical simulations, an accurate prediction, not to mention control, of the flow over an airfoil at a practical Reynolds number is a challenging task. The flow over an airfoil is inherently complex and exhibits a variety of physical phenomena including strong pressure gradients, flow separation, and confluence of boundary layers and wakes (e.g., Khorrami *et al.* 1999, 2000; Ying *et al.* 1998; Mathias *et al.* 1999). The complex unsteady flow is difficult to compute by traditional computational fluid dynamics (CFD) techniques based on Reynolds-Averaged Navier-Stokes (RANS) equations (Rumsey & Ying 2002). For prediction of such unsteady flows, large-eddy simulation (LES) offers the best promise in the foreseeable future because it provides detailed spatial and temporal information regarding a wide range of turbulence scales, which is precisely what is needed to gain better insight into the flow physics of this configuration.

Recently, Gilarranz *et al.* (2005) performed an experimental study of flow separation over a NACA 0015 airfoil with synthetic jet control. They reported the flow visualization,

mean pressure coefficients, and wake profiles in both controlled and uncontrolled cases. However, the mechanism for separation control and how the boundary layer is modified by the control have not been clearly identified. In the present study we address the issues using large-eddy simulation. A detailed understanding of the control mechanisms in the typical stall situations (e.g., a docile stall and a full stall) is valuable in reducing the effort for optimizing the control parameters.

In this study we employ an unstructured grid LES solver, CDP, to predict turbulent flow separation over an airfoil and its control by synthetic jets, and to understand the control mechanism for separation control. The unstructured grid capability of the solver allows us to effectively handle the complex flow configuration involving an embedded synthetic jet actuator and wind-tunnel walls. The present LES results are compared to the experimental data (Gilarranz *et al.* 2005) in both controlled and uncontrolled cases. The effects of flow control on the boundary layer properties, flow separation, and lift enhancement are discussed.

2. Computational methodology

2.1. Numerical method

The numerical algorithm and solution methods are described in detail by Mahesh *et al.* (2006) and Ham & Iaccarino (2004); the main features of the methodologies are summarized here. The spatially filtered Navier-Stokes equations for resolved scales in LES are

$$\frac{\partial \bar{u}_i}{\partial t} + \frac{\partial}{\partial x_j} \bar{u}_i \bar{u}_j = - \frac{\partial \bar{p}}{\partial x_i} + \frac{1}{\text{Re}} \frac{\partial}{\partial x_j} \frac{\partial \bar{u}_i}{\partial x_j} - \frac{\partial \tau_{ij}}{\partial x_j}, \quad (2.1)$$

$$\frac{\partial \bar{u}_i}{\partial x_i} = 0, \quad (2.2)$$

where τ_{ij} is the subgrid-scale (SGS) stress tensor modeled by the dynamic Smagorinsky model (Germano *et al.* 1991). All the coordinate variables, velocity components, and pressure are non-dimensionalized by the airfoil chord length C , the inflow freestream velocity U_∞ , and ρU_∞^2 , respectively. The time is normalized by C/U_∞ . The Cartesian velocity components and pressure are stored at the center of the computational elements. A numerical method that emphasizes discrete energy conservation was developed for the above equations on unstructured grids with hybrid, arbitrary elements. Controlling aliasing errors using kinetic energy conservation instead of employing numerical dissipation or filtering has been shown to provide good predictive capability for successful LES (You *et al.* 2006).

The temporal integration method used to solve the governing equations is based on a fully-implicit fractional-step method that avoids the severe time-step restriction that would occur in the synthetic jet orifice region with an explicit scheme. All terms in (2.1) and (2.2) are advanced using a second-order accurate fully-implicit method in time, and are discretized by the second-order central difference in space. A bi-conjugate gradient stabilized method (BCGSTAB) is used to solve the discretized nonlinear equations. The Poisson equation is solved by an algebraic multigrid method.

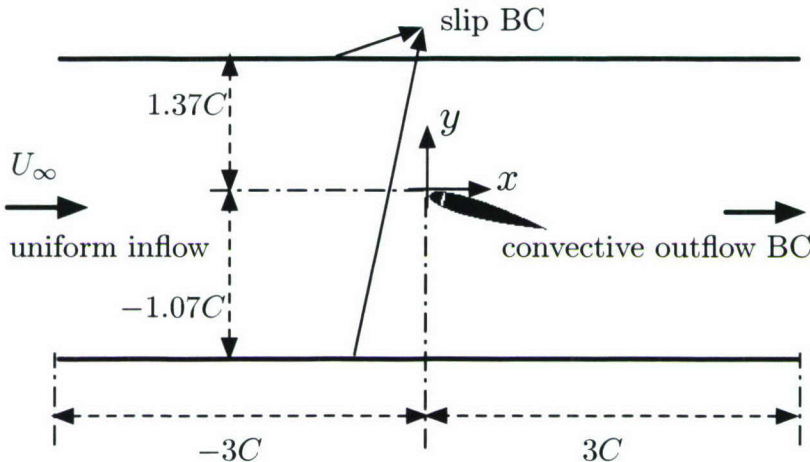


FIGURE 1. Flow configuration for LES of flow over a NACA 0015 airfoil with synthetic jet control.

2.2. Flow configuration

The flow configuration is shown in figure 1. This configuration was experimentally studied by a team at Texas A&M (Gilarranz *et al.* 2005). In the experiment, a NACA 0015 airfoil with a chord length of 375mm was installed in a wind tunnel. The slot of the actuator had a width of 2mm across the entire length of the span and was placed at 12% of the chord measured from the leading edge on the suction side of the airfoil. This location was selected to provide sufficient volume to accommodate the synthetic jet actuator inside the airfoil.

Figure 2 shows the maximum lift coefficient measured in the experiment (Gilarranz *et al.* 2005) as a function of angle of attack (α) in both the uncontrolled and controlled cases. The use of the synthetic jet actuator causes a dramatic increase in the maximum lift coefficient when the baseline (uncontrolled) flow separates. In the experiment, it was found that the angle of attack for which stall occurs is increased from 12° for an uncontrolled airfoil to approximately 18° for the controlled case. For the synthetic jet actuation, the frequency of the actuation in the range of $60 \sim 130\text{Hz}$ (or $fC/U_\infty = 0.65 \sim 1.40$) does not seem to have a significant effect on the maximum lift coefficient. Figure 2 indicates that the uncontrolled airfoil first suffers from a docile stall, which is also referred to as a trailing-edge stall when the angle of attack reaches approximately 12° . The separation point gradually moves upstream as the angle of attack increases. The leading-edge stall at approximately 19° produces an abrupt change in the lift coefficient.

With the synthetic jet actuation, the docile stall is effectively controlled and produces further enhanced lift coefficient up to the attack angle of approximately 18° . For an angle of attack greater than 18° , the controlled airfoil also suffers from a sharp drop of the lift coefficient due to the leading-edge stall, which is characterized by the formation of a separation bubble near the leading edge. Even after the massive stall (leading-edge stall) occurs, the synthetic jet actuation increases the maximum lift coefficient compared to the uncontrolled case, but the amount of the lift augmentation is relatively small.

The present study focuses on cases with the angle of attack of 16.6° , where flow separates from the mid-chord location of the airfoil in the uncontrolled case, and the control

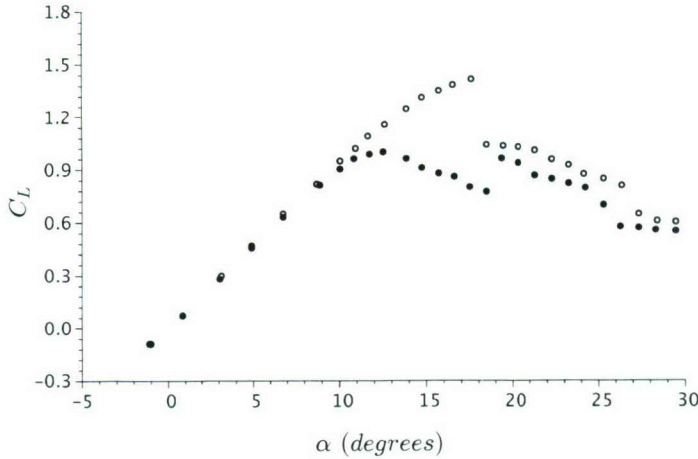


FIGURE 2. Lift coefficient as a function of angle of attack (α) measured by Gilarranz *et al.* (2005). \circ , controlled case ($f = 1.2U_\infty/C$); \bullet , uncontrolled case.

effect is most remarkable. For this angle of attack, experimental data such as the mean surface pressure coefficients and wake profiles are available for comparison (Gilarranz *et al.* 2005).

The computational domain is of size $L_x \times L_y \times L_z = 6C \times 2.44C \times 0.2C$. In the present LES, a smaller domain size than that in the experiment is employed in the spanwise direction to reduce the computational cost. The Reynolds number of this flow is 8.96×10^5 , based on the airfoil chord and inflow freestream velocity.

In this study, it is important to precisely predict the flow through the synthetic jet actuator because the directional variation of the jets during the oscillatory period greatly affects the boundary layer. Therefore, in the present study, the flow inside the actuator and resulting synthetic jets are simulated along with the external flowfield using an unstructured grid capability of the present LES solver. Figure 3a shows the synthetic jet actuator modeled with an unstructured mesh. In the experiment, a piston engine is utilized to generate a sinusoidal mass flux and generates synthetic jets through the spanwise cavity slot. To mimic the oscillatory motion of a piston engine in the experiment, we apply sinusoidal velocity boundary conditions to a cavity side wall as shown in figure 3b. Figure 3b shows the spanwise vorticity contours representing flow inside the cavity and the interaction between synthetic jets and boundary layer flow. The frequency of the sinusoidal oscillation of the cavity side wall is $f = 1.284U_\infty/C$, which corresponds to 120Hz in the experiment of Gilarranz *et al.* (2005); the peak bulk jet velocity at the cavity exit nozzle is $U_{max} = 2.14U_\infty$. The same momentum coefficient as in the experiment is produced as:

$$C_\mu = \frac{h(\rho U_{max}^2)}{C(\rho U_\infty^2)} = 1.23 \times 10^{-2}, \quad (2.3)$$

where h is the width of the cavity nozzle exit.

No-stress boundary conditions are applied along the top and bottom of the wind tunnel, and no-slip boundary conditions are applied on the airfoil surface and cavity wall. Periodic boundary conditions are used along the spanwise (z) direction. At the exit boundary, the convective boundary condition is applied, with the convection speed determined by the streamwise velocity averaged across the exit plane.

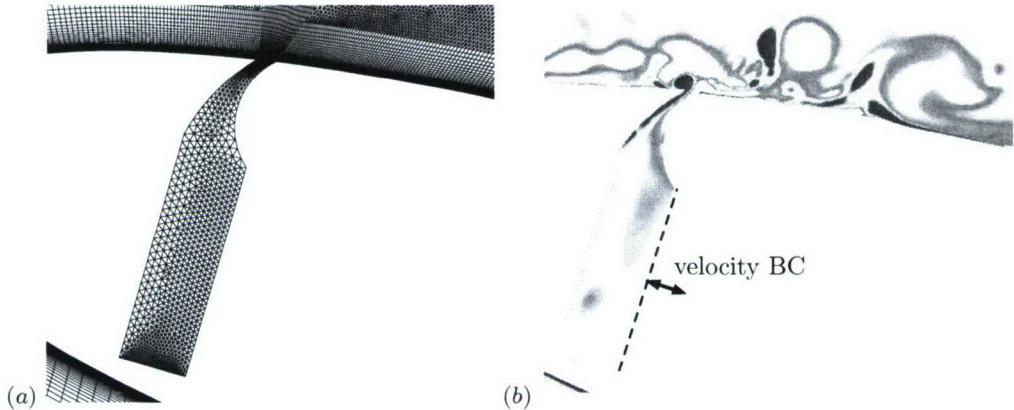


FIGURE 3. (a) Computational mesh and (b) instantaneous spanwise vorticity contours inside and around the synthetic jet actuator. 20 contour levels in the range of $-50 \sim 60$ are shown.

$\Delta x/C$	$\Delta y/C$	$\Delta z/C$	Δx^+	Δy^+	Δz^+
$2 \times 10^{-4} \sim 1 \times 10^{-2}$	$7 \times 10^{-5} \sim 1 \times 10^{-4}$	2×10^{-3}	≤ 60	≤ 1.2	≤ 16.2

TABLE 1. Grid spacing and resolution along the blade surface.

The mesh size used for the present simulation is approximately 8 million. A total of 24 mesh points are allocated along the cavity slot. The grid spacings and resolution in wall units are summarized in table 1. Prior to this simulation, coarser grid simulations were carried out to determine the resolution requirements, and the final mesh was subsequently constructed using this information.

The simulation is advanced in time with a maximum Courant-Friedrichs-Lowy (CFL) number equal to 3.5, which corresponds to $\Delta t U_\infty / C \approx 1.7 \times 10^{-4}$, and each time step requires a wallclock time of approximately 1.5 seconds when 128 CPUs of the ASC Linux Cluster (2.4GHz Intel Pentium 4 Prestonia) are used. The present results are obtained by integrating the governing equations over an interval of approximately $20C/U_\infty$.

3. Results and discussion

Gross features of the flow over uncontrolled and controlled airfoils are revealed in figure 4, showing iso surfaces of the instantaneous vorticity magnitude overlapped with pressure contours predicted by the present LES. The vortical structures present over the suction surface qualitatively indicate the degree of flow separation. In the uncontrolled case (figure 4a), flow massively separates from the half aft portion of the suction surface while the flow separation is dramatically prevented with the synthetic jet actuation in the controlled case (figure 4b). Qualitatively, these features are consistent with the change in

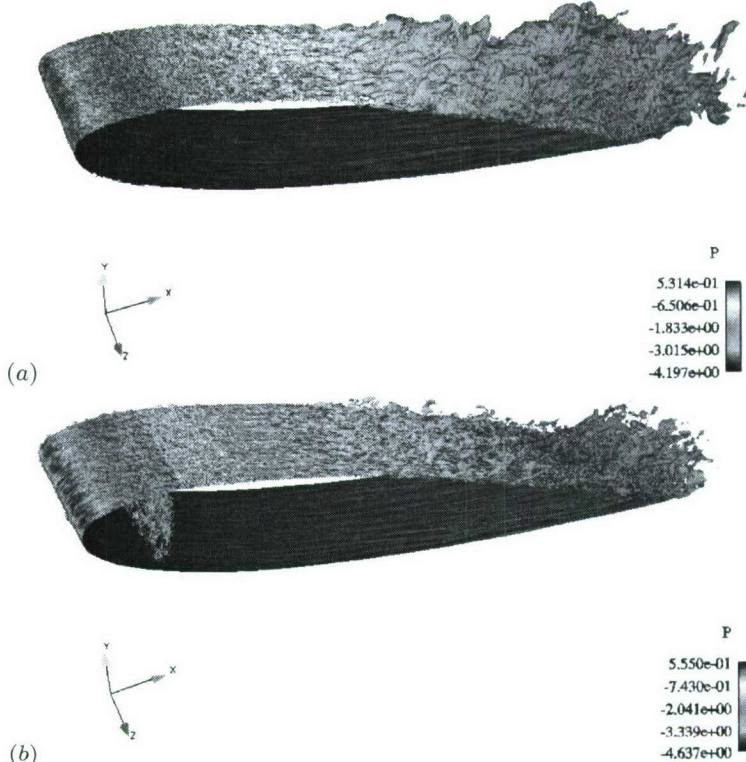


FIGURE 4. Iso surfaces of the instantaneous vorticity magnitude ($|\Omega|C/U_\infty$) of 40 overlapped with the pressure contours. (a) Uncontrolled case; (b) controlled case.

the experimentally measured maximum lift coefficient (Gilarranz *et al.* 2005) with flow control (see figure 2).

The pressure distributions over the airfoil surfaces in both uncontrolled and controlled cases are compared with the experimental data in figure 5. In general, the present LES shows favorable agreement with experimental measurements in both cases. The pressure distribution directly indicates the effect of synthetic jets on flow separation. As seen in figure 5, most of the lift enhancement is achieved in the upstream portion of the airfoil suction surface, while the control effect of synthetic jets on the pressure distribution in the pressure surface is negligible.

The lift and drag coefficients predicted by the present LES in the uncontrolled and controlled cases are in excellent agreement with the experimental data (Gilarranz *et al.* 2005) as shown in table 2. The present synthetic jet actuation with the momentum coefficient of 1.23% produces more than a 70% increase in the lift coefficient. The drag coefficient is found to decrease approximately 15% ~ 18% with the synthetic jet actuation.

The drag reduction due to the synthetic jet actuation is also indicated by the wake profiles. Figure 6 shows the mean streamwise velocity profiles in the uncontrolled (dashed line) and controlled (solid line) cases in a downstream location at $x/C = 1.2$. The width of the wake and the peak magnitude of velocity deficit decrease with synthetic jet control. The present wake profiles are in favorable agreement with experimental data (Gilarranz *et al.* 2005) in both uncontrolled and controlled cases.

Both the suction and blowing phases modify the boundary layer on the suction surface

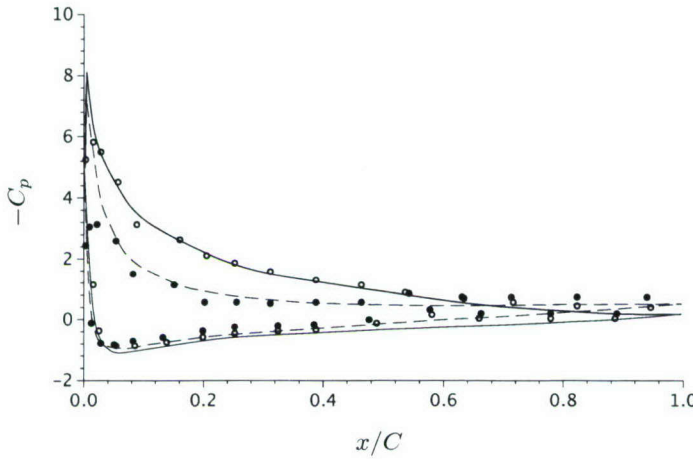


FIGURE 5. Mean pressure distribution over the airfoil surface. Solid line, controlled case; dashed line, uncontrolled case; symbols, experimental data (Gilarranz *et al.* 2005).

Case	Uncontrolled		Controlled	
	C_L	C_D	C_L	C_D
Present LES	0.83	0.28	1.43	0.23
Experiment (Gilarranz <i>et al.</i> 2005)	0.82	0.26	1.41	0.22

TABLE 2. Summary of lift and drag coefficients.

of the airfoil. The synthetic jet actuation not only stabilizes the boundary layer either by adding/removing the momentum to/from the boundary layer, but also enhances mixing between inner and outer parts of the boundary layer. The change of the blade boundary layer during a period of synthetic jet actuation is shown in figure 7 in terms of the phase-averaged streamlines. In the suction phase (figure 7a) the low momentum flow in the upstream boundary layer is removed by the suction and prevents downstream flow separation. On the other hand, synthetic-jet blowing (figure 7c) energizes the downstream boundary layer and prevents downstream flow separation.

4. Conclusions

We have performed a large-eddy simulation of separation control for flow over an airfoil and evaluated the effectiveness of synthetic jets as a control technique. The flow configuration consists of a flow over a NACA 0015 airfoil at Reynolds number of 896,000 based on the airfoil chord length and freestream velocity. A small slot across the entire span connected to a cavity inside the airfoil is employed to produce oscillatory synthetic

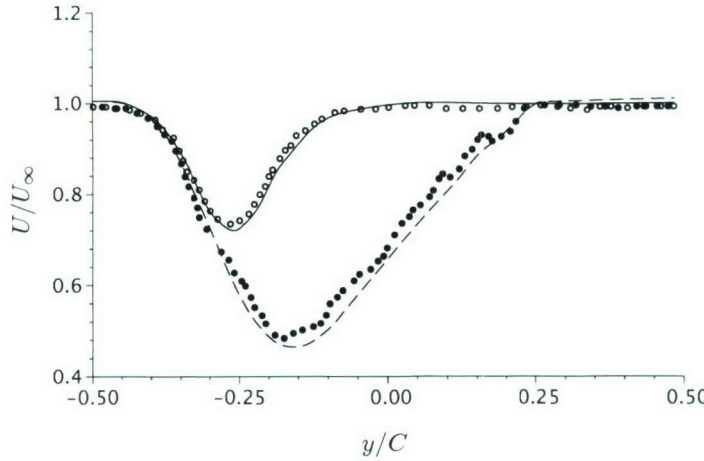


FIGURE 6. Mean streamwise velocity profiles at $x/C = 1.2$. Solid line, controlled case; dashed line, uncontrolled case; symbols, experimental data (Gilaranz *et al.* 2005).

jets. Detailed flow structures inside a synthetic jet actuator and the synthetic jet/cross-flow interaction have been simulated using an unstructured-grid finite-volume large-eddy simulation solver. Simulation results have been compared with the experimental data, and qualitative and quantitative agreements have been obtained for both uncontrolled and controlled cases in terms of mean pressure coefficients and wake profiles. As in the experiment, the present large-eddy simulation confirms that the synthetic jet actuation effectively delays the onset of flow separation and causes a significant increase in the lift coefficient.

Acknowledgments

The authors gratefully acknowledge support from Boeing company and valuable discussions with Dr. Arvin Shmilovich. The authors are also grateful to Dr. Frank Ham for his help with the unstructured LES solver CDP.

REFERENCES

GERMANO, M., PIOMELLI, U., MOIN, P. & CABOT, W. H. 1991 A dynamic subgrid-scale eddy-viscosity model. *Physics of Fluids (A)* **3** (7), 1760–1765.

GILARRANZ, J. L., TRAUB, L. W. & REDINOTIS, O. K. 2005 A new class of synthetic jet actuators - part II: application to flow separation control. *Journal of Fluids Engineering* **127**, 377–387.

GLEZER, A. & AMITAY, M. 2002 Synthetic jets. *Annual Review of Fluid Mechanics* **34**, 503–529.

HAM, F. & IACCARINO, G. 2004 Energy conservation in collocated discretization schemes on unstructured meshes. Annual Research Briefs, 3-14. Center for Turbulence Research, Stanford, California.

JIRASEK, A. 2004 A vortex generator model and its application to flow control. *AIAA Paper 2004-4965*.

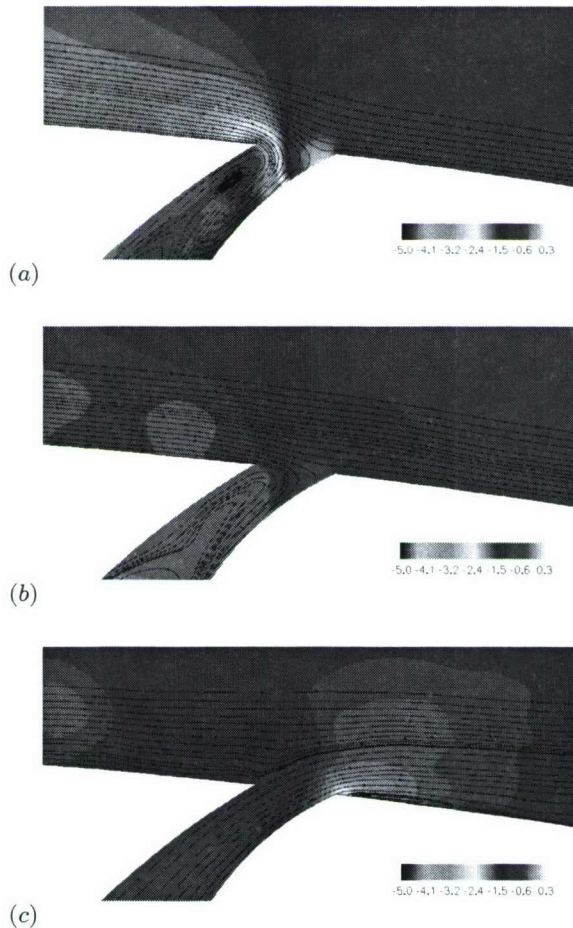


FIGURE 7. Mean streamlines overlapped by the mean pressure contours. (a) $(1/4)T$ (suction phase); (b) $(2/4)T$; (c) $(3/4)T$ (blowing phase).

KHORRAMI, M. R., BERKMAN, M. E. & CHOUDHARI, M. 2000 Unsteady flow computations of a slat with blunt trailing edge. *AIAA Journal* **38** (11), 2050–2058.

KHORRAMI, M. R., SINGER, B. A. & RADEZTSKY, R. H. 1999 Reynolds-averaged navier-stokes computations of a flap-side-edge flowfield. *AIAA Journal* **37** (1), 14–22.

MAHESH, K., CONSTANTINESCU, G., APTE, S., IACCARINO, G., HAM, F. & MOIN, P. 2006 Large-eddy simulation of reacting turbulent flows in complex geometries. *Journal of Applied Mechanics* **73**, 374–381.

MATHIAS, D. L., ROTH, K. R., ROSS, J. C., ROGERS, S. E. & CUMMINGS, R. M. 1999 Navier-Stokes analysis of the flow about a flap edge. *Journal of aircraft* **36** (6), 833–838.

RUMSEY, C. L., GATSKI, T. B., SELLERS III, W. L., VATSA, V. N. & VIKEN, S. A. 2004 Summary of the 2004 CFD validation workshop on synthetic jets and turbulent separation control. *AIAA Paper 2004-2217*.

RUMSEY, C. L. & YING, S. X. 2002 Prediction of high lift: Review of present CFD capability. *Progress in Aerospace Sciences* **38**, 145–180.

THIBERT, J. J., RENEAUX, J., MOENS, F. & PRIEST, J. 1995 ONERA activities on high lift devices for transport aircraft. *Aeronautical Journal* **99**, 395–411.

WOODWARD, D. S. & LEAN, D. E. 1993 Where is high-lift today a review of past UK research programs. *AIAA Paper 2004-2224*.

WYGNANSKI, I. 2004 The variables affecting the control of separation by periodic excitation. *AIAA Paper 2004-2505*.

YING, S. X., SPAID, F. W., McGINLEY, C. B. & RUMSEY, C. L. 1998 Investigation of confluent boundary layers in high-lift flows. *Journal of aircraft* **35** (3), 550–562.

YOU, D., WANG, M. & MOIN, P. 2006 Large-eddy simulations of flow over a wall-mounted hump with separation control. *AIAA Journal* **44** (11), 2571–2577.

Asymptotic analysis of the constant pressure turbulent boundary layer

By T. S. Lundgren†

1. Motivation and objectives

The Navier-Stokes equations are expanded in asymptotic power series in a small parameter ϵ ($= u_\tau/U_e$) which is determined as a function of Reynolds number by an asymptotic matching procedure. The present matched asymptotic expansion analysis differs from the more traditional approach by employing the unsteady Navier-Stokes equations instead of the unclosed Reynolds averaged equations. It is therefore not necessary to expand the Reynolds stress separately in the small parameter. The analysis is therefore simpler and requires fewer assumptions. The main result of this analysis is an instantaneous log-law in the overlap region, of form $u^+ = \kappa^{-1} \ln(y^+) + B$ where the additive “constant” B is independent of y but depends on the outer scaled x, z, t variables.

In this paper the constant pressure flat plate turbulent boundary layer is studied by the method of matched asymptotic expansions. This was first done as a formal procedure by Yajnik (1970) and Mellor (1972). They expanded the two-dimensional Reynolds-averaged Navier-Stokes equation, which has always defined this problem, in asymptotic power series in a small parameter, employing expansions in inner and outer regions which were then matched in an overlap region where both expansions are assumed valid. Since the equations are unclosed, the Reynolds stress terms must be expanded in addition to the velocity components. The present paper follows the same basic procedure, but makes use of the complete unsteady Navier-Stokes equations, and is therefore properly posed. This approach requires fewer assumptions. In particular no assumptions are required for the Reynolds stresses.

The present analysis is restricted to incompressible turbulent flow along a flat plate with constant free stream velocity U_e . A constant length scale l is introduced which is the boundary layer thickness at some position x_0 , $l = \delta(x_0)$. In the outer expansion all the spatial coordinates are scaled with l , not just the wall normal coordinate. This implies a turbulent boundary layer in which large scale vortical structures are convected with the free stream. It is assumed that the length scales of these structures are of the same order as the thickness of the boundary layer. These can be envisioned as long waves on the turbulent shear layer which originate from instabilities near the wall and interact back on the near wall disturbances in a complicated manner.

The inner layer is scaled with wall variables in the traditional way.

2. Outer expansion

The Navier-Stokes equations

$$\partial \mathbf{u} / \partial t + \mathbf{u} \cdot \nabla \mathbf{u} = -\nabla p + \nu \nabla^2 \mathbf{u} \quad (1)$$

$$\nabla \cdot \mathbf{u} = 0 \quad (2)$$

† Department of Aerospace Engineering and Mechanics, University of Minnesota

are scaled to outer variables by the change of variables

$$\mathbf{U} = \mathbf{u}/U_e, \quad P = p/U_e^2, \quad X = x/l, \quad Y = y/l, \quad Z = z/l, \quad T = U_e t/l. \quad (3)$$

This makes

$$\partial \mathbf{U} / \partial T + \mathbf{U} \cdot \nabla \mathbf{U} = -\nabla P + R_e^{-1} \nabla^2 \mathbf{U}, \quad R_e = U_e l / \nu \quad (4)$$

$$\nabla \cdot \mathbf{U} = 0 \quad (5)$$

Now make a change of variables to

$$\mathbf{U} = \hat{\mathbf{i}} + \epsilon \mathbf{U}_1(\xi, Y, Z, T_1), \quad \xi = X - T, \quad T_1 = \epsilon T, \quad P = \epsilon^2 P_1, \quad (6)$$

which puts the problem in a coordinate frame moving with the free stream; T_1 is the natural time scale in this frame. The unit vector $\hat{\mathbf{i}}$ is in the x direction. The velocity \mathbf{U}_1 satisfies the exact Navier-Stokes equation,

$$\partial \mathbf{U}_1 / \partial T_1 + \mathbf{U}_1 \cdot \nabla \mathbf{U}_1 = -\nabla P_1 + (\epsilon R_e)^{-1} \nabla^2 \mathbf{U}_1, \quad (7)$$

so no approximation has been made. At this stage ϵ is an arbitrary constant parameter. Now if we assume that ϵ is a function of R_e which tends to zero as $R_e \rightarrow \infty$ (tentatively identified as u_τ/U_e) and expand in an asymptotic power series, we find a time dependent “defect law”,

$$\mathbf{U} = \hat{\mathbf{i}} + \epsilon \mathbf{U}_1(X - T, Y, Z) + \dots \quad (8)$$

In this approximation $\mathbf{U}_1(X - T, Y, Z)$, without the explicit dependence on T_1 , satisfies the steady nonviscous version of (7). The vorticity is frozen into the external stream. At fixed x the velocity would be seen as a fluctuating function of time as vortical structures are convected past the observer. Viscosity is neglected since Mellor (1972) showed that R_e^{-1} is smaller than any power of ϵ as $\epsilon \rightarrow 0$ (transcendentally small), which will be verified below. This means that viscosity would be negligible to any order in the asymptotic expansion of (7) in powers of ϵ . With the viscous second derivative term neglected this is a singular perturbation problem which calls for a rescaling of the equations in order to describe a viscous boundary layer near the wall which can satisfy the no slip boundary condition.

3. Inner expansion

Rescale the Navier-Stokes equations using a velocity scale v_i and a length scale l_i in such a way as to retain the viscous terms in the infinite Reynolds number limit. Inner variables are defined by

$$\mathbf{u}_i = \mathbf{u}/v_i, \quad p_i = p/v_i^2, \quad y_i = y/l_i, \quad x_i = x/l_i, \quad z_i = z/l_i, \quad t_i = v_i t/l_i \quad (9)$$

When $l_i v_i / \nu = 1$ the rescaled equations become

$$\partial \mathbf{u}_i / \partial t_i + \mathbf{u}_i \cdot \nabla_i \mathbf{u}_i = -\nabla_i p_i + \nabla_i^2 \mathbf{u}_i. \quad (10)$$

with the viscous terms of the same order as inertial terms, without identifying v_i ; any constant velocity would do this. To make a definite physical identification the friction velocity will be used, $v_i \equiv u_\tau$ where $u_\tau = \sqrt{(\langle \tau_w \rangle / \rho)}$, with $\langle \tau_w \rangle$ the average shear stress at the wall. This is of course the scaling velocity which is always used for the wall layer, but it may not be the only possibility.

We reason as follows: $\langle \tau_w \rangle / \rho = \nu \langle du/dy \rangle_0 = \nu (v_i/l_i) \langle du_i/dy_i \rangle_0 = v_i^2 / l_i$

$du_i/dy_i > 0$. A scaling condition can be taken as $\langle du_i/dy_i \rangle_0 \equiv 1$, so $v_i = u_\tau$. Thus we have $v_i = u_\tau$ and $l_i = \nu/u_\tau$.

Solutions of (10) are sought in an asymptotic power series in ϵ . The lowest order term in the expansion, $\mathbf{u}_{i,1}$, satisfies the same equation and could depend parametrically on the outer variables which are slowly varying in inner variables. For instance the convecting vorticity in the outer flow can induce long irrotational waves near the wall which would enter the problem through boundary conditions. Townsend (1961) described this outer influence as an “inactive” component of the inner flow. Presumably the inner layer responds to this by an “active” ejection of vorticity and low speed fluid.

4. Matching

We have a two term outer expansion and a one term inner expansion,

$$\text{two term outer : } \mathbf{U} = \hat{\mathbf{i}} + \epsilon \mathbf{U}_1(X - T, Y, Z) \quad (11)$$

$$\text{one term inner : } \mathbf{U} = \epsilon \mathbf{u}_{i,1}(x_i, y_i, z_i, t_i) \quad (12)$$

where the inner and outer variables are related by $X = x_i/(\epsilon R_e)$, $Y = y_i/(\epsilon R_e)$, $Z = z_i/(\epsilon R_e)$. These will be matched in the y variables holding x, z, t fixed, assuming that they both express the same function in an overlap region. We will use the VanDyke (1964) matching principle, which states that the one term inner expansion of the two term outer expansion has to equal the two term outer expansion of the one term inner expansion. This is a little tricky because the matching process, as conceived here, also has to determine the R_e dependence of $\epsilon(R_e)$.

The two term outer expansion, expressed in the inner y variable is

$$\mathbf{U} = \hat{\mathbf{i}} + \epsilon \mathbf{U}_1(X - T, y_i/(\epsilon R_e), Z) . \quad (13)$$

This is to be expanded in inner variables, retaining one term in an inner expansion. Expressing this back in outer variables

$$\mathbf{U} = \hat{\mathbf{i}} + \epsilon \mathbf{U}_1(X - T, Y, Z) \text{ asymptotically as } Y \rightarrow 0. \quad (14)$$

The one term inner expansion expressed in the outer y variable is

$$\mathbf{U} = \epsilon \mathbf{u}_{i,1}(x_i, \epsilon R_e Y, z_i, t_i) . \quad (15)$$

This is to be expanded in outer variables retaining two terms in an outer expansion. This generates the large y_i asymptote of $\mathbf{u}_{i,1}$ which has to depend the same way for large y_i as the two term outer expansion does for small Y . (This is a little confusing because one can't see two terms explicitly. We will come back to this.) The matching principle means that (14) and (15) have to be equal for all Y when R_e is large. In general this will not be true without restrictions on the functions. For the x -component this requires

$$1 + \epsilon U_1(X - T, Y, Z) = \epsilon u_{i,1}(x_i, \epsilon R_e Y, z_i, t_i) . \quad (16)$$

This matches exactly for all Y if

$$u_{i,1} = \kappa^{-1} \ln(\epsilon R_e Y) + B_i(x_i, z_i, t_i) \quad (17)$$

and

$$U_1 = \kappa^{-1} \ln(Y) + B_o(X - T, Z) \quad (18)$$

since $\ln Y$ will cancel from both sides for any R_e and no other functional form can

accomplish this. Substituting (17) and (18) into (16) with $B = B_i - B_o$ results in the identity

$$1 = \epsilon \left(\kappa^{-1} \ln(\epsilon R_e) + B \right) . \quad (19)$$

This gives the required relationship between ϵ and R_e , with the added requirement that κ^{-1} and B must be constants (independent of coordinates and time), since ϵ and R_e are constants. This is the standard form for the friction law. It may be solved for R_e as a function of ϵ as

$$R_e = (b\epsilon)^{-1} \exp(\kappa/\epsilon) \quad \text{with } b = \exp(\kappa B) . \quad (20)$$

This shows that R_e^{-1} is transcendentally small compared to powers as was shown by Mellor.

Having determined $\epsilon(R_e)$ it is instructive to verify formally that the asymptotic matching procedure is satisfied. For the inner expansion in outer variables use (17) in (15) (for the x component) with $\epsilon R_e = b^{-1} \exp(\kappa/\epsilon)$:

$$U = \epsilon \left(\kappa^{-1} \ln(b^{-1}Y \exp(\kappa/\epsilon)) + B_i \right) . \quad (21)$$

This is supposed to be expanded to two terms in ϵ holding Y fixed. Because $\ln(\exp(\kappa/\epsilon)) \equiv \kappa/\epsilon$ this gives

$$U = 1 + \epsilon \left(\kappa^{-1} \ln(b^{-1}Y) + B_i \right) \equiv 1 + \epsilon \left(\kappa^{-1} \ln(Y) + B_o \right) \quad (22)$$

which is the two term outer expansion, as was to be shown. In the same way the outer expansion in inner variables is

$$U = 1 + \epsilon \left(\kappa^{-1} \ln(by_i \exp(-\kappa/\epsilon)) + B_o \right) \quad (23)$$

This is to be expanded to one term in ϵ holding y_i fixed. Here it gives exactly one term,

$$U = \epsilon \left(\kappa^{-1} \ln(by_i) + B_o \right) \equiv \epsilon \left(\kappa^{-1} \ln(y_i) + B_i \right) , \quad (24)$$

because the “1” is cancelled by the singular term in the logarithm.

For the y -component of velocity the matching condition is

$$0 = \epsilon \left(v_{i,1}(x_i, \epsilon R_e Y, z_i, t_i) - V_1(X - T, Y, Z) \right) . \quad (25)$$

This is only possible for all Y as R_e gets large if both functions are independent of y ,

$$V_1 = v_{i,1} = A_o(X - T, Z) . \quad (26)$$

Similarly, for the z -component

$$W_1 = w_{i,1} = C_o(X - T, Z) . \quad (27)$$

5. Conclusion

Therefore in the overlap region, we have

$$U = 1 + \epsilon \left(\kappa^{-1} \ln(Y) + B_o(X - T, Z) \right) \quad (28)$$

$$V = \epsilon A_o(X - T, Z) \quad (29)$$

$$W = \epsilon C_o(X - T, Z) \quad (30)$$

where the functions A_o, B_o, C_o are unknown. These can also be expressed in inner variables:

$$u^+ = \kappa^{-1} \ln(y^+) + B_o(X - T, Z) + B \quad (31)$$

$$v^+ = A_o(X - T, Z) \quad (32)$$

$$w^+ = C_o(X - T, Z) \quad (33)$$

At fixed X, Z the functions A_o, B_o, C_o are fluctuating random functions of time. Note that the logarithmic part is independent of time. Also note that in (31) $B_o(X - T, Z) + B \equiv B_i$ depends on outer variables because of the matching condition. The dependence on inner variables has dropped out as $y_i \rightarrow \infty$. This asymptotic boundary condition is where a parametric dependence on outer variables can enter solutions of the inner equations.

The averages of these expressions are:

$$\langle U \rangle = 1 + \epsilon \left(\kappa^{-1} \ln(Y) + \langle B_o \rangle \right) \quad (34)$$

$$\langle V \rangle = \epsilon \langle A_o \rangle \quad (35)$$

$$\langle W \rangle = \epsilon \langle C_o \rangle \quad (36)$$

where the angle brackets denote ensemble or time averages.

The fluctuating parts are obtained by subtracting:

$$U' = U - \langle U \rangle = \epsilon(B_o - \langle B_o \rangle) \equiv \epsilon B' \quad (37)$$

$$V' = V - \langle V \rangle = \epsilon(A_o - \langle A_o \rangle) \equiv \epsilon A' \quad (38)$$

$$W' = W - \langle W \rangle = \epsilon(C_o - \langle C_o \rangle) \equiv \epsilon C' \quad (39)$$

There are some empirical results which describe fluctuations of this kind. Lindgren (2003) have shown, using the KTH database for high Reynolds number zero pressure gradient turbulent boundary layers, that the PDF of fluctuations of u normalized by its rms value, i.e. $B'/\langle (B')^2 \rangle^{1/2}$, is self similar and approximately Gaussian in the overlap region and independent of Reynolds number and y . One might reasonably assume that the A' and C' fluctuations are of a similar nature.

It follows from (37), (38), and (39) that Reynolds stresses, which depend on averages of A', B', C' , are all constants in the overlap region:

$$\langle U'V' \rangle = \epsilon^2 \langle A'B' \rangle \quad (40)$$

$$\langle V'V' \rangle = \epsilon^2 \langle A'A' \rangle \quad (41)$$

$$\langle W'W' \rangle = \epsilon^2 \langle C'C' \rangle \quad (42)$$

$$\langle U'U' \rangle = \epsilon^2 \langle B'B' \rangle \quad (43)$$

The method of matched asymptotic expansions has been used here to study the constant pressure fully developed turbulent boundary layer. The new idea in the present analysis is the use of the unsteady Navier-Stokes equation. The conventional treatment of this problem has always made use of the Reynolds-averaged momentum equation, which requires a separate expansion of the Reynolds stresses. This is not required in the present approach. The result of the analysis is an instantaneous logarithmic law in the overlap region described by, (28), (29), and (30), in which the velocity fluctuations, (37), (38), and (39), are independent of the distance from the wall and are functions which

are “frozen” into the flow so that the dependence on t implies a dependence on x . This is Taylor’s frozen hypothesis, which is often assumed for processing experimental data. The analysis presented here, while making use of formal matched asymptotic methods, strongly resembles the Millikan (1939) classical overlap treatment in which empirical defect and wall laws were matched. Here (11) is the defect law and (12) the wall law; solutions of the Navier-Stokes equations have been substituted for the empirical laws and matching was done by a formally different method.

The number of assumptions required for the analysis is quite small. It was assumed that the boundary layer thickness is the proper outer scaling for all the coordinates, implying that the large eddies of the flow scale with the boundary layer thickness. It is also assumed that the velocity tends to uniform flow in the outer scaling as the Reynolds number tends to infinity.

6. Discussion

The existence of an overlap region implies a coupling or interaction between an outer problem and an inner problem. The inner problem is to solve the Navier-Stokes equations in inner variables with asymptotic boundary conditions as y_i tends to infinity. This looks much like a conventional boundary layer problem. The outer problem is to solve the inviscid Euler equations with boundary condition at $Y = 0$. The nature of the coupling between the two problems is described below.

There are three unknown functions of outer variables A_o, B_o, C_o which result from this analysis. However, it appears that only two of them are independent. We reason as follows. Suppose that the inner scaled Navier-Stokes equations (10) are solved with boundary conditions on the horizontal velocity components at infinity, therefore involving the B_o and C_o functions. These are the usual boundary conditions for boundary layers. Using this solution integrate the continuity equation from zero to infinity:

$$v_i(y_i \rightarrow \infty) = - \int_0^\infty \left(\frac{\partial u_i}{\partial x_i} + \frac{\partial w_i}{\partial z_i} \right) dy_i . \quad (44)$$

But $v_i(y_i \rightarrow \infty) = A_o$ and the right hand side of (44) depends only on the functions B_o and C_o . Therefore by this “displacement” argument A_o is a function of B_o and C_o . The implication of this is that the inner layer provides a boundary condition for the outer scaled equations at $Y = 0$ as in second order laminar boundary layer theory. Actually, one more condition is needed since there are two unknown functions. The continuity equation can be used in the overlap region. Since A_o is independent of Y , we have the condition $\partial B_o / \partial X + \partial C_o / \partial Z = 0$.

Fluctuations in the wall stress are related to fluctuations in the additive function B_o . Use $\tau_w / \rho = u_\tau^2 (du_i / dy_i)_0$ or the equivalent $\tau_w / \langle \tau_w \rangle = (du_i / dy_i)_0$. Now near the wall $u_i = y_i (du_i / dy_i)_0$ and from (31) $u_i = \kappa^{-1} \ln(y_i) + B_o + B$. Equating these two expressions at $y_i = 1$ gives the approximate result $\tau_w / \langle \tau_w \rangle = (du_i / dy_i)_0 = B_o + B$. This can be written as

$$\frac{\tau_w - \langle \tau_w \rangle}{\langle \tau_w \rangle} = B_o - \langle B_o \rangle .$$

This suggests that fluctuations in the shear stress at the wall are related to the outer problem boundary condition on V at $Y = 0$.

REFERENCES

LINDGREN, B., JOHANSSON, A. V. & TSUJI, Y. 2003 Universality of probability distributions in the overlap region in high Reynolds number turbulent boundary layers. *Physics of Fluids* **15**, 2587-2591.

MELLOR, G. L. 1972 The large Reynolds number, asymptotic theory of turbulent boundary layers. *International Journal of Engineering Science* **10**, 851-871.

MILLIKAN, C. B. 1939 A critical discussion of turbulent flows in channels and circular-tubes. Proceedings of 5th International Congress of Applied Mathematics, eds. J.P Den Hartog and H. Peters, Wiley, New York, 386-392.

TOWNSEND, A. A. 1961 Equilibrium layers and wall turbulence. *Journal of Fluid Mechanics* **11**, 97-120.

VAN DYKE, M. 1964 *Perturbation methods in fluid mechanics.*, Academic Press, New York.

YAJNIK, K. S. 1970 Asymptotic theory of turbulent shear flows. *Journal of Fluid Mechanics* **42**, 411-427.

Convection in an internally cooled fluid layer heated from below

By T. Hartlep AND F. H. Busse†

1. Motivation and objectives

Convection visible in the form of granulation on the sun represents the turbulent system with the highest Reynolds number that is accessible to direct observation. Also characterized by large Reynolds numbers is mesoscale convection in the Earth's atmosphere as visualized by the cloud patterns seen in satellite images. Both cases, though highly turbulent, exhibit surprisingly regular structures. Evidently, the presence of large-scale regular structures at asymptotically high Reynolds and Rayleigh numbers is compatible with a broad spectrum of highly chaotic motions at intermediate scales. Unfortunately, this aspect of turbulent convection cannot be easily investigated in laboratory experiments. In their attempts to reach high Rayleigh numbers Ra , experimenters have focused on convection layers with small aspect (height to horizontal width) ratios which do not permit the realizations of spontaneous large-scale patterns in highly turbulent convection. In fact, typical high Rayleigh number experiments are carried out with an aspect ratio of the order unity (e.g., Shang *et al.* 2003).

The numerical simulation of turbulent convection suffers from similar restrictions. High aspect ratios can be attained only through a corresponding reduction in the numerical resolution in the vertical direction. Since the thickness of the thermal boundary layers at the top and bottom plates decreases in proportion to $Ra^{-1/3}$ there are obvious limitations in reaching high Rayleigh numbers together with large aspect ratios. In contrast to laboratory experiments, periodic boundary conditions can be assumed in the horizontal directions. This allows the use of somewhat lower aspect ratios than would be needed to capture the large-scale spontaneous turbulent patterns in experiments.

A compromise in attaining the simultaneous goals of large aspect ratios and high Rayleigh numbers has been attempted in the numerical study of Hartlep *et al.* (2005). Using aspect ratios of 10 and 20 in both horizontal dimensions and Rayleigh numbers up to $Ra = 10^7$ convection in the presence of rigid boundaries at the top and bottom, i.e., Rayleigh-Bénard convection, has been simulated for a range of Prandtl numbers Pr between 0.7 and 60. In agreement with earlier experimental observations (Busse 1994), a network of large-scale square cells has usually been found at the highest Rayleigh numbers.

The square pattern is symmetric in both upward and downward plumes, and it could be argued that this reflects the symmetry of the upper and lower boundary conditions. For this reason it is of interest to study cases that are not symmetric in the conditions for the hotter and colder parts of the convection layer, especially since this situation is usually found in natural convection systems. In this paper we therefore consider the case when the upper boundary is thermally insulating and stress-free, while the temperature at the lower rigid boundary is assumed to be fixed. A time-averaged heat transport that is

† Institute of Physics, University of Bayreuth, D-95440 Bayreuth, Germany

steady can be achieved in this case when the layer is cooled homogeneously. More easily realizable in the laboratory is the mathematically equivalent case of a homogeneously heated layer with a fixed temperature at the cold upper boundary and a thermally insulating lower boundary. The stress-free lower boundary cannot be realized easily, of course, but this would be of minor importance.

Convection in an homogeneously cooled layer is of interest in its own right, since this case is often used as a model for convection in the Earth's atmosphere where the cooling is provided by infrared radiation (e.g., Parodi *et al.* 2003).

2. Mathematical formulation of the problem

We consider an infinitely extended horizontal fluid layer of height d between a lower rigid plate that is kept at the temperature T_0 and an upper, stress-free plate that is thermally insulating. The layer is cooled homogeneously with a cooling source density q . A cartesian coordinate system is used with the gravitational acceleration g acting in negative z -direction. Periodic boundary conditions are imposed in x - and y -directions with periodicity lengths l_x and l_y . The aspect ratio Γ is defined as $\Gamma = l_x/d = l_y/d$. Using d , d^2/κ , and $d^2q/\kappa c_p$ as units of length, time, and temperature, respectively, where κ is thermal diffusivity and c_p is the specific heat at constant pressure, one obtains non-dimensional equations for the velocity field $\mathbf{v}(\mathbf{r}, t)$ and the temperature $T(\mathbf{r}, t)$. When the fluid is at rest, the (dimensionless) temperature depends only on z and varies as $T_0 - (z - z^2/2)$. In the general case, it is convenient to specify the temperature through the deviation Θ from the static profile: $T(\mathbf{r}, t) = \Theta(\mathbf{r}, t) + T_0 - (z - z^2/2)$. The equations of motion for $\mathbf{v}(\mathbf{r}, t)$ and $\Theta(\mathbf{r}, t)$ are:

$$\partial_t \mathbf{v} + (\mathbf{v} \cdot \nabla) \mathbf{v} = -\nabla \pi + Pr \nabla^2 \mathbf{v} + Ra Pr \Theta \hat{\mathbf{z}}, \quad (2.1)$$

$$\nabla \cdot \mathbf{v} = 0, \quad (2.2)$$

$$\partial_t \Theta + \mathbf{v} \cdot \nabla \Theta = \nabla^2 \Theta + (1 - z) \mathbf{v} \cdot \hat{\mathbf{z}}, \quad (2.3)$$

where $\hat{\mathbf{z}}$ is the unit vector in z -direction and terms that can be written as gradients have been combined into $\nabla \pi$. Since we have employed the Boussinesq approximation, two dimensionless control parameters have entered the equations, the Rayleigh number Ra and the Prandtl number Pr ,

$$Ra = g\alpha d^5 q / (c_p \kappa \nu), \quad Pr = \nu / \kappa, \quad (2.4)$$

where ν is the kinematic viscosity of the fluid and α is its coefficient of thermal expansion.

The velocity field can be uniquely represented by a poloidal scalar $\phi(\mathbf{r}, t)$, a toroidal scalar $\psi(\mathbf{r}, t)$, and a mean flow $\mathbf{U}(z, t)$:

$$\mathbf{v} = \nabla \times \nabla \times \phi \hat{\mathbf{z}} + \nabla \times \psi \hat{\mathbf{z}} + \mathbf{U}, \quad (2.5)$$

where ϕ and ψ are bounded functions with vanishing average over the xy -plane, and the z -component of \mathbf{U} is zero. The boundary conditions are given by

$$\begin{aligned} \Theta &= \phi = \partial_z \phi = \psi = 0 & \text{at } z = 0, \\ \partial_z \Theta &= \phi = \partial_{zz}^2 \phi = \partial_z \psi = 0 & \text{at } z = 1, \end{aligned} \quad (2.6)$$

and

$$\begin{aligned} \mathbf{U} &= 0 & \text{at } z = 0, \\ \partial_z \mathbf{U} &= 0 & \text{at } z = 1. \end{aligned} \quad (2.7)$$

Equations of motion for ϕ , ψ , and \mathbf{U} are obtained from the z -component of the curl of the curl of Eq. (2.1), the z -component of the curl of Eq. (2.1), and the average over horizontal planes of Eq. (2.1), respectively,

$$\Delta_2 \nabla^2 [\partial_t - Pr \nabla^2] \phi = -\hat{\mathbf{z}} \cdot \left[\nabla \times \nabla \times [(\nabla \times \mathbf{v}) \times \mathbf{v}] \right] - Ra Pr \Delta_2 \Theta, \quad (2.8)$$

$$\Delta_2 [\partial_t - Pr \nabla^2] \psi = \hat{\mathbf{z}} \cdot \left[\nabla \times [(\nabla \times \mathbf{v}) \times \mathbf{v}] \right], \quad (2.9)$$

$$[\partial_t - Pr \partial_{zz}^2] \mathbf{U} = \langle (\nabla \times \mathbf{v}) \times \mathbf{v} \rangle, \quad (2.10)$$

where Δ_2 is the horizontal Laplacian, $\Delta_2 = \partial_{xx}^2 + \partial_{yy}^2$, and $\langle \dots \rangle$ denotes the average over horizontal planes.

A spectral method (Moser *et al.* 1983; Kerr 1996; Hartlep & Tilgner 2003) is used to solve Eqs. (2.3) and (2.8)–(2.10) numerically. Space is discretized with Chebychev polynomials in the z -direction and with Fourier modes in the x - and y -directions. Dealiasing using the two-thirds rule has been implemented. The time-marching procedure is a second-order Adams Bashforth scheme for the advection and buoyancy terms coupled to a Crank-Nicolson scheme for the diffusive terms. An adaptive time step is used to speed up the transients. Computations have been started from random noise as initial conditions or from cases with neighboring parameter values and have been run for several tens of convective time scales $\tau = (2E_{kin})^{-1/2}$, with E_{kin} being the average kinetic energy density. The code is a slightly modified version of the code used for the work of Hartlep *et al.* (2005). By restricting the expansion in terms of Chebychev polynomials for ϕ to those that are symmetric with respect to $z = 0.5$ and the Chebychev polynomials for Θ and ψ to those that are antisymmetric with respect to $z = 0.5$, we can satisfy boundary conditions (2.6) at $z = 0.5$ instead of $z = 1$. A simple rescaling will thus convert the numerical results to those obeying boundary conditions (2.6) at $z = 1$. Spatial resolution was 65 Chebychev polynomials, of which only those with the proper symmetry were actually used, and 128^2 grid points in horizontal planes.

3. Evolution of convection patterns

Convection is known for its rich variety of patterns which appear to persist even into the regime of fully developed turbulence as indicated by the examples of cloud patterns in the atmosphere and of solar granulation. Many of the characteristic patterns are associated with special boundary conditions or deviations from the Boussinesq approximation. Here we shall focus on the role of the up-down symmetry of the convection layer. Due to the asymmetric way in which the heat transport enters and exits the fluid layer, it may be expected that the pattern of turbulent convection will differ strongly from that seen under conditions of symmetry as visualized, for instance, in the work of Hartlep *et al.* (2005). As will be demonstrated in the following, the large-scale cells in which the turbulent convection organizes itself are rather similar in symmetric and asymmetric cases, while the small-scale structures and many quantitative properties differ considerably. Similar to the work of Hartlep *et al.* (2005), a series of Prandtl numbers ranging from $Pr = 0.3$ to $Pr = 30$ were considered. Some computations at $Pr = 0.1$ have also been made.

Figures 1 and 2 provide a good illustration of the convection flow which is dominated by sheets of hot rising flow that tend to entrain the colder surrounding fluid. As a result, the rising fluid cools and loses buoyancy until near the upper boundary only small hot plumes are left. The initial thickness of the rising sheets corresponds to the thickness of

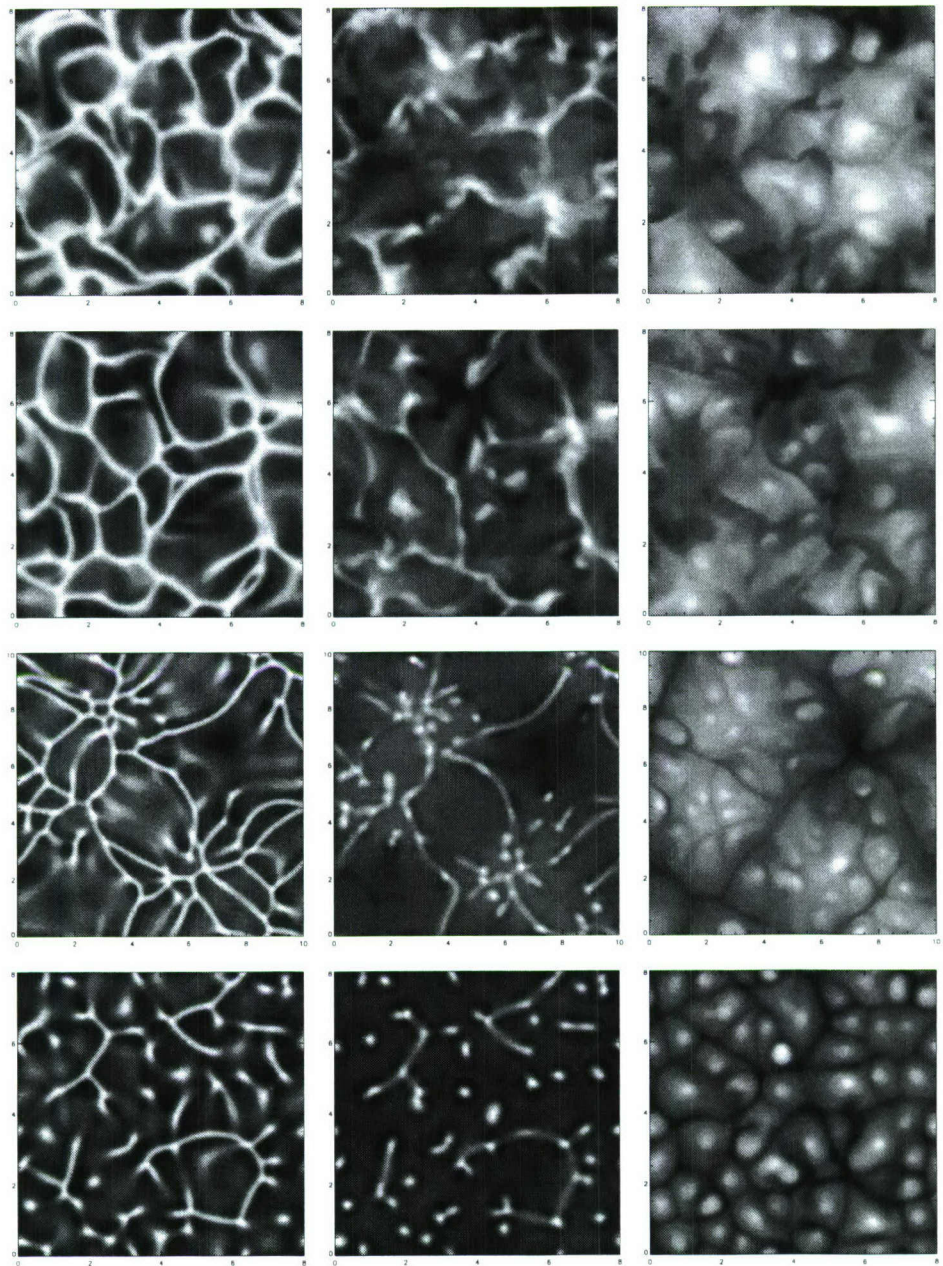


FIGURE 1. Contour plots of the instantaneous temperature distribution in horizontal planes near the bottom boundary ($z \approx 0.12$, left column), at the center ($z = 0.5$, center column), and near the top boundary ($z \approx 0.9$, right column) for simulations at Rayleigh number $Ra = 4 \times 10^5$ and four different Prandtl numbers Pr : 0.3, 0.7, 7, and 30 (from top to bottom row). The aspect ratio Γ in these simulations is 8, except for the case of $Pr = 7$ (third row), where $\Gamma = 10$. Dark and bright areas indicate cold and hot fluid, respectively.

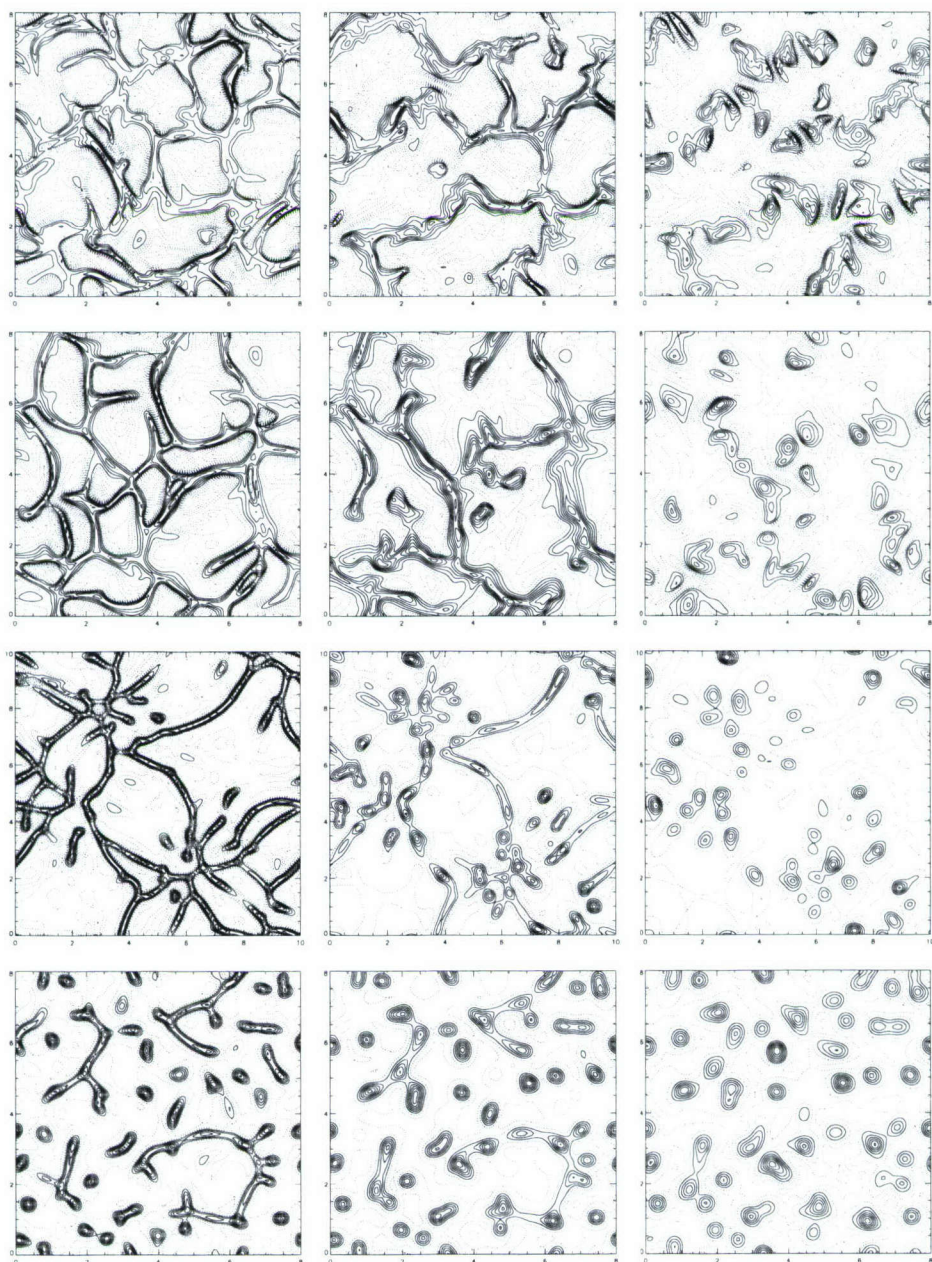


FIGURE 2. Contour lines of the vertical velocity for the same parameters and at the same instant in time as Fig. 1. Solid lines correspond to positive and broken lines to negative values of the vertical velocities.

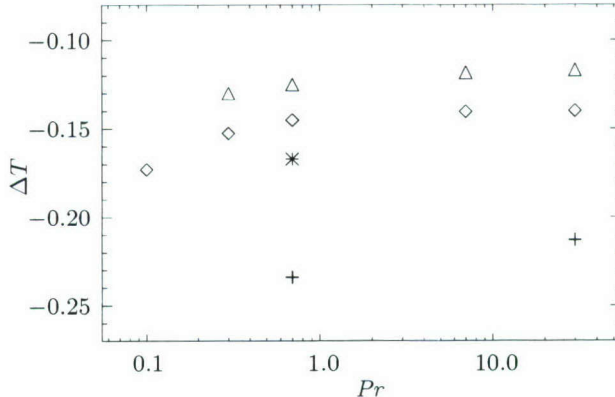


FIGURE 3. Horizontally averaged temperature difference ΔT between upper and lower boundary as a function of Prandtl number Pr . Rayleigh numbers are 2×10^4 (plus signs), 10^5 (star), 2×10^5 (diamonds), and 4×10^5 (triangles).

the thermal boundary layer at the bottom. At the highest Prandtl number, $Pr = 30$, the plume-like structures manifest themselves already close to the lower boundary. It is of interest to note that at the higher Prandtl numbers also cold sheet-like structures become visible in the temperature field near the upper boundary. These represent the cell-like downward flows generated by the rising plumes.

The distribution of the rising sheets is not uniform. They tend to organize themselves into a network of centers similar to the “spoke centers” in Rayleigh-Bénard convection (Busse & Whitehead 1974; Busse 1994; Hartlep *et al.* 2005). This phenomenon is especially apparent in the case $Pr = 7$ of figures 1 and 2, but the cases of lower values of the Prandtl number also show the tendency toward large wavelength structures. It is less evident, though, in the $Pr = 30$ simulation. The observed network structures in the Rayleigh-Bénard case are typically square-like.

4. Heat transport

The effectiveness of the heat transport in Rayleigh-Bénard convection is commonly measured by the Nusselt number Nu which is defined as the ratio between the actual, vertical heat flux through the convection cell and the heat flux that would be observed if there were no flows (i.e., pure conduction). In the present case, though, the constant cooling rate effectively prescribes the heat flux, and the Nusselt number cannot be used as a measure of the transport. The temperature at the upper boundary is not prescribed, though, and will assume different values depending on how effective heat is carried from the bottom to the top by the convection. The resulting temperature difference between the upper and lower boundary for the simulations performed for this study are shown in figure 3 as a function of Pr . Apparently, for a given Rayleigh number heat is transported most effectively at the highest Prandtl numbers considered here.

Averaged densities of the kinetic energy of the convection flow have been plotted as a function of the Prandtl number in figure 4 for given values of the Rayleigh number. The plot indicates that the optimal conversion of potential energy into kinetic energy occurs at a moderate value of the Prandtl number somewhere between 0.7 and 7. This

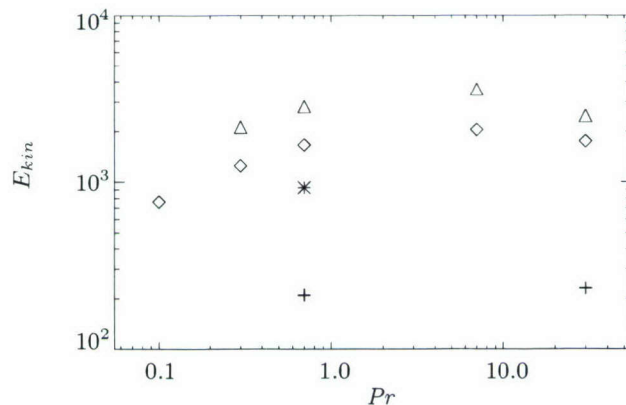


FIGURE 4. Time- and volume-averaged kinetic energy density $E_{kin} = \langle v^2/2 \rangle_{txyz}$ as a function of Prandtl number Pr . As in figure 3, Rayleigh numbers are 2×10^4 (plus signs), 10^5 (star), 2×10^5 (diamonds), and 4×10^5 (triangles).

is different from the behavior in standard Rayleigh-Bénard convection where, at least for values of Pr between 0.3 and 120, the kinetic energy increases monotonically with Prandtl number (Hartlep 2004).

5. Conclusion and future work

The preliminary results presented in the preceding sections indicate that convection with highly asymmetric transport of thermal energy can serve as an example for the study of changes in the structure of turbulent convection that occur when the flow is governed by a single thermal boundary layer instead of two antisymmetric ones. Instead of large scale hexagon-like cellular structures that might have been expected, it is found that the large-scale structure of the turbulent convection does not differ greatly from that seen in the case of Rayleigh-Bénard convection. Significant differences are found, though, in quantitative measures such as the kinetic energy density or the effectiveness of the heat transport. A more detailed study of the properties of this type of convection is still needed, and an extension of the computations to higher Rayleigh numbers is highly desirable.

Acknowledgment

This work was performed while F. H. Busse was visiting NASA Ames through the Senior Visiting Fellow Program of the Center for Turbulence Research.

REFERENCES

BUSSE, F. H. 1994 Spoke pattern convection. *Acta Mechanica* **4**, 11–17.
 BUSSE, F. H. & WHITEHEAD, J. A. 1974 Oscillatory and collective instabilities in large Prandtl number convection. *J. Fluid Mech.* **66**, 67–79.

HARTLEP, T. 2004 *Strukturbildung und Turbulenz. Eine numerische Studie zur turbulenten Rayleigh-Bénard Konvektion*. Doctoral thesis. Institute of Geophysics, University of Göttingen, Germany.

HARTLEP, T. & TILGNER, A. 2003 Rayleigh-Bénard convection at large aspect ratios. In *High Performance Computing in Science and Engineering '03*, pp. 343–357. Springer.

HARTLEP, T., TILGNER, A. & BUSSE, F. H. 2005 Transition to turbulent convection in a fluid layer heated from below at moderate aspect ratio. *J. Fluid Mech.* **554**, 309–322.

KERR, R. M. 1996 Rayleigh number scaling in numerical convection. *J. Fluid Mech.* **310**, 139–179.

MOSER, R. D., MOIN, P. & LEONARD, A. 1983 A spectral numerical method for the navier stokes equations with application to taylor couette flow. *J. Comp. Phys.* **54**, 524–544.

PARODI, A., EMANUEL, K. A. & PROVENZALE, A. 2003 Plume patterns in radiative-convective flows. *New J. Phys.* **5**, 106.1–106.17.

SHANG, X. D., QIU, X. L., TONG, P. & XIA, K. Q. 2003 Measured local heat transport in turbulent Rayleigh-Bénard convection. *Phys. Rev. Lett.* **90**, 074501.

Magnetic waves in a two-component model of galactic dynamo: metastability and stochastic generation

By S. Fedotov[†] AND S. Abarzhi

1. Motivation and objectives

The generation and propagation of magnetic fields in galaxies have been studied for many years (see, e.g., Moss *et al.* 2000). Nonetheless, many fundamental aspects of the galactic dynamo remain to be understood. The propagation of magnetic fronts is one such aspect of dynamo evolution. It is now accepted that the generation of the large scale magnetic field occurs as a result of the simultaneous action of differential rotation of the galactic disk and turbulent motions of the interstellar medium. Standard mathematical procedure consists of looking for exponentially growing solutions of the linear mean field dynamo equation (kinematic dynamo) (see, e.g., Beck *et al.* 1996). The propagation of a magnetic front then can be analyzed in terms of the classical Fisher-Kolmogorov-Petrovskii-Piskunov (FKPP) equation for the azimuthal magnetic field (Murray 1989). This equation is a generic model describing front propagation into an unstable state. If the dynamo excitation occurs within a certain radius $r \leq r_0$, then the magnetic front propagates into the unstable region $r > r_0$, where the linear growth rate γ is positive (*supercritical* case). One can find that the minimal propagation speed is $c = 2(\gamma\beta)^{\frac{1}{2}}$, where β is a magnetic diffusivity. This type of magnetic front is referred to as an "exterior front" (see, e.g., Moss *et al.* 2000). In fact, there are an infinite number of possible wave velocities that are determined by initial conditions. The front-like initial condition for a magnetic field ensures the minimal rate of propagation c .

The essential feature of early models for magnetic waves is that the minimal propagation rate is found from linear analysis. The main purpose of this work is to consider the *subcritical* case when the propagation of a magnetic wave is essentially a non-linear phenomenon. We are going to use recent results concerning non-normal growth and non-linear instability for the galactic dynamo (Fedotov 2003; Fedotov *et al.* 2004). The key insight gained from this theory is that although the trivial state with zero magnetic field is linearly stable, the non-normality due to differential rotation and the dependence of α -effect and turbulent magnetic diffusivity on a magnetic field can lead to the instability with respect to *finite* perturbations. Thus, in the *subcritical* case the generation of a large scale magnetic field can be regarded as a stochastic nucleation in a spatially extended dissipative system. Depending on the relative stability of stationary states, the finite localized perturbations (nuclei) either grow or shrink. When they grow, the propagation of magnetic fronts is observed. It should be noted that although the phenomenon of metastability occurs in many different situations in physics, it has received little attention in the context of magnetic field generation.

In this paper we use the comparatively simple thin-disk asymptotic approach to axisymmetric mean-field dynamo for disk galaxy (see, e.g., Beck *et al.* 1996). We restrict our-

[†] School of Mathematics, The University of Manchester, U.K.

selves to the *non-linear* $\alpha\Omega$ -dynamo when both alpha and magnetic diffusivity quenching are taken into account. The goal is to derive a closed stochastic partial differential equation for the order parameter describing the *subcritical* generation and propagation of magnetic fronts. Our intention is to describe the magnetic field generation as a stochastic process in a spatially extended system with multiple stationary states (a first-order phase transition). The magnetic front can be regarded as a trigger wave connecting an initial metastable state and an absolutely stable state (Murray 1989).

2. Thin-disk dynamo equation

We start with an axisymmetric turbulent dynamo in the galactic disk of thickness $2h$ and radius R that rotates with angular velocity $\Omega(r)$ ($R \gg h$). A mean field model for the evolution of the components of magnetic field $B_r(t, r)$ and $B_\varphi(t, r)$ can be written as

$$\begin{aligned}\frac{\partial B_r}{\partial t} &= -\frac{\alpha(B_\varphi)B_\varphi}{h} - \frac{\pi^2\beta(B_\varphi)B_r}{4h^2} + \nabla(\beta(B_\varphi)\nabla B_r) + F_r(t, r), \\ \frac{\partial B_\varphi}{\partial t} &= g_\Omega B_r - \frac{\pi^2\beta(B_\varphi)B_\varphi}{4h^2} + \nabla(\beta(B_\varphi)\nabla B_\varphi) + F_\varphi(t, r),\end{aligned}\quad (2.1)$$

where $\alpha(B_\varphi)$ is the non-linear function describing the α -effect, $\beta(B_\varphi)$ is the non-linear magnetic diffusivity, $g_\Omega = rd\Omega/dr$ is the measure of differential rotation and ($d\Omega/dr < 0$), ∇ is the gradient operator in the polar system of coordinates: $\nabla B = \partial B/\partial r \mathbf{e}_r$. To account for unresolved turbulent fluctuations, we add two stochastic terms $F_r(t, r)$ and $F_\varphi(t, r)$ on the right-hand side of (2.1). We average the magnetic field over the vertical cross-section of a turbulent disk and consider the spatial structure in the galactic plane only. Since $B_z/B_{r,\varphi} \sim h/R \ll 1$, we are only interested in the radial, B_r , and azimuthal, B_φ , components of the magnetic field \mathbf{B} . Here we introduce two functions $\alpha(B_\varphi)$ and $\beta(B_\varphi)$ describing the quenching mechanism. Theoretical disagreement currently exists regarding how the α -effect and turbulent diffusivity β are suppressed by the magnetic field. In this paper we use the following non-linear functions:

$$\alpha(B_\varphi) = \alpha_0 \left(1 + k_\alpha (B_\varphi/B_{eq})^2\right)^{-1}, \quad \beta(B_\varphi) = \beta_0 \left(1 + \frac{k_\beta}{1 + (B_{eq}/B_\varphi)^2}\right)^{-1}, \quad (2.2)$$

where k_α and k_β are positive constants, B_{eq} is the equipartition strength. It should be noted that while in this paper we choose specific forms of the dependence of α and β on the magnetic field B_φ , the core result is not dependent upon the precise forms of these functions. B_{eq} is defined as a field for which the magnetic energy is equal to the characteristic energy of the turbulent fluctuations: $B_{eq} = \rho v_T^2$. Here ρ is the density and v_T^2 is the characteristic velocity associated with the large-scale turbulent flow. Both functions $\alpha(B_\varphi)$ and $\beta(B_\varphi)$ decay with B_φ , thus describing the negative feedback on the magnetic field generation; α_0 and β_0 are chosen in such a way that $\alpha(0) = \alpha_0$ and $\beta(0) = \beta_0$. Note that the dependence of the magnetic diffusivity $\beta(B_\varphi)$ on the azimuthal component B_φ is crucial for the *subcritical* generation of the magnetic fields.

The mean field dynamo equations (2.1) can be non-dimensionalized by using a characteristic length $2h/\pi$, an angular velocity Ω_0 , and the equipartition strength B_{eq} :

$$\frac{\partial B_r}{\partial t} = -\delta\varphi_\alpha(B_\varphi)B_\varphi - \varepsilon\varphi_\beta(B_\varphi)B_r + \varepsilon\nabla(\varphi_\beta(B_\varphi)\nabla B_r) + f_r(t, r),$$

$$\frac{\partial B_\varphi}{\partial t} = -gB_r - \varepsilon\varphi_\beta(B_\varphi)B_\varphi + \varepsilon\nabla(\varphi_\beta(B_\varphi)\nabla B_\varphi) + f_\varphi(t, r), \quad (2.3)$$

where

$$\delta = \frac{R_\alpha}{R_\omega}, \quad \varepsilon = \frac{\pi^2}{4R_\omega}, \quad g = \frac{|g_\Omega|}{\Omega_0} \quad (2.4)$$

and R_α and R_ω are the dimensionless measures of relative strength of the α -effect and the differential rotation respectively:

$$R_\alpha = \frac{\alpha_0 h}{\beta_0}, \quad R_\omega = \frac{\Omega_0 h^2}{\beta_0}. \quad (2.5)$$

The random forces $f_r(t, r) = F_r(t, r)/\Omega_0$ and $f_\varphi(t, r) = F_\varphi(t, r)/\Omega_0$ are assumed to be Gaussian delta-correlated random fields with zero-mean

$$\langle f_r(t, r) f_r(t', r') \rangle = D_r \delta(t - t') \delta(r - r'), \quad (2.6)$$

$$\langle f_\varphi(t, r) f_\varphi(t', r') \rangle = D_\varphi \delta(t - t') \delta(r - r'). \quad (2.7)$$

The non-linear functions $\varphi_\alpha(B_\varphi)$ and $\varphi_\beta(B_\varphi)$ are

$$\varphi_\alpha(B_\varphi) = \frac{1}{1 + k_\alpha B_\varphi^2}, \quad \varphi_\beta(B_\varphi) = \frac{(1 + B_\varphi^2)}{1 + (k_\beta + 1)B_\varphi^2}. \quad (2.8)$$

In this paper we consider only the case of $\alpha\Omega$ -dynamo for which the differential rotation dominates over the α -effect: $\Omega_0 h \gg \alpha_0$, that is $R_\alpha \ll R_\omega$. The system (2.3) involves two small parameters δ and ε . The typical values are $\delta = 0.01$ and $\varepsilon = 0.1$. For small values δ , ε and $g \sim 1$, the linearized operator in (2.3) is highly non-normal which might lead to a large transient growth of the azimuthal component B_φ . Comprehensive survey and many examples of non-normal systems are given in (Grossmann 2000). One can also expect a high sensitivity of the second moments of a magnetic field to the stochastic perturbations $f_r(t, r)$ and $f_\varphi(t, r)$ (Fedotov 2003; Fedotov *et al.* 2004).

Linearization of a zero-dimensional dynamical system (2.3) about the equilibrium point $(0, 0)$ shows that in the *subcritical* case when both eigenvalues λ_1 and λ_2 are negative:

$$\lambda_1 = -\varepsilon + \sqrt{g\delta}, \quad \lambda_2 = -\varepsilon - \sqrt{g\delta} \quad (2.9)$$

the point $(0, 0)$ is a stable node. The corresponding eigenvectors are

$$\mathbf{h}_1 = (-\mu, 1)^T, \quad \mathbf{h}_2 = (\mu, 1)^T \quad \mu = \sqrt{\frac{\delta}{g}} \ll 1. \quad (2.10)$$

3. Stochastic normal form of dynamo equation

In this paper we consider only the *subcritical* case ($\varepsilon > \sqrt{g\delta}$) (Fedotov 2003; Fedotov *et al.* 2004). It is convenient to represent the system (2.3) in the stochastic normal form. By using the eigenvectors \mathbf{h}_1 and \mathbf{h}_2 as a basis, the change of variables $(B_r, B_\varphi) \rightarrow (u, v)$ can be introduced

$$B_r(t, r) = \mu(v(t, r) - u(t, r)), \quad B_\varphi(t, r) = v(t, r) + u(t, r). \quad (3.1)$$

The partial derivatives of the fields $u(t, r)$ and $v(t, r)$ are

$$\frac{\partial u}{\partial t} = \frac{1}{2\mu} \left(-\frac{\partial B_r}{\partial t} + \mu \frac{\partial B_\varphi}{\partial t} \right),$$

$$\frac{\partial v}{\partial t} = \frac{1}{2\mu} \left(\frac{\partial B_r}{\partial t} + \mu \frac{\partial B_\varphi}{\partial t} \right) \quad (3.2)$$

and the non-linear stochastic system (2.3) can be rewritten as:

$$\begin{aligned} \frac{\partial u}{\partial t} &= \frac{1}{2\mu} [\delta(\varphi_\alpha - 1)v + (\delta - 2\mu\varepsilon\varphi_\beta + \delta\varphi_\alpha)u] + \varepsilon\nabla(\varphi_\beta\nabla u) - \frac{1}{2\mu}f_r + \frac{1}{2}f_\varphi, \\ \frac{\partial v}{\partial t} &= \frac{1}{2\mu} [(-2\mu\varepsilon\varphi_\beta - \delta\varphi_\alpha - \delta)v + \delta(1 - \varphi_\alpha)u] + \varepsilon\nabla(\varphi_\beta\nabla v) + \frac{1}{2\mu}f_r + \frac{1}{2}f_\varphi, \end{aligned} \quad (3.3)$$

where

$$\varphi_\alpha = \varphi_\alpha(v + u), \quad \varphi_\beta = \varphi_\beta(v + u). \quad (3.4)$$

Since the parameter μ is small, the stochastic term $f_\varphi(t, r)$ can be neglected compared to $(2\mu)^{-1}f_r(t, r)$. Since the latter term is proportional to the large parameter μ^{-1} , it explains the sensitivity of the non-normal dynamical systems to random perturbations (Grossmann 2000). In the linear case, the system (3.3) can be rewritten in a decoupled form:

$$\begin{aligned} \frac{\partial u}{\partial t} &= -|\lambda_1|u + \varepsilon\Delta u - \frac{1}{2\mu}f_r(t, r), \\ \frac{\partial v}{\partial t} &= -|\lambda_2|v + \varepsilon\Delta v + \frac{1}{2\mu}f_r(t, r). \end{aligned} \quad (3.5)$$

These two equations can be easily solved to get the statistical moments of the random fields $u(t, r)$ and $v(t, r)$. For the large r for which $\Delta u = \partial^2 u / \partial r^2$, we can find from (3.5) that two-points equal time correlation functions are

$$\langle u(t, r)u(t, r') \rangle = \frac{D_\varphi}{4\mu^2 (|\lambda_1|\varepsilon)^{\frac{1}{2}}} \exp \left[-\left(\frac{|\lambda_1|}{\varepsilon} \right)^{\frac{1}{2}} |r - r'| \right], \quad (3.6)$$

$$\langle v(t, r)v(t, r') \rangle = \frac{D_\varphi}{4\mu^2 (|\lambda_2|\varepsilon)^{\frac{1}{2}}} \exp \left[-\left(\frac{|\lambda_2|}{\varepsilon} \right)^{\frac{1}{2}} |r - r'| \right]. \quad (3.7)$$

In what follows we consider only the case when

$$|\lambda_1| \ll |\lambda_2|. \quad (3.8)$$

One can see from (3.5) that under the condition (3.8), the random field $u(t, r)$ can be regarded as the "slow" field and $v(t, r)$ as the "fast" field. We can see from (3.6) and (3.7) that the ratio of the second moments $\langle v^2 \rangle$ and $\langle u^2 \rangle$ can be written as

$$\frac{\langle v^2 \rangle}{\langle u^2 \rangle} = \left(\frac{|\lambda_1|}{|\lambda_2|} \right)^{\frac{1}{2}} \ll 1. \quad (3.9)$$

This inequality allows us to neglect the random fluctuations of $v(t, r)$ compared to those of $u(t, r)$.

4. Stochastic equation for order parameter

4.1. Adiabatic elimination

Our purpose now is to derive the stochastic equation governing the slow evolution of the field u . Under conditions (3.8) and (3.9), the "fast" field $v(t, r)$ follows the "slow" field

$v(t, r)$. Neglecting partial structure of $v(t, r)$, one can find from (3.3) that

$$v = \frac{\delta(1 - \varphi_\alpha(u))u}{2\mu\varepsilon\varphi_\beta(u) + \delta\varphi_\alpha(u) + g\mu^2}. \quad (4.1)$$

Substitution of (4.1) into (3.3) and putting $v = 0$ in (3.4) gives the stochastic partial differential equation (PDE) for the order parameter $u(t, r)$

$$\frac{\partial u}{\partial t} = b(u) + \varepsilon \nabla (\varphi_\beta(u) \nabla u) - \frac{1}{2\mu} f_r(t, r), \quad (4.2)$$

where

$$b(u) = \frac{2\mu \left(g\delta\varphi_\alpha(u) - \varepsilon^2\varphi_\beta^2(u) \right) u}{2\mu\varepsilon\varphi_\beta(u) + \delta\varphi_\alpha(u) + g\mu^2}. \quad (4.3)$$

The main idea of this paper is that the stochastic reaction-diffusion equation (4.2) provides an universal description of magnetic field generation near the *subcritical* bifurcation point. It admits a large variety of solutions including propagating fronts connecting the different metastable states. The remarkable result here is the appearance of the deterministic potential

$$U(u) = - \int_0^u b(z) dz, \quad (4.4)$$

which is not obtained by considering the original equations (2.3). Recall that the azimuthal component of the magnetic field, B_φ , can be found as $B_\varphi = v + u$. The function u describes how the solution of the system (2.3), (B_r, B_φ) , moves along the eigenvector \mathbf{h}_1 . Eliminating the variable v we neglect the "fast" evolution of (B_r, B_φ) toward \mathbf{h}_1 from arbitrary initial conditions.

4.2. Steady uniform distributions

Next we find the steady uniform distributions for the equation (4.2). By using (2.8), (4.3), and equating $b(u)$ to zero, we find the equation

$$\frac{\varepsilon^2}{g\delta} (1 + u^2)^2 (1 + k_\alpha u^2) - (1 + (k_\beta + 1)u^2)^2 = 0 \quad (4.5)$$

determining non-trivial stationary points for the deterministic equation $du/dt = b(u)$. If we take $k_\alpha = k_\beta = 1$, then (4.5) can be rewritten as the equation

$$(1 + u^2)^3 - g_b(1 + 2u^2)^2 = 0 \quad (4.6)$$

with the bifurcation parameter

$$g_b = \frac{g\delta}{\varepsilon^2}. \quad (4.7)$$

It follows from (4.6) that when the parameter g_b is below approximately 0.844, there exists only one stable equilibrium point $u = 0$. For the range $0.844 < g_b < 1$, the system exhibits multi-stability in the bifurcation diagram (Fedotov 2003; Fedotov *et al.* 2004): there are two unstable states, u_1^\pm , and two non-trivial stable states, u_2^\pm . This is a classical *subcritical* pitchfork bifurcation. For example, if $g_b = 0.95$, then $u_1^\pm = \pm 0.243$ and $u_2^\pm = \pm 1.167$. The value $g_b = 1$ separates *subcritical* ($g_b < 1$) and *supercritical* ($g_b > 1$) zones. Here we are concerned only with the *subcritical* case: $0.844 < g_b < 1$.

Since

$$\frac{|\lambda_1|}{|\lambda_2|} = \frac{\sqrt{g\delta} - \varepsilon}{\sqrt{g\delta} + \varepsilon} = \frac{1 - g_b}{(1 + \sqrt{g_b})^2} \ll 1, \quad (4.8)$$

the main criteria for the adiabatic elimination procedure: $|\lambda_1| \ll |\lambda_2|$ is generic in the *subcritical* case.

4.3. Free energy functional and first-order phase transitions

One can introduce the free energy functional

$$F[u] = \int \left[\frac{\varepsilon \varphi_\beta(u)}{2} (\nabla u)^2 + U(u) \right] dr \quad (4.9)$$

such that the stochastic PDE (4.2) can be rewritten in the form

$$\frac{\partial u}{\partial t} = \frac{\delta F}{\delta u} - \frac{1}{2\mu} f_r(t, r). \quad (4.10)$$

This equation allows us to consider the problem of a galactic magnetic field generation as a first-order phase transition in a distributed non-equilibrium system. The additive noise term, $f_r(t, r)$, represents the stochastic forcing arising from the small-scale fluctuations in magnetic and turbulent velocity fields. Here we address the situation when these fluctuations generate the critical nucleus. The stable uniform distributions $u = 0$ and $u = u_2^\pm$ can be interpreted as phases. *Subcritical* instability of the metastable state $u = 0$ with respect to a finite spatially localized perturbation (nucleus) gives rise to a transient behavior of a magnetic field in the forms of trigger waves. They connect, for example, the local minimum of $F[u]$ at $u = 0$ and the global minimum at $u = u_2^\pm$. The critical nucleus, $u^*(t, \mathbf{r})$ can be found from $\frac{\delta F}{\delta u} = 0$, that is

$$b(u^*) + \varepsilon \nabla (\varphi_\beta(u^*) \nabla u^*) = 0, \quad (4.11)$$

$$\nabla u^*(0) = 0 \text{ and } u^* \rightarrow 0 \text{ as } r \rightarrow \infty. \quad (4.12)$$

As long as the critical nucleus u^* is formed as a result of random perturbations, it gives rise to traveling fronts. One can verify that the functional Fokker-Planck equation corresponding to (4.10) has a stationary solution

$$P[u] = \frac{1}{Z} \exp \left[-\frac{4\mu^2 F[u]}{D_\varphi} \right], \quad (4.13)$$

where Z is a normalization constant. The transition time, T , from the metastable uniform state $u = 0$ to the stable state u_2^+ is given by

$$T \sim \exp \left[\frac{4\mu^2 F[u^*]}{D_\varphi} \right]. \quad (4.14)$$

4.4. Magnetic fronts

In the *subcritical* case, galactic magnetic fronts can be analyzed by using the deterministic PDE

$$\frac{\partial u}{\partial t} = b(u) + \varepsilon \nabla (\varphi_\beta(u) \nabla u), \quad (4.15)$$

where the non-linear function $b(u)$ belongs to a generic class of bistable non-linearities: $b(u) < 0$ for u in $(0, u_1^+)$ and $b(u) > 0$ for u in (u_1^+, u_2^+) . (Note that $b(u)$ is the odd func-

tion). This is a classical reaction-diffusion equation with the field-dependent diffusivity $\varepsilon\varphi_\beta(u)$.

Let us consider the propagation of the effectively plane magnetic front neglecting all curvature effects. The equation (4.15) can be written as

$$\frac{\partial u}{\partial t} = b(u) + \varepsilon \frac{\partial}{\partial r} \left(\varphi_\beta(u) \frac{\partial u}{\partial r} \right). \quad (4.16)$$

One can expect that the long time development leads to the propagation of a traveling front of permanent form $u = u(z)$, where $z = r - ct$. The propagation rate c has to be found from the boundary value problem

$$-c \frac{du}{dz} = b(u) + \varepsilon \frac{d}{dz} \left(\varphi_\beta(u) \frac{du}{dz} \right), \quad (4.17)$$

$$u \rightarrow 0 \text{ as } z \rightarrow \infty, \quad u \rightarrow u_2^+ \text{ as } z \rightarrow -\infty. \quad (4.18)$$

One can also consider the front propagation when $u \rightarrow u_2^-$ as $z \rightarrow -\infty$. It should be noted that when the non-linear function $b(u)$ is bistable and the diffusivity $\varepsilon\varphi_\beta(u)$ depends on the field u , the direction of front propagation is controlled by the sign of the integral

$$\int_0^{u_2^+} \varphi_\beta(u) b(u) du \quad (4.19)$$

rather than $\int_0^{u_2^+} b(u) du$ (constant diffusion). To show this, we use the new variable $s = s(z)$ obtained from the equation

$$\frac{ds}{dz} = \frac{1}{\varphi_\beta(u(z))}. \quad (4.20)$$

We can rewrite the boundary value problem (4.17) in terms of the auxiliary function $\Phi(s(z)) = u(z)$:

$$-c \frac{d\Phi}{ds} = \varphi_\beta(\Phi) b(\Phi) + \varepsilon \frac{d^2\Phi}{ds^2}, \quad (4.21)$$

$$\Phi \rightarrow 0 \text{ as } s \rightarrow \infty, \quad \Phi \rightarrow u_2^+ \text{ as } s \rightarrow -\infty. \quad (4.22)$$

Multiplying both sides of (4.21) by $\frac{d\Phi}{ds}$ and integrating over $[0, u_2^+]$, we find that the propagation rate c is given by

$$c = \frac{\int_0^{u_2^+} \varphi_\beta(u) b(u) du}{\int_{-\infty}^{\infty} \left(\frac{d\Phi}{ds} \right)^2 ds}. \quad (4.23)$$

So the speed c is positive as long as the integral (4.19) is positive.

To get the formula for c we approximate the non-linear function $\varphi_\beta(u)b(u)$ by a cubic polynomial for $u \geq 0$

$$\varphi_\beta(u)b(u) = \frac{|\lambda_1|u}{u_1^+ u_2^+} (u_1^+ - u) (u - u_2^+), \quad (4.24)$$

such that $\varphi_\beta(0)b(0) = -|\lambda_1|u$. It follows from (4.21), (4.22) that the propagating rate c is given by

$$c = \sqrt{\frac{\varepsilon|\lambda_1|}{2u_1^+ u_2^+}} (u_2^+ - 2u_1^+). \quad (4.25)$$

This is a unique speed that does not depend on the initial conditions. Recall that for the supercritical case when $\lambda_1 > 0$, we have the minimal speed $c_{min} = 2\sqrt{\varepsilon\lambda_1}$.

5. Conclusions and future work

We have studied the stochastic $\alpha\Omega$ -dynamo model near the bifurcation point in the *subcritical* case. By using a two-component $\alpha\Omega$ -dynamo model, we have derived the equation for an order parameter in the form of a stochastic reaction-diffusion equation. This stochastic partial differential equation describes a *subcritical* generation of galactic magnetic field as a first-order phase transition in a spatially extended system. We have identified the free energy functional for galactic dynamo problem, which allows us to find the estimate for the mean transition time from the metastable uniform state with zero magnetic field. We have shown that the stochastic generation of magnetic field leads to a spontaneous front propagation.

So far we have considered the magnetic field propagation in the form of $1 - D$ traveling wave that propagates with a constant velocity. It is well known that the speed of a traveling wave in $2 - D$ depends on the radius of the expanding circle: $c(R) = c - D/R$, where D is a constant diffusivity, c is the propagation rate of a plane wave. So the excited domain with the radius less than the critical $R_{cr} = c/D$ does not propagate outward. The value of the critical radius corresponding to the equation with field-dependent diffusivity can be found from the critical "nucleus" problem (4.3) and (4.12). Note that in the subcritical case, the excited domain with the radius greater than R_{cr} can be formed as a result of random fluctuations. Clearly our results concerning the *subcritical* generation of magnetic field and front propagation are relevant for not only galactic dynamo but also for solar dynamo as where spatial and temporal structures emerge. However, the solar dynamo equations cannot be reduced to a single equation like (4.2) and therefore the computer simulations are required to analyze the *subcritical* dynamics.

6. Acknowledgments

We thank the Center for Turbulence Research for its support. S.F. was partially supported by the EPSRC Grant EP/D03115X/1.

REFERENCES

BECK, R., BRANDENBURG, A., MOSS, D., SHUKUROV, A. & SOKOLOFF, D. 1996 Galactic magnetism: recent perspectives and developments, *Ann. Rev. Astron. Astrophys.* **34**, 155–206.

FEDOTOV, S. 2003 Non-normal and stochastic amplification of magnetic energy in the turbulent dynamo: subcritical case, *Phys. Rev. E* **68**, 067301.

FEDOTOV, S., BASHKIRTSEVA, I. & RYASHKO, L. 2004 Stochastic analysis of subcritical amplification of magnetic energy in a turbulent dynamo, *Physica A* **342**, 491–506.

GROSSMANN, S. 2000 The onset of shear flow turbulence, *Reviews of Modern Physics* **72**, 603–618.

MOSS, D., PETROV, A. & SOKOLOFF, D. 2000 The motion of magnetic fronts in spiral galaxies, *Geophys. Astrophys. Fluid Dynamics* **92**, 129–149.

MURRAY, J.D. 1989 *Mathematical biology*. Springer-Verlag.

ROSTER

NAME/TERM	AREA OF RESEARCH
POSTDOCTORAL FELLOWS	
BENOIT, Dr. Fiorina 1/05-12/06	(Ph.D. Turbulent Combustion, 2004, Ecole Centrale Paris, France) LES of supersonic turbulent combustion
BODONY, Dr. Daniel 12/04-9/06	(Ph.D. Aeronautics and Astronautics, 2004, Stanford, USA) Acoustics of turbulent flows
BORONSKI, Dr. Piotr 11/05-11/06	(Ph.D. Computational Fluid Dynamics, 2005, Ecole Polytechnique, France) Magneto hydrodynamics turbulence
GHOSH, Dr. Debraj 10/06-present	(Ph.D. Civil Engineering, 2005, The Johns Hopkins University) Uncertainty quantification
HAHN, Dr. Seonghyeon 10/04-present	(Ph.D. Mechanical Engineering, 2002, Seoul National University, Korea) RANS simulation for rotorcraft applications
HARTLEP, Dr. Thomas 8/04-present	Ph.D. Physics, 2004, University of Gottingen, Germany) Solar convection
KIM, Dr. Seung, Hyun 6/04-present	(Ph.D. Mechanical Engineering, 2003, POSTECH, Korea) LES of partially pre-mixed combustion
LAMORGESE, Dr. Andrea 9/06-present	(Ph.D. Mechanical Engineering, 2006, Cornell University) Diffuse interface modeling of multiphase flows
LARSSON, Dr. Nils Johan 9/06-present	(Ph.D. Mechanical Engineering, 2006, University of Waterloo, Canada) Shock turbulence interaction

MARXEN, Dr. Olaf 7/06-present	(Ph.D. Aerospace Engineering, 1999, Universit?t Stuttgart, Germany)	Stability and separation analysis
MATTSSON, Dr. Ken 9/04-present	(Ph.D. Scientific Computing, 2003, Uppsala Universitet, Sweden)	Numerical analysis
MAGIN, Dr. Thierry 10/06-present	(Ph.D. Applied Sciences, 2004, Universite Libre de Bruxelles, Belgium)	Hypersonic flows
MOUREAU, Dr. Vincent 1/05-9/06	(Ph.D. Mechanical Engineering, 2004, Ecole Centrale Paris, France)	LES of premixed combustion in gas turbine engines
SVARD, Dr. Magnus 09/05-12/06	(Ph.D. Scientific Computing, 2004, Uppsala Universitet, Sweden)	Numerical analysis

SR. RESEARCH ASSOCIATES

WANG, Dr. Meng 9/92-12/05	(Ph.D. Mechanical Engineering, 1989, University of Colorado)	Aeroacoustics, LES
------------------------------	--	--------------------

RESEARCH ASSOCIATES

APTE, Dr. Sourabh 9/02-10/05	(Ph.D. Mechanical Engineering, 2000, Pennsylvania State University)	LES of multiphase flows
HAM, Dr. Frank 6/02-present	(Ph.D. Mechanical Engineering, 2001, University of Waterloo, Canada)	LES on unstructured grids and simulation of multiphase flows
HERRMANN, Dr. Marcus 3/02-present	(Ph.D. Mechanical Engineering, 2001, University of Technology, Aachen, Germany)	Turbulent combustion and simulation of multiphase flows
KALITZIN, Dr. Georgi 1/97-present	(Ph.D. Mechanical Engineering, 1992, University of Magdeburg, Germany)	Turbulence modeling and numerical methods

MEDIC, Dr. Gorazd 9/05-present	(Ph.D. Applied Math, 1999, Universite Pierre et Marie Curie, Paris 6, France)	Turbulence modeling and RANS/LES integration
SCHLUTER, Dr. Jorg 10/00-11/05	(Ph.D. Mechanical Engineering, 2000, CERFACS, France)	RANS/LES integration
WU, Dr. Xiaohua 7/03-9/06	(Ph.D. Mechanical Engineering, 1993, University of Manitoba, Canada)	Helicopter aerodynamics and RANS/LES Integration
YOU, Dr. Donghyun 6/04-present	(Ph.D. Mechanical Engineering, 2004, Stanford University, USA)	Numerical simulation of multi-scale and multi-phase flows

SR. VISITING FELLOWS

ABARZHI, Dr. Snezhana 9/02-12/06	Landau Institute for Theoretical Physics, Moscow	Hydrodynamic instabilities and turbulent mixing
BOYD, Prof. Iain 9/06-present	University of Michigan	Direct simulation Monte Carlo
ETEMADI, Prof. Nasrollah 8/06-present	University of Illinois, Chicago	Uncertainty quantification
KOBAYASHI, Dr. Hiromichi 3/05-present	Keio University, Japan	Subgrid scale modeling
NORDSTROM, Dr. Jan 12/05-6/06	Uppsala University, Sweden	Numerical analysis

SR. RESEARCH FELLOWS

JIMENEZ, Prof. Javier 1987-present	University of Madrid, Spain	Wall turbulence
---------------------------------------	-----------------------------	-----------------

2006 STEERING COMMITTEE

Prof. Gianluca Iaccarino
Mechanical Engineering, Stanford University

Prof. Parviz Moin
Director, Center for Turbulence Research
Professor, Mechanical Engineering, Stanford

Prof. Javier Jiménez
Sr. Research Fellow, Center for Turbulence Research, Professor, University of Madrid

Prof. Heinz Pitsch
Mechanical Engineering, Stanford University

Prof. Sanjiva K. Lele
Mechanical Engineering, Aeronautics and Astronautics, Stanford University

Dr. Alan Wray
Staff Scientist, NASA Ames Research Center

Dr. Nagi N. Mansour
Deputy Director, Center for Turbulence Research NASA Ames Research Center